# EVOLUTION OF THE LITHOSPHERE BENEATH TASMANIA AND WESTERN NORWAY


**by**

**Eloise Ellen Beyer**

BSc. (Hons), La Trobe University (1996)


A thesis submitted for the degree of
Doctor of Philosophy,
Department of Earth and Planetary Sciences,
Macquarie University

April, 2002

# TABLE OF CONTENTS

## ABSTRACT

Two suites of mantle-derived peridotites have been studied to evaluate the linkages between mantle geochemistry and crustal age in Proterozoic and Phanerozoic terrains.

Spinel-bearing peridotite xenoliths entrained in Tertiary alkali basalts have been erupted through Proterozoic and Phanerozoic crust in northern Tasmania. The xenoliths can be divided into three major compositional groups. The first, and most widespread, group consists of spinel lherzolites that are moderately fertile in terms of whole-rock $Al_2O_3$ and CaO contents and olivine Mg# and lie in, or adjacent to, the "oceanic peridotite trend" of Boyd (1989). The second group is less common and consists of harzburgites, which have depleted compositions and plot in the Proterozoic field on the olivine Mg# vs modal olivine diagram. The third group comprises highly fertile lherzolites and is restricted to the northwestern localities.

Modelling of compatible trace element abundances in clinopyroxene indicates that the fertile Tasmanian peridotites have experienced less than 5% (batch or fractional) partial melting in the spinel stability field while the highly fertile peridotites have experienced less than 2% melting. The depleted xenoliths require higher degrees of partial melting (8-15% fractional melting). Most Tasmanian xenoliths show evidence for cryptic metasomatism. Clinopyroxene trace element patterns show enrichment in the LREE, Sr, U and Th which can be modelled by simple mixing between moderately depleted (~5% melting) peridotite and 3-15% basalt.

The depth to the crust-mantle boundary across northern Tasmania has been determined by extrapolating xenolith temperatures to the SE Australian geotherm. The CMB is well-defined at 31-32 km beneath much of northern Tasmania and coincides with Moho depths derived from wide-angle seismic surveys. The CMB is poorly constrained beneath northwestern Tasmania but may be as shallow as 26 km. Estimates of crustal thickness are complicated in the northwest by high heat flow which would raise the local geotherm and thus raise the estimated depth to the crust-mantle boundary.

Rare depleted xenoliths found at some localities in Tasmania may represent relics of ancient lithosphere preserved in the shallow lithosphere. This is supported by an Archean Re-Os sulfide age for a depleted xenolith from northeastern Tasmania. A Re-Os isochron age of 1.45±0.7 Ga for sulfides from a fertile xenolith from the same locality suggests that the region might be underlain in part by refertilised Proterozoic lithospheric mantle. The extensive occurrence of hot, fertile lithosphere beneath northern Tasmania

suggests that there has been large-scale removal or refertilisation of the original depleted lithosphere. This is attributed to asthenosphere upwelling and lithosphere thinning during rifting between Australia and Antarctica.

Mantle peridotites preserved in orogenic massifs in the Western Gneiss Region (WGR), Norway are thought to represent slices of lithospheric mantle tectonically emplaced into continental crust during subduction. The WGR peridotites have whole-rock compositions that are depleted relative to estimates for primitive mantle. The relatively fertile Almklovdalen garnet peridotites have the least depleted bulk compositions and have been modelled as residues after ~20-35% partial melting at low pressure (2 GPa). The more depleted garnet peridotites from Gurskøy and Otrøy have been modelled as residues after 20-40% melt extraction at high pressure. The extremely depleted dunites from Almklovdalen appear to be residues after high degrees (60%?) of partial melting at high-pressure (7 GPa). The discrepancy in the pressure estimates for the garnet peridotites and dunites at Almklovdalen suggests that these rock types are not related by a simple melt-depletion process.

Rare earth patterns for the WGR garnets have high HREE and depleted LREE similar to garnets from high-T sheared peridotite xenoliths in kimberlites. This suggests that the WGR rocks represent refertilisation of a depleted precursor. The close structural relationship between the fertile garnet peridotites and the highly depleted dunites at Almklovdalen suggests that the garnet peridotite bodies represent zones of refertilised dunite. Whole-rock compositions for the Almklovdalen garnet peridotites indicates that the refertilising agent was rich in Fe, Ca, Al and Na but not Ti, similar to pyroxenites within the garnet peridotites.

Re-Os $T_{RD}$ model ages for Almklovdalen sulfides define a series of peaks, some of which can be matched with known crustal events. However, peaks in the Archean do not correspond with any known event in the WGR crust and suggest that the peridotites experienced an Archean partial melting event. The preservation of Archean ages in the WGR garnet peridotites supports compositional evidence that some Proterozoic mantle sections elsewhere represent strongly modified Archean lithospheric mantle.

In conclusion, this study has shown that crustal age is not a definitive indicator of the composition and age of the underlying mantle due to processes such as lithosphere removal and modification which can spatially or temporally decouple crust and mantle. These processes also may leave residual ancient mantle beneath relatively young crust.

## DECLARATION

This thesis is based on work carried out in the Department of Earth and Planetary Sciences of Macquarie University, Australia over the period from April 1997 to April 2002. I hereby declare that all data and interpretations presented in this thesis are my own work except for information cited from published or unpublished work of others that has been fully acknowledged. No part of this thesis has ever been submitted for any degree in any form at any university or institute of education.

Eloise E. Beyer

17th April, 2002.

his expertise on the Western Gneiss Region peridotites and for taking the time to correct my chapter on western Norway even though he was on the other side of the world.

A big heartfelt thank-you to my past and current office mates, William Powell, Olivier Alard and Stéphanie Touron, who provided a lot of laughs and made Room 511 a pleasant environment to work in. Will is especially thanked for his friendship and help over the years. Thanks also to Mark C. Pirlo, Guillaume Delpech and Sonja Aulbach, and the rest of the lunchtime crew.

Last, but not least, I would like to thank, and dedicate this thesis to, my parents, Max and Margaret, and my sister Claire. Thank-you for your unwavering love and support, and for always believing I could do it.

# LIST OF TABLES

# LIST OF FIGURES

## CHAPTER 1



## CHAPTER 2



## CHAPTER 3



## CHAPTER 4

## CHAPTER 6



## CHAPTER 7

# CHAPTER 1
# INTRODUCTION

The subcontinental lithospheric mantle (SCLM) is a geochemically distinct region of the mantle that underlies and is mechanically coupled to the crust. Direct samples of this region are brought to the surface as accidental inclusions (xenoliths) entrained in alkali basalts and kimberlites, and as tectonically emplaced massif complexes within mountain systems. Fundamental differences in the composition of Archean and Phanerozoic lithospheric mantle have been well documented over the last decade, but little attention has been paid to the nature of Proterozoic mantle and how it compares with mantle of different ages. This study investigates two regions that potentially provide samples of Proterozoic mantle, Tasmania (Australia) and the Western Gneiss Region (Norway). While the two terrains are radically different in terms of geology and tectonic setting, and while the samples of the mantle were delivered to the surface in two completely different ways, it is hoped that this study will reveal global similarities in subcontinental lithospheric mantle of Proterozoic age, as already discovered for Archean and Phanerozoic lithosphere in other parts of the world.

## 1.1 AIMS AND OBJECTIVES OF THIS STUDY

The primary aim of this thesis is to investigate the composition and origin of Proterozoic mantle.

The four principal goals of this study are:

1. to characterise the geochemistry of the mantle rocks beneath Tasmania and in the Western Gneiss Region.
2. to establish if a link can be made between mantle geochemistry and the overlying crustal terrains of Proterozoic age (and Phanerozoic age in Tasmania).
3. to compare the geochemical "fingerprints" of the Tasmanian and Norwegian mantle sections with each other.
4. to determine lithosphere ages for both regions using the Re-Os isotopic system to date whole rock samples and sulfide phases.

To achieve these objectives a suite of mantle xenoliths entrained in Tertiary basalts from Tasmania, Australia was selected. Tasmania is a natural choice for this study as its

crustal regions can be broadly divided into Proterozoic and Phanerozoic terrains and xenolith-bearing mantle-derived volcanics are widespread in both terrains. If lithospheric mantle and crust formed together the xenoliths may be samples of Proterozoic and Phanerozoic lithosphere.

Mantle xenoliths provide a basic but very powerful tool for investigating the nature of the lithosphere in space and time. Results from microanalysis, in conjunction with regional geophysical data, make it possible to determine vertical and lateral changes in the structure and chemistry of Tasmanian lithospheric mantle, which can then be related to temporal differences between terrains. This methodology is known as 4-D Lithosphere Mapping (O'Reilly and Griffin, 1996) and is outlined in section 1.2.2.

The second suite selected is from (locally garnet-bearing) orogenic peridotites from the Western Gneiss Region (WGR) of the Caledonides, Norway. A Proterozoic age for these rocks has already been established by Sm-Nd dating (Jamtveit *et al.*, 1991; Brueckner *et al.*, 1996). Previous studies (Jamtveit *et al.*, 1991; Krogh and Carswell, 1995; Brueckner *et al.*, 1996) have also shown that some of these rocks bear a remarkable resemblance to some kimberlite-borne xenoliths and it is thought they represent slices of lithospheric mantle tectonically emplaced into continental crust during crustal subduction. Garnet peridotites preserved in massifs within collisional orogenic belts provide windows into deeper levels (100 to possibly >400km) of the lithospheric mantle than do spinel peridotites (e.g. Brueckner and Medaris, 1998).

The mantle samples investigated in this study were analysed using a variety of whole rock and *in situ* methods. Whole rock techniques include X-ray fluorescence and solution ICPMS, while *in situ* techniques involved electron microprobe and laser ablation-ICPMS analysis.

The fourth objective involves the use of the recently acquired multi-collector-laser-ablation-ICPMS at Macquarie University which allows high-precision *in situ* analysis of isotopic ratios in geological materials. A combination of *in situ* Re-Os data obtained from sulfide inclusions in xenolith phases, and whole-rock Re-Os analysis, will allow model ages for individual samples to be determined and therefore constrain ages of melt depletion in the mantle.

## 1.2 THE SUBCONTINENTAL LITHOSPHERIC MANTLE

### *1.2.1 Definitions*

The distinction between the lithosphere and asthenosphere is of fundamental

importance to lithospheric research. The term lithosphere was first introduced by Barrell (1914) to describe the strong outer shell of the Earth, which overlies the weaker, less rigid asthenosphere. This is a definition that is difficult to apply quantitatively and for the purposes of this study a thermal definition of the lithosphere is used.

A thermal definition of lithosphere is based on the knowledge that the Earth is losing heat, from both primordial and radiogenic sources. The thermal lithosphere acts as a conductive boundary layer (also mechanical boundary layer or MBL) overlying the convecting mantle system (Anderson, 1995), allowing a definition of the thermal lithosphere as the outer layer of the Earth where heat transfer is by conduction. Conduction is the transfer of heat through vibrational energy between adjacent particles, whereas convection is the transfer of heat through mass movement of material. Conduction is relatively inefficient in redistributing heat through rocks compared to convection, and as a result temperature gradients are higher in the conductive lithosphere than in the asthenosphere where heat transfer is by convection (and the thermal gradient is therefore adiabatic).

The thermal lithosphere should not be confused with the thermal boundary layer (TBL) which is the narrow transition zone separating the outer mechanical boundary layer, where heat transfer is by conduction, from the adiabatic asthenosphere where heat is transferred by convection (Fig. 1-1). Many workers, such as Griffin *et al.* (1999a), consider the MBL to be synonymous with the lithosphere and use the term lithospheric mantle "to refer to the uppermost part of the mantle, comprising both a mechanical and chemical boundary layer, and characterised by conductive heat transfer". Likewise, Anderson (1995) debates the validity of including the TBL in any definition of the lithosphere arguing that '"lithosphere" is a mechanical concept implying strength and relative permanence', features not usually associated with the TBL.

The boundary between the thermal lithosphere and asthenosphere is commonly at or about the temperature where mantle material undergoes significant melting (McKenzie and Bickle, 1988) as the presence of melt weakens the mantle and allows the mass movement of material necessary for convection to occur. The lithosphere-asthenosphere boundary (LAB) in Archean cratons probably coincides with the base of the TBL while the LAB in younger or reworked tectonic regions is shallower and closer to the base of the mechanical boundary layer (Menzies, 1990a) (Fig. 1-1).

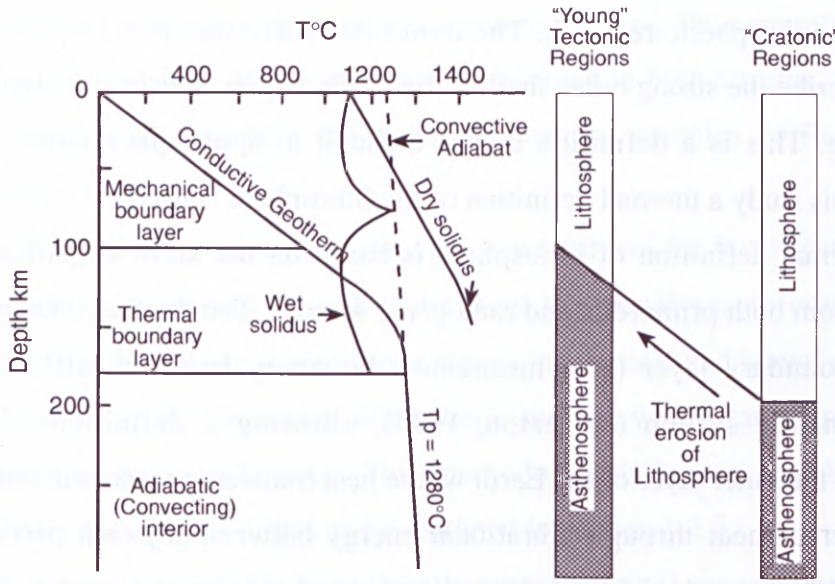


**Figure 1-1.** Definitions of the thermal and mechanical layers of the lithosphere and asthenosphere from McKenzie and Bickle (1988). The relative thicknesses of undisturbed Archean and younger lithosphere are shown in the right and left columns respectively after Menzies (1990a) and O'Reilly and Griffin (1996).

Evidence from thermobarometric and isotopic studies on mantle xenoliths in old cratonic areas suggests that the mechanical boundary layer, at least beneath continents, is also a chemical boundary layer that is depleted relative to the underlying mantle (Griffin *et al.*, 1999a). This notion of the MBL as a chemical boundary layer has been complicated by some isotopic studies which tend to equate different layers in Earth's structure with isotopically recognisable geochemical reservoir (Menzies, 1990b). These reservoirs are the result of the relatively fixed nature of the lithosphere which, unlike the convecting and therefore chemically well-mixed asthenosphere, tends to sustain geochemical heterogeneities on a long time scale (McKenzie and Bickle, 1988; Hofmann, 1997).

The seismic lithosphere refers to the high velocity zone (or LID) at the top of the mantle (Anderson, 1995). The base of this LID is marked by a decrease in velocity known as the low velocity zone (LVZ) which is sometimes equated with the asthenosphere. This drop in velocity implies a change in phase such as dehydration or partial melting, or a change in composition or mineralogy. As already discussed the presence of partial melts is likely to occur at the base of the thermal lithosphere indicating a broad correlation between the thermal lithosphere and the LID.

### *1.2.2 4-D Lithosphere Mapping*

4-D Lithosphere Mapping represents a holistic approach to understanding the composition, stratigraphy and thermal state of the lithosphere, the nature and significance of its major boundaries (e.g. the crust-mantle boundary and the lithosphere-asthenosphere

boundary) and its evolution (O'Reilly and Griffin, 1996). This method involves the integration of petrological, geochemical and geophysical information to construct realistic geological sections of the lithospheric mantle, and is the key to reconstructing the mechanisms and stages in the evolution of Earth's crust and mantle (O'Reilly and Griffin, 1996).

The basis of Lithosphere Mapping is the direct evidence for the petrology and geochemistry of the lower crust and upper mantle provided by xenoliths and xenocrysts (garnet and chromite) entrained in mantle-derived volcanics e.g. basalts, kimberlites and lamproites (O'Reilly *et al.*, 1999). In areas where sufficient xenoliths and/or xenocrysts of appropriate composition are available it is possible to establish the regional paleogeotherm (i.e. the geotherm at the time of eruption), the detailed distribution of rock types with depth, the depths to the crust-mantle and lithosphere-asthenosphere boundaries, and the spatial distribution of fluid-related processes such as metasomatism, within the mantle section under investigation (O'Reilly and Griffin, 1996). Geophysical data (seismic, gravity, magnetic, thermal) can be used in conjunction with geochemical data to give a 3-D picture of the composition, structure and thermal state of the lower crust and upper mantle, and allow the extrapolation of vertical lithosphere sections laterally beyond the occurrence of xenoliths. In regions where there have been volcanic episodes of different ages it is possible to add the fourth dimension, time, to lithosphere mapping by looking at different time-slices corresponding to the timing of volcanism (O'Reilly *et al.*, 1999).

The geochemistry of mantle-derived material is an integral part of Lithosphere Mapping and the basis of this study. Unfortunately direct samples of the mantle are rare and, in the case of xenoliths and xenocrysts, are limited to areas with suitable volcanism. Many of these areas are isolated point sources and therefore an important part of 4-D Lithosphere Mapping is the comparison of, and interpolation between, sample localities.

Volcanic activity samples mantle material from a range of depths so a necessary part of Lithosphere Mapping is determining depth relationships between samples. This can be done using geothermobarometry calculations for xenolith mineral assemblages. Using these methods of calculating equilibrium conditions it is possible to construct an empirical geotherm for the sample locality (O'Reilly and Griffin, 1996). Additional geochemical information can then be correlated with depth to build up a two-dimensional picture of how various characteristics change with depth in the lithosphere. Regional geophysical information can then be used to extrapolate lithosphere composition and structure laterally over large areas. However, this extrapolation must be used with caution, as discussed

below.

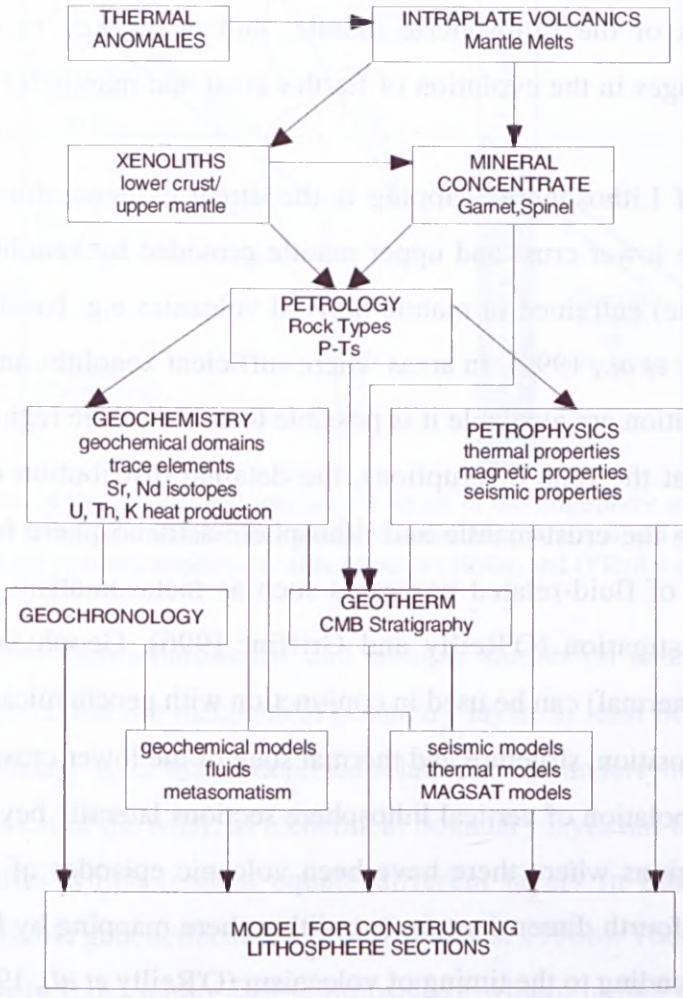


**Figure 1-2.** Flowchart displaying linked strands that illustrate the approach used for 4-D Lithosphere Mapping (after O'Reilly and Griffin, 1996).

When selecting samples for thermobarometric study it is important to use samples that show mineralogical equilibrium and are statistically representative of the xenolith population being studied for each locality. The sampling mechanism, both volcanic and human, is selective and ultimately controls the way in which the Earth's deep stratigraphy is interpreted (O'Reilly and Griffin, 1996). It is also crucial to recognise, when interpreting the results of such studies, that the results represent the state of the lithosphere at the time of entrainment of the mantle samples. The use of techniques that reflect present-day properties, such as surface heat flow measurements and seismic data, restricts direct comparisons to areas of recent sampling or where it is clear that there has been tectonic stability since the time the mantle was sampled. This is possible in areas which have not undergone any major tectonothermal activity since the volcanic episode that brought the mantle samples to the surface.

4-D Lithosphere Mapping is a xenolith-based methodology and therefore is an ideal approach to the characterisation of the lithospheric mantle beneath Tasmania.

### *1.2.3 Composition and structure of the SCLM*

The subcontinental lithospheric mantle (SCLM) is composed predominantly of peridotitic material. Lherzolite is a four-phase ultramafic rock consisting of up to 90% olivine and lesser proportions of orthopyroxene, clinopyroxene and an aluminous phase that is usually either spinel or garnet. The aluminous phase present in lherzolite is a function of temperature and pressure as spinel will transform to garnet at higher pressures over a relatively narrow transition zone (O'Neill, 1981; Carroll Webb and Wood, 1986). Lherzolite is considered to be relatively fertile based on its significant Ca and Al abundances (equivalent to basaltic components) as evidenced by the presence of clinopyroxene. Harzburgite has a similar mineral assemblage to lherzolite but is clinopyroxene-free as reflected in its low bulk Ca and Al contents (Griffin *et al.*, 1999a).

The first realistic estimates of the composition of the Earth's mantle were provided by the pyrolite model of Ringwood (1962, 1966). This model uses the complementary melt-residuum relationship between basalts and peridotites as a basis for estimating the major and minor element composition of the Earth's upper mantle. Ringwood (1966) found that the refractory lithophile element composition of the pyrolite model closely matched the composition of CI carbonaceous chondrites, minus the core components. Subsequent models (e.g. Jagoutz *et al.*, 1979; Sun, 1982; Hart and Zindler, 1986; McDonough and Sun, 1995; Niu, 1997) have also used the compositions of fertile peridotites and/or high-temperature melts derived from peridotite to establish the composition of the Earth's primitive mantle. The model of McDonough and Sun (1995) has been used in this study as it avoids unnecessary assumptions inherent in several existing models, and results in an internally consistent Silicate Earth composition having chondritic proportions of the refractory lithophile elements at ~2.75 times that in CI carbonaceous chondrites.

Early compilations of compositional data (Maaløe and Aoki, 1977; Jordan, 1979) on the major element compositions of mantle xenoliths indicated significant geochemical differences between garnet peridotites and spinel peridotites. These studies, however, failed to recognise the potential importance of age differences between the garnet peridotites, drawn largely from Archean cratonic settings, and the spinel peridotites, drawn almost entirely from Phanerozoic settings. It has been demonstrated that there are

fundamental differences in the composition of Archean lithospheric mantle, as represented by xenoliths in kimberlites from the Kaapvaal and Siberian cratons, and Phanerozoic mantle, as represented by both ocean-floor peridotites (including abyssal peridotites, harzburgite tectonites in ophiolites and some alpine massifs) and xenoliths entrained in young (mostly intraplate) alkali basalts erupted through Phanerozoic crust (Boyd, 1989; Griffin *et al.*, 1998b, 1999a).

Oceanic peridotites have compositions that reflect their origin as residues from the extraction of variable proportions of basaltic components from a primitive mantle source. Average compositions and modes for depleted abyssal peridotites, ophiolite tectonites and alpine peridotites combined with those for model, fertile peridotite have been used to define two geochemical "oceanic trends". The first trend is defined by plotting Mg# (100 x Mg/(Mg+Fe)) of rock or olivine against Mg/Si (or modal olivine) (Fig. 1-3), and is particularly useful in characterising peridotites, as progressive depletion of a fertile peridotite causes an increase in both Mg# and Mg/Si. This plot can be used in conjunction with a plot of whole rock CaO against $Al_2O_3$ (Fig. 1-4), both of which are reduced with increasing depletion (Boyd, 1997; O'Reilly *et al.*, 2001).

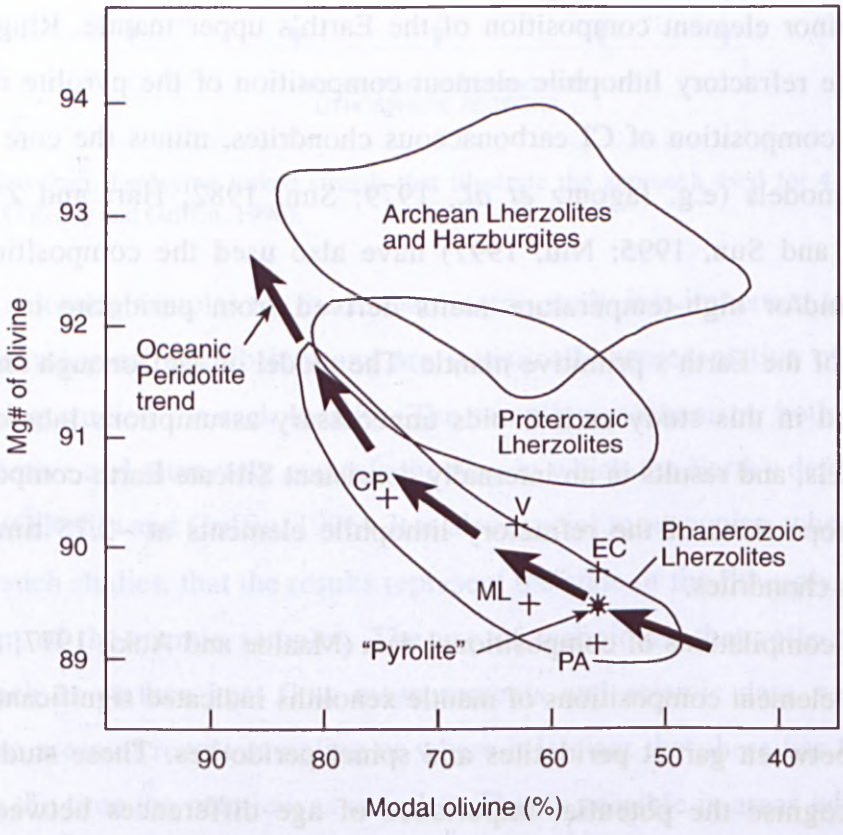


**Figure 1-3.** Mg# (%Fo) of olivine plotted against modal olivine content for mantle-derived xenoliths from Archean, Proterozoic and Phanerozoic terrains (Grffin *et al*, 1998b, modified after Boyd, 1996). Average values for selected Phanerozoic xenolith suites: PA, Pali-Aike; EC, Eastern China; V, Vitim; CP, Colorado Plateau; ML, Malaita (from Griffin *et al.*, 1998b).

Xenoliths from Phanerozoic terrains (in both oceanic and continental settings) follow the oceanic trend shown in Fig. 1-3 leading to progressively higher olivine contents and more magnesian olivine with increasing depletion. Mg# for these rocks ranges from 89-92 with modal olivine contents varying from 50-80%. There is considerable variation in the levels of depletion for Phanerozoic suites, but many are much less depleted than typical cratonic peridotites, and on average they are only marginally depleted in Ca and Al in comparison to estimated primitive upper mantle compositions (Griffin *et al.*, 1998b, 1999a).

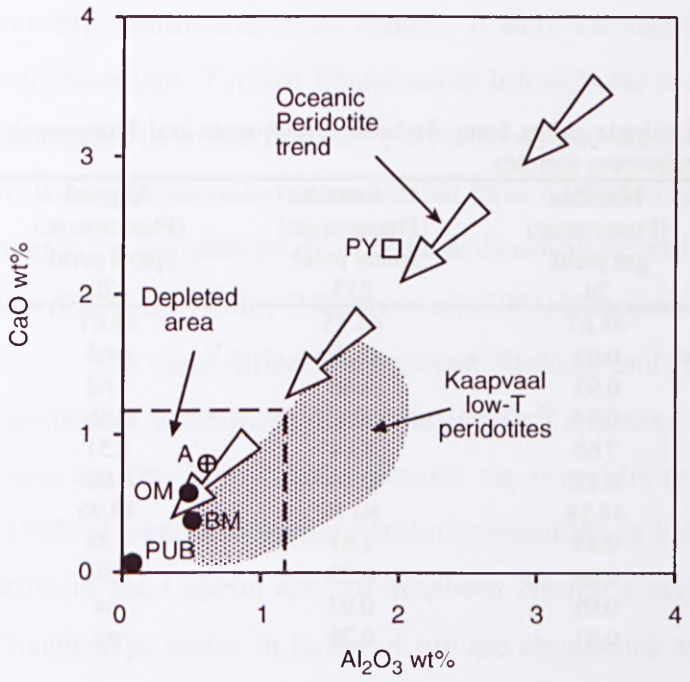


**Figure 1-4.** $AL_2O_3$ plotted against CaO for oceanic and cratonic peridotites (after Boyd, 1989). Point PY is pyrolite, A is average abyssal peridotite, OM is average Oman harzburgite, BM is Burro Mountain harzburgite and PUB is Papua Ultramafic Belt harzburgite. Field for Kaapvaal low-T peridotites is from (Boyd *et al.*, 1997).

Archean garnet peridotite xenoliths are generally highly depleted in Ca and Al and have lower Ca/Al compared to xenoliths from Phanerozoic terrains (see Table 1-1). They typically contain more magnesian olivine ($Fo_{92-94}$) and a plot of olivine Mg# against modal olivine for a suite of Kaapvaal and Siberian garnet peridotites defines a field that lies significantly above the oceanic trend (Boyd, 1989). In these rocks, modal olivine ranges from 40-80%, and the average enstatite content is 31%, contrasting with an average value of 13% for abyssal peridotites (Boyd, 1989). The high opx/olivine ratios observed in Archean garnet peridotites reflect a lower Mg/Si ratio at any Mg# (Griffin *et al.*, 1998b). These features are not restricted to garnet peridotites, but are shared by spinel-bearing peridotites from Archean settings (Carswell *et al.*, 1984; Boyd *et al.*, 1997).

The observed differences in Ca/Al and Mg/Si at any Mg# suggest that Archean peridotites have not been formed by the same processes as Phanerozoic peridotites. The

geochemistry of most Archean lithospheric mantle with low Mg/Si suggests it is the product of high-degree melting at depths ≥150 km, with no Cr-Al phase (i.e. garnet, spinel) present in the residue (see arguments by Griffin *et al.*, 1999a, 2002). Most Phanerozoic continental lithospheric mantle probably has been generated in extensional environments involving ≤10% partial melting and with a Cr-Al phase present on the liquidus. Another major mechanism for the generation of Phanerozoic lithosphere in intraplate environments may be accumulation and cooling of material from rising plumes (Stein and Hofmann, 1994). Griffin et al. (1999a) have suggested that much Proterozoic lithosphere was produced in extensional environments, but with higher average degrees of melting and possibly at greater depth .

**Table 1-1.** Median bulk compositions of sample suites from Archean, Proterozoic and Phanerozoic terrains (data from Griffin *et al.*, 1999a and references therein).

| Locality | Kaapvaal | | Namibia | E. Australia | Abyssal |
|---|---|---|---|---|---|
| Age | (Archean) | | (Proterozoic) | (Phanerozoic) | (Phanerozoic) |
| Rock type | gnt lherz. | sp. perid. | gnt perid. | spinel perid. | spinel perid. |
| No. analyses | 79 | 17 | 24 | 253 | 120 |
| $SiO_2$ | 46.39 | 45.07 | 44.67 | 44.55 | 43.61 |
| $TiO_2$ | 0.06 | 0.05 | 0.03 | 0.08 | 0.02 |
| $Al_2O_3$ | 1.42 | 0.71 | 0.93 | 2.46 | 1.62 |
| $Cr_2O_3$ | 0.35 | 0.37 | 0.34 | 0.4 | 0.66 |
| FeOt | 6.56 | 6.43 | 7.65 | 8.64 | 8.51 |
| MnO | 0.11 | 0.11 | 0.12 | 0.14 | 0.00 |
| MgO | 43.35 | 45.59 | 44.58 | 40.76 | 43.96 |
| CaO | 0.95 | 0.52 | 0.84 | 2.43 | 1.38 |
| $Na_2O$ | 0.10 | 0.10 | 0.04 | 0.23 | 0.04 |
| $K_2O$ | 0.08 | 0.10 | 0.01 | 0.03 | na |
| NiO | 0.28 | 0.03 | 0.31 | 0.26 | na |
| Mg# | 92.2 | 92.7 | 91.1 | 89.1 | 90.2 |
| Mg/Si | 1.40 | 1.54 | 1.48 | 1.35 | 1.51 |
| Ca/Al | 0.61 | 0.64 | 0.72 | 0.87 | 0.84 |
| Aver% Ol. | 61 | 69 | - | 69 | 74 |
| %Fo in Ol | 92.3 | 92.8 | - | 88.8 | 90.0 |

Both petrologic and geophysical studies have provided evidence that the lithosphere beneath cratons is thicker than that in oceanic plates (Boyd, 1989). Experimental data on diamond stability in the mantle and thermobarometric studies of mantle minerals have led to the concept of a thick, cool "keel" or "root" beneath Archean cratons (Pearson *et al.*, 1995a; Griffin *et al.*, 1998b, 1999a). By inference, the lithospheric mantle beneath younger terrains is thinner and hotter to explain the paucity of diamonds in areas with Phanerozoic crustal ages (assuming carbon is equally available). This predicted difference in lithosphere thickness is supported by seismic tomography which shows regions of high seismic velocity extending to 150-300 km beneath some Archean cratons

but not beneath younger terrains (Griffin *et al.*, 1998b, 1999a). This is evident in the Australian continent where a three-dimensional model of seismic wave heterogeneities in the upper mantle shows that, in the upper 200km of the model, seismic velocities are lower beneath the eastern Phanerozoic part of Australia compared to the Precambrian central and western cratons (Debayle and Kennett, 2000).

Density calculations for average Archean lherzolite indicate that it is ca 0.04 g/cm$^3$ less dense than typical Phanerozoic lherzolite at any temperature (Griffin *et al.*, 1999a; Poudjom Djomani *et al.*, 2001). This means that the melt-depleted Archean lithosphere is intrinsically buoyant with respect to more "fertile" mantle and may therefore be stable beneath continents, even though it may be significantly cooler than the underlying asthenosphere. Typical Phanerozoic lithospheric sections (~110-120 km) with advective geotherms decrease in density with depth and are very buoyant relative to asthenosphere. However, Phanerozoic sections that have cooled to typical stable conductive geotherms are negatively buoyant relative to the asthenosphere and are therefore gravitationally unstable (Griffin *et al.*, 1998b; O'Reilly *et al.*, 2001; Poudjom Djomani *et al.*, 2001).

The clear difference between Archean and Phanerozoic mantle samples raises the question of when these dissimilarities first appeared in the geologic record. Unfortunately there are few comparable datasets on xenoliths from Proterozoic terrains. Hoal *et al.* (1995) showed that garnet peridotite xenoliths in kimberlites erupted through Proterozoic crust in the Gibeon area of southern Namibia are intermediate between Archean and Phanerozoic suites in terms of olivine abundance and composition. Likewise a xenolith suite from another Namibian kimberlite at Louwrensia has been shown to be transitional between Kaapvaal and oceanic peridotites in terms of its modal mineralogy and Mg# (Pearson *et al.*, 1994). The Obnazhennaya kimberlite, which intrudes a Proterozoic terrain in northern Siberia, contains garnet lherzolite xenoliths that have higher Mg/Si and higher (Ca+Al) than those from the kimberlites penetrating the Archean terrains further south (Spetsius, 1995). These data suggest that Proterozoic lithospheric mantle is intermediate in composition between Archean and Phanerozoic mantle, with some localities tending toward Phanerozoic mantle compositions (Griffin *et al.*, 1998b).

### *1.2.4 Secular variation in the composition of the SCLM*

A recent study by Griffin *et al.* (1998b) of modal and trace element data for mantle-derived peridotites and compositions of mantle-derived Cr-pyrope garnets provides evidence for a secular change in the chemical composition of newly-created lithospheric

mantle from Archean times to the present. For the purposes of that study the samples were divided into three main groups based on the "tectonothermal age" of the crust intruded by the volcanic rock from which the sample is derived. Using a modified version of a scheme proposed by Janse (1994) the samples were divided into those from Archons (>2.5 Ga), Protons (2.5-1 Ga) and Tectons (<1 Ga).

Garnet concentrates derived from kimberlites, lamproites and other volcanic rocks are interpreted as disaggregated mantle wall rock. Comparison with data from mantle-derived xenoliths allows determination of the parent rock type of each garnet and this was used to estimate relative abundances of these rock types in individual mantle sections. As a result of this work Griffin *et al.* (1998a, 1998b) have shown that subcalcic (low Ca/Al) harzburgites are restricted to lithospheric mantle beneath Archons, and that calcic harzburgites are common beneath Archon terrains, less abundant beneath Proton terrains, and essentially absent beneath Tectons. It was also demonstrated that there are significant differences in the composition of the average lherzolitic garnets from Archon, Proton and Tecton suites. A steady decrease in the mean Cr content and Zr/Y of the garnet suites with decreasing tectonothermal age is accompanied by an increase in mean Y content and Y/Ga (Griffin *et al.*, 1998b). These changes, coupled with a rise in average Ca and Al contents and Ca/Al (expressed as modal cpx/gnt and (cpx+gnt)) and a decrease in average Mg#, document the evolution of the lithospheric mantle toward less depleted average compositions from the Early Proterozoic to the present (Griffin *et al.*, 1998b).

### *1.2.5 Stability of the SCLM*

The correlation between mantle composition and the age of the overlying crust has led to the concept of crust-mantle coupling where crustal volumes and the underlying lithospheric mantle are thought to have formed together and in most cases to have remained coupled together since that time. Mantle roots extending to depths of 200-300 km beneath Archean cratons apparently have been able to survive large-scale movement of cratons and cratonic fragments over large distances without being detached from their crust. While the present data suggest long-term coupling of the crust and mantle there also is evidence to suggest that in some regions decoupling (or "lithosphere erosion") has occurred (Griffin *et al.*, 1998a, 1998b).

One of the first documentations of lithosphere erosion was reported by Eggler *et al.* (1988) based on studies of kimberlite-borne and basalt-borne mantle xenoliths in the Wyoming Province of North America. Garnet-bearing peridotite xenoliths were used to

establish that by the end of the Archean a thick (175-200km) keel existed beneath the Wyoming Province. It is thought that this keel remained tectonically stable throughout the Paleozoic and probably existed into Cretaceous time, when processes associated with subduction or back-arc advection may have begun to destroy it. Evidence for a significantly thinner lithosphere in the present day comes from gravity and seismic surveys and heat-flow measurements that indicate that today only fragments of the mantle keel remain (Eggler *et al.*, 1988). Further evidence comes from xenoliths brought up in Tertiary kimberlites and other volcanic rocks, which define an elevated geotherm and a thin lithosphere (Eggler *et al.*, 1988).

A more recent investigation into lithosphere erosion has been carried out on the Sino-Korean Craton in northern China (Griffin *et al.*, 1998a). Analysis of garnet and spinel concentrates from kimberlites intruding the eastern part of the craton shows that an Archean lithospheric keel ca 200 km thick, characterised by low heat flow and containing abundant harzburgites, existed beneath Shandong and Liaoning Provinces during the mid-Ordovician (Griffin *et al.*, 1998a). Geochemical evidence from garnets entrained in Mesozoic-Tertiary kimberlites and mantle xenoliths found in Tertiary basalts suggest that the lithosphere is now predominantly fertile Phanerozoic lherzolite and less than 80-100 km thick. Geophysical data from the region show a thin lithosphere (60-120 km) and an elevated geotherm in agreement with these findings (Griffin *et al.*, 1998a). Recent work by Zheng *et al.* (2000) on high-Mg xenoliths from Hebi county, 400 km west of the Tanlu fault zone and Shandong province, has led to their interpretation as relics of the Archean lithosphere preserved locally at shallow levels.

The decoupling and removal of a Archean keel and its replacement by a thin, hot lithosphere will have significant tectonic consequences, firstly because of the differences in intrinsic density between the two volumes, and secondly because it will be accompanied by a rise in isotherms (Griffin *et al.*, 1998b). The results are likely to include rifting and uplift, as seen in Shandong and Liaoning Provinces during Jurassic-Cretaceous time, heating, magmatism and extensive fluid-mobilisation within the crust (Griffin *et al.*, 1998a, 1998b).

## 1.3 MANTLE SAMPLES

### *1.3.1 Xenoliths*

Xenoliths are accidental inclusions entrained from lithospheric mantle levels in rising magmas and brought rapidly to the Earth's surface. The ability of a magma to

transport mantle xenoliths to the surface is primarily dependent on the rheology of the magma (O'Reilly, 1989b). A magma such as a tholeiitic basalt ascends relatively slowly allowing time for denser mantle xenoliths to settle out, as shown by the paucity of mantle xenoliths in mid-ocean ridge basalts (Kushiro *et al.*, 1976). Kimberlites and alkaline basalts have higher ascent velocities (on the order of tens of hours to days) increasing the likelihood of retention of mantle inclusions (Kushiro *et al.*, 1976; O'Reilly, 1989b; O'Reilly *et al.*, 1990; Kelley and Wartho, 2000). The short duration of ascent decreases the likelihood of contamination by the host basalt, although entrainment in high temperature magmas combined with rapid decompression makes melting of hydrous phases during ascent likely (Frey and Green, 1974).

Eastern Australia contains one of the largest concentration of mantle xenoliths in the world. Hundreds of xenolith-bearing localities are found in the belt of Jurassic to Holocene basaltic rocks that stretches nearly 4000 km from northern Queensland to Tasmania (O'Reilly and Griffin, 1987). Mantle xenoliths are found in all forms of volcanic deposits including flows, cinder cones, pyroclastic rocks, diatremes and maars, and also in high-level intrusions such as dykes and sills (O'Reilly, 1989b).

Mantle xenolith suites in basaltic rocks include a relatively restricted range of rock types, the proportions of which may vary widely between localities. The classification scheme used here for mantle-derived xenoliths divides mantle samples into three suites; the Cr-diopside suite (Wilshire and Shervais, 1975; Group I of Frey and Prinz, 1978), the Al-augite suite (Wilshire and Shervais, 1975; Group II of Frey and Prinz, 1978), and the Fe-rich Cr-diopside suite which is intermediate between the two. Cr-diopside spinel lherzolite is the most abundant and ubiquitous xenolith type in eastern Australia, making up 80-100% of the population at most xenolith localities (O'Reilly, 1989b). This is also evident in Tasmania where the 130 mantle samples collected for the purposes for this study belong almost exclusively to the Cr-diopside suite.

The Cr-diopside suite is characterised by grass-green (in hand specimen) Cr-diopside and olivine with $Fo_{88-92}$. Rock types range from lherzolite to harzburgite, pyroxenite and rare dunite and can be further divided into anhydrous and hydrous types (O'Reilly, 1989b). The anhydrous xenoliths are typical four-phase spinel lherzolites (olivine, orthopyroxene, clinopyroxene, spinel) with rarer samples having garnet as an additional phase. Garnet-bearing xenoliths are extremely rare in Tasmania and have only been documented at two localities; Bow Hill in central Tasmania, and Table Cape in the northwest (Sutherland *et al.*, 1984; Sutherland *et al.*, 1994; Sutherland *et al.*, 1996). Counts

of xenoliths at Bow Hill give a ratio of garnet lherzolite to spinel lherzolite of about 1 to 500 (Sutherland *et al.*, 1984).

Hydrous, or volatile-bearing, xenoliths are all garnet-free and may contain any combination of amphibole, mica, apatite and calcite (O'Reilly, 1989b). The presence of these minerals reflects modal or patent metasomatism (Dawson, 1984; Harte, 1987). No evidence for this type of metasomatism has been found in Tasmania, though cryptic metasomatism is widespread as will be discussed in a later section.

The Fe-rich Cr-diopside suite includes most of the rock types of the Cr-diopside suite and is characterised by mineral compositions intermediate between those of the Cr-diopside and Al-augite suites. Olivine is more fayalitic ($Fo_{86}$) and clinopyroxene contains higher $Al_2O_3$, $TiO_2$ and FeO concentrations than do normal Cr-diopside suite equivalents (O'Reilly and Griffin, 1987). These xenoliths are thought to be the result of the interaction of lherzolite wall rock with basaltic melts (O'Reilly and Griffin, 1987). Sample WH13 from Wagners Hill is a spinel lherzolite which shows many characteristics of this suite including fayalitic olivine ($Fo_{84}$) and clinopyroxene enriched in Al, Ti and Fe.

The Al-augite suite is characterised by an Al-rich clinopyroxene that is black in hand-specimen and generally more Fe-and Ti-rich than those of the Cr-diopside suite. Al-augite series xenoliths have a wide range in modal assemblages, microstructures and geochemistry and are interpreted as having originated as cumulates from basaltic melts within the mantle. The suite can be divided into three distinct series: (1) the *wehrlite* series, characterised by igneous microstructures and dominated by clinopyroxene+olivine assemblages; (2) the *metapyroxenite* series, representing microstructural and mineralogical re-equilibration of wehrlite series xenoliths; and (3) the *apatite/amphibole* series, representing precipitates from magmas enriched in volatiles and incompatible elements (O'Reilly, 1989b). Xenoliths of the Al-augite series have been reported at several localities in Tasmania (Wass and Irving, 1976 and references therein; Sutherland *et al.*, 1984). Samples are typically wehrlites and websterites and include some rare garnet-bearing varieties (Sutherland *et al.*, 1984).

### *1.3.2 Massif peridotites*

Orogenic or alpine massifs are tectonically emplaced bodies within compressional mountain systems, of ultramafic rock of various sizes that are composed of metamorphic lherzolite and/or harzburgite with associated pyroxenites, gabbros and basalts (Menzies and Dupuy, 1991). Massif peridotites are distinguished from ophiolitic peridotites by a

lack of any obvious association with other rocks of oceanic provenance (Griffin *et al.*, 1999a). They are usually associated with high-grade metamorphic rocks. Recent studies of orogenic massifs have revealed a diversity of rock types that bear a remarkable chemical and mineralogic resemblance to kimberlite- and basalt-borne mantle xenoliths. Most massif peridotites are spinel-bearing but garnet-bearing examples are found in some mountain chains. Garnet-bearing rock types include lherzolite, harzburgite, wehrlite, dunite and pyroxenite and all have been recrystallised to varying degrees to lower-pressure anhydrous and hydrous mineral assemblages (Brueckner and Medaris, 2000).

Peridotites in orogenic massifs are further described as being either cumulate or tectonite in nature and exist in either the plagioclase, spinel or garnet lherzolite fields (Menzies, 1976). Moore and Qvale (1977) identified three types of alpine peridotites in the Norwegian Caledonides. Moore and Qvale's Type-one peridotites contain primary (magmatic) olivine, clinopyroxene, orthopyroxene and chromite, are highly serpentinised and are restricted to Cambro-Silurian metasedimentary sequences in the Caledonian fold belt. The other two types are recognised in the Western Gneiss Region. The first (Type-two of Moore and Qvale, 1977) are polymetamorphic carbonate-bearing peridotites which are not part of this study and will not be discussed further. The second type seen in the WGR (Type-three of Moore and Qvale, 1977) shows a metamorphic mineral association of olivine, orthopyroxene and minor chromite with garnet, clinopyroxene, amphibole and Cr-chlorite present in some samples.

The origin(s) of garnet in massif peridotites is widely debated. Brueckner and Medaris (2000) have proposed that garnet-bearing alpine peridotites be classified into two broad categories: "*crustal*" peridotite and "*mantle*" peridotite. Crustal peridotite (Class I) originated as cumulates from mafic magmas residing in the crust and acquired its garnet-bearing assemblage during metamorphism associated with subduction. Mantle peridotite (category II) is derived from the mantle wedge above underthrust continental crust, and can be subdivided into two classes. Class IIA or "*subduction zone*" peridotites occurred above subducting oceanic crust prior to continental underthrusting. Depending on depth of derivation and intrusion subduction peridotites are further divided into "*high-pressure-high temperature*" (HP-HT) and "*ultrahigh-temperature*" (UHT) depending on the P-T conditions associated with garnet formation. Class IIB or "*relict*" peridotite was derived from ancient, subcontinental lithospheric mantle and shows no evidence for involvement in subduction. The garnets in "relict" peridotites formed in the mantle before the tectonic processes that emplaced them into the crust.

It is the garnetiferous variants of Moore and Qvale's Type-three peridotites that are of prime importance to this thesis. According to the classification scheme of Brueckner and Medaris (2000) they fall into category IIB, that is they are relict mantle peridotites. This interpretation is based on previous studies of their geochemistry (Krogh and Carswell, 1995), ages and isotopic signatures (Mearns, 1986; Jamtveit *et al.*, 1991; Brueckner *et al.*, 1996). Previous work has also shown that these garnet-bearing rocks can be divided into two compositional groups; a Mg-Cr type and an Fe-Ti type, (Carswell *et al.*, 1983).

Mg-Cr garnet peridotites are relatively magnesian (whole rock Mg#=80-92) with low $TiO_2$ (~0.25 wt%) and high $Cr_2O_3$ (~0.5 wt%) and NiO (Carswell *et al.*, 1983). These high-pressure garnetiferous assemblages are preserved at only a few localities and most are close to the coast, since the degree of retrogressive replacement by late amphibolite facies assemblages generally increases in an easterly direction across the WGR (Krogh and Carswell, 1995). There is petrographic evidence that garnet was originally much more widely developed in these peridotite bodies than is currently apparent, but has been extensively retrograded to foliated chlorite and tremolite bearing assemblages (Carswell *et al.*, 1983).

The Fe-Ti type peridotites and associated garnet pyroxenites are crustal in origin (Brueckner and Medaris' Class I) and are thought to have formed from layered intrusive complexes of olivine norite-peridotite originally crystallised from crustal cumulates at ≤10 kbar pressure and subsequently metamorphosed under eclogite-facies conditions (Carswell *et al.*, 1983; Jamtveit *et al.*, 1991; Medaris and Carswell, 1990). Although Fe-Ti garnet peridotites are a significant component of the WGR they will not be discussed here.

### *1.3.3 Microstructural classification scheme for mantle rocks*

A microstructural classification scheme for peridotite xenoliths in kimberlites and basalts, devised by Harte (1977), defines the principal xenolith textural types as: coarse, porphyroclastic, mosaic-porphyroclastic and granuloblastic (later termed granoblastic by O'Reilly *et al.*, 1989b). These principal types can be further subdivided into tabular, equant, laminated, fluidal and disrupted on the basis of other textural characteristics. The terminology proposed by Harte (1977) is also applicable to orogenic peridotites (Nicolas *et al.*, 1971).

Harte's *coarse* textural type describes a rock lacking porphyroclasts and which is predominantly formed by mineral grains 2 mm or greater in average dimension and with grain boundaries that may be straight, smoothly curved, or less regular. This textural type

can be divided into two subtypes, *coarse equant* and *coarse tabular*, based on the dominant olivine habit (O'Reilly *et al.*, 1989b). The typical grain-size range for olivine and orthopyroxene in coarse equant peridotites is 2-5 mm while olivines in tabular types have aspect ratios of about 3:1 (O'Reilly *et al.*, 1989b). Most coarse xenoliths have deformation and exsolution features affecting olivine (kink bands and undulose extinction) and orthopyroxene (Ca-clinopyroxene exsolution lamellae).

**Table 1-2.** Summary of microstructural classification for peridotite xenoliths based on the nomenclature of Harte (1977).

| Texture | Porphyroclasts | Grain size | Grain boundaries | Subtypes |
|---|---|---|---|---|
| *Coarse* | Absent | Average grain-size >2.0mm | Variable. Largely straight or smoothly curving | Equant<br>Tabular |
| *Porphyroclastic* | Present.<br>>10% olivine as porphyroclasts | Bimodal<br>-porphyroclasts<br>-neoblasts | Irregular in porphyroclasts<br>Straight in neoblasts | Disrupted<br>Fluidal<br>Laminated |
| *Mosaic-porphyroclastic* | Present.<br><10% olivine as porphyroclasts | Bimodal<br>-porphyroclasts<br>-neoblasts | Irregular in porphyroclasts<br>Straight in neoblasts | Disrupted<br>Fluidal<br>Laminated |
| *Granoblastic*[1] | Absent or <5% in all mineral phases | Average grain size <2.0mm | Straight or smoothly curving triple-point boundaries between polygonal grains | Equant<br>tabular |

1. O'Reilly *et al.* (1989). Harte's original term was "granuloblastic".

Recrystallisation of olivine evidenced by the appearance of olivine neoblasts marks the transition to Harte's *porphyroclastic* textural type. This microstructure describes olivine-rich xenoliths in which at least 10% of olivine is present as porphyroclasts (Harte, 1977). *Mosaic-porphyroclastic* is used to describe xenoliths in which porphyroclasts make up less than 10% of the total olivine (O'Reilly *et al.*, 1989b). Other porphyroclast species, such as orthopyroxene, may be abundant. Within both porphyroclastic and mosaic-porphyroclastic groups subdivisions may be made according to whether or not the spinel or garnet shows a disrupted texture and whether the rock is laminated or fluidal (Harte, 1977). The terms "laminated" and "fluidal" denote the presence of sub-parallel, semi-continuous layers and lenticles enriched in particular minerals though (O'Reilly *et al.*, 1989b) point out that these terms can rarely be applied. However, "disrupted" textures, described by linear or planar trains of spinel grains parallel to planar fabrics defined by olivine, are common in olivine-rich xenoliths (O'Reilly *et al.*, 1989b).

Continuing recrystallisation leads to the ubiquitous strain and exsolution features of the porphyroclastic texture becoming less pronounced in the mosaic-porphyroclastic texture and culminating in strain-free *granoblastic* microstructures (O'Reilly *et al.*, 1989b).

*Granoblastic* textures are defined as having less than 5% of total olivine as porphyroclasts (Harte, 1977). Most minerals have narrow grain-size ranges (typically <2 mm), are dominantly polygonal in shape and are characterised by straight boundaries and triple-point grain junctions (O'Reilly *et al.*, 1989b). Harte's granoblastic microstructure can be subdivided into equant and tabular types based on dominant olivine habit.

# CHAPTER 2

# METHODOLOGY

## 2.1 INTRODUCTION

This chapter outlines both the whole rock and *in situ* analytical methods used and their application to this study. All analyses were carried out in the Geochemical Analysis Unit (GAU), ARC National Key Centre GEMOC, Macquarie University.

## 2.2 WHOLE ROCK ANALYTICAL TECHNIQUES

### *2.2.1 X-Ray Fluorescence*

Samples were cut into 2 cm thick slabs and coarsely crushed between plastic sheets with a hammer. The coarse crush was then powdered in an agate mill. Some samples which would not powder adequately in the agate mill were instead processed in a tungsten carbide mill to ensure that the powder would be fine enough to fuse.

Major elements and some trace elements (Ba, Cr, Cu, Ni, V and Zn) were analysed by XRF by C. Lawson using a Siemens SRS-1 instrument. Major elements were determined using glass fusion discs (Norrish and Hutton, 1969). Trace elements were analysed using pressed-powder pellets and corrected using mass absorption coefficients calculated from major element analyses (Norrish and Chappell, 1977). International rock standards provided calibration for both major and trace elements and an appropriate range of international or internal standards was included as unknowns in each run. All samples were run in duplicate. Detection limits and precision are as described by O'Reilly and Griffin (1988).

FeO was determined by HF digestion and titration with ceric sulfate. $H_2O^+$ and $CO_2$ were determined using a LECO induction furnace while $H_2O^-$ was determined separately by drying at 110°C for 2 hours.

### *2.2.2 Solution ICPMS*

Trace elements

Trace elements in whole rock samples were analysed by A. Sharma and S. Elhlou using solution Inductively Coupled Plasma Mass Spectrometry (ICPMS). REE, LILE ( Cs, Rb, Ba, Th, U, Sr), HFSE (Nb, Ta, Zr, Hf), as well as minor and transition elements (Ti, V, Cr,

Ni, Cu, Zn, Ga, Mo) were analysed. The ICPMS instruments used were a Perkin Elmer Sciex Elan 6000 and a Hewlett Packard 4500 with a shield torch. Rock digestion was performed using the $HF/HClO_4$ procedure outlined in the flow diagram below (Fig. 2-1).

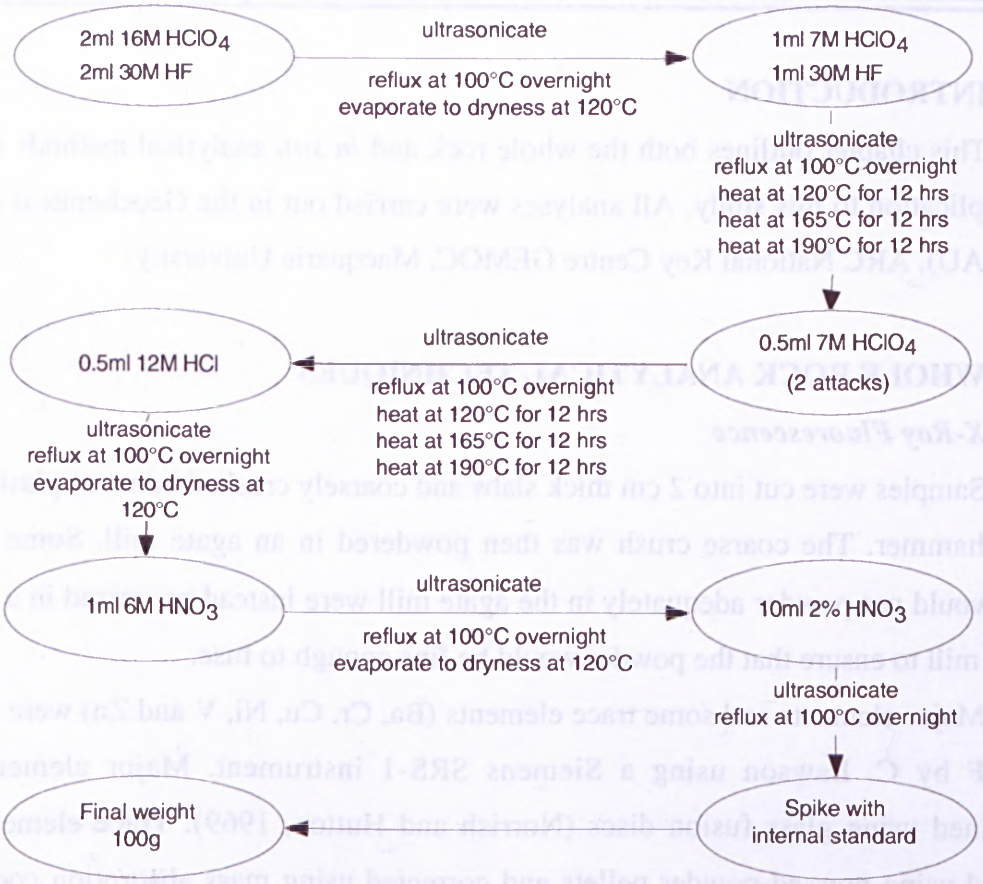


**Figure 2.1** Flow diagram for $HF/HClO_4$ rock digestion procedure for solution ICPMS.

For each batch, USGS and JGS rock standards have been included in order to check the accuracy of the analyses. Drift was corrected using $^{6}Li$, Ru, In and Bi as doping elements. A comparison of detection limits for elements analysed on the PE Elan 6000 and Agilent 4500 ICPMS systems is outlined in Table 2-1.

**Table 2-1** Detection limits for elements analysed by solution ICPMS. Values are given in ppb.

| | Ni | Ga | Rb | Sr | Y | Zr | Nb | Ba | La | Ce | Pr | Nd |
|---|---|---|---|---|---|---|---|---|---|---|---|---|
| PE6000 | 120 | 6 | 5 | 16 | 0.8 | 6.8 | 3 | 48 | 1.1 | 18 | 0.3 | 1.1 |
| HP4500 | 160 | 20 | 10 | 80 | 1.2 | 8 | 12 | 37 | 1.0 | 2 | 0.8 | 1.4 |
| | Sm | Eu | Gd | Ho | Er | Yb | Lu | Hf | Ta | Pb | Th | U |
| PE6000 | 0.3 | 0.1 | 0.3 | 0.2 | 0.3 | 0.5 | 0.3 | 0.2 | 0.3 | 72 | 0.2 | 0.3 |
| HP4500 | 2.0 | 0.9 | 0.5 | 0.5 | 1.2 | 1.0 | 0.2 | 1.0 | 1.2 | 46 | 0.2 | 0.3 |

Re-Os

Analysis of Re-Os isotopes in whole rock samples was carried out by Dr S. Graham using the GEMOC isotope dilution method for Os concentrations, and Carius tube digestion (after Shirey and Walker, 1995) and solvent extraction for $^{187}Os/^{188}Os$ ratio determination. The Carius tube method is still the only method that ensures spike calibration. Os extraction is achieved using a chloroform solvent extraction method as developed by Pearson and Woodland (2000). After Carius tube digestion and opening the content is then centrifuged. The chloroform layer is removed and added to 4 ml of chilled HBr. This process is repeated three times. The remaining solution is dried down, taken up in $HNO_3$ and Re is extracted by cation exchange chemistry as described in Shirey and Walker (1995). The chloroform-HBr solution is heated (80-90°C) for an hour to facilitate the back-extraction of Os into the HBr. The solution is then allowed to cool and is decanted. The chloroform is discarded and the HBr solution is gently dried down. The Os blank is ca. 5 pg and the Re blank varies from 8-17 pg. Full details on sample preparation, spike calibration and the Re-Os chemical procedure are given on the Analytical Methods page at GEMOC's website (http://www.es.mq.edu.au/GEMOC/).

*Mass spectrometry*

Os was analysed using a *Nu Plasma* multi-collector ICPMS (see Section 2.3.3). Peak centering and the optimum torch position for maximum sensitivity on the MC-ICPMS were determined using a 92 ppb Os solution that was vaporised by a CETAC MCN6000 microconcentric nebuliser. This minimises sample consumption and improves sensitivity, though a possible downside to this method is Os memory in the MCN. Once the peaks were centred and the sensitivity maximised, the MCN was disconnected, and the sparging system connected.

The sample is loaded into a glass vessel with a mixture of $H_2SO_4$ and Nochromix® (a powerful oxidant) and then vigorously shaken and heated to about 120°C. This method allows rapid oxidation and release of the Os, yielding a high signal for a few minutes (typically 10 mins). Following signal acquisition a previously prepared reaction vessel was connected to the gas flow and the mass spectrometer monitored until background voltages on the Faraday cups were detected. Background intensities were usually reach within 15 mins, although longer periods of time were required following samples that had high signal intensity.

Sample acquisition was performed using an "all Faraday" setup, in which masses 194, 192, 190, 189, 187, 186 and 185 were measured. This configuration allowed monitoring and correction of possible isobaric mass interferences from Re (185) and Pt (194) on $^{187}$Os and $^{192}$Os, respectively. Os signals could usually be detected over periods of 5-20 mins and measured Os isotopic ratios were then reported relative to 188Os. Mass fractionation correction and spike stripping were performed off-line.

Re isotopic data ($^{185}$Re and $^{187}$Re) were measured using either the Agilent 4500 or 7500 ICPMS. Samples were interspersed with a Re standard solution every 5 samples to monitor drift and fractionation. Both were found to be negligible. Data reduction was performed off-line.

*Os standard*

Os isotope composition analyses for the WPR-1 PGE standard obtained by MC-ICPMS are presented in Table 2-2. The Os isotopic result is in excellent agreement with the published N-TIMS values available for the same standard: $^{187}$Os/$^{188}$Os =0.14559±0.00073 (n=7; Lambert *et al.*, 1999) and $^{187}$Os/$^{188}$Os =0.14543±0.00018 (n=3; Cohen, 1996). The external reproducibilities are also comparable, demonstrating that MC-ICPMS isotopic measurements are as reliable in terms of long term reproducibility and stability as those determined using N-TIMS. Internal precision (±2SE) of the $^{187}$Os/$^{188}$Os on individual runs for the all-Faraday collector setup ranges from 0.01-0.2% for Os contents varying between ~10 and 100ppb (Alard, 2000).

**Table 2-2.** Results obtained for the WPR-1 PGE standard. Os and Re concentrations are reported in ppb.

| GEMOC: Os MC-ICPMS, Re ICPMS | | | | | |
|---|---|---|---|---|---|
| | Os | Re | Re/Os | $^{187}$Os/$^{188}$Os | $^{187}$Re/$^{188}$Os |
| Mean | 16.78 | 11.63 | 0.69 | 0.14524 | 3.29783 |
| 2SE (M) | 0.28 | 0.09 | 0.01 | 0.00035 | 0.09386 |
| 2SE(M)% | 1.68% | 0.78% | 1.08% | 0.24% | 2.85% |
| Number | 17 | 13 | 13 | 22 | 13 |
| Minimum | 15.92 | 11.36 | 0.67 | 0.14388 | 2.77719 |
| Maximum | 18.29 | 11.93 | 0.72 | 0.14697 | 3.44845 |

## 2.3 *IN SITU* ANALYTICAL TECHNIQUES

### *2.3.1 Electron Microprobe*

Electron microprobe analysis provides major element compositions of individual mineral phases *in situ*. Analyses were carried out using a Cameca Camebax SX50 electron

microprobe fitted with five wavelength-dispersive spectrometers. Normal operating conditions were an accelerating voltage of 15 kV and a sample current of 20 nA. The diameter of the electron beam was 2-3 μm. Standards used were natural minerals (Si; Al-kyanite; Mg-forsterite; Na-albite; K-orthoclase; Ca-wollastonite; Ti-rutile; Cr-chromite; Mn-spessartine; Fe-haematite). Lower limits of detection for silicates are listed in Table 2-3.

Count times used were 10 seconds for peaks with 5 seconds for backgrounds on either side of the peak. Corrections were performed using the Pouchou and Pichoir (1984) method.

**Table 2-3.** Lower levels of detection for 15kV silicates.

| Element | wt % | c/s (20 na) | c/s/wt% | cts bkg | Pk (secs) | Bkg (secs) | LLD (wt%) | % rsd | wt % oxide |
|---|---|---|---|---|---|---|---|---|---|
| $SiO_2$ | 37.000 | 5421.62 | 146.53 | 55.00 | 10 | 10 | **0.07** | 0.429 | 0.159 |
| $TiO_2$ | 100.000 | 11248.32 | 112.48 | 22.00 | 10 | 10 | **0.06** | 0.298 | 0.298 |
| $Al_2O_3$ | 62.700 | 12899.68 | 205.74 | 25.00 | 10 | 10 | **0.03** | 0.278 | 0.175 |
| $Cr_2O_3$ | 45.650 | 1270.78 | 27.84 | 3.50 | 10 | 10 | **0.09** | 0.887 | 0.405 |
| FeO | 89.981 | 3398.98 | 37.77 | 5.70 | 10 | 10 | **0.08** | 0.542 | 0.488 |
| MnO | 40.710 | 1339.78 | 32.91 | 4.60 | 10 | 10 | **0.09** | 0.864 | 0.352 |
| MgO | 50.780 | 7953.06 | 156.62 | 54.00 | 10 | 10 | **0.06** | 0.355 | 0.180 |
| CaO | 48.270 | 5365.12 | 111.15 | 19.60 | 10 | 10 | **0.05** | 0.432 | 0.208 |
| $Na_2O$ | 11.460 | 1293.48 | 112.87 | 10.30 | 10 | 10 | **0.04** | 0.879 | 0.101 |
| $K_2O$ | 15.400 | 1675.22 | 108.78 | 8.80 | 10 | 10 | **0.04** | 0.773 | 0.119 |
| NiO | 71.340 | 2297.86 | 32.21 | 7.30 | 20 | 20 | **0.08** | 0.466 | 0.333 |
| $P_2O_5$ | 17.860 | 936.92 | 52.46 | 1.80 | 10 | 10 | **0.03** | 1.033 | 0.185 |
| Cl | 6.200 | 599.8 | 96.74 | 1.40 | 10 | 10 | **0.02** | 1.291 | 0.080 |
| F | 15.970 | 1879.3 | 117.68 | 18.00 | 10 | 10 | **0.05** | 0.729 | 0.116 |

Mineral compositions were obtained for both cores and rims. In each rock section analyses were made on multiple grains of each phase to determine the degree of intergrain heterogeneity. Analyses used for geothermobarometry were done on touching grain clusters to ensure assemblage equilibrium.

Sulfide inclusions were also analysed using the electron microprobe. Normal operating conditions were an accelerating voltage of 20 kv and a 20 nA sample current. Electron beam diameter was ~5 μm. Count times used were the same as those used for silicate analyses. Standards used were natural minerals (S, Fe, Cu, chalcopyrite, Ni, Co, O). Back-scattered electron images were used to construct maps of sulfide grains. X-ray maps of sulfide grains were produced by a LINK ISIS EDS system. Typically 50-150 frames were acquired in order to obtain the resolution necessary for recognizing the various phases.

### 2.3.2 *LAM-ICPMS*

Minor and trace elements in mineral phases were analysed using the Laser Ablation Microprobe-ICPMS facility in the GAU at Macquarie University. This technique allows rapid and precise (<5%) *in situ* determination of trace element abundances to sub-ppm levels (Norman *et al*, 1996).

The instrument consists of two parts; a laser ablation microprobe in which the sample is ablated, and an ICPMS where the ablated material is ionised and analysed. Two different lasers have been used over the course of this study; an in-house system, based on a Continuum Surelite I-20 Q-switched laser, and designed by S. E. Jackson and H. Longerich, and a Merchantek LUV266. Both are frequency quadrupled Nd-YAG lasers with a beam wavelength of 266 nm and typical operating frequencies of 4-10 Hz. In both cases the beam is directed through a focussing lens onto the polished sample with a typical spot size of 20-200 μm. The ablated material is then carried from the sample chamber to the ICPMS by a stream of high purity argon or helium.

Three quadrupole ICPMS instruments have been used during this study; the Perkin-Elmer Sciex ELAN 6000, Hewlett Packard 4500 (series 300) and the Agilent 7500s, the latter two featuring the shield torch option. Most of the work presented in this thesis has been done with the PE 6000. Typical operating conditions for each ICPMS are reported in Table 2-4. Typical detection limits for elements in silicates for each instrument are reported in Table 2-5.

**Table 2-4** Typical operating conditions for laser-ablation run.

| ICPMS | PE Elan 6000 | Agilent 4500 (s300) Shield torch option | Agilent 7500s Shield torch option |
|---|---|---|---|
| Forward (reflected) power (W) | 1050 | 1300 | 1300 |
| Gas flow (l/min) | | | |
| Plasma | 15 | 15 | 15 |
| Auxiliary | 0.8 | 0.8 | 0.8 |
| Carrier - Ar | 0.9 | 1.0 | 1.35 |
| - He | 0.8 | 0.93 | |
| Detector mode | Dual stage | Dual stage | Dual stage |
| Scanning mode | Peak hopping | Peak hopping | Peak hopping |
| Dwell time (ms) | 50 | 30 | 30 |

Analyses are generally made over 3-4 minutes with over 100 replicates. Each replicate is a sweep of the mass range with dwell times of 50-100 ms. Typically the first 40-60 seconds of the analysis are used to measure the background of the nebulizer gas before ablation is begun. Analyses are normalised to $^{43}Ca$ or $^{25}Mg$ contents previously determined by EMP. The external standards used were the NIST 610 and 612 glasses. This

double normalisation to an internal and external standard allows efficient correction for variations in instrument and ablation yield as well as instrumental drift (Longerich *et al.*, 1996).

**Table 2-5.** Typical detection limits for elements analysed in silicates by LAM-ICPMS. Values are given in ppm.

| | Ni | Ga | Rb | Sr | Y | Zr | Nb | Ba | La | Ce | Pr | Nd |
|---|---|---|---|---|---|---|---|---|---|---|---|---|
| PE6000 | 0.19 | 0.063 | - | 0.01 | 0.009 | 0.022 | 0.01 | - | 0.007 | 0.007 | 0.005 | 0.044 |
| HP4500 | 0.078 | 0.055 | 0.022 | 0.002 | 0.005 | 0.007 | 0.008 | 0.03 | 0.004 | 0.003 | 0.003 | 0.014 |
| HP7500 | 0.08 | 0.016 | 0.01 | 0.006 | 0.006 | 0.014 | 0.007 | 0.025 | 0.005 | 0.004 | 0.003 | 0.015 |

| | Sm | Eu | Gd | Ho | Er | Yb | Lu | Hf | Ta | Pb | Th | U |
|---|---|---|---|---|---|---|---|---|---|---|---|---|
| PE6000 | 0.024 | 0.015 | 0.03 | 0.007 | 0.017 | 0.02 | 0.009 | 0.023 | 0.005 | 0.061 | 0.004 | 0.004 |
| HP4500 | 0.01 | 0.005 | 0.009 | 0.003 | 0.014 | 0.007 | 0.003 | 0.008 | 0.003 | 0.031 | 0.003 | 0.003 |
| HP7500 | 0.01 | 0.005 | 0.01 | 0.003 | 0.012 | 0.012 | 0.003 | 0.01 | 0.004 | 0.036 | 0.004 | 0.005 |

Data reduction was carried out on-line using GLITTER (GEMOC Laser ICPMS Total Trace Element Reduction) an interactive program developed by GEMOC (van Achterbergh *et al.*, 1999). This software allows real-time interactive data reduction for LAM-ICPMS analysis, allowing inspection and evaluation of each result before the next analysis spot is chosen (GEMOC Annual Report, 1998. http://www.es.mq.edu.au/GEMOC/).

### *2.3.3 Multi-Collector LAM-ICPMS*

The recent acquisition of a multi-collector LAM-ICPMS at GEMOC has enabled the development of a method for high-precision *in situ* analysis of Re-Os isotopes in sulfide minerals. The multi-collector LAM-ICPMS consists of a Merchantek LUV266 nm laser microprobe attached to a *Nu Plasma* multi-collector magnetic sector ICPMS (Griffin *et al.*, 2000; Pearson *et al.*, 2002). The *Nu Plasma* instrument is a double-focussing Nier Johnson design with an array of 12 fixed Faraday cup detectors, 3 ETP ion counters and a unique pair of quadrupole lenses, which adjusts the image magnification of the detector array (Belshaw *et al*, 1998; Griffin *et al.*, 2000). The sample cell for the Merchantek laser was replaced with a cell designed by S.E. Jackson for improved signal stability and precision. Analyses were carried out by Prof. W.L. Griffin, O. Alard and Dr S. Graham.

Typical laser operating conditions used in this study were a frequency of 5 Hz and beam energy of 3-5 mJ/pulse producing spot sizes in the range 60-120 microns. Ablation was carried out in a He atmosphere and the He-sample mixture was passed through a

mixing chamber before blending with Ar prior to introduction into the ICP. Measurements were made in static collection mode using a "mixed array" of Faraday cups and ion counters:

masses 194, 193, 192, 191, 190, 189, 188, 186 were measured in Faraday cups; masses 187 and 185 were measured in ion counters.

The combined Faraday-ion counter technique was developed to make it possible to measure lower Os abundances by placing the smaller $^{187}$Os isotope and both Re isotopes in the ion counters. This has been shown to improve the precision on $^{187}$Os and on the Re overlap correction. Relative fractionation coefficients for Os, Re and Ir (introduced as dry sample and used as an internal isotope standard) can be considered as being internally consistent based on results from Ir-Os and Ir-Re solutions (Pearson *et al.*, 2002). All analyses were corrected for mass bias using the exponential law and normalised to $^{191}$Ir/$^{193}$Ir = 0.59359 (http://www.es.mq.edu.au/ GEMOC/).

Analyses of a synthetic NiS bead (PGE-A), with 204±14 ppm of Os of known isotopic composition, were undertaken to assess the precision of the measured $^{187}$Os/$^{188}$Os as a function of signal intensity, laser spot size and analysis duration. Average $^{187}$Os/$^{188}$Os ±2sd for PGE-A using the "mixed array" setup is approximately 0.10635±0.0003 with precision between 0.1% and 0.5%. Drift correction was carried out by running each unknown analysis in between analyses of PGE-A, and then normalising to PGE-A. Drift was demonstrated to be linear with time.

## 2.4 GEOTHERMOBAROMETRY

### *2.4.1 Spinel peridotites*

Introduction

Equilibrium temperatures for spinel peridotites can be calculated by a variety of thermometers. Two-pyroxene thermometers are based on the compositions and mixing properties of co-existing clinopyroxene and orthopyroxene (e.g. Wood and Banno, 1973; Wells, 1977 [W]; Kretz, 1982; Brey and Kohler, 1990 [BKN]). An empirical thermometer based on the CaO contents and the solubilities of $Al_2O_3$ and $Cr_2O_3$ in orthopyroxene coexisting with olivine, clinopyroxene and spinel has been developed by Sachtleben and Seck (1981) [SS]. This thermometer has since been recalibrated by Witt-Eickschen and Seck (1991) [WES-1], who also developed another empirical thermometer based on the

solubilities of Cr and Al in orthopyroxene [WES-2]. A third type of thermometer is based on Ca content in orthopyroxene e.g. Brey and Kohler (1990) [BKCa].

Xu *et al.* (1998) reassessed geothermobarometry techniques for spinel peridotites in light of ongoing new calibrations. A comparison of the [SS], [WES-2] and [BKCa] on spinel±garnet lherzolites from eastern China and western Victoria led to the conclusion that these three thermometers give very similar temperatures with [SS] slightly higher at higher temperatures. Comparison of the Wells (1977) two-pyroxene thermometer with Sachtleben and Seck (1981) for the eastern China lherzolites shows [W] consistently underestimates temperatures by ~50°C. Another recent review of geothermobarometric methods by Smith (1999) concludes that, potentially, the most accurate thermometers for spinel peridotites at temperatures below 1000°C are [BKCa] and [WES-2].

There is no reliable geobarometer for spinel lherzolites. The Ca-in-olivine barometer developed by Kohler and Brey (1990) is not appropriate for these rocks due to the low concentration of calcium in olivine and the strong temperature dependence of this barometer. O'Reilly *et al.* (1997) have shown that the uncertainty in pressure (calculated by this method) is ca ±8 kbar, which corresponds to the entire pressure range of the spinel lherzolite field at 900-1200°C. However, this barometer is useful in the garnet lherzolite P-T field for which it was calibrated (O'Reilly *et al.*, 1997).

An alternative to directly calculating equilibrium pressures is outlined in O'Reilly and Griffin (1985) and involves extrapolating calculated temperatures to the relevant regional geotherm. In the case of Tasmanian spinel lherzolites the southeastern Australian (SEA) geotherm (O'Reilly and Griffin, 1985) is used as discussed in section 2.4.2 below.

Sachtleben and Seck (1981) thermometer [SS]

The solubility of Al in orthopyroxene coexisting with olivine and spinel can be expressed by the reaction enstatite + spinel ↔ Mg-Tschermaks + forsterite (Fujii, 1976; Danckwerth and Newton, 1978; Gasparik and Newton, 1984). This reaction is primarily a function of temperature with very minor pressure effects and has led to the widespread view that Al-solubility in orthopyroxene has the potential to be a useful tool for geothermometry of natural spinel peridotites. Additional work on the dependence of Al in opx temperatures on Cr content of spinel led Sachtleben and Seck (1981) to formulate their thermometer. The authors suggest that, providing equilibrium was reached, this geothermometer should be applicable to peridotitic rocks in the temperature range 950-1150°C.

Witt-Eickschen and Seck (1991) revised Sachtleben and Seck (1981) based on temperatures derived from the re-evaluation of Ca content in orthopyroxene (Brey and Kohler, 1990). Fitting of $X_{Al}^{opx}$ and $X_{Cr}^{opx}$ to temperatures derived from [BKCa] also allowed Witt-Eickschen and Seck (1991) to develop their Cr-Al-opx thermometer [WES-2]. It must be remembered when applying this thermometer that is valid only over a limited range of $X_{Al}^{opx}$ and $X_{Cr}^{opx}$ in orthopyroxene (see Fig. 5-18 in Chapter 5). Testing by Xu *et al.* (1998) shows very little difference between [SS] and [WES-2] temperatures for eastern China and southeastern Australian spinel peridotites and suggested that [SS] is still a reliable geothermometer for spinel-bearing lherzolites.

Brey and Kohler (1990) thermometer [BKCa]

This geothermometer is based on the solubility of Ca in orthopyroxene in equilibrium with clinopyroxene and was derived from experimental results in the CMS ($CaO$-$MgO$-$SiO_2$) system (Brey *et al.*, 1990). While the geothermometer was able to reproduce experimental temperatures the authors suggest that it should be used with caution in its application to natural systems as the influence of Na on Ca content in orthopyroxene is uncertain and they were not able to devise a reasonable correction scheme for natural mineral compositions. Brey and Kohler (1990) point out that this thermometer is calibrated only for magnesian ultramafic compositions and advise against its application to other compositions. Likewise Xu *et al.* (1998) recommend that this thermometer only be used for Mg-rich spinel and garnet pyroxenites, and spinel and garnet lherzolites. A pressure of 15 kbar was assumed in applying this thermometer to spinel lherzolites.

Wells (1977) thermometer [W]

This thermometer was developed by applying simple mixing models to orthopyroxene and clinopyroxene solid solutions and extracting a semi-empirical equation of state from available experimental data for the diopside-enstatite miscibility gap. Calibrated over a temperature range of 785-1500°C, the Wells thermometer is only valid for compositions $X_{Fe}^{opx}$=0.0-1.0, and ($Al_2O_3$ in cpx)=0.0-10 wt%. Temperatures calculated within these calibration ranges should be accurate to 70°C. Xu *et al.* (1998) recommend that this thermometer only be applied to Fe-rich spinel pyroxenites.

### 2.4.2 *Southeastern Australian Geotherm*

The southeastern Australian geotherm was constructed originally from a suite of well-equilibrated garnet websterites from Lakes Bullenmerri and Gnotuk, two Quaternary maars in western Victoria. P-T estimates for these rocks were calculated using the Ellis and Green (1979)/Wood (1974) combination for garnet-two pyroxene (± olivine) assemblages (O'Reilly and Griffin, 1985). Data from other localities with appropriate mineral assemblages plot very close to the SEA geotherm and have allowed its extension to higher and lower P (O'Reilly and Griffin, 1985).

This geotherm lies well above the conventional oceanic geotherm of Pollack and Chapman (1977) reflecting high heat flow. The high T at shallow depths (ca. 25-40 km) as indicated by the curve implies significant advective heat transfer which is probably related to the intrusion of basaltic melts at the crust-mantle boundary (Griffin *et al.*, 1984; O'Reilly and Griffin., 1996). At depths greater than 100 km the geothermal gradient converges towards more normal adiabatic values (Griffin *et al.*, 1984). Data from Tertiary to Mesozoic localities (Jugiong, Delegate) define essentially the same geotherm suggesting that the high heat flow observed in southeastern Australia today has characterised the region during volcanic episodes since Mesozoic time (Griffin *et al.*, 1984).

The occurrence of composite spinel lherzolite/garnet-pyroxenite xenoliths in the western Victorian suite allows the referral of Sachtleben and Seck (1981) or Brey and Kohler [BKCa] (1990) temperatures to the SEA to give depths of equilibration in the mantle (O'Reilly and Griffin, 1985). These xenoliths show contacts between spinel lherzolite and garnet pyroxenite which have originated at the same depth in the mantle and therefore should give similar equilibrium temperatures. Griffin *et al.* (1984) determined that the SS geothermometer for spinel lherzolites was directly comparable with the EG geothermometer used for the garnet websterites. It was concluded that the SEA can be justifiably used to estimate P for spinel lherzolites as discussed below.

Although the southeastern Australian geotherm was constructed using data from one lithospheric section beneath western Victoria, it has been found that pressure-temperature estimates fulfilling the criteria specified by Griffin and O'Reilly (1987a), and calculated for other appropriate xenolith assemblages from eastern Australia, fall along this geotherm (O'Reilly, 1989a). These include garnet websterites and garnet granulites from various localities in Victoria and New South Wales, and garnet lherzolites from Jugiong, New South Wales and Bow Hill, Tasmania. In addition, a detailed study of lower-crustal granulites and garnet-bearing websterites from a depth range of 15-55 km beneath central

Queensland (Griffin *et al.*, 1987) produced equilibration pressure-temperature values that coincide with those for the SEA geotherm (O'Reilly, 1989a). Based on evidence, that this geotherm appears to apply to all eastern Australian basaltic provinces sampled thus far, it has been chosen as the most appropriate geotherm for estimating equilibration pressures for Tasmanian spinel lherzolites.

### *2.4.3 Garnet peridotites*

There are numerous geothermometers and geobarometers that are applicable to garnet-bearing ultramafic assemblages.

Geothermometers

The most useful geothermometers for four-phase lherzolite assemblages are mineral thermometers based on $Ca^{2+}$-$Mg^{2+}$ exchange between co-existing pyroxenes (two pyroxene solvus) and those based on $Fe^{2+}$-$Mg^{2+}$ exchange between garnet and the other mineral phases (Jamtveit *et al.*, 1991). Evaluation of the $Fe^{2+}$-$Mg^{2+}$ exchange reaction thermometers (Carswell and Gibb, 1987) has indicated that the most reliable temperature estimates are provided by the formulations of Powell (1985) and Ellis and Green (1979) for garnet-clinopyroxene pairs, Harley (1984) for garnet-orthopyroxene pairs, and O'Neill and Wood (1979; correction 1980) for garnet-olivine pairs. Krogh (1988) constructed a new expression for the garnet-clinopyroxene geothermometer using the experimental $Fe^{2+}$-Mg partitioning data of Ellis and Green (1979) and others. The main uncertainty in applying these thermometers to natural samples arises from the assumption that all Fe is present as $Fe^{2+}$ in electron microprobe analyses of the mineral phases. Calculation of $Fe^{3+}$ contents by stoichiometric charge balance in the minerals concerned suggests the presence of, at most, only minor amounts of $Fe^{3+}$ which, when set against the level of analytical precision, can probably be ignored (Jamtveit *et al.*, 1991).

This problem with Fe oxidation state can be avoided by the use of two-pyroxene solvus thermometers, though it is unfortunately less sensitive throughout the whole P-T range of interest in these rocks (Carswell and Gibb, 1987). The formulations considered to provide the best temperature estimates are Wells (1977), and Brey and Kohler (1990), although the thermometer of Wells (1977) has a tendency to underestimate T at pressures greater than 37 kbar. This is possibly because it lacks a term to correct for the influence of pressure on the pyroxene miscibility gap. Another thermometer which avoids the $Fe^{3+}/Fe^{2+}$

problem is the Ca-in-opx thermometer of Brey and Kohler (1990) which has been calibrated for Mg-rich garnet lherzolites and pyroxenites.

The Ni-in-garnet geothermometer (Griffin *et al.*, 1989; recalibrated by Ryan *et al.*, 1996) is a single-mineral thermometer based on a empirical calibration of the partitioning of Ni between co-existing Cr-pyrope garnet and olivine in mantle-derived materials. The distribution co-efficient $D_{Ni}^{gnt/ol}$ is strongly temperature dependent, varying by two orders of magnitude over temperatures encountered in the lithosphere. The variation in $D_{Ni}^{gnt/ol}$ is almost entirely due to the temperature dependence of the Ni content of the garnet and it is assumed that each garnet has equilibrated with olivine of uniform Ni content. The thermometer has been calibrated for a temperature range of 640-1550°C, a pressure range of 20-68 kbar, and a range of geotherms and rock types. The thermometer appears to be insensitive to large variations in the Ca, Al and Cr contents of the garnet.

Geobarometers

Geobarometers for garnet-bearing mantle peridotites are based on the Tschermak's molecule content of orthopyroxene coexisting with garnet. Testing of twelve barometers by Carswell and Gibb (1987) found that only the calibration by Nickel and Green (1985) yielded satisfactory results. The Nickel and Green (1985) barometer was derived through thermodynamic calculations in the CMAS (CaO, MgO, $Al_2O_3$, $SiO_2$) and SMACCR ($SiO_2$, MgO, $Al_2O_3$, CaO, $Cr_2O_3$) systems and calibrated for pressures of 20-40kbar and temperatures of 1000-1400°C. With thermodynamic/empirical corrections for the influence of Fe this barometer most closely models the compositions of naturally occurring garnet lherzolites (Carswell and Gibb, 1987).

Brey and Kohler (1990) reached a similar conclusion from tests of these barometers with the experimental data presented in Brey *et al.* (1990), and from their own experiments which are reproduced best with the formulation of Nickel and Green, though only in the pressure range of the experiments on which their calibration was based. The barometer of Brey and Kohler (1990) is based on the thermodynamic evaluation of the $MgO$-$Al_2O_3$-$SiO_2$ (MAS) system by Gasparik and Newton (1984) and calibrated against experimental P/T data in both simple and natural systems.

## 2.5 OXYGEN FUGACITY

### *2.5.1 Introduction*

Oxidation states of mantle material can be measured using either oxygen-specific

electrochemistry which determines the "intrinsic" oxygen fugacity ($fO_2$) of the rock (Arculus and Delano, 1981) or by employing any of a number of thermobarometric calculations which determine oxygen fugacity from mineral compositions (Chen *et al.*, 1991). The thermobarometric method is considered by Wood *et al.* (1990) to be the most promising of the two because it relies on properties of the minerals that cannot be rapidly reset during cooling or perturbed by normal measurement techniques. The oxygen barometers of Nell and Wood (in Wood *et al.*, 1990), Mattioli and Wood (1988) and Ballhaus *et al.* (1991) have been used in this thesis to calculate oxygen fugacities for spinel lherzolite xenoliths from Tasmania and descriptions of the three methods are outlined in Section 2.5.2.

As has been done in other studies (Mattioli *et al.*, 1989; Ballhaus *et al.*, 1991; Chen *et al.*, 1991; Amundsen and Neumann, 1992) the amount of $Fe^{3+}$ in spinel has been calculated on the basis of microprobe analyses, assuming that this phase maintains stoichiometry in the $fO_2$ range of concern (Wood *et al.*, 1990); iron in olivine and orthopyroxene is assumed to be entirely $Fe^{2+}$. Concern for the accuracy in ferric contents calculated in this way (Dyar *et al.*, 1989; Wood and Virgo, 1989) has led to several studies which have compared $Fe^{3+}$ contents determined by stoichiometry with those obtained from Mössbauer spectroscopy, a method which greatly reduces systematic errors in measured $Fe^{2+}/Fe^{3+}$ (Wood and Virgo, 1989; Canil *et al.*, 1990; Canil *et al.*, 1994). Ballhaus *et al.* (1991) re-evaluated this matter and concluded that $Fe^{3+}$ calculation from EMP analyses gives reasonable results. In terms of calculated $\Delta \log fO_2$ the differences between ferric iron determined by stoichiometry and by Mössbauer spectroscopy was found to be less than 0.4 log units, and the differences are random (Ballhaus *et al.*, 1991).

Oxygen fugacities calculated for natural mantle assemblages are normally compared to the values of well-known end-member reactions for Fe in all three oxidation states i.e. Fe(O), Fe(II) and Fe(III) (Wood *et al.*, 1990). The reactions of importance for upper mantle compositions are:

IW $\quad Fe(metal) + 1/2\ O_2 = FeO$ (wüstite)

WM $\quad 3FeO$ (wüstite) $+ 1/2\ O_2 = Fe_3O_4$ (magnetite)

QFM $\quad 3SiO_2$ (quartz) $+ 2Fe_2O_3$ (magnetite) $= 3Fe_2SiO_4$ (fayalite) $+ O_2$.

The convention is to report oxygen fugacities as the difference ($\Delta \log fO_2$) between the calculated $\log fO_2$ and the quartz-fayalite-magnetite (QFM) buffer.

### 2.5.2 *Oxygen barometers*

Nell and Wood (1990)

Nell and Wood's formulation is based on the reaction:

$$\underset{\text{olivine}}{6Fe_2SiO_4} + O_2 = \underset{\text{opx}}{6FeSiO_3} + \underset{\text{spinel}}{2Fe_3O_4}$$

and involves measuring the concentrations of $Fe_2SiO_4$, $FeSiO_3$ and $FeO_4$ components in the olivine, orthopyroxene and spinel phases, respectively, and calculating $fO_2$ from thermodynamic data on the end-member reactions with the use of activity-composition relations for the complex phases (Wood *et al.*, 1990). By incorporating datasets of earlier versions of this barometer and using new measurements of cation disorder they produced the following equation for calculating oxygen fugacity:

$$\Delta \log(fO_2)^{QFM} = 220T + 0.35 - 0.0369P/T - 12\log X_{Fe}^{sp} - 2620/T(X_{Mg}^{ol})^2$$
$$+3\log(X_{Fe}^{M1} \cdot X_{Fe}^{M2})^{opx} + 2\log a_{Fe_3O_4}^{sp}$$

This version has no apparent composition dependence and yields good agreement between calculated and actual experimental $fO_2$ (Wood *et al.*, 1990). Other versions of this barometer include those of Mattioli and Wood (1988) and O'Neill and Wall (1987).

Ballhaus *et al* (1991)

Synthetic spinel harzburgite and lherzolite assemblages were equilibrated under P-T-$fO_2$ conditions representative of the upper mantle and the compositional variations in the olivine-orthopyroxene-spinel assemblage produced in the experiments were used to formulate a semi-empirical oxygen barometer. A linear least-square fit through the experimental data gives

$$\Delta \log(fO_2)^{QFM} = 0.27 + 2505/T - 400P/T - 6\log(X_{Fe}^{olv}) - 3200(1 - X_{Fe}^{olv})^2/T$$
$$+2\log(X_{Fe^{2+}}^{sp}) + 4\log(X_{Fe^{3+}}^{sp}) + 2630(X_{Al}^{sp})^2/T.$$

This equation is specifically designed for upper mantle-derived rocks and, while applicable to the entire spectrum of spinel compositions occurring in mantle rocks, should not be applied to assemblages that are significantly enriched in iron i.e. $X_{Fe}^{olv} \geq 0.15$. Equilibration temperatures used in the calculation can be determined with any thermometer with proven reliablity for mantle assemblages and in this case the olivine-opx-spinel thermometer of Sachtleben and Seck (1981) has been used. In the absence of an accurate geobarometer for spinel lherzolite assemblages, pressures were set at 1.5 GPa which

essentially is in the middle of the spinel stability field. Application of the Ballhaus *et al.* (1991) barometer to natural assemblages suggests that it gives reasonable results down to temperatures as low as 800°C.

# CHAPTER 3
# TASMANIAN GEOLOGY

## 3.1 INTRODUCTION

On a broad scale Tasmania can be divided into two major terrains. The western terrain, which makes up about two-thirds of the state, is composed of a number of Precambrian blocks separated and/or overlain by belts of lower to middle Palaeozoic rocks of highly variable provenance and composition (Berry *et al.*, 1990). The northeastern terrain is characterised by lower Palaeozoic turbiditic shales and sandstones (the Mathinna Group) which have been folded and intruded by Devonian granitoids, and by an absence of known Precambrian rocks (Berry *et al.*, 1990; Seymour and Calver, 1995). The boundary between the two terrains is not exposed but is believed to lie within the Tertiary graben occupied by the Tamar River.

Tasmania can be further divided into seven Proterozoic-lower Palaeozoic regions or "elements" (Seymour and Calver, 1995). These elements comprise King Island, the Rocky Cape Element, the Dundas Element, the Sheffield Element, the Tyennan Element, the Adamsfield-Jubilee Element, which are all part of the western terrain, and the Northeast Tasmania Element which is equivalent to the eastern terrain (see Fig.3-1).

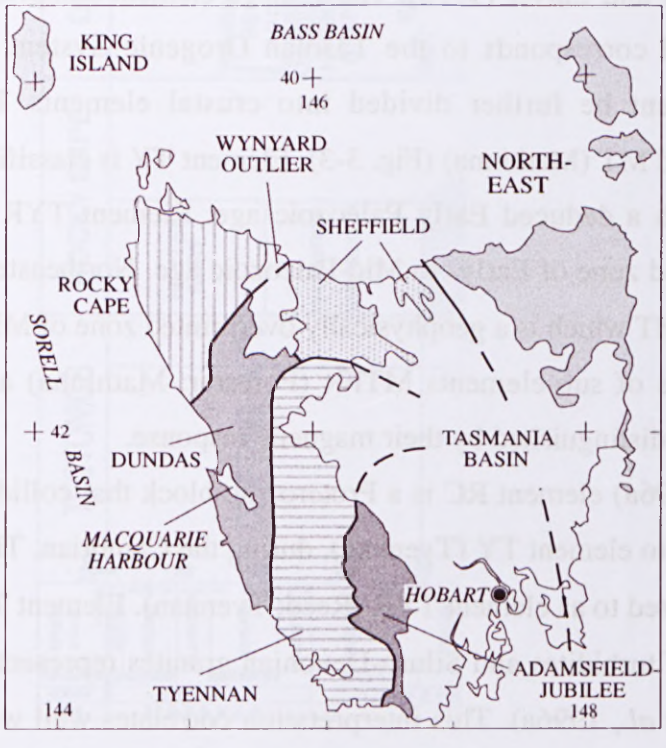


**Figure 3-1.** Main subdivisions or "Elements" in Tasmania. Heavy dashed lines are concealed Element boundaries (Fig. 375 from Veevers, 2000a, after Seymour and Calver, 1995)

Seymour and Calver's subdivision of Tasmania is based on geological mapping and results from the 'Magnetic anomaly map of Australia' (Milligan and Tarlowski, 1999). Each of the elements has a geological history and internal structure that differs in at least some respects from those of the other elements. The geological and tectonic history of Tasmania presented in Section 3.2.1, and summarised in a time-space diagram in Fig. 3-2 (p. 38A), is a brief overview of the events given in Seymour and Calver (1995) and supporting references.

An alternate subdivision for Tasmania is based on the Australian Crustal Elements map (Shaw *et al.*, 1996b). This map delineates upper-crustal elements defined primarily on composite geophysical domains, each of which shows a distinctive pattern of gravity and magnetic anomalies. Australia can be divided into eight "mega-elements" which represent groups of crustal elements having similar geological and geophysical characteristics (see inset in Fig. 3-3). Crustal elements are classified on the basis of their geophysical character, their spatial relationships to each other and the deduced relative age of their source rocks. Age limits for each element were deduced by determining relative ages of the domains from structural relationships between adjoining elements and then assigning an age-range for the sources of the dominant magnetic and gravity signals.

Tasmania consists of two mega-elements; the South Australia mega-element (SA) and the Tasman mega-element (T) (see inset in Fig. 3-3). The SA mega-element corresponds to the Rocky Cape (RC) crustal element of Shaw *et al.* (1996b) and the Rocky Cape element as defined by Seymour and Calver (1995). The T mega-element comprises the remaining part of the state and corresponds to the Tasman Orogenic System of Wellman (1995). This mega-element be further divided into crustal elements TY (Tyennan), TYR (Reed; Tyennan) and MT (Mathinna) (Fig. 3-3). Element TY is classified as a "standard" crustal element with a deduced Early Paleozoic age. Element TYR is classed as a geophysically overprinted zone of Early- to Mid-Paleozoic age. Northeastern Tasmania is represented by element MT which is a geophysically overprinted zone of Mid-Paleozoic age. Element MT consists of sub-elements MTFR (Forester; Mathinna) and MTLE (Lefroy; Mathinna) which are distinguished by their magnetic response.

According to Shaw *et al.* (1996a) element RC is a Proterozoic block that collided with a younger block, corresponding to element TY (Tyennan), during the Cambrian. This produced a zone of overprinting referred to as element TYR (Reed; Tyennan). Element TY is bordered and overlain by a unit of turbidites and Siluro-Devonian granites represented by element MT (Mathinna) (Shaw *et al.*, 1996a). This interpretation correlates well with

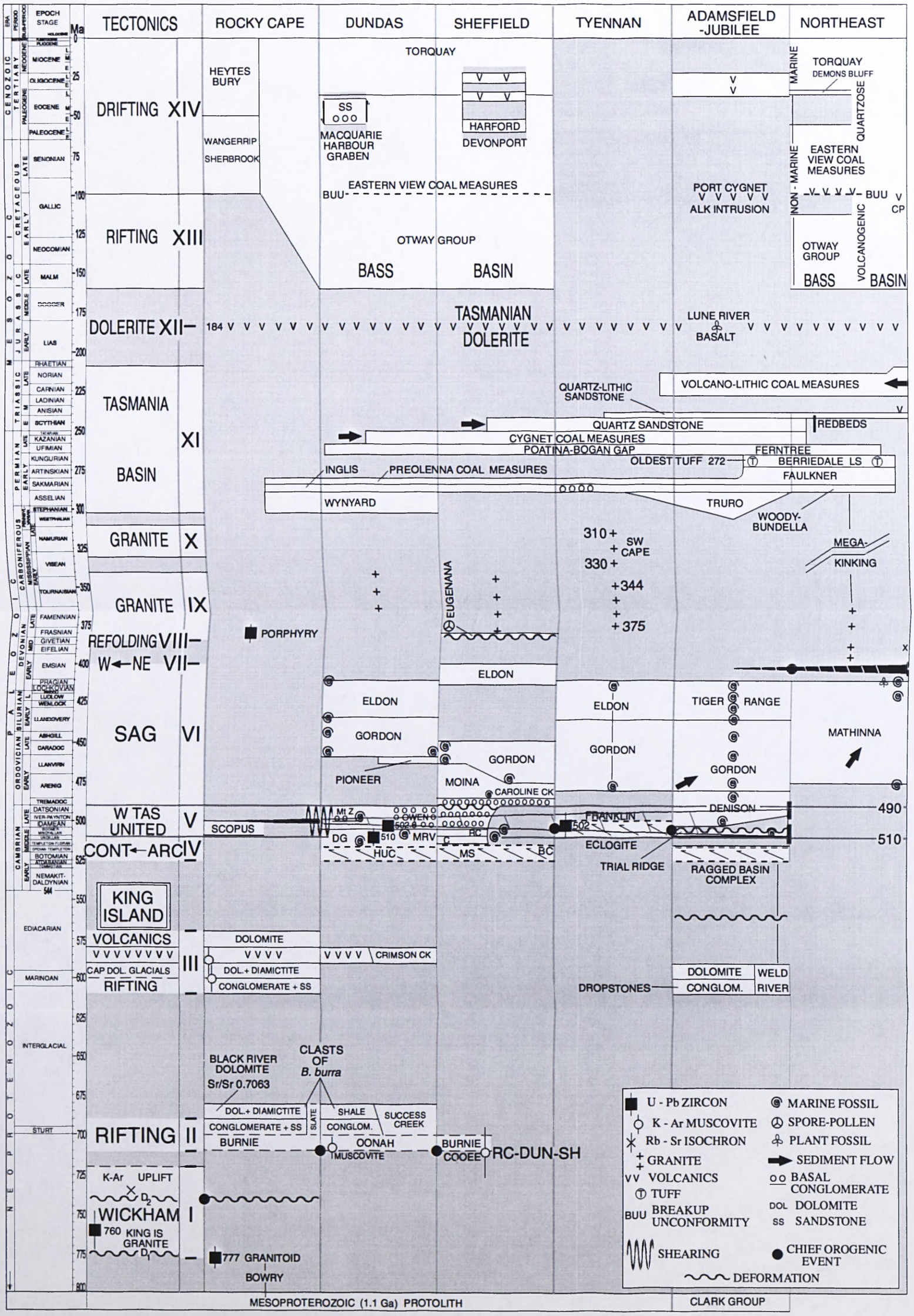


**Figure 3-2.** Time-space diagram across Tasmania (after Veevers, 2000a)

the geological evidence and illustrates the importance of incorporating geophysical datasets when constructing, and constraining, tectonic models.

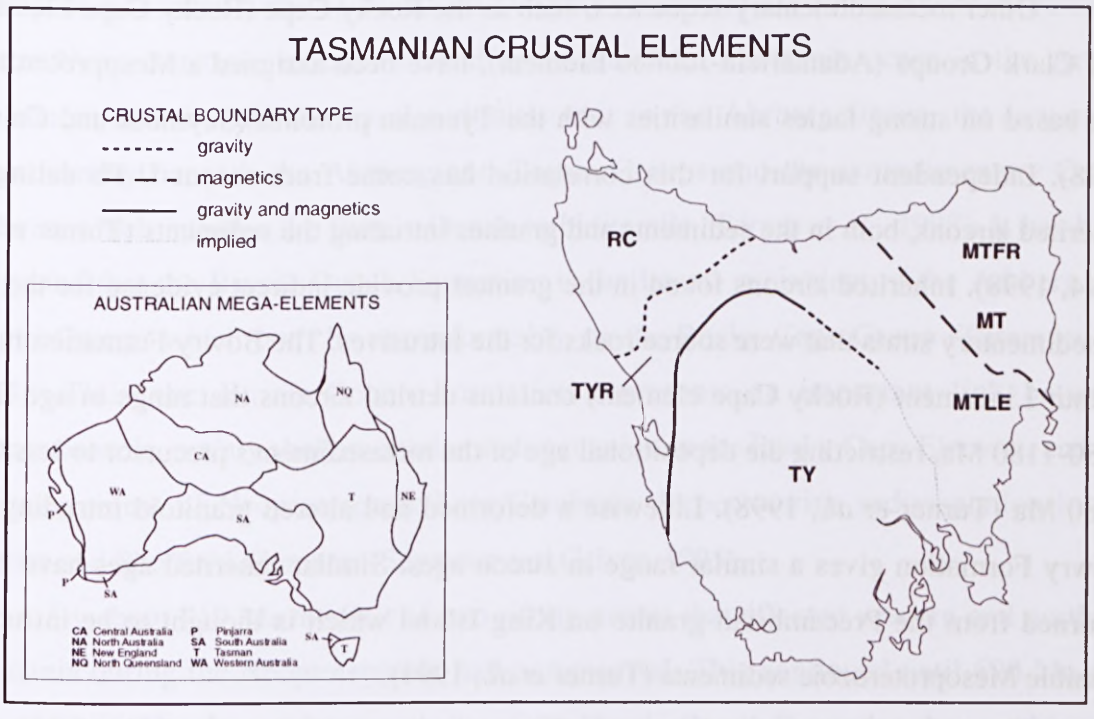


**Figure 3-3.** Map of Tasmanian crustal elements. After Shaw *et al.* (1996b). See text for description of elements. Inset. Australian mega-elements map (Shaw *et al.*, 1996b).

For the purposes of this thesis the stratotectonic elements of Seymour and Calver (1995) will be used as the preferred subdivision of Tasmania. The crustal elements of Shaw *et al.* (1996b), while not geologically defined features, do delineate differing geophysical domains in Tasmania, albeit on a broad scale, and may help shed some light on the tectonic development of the state.

## 3.2 GEOLOGICAL SETTING

### *3.2.1 Geological and tectonic history*

Proterozoic rock sequences occupy about one-third of the surface area of Tasmania. The largest areas of Proterozoic rocks are the contiguous Tyennan and Adamsfield-Jubilee regions which form a belt in the centre of the state, and the Rocky Cape region which makes up the northwestern corner of Tasmania (Seymour and Calver, 1998). The oldest exposed rocks in Tasmania are metapelites occurring in the Tyennan Element and interpreted to be Mesoproterozoic in age. These rocks are dominated by polydeformed and variably metamorphosed (lower amphibolite to eclogite facies) quartzarenite, pelite and minor carbonate (Seymour and Calver, 1998). The original age of the sedimentary protolith is indicated by Rb-Sr model ages which range from 1100-1150

Ma and are considered likely to correspond to the age of deposition (Råheim and Compston, 1977).

Other metasedimentary sequences, such as the Rocky Cape (Rocky Cape Element) and Clark Groups (Adamsfield-Jubilee Element), have been assigned a Mesoproterozoic age based on strong facies similarities with the Tyennan protolith (Seymour and Calver, 1998). Independent support for this correlation has come from recent U-Pb dating of inherited zircons, both in the sediments and granites intruding the sediments (Turner *et al.*, 1994, 1998). Inherited zircons found in the granites provide indirect evidence for the age of sedimentary strata that were source rocks for the intrusives. The Bowry Formation in the Arthur Lineament (Rocky Cape element) contains detrital zircons that range in age from 1880-1180 Ma, restricting the depositional age of the metasediment's precursor to less than 1180 Ma (Turner *et al.*, 1998). Likewise a deformed and altered granitoid intruding the Bowry Formation gives a similar range in zircon ages. Similar inherited ages have been returned from the Precambrian granite on King Island which is thought to be intruding possible Mesoproterozoic sediments (Turner *et al.*, 1994).

The oldest demonstrated event in Tasmania is recorded as the 760±12 Ma syn-kinematic intrusion of the King Island Granitoid (Turner *et al.*, 1994). Partly synchronous with intrusion was polyphase deformation of the ?Mesoproterozoic sequence and metamorphism to amphibolite facies (Cox, 1989). This deformation has been recognised as the Wickham (previously Tyennan) Orogeny which is interpreted as reflecting docking of King Island and Rocky Cape Elements (Veevers, 2000a p. 352, based on U-Pb zircon ages from Black *et al.*, 1997). The Wickham Orogeny appears to have had only a weak effect on the Tasmanian mainland (see below), and has been provisionally correlated with the granite (777±7 Ma) intruding the Bowry Formation (Seymour and Calver, 1998).

The Rocky Cape Group is considered to represent the oldest exposed sequence in the Rocky Cape Element (Turner *et al.*, 1992). It is separated from the younger Burnie-Oonah Formation to the east by the Arthur Lineament. The Arthur Lineament (or Arthur Metamorphic Complex) is a linear belt of regionally metamorphosed and highly deformed rocks that are equivalent to the Rocky Cape Group and Oonah Formation (Seymour and Calver, 1995). The Rocky Cape Group forms the most areally extensive outcrop in the region and consists of several kilometres of relatively unmetamorphosed shallow marine quartzarenite, siltstone, mudstone and subordinate dolomite (Turner, 1989).

The Burnie-Oonah quartz turbidite overlies the Bowry Formation and extends east of the Arthur Lineament and into the Dundas and Sheffield Elements. The Burnie-Oonah

sequence has been dated as 710-690 Ma (Veevers, 2000a) and it is likely that its deposition was the major event in northwestern Tasmania reflecting the general period of instability and uplift associated with the Wickham Orogeny (Turner *et al.*, 1998). Other expressions of the Neoproterozoic mountain-building in mainland Tasmania occur in the Arthur Lineament and include the basal turbiditic unit in the Ahrberg Group, the low-angle unconformity beneath the Ahrberg and Togari Groups and the synsedimentary Cooee Dolerite which intrudes the Burnie-Oonah turbidite pile (Turner *et al.*, 1998). It has been suggested that the Burnie-Oonah Formation is the lateral equivalent of the Arhberg and Togari Groups which both lie unconformably on the Rocky Cape Group (Turner *et al.*, 1994). Thus the Burnie-Oonah Formation represents an important link between Neoproterozoic, mainly shallow-marine sedimentation in the Rocky Cape Element, and the commencement of Neoproterozoic-Late Cambrian deeper marine sedimentation in the Dundas and Sheffield Elements (Seymour and Calver, 1995).

By about 710 Ma the first of two rifting events that affected western and northern Tasmania during the Neoproterozoic had commenced. This continued until 690 Ma and was dominated by the overlap succession of the Burnie-Oonah Formation thus marking the minimum age of accretion of Rocky Cape, Dundas and Sheffield Elements (Veevers, 2000a). Basins and troughs produced during rifting include the Dundas and contiguous Dial Range and Fossey Mountain Troughs, the Smithton Basin and the Adamsfield Trough (Williams, 1989). Shallow marine sediments accumulated in the these troughs and basins until the second rifting event when they began to fill with mafic volcanics. The second event started around 600 Ma and involved a broad zone of extensive tholeiitic volcanism that continued until 570 Ma (Berry, 1994; Veevers, 2000a).

The next major tectonic event to affect Proterozoic Tasmania was E-W arc-continent collision and obduction that has been dated at 525-510 Ma. It is thought that the passive margin of eastern Australia collided with an oceanic arc, resulting in major slices of forearc lithologies being thrust over Tasmania (Berry, 1994). The outcome of this collision was widespread orogenesis (Tyennan Orogeny) and structural emplacement of allochthonous elements as major thrust sheets in western Tasmania. These exotic units include mafic/ultramafic complexes, the Forth and Badger Head Metamorphic Complexes (Sheffield Element) and eclogites in the Tyennan Massif (Berry, 1994). The Tyennan Orogeny is thought to be responsible for most of the deformation in the Rocky Cape Group, the Arthur Lineament and the Burnie-Oonah Formation.

There are some conflicting views in the literature on the naming and timing of the Tyennan Orogeny and whether or not it is a separate orogeny or simply an early phase of the Delamerian Orogeny. Seymour and Calver make no mention of the Tyennan orogeny in their 1995 paper but refer to the deformation event ca 510 Ma as the Penguin Orogeny as does Corbett (1994). Their later paper, Seymour and Calver (1998), revises this name and now refers to the Tyennan Orogeny as taking place between 514-510 Ma with no mention of the Penguin Orogeny. The Penguin Orogeny has been reported by Berry (1994) as occurring around 700 Ma though the author expresses some doubt at the validity of this age. Turner *et al.* (1998) define a minimum age for the Penguin Orogeny at ca 500 Ma making it indistinguishable from the Tyennan Orogeny which the authors define as commencing with high-pressure metamorphism at 502±8 Ma and ending with uplift and volcanism in the Early Ordovician. The Delamerian Orogeny is almost universally reported as taking place in Tasmania from 510-490 Ma (Turner *et al.* (1998) define the Tyennan Orogeny as being related to the Delamerian Orogeny in South Australia but do not appear to recognise the Delamerian as an event affecting Tasmania).

As the descriptions and definitions of the Penguin and Tyennan Orogenies are very similar, i.e. their timing (c. 510-500 Ma), emplacement of allochthonous elements, high-pressure metamorphism, the two can probably be considered synonymous. This does lead to some overlap with the Delamerian Orogeny and it has been suggested by N. Turner (see Leaman, 1994b) that the two orogenies are part of the same ongoing tectonic event that extends to the end of the Cambrian.

The Delamerian Orogeny in Tasmania was a complex event that involved E-W extension and the eruption of the Mount Read Volcanics, metamorphism and emplacement of eclogite, and N-S and E-W compression, the former producing E-W trending folds and the latter reactivating faults and causing major uplift of the Tyennan block and deposition of syn-orogenic sediments (Owen Conglomerate in the Sheffield Element) (Berry, 1994; Veevers, 2000a). It is also thought that during this period that western Tasmania amalgamated as the Tyennan and Adamsfield-Jubilee elements docked with the King Island-Rocky Cape-Dundas-Sheffield composite (Veevers, 2000a).

The time following the Delamerian Orogeny was a relatively quiet time in Tasmania. The period 490-400 Ma was dominated by sag and shallow water platform sedimentation across much of the state (Berry, 1994). The Wurawina Supergroup is a thick, essentially conformable succession that unconformably overlies older rocks. The Supergroup can be divided into the Denison, Gordon and Tiger Range Groups (Seymour

and Calver, 1995). The Denison Group, which forms the basal unit of the Wurawina Supergroup in the Adamsfield-Jubilee Element, was derived predominantly from emerging regions of Proterozoic rocks during the Delamerian Orogeny with deposition continuing into the Early Ordovician (Williams, 1989; Seymour and Calver, 1995). The Denison Group is conformably overlain by the Gordon Group which was deposited over an extensive area of western Tasmania, including the Dundas and Sheffield Elements, and part of the Tyennan Element (Seymour and Calver, 1995). The Gordon Group is dominated by micrite and dolomitic micrite, deposited in supratidal, intertidal, and subtidal shallow marine environments (Seymour and Calver, 1995). The Tiger Range Group overlies the Gordon Group in the Adamsfield-Jubilee Element and consists of shallow marine siliciclastic rocks. The western Tasmania correlate of the Tiger Range Group is the Eldon Group which is predominantly clastic, consisting of sandstone and siltstone with minor conglomerate horizons and limestone lenses (Seymour and Calver, 1995).

During deposition of the Wurawina Supergroup in western Tasmania the Mathinna Group in the Northeast Element was also being deposited. The Mathinna Group consists of lower Palaeozoic turbiditic rocks that young regionally from west to east and resemble the fill of the Melbourne Trough (Veevers, 2000a). Age-diagnostic fossils are rare in this succession but graptolites of late Arenigian (475 Ma), late Ludlow (420 Ma) and Pragian (410 Ma) have been identified (Veevers, 2000a).

Deformation during the late Early to early Middle Devonian affected much of Tasmania and has been interpreted as reflecting docking between western and northeastern Tasmania at c. 400 Ma (Veevers, 2000a). Devonian deformation throughout Tasmania is complex and in many areas is controlled by existing Cambrian fold trends. Four phases of deformation have been recognised, ranging in trend from E-W to N-S and in style from open and upright to tight and inclined with axial plane cleavage seen in all but the initial phase (Seymour and Calver, 1995). The regional metamorphic grade associated with orogenesis is prehnite-pumpellyite with local zones of greenschist facies in the vicinity of syn- to post-orogenic granites. The Tasmanian Devonian deformation event has been correlated with the Tabberabberan Orogeny of southeastern Australia.

In western Tasmania, middle Palaeozoic (375-310 Ma) granitoids were emplaced after the Devonian deformation with narrow aureoles at high crustal level though have only been partly unroofed. Most of the granitoids, both S- and I-types, have intruded rocks ranging in age from Precambrian to Early Devonian (Williams, 1989). Lower Palaeozoic (395-368 Ma) granitoids in northeastern Tasmania, which are now largely unroofed, were

emplaced at relatively shallow depths (6 km) after the main Devonian deformation. The granitoid bodies outcrop over an area of 2500 km$^2$ and include three large composite batholiths; Scottsdale, in the west, and Blue Tier and Eddystone, in the east. The granitoids of the Scottsdale batholith are entirely I-type and the proportion of I-type granitoids decreases to the east, and unequivocal S-type granites are restricted to the Eddystone batholith in the far northeast (Williams, 1989; Seymour and Calver, 1995).

The Tasmania Basin covers most of central and eastern Tasmania and overlaps most of the older Elements. The basin contains a 1.5 km thick succession of predominantly flat-lying sedimentary rocks of Late Carboniferous to Late Triassic age known as the Parmeener Supergroup (Seymour and Calver, 1995). The supergroup is divided into two units. the lower unit, the Lower Parmeener Supergroup, is composed of upper Carboniferous to Permian glacigene and glacimarine deposits with a horizon of freshwater coal measures. The upper unit, the Upper Parmeener Supergroup, comprises upper Permian and Triassic fluviatile sequences with relatively thick freshwater coal measures (Williams, 1989). The Parmeener Supergroup was injected with thick (400-500 m) sheets and sills of dolerite at ca 184 Ma.

**Table 3-1.** Tectonic summary for Tasmania from the Mesoproterozoic to the present. (After Veevers, 2000a).

| Code | Age Ma | Event |
|---|---|---|
| XIV | 99-0 | drifting of Australia from Antarctica |
| XIII | 160 | rifting between Antarctica and Australia |
| XII | 184 | dolerite injected along Panthalassan margin of Gondwanaland |
| XI | 302-209 | sag accumulates Tasmania basin |
| X | 330-310 | SW Cape Granite in Tyennan Element |
| IX | ~385-340 | syn- to post-kinematic granite |
| VIII | 385 | tightening of Cambrian folds |
| VII | 400 | deformation: interpreted as reflecting docking of NE and W Tasmania |
| VI | 490-400 | sag and platform sedimentation in shallow water |
| V | 510-490 | Delamerian Orogeny: E-W extension and eruption of Mount Read Volcanics, metamorphism and emplacement of eclogite, N-S and E-W compression. W Tasmania formed as Tyennan and Adamsfield-Jubilee elements dock with King Island-Rocky Cape-Dundas-Sheffield composite. |
| IV | 525-510 | E to W arc-continent collision and obduction: Tyennan Orogeny, structural emplacement of allochthonous units |
| III | 600-570 | rifting and tholeiitic volcanism |
| II | 710-690 | rifting; overlap succession (Burnie-Oonah Formation) marks minimum age of accretion of Rocky Cape, Dundas and Sheffield elements |
| I | 777-720 | syntectonic emplacement of granite and uplift (Wickham Orogeny): interpreted as reflecting docking of King Island and Rocky Cape |
| | 1150-1100 | deposition of sedimentary protolith |

Intrusion of the Jurassic dolerite has been linked to tensional stresses heralding the eventual drifting of Australia and Antarctica in the mid-Cretaceous (for more detail on the Jurassic dolerites see Section 3.2.4). Continental extension of Australia-Antarctica began in the mid-Jurassic (160 Ma) with separation during the mid-Cretaceous (95±5 Ma) (Veevers and Ettreim, 1988). Associated with breakup was the development of a number of extensional basins, both offshore (Bass, Sorell, Otway, Durroon and Gippsland) and onshore (extensions of the Bass and Sorell), and widespread normal faulting from the Late Mesozoic to the Tertiary (Seymour and Calver, 1995). The Tertiary in Tasmania saw widespread eruption of basalts as dominantly mafic subaerial flows forming extensive lava plains up to 400 m thick (Williams, 1989). Tasmanian Tertiary volcanism is discussed in detail in Section 3.2.3. Most of the present Tasmanian landscape was determined in the Tertiary, however much has been developed during the Quaternary, particularly in periods of extensive Pleistocene glaciation (Colhoun, 1989).

### *3.2.2 The Tasman Line and the Tamar Fracture System*

The contrast in geology between western and northeastern Tasmania has logically led to the question of where the boundary between the two terrains is located. This has been hampered by the Tasmania Basin whose sediments blanket the postulated suture between western and northeastern Tasmania. In eastern Australia, the principal suture is known as the Tasman Line which marks the boundary between the Proterozoic Australian Craton to the west and the Paleozoic Tasman Fold Belt System to the east (a recent revision of the Tasman Line by Scheibner and Veevers (2000) has redefined the suture as the outcrop of the inclined 2-dimensional Tasman Surface). Previously the Tasman Line in Tasmania has been defined as the approximate N-S trending boundary between the Proterozoic Tyennan and Rocky Cape Blocks in the west from the younger Tasman Fold Belt in the east based on the crustal subdivisions devised by Plumb (1979). It is not certain, however, that the Tasman Line can be extrapolated to Tasmania. Murray *et al.* (1989) report Tasmania as lying east of the Tasman Line while Scheibner and Veevers (2000) take the view that Tasmania is wholly allochthonous and therefore unrelated to the Tasman Line as determined for mainland Australia.

It has been suggested that the Tamar River is the site of a fracture system along which the two terrains have been juxtaposed. This is based on the observation that the geology of the pre-Carboniferous rocks of the Western Tasmania Terrain, west of the Tamar River, differs significantly from that of the Eastern Tasmania Terrain, east of the

river. The Lower Ordovician and Lower Devonian Mathinna beds of the Eastern Terrain are turbidite quartzwacke sequences whereas the time equivalent sequences west of the Tamar River are dominantly carbonate and quartz-rich shelf deposits (Williams, 1989). Further, folds produced during Devonian deformation in Tasmania indicate tectonic transportation from the southwest in the Eastern Terrain whilst those in the Western Terrain were developed during transportation from the northeast (Williams, 1978).

According to Richardson (1989b) the Tamar Fracture System (TFS) is defined over much of its length by gravity, magnetic and conductivity data. However, recent seismic work has not shown any evidence for the boundary between the eastern and western terrains (Leaman, 1994a; Barton, 1998; Drummond *et al.*, 2000). Likewise new gravity data has shown that the principal gravity gradient across the centre of the island extends SSE from Devonport and is not geographically related to the Tamar River (Leaman, 1992). In light of this, Leaman (1994a) suggests that the term "Tamar Fracture System" be discontinued. Leaman also suggests that a major conductivity anomaly between the Tiers Fault and the western face of the eastern batholiths should be further investigated as a possibility as it is a zone of thickened crust and the anomaly extends at least 10 km into the crust.

Given the uncertainty in identifying and defining the boundary between the Western and Eastern Terrains of Tasmania it will be simply referred to here as the Tasmanian suture.

### *3.2.3 Tertiary Volcanism*

During the last 70 million years there has been widespread lava-field volcanism in eastern Australia (Wellman and McDougall, 1974). The basaltic provinces stretch nearly 4000 km in a 200 km wide belt along the eastern Australia coast, from North Queensland to Tasmania. Most of the basalts have erupted through a variety of terrains of the Phanerozoic Fold belt, but some provinces in North Queensland and Tasmania are located in Proterozoic terrains (Zhang *et al.*, 2001, in press). Three types of volcanic provinces have been recognised in eastern Australia: (i) leucitite provinces, (ii) central-volcano provinces, and (iii) lava-field provinces (Wellman and McDougall, 1974).

The Tertiary basalts of Tasmania form the southernmost extent of the mafic lava-field province of eastern Australia (the leucitite and central volcano provinces are not represented in Tasmania). Tasmania has approximately 400 $km^3$ of Tertiary basalts, in lava fields, eroded valley fills, and other scattered remnants. They are mainly distributed

diagonally across the state, are absent in the southwest (see Fig. 3-4) and form only minor outcrops on the larger Bass Strait islands (Sutherland *et al.*, 1989). Over 120 identified and inferred centres are exposed as lava cones, plugs and dykes, and many are located and aligned on fault lines, or on steep intrusive Jurassic dolerite contacts (Sutherland, 1969b). Exposures are dominated by subaerial flows which fed into the Tertiary drainages, but pillow-like lavas and breccias occur and may represent eruption in marine and lacustrine environments (Sutherland, 1969b; Sutherland *et al.*, 1989). In most areas the flows include a variety of basalt types and their field relationships often suggest separate volcanic episodes with intervening sedimentation and/or erosion (Sutherland and Wellman, 1986).

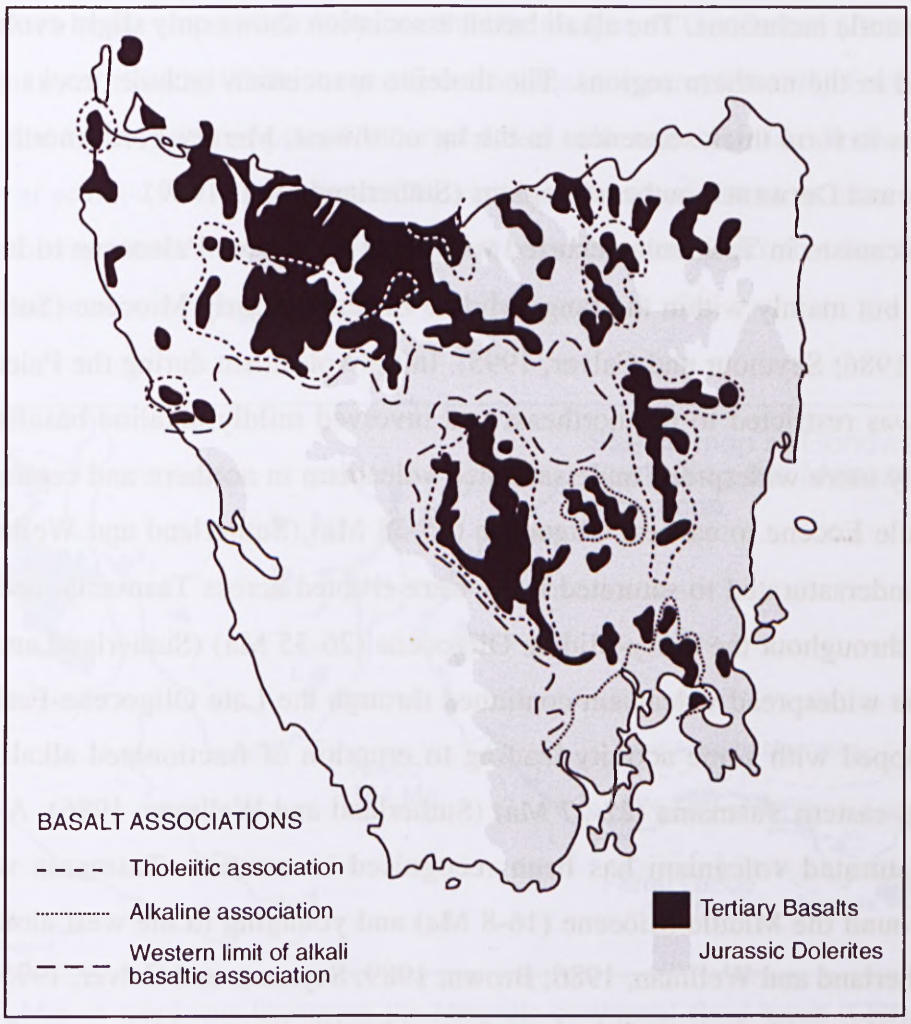


**Figure 3-4.** Map showing the distribution of Tertiary basalts and Jurassic dolerites in Tasmania. Also shown are the three main regional associations of basalt types (after Sutherland, 1989a).

Unlike the trachyte-rhyolite and olivine leucitite suites that typify central volcano migrational volcanism of mainland eastern Australia, the Tasmanian Cainozoic volcanic rocks form a mixed but predominantly alkaline province. The basalts range from tholeiitic

to alkaline and include olivine tholeiite, olivine-free tholeiite and alkali olivine basalt (Varne, 1977). Related but more undersaturated varieties include basanite, olivine nephelinite and olivine melilitite which, along with alkali basalt, represent primary magmas in Tasmania (Varne, 1977; Sutherland *et al.*, 1989). More fractionated alkaline lineages of the hawaiite-mugearite series and similar but more feldspathoidal-rich varieties have also been recognised (Sutherland, 1974).

Basalt types are irregularly distributed through the island, however, on a broad scale, the magmas can be grouped into three separate geographic associations (see Fig. 3-4). The alkaline association is found predominantly in the southeast and includes restricted areas of fractionated lineages, with abundant pyroclastics, many K-rich members and common mantle inclusions. The alkali basalt association shows only slight evolution and is widespread in the northern regions. The tholeiite association includes rocks of the other associations to form thick sequences in the far northwest, Mersey-Forth (north coast), and the Central and Derwent (southeast) regions (Sutherland *et al.*, 1989).

Volcanism in Tasmania occurred within the span from Paleocene to late Miocene (58-8 Ma) but mainly within the range Middle Eocene to Early Miocene (Sutherland and Wellman, 1986; Seymour and Calver, 1995). Initial volcanism during the Paleocene-early Miocene was restricted to the northeast and involved mildly alkaline basalts. This was followed by more widespread undersaturated volcanism in northern and central Tasmania from Middle Eocene to earliest Oligocene (35-38 Ma) (Sutherland and Wellman, 1986). Strongly undersaturated to saturated lavas were erupted across Tasmania, apart from the northeast, throughout the Early-Middle Oligocene (26-35 Ma) (Sutherland and Wellman, 1986). This widespread volcanism continued through the Late Oligocene-Early Miocene but overlapped with some activity leading to eruption of fractionated alkaline lavas in central and eastern Tasmania (22-27 Ma) (Sutherland and Wellman, 1986). A final phase of undersaturated volcanism has been recognised in northern Tasmania with basalts erupted around the Middle Miocene (16-8 Ma) and younging to the west along the north coast (Sutherland and Wellman, 1986; Brown, 1989; Seymour and Calver, 1995).

Mantle peridotite xenoliths have been identified in a wide range of Tasmanian basalt types extending from strongly undersaturated olivine melilitites and olivine nephelinites through to olivine tholeiite (Sutherland, 1974). The widespread lherzolite occurrences also encompass more fractionated alkaline lineages of the hawaiite-mugearite and equivalent feldspathoidal series (Sutherland, 1974). Apart from peridotite xenoliths, many of these rocks also contain a variety of lower-crustal xenoliths and high-pressure

megacrysts including alkali feldspars, olivine, plagioclase, aluminous augite and bronzite, kaersutitic amphibole, titano-magnetites and spinels (Sutherland, 1974, 1989b).

### *3.2.4 Jurassic Dolerites*

During the Mesozoic, the extrusion of large volumes of tholeiitic magmas preceded the continental break-up of Gondwana. The majority of these tholeiites form the three major continental flood basalt (CFB) provinces of the southern hemisphere: i.e. Paranà (ca 130 Ma), Karoo (ca 184 Ma) and Ferrar (184 Ma) (see Fig.3-5; dolerite ages from Veevers, 2000b). The Ferrar magmatic province stretches >4000 km from Tasmania, through the Transantarctic Mountains into Queen Maud Land and represents the Mesozoic CFB province which tends to parallel the proto-Pacific margin of Gondwana (Antonini *et al.*, 1999; Brauns *et al.*, 2000). While the province includes lava erupted at the Earth's surface, it is dominated by magmas emplaced as large sheets, sills and dyke-like bodies at shallow depths (Hergt *et al.*, 1989). The Ferrar CFBs possess some of the most extreme isotopic and elemental signatures observed in tholeiitic rocks, characteristics that are shared right across the vast province (Hergt *et al.*, 1989).

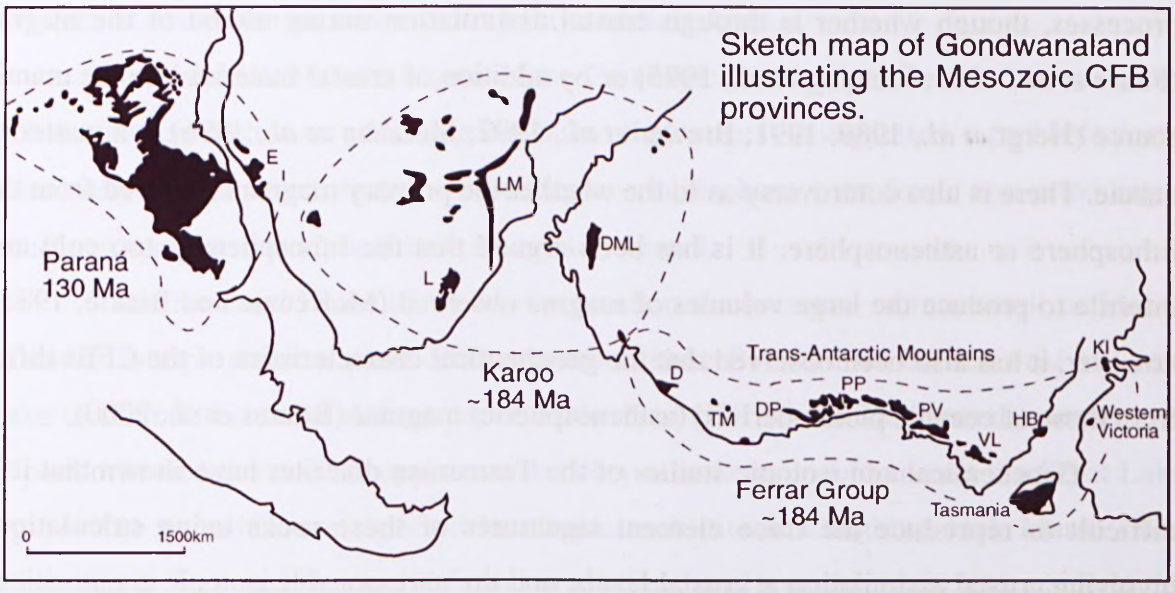


**Figure 3-5.** Map of Gondwana illustrating the Mesozoic continental flood basalt (CFB) provinces. Abbreviations are D=Dufek intrusion, DML=Dronning Maud Land, DP=Dawson Peak, E=Etendeka, HB=Horn Bluff, KI=Kangaroo Island, L=Lesotho, LM=Lebombo monocline, PP=Portal Peak, PV=Pearse Valley, TM=Thiel Mountains and VL=Victoria Land. Map modified after Hergt *et al.* (1991).

The Tasmanian dolerites represent a comparatively small part of the Mesozoic CFB province. They are entirely represented by intrusive rocks which form sheets, sills (~100-400 m thick) and dykes (~1 km wide) and are generally confined to the essentially flat-

lying Permo-Triassic sediments of the Parmeener Supergroup (Tasmania Basin) (Hergt *et al.*, 1989) (see Section 3.2.1). The volume of dolerite in Tasmania is currently estimated at 15000 $km^3$, based on the extent of outcrop (30000 $km^2$) and average thickness of sheets (Hergt *et al.*, 1989). Recent age estimates for the Tasmanian dolerites using the Re-Os isotopic system have yielded an age of 177.3±3.5 Ma (Brauns *et al.*, 2000). This result is consistent with the 174.5±8 Ma K-Ar age for the Tasmanian dolerites (Schmidt and McDougall, 1977), but younger than the183.6±1.0 Ma age for two sills in the Transantarctic Mountains calculated from $^{206}Pb/^{238}U$ zircon and baddeleyite data (Encarnacion *et al.*, 1996) and the 184-179 Ma $^{40}Ar/^{39}Ar$ age range for feldspars and whole rocks from the Karoo province (Duncan *et al.*, 1997).

The Mesozoic CFBs are the result of dramatic partial melting episodes within the Earth's mantle. These magmas are not primary and have compositions that differ from typical mid-ocean ridge and ocean island basalts (Brauns *et al.*, 2000). On a broad scale the basalts can be divided into high- and low-Ti sub-provinces which also display contrasting trace element and isotopic compositions. In the case of low-Ti rocks, this can include unusual features, more reminiscent of continental crust than mantle-derived magmas (Brauns *et al.*, 2000). This "crustal signature" has been attributed to crustal contamination processes, though whether is through crustal assimilation during ascent of the magma (Faure *et al.*, 1982; Fleming *et al.*, 1995) or by addition of crustal material into the mantle source (Hergt *et al.*, 1989, 1991; Brewer *et al.*, 1992; Molzahn *et al.*, 1996) is a matter of debate. There is also controversy as to the whether the primary magma is derived from the lithosphere or asthenosphere. It is has been argued that the lithosphere is too cold and infertile to produce the large volumes of magma observed (McKenzie and Bickle, 1988), however, it has also been observed that the geochemical characteristics of the CFBs differ from those of oceanic plume-derived (asthenospheric) magmas (Brauns *et al.*, 2000).

Geochemical and isotopic studies of the Tasmanian dolerites have shown that it is difficult to reproduce the trace element signatures of these rocks using calculations involving crustal assimilation at crustal levels, and the unreasonable isotopic compositions required of the contamination make such models unlikely (Hergt *et al.*, 1989). A more likely explanation, it is argued, involves the introduction of a small quantity of sediment (≤3 wt%) into a depleted MORB mantle source by the process of subduction. This model has also been applied to Ferrar rocks from Antarctica (Molzahn *et al.*, 1996), though Antonini *et al.* (1999) prefer a model whereby Antarctic Ferrar magmas were generated through melting of an E-MORB Dupal type mantle source with the subsequent "primary"

melts then undergoing assimilation-fractional crystallisation processes. New Os isotope data for the Tasmanian dolerites presented by Brauns *et al.* (2000) has been used to demonstrate that the unradiogenic initial Os ratios measured in these rocks are inconsistent with petrogenetic models involving the assimilation of continental crust with mantle-derived magmas.

## 3.3 PREVIOUS WORK

Early reports of mantle xenoliths in Tasmanian Tertiary basalts are generally only included as an aside to discussion of the host rock and tend to be brief and lacking in detail. Burns (1964) mentions xenoliths in lavas in the Devonport area but does not indicate whether they are of mantle or crustal origin. Sutherland's paper on the Tamar lavas of northern Tasmania includes a short section on both crustal and mantle xenoliths (Sutherland, 1969a). The latter are described as small and composed predominantly of olivine and augitic clinopyroxene with minor enstatite, calcic plagioclase and spinel. Major oxide abundances for a clinopyroxene grain from one of these nodules and a spinel xenocryst are provided. Sutherland (1971) expands on the previous paper by looking at each locality separately and providing more specific petrographic descriptions of the xenoliths at two of the localities (Spring Bay and East Arm).

Sutherland (1969b) is a review of the Cainozoic volcanic province in Tasmania and includes a short section on peridotite inclusions that have, it is suggested, a probable deep-seated origin. Apart from listing where these xenoliths have been found and providing a broad petrographic description there is very little detail.

Sutherland and Hale (1970) briefly mention the presence of rare small peridotite xenoliths in a porphyritic alkali olivine basalt at Lake Botsford which lies west of Great Lake in central Tasmania. A later paper, Sutherland (1973), also mentions the occurrence of peridotite nodules and clinopyroxene xenocrysts in lavas in and around the Great Lake region. The xenoliths are reported in olivine melilitite at Laughing Jack Marsh (also referred to in Brey and Green, 1975) and in alkaline basalts on the southeastern side of the Central Plateau.

In 1974, Sutherland reported the occurrence of mantle xenoliths in a tholeiitic basalt near Andover in the Tasmanian Midlands (Sutherland, 1974). The inclusions are described as predominantly spinel-bearing lherzolites with lesser amounts of dolerites and pyroxenites and olivine, orthopyroxene, clinopyroxene and plagioclase xenocrysts. There is little discussion about these xenoliths other than their unusual occurrence in a tholeiitic

basalt, a brief petrographic description and a note that they closely resemble lherzolites found abundantly in many other undersaturated Tasmanian lavas.

Sutherland (1976) provides a detailed examination of mantle xenolith occurrences in the lavas of the Hobart region. The volcanic rocks in this area include members of the tholeiitic and alkali olivine basalts and more undersaturated and alkaline varieties. Over half of the alkaline centres were reported to contain rocks bearing peridotitic xenoliths and xenocrysts. The xenoliths are generally small, with rare samples at some localities ranging to 100mm, and lherzolitic in composition. Xenocrysts include olivine, enstatite, clinopyroxene and spinel suggesting derivation from fragmented lherzolites. Pyroxenites are rare and only noted at one locality. Megacrysts are reported in a tuff and a lherzolite-bearing alkali olivine basalt plug in the Risdon area and consist of kaersutitic pargasite, enstatite, diopside and augite.

Wass and Irving (1976) is a catalogue of occurrences of xenoliths and megacrysts in basic volcanic rocks of eastern Australia that includes thirty-five Tasmanian localities. For each locality there is listed the location (as a latitude/longitude or easting/northing co-ordinate), geologic setting, age, host rock type, brief descriptions and relative abundances of xenoliths and megacrysts, and references where further data may be obtained. Xenolith-bearing lavas are reported from localities across northern and central Tasmania in a variety of basaltic rocks. Xenoliths are predominantly spinel-bearing Cr-diopside lherzolites though other rock types such as pyroxenites, dunites, and wehrlites and websterites of the Al-augite series, including some rare garnet-bearing types, were recognised at a few localities. Frequency of xenoliths ranges from rare to abundant and xenolith size is generally less than 4cm though larger samples, up to 10-11cm, are also reported. Megacrysts identified in Tasmanian basalts include clinopyroxene, olivine, bronzite, labradorite, kaersutitic amphibole, Al-augite, albite, and ferroan spinel.

A comprehensive report on mantle xenoliths in Tasmania was published in 1977 by R. Varne. His study was primarily concerned with the description, interpretation, and implications of reactions involving spinel that have been observed in some of the inclusions. The samples were collected from localities in northern Tasmania and Flinders Island from a variety of rock types including olivine basanite, nepheline hawaiite and olivine nephelinite. The xenoliths are described as being exclusively spinel lherzolite with predominantly granoblastic textures. Mineral compositions, determined by electron microprobe, and modal abundances are presented for nine samples. Comparison of the Tasmanian geochemical data with that for spinel lherzolites from southeastern Australia

and Hawaii leads Varne to conclude that the Tasmanian inclusions are not unusual mineralogically.

The only reference found to date on the occurrence of mantle xenoliths in far northwest Tasmania is a paper published in 1980 by Sutherland which mentions the presence of small lherzolitic xenoliths in pillowy and massive lavas on Robbins Island (Sutherland, 1980).

Spinel lherzolite and websterite xenoliths are reported in basaltic rocks at seven localities in the Ringarooma Quadrangle of northeastern Tasmania in Brown and McClenaghan (1982). A broad handspecimen description is provided for both lherzolites and websterites as well as basic mineral chemical compositions. Electron probe analyses of minerals and whole rock compositions from two spinel lherzolites and two websterites are included.

The first mention of garnet-bearing mantle xenoliths in Tasmania appears in a discussion on mantle and lower crustal xenoliths in eastern Australia (Sutherland and Hollis, 1982). Garnet lherzolites and pyroxenites are reported from Bow Hill and garnet pyroxenites are shown to occur at a locality on the northwest coast that is presumably Table Cape. Major oxide analyses are provided for one garnet lherzolite and one garnet pyroxenite from Bow Hill. A further and more detailed geochemical study of the Bow Hill xenolith suite and the host basalt is presented in Sutherland *et al.* (1984). Mineral major oxide analyses are used to determine pressure-temperature estimates for the garnet peridotites using a variety of geothermobarometers. It is concluded that these rocks were derived from within or just below the spinel/garnet lherzolite transition zone which the authors favour at a depth of ~70 km. Preliminary P/T estimates for spinel lherzolites and crustal xenoliths are used to constrain Moho depth at approximately 35 km. In light of their geochemistry and P/T limits the garnet-bearing peridotites are found to resemble xenoliths entrained in diamondiferous kimberlites associated with Precambrian shield geotherms.

Apart from Bow Hill there are numerous localities in central Tasmania that are reported to contain mantle peridotite xenoliths (Sutherland, 1984). The xenoliths are described as generally small and predominantly lherzolites, though rare pyroxenites are recorded at a few localities. Other basalts in central Tasmania (Western, Northern and Central Plateau volcanics) also contain numerous mantle xenoliths with one locality (East Round Lagoon) noteworthy for having large composite xenoliths of spinel lherzolite in contact with wehrlite (Sutherland, 1989c).

In the last decade, mantle xenoliths have mainly been mentioned in the literature only when observed in the particular basalts under investigation (Sutherland, 1989b; Sutherland *et al.*, 1989; Sutherland *et al.*, 1996). The majority of xenoliths are identified as spinel lherzolites as already observed in previous reports. Description of the inclusions is generally brief and usually includes their abundance, size and basic petrography. Mineral compositions and temperature estimates when provided form the basis for speculation on the genetic relationship between the mantle sample and its host rock.

A paper in 1994 by Sutherland *et al.* re-evaluates the spinel-garnet transition and the southeastern Australian geotherm in light of new mineral analyses and thermobarometry for eastern Australian xenolith suites, including those from Table Cape and Bow Hill in Tasmania (Sutherland *et al.*, 1994). This study concludes that the spinel/garnet lherzolite transition is hotter and deeper under Tertiary Tasmania (60 km depth at 1090°C) than under Mesozoic New South Wales (50 km depth at 980°C). Paleogeotherms constructed for Table Cape and Bow Hill indicate higher temperature gradients for these localities than determined for southeastern Australia, and this is related to an abnormally hot mantle beneath Tasmania. Supplementary papers with this publication provide mineral major oxide analyses for nine Tasmanian garnet peridotites as well as temperature and pressure estimates calculated from several different geothermobarometers.

# CHAPTER 4
# TASMANIAN MANTLE XENOLITHS

## 4.1 LOCALITIES

Past studies of the Tasmanian mantle xenoliths have focussed on single localities which, while providing significant insights into the vertical structure of the lithosphere mantle, have not delineated any lateral change that may occur from east to west. This investigation into Tasmania's SCLM seeks to address this by carrying out sampling at nine localities along a 250km E-W traverse across northern Tasmania (see Fig.4-1). This traverse cuts across three of the elements defined by Seymour and Calver (1995) and discussed in Chapter 3. Two localities (Coates Road and Arthur River) lie within the Rocky Cape element and another two localities (Table Cape and Doctors Rocks) lie close to the boundary between the Rocky Cape and Sheffield elements. South Riana and Don Heads both lie within the Sheffield element while the remaining three localities (the Sideling, Blessington and Wagners Hill) are all part of the Northeast Tasmania element.

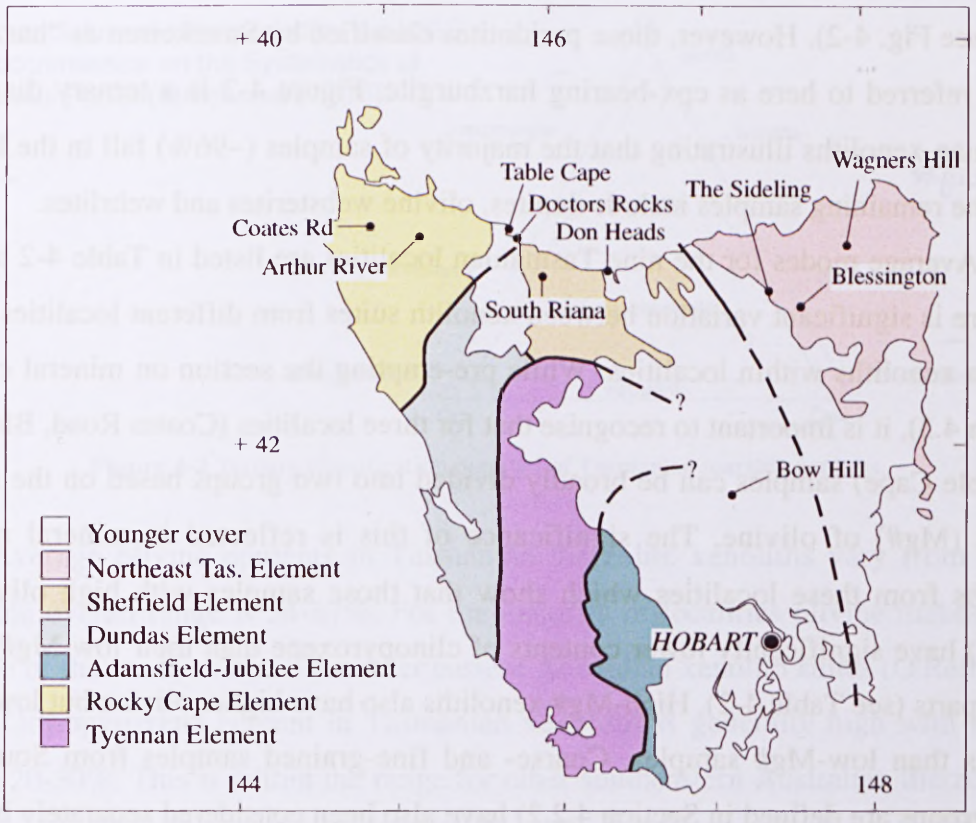


**Figure 4-1.** Map of Tasmania showing sample localities and crustal Elements (after Seymour and Calver, 1995).

**Table 4-1.** Co-ordinates for sample localities.

| Locality | Latitude | Longitude | 1:50 000 Map Sheet |
|---|---|---|---|
| Coates Road | 40°54'45" | 144°57'17" | Woolnorth |
| Arthur River | 41°06'46" | 145°24'26" | Trowutta |
| Table Cape | 40°57'18" | 145°43'48" | Table Cape |
| Doctors Rocks | 41°00'40" | 145°47'01" | Burnie |
| South Riana | 41°16'07" | 145°59'40" | St Valentines |
| Don Heads | 41°09'26" | 146°19'49" | Devonport |
| The Sideling | 41°16'24" | 147°24'16" | Launceston |
| Blessington | 41°31'21" | 147°27'38" | Longford |
| Wagners Hill | 41°04'32" | 147°51'28" | Ringarooma |

## 4.2 PETROGRAPHY

### *4.2.1 Mineral Modes*

The modal compositions of the Tasmanian xenoliths have been determined by pointcounting more than 1000 points in each thin section. Mineral modes for each locality are listed in Appendix I. Several samples were considered too small or too altered by heating, making it difficult to correctly identify clinopyroxene, to give meaningful modal data. Classification of the ultramafic xenoliths is based on the IUGS scheme (Streckeisen, 1976) (see Fig. 4-2). However, those peridotites classified by Streckeisen as "harzburgite" will be referred to here as cpx-bearing harzburgite. Figure 4-2 is a ternary diagram for Tasmanian xenoliths illustrating that the majority of samples (~96%) fall in the lherzolite and harzburgite field. The remaining samples include dunites, olivine websterites and wehrlites.

Average modes for the nine Tasmanian localities are listed in Table 4-2 and show that there is significant variation between xenolith suites from different localities and also between xenoliths within localities. While pre-empting the section on mineral chemistry (Section 4.3), it is important to recognise that for three localities (Coates Road, Blessington and Table Cape) samples can be broadly divided into two groups based on the forsterite content (Mg#) of olivine. The significance of this is reflected in mineral modes of xenoliths from these localities which show that those samples with high olivine-Mg# (Fo>91) have significantly lower contents of clinopyroxene than their low-Mg# (Fo<91) counterparts (see Table 4-2). High-Mg# xenoliths also have higher olivine but lower spinel contents than low-Mg# samples. Coarse- and fine-grained samples from South Riana (these groups are defined in Section 4.2.2) have also been considered separately but as can

be seen in Table 4-2 there is little modal difference between the two textural types other than the fine-grained xenoliths having somewhat higher spinel contents.

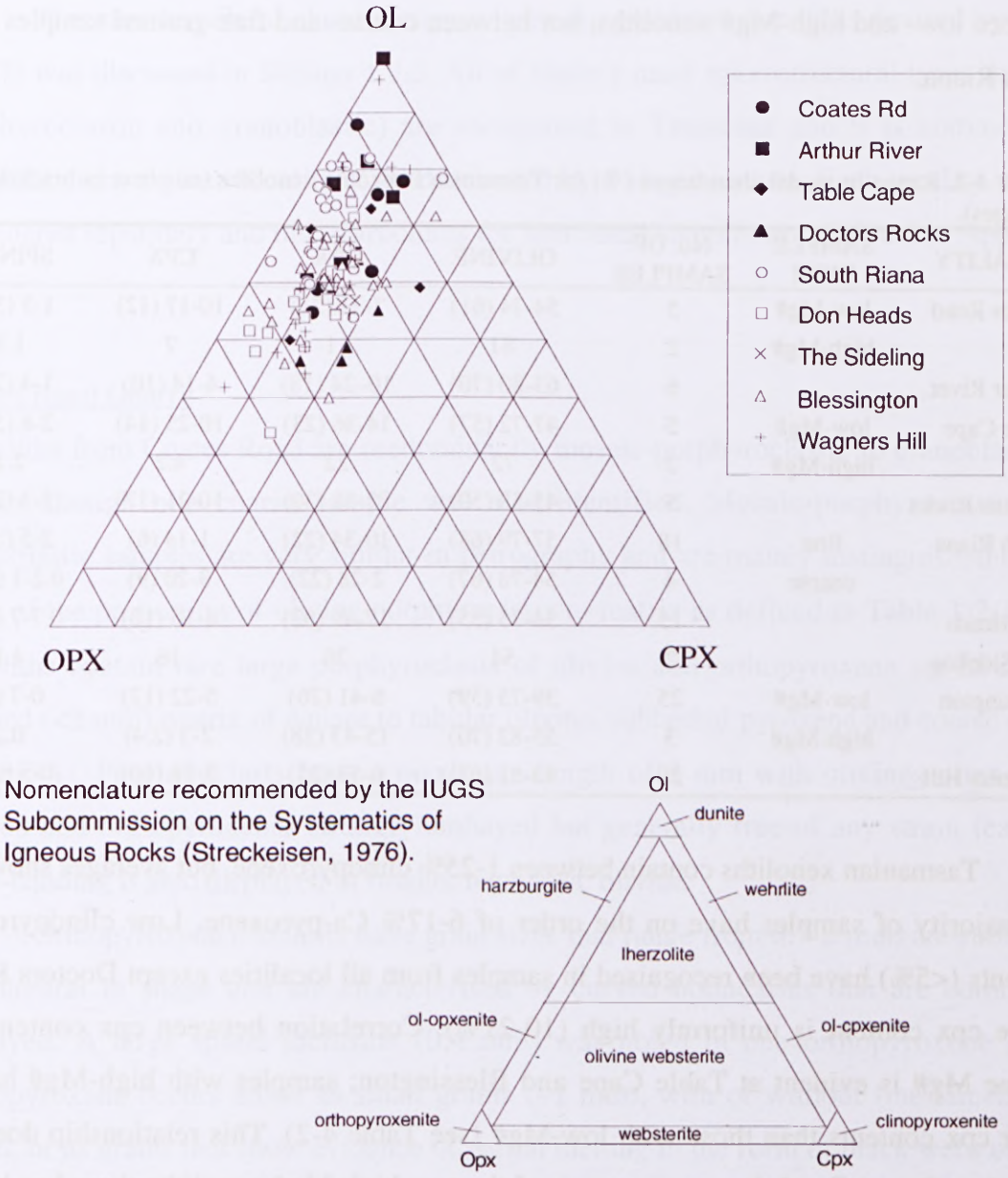


**Figure 4-2** Ternary classification diagram of Tasmanian mantle xenoliths.

Average olivine contents in Tasmanian lherzolite xenoliths vary from 54-81% though the overall range is 34-87%. For the majority of localities olivine makes up less than 70% of the mode as noted for other eastern Australian xenolith suites (O'Reilly *et al.*, 1989b). Orthopyroxene content in Tasmanian xenoliths is generally high with averages between 20-30%. This is within the range for other southeastern Australian lherzolites (5-30%) as reported in O'Reilly *et al.* (1989b). Very low orthopyroxene contents (2-8%) are rare and only seen in a few samples. High orthopyroxene contents (>30%) are more

common and are particularly prevalent in the localities east of, and including, Don Heads. In some samples from these localities orthopyroxene makes up to 40 or 50% of the mode, and it was found that between 25 and 50% of a given xenolith suite consists of these opx-rich xenoliths. There does not appear to be any significant difference in opx content between low- and high-Mg# xenoliths, nor between coarse- and fine-grained samples from South Riana.

**Table 4-2.** Range in modal abundances (%) for Tasmanian lherzolite xenoliths (numbers in brackets are averages).

| LOCALITY | SAMPLE TYPE | No. OF SAMPLES | OLIVINE | OPX | CPX | SPINEL |
|---|---|---|---|---|---|---|
| Coates Road | low-Mg# | 5 | 54-74 (61) | 7-33 (24) | 10-17 (12) | 1-5 (3.4) |
| | high-Mg# | 2 | 81 | 11 | 7 | 1.3 |
| Arthur River | | 6 | 63-80 (70) | 10–24 (18) | 4-14 (10) | 1-4 (2.1) |
| Table Cape | low-Mg# | 5 | 47-72 (57) | 14-36 (23) | 10-25 (14) | 2-8 (5.6) |
| | high-Mg# | 2 | 72 | 22 | 4.2 | 2.1 |
| Doctors Rocks | | 5 | 45-58 (50) | 22-38 (30) | 10-21 (17) | 2-3 (2.8) |
| South Riana | fine | 18 | 57-79 (68) | 10-34 (22) | 1-14 (6) | 2-5 (3.9) |
| | coarse | 4 | 54-78 (67) | 2-28 (22) | 3-20 (9) | 0.2-1 (1.1) |
| Don Heads | | 15 | 34-73 (55) | 17-49 (32) | 4-16 (10) | 0.7-7 (2.5) |
| The Sideling | | 2 | 54 | 26 | 16 | 4.1 |
| Blessington | low-Mg# | 25 | 39-75 (59) | 6-41 (26) | 5-22 (12) | 0-7 (3) |
| | high-Mg# | 3 | 55-82 (70) | 15-43 (28) | 2-3 (2.4) | 0.2 |
| Wagners Hill | | 20 | 43-81 (62) | 6-53 (25) | 3-18 (10) | 0-5 (2.2) |

Tasmanian xenoliths contain between 1-25% clinopyroxene, but averages show that the majority of samples have on the order of 6-17% Ca-pyroxene. Low clinopyroxene contents (<5%) have been recognised in samples from all localities except Doctors Rocks where cpx content is uniformly high (10-21%). Correlation between cpx content and olivine Mg# is evident at Table Cape and Blessington; samples with high-Mg# having lower cpx contents than those with low-Mg# (see Table 4-2). This relationship does not extend to Coates Road, however, as one of the two high-Mg# xenoliths there has higher modal cpx (11%) than expected (the other high-Mg# sample has 2% cpx). The fine-grained xenoliths from South Riana have overall lower clinopyroxene modes than the coarse-grained samples though this must be treated with some caution as cpx in the latter was often difficult to identify (see Section 4.2.2) and may have been overestimated.

Spinel content varies little between localities with most samples containing less than 5% of this phase. High-Mg# samples typically have less spinel than those with low-Mg#, and samples from the South Riana coarse-grained group are poor in spinel compared

to those from the fine-grained group. Two localities (Blessington and Wagners Hill) have lherzolites that are spinel-free.

### *4.2.2 Microstructure*

The microstructural classification scheme for peridotite xenoliths devised by Harte (1977) was discussed in Section 1.3.3. All of Harte's main microstructural types (coarse, porphyroclastic and granoblastic) are recognised in Tasmania and it is common for xenoliths from a given locality to be dominated by a single texture. Each locality will be considered separately and microstructures for individual samples are reported in Appendix I.

Coates Road Quarry

Xenoliths from Coates Road are predominantly mosaic-porphyroclastic to granoblastic in texture though one coarse sample was also identified. Mosaic-porphyroclastic and granoblastic samples are very similar in petrography and are mainly distinguished on the basis of the proportion of olivine porphyroclasts to matrix as defined in Table 1-2. These xenoliths contain rare large porphyroclasts of olivine and orthopyroxene set in a fine-grained (<2 mm) matrix of equant to tabular olivine, subhedral pyroxene and coarse spinel (Fig.4-3A). Porphyroclasts have a maximum length of 3 mm with olivines often kink-banded and orthopyroxenes strongly embayed but generally free of any strain features. Kink-banding is also displayed in smaller neoblastic olivine.

Orthopyroxene neoblasts have grain sizes that range from 0.7-2 mm, are subhedral to anhedral in shape and are characterised by curved boundaries that are commonly embayed. A large spinel inclusion (0.4 mm) was noted in one orthopyroxene grain. Clinopyroxene occurs either as small grains (~1 mm), with or without fine lamellae of spinel, or as grains that show evidence of partial melting in the form of black webs of melt that have partly, or in some cases completely, consumed the original grain. Spinel occurs as individual interstitial blebs (>1.5 mm), or as trains, in association with orthopyroxene. The trains define a weak fabric that is not paralleled by the other phases.

In the coarse sample (CQ4), phases are typically anhedral to subhedral with olivine occurring as large (2-4 mm) equant grains that often display undulose extinction and broad kink-banding or as smaller strain-free grains (<1 mm) that form small (3-4 mm across) polygonal aggregates with pyroxene and spinel (Fig.4-3B). Orthopyroxene grains are up to 3 mm in diameter (average 1 mm) with the larger grains displaying fine discontinuous

exsolution lamellae of Ca-pyroxene and smaller grains (<1 mm) generally fresh and clear. Clinopyroxene occurs as small pale green (<1 mm) grains that are nearly always in contact with orthopyroxene and which contain short broad lamellae of spinel. Fine-grained chromian spinel occurs as rare discrete grains but is more typically seen as rims on pyroxene grains.

Sulfides in Coates Road xenoliths occur as rare interstitial grains generally less than 100 μm in size, although one large grain of 230 μm was noted.

Arthur River

Spinel lherzolite xenoliths from Arthur River are fine-grained with granoblastic microstructures (Fig. 4-4A). Relict porphyroclasts (<5% of the mode) occur in several samples and are either olivine or, more commonly, orthopyroxene. These large grains have an average length of 3-4 mm and show strain features such as kink-banding and undulose extinction. Very fine exsolution lamellae of clinopyroxene are seen in some of the orthopyroxene porphyroclasts. Olivine and pyroxene neoblasts are polygonal and less than 2mm in size, with most grains averaging between 0.5 and 1 mm.

Triple-points are common in most samples though they are not always easy to recognise as most samples show evidence of melting such as extensive networks of brown glass and thick black reaction rims on clinopyroxene and spinel. Where clinopyroxene is relatively fresh it occurs as anhedral to subhedral grains that are pale green in colour though often with a dusty appearance (sieve texture) from numerous fine dark inclusions. Dark red/brown spinel occurs as small (<1 mm) interstitial grains that either are disseminated through the sample or, in the case of sample AR1, form long trains that lie parallel to the long axes of tabular olivine neoblasts.

Sample AR2 is a dunite which has a coarse microstructure that is dominated by large olivine grains up to 5 mm across though some grains are as small as 1 mm. Undulose extinction is common. Spinel occurs as small (<1 mm), dark interstitial grains. Brown glass occurs throughout the xenolith usually along grain boundaries and fractures.

Sulfides in xenoliths from Arthur River are generally interstitial though a few enclosed grains were noted. Grain size for the interstitial sulfides ranges from <10 μm up to 450 μm. Enclosed sulfides occur as discrete grains or as fine trains and are less than 20 μm in size.

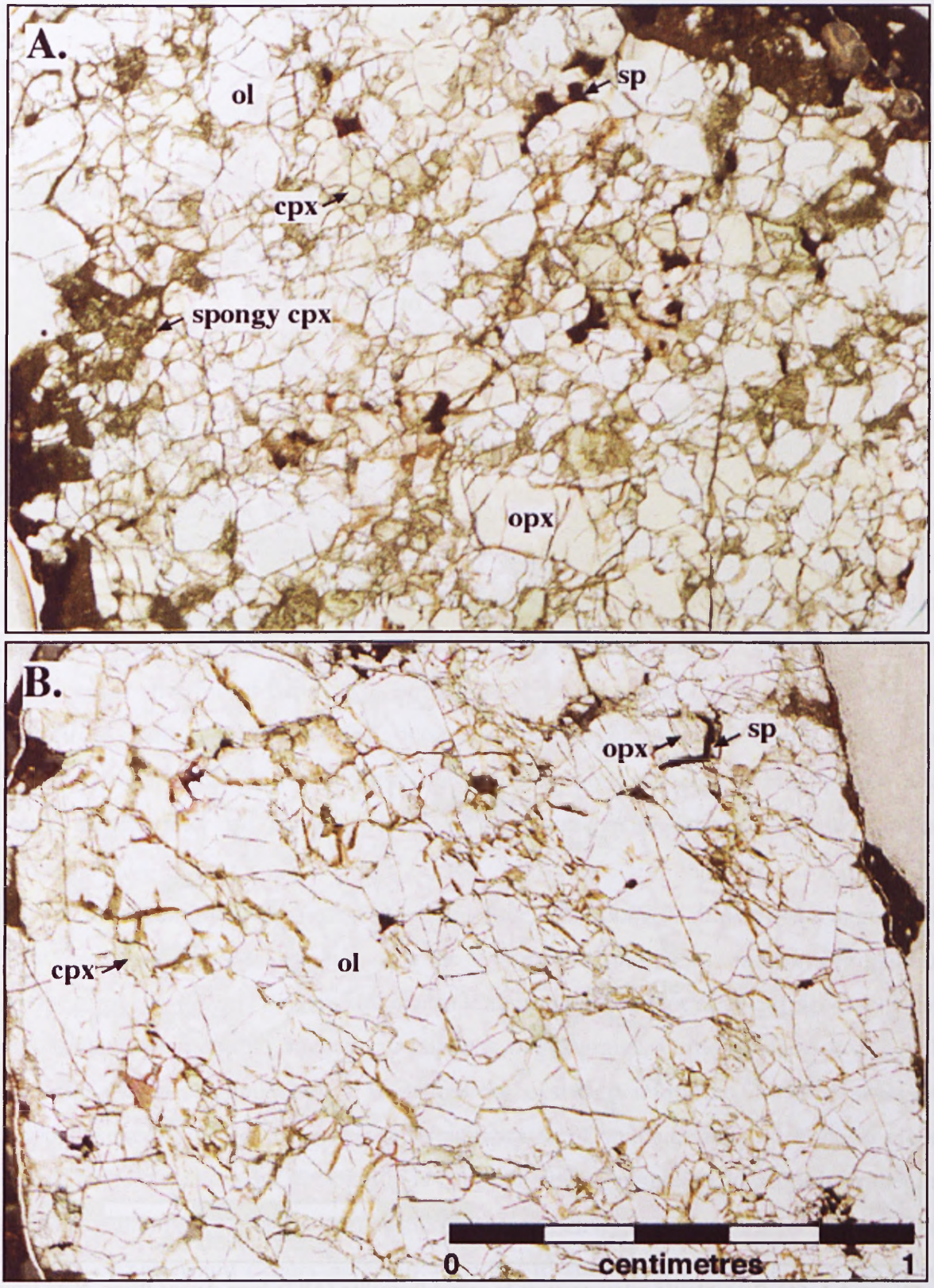


**Figure 4-3.** (A) Granoblastic microstructure in spinel lherzolite (CQ6) from Coates Road Quarry. (B) Coarse microstructure in cpx-poor spinel lherzolite (CQ4) from Coates Road Quarry. Note spongy rims and/or complete resorbtion of cpx in A.

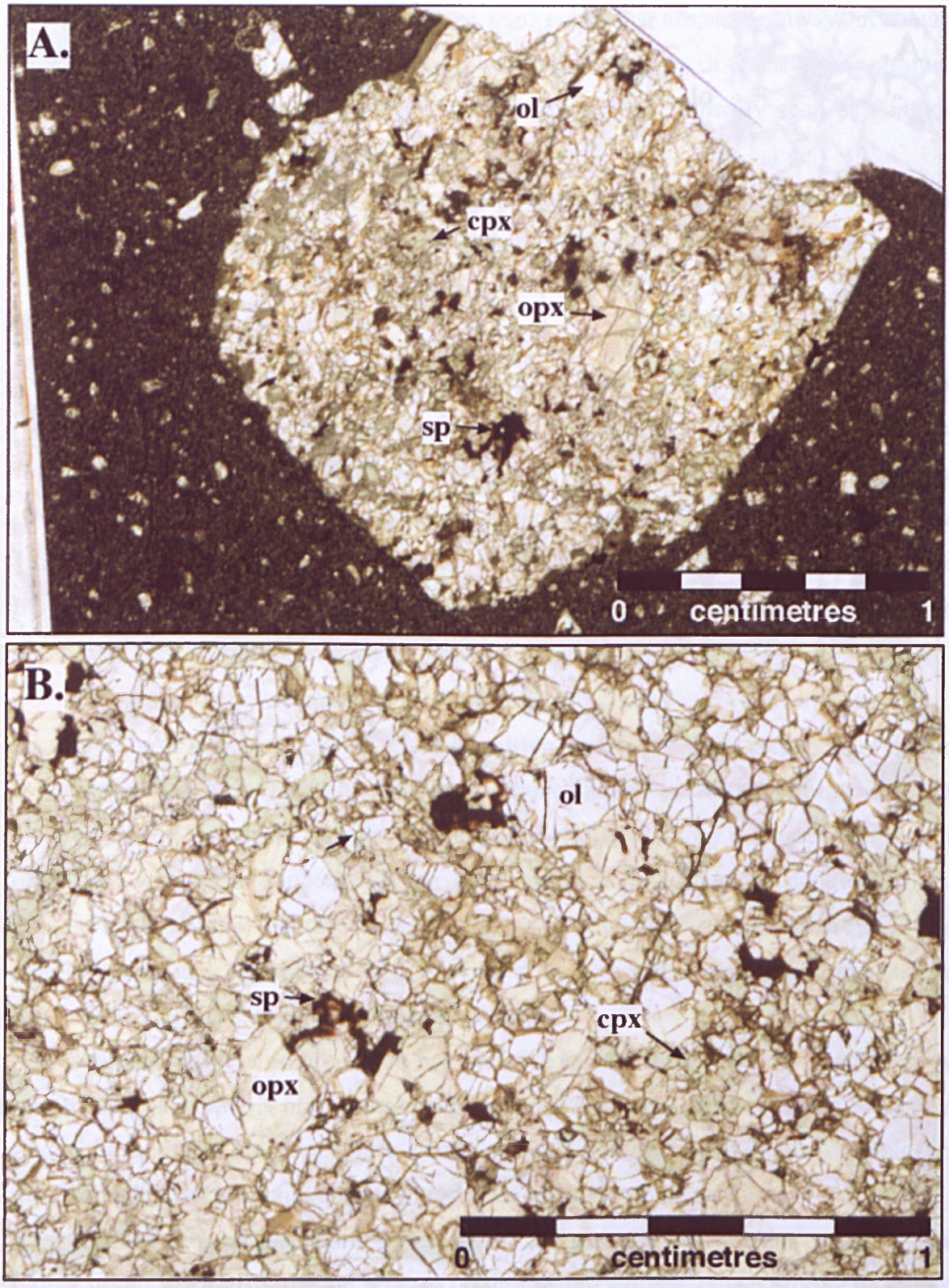


**Figure 4-4.** (A) Granoblastic microstructure in spinel lherzolite (AR7) from Arthur River. Note large orthopyroxene porphyroclast and resorbed clinopyroxene. (B) Granoblastic microstructure in spinel lherzolite (DR1) from Doctors Rocks.

Table Cape

Mantle xenoliths from Table Cape display predominantly granoblastic microstructures with one sample having a coarse microstructure (Fig. 4-5). In the granoblastic xenoliths mineral grains typically form polygonal aggregates with poorly-developed triple junctions. Olivine grains range from equant to tabular in shape and have an average size of 1 mm. Kink banding is common in olivine and many grains display undulose extinction. Orthopyroxene grains have an average size of 1mm though larger grains (1-2 mm diameter) are common in some samples. These grains are generally free of deformation features. Large (maximum length 7 mm) rare porphyroclasts of orthopyroxene were noted in a few samples. Porphyroclasts have irregular grain boundaries that are often embayed and generally show little evidence for strain; fine, short lamellae of clinopyroxene are uncommon and seen only in a few grains.

Clinopyroxene in several of the granoblastic xenoliths shows evidence for heating during ascent in the host basalt, ranging from spongy rims on grains closest to the xenolith/basalt contact to complete resorbtion of the grain. Where clinopyroxene has been totally resorbed it is olive-green in colour and cloudy in appearance. Fresh clinopyroxene is pale green and free of exsolution, with a grain size less than 1 mm. Spinel occurs as interstitial grains (>1.5 mm) that occur as discrete blebs or as trains which are characteristic of disrupted microstructures. Spinel trains are fine, discontinuous and parallel to each other and, in one sample (TC4), to a weak fabric defined by aligned tabular olivines (Fig. 4-5A).

The xenolith with the coarse microstructure (TC1) consists of polygonal aggregates of large equant olivines (1-4 mm, average 2 mm) and smaller pyroxenes (Fig. 4-5B). Olivine grains commonly display kink bands that can be parallel or crosscutting. Patches of fine-grained olivine (0.5-1 mm) occur between larger grains. Orthopyroxene (average 1 mm, rare grains >4 mm across) is commonly exsolved with fine, long lamellae of clinopyroxene. Clinopyroxene occurs as aggregates of small grains (>2 mm) in close contact with orthopyroxene. Exsolution is common in clinopyroxene and appears either as fine, short lamellae of spinel or as closely packed rounded inclusions of spinel. Interstitial spinel is common and occurs as small anhedral to subhedral grains (1 mm) between pyroxenes. Spongy rims are seen occasionally on clinopyroxenes and spinels.

Sulfides range from common to rare in Table Cape xenoliths. Interstitial sulfides are common and often large in size (50-350 μm). Enclosed sulfides are rare and occur as small (<50 μm) rounded grains that sometimes form fine trails in the host mineral.

Doctors Rocks

Doctors Rocks xenoliths are exclusively granoblastic with most sections containing at least one large relic orthopyroxene porphyroclast (Fig. 4-4B). These samples are characterised by polygonal grains (range in size from 0.7-2 mm, average ~1 mm) with straight to curved boundaries that meet at triple junctions. Larger grains (1-2 mm diameter) show evidence for incipient recrystallisation as they are embayed and surrounded by smaller subgrains of olivine and pyroxene. Olivine neoblasts are generally free of deformation features though undulose extinction and rare kink-banding were noted in some grains. Exsolution is uncommon in pyroxenes and when seen in clinopyroxene appears as fine short lamellae of, what is assumed to be, orthopyroxene. Spongy rims on clinopyroxene and spinel are common in two samples and best developed close to the xenolith/basalt contact.

Porphyroclasts range in size from 2-4 mm in length and are often strongly embayed. Exsolution lamellae of clinopyroxene in large orthopyroxenes are common, though not ubiquitous, and are typically fine, continuous and closely spaced. Spinel occurs as >1 mm interstitial grains between pyroxenes or as inclusions in orthopyroxene porphyroclasts. Brown glass is common along grain boundaries and fractures.

Sulfides are rare in xenoliths from Doctors Rocks. They are generally less than 50 μm in diameter, though a couple of grains were close to 100 μm, and occur as discrete blebs or fine veins along grain boundaries. Enclosed sulfides are extremely rare and found to be less than 5 μm across.

South Riana

Xenoliths from South Riana can be broadly divided into two groups; fine-grained (Fig. 4-6A) and coarse-grained (Fig. 4-6B). The fine-grained group consists of samples that are either porphyroclastic, granoblastic, or transitional to granoblastic, in structure, while the coarse-grained samples are granoblastic but with an overall larger grain size than those from the fine-grained group. The fine-grained granoblastic xenoliths with the best developed microstructures have an average grain size of about 0.4 mm, and are characterised by polygonal neoblast grains with straight to curved boundaries and well-developed triple-point grain junctions (Fig. 4-6A). A few samples display a weak fabric defined by the preferred orientation of coarse-grained (>1 mm) tabular olivine and, in some cases, trains of fine-grained spinel. Exsolution is occasionally seen in orthopyroxene and clinopyroxene and appears as fine lamellae of the corresponding pyroxene. Spinel occurs in these rocks as fine (<0.5 mm) disseminated grains.

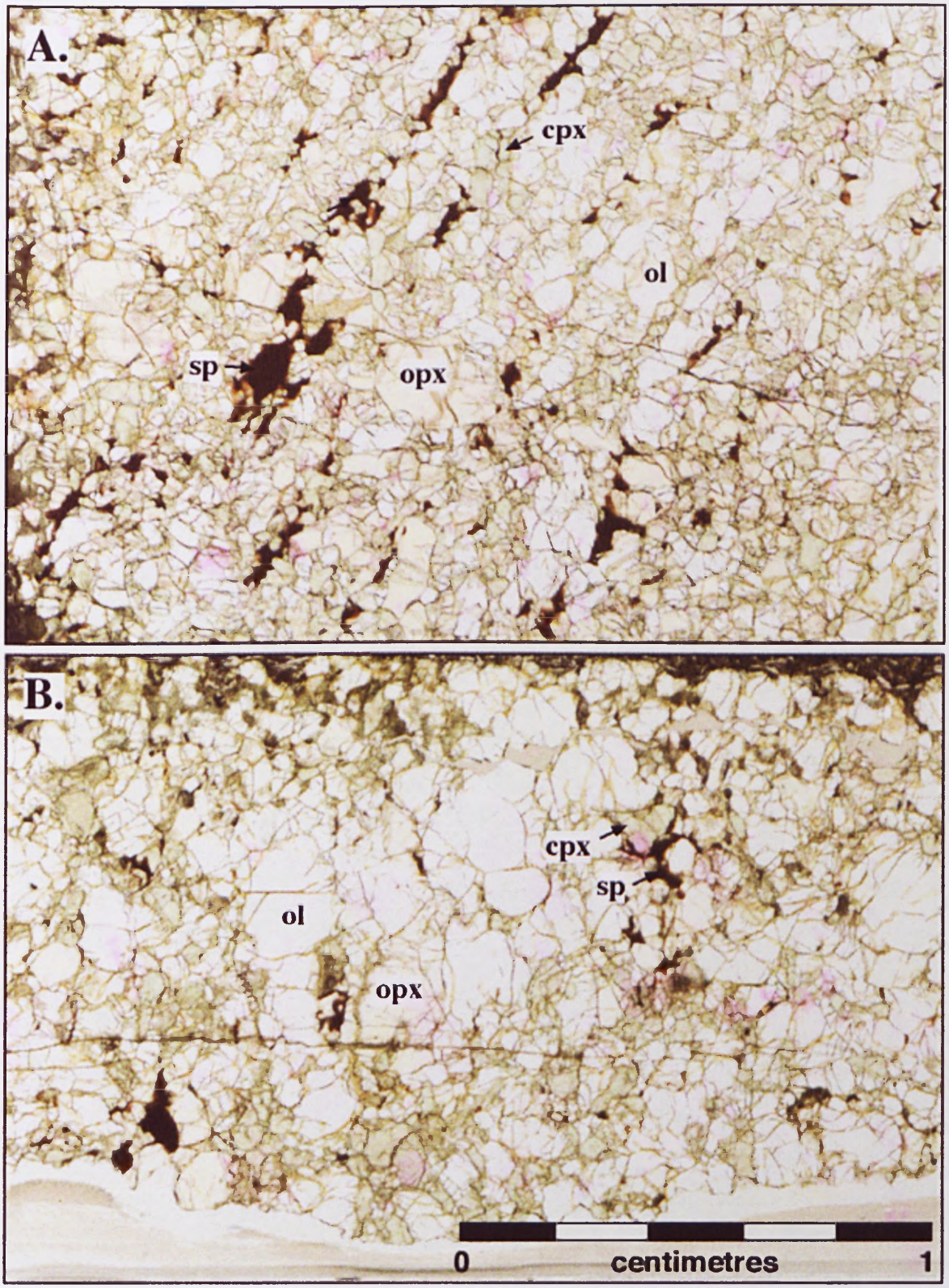


**Figure 4-5.** (A) Granoblastic microstructure in spinel lherzolite (TC4) from Table Cape. Note parallel alignment of spinel trains. (B) Coarse microstructure in spinel lherzolite (TC1) from Table Cape.

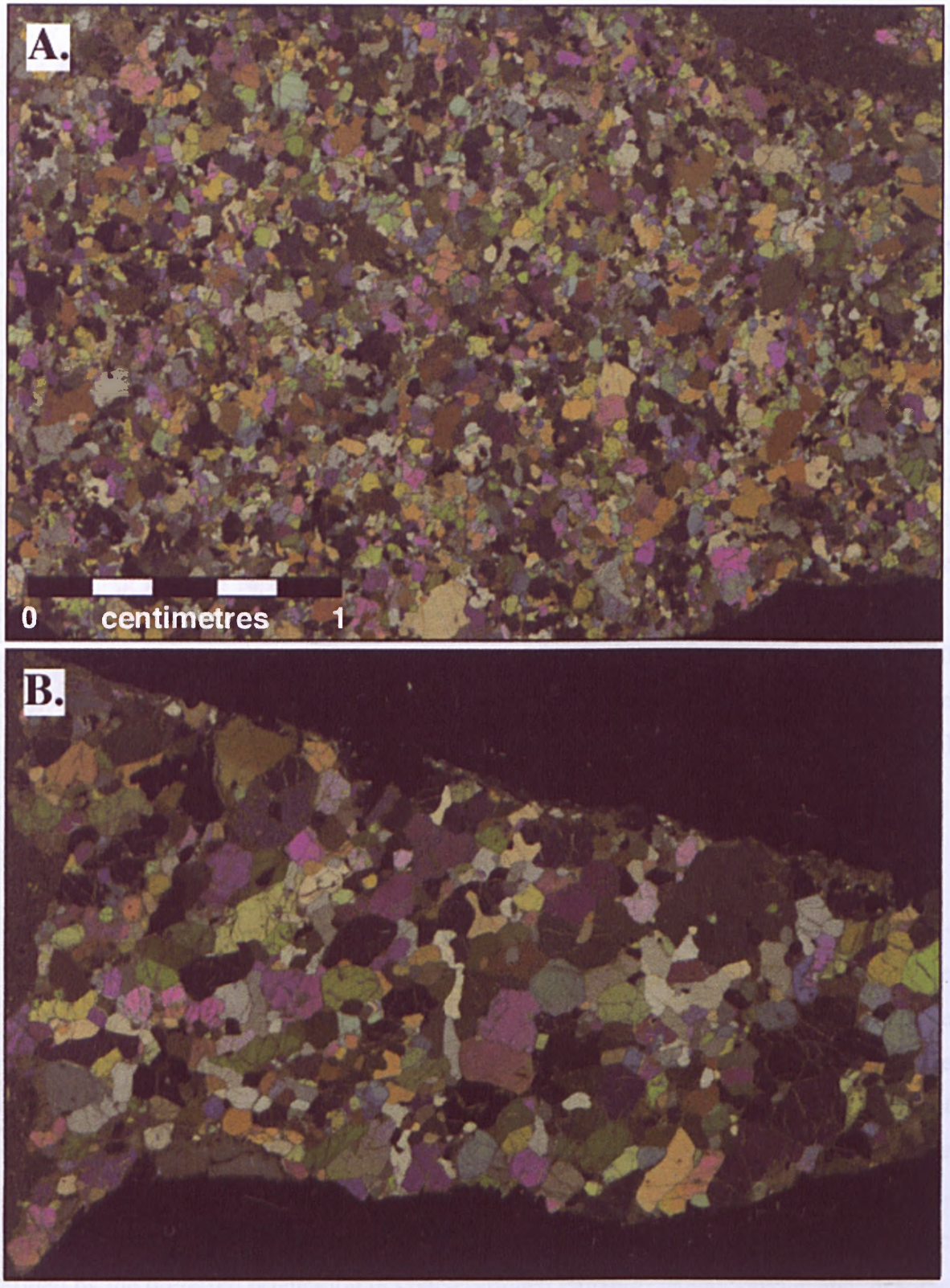


**Figure 4-6.** (A) Granoblastic microstructure in fine-grained spinel lherzolite (SR9) from South Riana. (B) Granoblastic microstructure in coarse-grained spinel lherzolite (SR2) from South Riana. Scans taken with crossed polars.

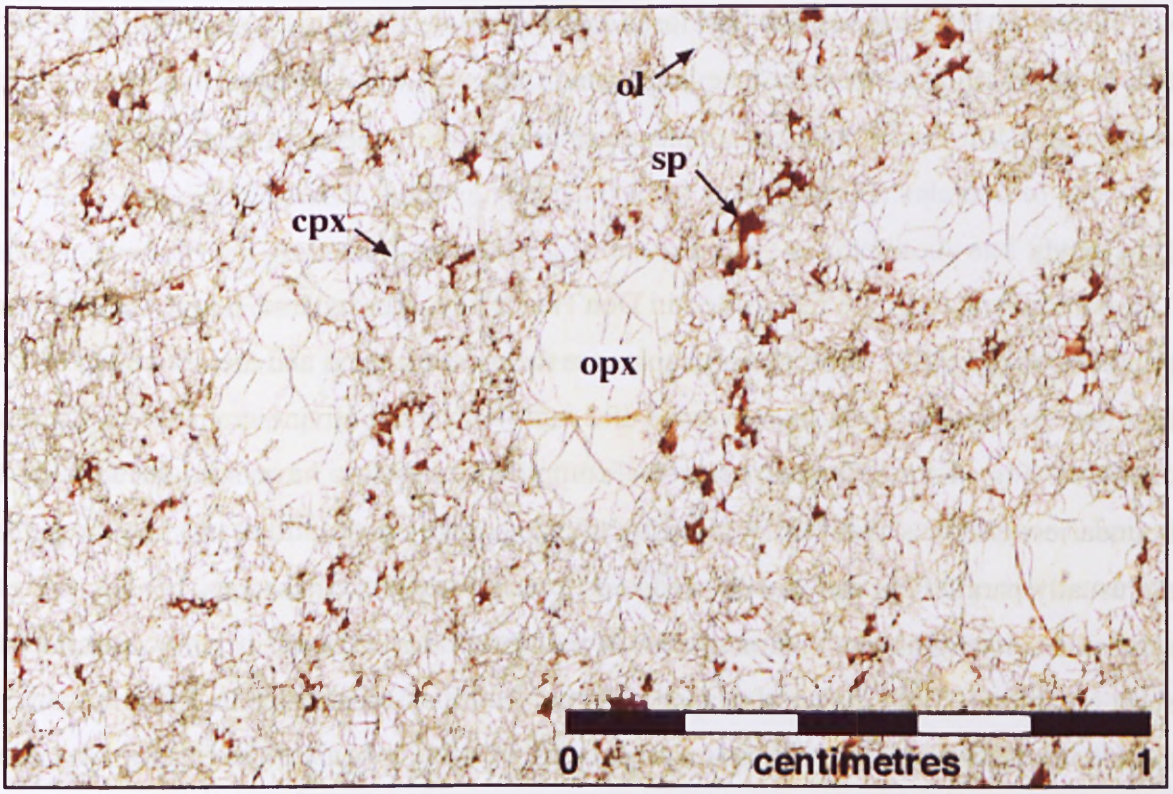


**Figure 4-7** Porphyroclastic microstructure in spinel lherzolite SR12 from South Riana. This structure is well-developed with large orthopyroxene porphyroclasts and a fine-grained granoblastic matrix.

Relict porphyroclasts of orthopyroxene are common in the granoblastic samples and make up less than 5% of the sample; one or two per section. Porphyroclastic xenoliths, where porphyroclasts comprise more than 10% of the mode, are rare (Fig. 4-7). Porphyroclasts are exclusively orthopyroxene and grains are typically elongate (maximum diameter 6 mm) in shape and strongly embayed. Strain features are common and appear as kink-banding and thick discontinuous exsolution lamellae of clinopyroxene though there are a few grains that are clear and free of deformation.

Coarse-grained granoblastic samples have average grain sizes between 1 and 2 mm (Fig. 4-6B). These samples show evidence for varying degrees of heating ranging from spongy rims on clinopyroxene and spinel to complete resorbtion of grains, the latter usually only seen in clinopyroxene. Microstructures are dominated by polygonal grains with straight to curving grain boundaries intersecting at triple junctions. Olivine is unstrained and pyroxenes rarely display exsolution. Modal clinopyroxene varies from 3-20% in these xenoliths. Brown glass is abundant in one sample.

Sulfides are absent or rare in most South Riana xenoliths. A few samples contain small amounts of sulfide, typically as fine interstitial grains along silicate grain boundaries or as larger polygonal grains at triple point junctions. Polygonal sulfides range from

subhedral and euhedral, to more irregular shapes. Grain size can be quite large with some sulfides up to 150 µm in length. Enclosed sulfides are very rare and usually occur as very fine trains in silicate minerals. One large grain (150 µm) was identified in coarse-grained sample SR2. The coarse-grained samples were found to be generally free of sulfide.

Don Heads

Three microstructures are recognised in Don Heads xenoliths; coarse, porphyroclastic and granoblastic (Fig. 4-8). The coarse samples are the most common and are of two types. The first type has a large grain size (average of 2 mm) with some olivine grains up to 7 mm in diameter (Fig. 4-8A). Triple points are common and grains have straight to curving boundaries. Olivines are characterised by undulose extinction and broad kink bands that are usually parallel but can also be wedge-shaped. Orthopyroxene occurs as large (>4 mm across) exsolved grains with lamellae of Ca-pyroxene ranging from fine and continuous to short and broad (often diamond-shaped). Two generations of lamellae in the one grain are quite common with one type cross-cutting the other, usually at a high angle. Kink-banding is occasionally observed in orthopyroxene.

Clinopyroxene is found in close association with orthopyroxene and occurs as clusters of 2 or more grains. Grains range from 1-3 mm in size with an average of about 2 mm. Exsolution is common and appears as very short, fine orthopyroxene lamellae which are concentrated towards grain centres. Spinel is red/brown in colour and occurs adjacent to pyroxene along grain boundaries or at triple point junctions. It also appears as large patches up to 4 mm across between pyroxene grains.

The second type of coarse microstructure is recognised in rare samples and is characterised by a similar average grain size as type 1 but with an overall more equigranular texture (Fig. 4-8B). Triple points are very common with smaller recrystallised grains often seen at the junctions. These smaller neoblasts are common and often occur in patches or along grain boundaries indicating that this sample is transitional to a porphyroclastic microstructure. Deformation features recognised in the type one xenoliths are apparent in type 2 samples including kink-banding in olivine, which is widespread and commonly wedge-shaped, and exsolution in pyroxenes, which is similar in form but not as common. Spinel is pale greenish brown and either interstitial at triple junctions or along pyroxene grain boundaries. Aggregates of very fine-grained minerals (<0.05 mm) and dark brown glass occur in these samples and are probably patches of melt. The minerals are difficult to identify but appear to be olivine and pyroxene.

A well-developed porphyroclastic microstructure was only evident in one sample. Large porphyroclasts of olivine and orthopyroxene (>3 mm across) are common in this xenolith. These grains are strongly embayed and rimmed by smaller subgrains of olivine, spinel and pyroxene. The large orthopyroxenes contain very fine, closely spaced lamellae of clinopyroxene. Neoblasts range in size from 0.2-1 mm. Spinel is anhedral to subhedral and occurs between grains at triple junctions. Brown glass is ubiquitous and found along grain boundaries and fractures.

The granoblastic sample has an average grain size of 1mm and is characterised by tabular olivines that produce a well-defined fabric. Pyroxenes are polygonal with exsolution uncommon in orthopyroxene but well-developed in clinopyroxene. Lamellae in clinopyroxene are fine, long and closely-spaced or short, broad and widely-spaced. Spinels are small and interstitial between pyroxenes. This sample is strongly fractured and fractures typically lie parallel to the fabric and crosscut grains. Brown glass is common and found along grain boundaries or infilling fractures.

Sulfides are absent to rare in Don Heads xenoliths. Both interstitial and enclosed sulfides are recognised though the former is the most common type. Interstitial grains commonly occur as fine trains along grain boundaries or as polygonal grains at triple point junctions. Grain size is generally very small (<20 μm) with rare grains up to 75 μm. Enclosed sulfides are rounded to sub-rounded and are often embayed. These grains are typically less than 50 μm in size and occur singly or as fine trains.

The Sideling

Both xenoliths from the Sideling have coarse mosaic microstructures. These samples are rich in pyroxene and have an average grain size of 3 mm. Olivine grains are up to 5 mm in diameter and display kink-banding which, in some cases, is wedge-shaped. The pyroxenes occur as coarse-grained aggregates. Exsolution is very common in both pyroxenes and usually involves the complementary pyroxene. Lamellae show a wide range in form from fine and closely-spaced to broad and widely-spaced. In grains where lamellae are very dense they are non-parallel and overlapping. Some pyroxenes have thick dark reaction rims especially those close to the xenolith/ basalt contact. Spinel occurs as large (average 1 mm) interstitial grains between pyroxene grains. Brown glass is common along grain boundaries. No sulfide was identified in these xenoliths.

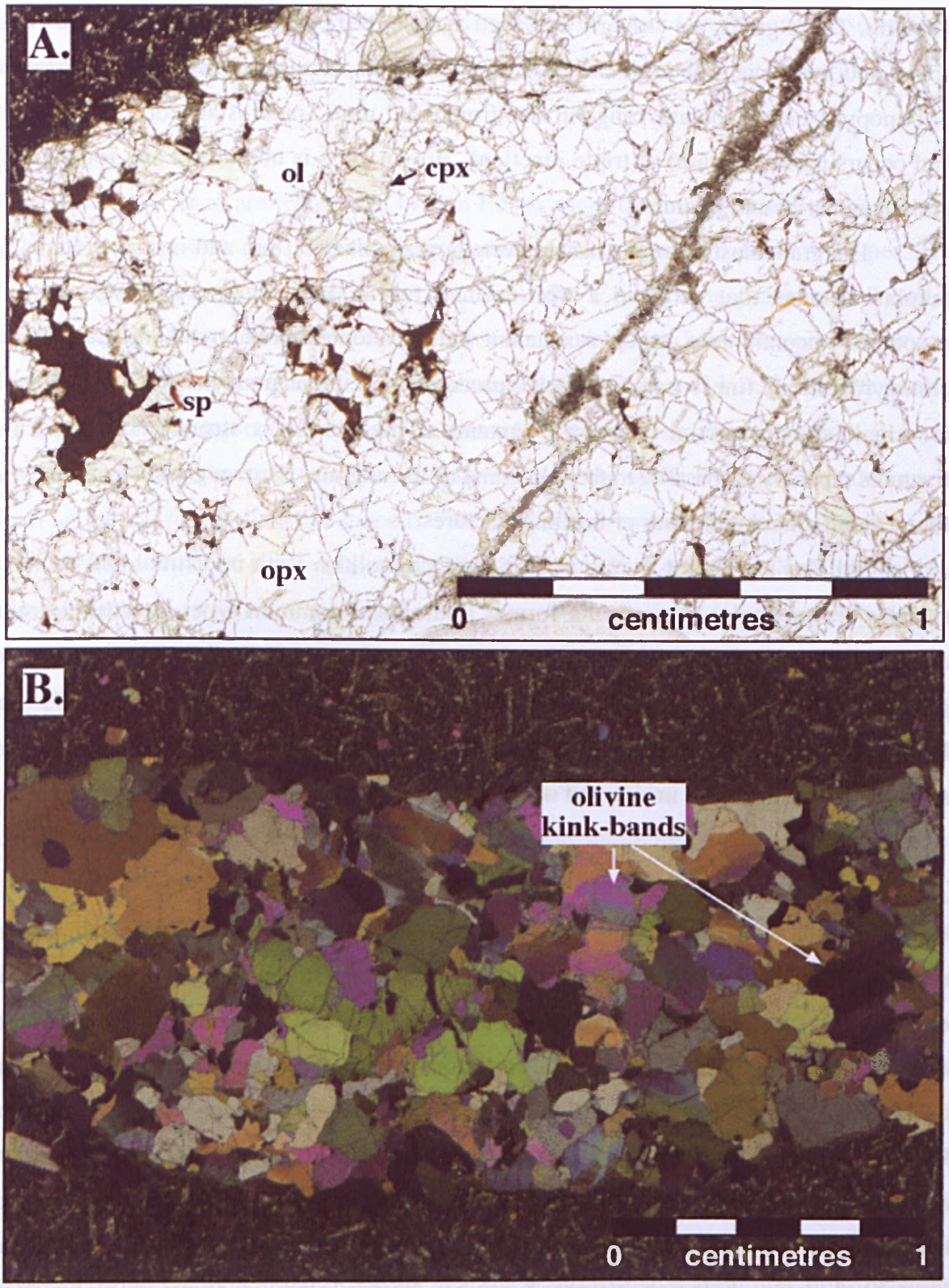


**Figure 4-8** (A) Type 1 coarse microstructure in spinel lherzolite (DH1) from Don Heads. (B) Type 2 coarse microstructure in spinel lherzolite (DH6) from Don Heads. Note kink-bands in olivine. Scan taken under crossed polars.

Blessington

Blessington xenoliths are restricted to coarse equant microstructures apart from a few samples which appear to be transitional between coarse and porphyroclastic textures (Fig. 4-9). Structurally there is no discernible difference between the cpx-poor (Fig. 4-9A) and cpx-rich (Fig. 4-9B) samples. Lherzolites from Blessington are extremely coarse-grained with olivine up to 15 mm in diameter seen in some samples. Grains typically form polygonised aggregates with straight to smoothly curving boundaries. Triple junctions are common and range from poorly- to well-developed.

Average size for olivine ranges from 3-5 mm in diameter and grains are typically colourless and anhedral to subhedral in shape. Undulose extinction in olivine is very common and broad kink-bands were noted in several samples. Pale brown orthopyroxene (average 3 mm and up to 8 mm+) is anhedral to subhedral in shape and commonly embayed. Exsolution lamellae of clinopyroxene in orthopyroxene are common and range from fine, long and regularly spaced to short and broad. One sample contains orthopyroxenes that display two sets of lamellae crosscutting each other at acute angles.

Clinopyroxene is pale green and is generally found in close association with orthopyroxene and spinel. Grain size of clinopyroxene is much finer than that of olivine and orthopyroxene with a range of 0.5 to 2 mm and an average of about 1 mm. While grains are often fresh and free of exsolution features there are many that display mild to strongly developed lamellae of orthopyroxene and spinel. These lamellae are generally short and broad. Partial melting of clinopyroxenes was noted in several samples and typified by thick spongy rims and well-developed sieve textures; grains closest to the xenolith/basalt boundary were found to be most strongly affected.

Dark red/brown spinel is fine-grained, less than 1 mm across, though large patches up to 3 mm across also occur in some samples. Spinel occurs either as discrete interstitial grains or as intergrowths, of which the most well-developed form symplectites with olivine and pyroxene. Interstitial grains are found in triple-point junctions between pyroxene grains. They are anhedral to subhedral in shape and generally less than 1 mm in size. Spinel intergrowths occur between pyroxenes and are typically vermicular in form; rimming and, in some cases, enclosing grains. Symplectites are rare and appear as patches of fine, wormy intergrowths of spinel, pyroxene and olivine.

Several samples show evidence of recrystallisation in the form of patches of fine-grained mosaic aggregates of olivine and pyroxene with an average grain size of 1 mm. Grains have straight boundaries and are generally free of features such as exsolution and

kink-banding. Melting features in the Blessington xenoliths include dentritic networks of pale brown glass and dark reaction rims on pyroxenes, usually clinopyroxene, and spinel.

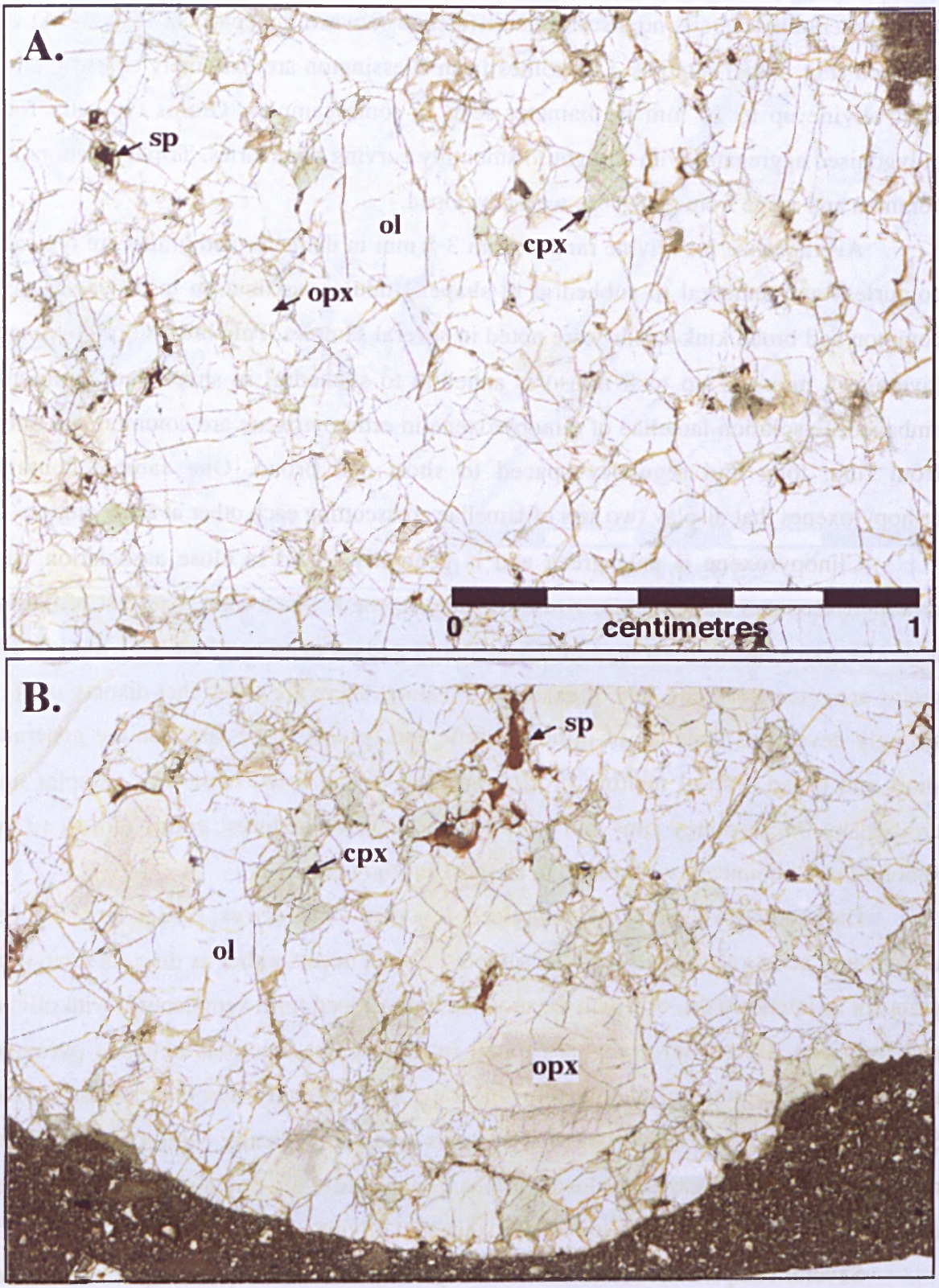


**Figure 4-9.** (A) Coarse microstructure in cpx-poor spinel lherzolite (BL10) from Blessington. Note spinel grain enclosed by clinopyroxene in top lefthand corner. (B) Coarse microstructure in cpx-rich spinel lherzolite (BL20) from Blessington.

Sulfides are common in Blessington xenoliths and were identified in nearly all samples. Most Blessington sulfides occur along silicate grain boundaries as disseminated grains or more rarely as fine veins. Grain size ranges from <10 μm up to 250 μm with many >50 μm. Enclosed sulfides are uncommon and are found as rounded inclusions in olivine and orthopyroxene. These grains are as small as 10-20 μm but many are >50 μm and some up to 100 μm in diameter.

Wagners Hill

Xenoliths from Wagners Hill display predominantly coarse microstructures (Fig. 4-10). These samples are very coarse-grained with both olivine and orthopyroxene ranging up to 1 cm across. Grains typically form polygonised aggregates with straight to curved grain boundaries and well-developed triple points. Olivine has an average grain diameter of 3 mm and is characterised by undulose extinction and kink bands which are commonly broad, but may be narrow, and which are usually parallel but also occur as wedges or, in rare cases, as bands that crosscut at right angles. Olivine also occurs as small (~0.5 mm) rounded to sub-rounded inclusions in orthopyroxene.

Orthopyroxene is fawn in colour and has an average grain size of 4 mm. Exsolution is common in this phase and occurs as fine lamellae of clinopyroxene. Lamellae are typically long and densely packed though shorter and more widely spaced lamellae are also seen. Short, broad lamellae of spinel in orthopyroxene were seen in a few samples. Bright green clinopyroxene is abundant (6-22 modal%) in most Wagners Hill lherzolites. Grains range in size from 0.5-3 mm with an average of 2 mm. Most grains contain exsolved orthopyroxene, and rarely spinel, with lamellae displaying a wide range in style. Spongy rims on clinopyroxene are common in samples that show obvious interaction with their host basalt i.e. stringers and patches of basalt within the xenolith.

Spinel occurs in a variety of forms in Wagners Hill xenoliths though it is always intimately associated with pyroxene. It primarily appears as interstitial, anhedral to subhedral, grains (>2 mm) between pyroxene grains. In several samples it occurs as fine wormy intergrowths with pyroxene (symplectites) (Fig. 4-10). The intergrowths are typically complex, in which the spinel is intergrown with two or more silicate grains that are not necessarily of the same species. Spinel-silicate symplectites in spinel-bearing mantle xenoliths have been attributed to decomposition of pre-existing garnet, co-existing with olivine, to pyroxene+spinel which suggests that the xenolith originated in the garnet

stability field and was transported to the depth of equilibrium, where it was entrained in the host magma (Carswell *et al.*, 1984; Green and Burnley, 1988).

Several samples contain patches of fine-grained (<2 mm) minerals indicating incipient recrystallisation to a more granoblastic microstructure. Recrystallisation is particularly evident in two samples (WH13 and WH18) from Wagners Hill which have well-developed porphyroclastic microstructures. Sample WH13 is olivine-rich, about 95% olivine, which occurs mainly as large porphyroclasts (average 5 mm) (Fig. 4-11). The porphyroclasts commonly display undulose extinction and kink-banding. Kink-bands are broad, often wedge-shaped, and are occasionally seen to crosscut each other at right angles in the one grain. Olivine also occurs as smaller subgrains (<1 mm) along porphyroclast margins or as neoblasts in polygonal aggregates with pyroxene between porphyroclasts.

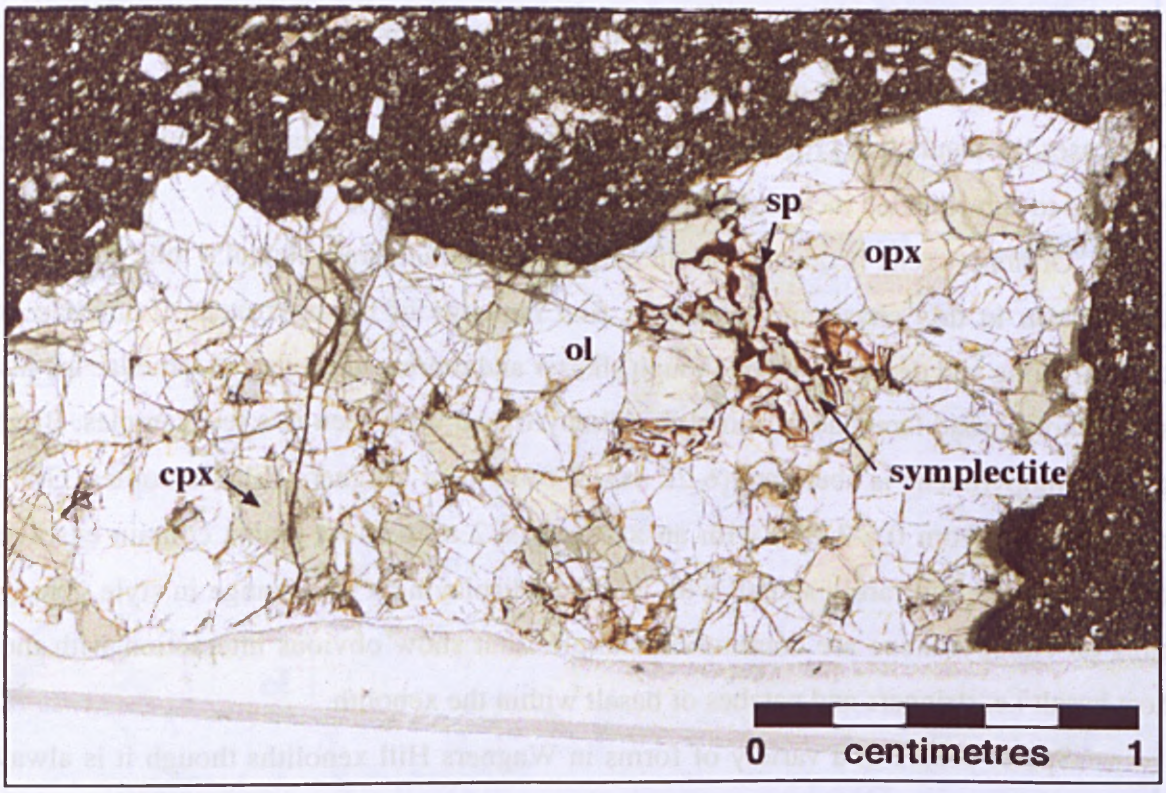


**Figure 4-10.** Coarse microstructure in spinel lherzolite WH15 from Wagners Hill. Note the symplectitic spinel/pyroxene intergrowth.

Sample WH18 contains porphyroclasts of olivine and both pyroxenes. These relict grains range in size from 2-8 mm and are often strongly embayed. Olivines are kink-banded (wedge-shaped, crosscutting) and commonly display undulose extinction. Pyroxenes are exsolved and usually involve a complementary pyroxene. Lamellae in orthopyroxenes are long and fine and are gently curved. In clinopyroxene lamellae are broader and discontinuous. The matrix in this xenolith is composed predominantly of fine-

grained (0.1-0.5 mm) polygonal aggregates of olivine and pyroxene with isolated patches of coarser-grained (~1 mm) olivine. Spinel occurs as interstitial blebs (<0.5 mm) between grains, and is often concentrated in patches, or as very fine-grained inclusions in pyroxene neoblasts. Larger spinels (>1 mm) are found in association with pyroxene porphyroclasts and typically appear as rims or interstitial grains.

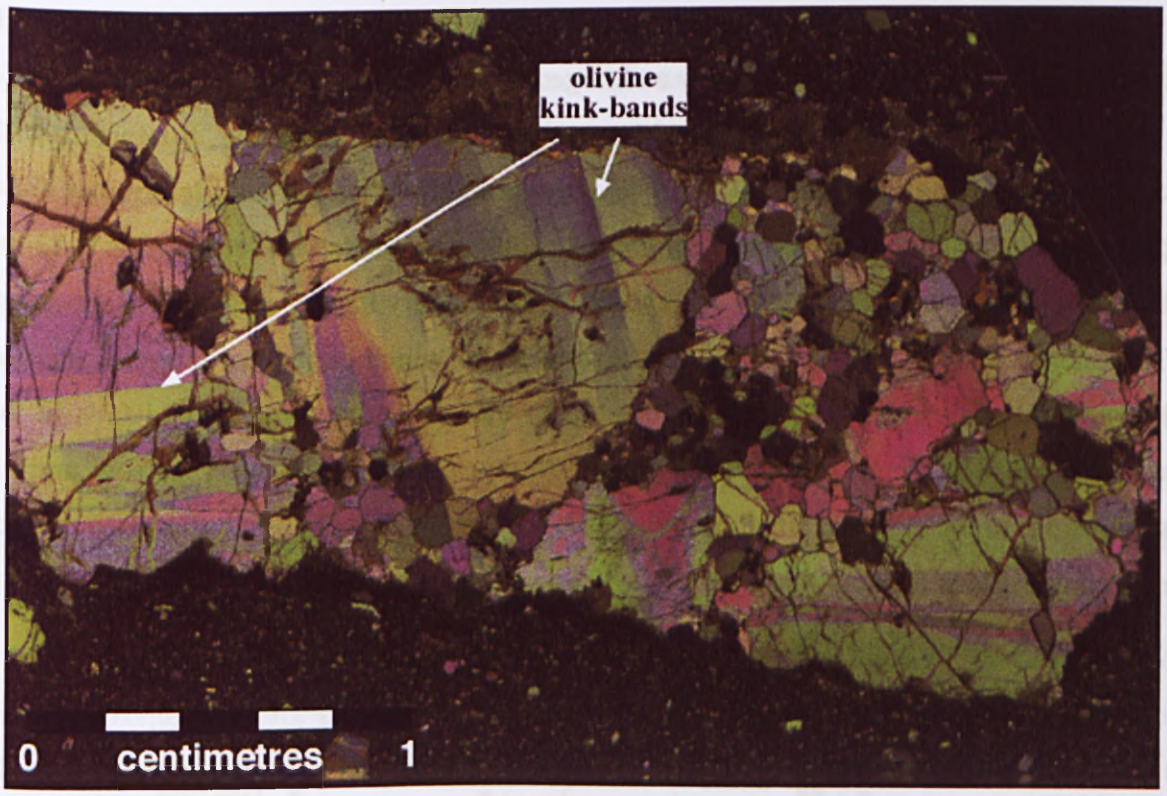


**Figure 4-11.** Porphyroclastic microstructure in olivine-rich spinel lherzolite (WH13) from Wagners Hill showing well-developed kink-bands in the large olivine porphyroclasts.

Sulfides are rare in Wagners Hill xenoliths and usually small (<20 μm) and interstitial. They occur as fine grains along silicate grain boundaries, rarely as veins, and, in one case, concentrated along the xenolith/basalt margin. Although generally small, larger sulfides (>100 μm) were identified in a few samples. Enclosed sulfides occur as discrete rounded grains ranging up to 100 μm across (average ~50 μm), or as trails of fine grains (<20 μm), in olivine and pyroxene.

## 4.3 MINERAL GEOCHEMISTRY

### *4.3.1 Major Elements*

The GEMOC electron microprobe was used to analyse major element abundances in all phases of one hundred and thirty ultramafic xenoliths collected at nine localities across northern Tasmania. A minimum of three grains for each mineral phase was analysed

with a minimum of four analyses per grain (two rim; two core). Analyses outside analytical error were discarded as were analyses giving poor totals. Analyses for each phase were averaged and the standard deviation calculated (1σ). Mineral phases are typically homogeneous within analytical error and results are given in Appendix IIA along with Mg# numbers for all phases and Cr# numbers for clinopyroxene and spinel. Where there was significant difference between core and rim analyses for any phase these values were averaged separately and are tabulated in Appendix IIB. In the following discussion each locality will be dealt with individually and in geographical order from west to east.

Olivines in Tasmanian mantle xenoliths are predominantly forsteritic with compositions lying between $Fo_{84}$ and $Fo_{92}$. Pyroxene classification was determined from plotting end-member compositions on a ternary diagram. As can be seen in Fig. 4-12 the bulk of clinopyroxenes are diopsides and fall within a very narrow range in composition. The one exception is sample AR5 from Arthur River which contains clinopyroxene that has a slightly higher En component ($Mg_2Si_2O_6$) than the other samples and falls in the augite field. The compositional range for orthopyroxenes is also very narrow and all samples lie in the enstatite field. Sample WH13 from Wagners Hill has slightly more Fe-rich compositions for both pyroxenes.

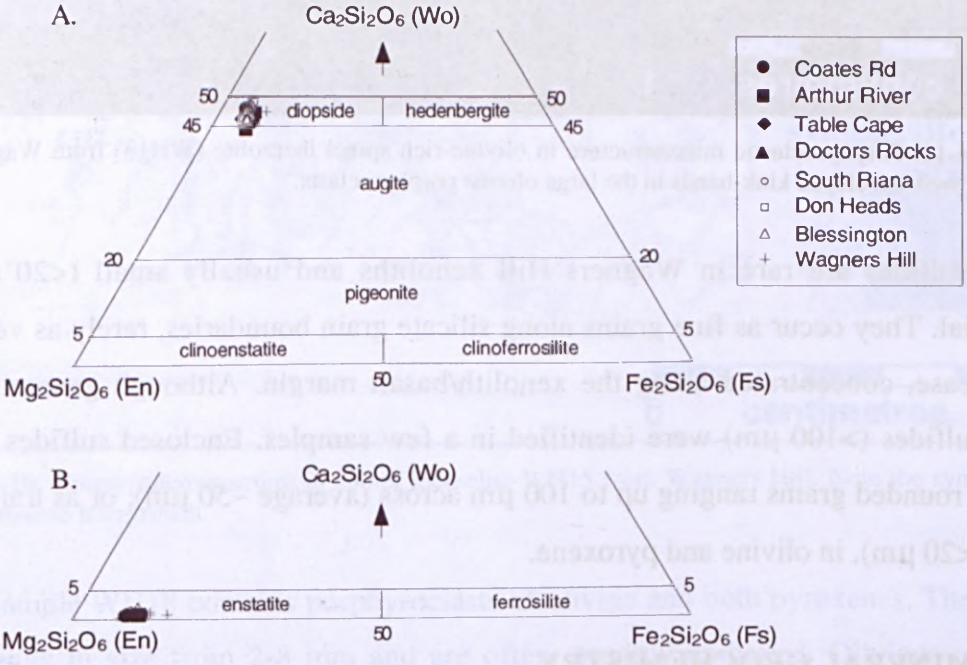


**Figure 4-12.** Composition ranges and nomenclature for A. clinopyroxenes and B. orthopyroxenes from Tasmanian mantle xenoliths.

Spinels rich in Cr, such as those found in Tasmanian mantle xenoliths, are variably referred to as chromites or chromian spinels. Yao (1999) recommends that the term

"chromite" be used except where the grains are low in Cr ($Cr_2O_3$<10%) in which case "chromian spinel" is preferred. The majority of Tasmanian spinels have between 9-12wt% $Cr_2O_3$ and in this study are referred to as chromian spinels. Spinels with very high-Cr (>30wt% $Cr_2O_3$) are referred to as chromites.

Coates Road Quarry

Seven xenoliths from Coates Road Quarry have been studied and all are spinel lherzolites. Olivine compositions define two groups based on olivine Mg# as illustrated in Fig. 4-13. The first group or low-Mg# group contains most of the samples and has olivine Mg# ranging from 88.9-90.3. The second group or high-Mg# group contains two samples (CQ1 and CQ4) which have olivine Mg# of 91.5 and 91.4 respectively.

The orthopyroxenes ($En_{88-90}Fs_{9-10}Wo_{1.4-1.6}$) in the low-Mg# group have low Mg# (89.7-90.3), but high contents of $Al_2O_3$ (see Fig. 4-13), $TiO_2$ and CaO relative to the high-Mg# orthopyroxenes ($En_{91}Fs_8Wo_{0.7-0.8}$). $Cr_2O_3$ contents for the two groups show an overall range of 0.31-0.45 with the high-Mg# group lying at mid-range.

Clinopyroxenes show a dichotomy in Mg# as seen already in olivine and orthopyroxene. Mg# for clinopyroxenes of the low-Mg# group range from 90-91.5 while those of the high-Mg# are 94.1 for CQ1 and 93.9 for CQ4. High-Mg# clinopyroxenes have significantly higher Cr# (CQ1,16.2; CQ4,17.9) than low-Mg# clinopyroxenes (5.6-9.7), but lower $Na_2O$, $Al_2O_3$ and $TiO_2$. A single clinopyroxene grain in CQ5 displays strong zoning with the core rich in $Al_2O_3$ and $Na_2O$, but poor in MgO and CaO, compared to the rim. Rim composition is very similar to the other clinopyroxene analyses for this sample suggesting that the core represents an older more aluminous composition.

The spinels of the high- and low-Mg# groups are distinguished by their Cr# where the former have Cr# of 29.9 and 32.2 and the latter have Cr# ranging from 8.5-15.5. Spinels with high-Cr# are high in $Cr_2O_3$ (26.1wt% and 28.0wt% respectively for samples CQ1 and CQ4) and FeO (CQ 1,11.5wt%; CQ4, 12.2wt%), but low in $Al_2O_3$ (CQ1, 41.0wt%; CQ4, 39.6wt%), MgO (CQ1, 18.2wt%; CQ4, 17.6wt%) and NiO (CQ1, 0.24wt%; CQ4, 0.19wt%), compared to their low-Cr# counterparts. These grains are moderately zoned with cores rich in FeO and poor in MgO and the opposite true for rims. Spinels with low-Cr# are unzoned and contain 52.4-57.7wt% $Al_2O_3$, 8.04-14.3wt% $Cr_2O_3$, 10.4-10.9wt% FeO and 20.3-21.1wt% MgO.

Arthur River

Nine samples from Arthur River have been studied. These xenoliths consist of lherzolites ± spinel and one spinel-bearing dunite. Arthur River peridotites show a very narrow range in olivine compositions from $Fo_{89.1-89.7}$ and there is no correlation between olivine Mg# and MnO as seen in the Coates Road xenoliths (see Fig. 4-13). Zoning occurs in two olivines from sample AR3. Grain 1 shows a decrease in FeO from core to rim coupled with an increase in MgO and NiO. Grain 2 shows a strong increase in FeO from core to rim (10.0 to 12.6wt%) and a strong decrease in MgO (49.4 to 47.0wt%).

Mg# for orthopyroxene has a narrow range from 89.8-90.2. There is also a very small range in orthopyroxene composition ($En_{88-89}Fs_{10}Wo_{0.5-1.6}$). There is a wide range in $Al_2O_3$ contents with sample AR5 showing the highest abundance at 4.91wt%. This orthopyroxene also has twice the CaO of the other Arthur River samples.

Clinopyroxene compositions display a good negative correlation between $Al_2O_3$ and CaO with AR5 again having the highest $Al_2O_3$ content (7.12wt%). Other samples lie at lower $Al_2O_3$ values but with increasing CaO contents (highest CaO value is 21.7wt%). Mg- and Cr-numbers for clinopyroxene do not show any correlation; Cr# are fairly uniform (~5.5-6.5) as are Mg# (90-91).

Spinels from the lherzolites all show very similar compositions and on a Mg# vs Cr# plot they lie in a tight cluster at high Mg# (76-79) and low Cr# (6-10). The dunite contains spinel which is more Fe- and Cr-rich and plots, therefore, at a lower Mg# and higher Cr#. A spinel grain from the dunite shows strong zoning with $Al_2O_3$ and MgO increasing, and FeO decreasing, from core to rim. Mg# is 49.2 for the core and 64.7 at the rim.

Table Cape

Nine spinel lherzolites have been studied from Table Cape. Mineral phases are typically homogeneous and no significant zoning has been detected. These peridotites show a range in olivine Mg# from 89-91.2 that is negatively correlated with olivine MnO contents (see Fig. 4-14).

Orthopyroxene shows a wide variation in composition that delineates two distinct geochemical types. The first type is characterised by high $Al_2O_3$ and FeO abundances in orthopyroxene and low CaO and MgO ($En_{89}Fs_{9.4-10.1}Wo_{0.9-1.4}$) The second type (TC3 and

TC7) has low $Al_2O_3$ (2.95 and 2.56wt% respectively) and FeO and high CaO ($En_{90}Fs_8Wo_{1.4}$). These two samples have the highest olivine Mg# for this locality and both lie in the same part of an olivine Mg# vs MnO plot as the high-Mg# samples of Coates Road (see Fig.4-14).

The geochemical differences recognised in orthopyroxene are also evident in clinopyroxene. Samples can again be separated into high- and low-$Al_2O_3$ groups. The first group is characterised by high $Al_2O_3$ (4.66-6.92wt%) and $Na_2O$ (1.33-1.89wt%), and low MgO (14.7-15.3wt%) and CaO (19.9-21.9wt%), and the second group by low $Al_2O_3$ (TC3, 3.37wt%; TC7, 2.79wt%) and $Na_2O$ (TC3, 0.67wt%; TC7, 0.66wt%), and high MgO (TC3, 17.0wt%; TC7, 17.2wt%) and CaO (TC3, 22.1wt%; TC7, 22.2wt%). FeO contents are similar for both groups. The low-$Al_2O_3$ clinopyroxenes are very similar in composition to those from the high-olivine-Mg# group of the Coates Road locality. These similarities include $Al_2O_3$ and CaO content, and Cr# and Mg#. $Na_2O$ is low for both localities but particularly so for Table Cape.

Spinels from Table Cape define two groups based on Mg# and Cr# which coincide with the two groups defined for the Coates Road spinels. The first group is characterised by high-Mg# and low-Cr#. These spinels are unzoned and contain 56.5-58.2wt% $Al_2O_3$, 8.89-10.3wt% $Cr_2O_3$, 9.72-11.4wt% FeO, and 20.0-21.3wt% MgO. The two samples from the second group has lower Mg# and higher Cr#. Sample TC3 has the composition 38.7wt% $Al_2O_3$, 28.7wt% $Cr_2O_3$, 12.6wt% FeO and 18.2wt% MgO. Sample TC7 is more chromiferous with the composition 33.5wt% $Al_2O_3$, 34.5wt% $Cr_2O_3$, 12.9wt% FeO and 16.2wt% MgO.

Doctors Rocks

Six samples from Doctors Rocks were studied including five spinel lherzolites and one clinopyroxene-free harzburgite. These peridotites display a very narrow range in olivine composition ($Fo_{88.9-89.5}$) and plot with the bulk of olivines from Tasmanian mantle xenoliths on a olivine Mg# vs MnO diagram (Fig. 4-15).

Orthopyroxene shows little variation in elements such as MgO (32.9-33.7wt%), FeO (6.56-6.84wt%), $Cr_2O_3$ (0.26-0.31wt%) and CaO (0.54-0.74wt%) and has a typical composition of $En_{89}Fs_{10}Wo_{1.1}$. $Al_2O_3$ shows some variation with values ranging from 3.58-4.57wt% as illustrated in Fig. 4-15.

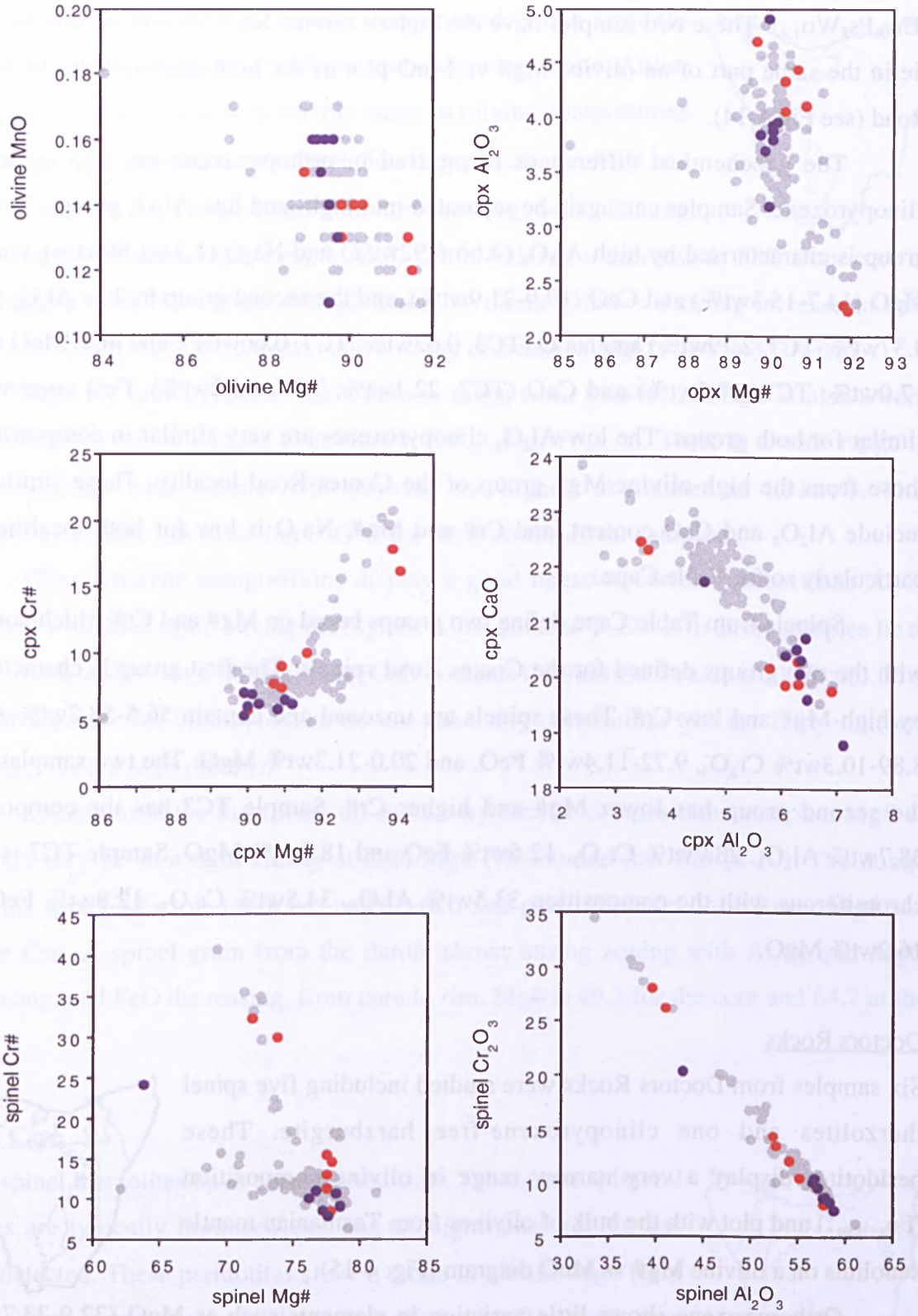


**Figure 4-13.** Composition variation diagrams for minerals in Tasmanian mantle xenoliths. Grey symbols represent the entire dataset for Tasmania. Red symbols are Coates Road Quarry xenoliths. Blue symbols are Arthur River xenoliths.

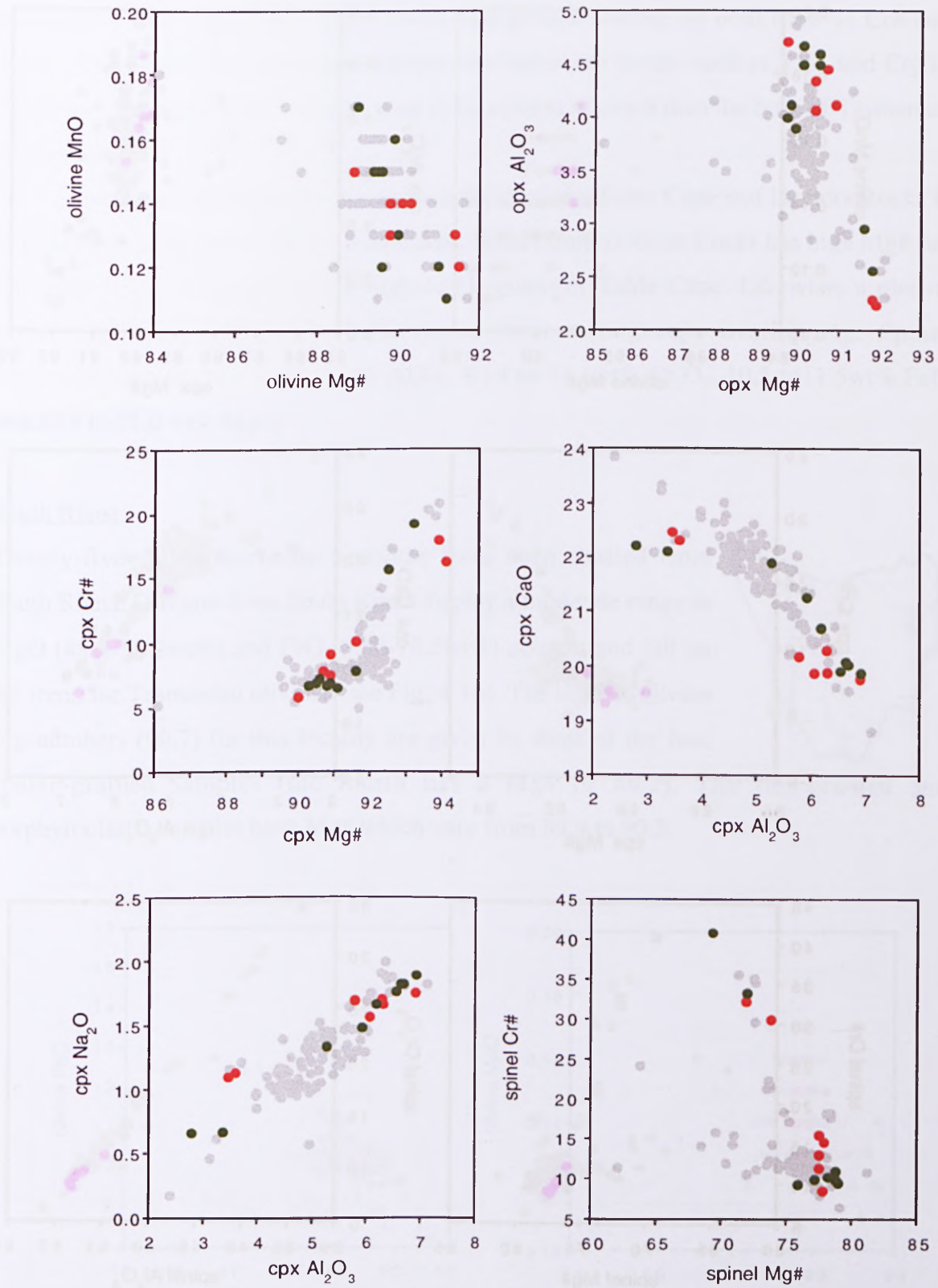


**Figure 4-14.** Composition variation diagrams for Tasmanian mantle xenoliths. Grey symbols represent the entire dataset for Tasmania. Red symbols are Coates Road Quarry xenoliths. Green symbols are Table Cape xenoliths.

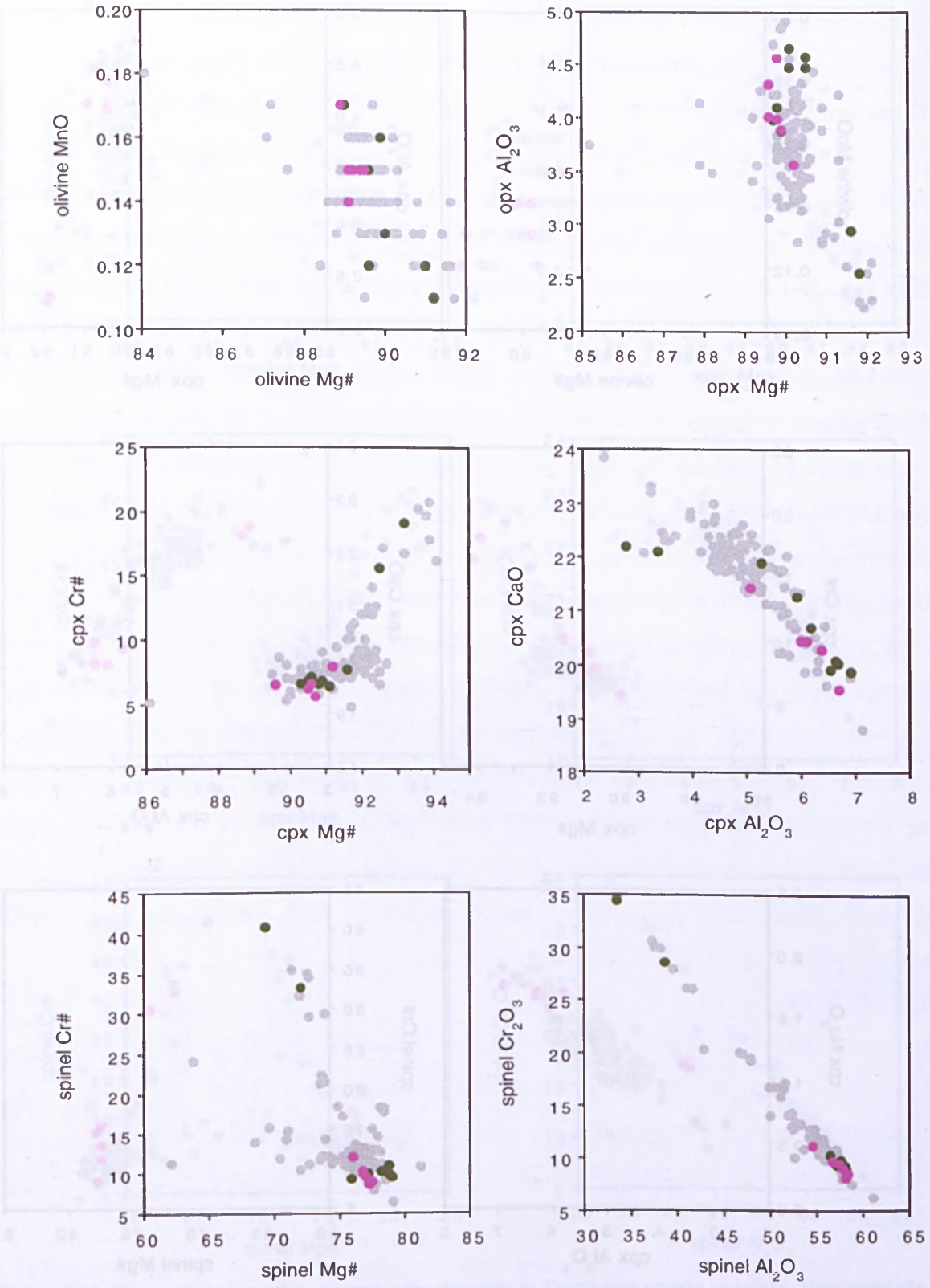


**Figure 4-15.** Composition variation diagrams for minerals in Tasmanian mantle xenoliths. Grey symbols represent the entire dataset for Tasmania. Green symbols are Table Cape xenoliths. Purple symbols are Doctors Rocks xenoliths.

Clinopyroxenes from Doctors Rock are very similar in composition to the high-$Al_2O_3$-cpx group from Table Cape. These two groups overlap on both Mg# vs Cr# and $Al_2O_3$ vs CaO plots and also show comparable values for oxides such as $TiO_2$ and $Cr_2O_3$. Clinopyroxene from these localities tend to be more $Al_2O_3$-rich than the bulk of Tasmanian clinopyroxenes.

Geochemical similarities between xenoliths from Table Cape and Doctors Rocks is also apparent in spinels from these localities. Spinel from Doctors Rocks has high Mg# but relatively low Cr# as seen in the high-$Al_2O_3$ group of Table Cape. Likewise, a plot of spinel $Al_2O_3$ against spinel $Cr_2O_3$ shows these two groups overlapping. Spinel compositions have 54.6 to 58.3wt% $Al_2O_3$, 8.14 to 11.1wt% $Cr_2O_3$, 10.5 to11.5wt% FeO and 20.5 to 21.0 wt% MgO.

South Riana

Twenty-five spinel lherzolite xenoliths have been studied from South Riana. Olivines from South Riana display a moderate range in MgO (48-8-50.2wt%) and FeO (8.88-10.5wt%) content and fall on the trend for Tasmanian olivines (see Fig. 4-16). The highest olivine Mg-numbers (90.7) for this locality are given by three of the four coarse-grained samples (the fourth has a Mg# of 89.2). The fine-grained and porphyroclastic samples have Mg# which vary from 89.4 to 90.3.

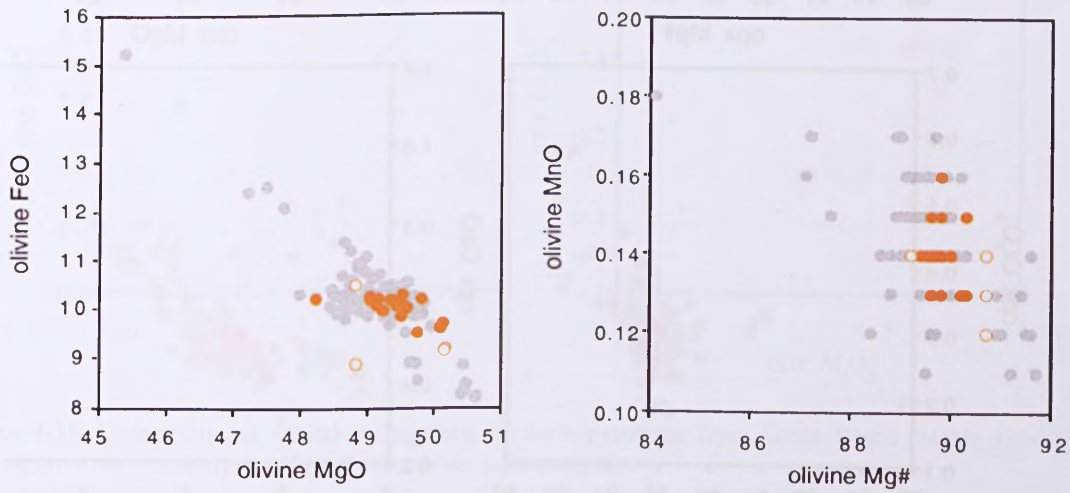


**Figure 4-16.** Compositional variation diagrams for olivine from Tasmanian mantle xenoliths. Grey symbols represent the entire dataset for Tasmania. Orange symbols are South Riana xenoliths. Closed circles are fine-grained and porphyroclastic samples. Open circles are coarse-grained samples.

Orthopyroxene composition shows considerable variation though overall the majority of samples tends to plot within a tight compositional range (Fig.4-17). Mg-number for most orthopyroxenes falls in the range 89.9-90.5 with a few outliers ranging up to 91.3. These high-Mg# orthopyroxenes belong exclusively to the coarse-grained xenoliths. $Al_2O_3$ content varies from 2.84 wt% to 4.85wt% with most samples lying between 3.2 and 3.8wt%. The coarse-grained samples are responsible for both the highest and lowest $Al_2O_3$ contents. Plots of $Cr_2O_3$ and CaO against Mg# or $Al_2O_3$ show that the orthopyroxenes from the coarse-grained xenoliths are uniformly enriched in Cr and Ca in comparison to those from the fine-grained xenoliths (see Fig. 4-17). Sample SR1b-2, though microstructurally belonging to the coarse-grained group, is compositionally distinct from the other coarse samples as it has a low Mg# (89.2) and $Cr_2O_3$ content (0.35wt%), and high FeO (6.52wt%), though it does have a comparable CaO (0.79wt%) abundance.

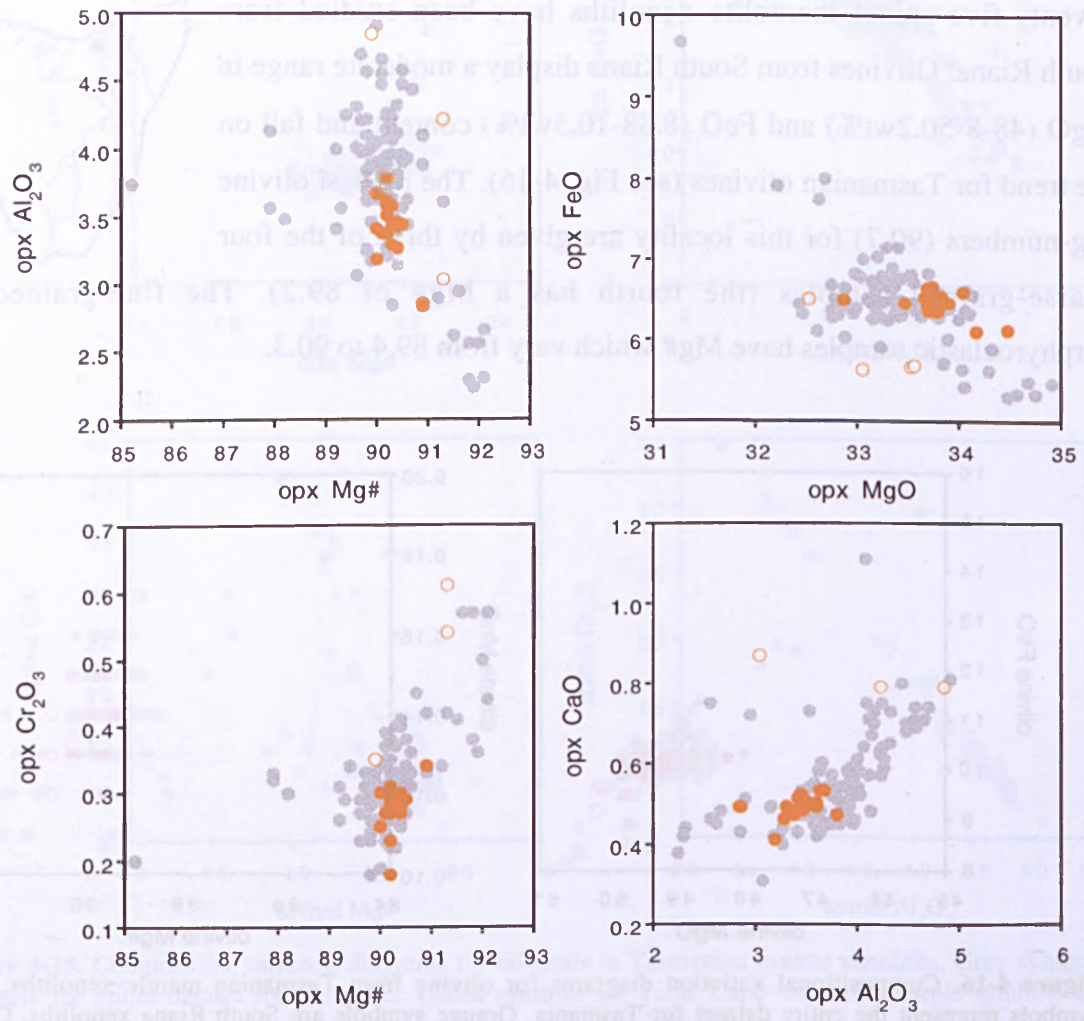


**Figure 4-17** Compositional variation diagrams for orthopyroxene from Tasmanian mantle xenoliths. Grey symbols represent the entire dataset for Tasmania. Orange symbols are South Riana xenoliths. Closed circles are fine-grained and porphyroclastic samples. Open circles are coarse-grained samples.

Zoning in orthopyroxenes is restricted to the large porphyroclasts in the porphyroclastic samples. These grains display strong zoning in $Al_2O_3$ content from core to rim as can be seen in Fig. 4-18. $Al_2O_3$ content for cores ranges from 3.43-4.75wt% while rims contain between 2.97-3.62wt% $Al_2O_3$. This range for rims closely matches the $Al_2O_3$ content of the orthopyroxene neoblasts (2.99-3.66wt%) in these samples suggesting that porphyroclast rims are in equilibrium with the neoblasts but cores are not. Cores are also considerably enriched in CaO and $Cr_2O_3$ in comparison to rims. Rims tend to be more Mg- and Fe-rich than cores though not all samples show a significant difference between cores and rims for these elements.

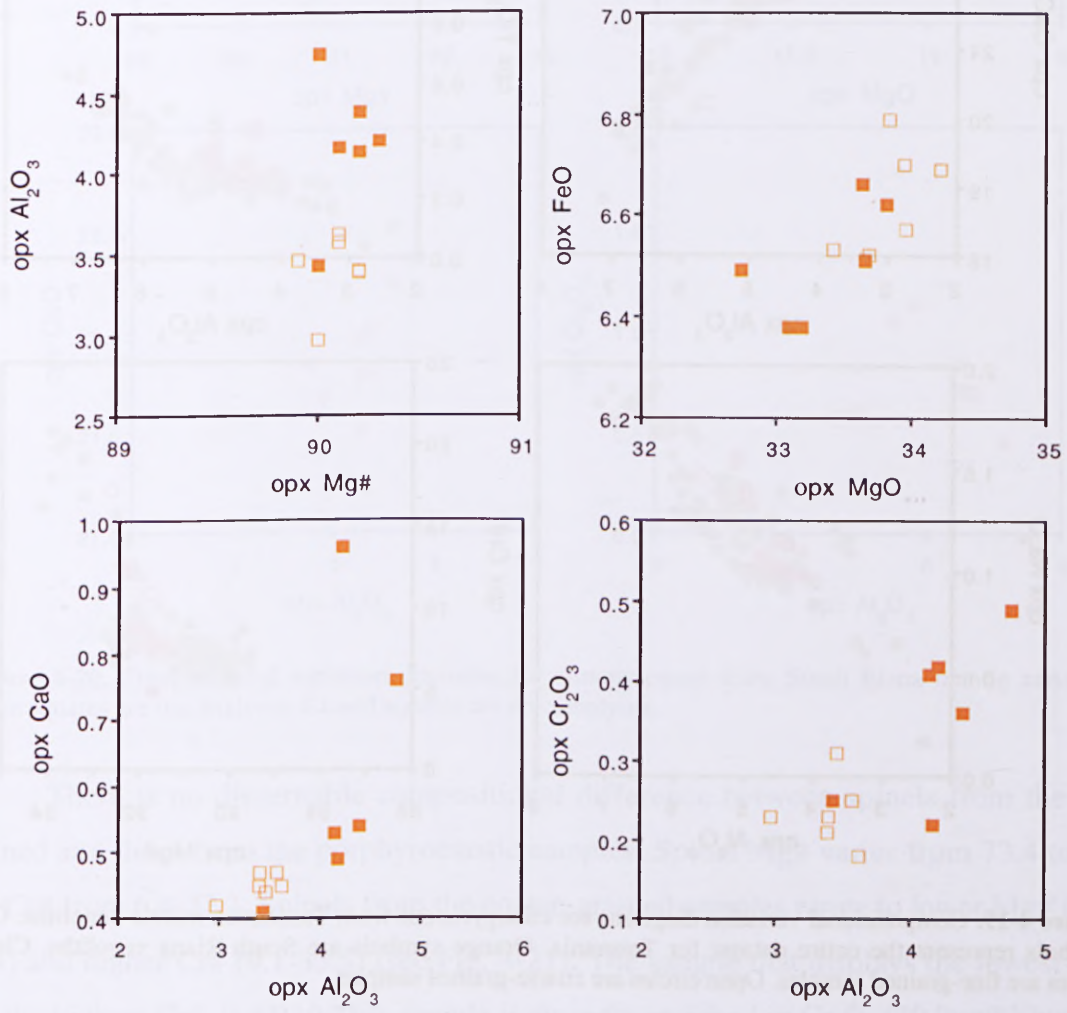


**Figure 4-18.** Compositional variation diagrams for orthopyroxene from South Riana mantle xenoliths. Open squares are rim analyses. Closed squares are core analyses.

Clinopyroxene composition ranges from $Al_2O_3$-poor (3.04wt%) to $Al_2O_3$-rich (5.66wt%) (Fig.4-19). The bulk of clinopyroxenes from this locality plot over a narrow range in $Al_2O_3$ (4.12-5.03wt%) and CaO (21.4-22.5wt%). The most extremes $Al_2O_3$ values

belong to the coarse-grained samples except for sample SR1b-2 which plots within the range for the other samples though at a slightly higher CaO content. The coarse-grained clinopyroxenes, including sample SR1b-2, also show deviation from the rest of the samples in terms of $TiO_2$, $Cr_2O_3$ and $Na_2O$ contents as illustrated in Fig. 4-19. There does not appear to be any significant difference in FeO or MgO content between coarse-grained and fine-grained samples except for sample SR 10 which is enriched in MgO (16.9wt%).

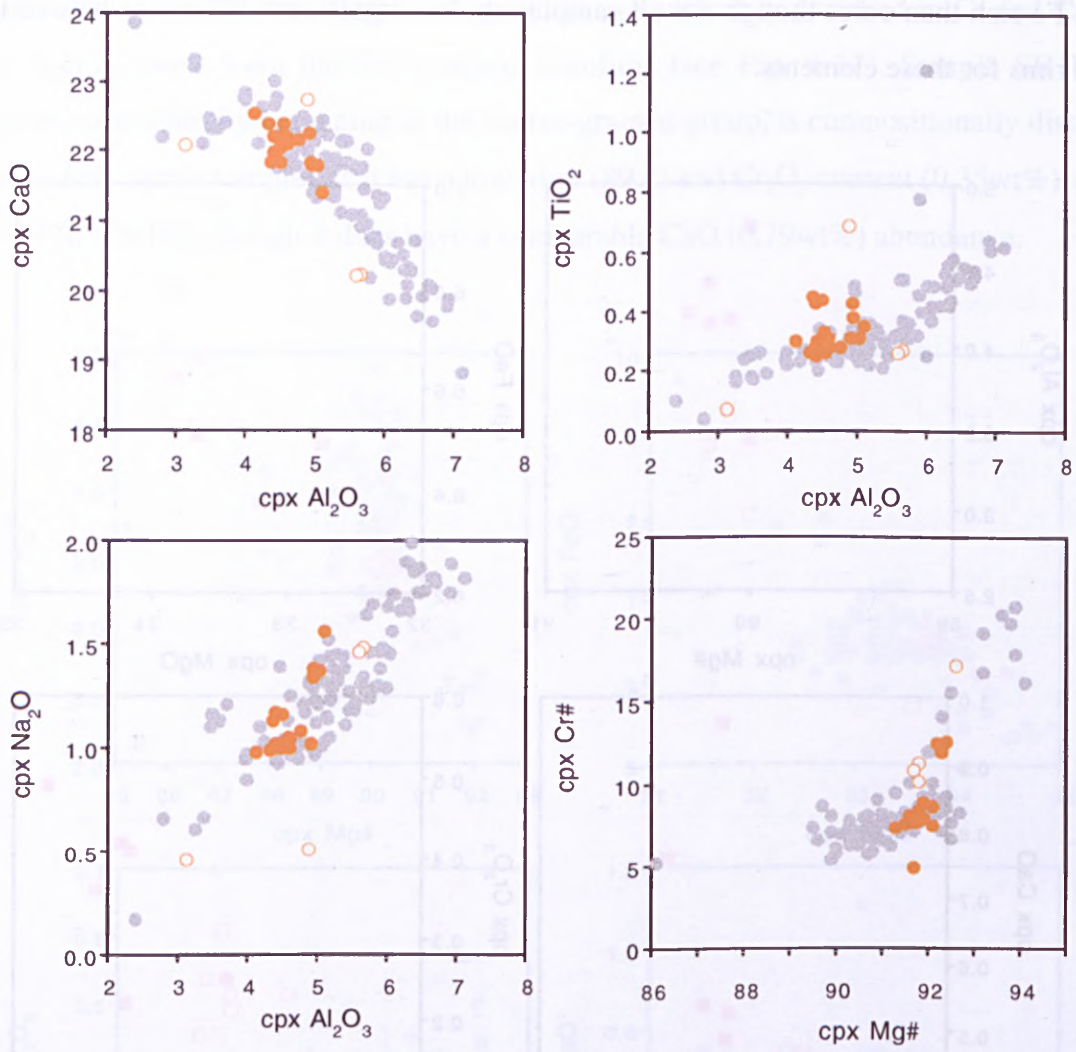


**Figure 4-19.** Compositional variation diagrams for clinopyroxene from Tasmanian mantle xenoliths. Grey symbols represent the entire dataset for Tasmania. Orange symbols are South Riana xenoliths. Closed circles are fine-grained samples. Open circles are coarse-grained samples.

Zoning in clinopyroxene is recognised in fine-grained and porphyroclastic xenoliths but is absent in coarse-grained samples. Zoning in these pyroxenes is characterised by variations in $Al_2O_3$ and MgO content from core to rim, where cores are MgO-poor and $Al_2O_3$-rich and rims are MgO-rich and $Al_2O_3$-poor (see Fig. 4-20). There is no evidence for zoning in other elements such as Fe, Ca and Cr, nor is there any major

difference in Mg# between cores and rims. Cr# is slightly higher in cores than in rims for some samples.

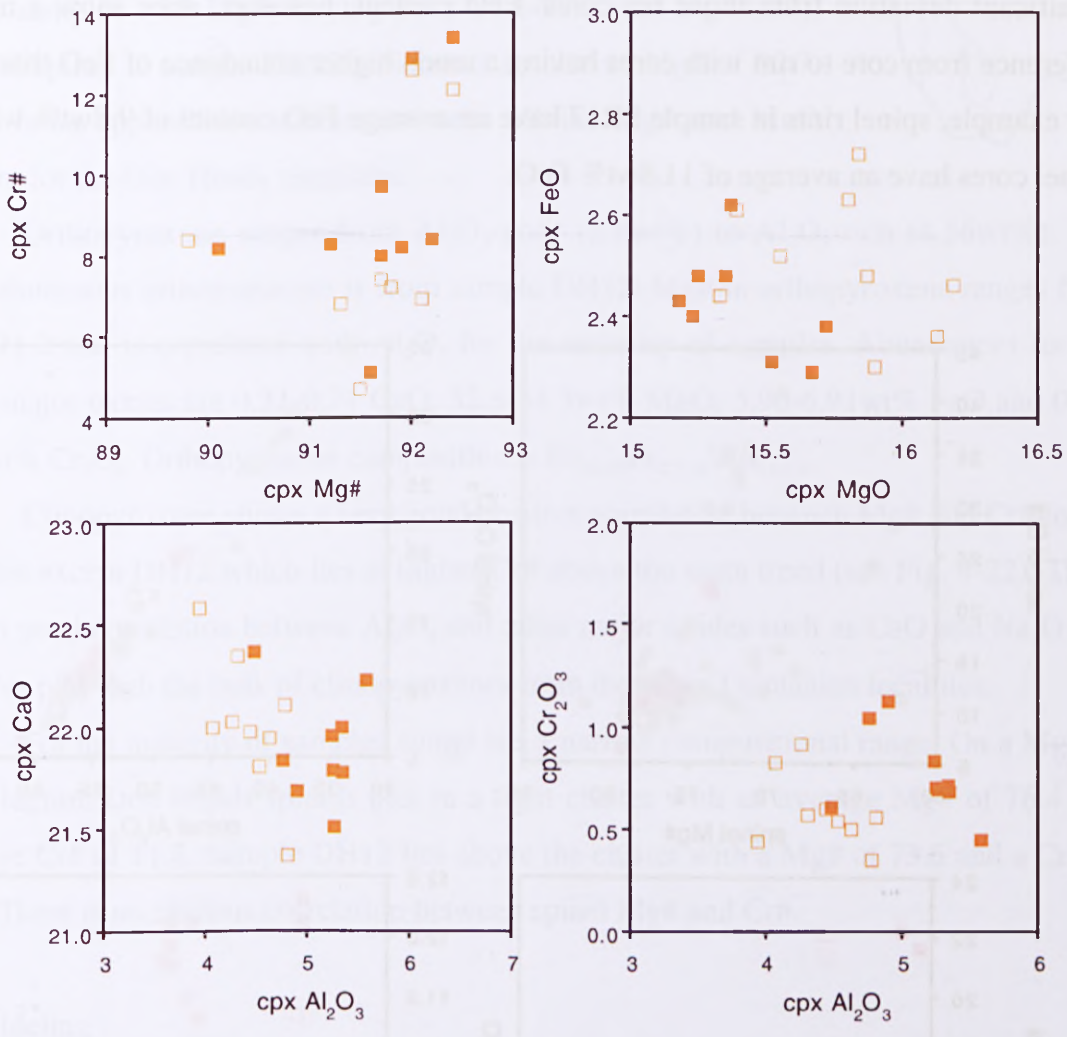


**Figure 4-20.** Compositional variation diagrams for clinopyroxene from South Riana mantle xenoliths. Open squares are rim analyses. Closed squares are core analyses.

There is no discernable compositional difference between spinels from the fine-grained and those from the porphyroclastic samples. Spinel Mg# varies from 73.4 to 79.1 and Cr# from 6.4-22.1. Spinels from the coarse-grained samples range to lower Mg# (71.3-78.4) and higher Cr# (9.1-35.5) (see Fig. 4-21). The sample that displays the lowest Mg#, and the highest Cr#, is SR10 This sample is strongly enriched in $Cr_2O_3$ (30.7wt%) but very poor in $Al_2O_3$ in comparison to the other samples. The other coarse-grained xenoliths contain spinel which has $Al_2O_3$ and $Cr_2O_3$ contents that fall within the ranges for spinels from the fine-grained and porphyroclastic peridotites.

Zoning in spinels is common and occurs in grains from all three xenolith types identified at South Riana. Fig. 4-21 shows that Cr# does not vary from core to rim as both

$Al_2O_3$ and $Cr_2O_3$ appear to be homogeneously distributed across the grains. However, Mg# does show variation from core to rim with rims typically having higher Mg# than cores. This a function of FeO rather than MgO content as rim MgO values do not show significant deviation from those for cores. FeO content, however, does show a marked difference from core to rim with cores having a much higher abundance of FeO than rims. For example, spinel rims in sample SR17 have an average FeO content of 9.8wt% whereas spinel cores have an average of 11.8wt% FeO.

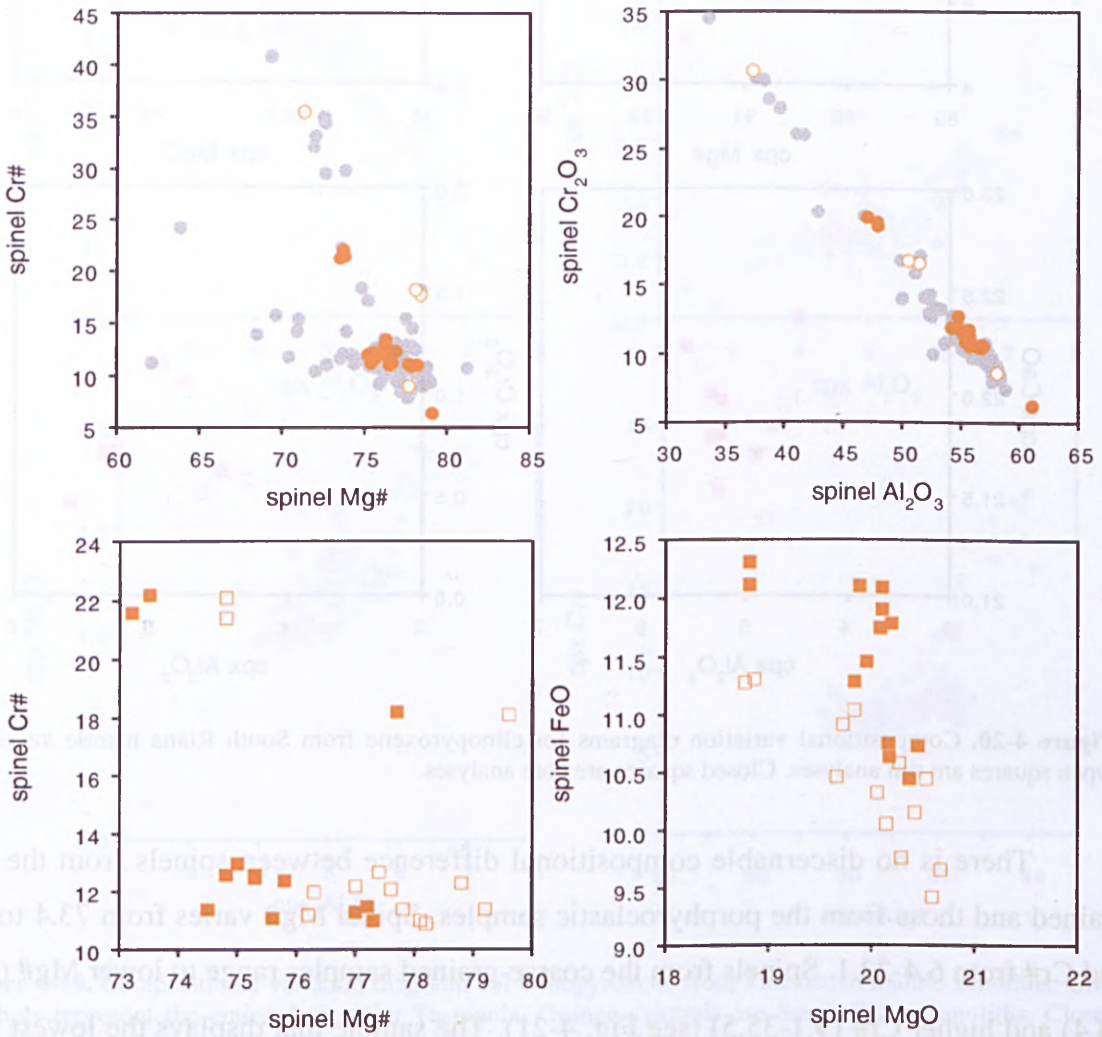


**Figure 4-21.** Top. Compositional variation diagrams for spinel from South Riana mantle xenoliths. Grey symbols represent the entire dataset for Tasmania. Orange symbols are South Riana xenoliths. Closed circles are fine-grained samples. Open circles are coarse-grained samples. Bottom. Compositional variation diagrams for spinel from South Riana mantle xenoliths. Open squares are rim analyses. Closed squares are core analyses.

Don Heads

Fifteen samples were studied from Don Heads and all are spinel lherzolites. Olivine composition shows little variation for the bulk of the samples with Mg# varying from 89.4-90.2 (see Fig. 4-22). The exception is sample DH12 which has an olivine Mg# of 90.7. There is no apparent correlation between olivine Mg# and MnO content for the Don Heads xenoliths.

Orthopyroxene ranges from $Al_2O_3$-poor (2.9wt%) to $Al_2O_3$-rich (4.56wt%). The least aluminous orthopyroxene is from sample DH12. Mg# in orthopyroxene ranges from 89.6-91.2 and is correlated with $Al_2O_3$ for the majority of samples. Abundances for the other major oxides are 0.31-0.71 CaO, 32.8-34.3wt% MgO, 5.90-6.91wt% FeO and 0.22-0.36wt% $Cr_2O_3$. Orthopyroxene composition is $En_{88-90}Fs_{8.7-10}Wo_{0.6-1.4}$.

Clinopyroxene shows a very good positive correlation between Mg# and Cr# for all samples except DH12 which lies at higher Cr# above the main trend (see Fig. 4-22). There is also good correlation between $Al_2O_3$ and other major oxides such as CaO and $Na_2O$ and samples plot with the bulk of clinopyroxenes from the other Tasmanian localities.

For the majority of samples spinel has a narrow compositional range. On a Mg# vs Cr# diagram Don Heads spinels plot in a tight cluster with an average Mg# of 76.4 and average Cr# of 11.8. Sample DH12 lies above the cluster with a Mg# of 73.6 and a Cr# of 22.3. There is no obvious correlation between spinel Mg# and Cr#.

The Sideling

Only two samples (SD2a and SD2b) from the Sideling have been studied and both are spinel lherzolites. These samples have similar compositions. They have an average olivine Mg# of 89.4 and plot with the bulk of Tasmanian olivines on a Mg# vs MnO diagram.

Orthopyroxene is rich in $Al_2O_3$ (~3.8wt%), has a Mg# of 90.1 and a composition of $En_{89.3}Fs_{9.8}Wo_{0.9}$. Clinopyroxene is also Al-rich (~5wt% $Al_2O_3$) and has an average Mg# of 91.9. Both pyroxenes are similar in composition to low-Mg# orthopyroxenes and clinopyroxenes from the other Tasmanian localities.

Spinel from the Sideling is typical low-Mg# spinel with an average Mg# of 76.3 and average Cr# of 11.2. Zoning in two spinels from sample SD2a shows an increase in $Al_2O_3$, and FeO, and a decrease in MgO and $Cr_2O_3$, from core to rim for one grain and the opposite true for the other grain.

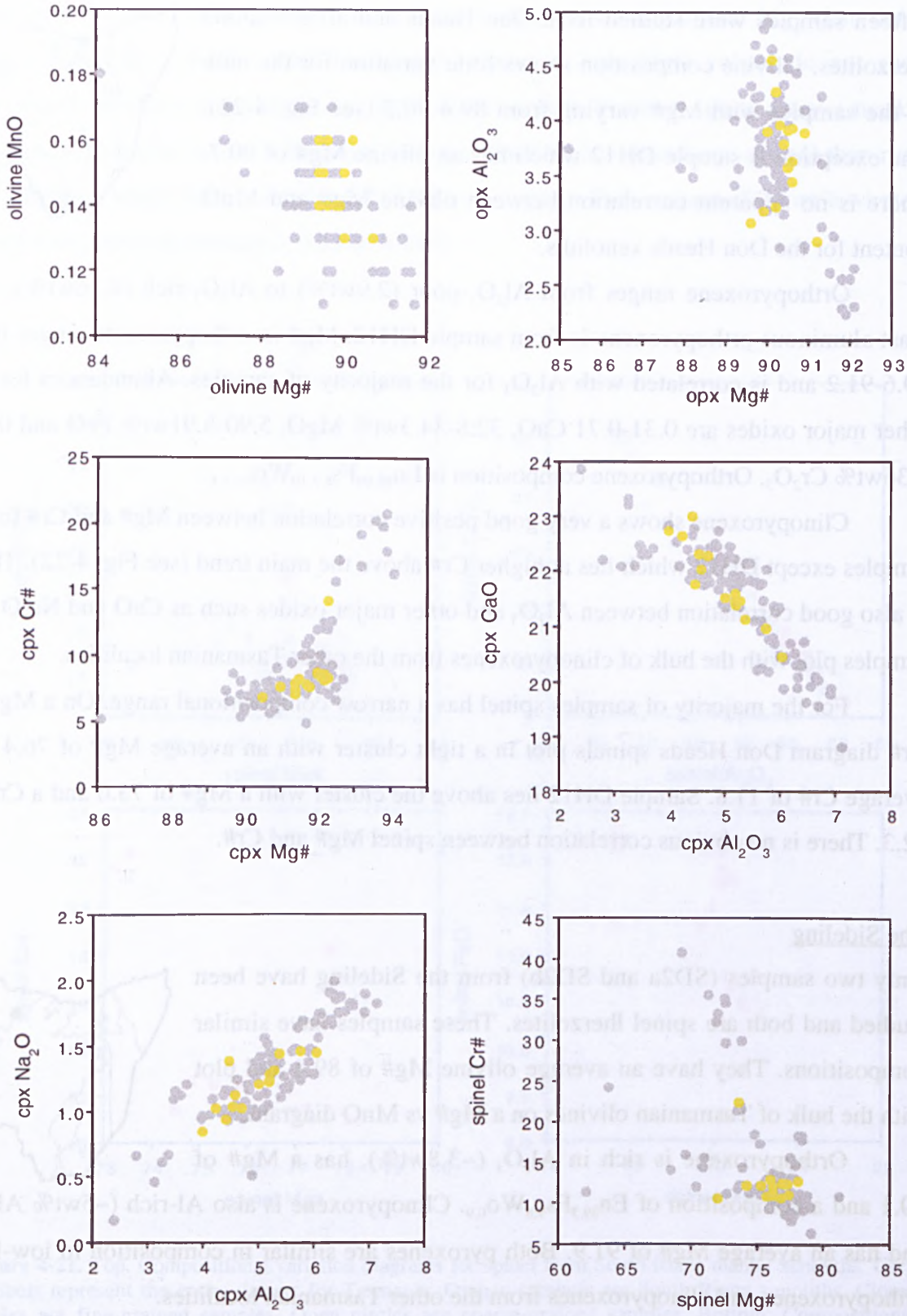


**Figure 4-22.** Composition variation diagrams for minerals in Tasmanian mantle xenoliths. Grey symbols represent the entire dataset for Tasmania. Yellow symbols are Don Heads xenoliths.

Blessington

Thirty-three xenoliths were studied from Blessington. The rocks types recognised in this suite are cpx-bearing harzburgites and lherzolites±spinel. Olivines in these samples can be divided into two compositional types; high-Mg# and low-Mg#. The high-Mg# group of Blessington consists of three xenoliths (samples BL1, BL3 and BL10) that are all cpx-bearing harzburgites. This group has an average olivine Mg# of 91.6, similar to that seen in the high-Mg# samples from Coates Road. The low-Mg# group are all lherzolites, with or without spinel. Olivine in these samples shows a narrow range in Mg# from 89.4-90. Sample BL22 has an olivine Mg# (90.9) that is intermediate between the high- and low-Mg# groups.

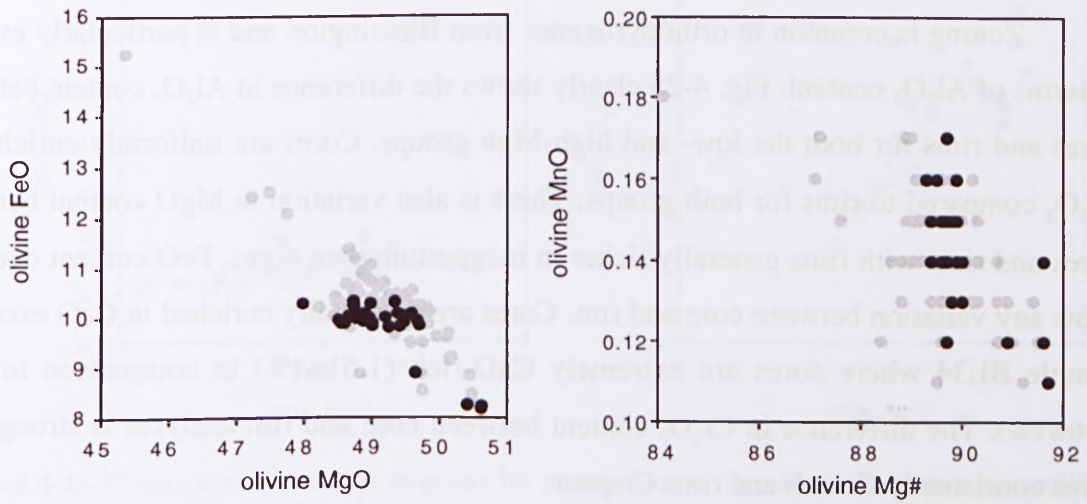


**Figure 4-23.** Composition variation diagrams for olivine from Tasmanian mantle xenoliths. Grey symbols represent the entire Tasmanian dataset. Black symbols are Blessington samples.

Orthopyroxene composition clearly separates the Blessington samples into two distinct groups based on $Al_2O_3$ content and Mg# (Fig. 4-24). The low-olivine-Mg# group plots with a narrow range in orthopyroxene Mg# (89.9-90.4) over a wide range in $Al_2O_3$ (2.85-4.24wt%). The high-Mg# group lies at higher Mg# (92.1) and much lower $Al_2O_3$ (2.33-2.66) than the low-Mg# samples and again overlaps the high-Mg# group of Coates Road. Sample BL22 has an orthopyroxene Mg# of 91.5 and an $Al_2O_3$ content of 2.62 and therefore plots closer to the high-Mg# group than the low-Mg# group. The dichotomy in orthopyroxene chemistry is also seen in $Cr_2O_3$ contents, and MgO and FeO abundances as indicated by differences in Mg# (see Fig. 4-24). Orthopyroxene composition for the low-Mg# group is $En_{88.8\text{-}90.7}Fs_{8.5\text{-}10}Wo_{0.8\text{-}1.4}$ and for the high-Mg# group is $En_{91}Fs_{7.8}Wo_{0.8\text{-}0.9}$.

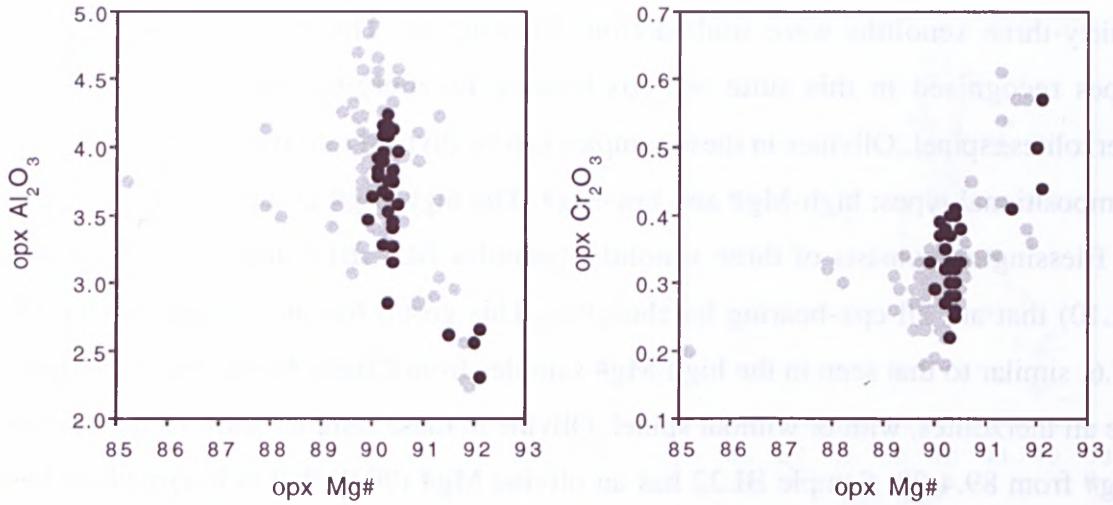


**Figure 4-24.** Composition variation diagrams for orthopyroxene from Tasmanian mantle xenoliths. Grey symbols represent the entire Tasmanian dataset. Black symbols are Blessington samples.

Zoning is common in orthopyroxenes from Blessington and is particularly evident in terms of $Al_2O_3$ content. Fig. 4-25 clearly shows the difference in $Al_2O_3$ content between cores and rims for both the low- and high-Mg# groups. Cores are uniformly enriched in $Al_2O_3$ compared to rims for both groups. There is also variation in MgO content between cores and rims with rims generally richer in magnesium than cores. FeO content does not show any variation between core and rim. Cores are marginally enriched in CaO except in sample BL34 where cores are extremely CaO-rich (1.61wt%) in comparison to rims (0.6wt%). The difference in $Cr_2O_3$ content between core and rim analyses is strong with cores consistently Cr-rich and rims Cr-poor.

Variations in Mg# seen in olivine and orthopyroxene are also apparent in clinopyroxenes from Blessington. This can be seen in a Mg# vs Cr# plot (Fig. 4-26) which separates clinopyroxene data into a low-Mg#, low-Cr# group and a high-Mg#, high-Cr# group. Both groups show good correlation between $Al_2O_3$ and major element oxides such as CaO, $Na_2O$ and $TiO_2$. On average, the high-Mg# group has lower $Al_2O_3$ contents (3.58wt%) than the low-Mg# group (4.82wt%), though it is sample BL25a from the low-Mg# group which records the lowest $Al_2O_3$ content at 2.39wt%. Sample BL22 has a Mg# of 93.2 and $Al_2O_3$ content of 4.17wt%. The high-Mg# clinopyroxenes have the lowest FeO contents (1.87-1.93wt%) and plot below the trend for the low-Mg# group on the $Al_2O_3$ vs FeO diagram in Fig. 4-26. Clinopyroxenes from Blessington do not show any evidence for zoning.

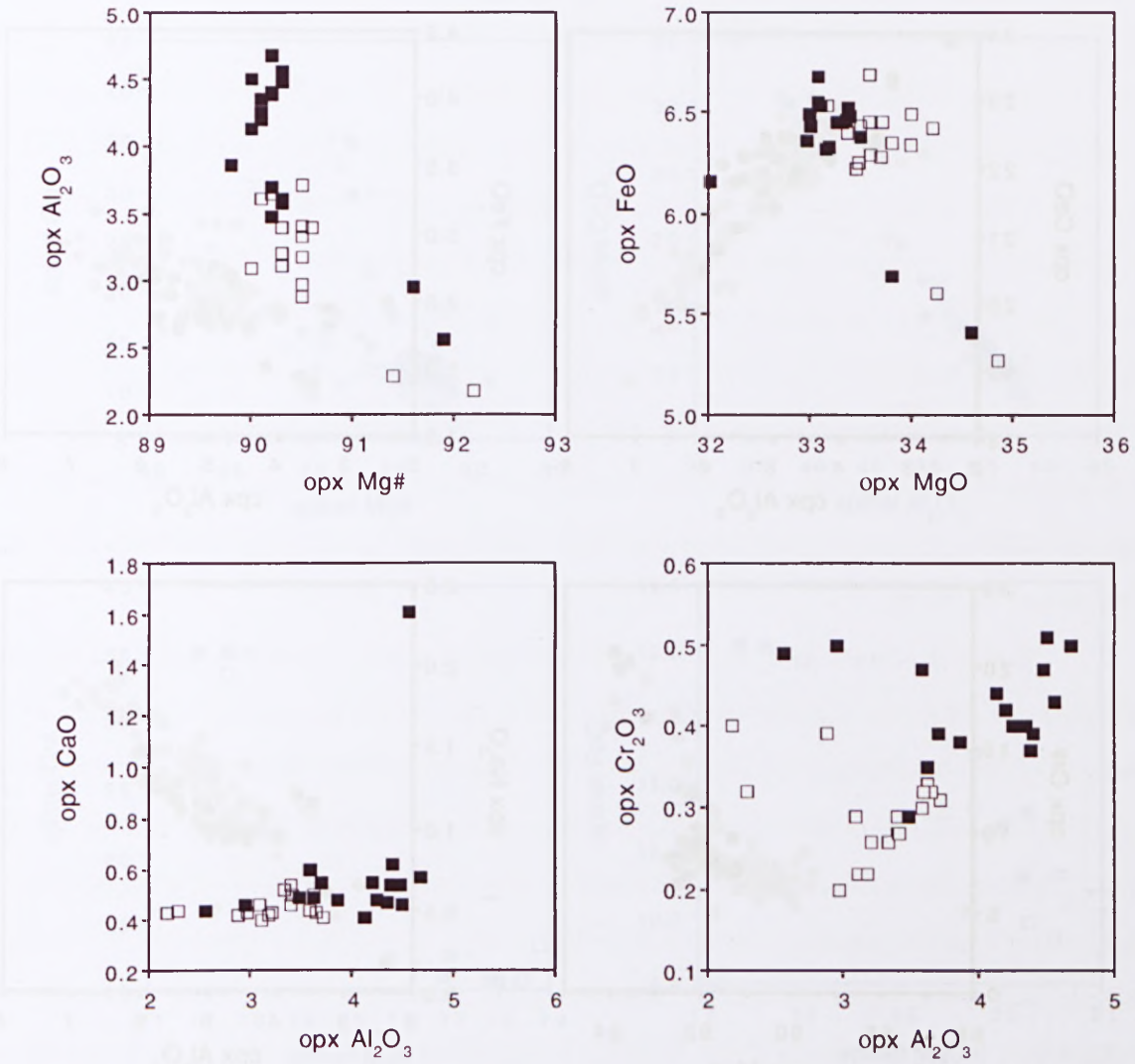


**Figure 4-25.** Compositional variation diagrams for orthopyroxene from Blessington mantle xenoliths. Open squares are rim analyses. Closed squares are core analyses.

As with the two pyroxenes, spinels can be divided into two groups based on Mg# and Cr#. Only two samples of the previously defined high-Mg# group contain spinel but both are Mg-poor and Cr-rich as can be seen in Fig. 4-27. These spinels are similar in composition to the high-Mg# spinels of Coates Road and Table Cape. The low-Mg# group has low MgO, $Al_2O_3$ and $Cr_2O_3$ in comparison to the high-Mg# group, and the majority of samples plots over a restricted range in Mg# and Cr# (see Fig. 4-27). Spinels from sample BL22 plot intermediate between the low- and high-Mg# groups. Zoning has been noted in a few instances in both low- and high-Mg# group spinels. The trend is for Fe-poor, Mg-rich rims and Fe-rich, Mg-poor cores as illustrated in Fig. 4-27. Rims tend to have higher Mg# than cores as expected from results for MgO and FeO though there does not appear to be any significant variation in Cr# from core to rim.

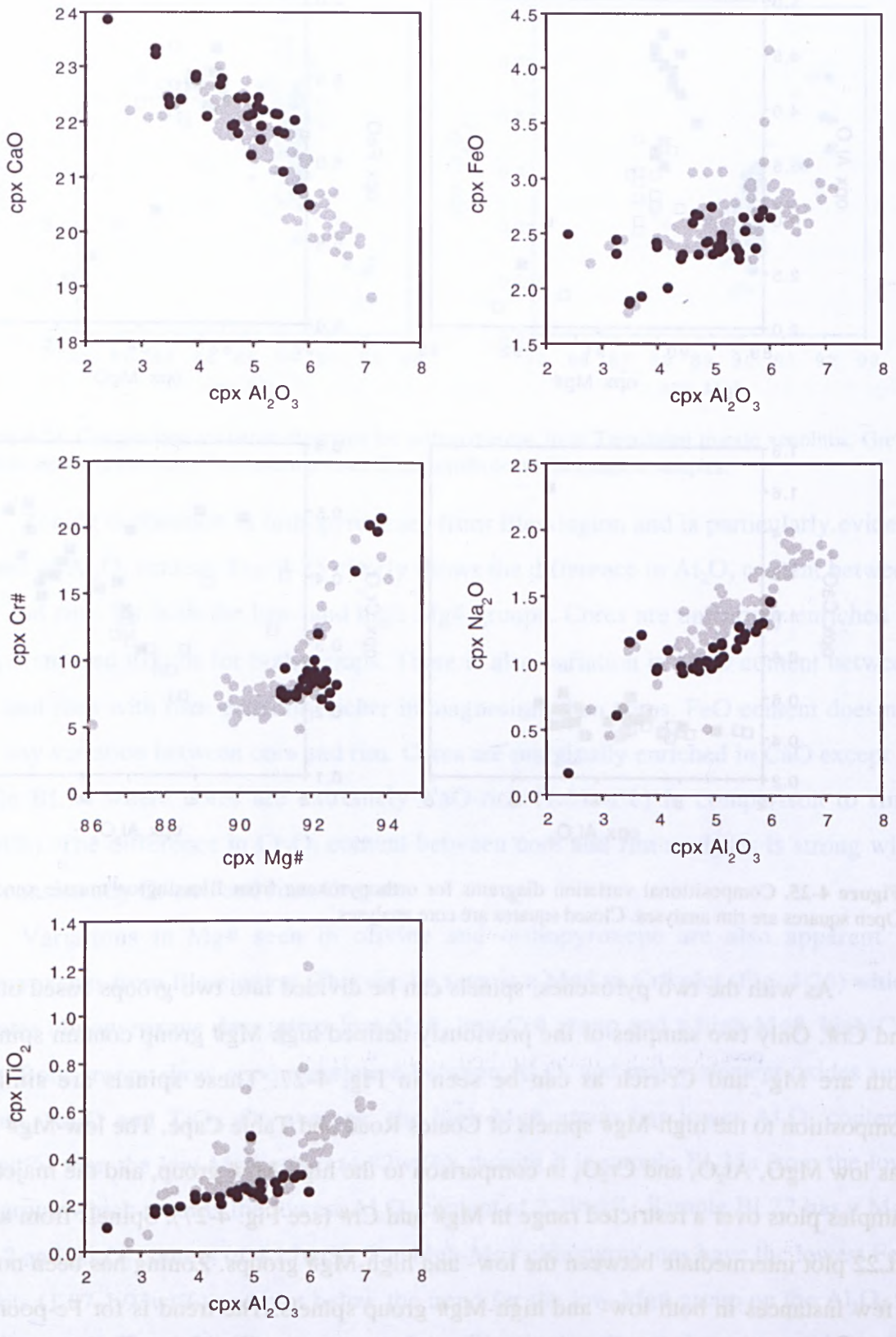


**Figure 4-26.** Composition variation diagrams for clinopyroxene from Tasmanian mantle xenoliths. Grey symbols represent the entire Tasmanian dataset. Black symbols are Blessington samples.

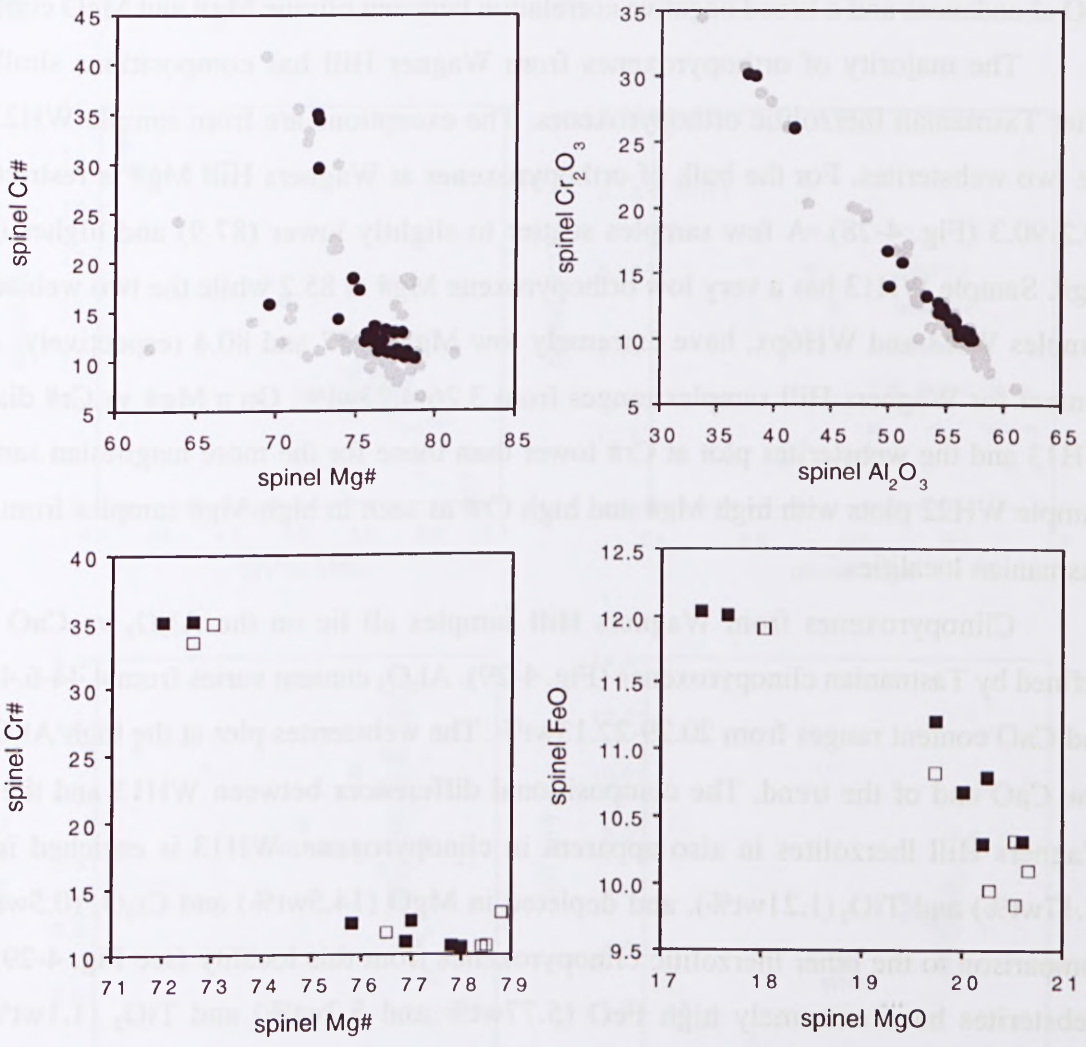


**Figure 4-27.** Top. Composition variation diagrams for spinel from Tasmanian mantle xenoliths. Grey symbols represent the entire Tasmanian dataset. Black symbols are Blessington samples. Bottom. Open squares are rim analyses. Closed squares are core analyses.

Wagners Hill

Twenty-four samples have been studied from Wagners Hill and these include lherzolites±spinel and two pyroxenites. Olivine from Wagners Hill lherzolites has a very wide range in Mg# from 84.1 to 90.9 (Fig. 4-28). The majority of olivines plot with high MgO (48.7-49.7wt%) and moderately low FeO (10.0-11.4wt%). A group of three samples plot with slightly lower MgO (47.2-47.7wt%) and higher FeO (12.1-12.5wt%) contents. Olivine from sample WH22 has the highest MgO (49.7wt%) and lowest FeO (8.88wt%) content and correspondingly gives the highest Mg# (90.9). Sample WH13 gives the very low Mg# (84.1) and based on this, and other geochemical characteristics which will be discussed below, belongs to the Fe-rich Cr-diopside suite

(refer to Section 1.3.1). There is a strong negative correlation between olivine MgO and FeO abundances and a broad negative correlation between olivine Mg# and MnO content.

The majority of orthopyroxenes from Wagner Hill has compositions similar to other Tasmanian lherzolitic orthopyroxenes. The exceptions are from sample WH22 and the two websterites. For the bulk of orthopyroxenes at Wagners Hill Mg# is restricted to 89.2-90.3 (Fig. 4-28). A few samples scatter to slightly lower (87.9) and higher (91.3) Mg#. Sample WH13 has a very low orthopyroxene Mg# at 85.2 while the two websterites, samples WH3 and WH6px, have extremely low Mg# at 77 and 80.4 respectively. $Al_2O_3$ content for Wagners Hill samples ranges from 3.26-4.23wt%. On a Mg# vs Cr# diagram WH13 and the websterites plot at Cr# lower than those for the more magnesian samples. Sample WH22 plots with high Mg# and high Cr# as seen in high-Mg# samples from other Tasmanian localities.

Clinopyroxenes from Wagners Hill samples all lie on the $Al_2O_3$ vs CaO trend defined by Tasmanian clinopyroxenes (Fig. 4-29). $Al_2O_3$ content varies from 4.44-6.47wt% and CaO content ranges from 20.29-22.13wt%. The websterites plot at the high $Al_2O_3$ and low CaO end of the trend. The compositional differences between WH13 and the other Wagners Hill lherzolites in also apparent in clinopyroxene. WH13 is enriched in FeO (4.17wt%) and $TiO_2$ (1.21wt%), and depleted in MgO (14.5wt%) and $Cr_2O_3$ (0.5wt%) in comparison to the other lherzolitic clinopyroxenes from this locality (see Fig. 4-29). The websterites have extremely high FeO (5.77wt% and 5.7wt%) and $TiO_2$ (1.1wt% and 0.88wt%) contents and at slightly higher $Al_2O_3$ contents than the clinopyroxenes from the lherzolites. There is little difference in $Na_2O$ abundance between samples though the websterites fall slightly off to higher $Al_2O_3$ values on a $Na_2O$ vs $Al_2O_3$ diagram. Mg# and Cr# in clinopyroxene clearly separates the magnesian samples from the more Fe-rich. WH13 lies intermediate between the websterites and lherzolites. The lherzolitic clinopyroxenes show a strong positive correlation between Mg# and Cr#. Sample WH22 lies off this trend at elevated Cr#.

Of the twenty-two lherzolites studied only seventeen contain spinel. There is considerable scatter in spinel composition on a Mg# vs Cr# diagram for Wagners Hill samples (Fig.4-29). The spinels plot over a relatively narrow range in Cr# (10.8-18.2) and a wide range in Mg# (62.1-81.2). Sample WH13 lies at low Mg# and Cr# as already seen in orthopyroxene and clinopyroxene. The sample with the highest Cr# is again WH22 confirming its Cr-rich composition as indicated by its pyroxenes. Spinels from Wagners

Hill fall on the strong negative trend for $Al_2O_3$ vs $Cr_2O_3$ abundances defined for Tasmanian spinels.

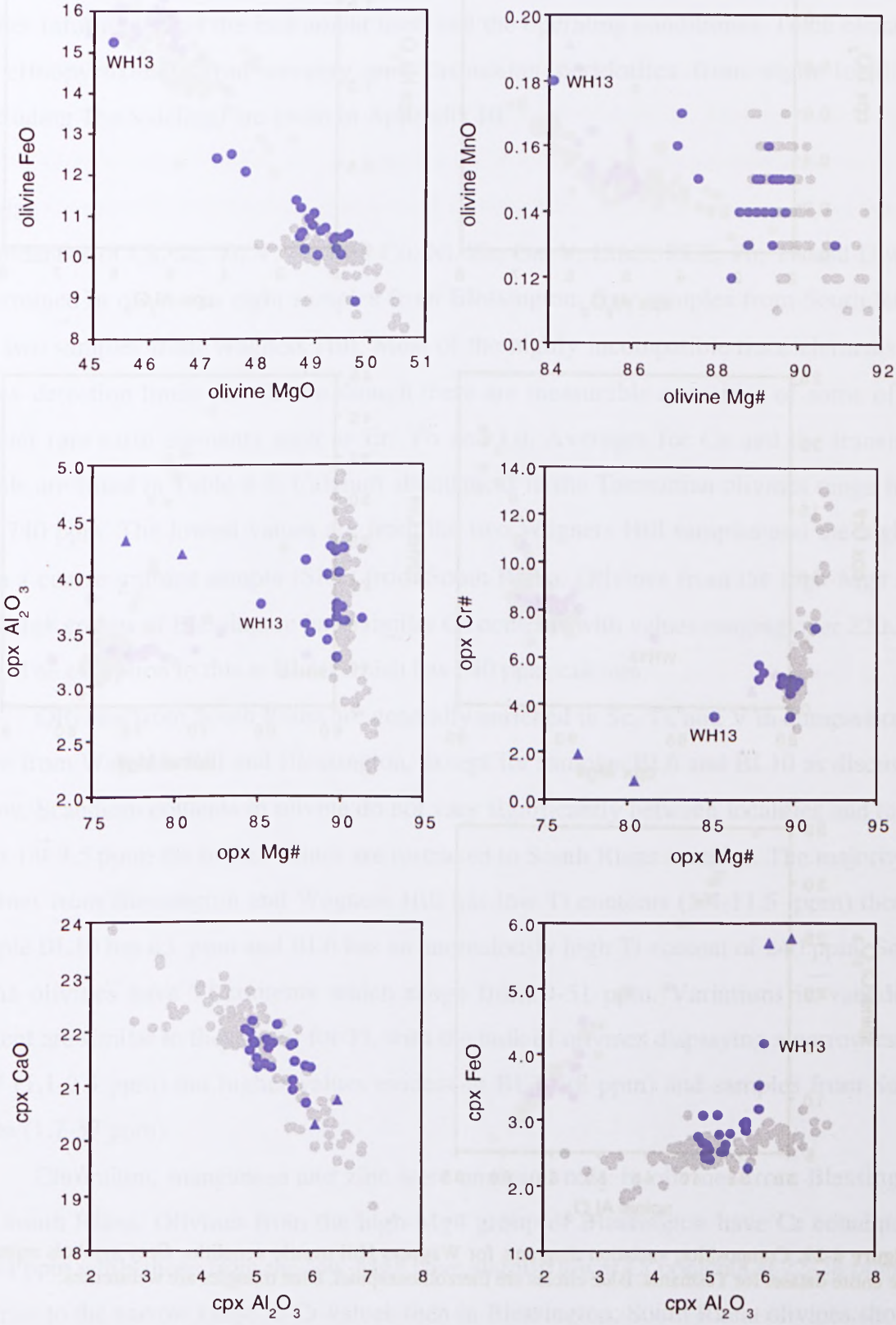


**Figure 4-28.** Composition variation diagrams for Wagners Hill mantle xenoliths. Grey symbols represent the entire dataset for Tasmania. Blue circles are lherzolites±spinel. Blue triangles are websterites.

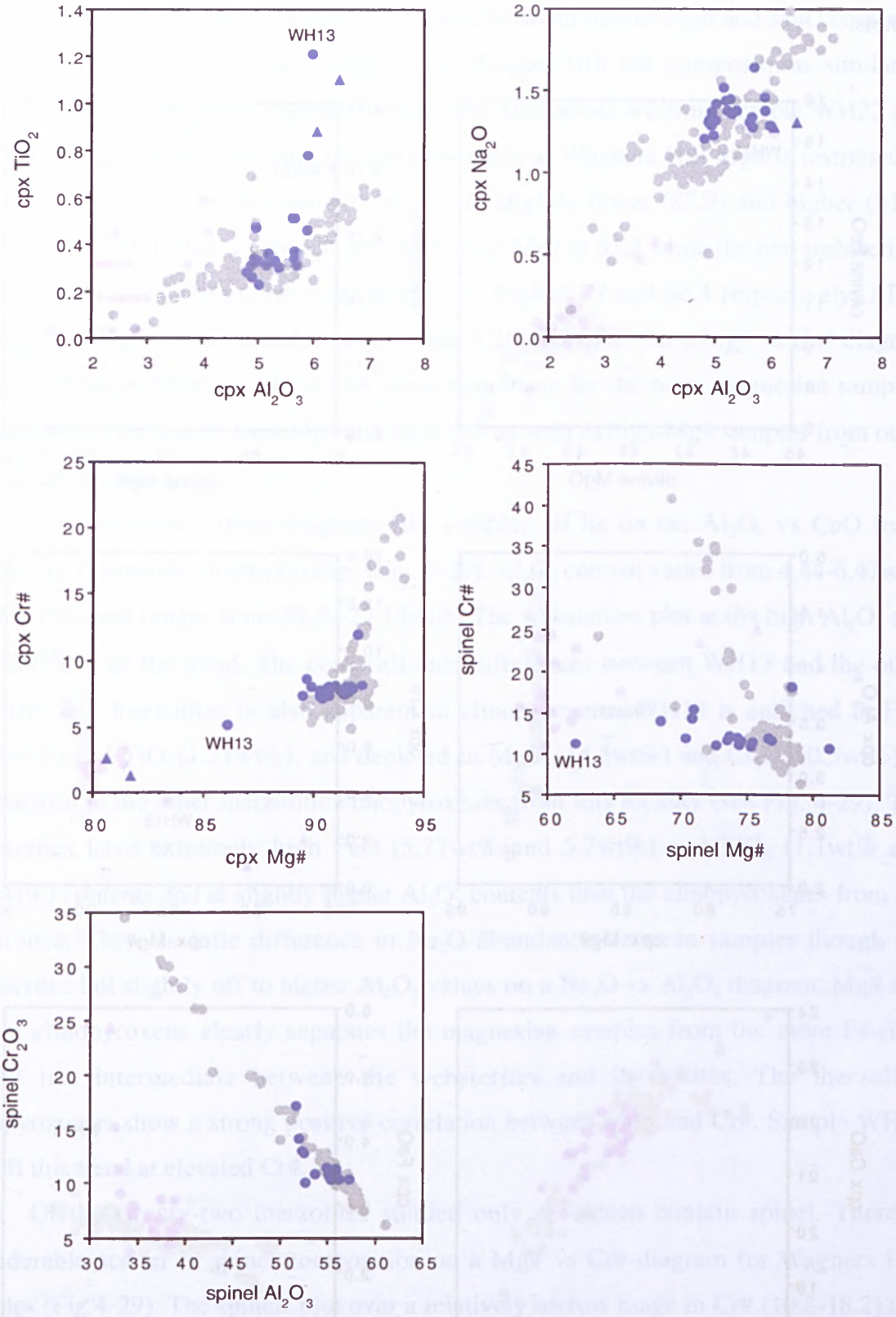


**Figure 4-29.** Composition variation diagrams for Wagners Hill mantle xenoliths. Grey symbols represent the entire dataset for Tasmania. Blue circles are lherzolites±spinel. Blue triangles are websterites.

### *4.3.2 Trace Elements*

Trace elements were analysed in olivine, orthopyroxene, clinopyroxene and spinel using the GEMOC laser ablation microprobe coupled to an ICPMS (see Section 2.3.2 for further information on the instrument used and the operating conditions). Trace elements for clinopyroxenes from seventy-one Tasmanian peridotites from eight localities (excluding The Sideling) are given in Appendix III.

Olivine

Abundances of Ca, Sc, Ti, V, Cr, Mn, Co, Ni, Zn, Ga, Y, LILE, REE, Pb, Th and U were determined in olivine in eight samples from Blessington, four samples from South Riana and two samples from Wagners Hill. Most of the highly incompatible trace elements are below detection limits for olivine though there are measurable quantities of some of the heavier rare earth elements such as Er, Yb and Lu. Averages for Ca and the transition metals are listed in Table 4-3. Calcium abundances in the Tasmanian olivines range from 170-740 ppm. The lowest values are from the two Wagners Hill samples and the highest from a coarse-grained sample (SR2) from South Riana. Olivines from the high-Mg# and low-Mg# groups of Blessington have similar Ca contents with values ranging over 220-370 ppm. The exception to this is BL10 which has 540 ppm calcium.

Olivines from South Riana are generally enriched in Sc, Ti, and V in comparison to those from Wagners Hill and Blessington, except for samples BL6 and BL10 as discussed below. Scandium contents in olivine do not vary significantly between localities and range from 1.9-3.5 ppm; the higher values are restricted to South Riana samples. The majority of olivines from Blessington and Wagners Hill has low Ti contents (5.4-11.5 ppm) though sample BL10 has 63 ppm and BL6 has an anomalously high Ti content of 240 ppm. South Riana olivines have Ti contents which range from 9-51 ppm. Variations in vanadium content are similar to those seen for Ti, with the bulk of olivines displaying a narrow range in V (1.1-2.4 ppm) but higher values evident in BL10 (8 ppm) and samples from South Riana (1.7-37 ppm).

Chromium, manganese and zinc were analysed only in olivines from Blessington and South Riana. Olivines from the high-Mg# group of Blessington have Cr contents of 36-44 ppm while those from the low-Mg# have slightly lower Cr contents at 22-28 ppm. In contrast to the narrow range in Cr values seen in Blessington, South Riana olivines show a very large variation in chromium from 21-6880 ppm. The very high Cr value is from coarse-grained sample SR2 and may reflect the presence of tiny spinel inclusions in the

analysed olivines. Manganese is slightly lower in the high-Mg# olivines (900-990 ppm) than in the low-Mg# olivines (1130-1210 ppm) of Blessington. Values for the South Riana samples range from1160-1630 ppm and do not show any correlation with texture. Zinc varies from 42-66 ppm in Blessington olivines and does not appear to be related to olivine Fo content. South Riana olivines have Zn abundances that range to higher values (41-120 ppm) with sample SR2 being the most enriched.

Nickel content for Tasmanian olivines ranges from 1980-4470 ppm with the lowest values from Wagners Hill and the highest values from South Riana. Cobalt ranges from 100-230 ppm with the lowest values found in olivines from Wagners Hill and the highest seen in a fine-grained sample from South Riana.

**Table 4-3.** Trace element abundances in olivine from Tasmanian spinel peridotites. All values are given in ppm.

| | BL1 Blessington | BL3 Blessington | BL4 Blessington | BL6 Blessington | BL10 Blessington | BL31 Blessington | BL33 Blessington |
|---|---|---|---|---|---|---|---|
| Ca | 280 | 300 | 340 | 370 | 540 | 260 | 330 |
| Sc | 2.5 | 2.6 | 2.2 | 2.3 | 2.5 | 2.4 | 2.0 |
| Ti | 5.8 | 5.4 | 7.5 | 242 | 63 | 8.6 | 6.8 |
| V | 1.6 | 1.6 | 2.4 | 1.7 | 8.0 | 1.8 | 1.4 |
| Cr | 36 | 38 | 22 | 28 | 44 | n.a. | n.a. |
| Mn | 900 | 910 | 1130 | 1210 | 990 | n.a. | n.a. |
| Co | 140 | 140 | 160 | 170 | 160 | 110 | 100 |
| Ni | 3110 | 3090 | 3380 | 3430 | 3540 | 2300 | 2080 |
| Zn | 43 | 42 | 48 | 64 | 66 | n.a. | n.a. |
| | BL35 Blessington | SR1 South Riana | SR1b-2 South Riana | SR2 South Riana | SR2b South Riana | WH21 Wagners Hill | WH22 Wagners Hill |
| Ca | 220 | 460 | 520 | 740 | 530 | 170 | 210 |
| Sc | 1.9 | 2.6 | 3.1 | 3.4 | 3.5 | 2.2 | 2.4 |
| Ti | 8 | 9 | 29 | 51 | 18 | 9.4 | 11.5 |
| V | 1.5 | 1.7 | 5 | 37 | 12 | 1.1 | 1.4 |
| Cr | n.a. | 21 | 180 | 6880 | 1210 | n.a. | n.a. |
| Mn | n.a. | 1170 | 1190 | 1160 | 1630 | n.a. | n.a. |
| Co | 110 | 160 | 170 | 180 | 230 | 110 | 100 |
| Ni | 2070 | 3280 | 3220 | 3580 | 4470 | 1980 | 2030 |
| Zn | n.a. | 120 | 130 | 200 | 190 | n.a. | n.a. |

There is a very good positive correlation between Ni and Co in Tasmanian olivines as illustrated in Fig. 4-30. Ni/Co ratios of 18.5-22.2 are close to the chondritic value (21; McDonough and Sun, 1995) and show an overall increase with increasing olivine Mg# (Fig. 4-30). There is reasonably good correlation between olivine FeO content and Mn

with sample SR2 lying well above the main trend. Zinc does not correlate with FeO in the Tasmanian lherzolites. Zn and Fe have been shown to be well-correlated in garnet peridotite olivine, but in spinel peridotites this relationship is perturbed by partitioning of Zn into spinel (O'Reilly *et al.*, 1997).

Other elements analysed in olivine are generally very low in abundance and close to detection limits. Germanium occurs in some samples up to 2 ppm, and Y and Zr content is typically less than 1 ppm. Sample BL10 is enriched in the large ion lithophile elements and Zr compared to the other samples with 0.46 ppm Rb, 1.9 ppm Ba, 0.41 ppm Sr and 1.2 ppm Zr.

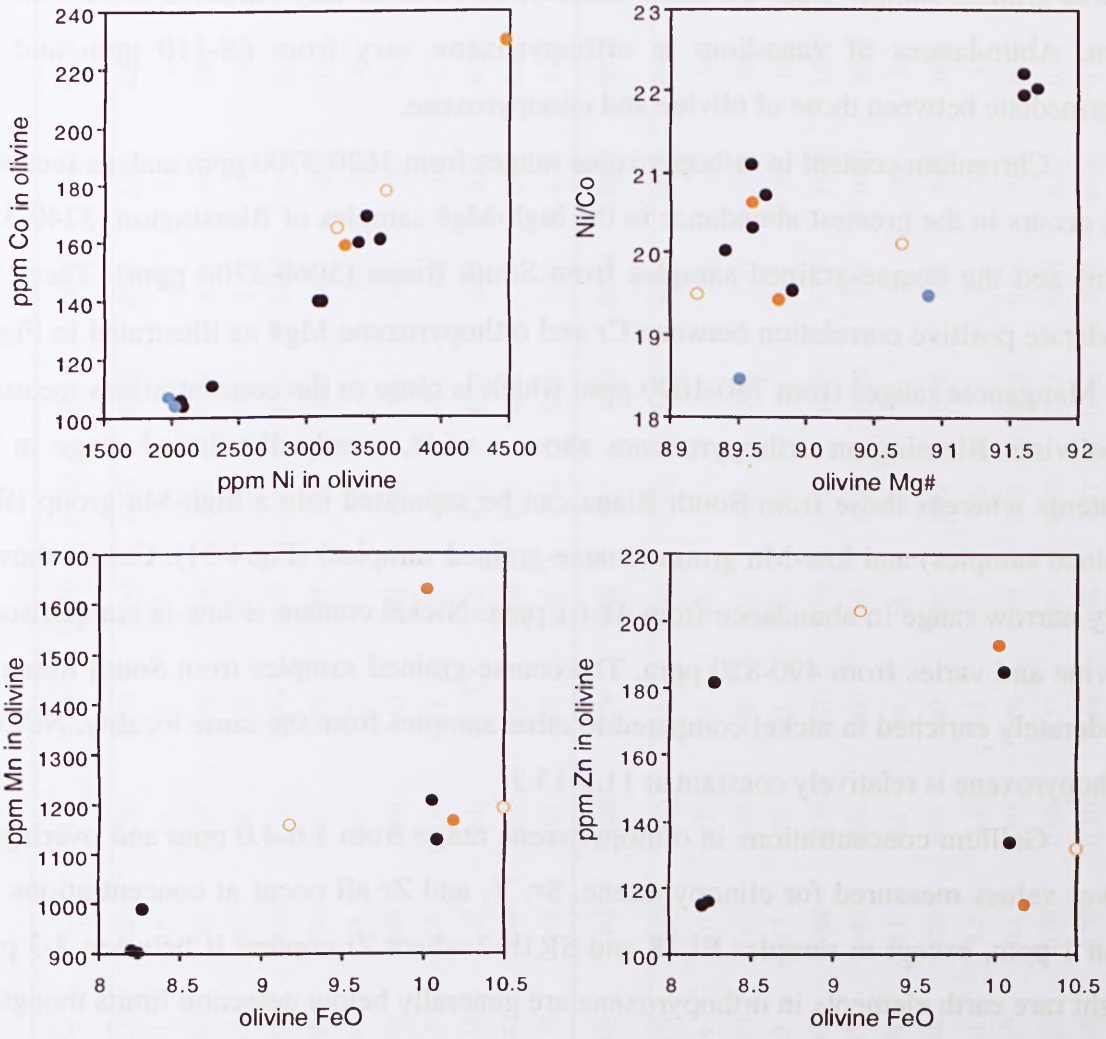


**Figure 4-30.** Trace element variation diagrams for Tasmanian olivines. Black symbols are Blessington samples. Orange symbols are South Riana samples (closed circles-fine grained; open circles-coarse grained). Blue symbols are Wagners Hill samples.

## Orthopyroxene

The elements analysed in olivine have also been analysed in orthopyroxenes from the same three localities. As for olivine, most of the highly incompatible trace elements are below

detection limits for orthopyroxene, although it was possible to measure abundances of Ga, Sr, Y, Zr and some of the heavy rare earth elements (HREE), as well as the transition metals.

Calcium content in Tasmanian orthopyroxenes ranges from 2930-5900 ppm. The highest Ca values are seen in the high-Mg# group of Blessington (4870-5120 ppm) and the coarse-grained samples from South Riana (5330-5900 ppm). Scandium ranges from 12-20 ppm and does not show any correlation with major element composition or sample textural type. The majority of orthopyroxene grains have between 260 ppm and 480 ppm Ti although coarse-grained sample SR10 from South Riana has only 170 ppm Ti and another coarse-grained sample from the same locality, SR1b-2, in very enriched in Ti with 810 ppm. Abundances of vanadium in orthopyroxene vary from 68-110 ppm and are intermediate between those of olivine and clinopyroxene.

Chromium content in orthopyroxene ranges from 1620-3700 ppm and, as seen with Ca, occurs in the greatest abundance in the high-Mg# samples of Blessington (3240-3520 ppm) and the coarse-grained samples from South Riana (3060-3700 ppm). There is a moderate positive correlation between Cr and orthopyroxene Mg# as illustrated in Fig. 4-31. Manganese ranges from 780-1090 ppm which is close to the concentrations measured in olivine. Blessington orthopyroxenes show a wide, evenly-distributed range in Mn contents whereas those from South Riana can be separated into a high-Mn group (fine-grained samples) and low-Mn group (coarse-grained samples) (Fig.4-31). Cobalt shows a very narrow range in abundance from 41-61 ppm. Nickel content is low in comparison to olivine and varies from 490-820 ppm. The coarse-grained samples from South Riana are moderately enriched in nickel compared to other samples from the same locality. Ni/Co of orthopyroxene is relatively constant at 11.3-13.5.

Gallium concentrations in orthopyroxene range from 1.6-4.0 ppm and overlap the lower values measured for clinopyroxene. Sr, Y, and Zr all occur at concentrations less than 1 ppm, except in samples BL18 and SR1b-2 where Zr content is between 2-3 ppm. Light rare earth elements in orthopyroxene are generally below detection limits though Ce is detectable to the 0.2 ppm level in a couple of samples from Blessington. Heavy rare earth elements are present in amounts of less than 0.2 ppm with Er and Yb abundances typically less than 0.05 ppm. Positive correlation occurs between Ti and compatible trace elements such as Y and Yb, while the HREE show an overall decrease with increasing orthopyroxene Mg#.

**Table 4-4.** Trace element abundances in orthopyroxene from Blessington, South Riana and Wagners Hill lherzolite xenoliths. All values are given in ppm.

| | BL1 | BL3 | BL4 | BL6 | BL10 | BL12 | BL13 | BL17 | BL18 | BL26 | BL31 | BL33 | BL35 | SR1 |
|---|---|---|---|---|---|---|---|---|---|---|---|---|---|---|
| Ca | 5120 | 5020 | 4200 | 4270 | 4850 | 4750 | 4060 | 4990 | 5380 | 4260 | 2930 | 2980 | 4310 | 3500 |
| Sc | 19 | 18 | 16 | 19 | 17 | 14 | 13 | 19 | 15 | 14 | 15 | 15 | 17 | 16 |
| Ti | 340 | 280 | 310 | 290 | 290 | 300 | 310 | 450 | 410 | 290 | 260 | 280 | 320 | 370 |
| V | 84 | 80 | 94 | 100 | 80 | 83 | 84 | 110 | 96 | 75 | 84 | 89 | 99 | 95 |
| Cr | 3350 | 3520 | 2330 | 2340 | 3240 | 2070 | 2250 | 2420 | 2140 | 2630 | n.a. | n.a. | n.a. | 1740 |
| Mn | 830 | 790 | 940 | 1030 | 800 | 870 | 880 | 980 | 1060 | 780 | n.a. | n.a. | n.a. | 1000 |
| Co | 46 | 43 | 50 | 52 | 45 | 50 | 49 | 52 | 58 | 41 | 45 | 44 | 49 | 51 |
| Ni | 570 | 540 | 610 | 610 | 560 | 600 | 590 | 600 | 730 | 490 | 510 | 510 | 560 | 630 |
| Ga | 1.6 | 1.6 | 2.8 | 2.7 | 1.7 | 2.8 | 3.0 | 3.0 | 3.6 | 2.4 | 2.3 | 2.1 | 2.6 | 3.0 |
| Sr | 0.19 | 0.22 | 0.1 | <0.03 | 0.2 | 0.18 | 0.08 | 0.12 | 0.81 | 0.12 | 0.04 | 0.01 | 0.04 | 0.1 |
| Y | 0.42 | 0.40 | 0.61 | 0.41 | 0.76 | 0.67 | 0.87 | 1.05 | 0.51 | 0.47 | 0.44 | 0.54 | 0.64 | 0.64 |
| Zr | 0.79 | 0.69 | 0.07 | 0.07 | 0.70 | 0.28 | 0.30 | 0.30 | 2.76 | 0.26 | 0.08 | 0.02 | 0.06 | 0.09 |

| | SR1b-2 | SR2 | SR2b | SR3a | SR6 | SR7 | SR8 | SR10 | SR11 | SR12 | SR14 | WH21 | WH22 |
|---|---|---|---|---|---|---|---|---|---|---|---|---|---|
| Ca | 5330 | 5610 | 3630 | 3270 | 5430 | 2760 | 3270 | 5900 | 5070 | 4250 | 3840 | 4280 | 4250 |
| Sc | 16 | 16 | 17 | 15 | 15 | 12 | 16 | 20 | 17 | 16 | 17 | 16 | 14 |
| Ti | 810 | 410 | 340 | 440 | 410 | 460 | 360 | 170 | 450 | 480 | 380 | 470 | 350 |
| V | 93 | 87 | 93 | 98 | 90 | 76 | 92 | 93 | 94 | 100 | 94 | 92 | 68 |
| Cr | 2000 | 3060 | 1730 | 1620 | 3170 | 1550 | 1900 | 3700 | 1890 | 1820 | 1750 | n.a. | n.a. |
| Mn | 1010 | 940 | 1030 | 1090 | 950 | 1020 | 1020 | 930 | 1060 | 1010 | 990 | n.a. | n.a. |
| Co | 58 | 61 | 54 | 56 | 58 | 51 | 53 | 56 | 54 | 51 | 52 | 48 | 44 |
| Ni | 740 | 820 | 670 | 660 | 780 | 590 | 630 | 750 | 630 | 600 | 590 | 560 | 590 |
| Ga | 4.1 | 3.5 | 2.3 | 2.4 | 3.2 | 2.3 | 2.3 | 2.2 | 2.3 | 2.5 | 2.3 | 2.7 | 2.3 |
| Sr | 0.17 | 0.1 | 0.03 | 0.06 | 0.09 | 0.03 | 0.15 | 0.04 | 0.22 | 0.29 | 0.16 | 0.05 | 0.59 |
| Y | 1.17 | 0.70 | 0.66 | 0.57 | 0.67 | 0.69 | 0.71 | 0.35 | 0.87 | 0.72 | 0.72 | 0.63 | 0.51 |
| Zr | 2.08 | 0.76 | 0.10 | 0.16 | 0.76 | 0.17 | 0.28 | 0.27 | 0.16 | 0.30 | 0.10 | 0.11 | 0.43 |

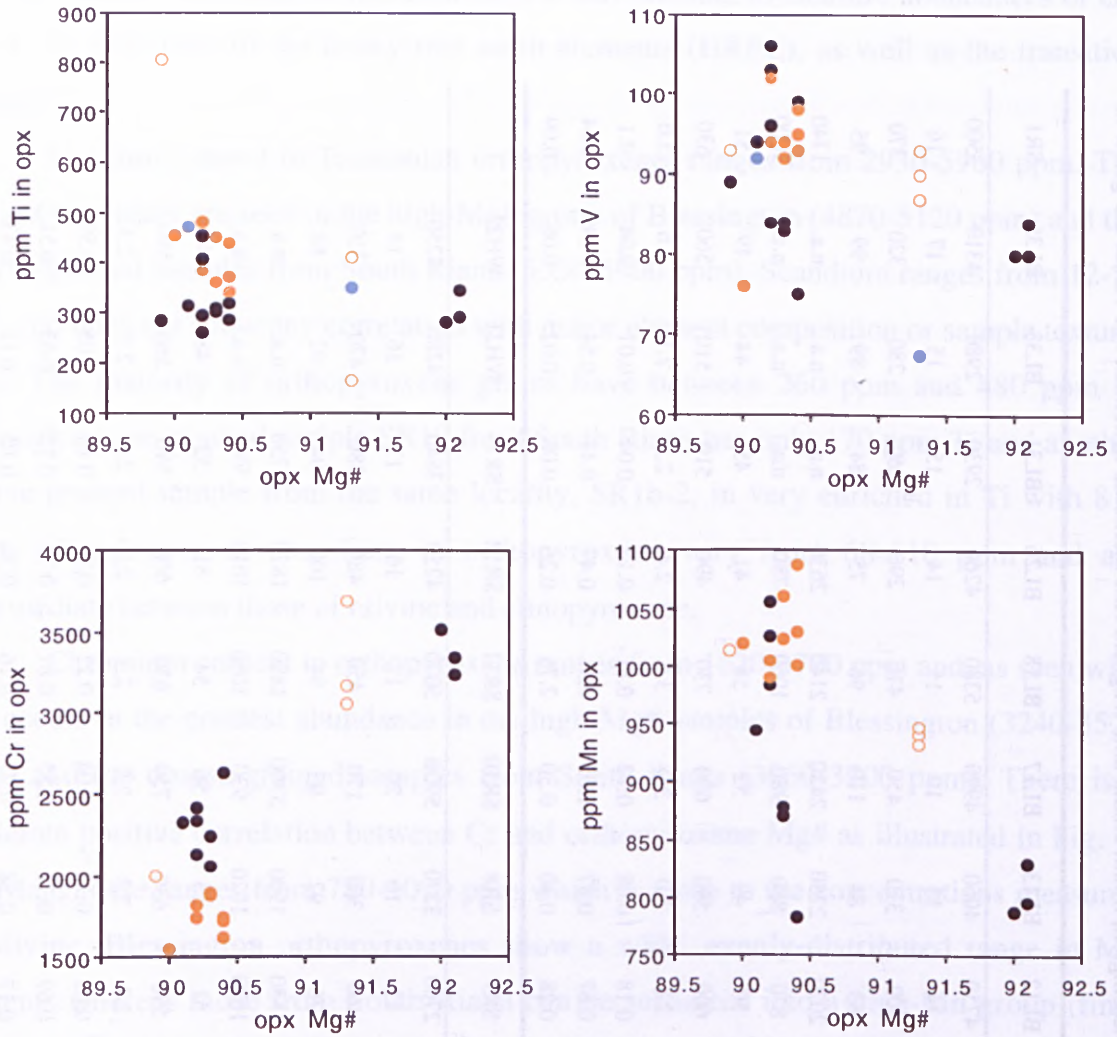


**Figure 4-31.** Trace element variation diagrams for Tasmanian orthopyroxenes. Black symbols are Blessington samples. Orange symbols are South Riana samples (closed circles-fine grained; open circles-coarse grained). Blue symbols are Wagners Hill samples.

Clinopyroxene

Clinopyroxene contains measurable contents of LREE, U, Th, Pb, Nb and Hf, in addition to those elements determined in olivine and orthopyroxene. Abundances of the transition metals Sc and Ti are high in clinopyroxene compared to the other phases. The majority of samples contain between 58-74 ppm Sc which is 3 to 4 times that seen in orthopyroxene. The high-Mg# samples from Blessington and Coates Road are enriched in Sc (79-95 ppm) compared to the low-Mg# samples (58-71 ppm) (see Fig.4-32). The lowest Sc value contents are seen in BL25a (40 ppm) and the coarse-grained samples of South Riana (56-60 ppm) except for SR1b-2 which has high Sc at 70 ppm.

Titanium shows considerable variation with most samples containing 1000-3500 ppm Ti. The high-Mg# samples from Blessington have low Ti (960-1060 ppm) while those from Coates Road are slightly higher with ~1370 ppm Ti. Coarse-grained samples from

South Riana give both the lowest (390 ppm in SR10) and the highest (4120 ppm in SR1b-2) titanium concentrations. Clinopyroxenes from Arthur River, Table Cape and Doctors Rocks show overall enrichment in Ti in comparison to the other localities though there is overlap with some Ti-rich samples from Wagners Hill as can be seen in Fig. 4-32.

There is considerable overlap in vanadium content for Tasmanian clinopyroxenes from the different localities. The majority of samples contain between 240-280 ppm V though some samples range to slightly higher or lower values (Fig. 4-32). Sample BL25a has only 130 ppm V and SR10 contains 180 ppm, which is similar to V measured in the other coarse-grained samples. Sample SR1b-2 has the highest V content with 320 ppm. Arthur River and Doctors Rocks samples are generally enriched in V with concentrations that range from 270-290 ppm.

Cobalt and nickel abundances are low in clinopyroxene compared to the other mineral phases. Both cobalt and nickel content in clinopyroxene is lower by an order of magnitude than that in olivine and spinel, and is approximately half that seen in orthopyroxene. The majority of samples contain 15-26 ppm Co and 250-400 ppm Ni (Fig.4-32). There is a very good positive correlation between Co and Ni so that samples with high Co (29-33 ppm) have correspondingly high Ni (370-460 ppm). Low Ni and Co abundances are seen in the high-Mg# group of Blessington while the coarse-grained South Riana samples plot off the main trend at constant Co values but widely varying Ni contents. This is reflected in Ni/Co ratios; the bulk of samples lie between 13 and 18 but the most extreme values belong to SR1b-2 (10.5) and SR2 (20.1). Ni/Co shows reasonably good correlation with clinopyroxene Mg# for Blessington, Coates Road and Doctors Rocks but shows little or no correlation for the other localities.

Gallium is equally partitioned between clinopyroxene and orthopyroxene, and contents fall in between those for olivine and spinel. The range in Ga is 1.6-10 ppm though most samples contain less than 4.6 ppm. Clinopyroxenes from Blessington fall into two groups that are correlated with Mg#. The high-Mg# group contains 1.9-2.1 ppm Ga whereas the low-Mg# typically have Ga concentrations of 2.8-4.6 ppm. Low Ga contents are seen in BL25a and SR10 while the highest value is from SR1b-2. Wagners Hill clinopyroxenes are generally quite rich in Ga and concentrations range up to 7 ppm. There is good correlation between Ga and Ti for all localities except Wagners Hill suggesting there has been some disturbance in Ga content at this locality. The yttrium content of Tasmanian clinopyroxenes varies from 3.7-24 ppm though the majority of samples fall in the narrow range of 9-18 ppm. Low Y concentrations (8-9 ppm) are typical of the high-

Mg# samples from Blessington, Coates Road and Table Cape. The highest Y content occurs in clinopyroxenes from sample SR1b-2.

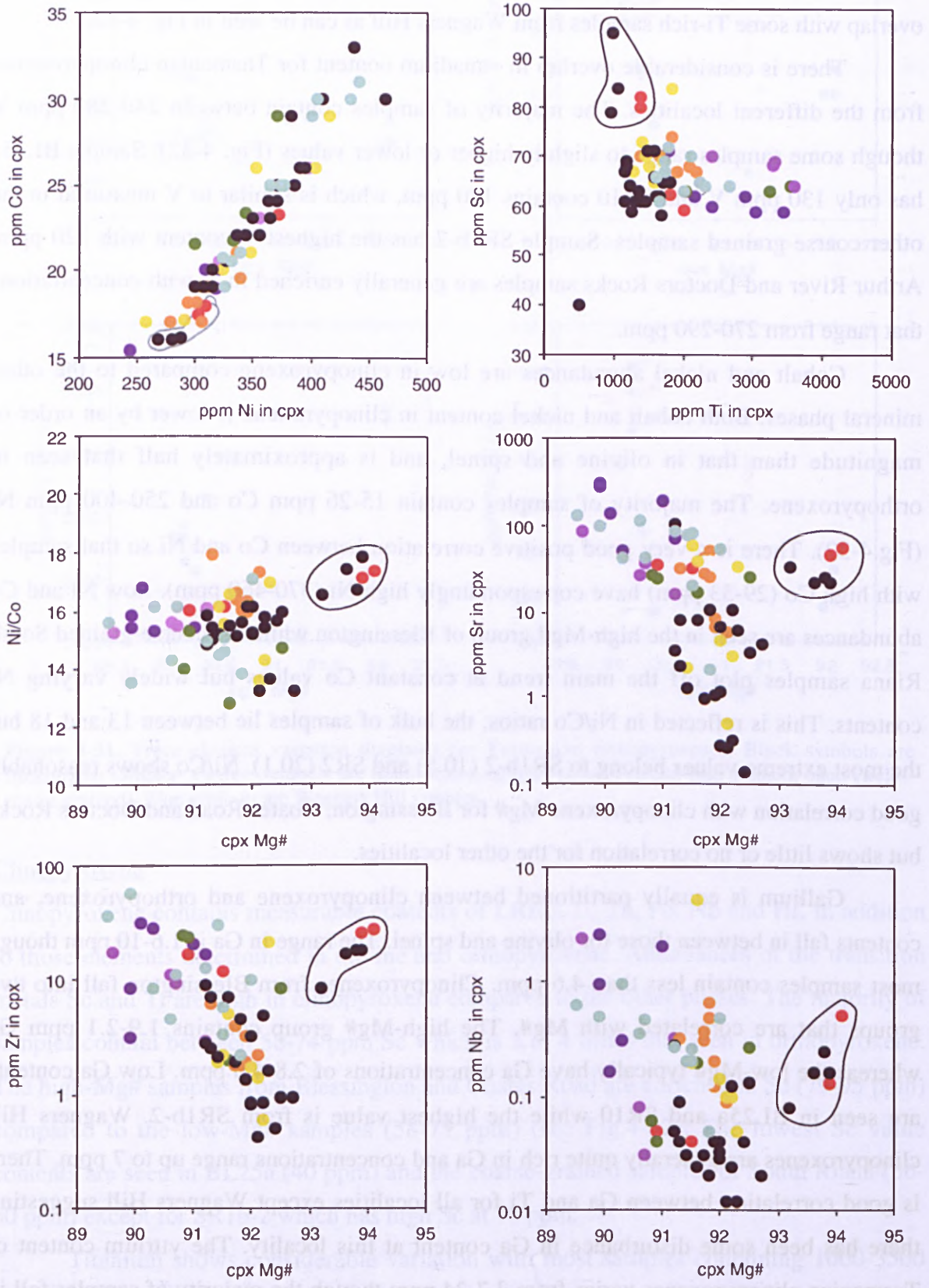


**Figure 4-32** Composition variation diagrams for Tasmanian clinopyroxenes. Localities are keyed according to the colours used in the mineral major element plots (see Section 4.3.1). High-Mg# group is circled.

Of the large ion lithophile elements only strontium has been analysed in every sample. Barium and rubidium were only analysed in some samples from Table Cape, Doctors Rocks, Blessington and Wagners Hill. Strontium shows extreme variation (0.14-300 ppm) in Tasmanian clinopyroxenes and, for the low-Mg# xenoliths, is negatively correlated with clinopyroxene Mg# (see Fig. 4-32). The lowest Sr values occur in the low-Mg# group xenoliths from Blessington. These samples typically contain between 0.14-10 ppm Sr although BL18 has an anomalously high Sr content of 110 ppm. Clinopyroxenes from the other localities generally show Sr-enrichment (16-300 ppm) in comparison to the low-Mg# Blessington samples, though South Riana and Don Heads do range to lower Sr contents. Samples from the Blessington and Coates Rd high-Mg# group are enriched in Sr (22-58 ppm) relative to their low-Mg# equivalents and lie off the main trend. Rubidium is typically below detection in the samples investigated particularly in those from Blessington and Wagners Hill. Table Cape clinopyroxenes contain from 0.03-0.23 ppm Rb and one sample from Doctors Rocks gave a Rb concentration of 0.05 ppm. Barium is also present only in low concentrations ranging from 0.04-1.3 ppm. Blessington samples contain little Ba with an average content of 0.05 ppm. This is similar to concentrations measured in Table Cape though sample TC2 contains 1.3 ppm Ba. Clinopyroxenes from Doctors Rocks have a narrow range in Ba content containing between 0.10-0.32 ppm.

Zirconium and niobium contents in low-Mg# clinopyroxenes are negatively correlated with clinopyroxene Mg# as already seen for Sr. The overall range in zirconium abundance is 0.43-57 ppm with most localities displaying a wide variation in this trace element (see Fig. 4-32). Clinopyroxenes from fine-grained South Riana samples generally have low Zr contents (<6 ppm) while the coarse-grained samples have high Zr (12-24 ppm). Niobium content is generally low for most Tasmanian clinopyroxenes (<0.5 ppm) as illustrated in Fig. 4-32. The high-Mg# samples from Blessington and Coates Road have slightly higher Zr and Nb than their low-Mg# equivalents and plot off the main trend. This suggests that the high-Mg# xenoliths have been modified by addition of Zr, Nb and Sr, an event that has not affected the low-Mg# samples from those same localities. This is further discussed in Section 5.4 which looks at trace element enrichment and metasomatic signatures.

In the absence of amphibole and phlogopite, clinopyroxene is usually the main repository for rare earth elements in spinel lherzolites. Primitive mantle-normalised REE patterns in Tasmanian clinopyroxenes vary from LREE depleted to LREE enriched relative to chondrite. Three main patterns have been recognised: (1) enriched LREE [$(La/Yb)_N>1$],

(2) depleted LREE [$(La/Yb)_N<1$], and (3) flat LREE [$(La/Yb)_N\approx1$). Pattern 1 has two subtypes based on the shape of the LREE; subtype 1a typically has smooth to upwardly-concave LREE while subtype 1b has upwardly-convex LREE (Fig. 4-33). Depleted LREE patterns (type 2) are either upwardly-convex or V-shaped where there has been enrichment in La relative to Ce (Fig. 4-33). Type 3 patterns (not illustrated) are flat and are either enriched or depleted relative to primitive mantle values.

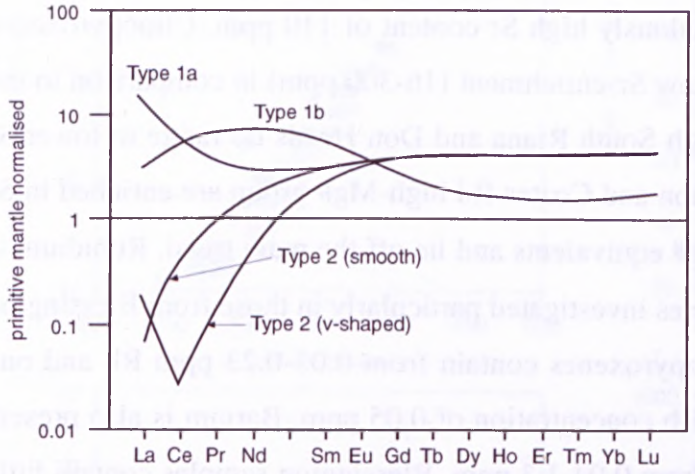


**Figure 4-33** Diagram illustrating the different REE patterns recognised in Tasmanian clinopyroxenes.

Extended normalised trace-element plots have been used to identify anomalies in elements such as Ti, the HFSE and U and Th relative to the rare earth elements. Anomalies for Ti and Zr have been calculated as Ti/Ti* and Zr/Zr* where Ti*=(Gd+Eu)/2 and Zr*=(Sm+Nd)/2 after the method of Zheng (1998) (modified after Rampone *et al.*, 1991).

Coates Road clinopyroxenes show either type 2 or type 3 REE patterns (Fig. 4-34). The clinopyroxenes with the type 3 patterns are from the high-Mg# group and show low abundances of HREE with flat patterns and only marginal enrichment in the LREE ($(La/Yb)_N$=1.31, 1.07). The clinopyroxenes with the type 2 patterns have smooth LREE and LREE/HREE<1 ($(La/Yb)_N$=0.23, 0.09), and higher HREE abundances (~3 x primitive mantle) compared to the high-Mg# samples (~1.5 x PM). All samples are characterised by small negative Ti (Ti/Ti*=0.37-0.50) and Zr (Zr/Zr*=0.61-0.88) anomalies and a deep negative anomaly in Nb (Fig. 4-35). Ta shows negative anomalies in the low-Mg# samples and sample CQ4 of the high-Mg# group.

Clinopyroxenes from Arthur River have REE patterns which range from type 2 to type 1a (Fig. 4-34) reflecting increases in LREE abundances relative to HREE ($(La/Yb)_N$=0.20 to 4.94). This systematic increase in LREE has been attributed to metasomatic addition of incompatible elements by infiltration of fluids or melts enriched in these elements (this is discussed in detail in Chapter 5). Enrichment in the LREE is accompanied by enrichment in U and Th in all samples except AR5 which also has the

lowest abundances of LREE (Fig. 4-35). Negative anomalies relative to the REE are particularly strong for Nb and Ta though large anomalies are also present in Zr and Hf for some samples. Ti anomalies range from 0.23 to 0.64.

Table Cape clinopyroxenes have a range of REE patterns including types 1a and b and type 2 (Fig. 4-34). Samples TC4 and TC5 have very similar patterns to the low-Mg# group of Coates Road and have a $(La/Yb)_N$ of 0.13 and 0.19 respectively. The high-Mg# sample TC7 has LREE/HREE>1 ($(La/Yb)_N$=1.75) and low abundances of HREE (primitive mantle values) similar to the high-Mg# clinopyroxenes of Coates Road. Sample TC2 has a distinctive spoon-shaped REE pattern resulting from enrichment in La and Ce relative to the other LREE ($(La/Nd)_N$=6.59). TC2 is also characterised by strong negative Nb and Zr anomalies, a small positive Pb anomaly and extreme enrichment in U and Th (Fig. 4-35). Small negative Ti anomalies (0.63-0.70) are common to all samples.

Doctors Rocks clinopyroxenes have REE patterns that vary from type 2 to type 1a (Fig. 4-36) as LREE abundances increase relative to HREE from $(La/Yb)_N$=0.21 to 2.1. MREE and HREE have flat abundance patterns and concentrations that are typically 3 x PM. Increasing LREE-enrichment is accompanied by increasing U and Th (Fig. 4-37). Anomalies in Ti are very shallow (0.73-0.84) and Zr anomalies range from 0.20 to 0.49. Deep negative Nb anomalies in clinopyroxene were recognised in two samples while Ta is generally below detection.

Clinopyroxenes from the fine- and coarse-grained samples of South Riana have very different REE patterns (Fig. 4-36). Fine-grained samples typically have shallow spoon-shaped patterns (types 1a and 2) that are characterised by progressive LREE-enrichment ($(La/Yb)_N$ ratios range from 0.05 to 1.12), $(La/Sm)_N$=0.13-1.77 and HREE abundances that are 3-4 x PM. Coarse-grained samples have much flatter type 3 patterns ($(La/Yb)_N$=0.29-0.43), a narrow range in $(La/Sm)_N$ (0.33-0.66) and HREE abundances that vary from close to primitive mantle values in sample SR10 to 5 x PM in SR1b-2. Behaviour of the other incompatible elements is similar between fine- and coarse-grained samples however element concentrations range to higher values in the latter (Fig. 4-37). Ti anomalies in clinopyroxenes from South Riana range from 0.45-0.57, and abundances of Ti show considerable variation in the coarse-grained samples (0.3-3 x PM) but not in the fine-grained samples (1-2 x PM). All samples have a negative Zr anomaly though anomalies in the fine-grained samples are more pronounced and typically at lower concentrations (0.2-0.6 x PM) than those in the coarse-grained samples (0.2-4.0 x PM).

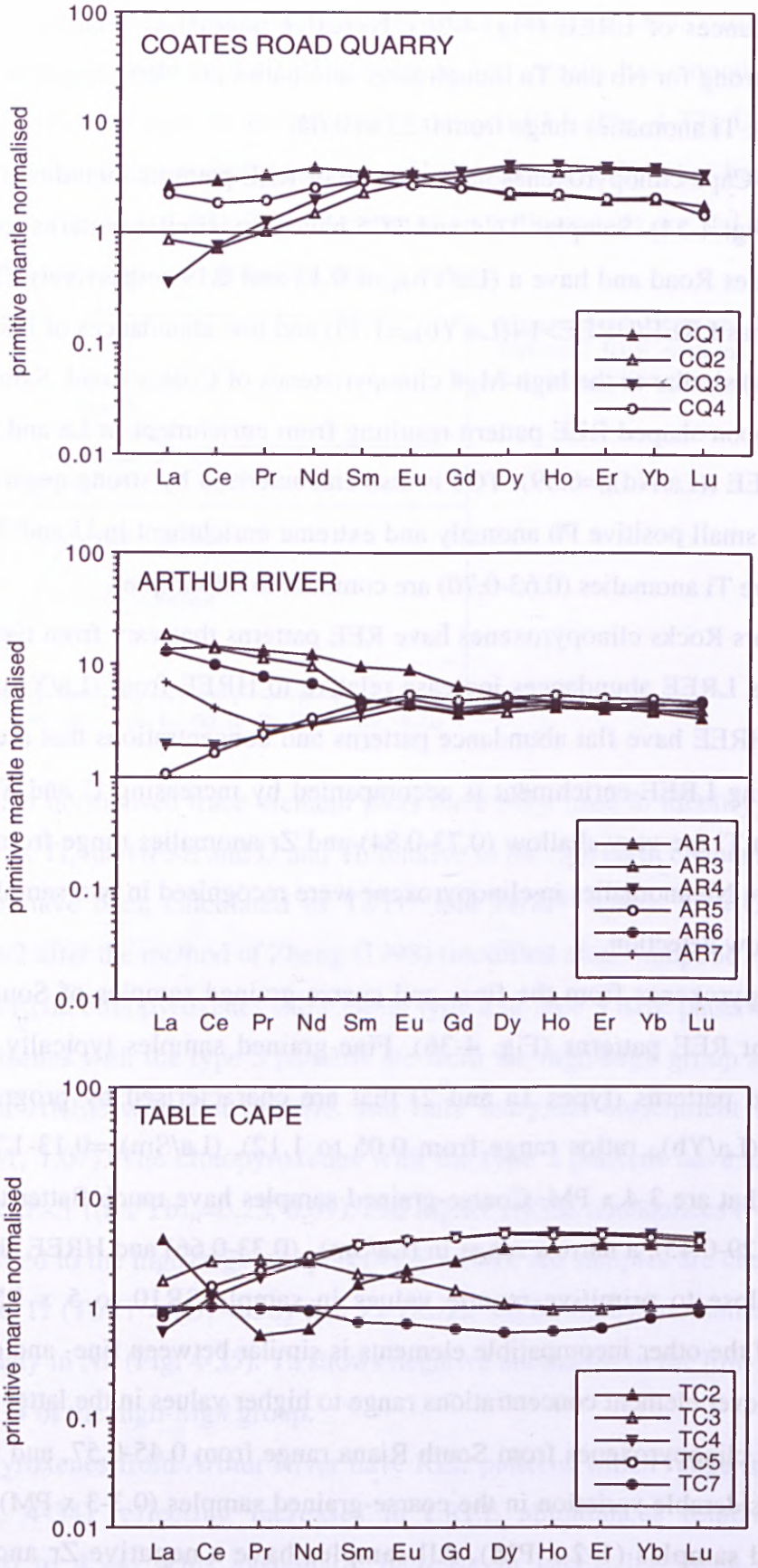


**Figure 4-34.** Primitive mantle normalised REE patterns of clinopyroxene in mantle peridotites from Coates Road Quarry, Arthur River and Table Cape.

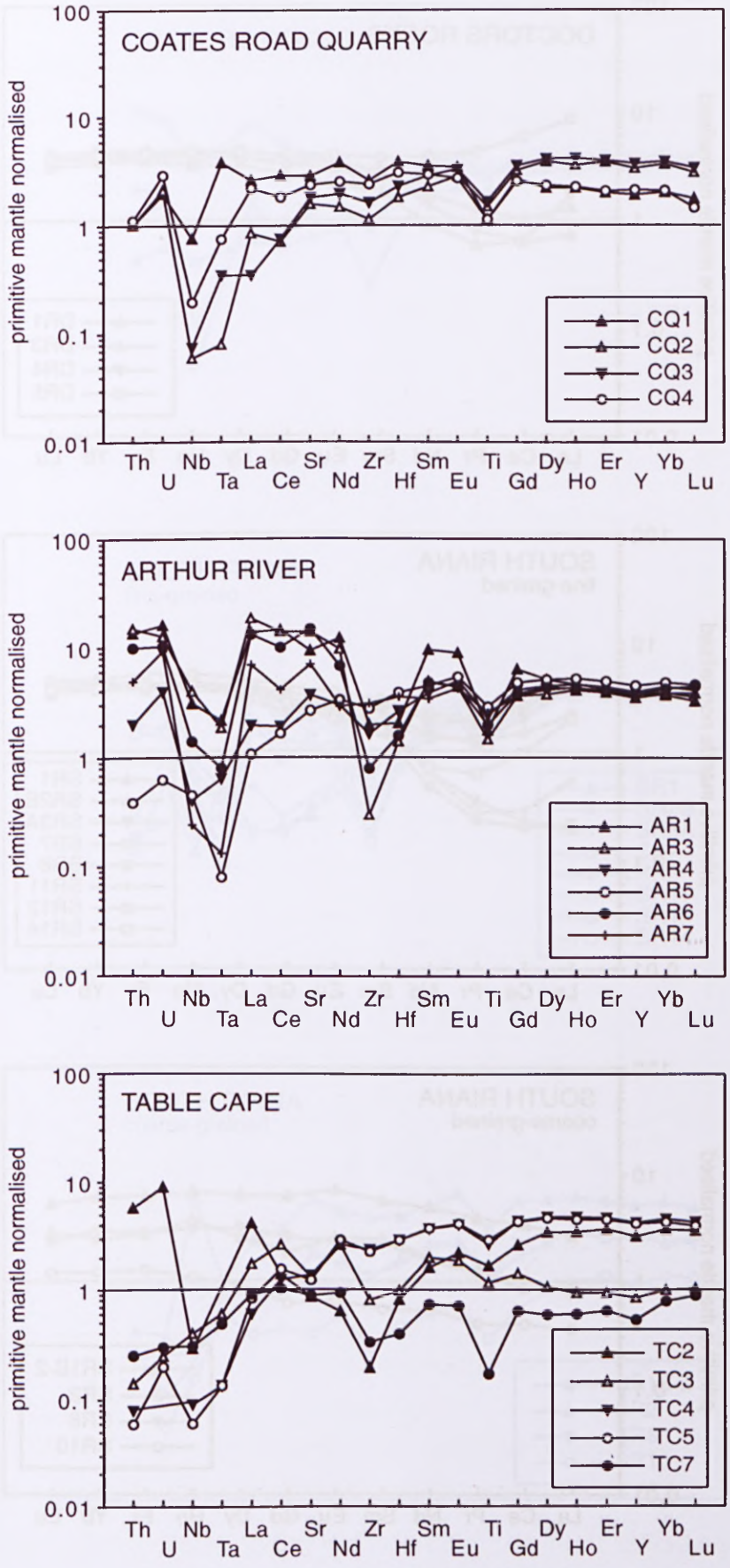


**Figure 4-35** Primitive mantle normalised trace element abundance patterns of clinopyroxene in mantle peridotites from Coates Road Quarry, Arthur River and Table Cape.

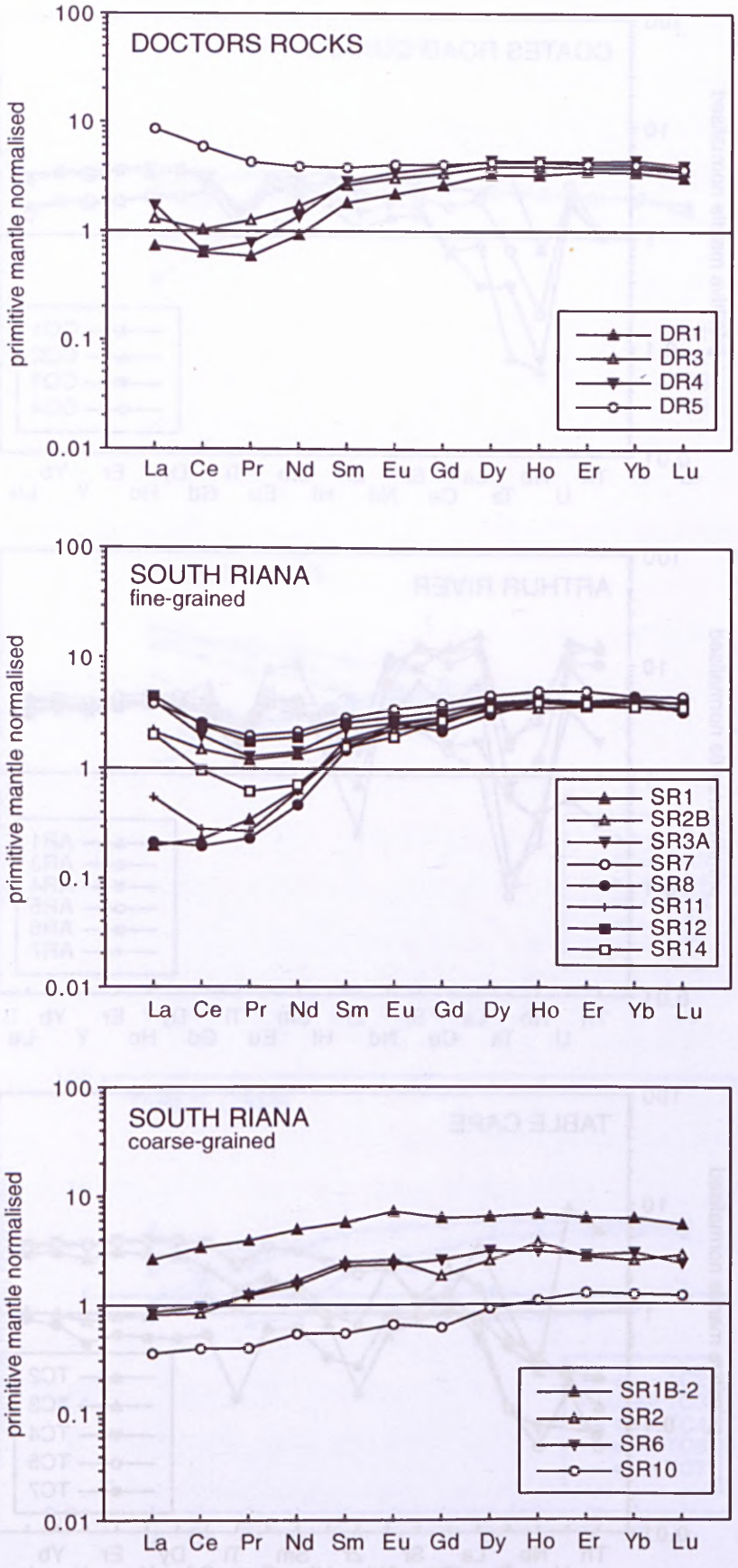


**Figure 4-36.** Primitive mantle normalised REE patterns of clinopyroxene in mantle peridotites from Doctors Rocks and South Riana

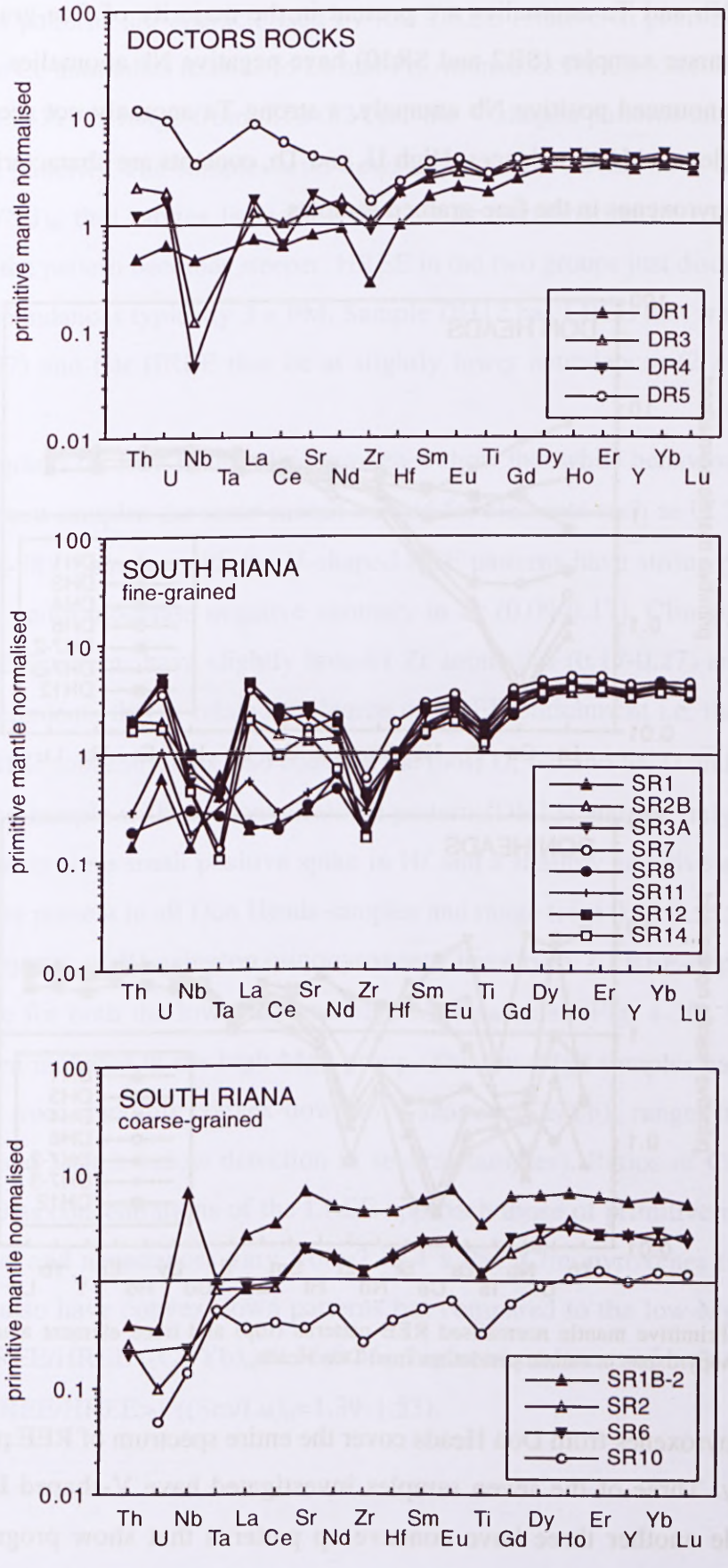


**Figure 4-37.** Primitive mantle normalised trace element abundance patterns of clinopyroxene in mantle xenoliths from Doctors Rocks and South Riana.

Deep Nb and Ta anomalies are present in the majority of fine-grained samples. Two of the coarser samples (SR2 and SR10) have negative Nb anomalies while SR1b-2 has a very pronounced positive Nb anomaly, a strong Ta anomaly not seen in the other samples, and elevated U abundances. High U, and Th, contents are characteristic of LREE-enriched clinopyroxenes in the fine-grained samples.

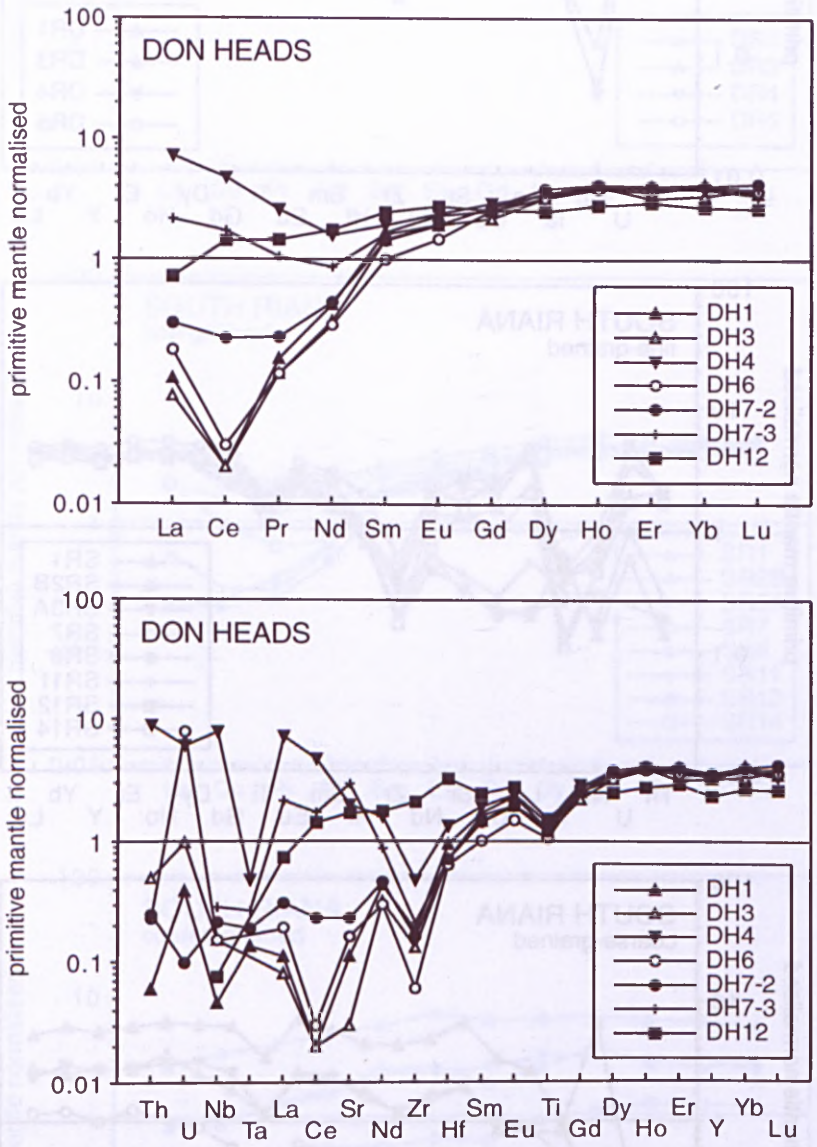


**Figure 4-38.** Primitive mantle normalised REE patterns (top) and trace element abundance patterns (bottom) of clinopyroxene in mantle peridotites from Don Heads.

Clinopyroxenes from Don Heads cover the entire spectrum of REE patterns defined for this study. Three of the seven samples investigated have V-shaped LREE-depleted patterns while another three have concave-up patterns that show progressive LREE-enrichment like that seen at Doctors Rocks and South Riana (Fig. 4-38). Sample DH12 has a depleted convex-down LREE pattern similar to the low-Mg# samples of Coates Road.

The V-shaped patterns are characterised by low LREE relative to primitive mantle and sharp negative Ce anomalies relative to La and Pr. Anomalies for Ce (calculated as Ce/Ce* where Ce*=(La+Pr)/2) range from 0.13-0.24 for the V-shaped patterns and 0.85-1.30 for the remaining patterns. The samples with upwardly-concave LREE have $(La/Yb)_N$=0.08-1.87 and $(La/Nd)_N$ that ranges from 0.67 to 4.53 as fractionation between La and Nd increases and the pattern becomes steeper. HREE in the two groups just discussed have flat patterns and abundances typically 3 x PM. Sample DH12 has LREE that are convex down ($(La/Yb)_N$=0.27) and flat HREE that lie at slightly lower abundances (2 x PM) than the other samples.

Spidergrams for Don Heads clinopyroxenes show that while behaviour in Zr and Ti is similar between samples the same cannot be said for elements such as U, Th, Nb, Ta, Sr and Pb (Fig. 4-38). Samples with the V-shaped REE patterns have strong positive U and Pb anomalies, and a moderate negative anomaly in Zr (0.09-0.17). Clinopyroxenes with concave-up REE patterns have slightly broader Zr anomalies (0.17-0.27) and variation in incompatible elements that is related to degree of LREE-enrichment i.e. the sample with the highest LREE concentrations also contains the most U, Nb and Sr. U and Th are below detection in the sample with the convex-down pattern (DH12) and the only anomalies in the other elements are a small positive spike in Hf and a shallow negative anomaly in Ti. Ti anomalies are present in all Don Heads samples and range from 0.51-0.57.

The majority of Blessington clinopyroxenes have type 2 LREE-depleted patterns and this is true for both the low-Mg# and high-Mg# samples (Fig. 4-39). Sample BL22 ($Fo_{90.9}$) has been included in the high-Mg# group. The low-Mg# samples have LREE that range in shape from smoothly convex-down to V-shaped. $(Ce/Yb)_N$ ranges from 0.01-0.15 (La was not used as it is below detection in several samples). Ratios of Ce to Nd range from 0.02-0.60 as concentrations of the LREE approach those of primitive mantle. HREE patterns are flat and abundances vary from 2 to 4 x PM. Clinopyroxenes from the high-Mg# samples also have convex-down patterns but compared to the low-Mg# group they have higher LREE/HREE ($(Ce/Yb)_N$=0.36-0.46), higher abundances of both the LREE and MREE, and MREE/HREE>1 ($(Sm/Lu)_N$=1.39-1.53).

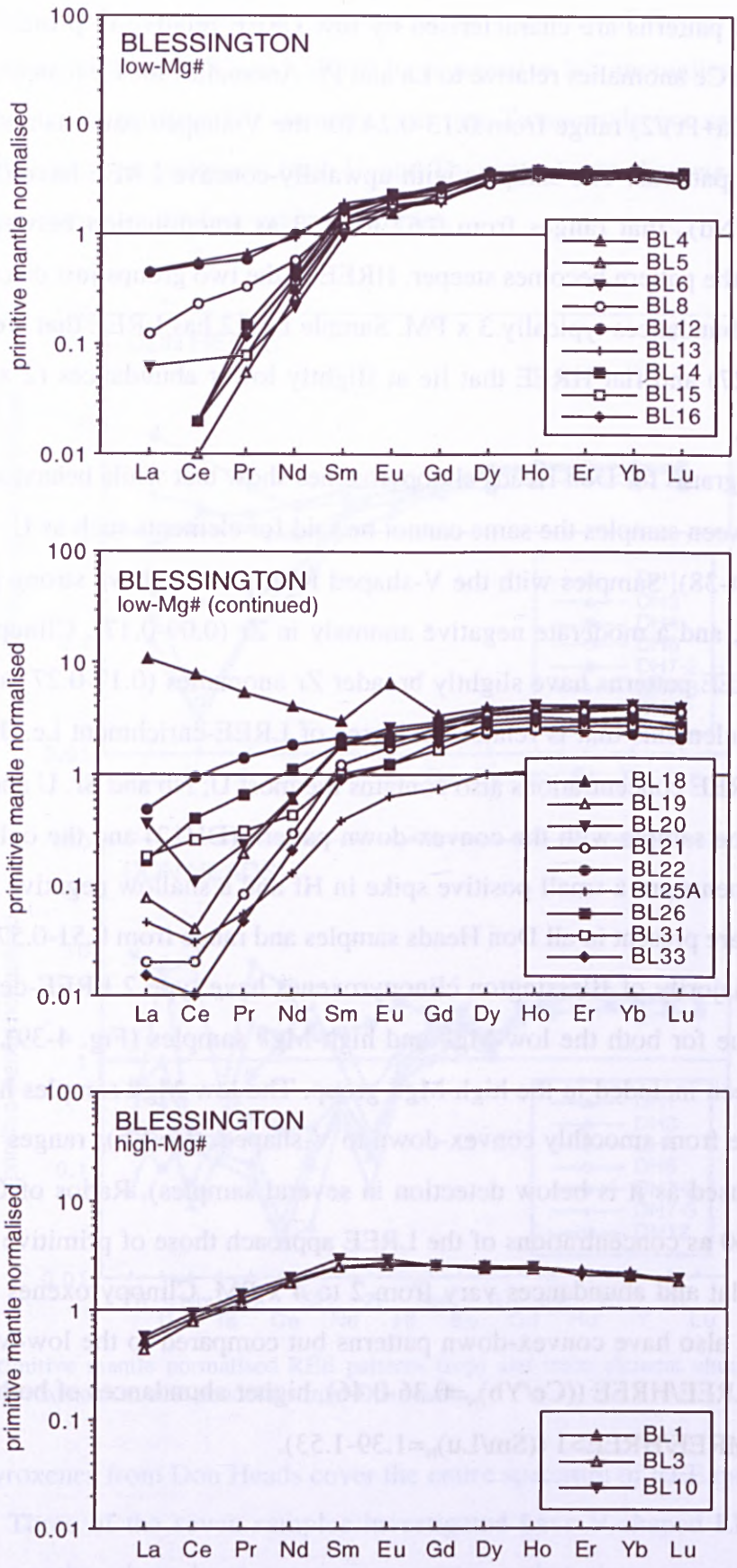


**Figure 4-39.** Primitive mantle normalised REE patterns of clinopyroxene in mantle xenoliths from Blessington.

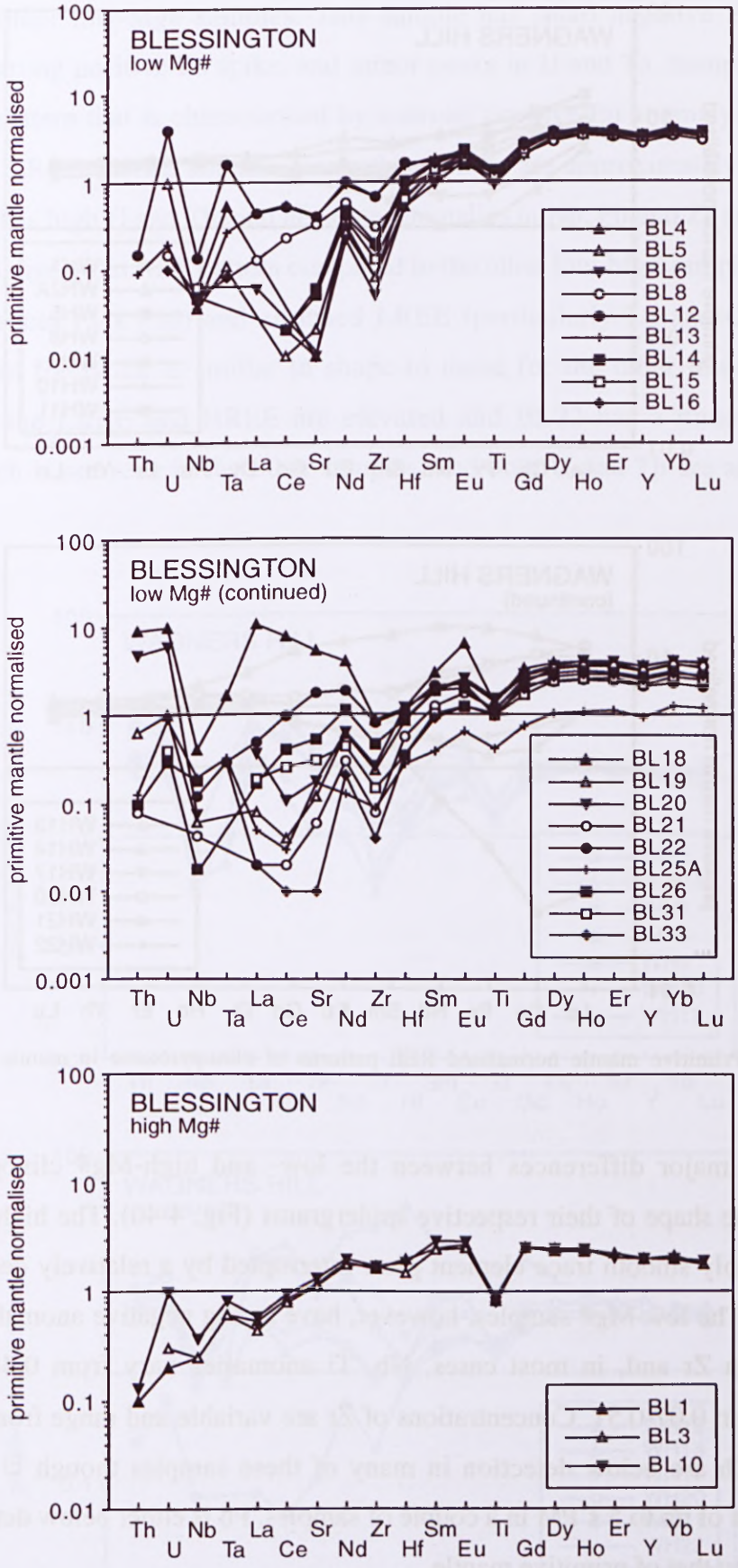


**Figure 4-40.** Primitive mantle normalised trace element abundance patterns of clinopyroxene in mantle xenoliths from Blessington.

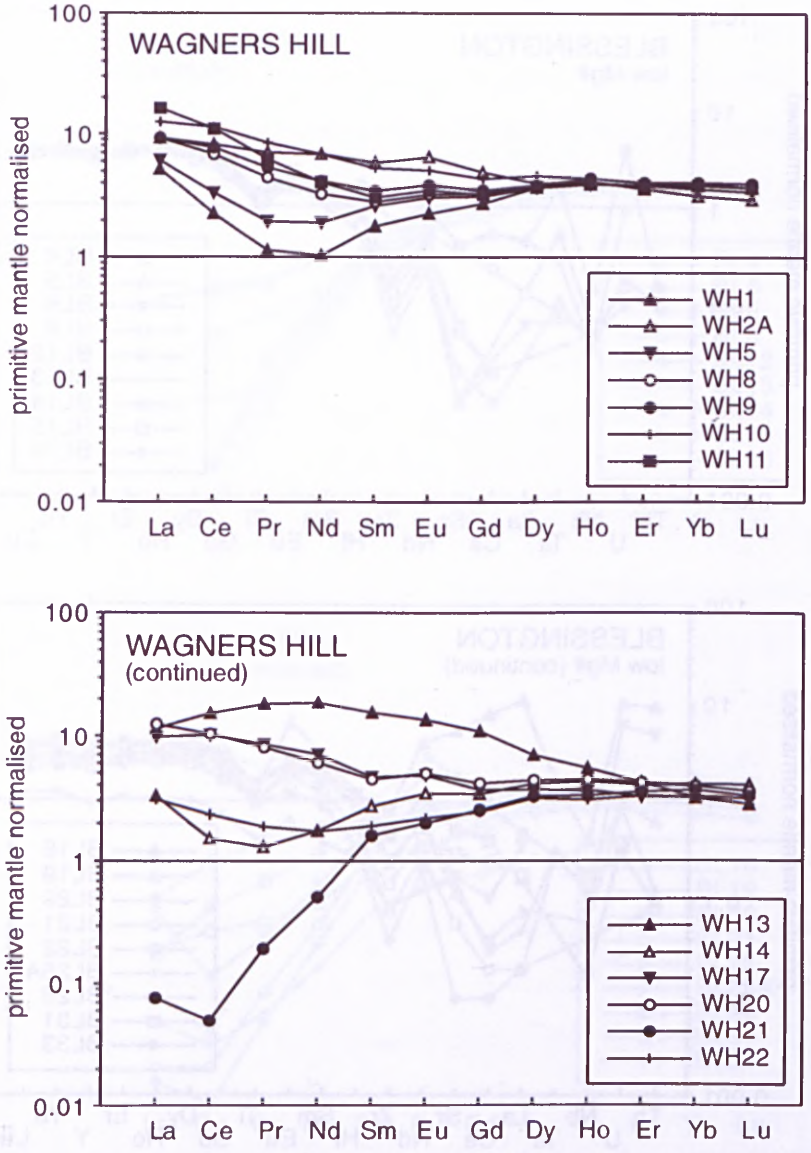


**Figure 4-41.** Primitive mantle normalised REE patterns of clinopyroxene in mantle xenoliths from Wagners Hill.

Other major differences between the low- and high-Mg# clinopyroxenes are apparent in the shape of their respective spidergrams (Fig. 4-40). The high-Mg# samples have remarkably smooth trace element plots interrupted by a relatively deep Ti anomaly (0.29- 0.33). The low-Mg# samples, however, have strong negative anomalies not only in Ti but also in Zr and, in most cases, Nb. Ti anomalies vary from 0.48-0.74 and Zr anomalies from 0.07-0.51. Concentrations of Zr are variable and range from 0.04 to 0.7 x PM. U and Th are below detection in many of these samples though U does occur at concentrations of up to 5 x PM in a couple of samples. Pb is either below detection or has a value similar to that of primitive mantle.

There are three samples from Blessington which have REE patterns that are slightly unusual and deserve a separate mention. Clinopyroxenes from sample BL25a have spoon-shaped depleted-LREE patterns with very low HREE abundances (primitive mantle values)

compared to other low-Mg# samples. This sample has small negative Zr, Ti and Nb anomalies, a strong positive Pb spike, and minor peaks in U and Ta. Sample BL18 has a type 1a REE pattern that is characterised by a strong positive Eu anomaly and moderate enrichment in LREE. HREE abundances in this sample are approximately 3 x primitive mantle. BL18 has high U and Th, and negative anomalies in Nb, Pb and Zr and Hf. Sample BL22 has a relatively flat REE pattern compared to the other low-Mg# samples with higher HREE abundances (3 x PM) and enriched LREE (particularly La and Ce). The trace element pattern for BL22 is similar in shape to those for the other low-Mg# samples though again the LREE and HREE are elevated and BL22 has a minor negative Zr anomaly, which is not seen in the other samples, and both U and Th are at levels below detection.

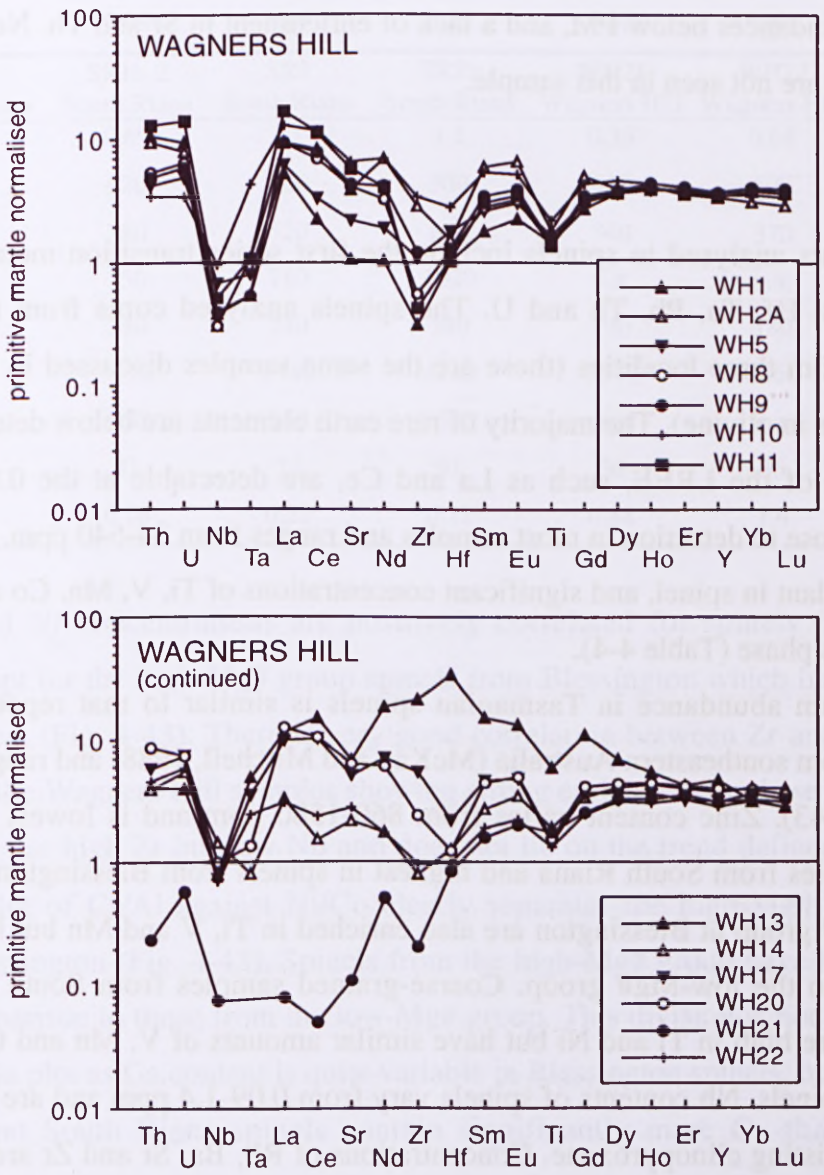


**Figure 4-42.** Primitive mantle normalised trace element abundance patterns of clinopyroxene in mantle xenoliths from Wagners Hill.

There is little variation in the shape of REE patterns for the majority of Wagners Hill clinopyroxenes. All except one (WH21) have upwardly-concave type 1a patterns ($(La/Yb)_N$=0.81-4.25) with flat HREE at abundances of approximately 3.5 x PM (Fig. 4-41). These clinopyroxenes have extremely enriched LREE signatures with LREE abundances which are up to eleven times PM. Uniformly high concentrations of other incompatible elements such as U, Th and Sr, and deep negative anomalies in Nb, Ta, Zr, Ti, and in some cases Hf, are characteristic of these samples (Fig.4-42). Ti anomalies show a range of 0.32-0.59 and Zr anomalies vary from 0.12-0.92. Sample WH21 has a V-shaped type 2 pattern that has similar MREE and HREE abundances as the other samples but very low LREE ($(La/Yb)_N$=0.02). $(Ce/Nd)_N$ equals 0.1 in this sample compared to a range of 0.87-2.7 in those that are LREE-enriched. A trace element plot for WH21 shows Zr and Ti anomalies similar to those seen in the other samples, high U and Nd relative to the REE, though at abundances below PM, and a lack of enrichment in Sr and Th. Negative Nb and Ta anomalies are not seen in this sample.

Spinel

Trace elements analysed in spinels include the first series transition metals, Ga, Y, Zr, LILEs, REEs, Hf, Ta, Pb, Th and U. The spinels analysed come from thirteen spinel peridotites from three localities (these are the same samples discussed in the section on trace elements in olivine). The majority of rare earth elements are below detection in spinel though some of the LREE, such as La and Ce, are detectable at the 0.01 ppm level. Calcium is close to detection in most samples and ranges from 34-640 ppm. Ga and Zn are notably abundant in spinel, and significant concentrations of Ti, V, Mn, Co and Ni are also present in this phase (Table 4-4).

Gallium abundance in Tasmanian spinels is similar to that reported for spinel lherzolites from southeastern Australia (McKay and Mitchell, 1988) and ranges from 35-91 ppm (Fig. 4-43). Zinc content varies from 860-1580 ppm and is lowest in the coarse-grained samples from South Riana and highest in spinels from Blessington. Spinels from the high-Mg# group at Blessington are also enriched in Ti, V and Mn but have low Ni in comparison to the low-Mg# group. Coarse-grained samples from South Riana contain spinels that are high in Ti and Ni but have similar amounts of V, Mn and Co to the other Tasmanian spinels. Nb contents of spinels vary from 0.09-1.4 ppm and are comparable to those in coexisting clinopyroxene. Concentrations of Rb, Ba, Sr and Zr are typically less

than 0.5 ppm for the majority of samples except for sample BL10 which contains 0.69 ppm Rb, 0.97 ppm Sr. 1.2 ppm Zr and close to 3 ppm Ba.

**Table 4-5.** Trace element abundances in spinel from Tasmanian spinel peridotites. All values are given in ppm.

| | BL1 Blessington | BL4 Blessington | BL6 Blessington | BL10 Blessington | BL31 Blessington | BL33 Blessington | BL35 Blessington |
|---|---|---|---|---|---|---|---|
| Sc | 1.6 | 0.41 | 0.58 | 4.0 | 0.57 | 0.49 | 0.50 |
| Ti | 790 | 330 | 540 | 710 | 280 | 250 | 240 |
| V | 960 | 500 | 550 | 880 | 390 | 390 | 360 |
| Mn | 950 | 770 | 810 | 920 | n.a. | n.a. | n.a. |
| Co | 300 | 290 | 310 | 290 | 190 | 180 | 190 |
| Ni | 1660 | 3020 | 2980 | 1610 | 2020 | 1730 | 1930 |
| Zn | 1390 | 1320 | 1360 | 1580 | n.a. | n.a. | n.a. |
| Ga | 47 | 72 | 73 | 48 | 41 | 36 | 40 |
| Nb | 0.21 | 0.09 | 0.14 | 0.29 | 0.39 | 0.41 | 0.36 |

| | SR1 South Riana | SR1b-2 South Riana | SR2 South Riana | SR2b South Riana | WH21 Wagners Hill | WH22 Wagners Hill |
|---|---|---|---|---|---|---|
| Sc | 0.56 | 0.69 | 1.1 | 1.1 | 0.35 | 0.64 |
| Ti | 390 | 920 | 720 | 500 | 410 | 600 |
| V | 520 | 380 | 520 | 690 | 340 | 370 |
| Mn | 770 | 750 | 780 | 1020 | n.a. | n.a. |
| Co | 280 | 230 | 240 | 380 | 190 | 180 |
| Ni | 2930 | 3110 | 2740 | 4140 | 1840 | 1560 |
| Zn | 1110 | 860 | 940 | 1380 | n.a. | n.a. |
| Ga | 67 | 81 | 73 | 91 | 36 | 35 |
| Nb | 0.10 | 0.16 | 0.22 | 0.12 | 0.88 | 1.4 |

Co and Ni concentrations are positively correlated for spinels from all three localities except for the high-Mg# group spinels from Blessington which have low Ni for their Co content (Fig. 4-43). There is very good correlation between Zr and Nb for most samples with the Wagners Hill samples showing strong enrichment in these two elements. Sample BL10 has high Zr but low Nb and does not lie on the trend defined by the other samples. A plot of Cr/Al against Ni/Co clearly separates the high-Mg# and low-Mg# groups of Blessington (Fig. 4-43). Spinels from the high-Mg# group have low Cr/Al and Ni/Co in comparison to those from the low-Mg# group. This division is not so obvious on the Cr/Al vs Ga plot as Ga content is quite variable in Blessington spinels, but this diagram does show that South Riana spinels contain significantly more Ga than those from Wagners Hill.

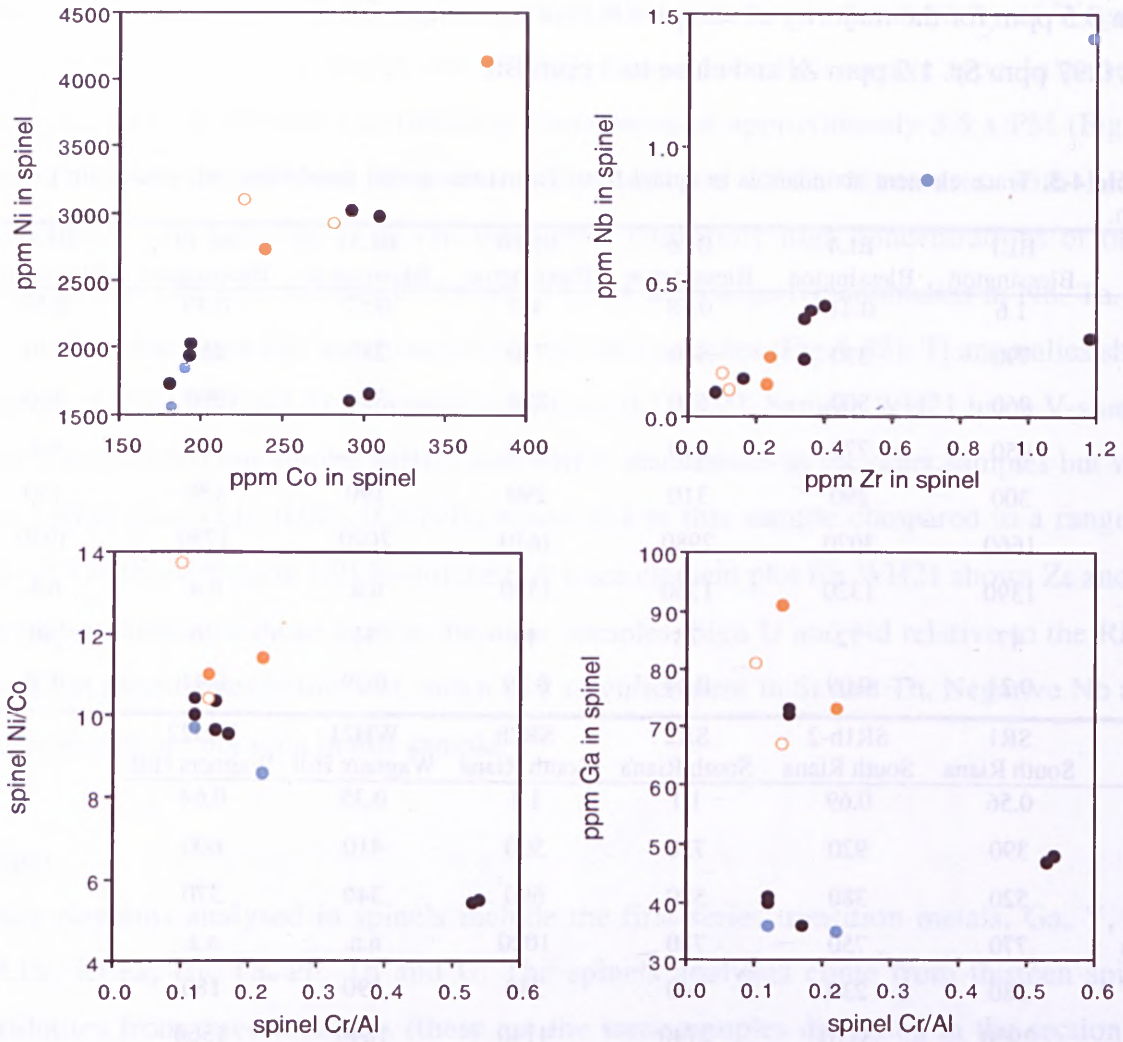


**Figure. 4-43.** Trace element variation diagrams for Tasmanian spinels. Black symbols are Blessington samples. Orange symbols are South Riana samples (closed circles-fine grained; open circles-coarse grained). Blue symbols are Wagners Hill samples.

## 4.4 WHOLE ROCK GEOCHEMISTRY

### *4.4.1 Major and trace elements*

The majority of Tasmanian xenoliths are small (<10cm in diameter) making them unsuitable for whole rock geochemical analysis. Of the 130 xenoliths studied five samples (three from Blessington and two from Wagners Hill) were considered large enough for whole-rock major and trace-element analysis. Results from XRF and ICPMS analysis for these five samples are presented in Table 4.5. Bulk-rock major-element compositions were reconstructed for 105 of the remaining samples using their mineral major-element chemistry and pointcounted modes (see Section 4.2). Reconstructed bulk rock analyses are given in Appendix IV.

Major Elements

Whole-rock $Al_2O_3$ contents in Tasmanian peridotites vary from 0.32-6.42wt% (see Fig. 4-44). Low $Al_2O_3$ contents are typical of the high-Mg# xenoliths while strong Al-enrichment is seen in a group of three samples from Table Cape. In general, Tasmanian mantle xenoliths show a broad positive correlation between $TiO_2$ and $Al_2O_3$ (Fig. 4-44). This trend is most strongly defined for Blessington, Wagners Hill and South Riana, while xenoliths from Table Cape and Doctors Rocks show scattered data with no systematic correlation. Correlation between CaO and $Al_2O_3$ (Fig. 4-44) is generally poor for Tasmanian xenoliths with the exception of samples from South Riana which show a broad positive correlation between Ca and Al content. While Blessington lherzolites show considerable scatter on a CaO vs $Al_2O_3$ plot, the high-Mg# group xenoliths do lie at lower $Al_2O_3$ and CaO compared to the low-Mg# group. This is expected as clinopyroxene controls Ca content in spinel lherzolites and it has already been shown that clinopyroxene from the high-Mg# group has considerably lower Ca, and Al, than that from the low-Mg# group.

Tasmanian lherzolites define a broad negative correlation between MgO and $Al_2O_3$ and little or no correlation between FeO and $Al_2O_3$ (Fig. 4-44). The majority of xenoliths have relatively constant FeO for any given $Al_2O_3$ value except for a few samples from Wagners Hill which range to higher FeO contents; WH13 has 14.9wt% FeO as expected from its mineral chemistry. Fe-enrichment in Wagners Hill xenoliths is more apparent on a Mg# vs $Al_2O_3$ plot where those samples rich in Fe scatter away from the main trend to very low Mg#. This plot also delineates the high- and low-Mg# groups of Blessington and Coates Road.

Correlation between $Cr_2O_3$ and $Al_2O_3$ content is strong and positive for the bulk of Tasmanian xenoliths though there are a few samples that lie off the main trend at higher Cr values (Fig. 4-44). This relationship is unusual as spinel peridotites from young continental intraplate settings typically show no overall correlation between Cr and Al (Griffin *et al.*, 1999a). Positive correlation between Cr and Al has, however, been recognised in abyssal oceanic peridotites and interpreted as an artefact resulting from a small overestimation of the modal abundance of spinel when pointcounting (Griffin *et al.*, 1999a). This may also be the case for the Tasmanian xenoliths. $Na_2O$ does not show a strong correlation with $Al_2O_3$ though there is an overall trend of increasing $Na_2O$ content with increasing $Al_2O_3$. The highest Na contents occur in samples from Table Cape and Doctors Rocks and the lowest in the high-Mg# xenoliths and Fe-rich sample WH13. High whole rock $P_2O_3$ contents (>0.03 wt%) have been shown to be indicative of the presence of modal apatite

(O'Reilly and Griffin, 1988). However, samples WH21 and WH22, with $P_2O_5$ contents of 0.11 wt% and 0.03 wt% respectively, do not show any petrographic evidence for apatite. An alternative explanation for their high phosphorus is contamination by the host basalt. There is good evidence for pervasive interaction between xenolith and host rock in sample WH21 which contains numerous stringers and blebs of basalt.

**Table 4-6.** Major (XRF) and trace element (solution ICPMS) data for Tasmanian spinel lherzolites from Blessington and Wagners Hill. XRF data are presented as wt% and ICPMS data as ppm.

| Sample no. | BL31 | BL33 | BL35 | WH21 | WH22 |
|---|---|---|---|---|---|
| Locality | Blessington | Blessington | Blessington | Wagners Hill | Wagners Hill |
| $SiO_2$ | 44.9 | 44.1 | 44.5 | 44.4 | 44.9 |
| $TiO_2$ | 0.04 | 0.03 | 0.04 | 0.07 | 0.05 |
| $Al_2O_3$ | 2.75 | 2.01 | 2.52 | 2.44 | 1.84 |
| $Cr_2O_3$ | 0.45 | 0.39 | 0.41 | 0.39 | 0.36 |
| $Fe_2O_3$ | 8.68 | 9.42 | 9.13 | 9.4 | 8.95 |
| MnO | 0.13 | 0.13 | 0.14 | 0.13 | 0.13 |
| MgO | 39.3 | 39.3 | 39.8 | 41.0 | 42.2 |
| CaO | 2.85 | 2.48 | 2.40 | 2.49 | 2.13 |
| $Na_2O$ | 0.06 | 0.13 | 0.07 | 0.22 | 0.16 |
| $K_2O$ | 0.01 | 0.01 | 0.02 | 0.05 | 0.04 |
| NiO | 0.25 | 0.28 | 0.26 | 0.27 | 0.29 |
| $P_2O_5$ | 0.01 | 0.01 | 0.01 | 0.11 | 0.03 |
| $H_2O+$ | 1.22 | 0.68 | 1.00 | 0.44 | 0.54 |
| H2O- | 0.16 | 0.09 | 0.13 | 0.08 | 0.09 |
| CO2 | 0.13 | 0.03 | 0.03 | 0.08 | 0.03 |
| Total | 100.2 | 100.7 | 99.9 | 100.9 | 101.1 |
| Mg# | 89.9 | 89.2 | 89.6 | 89.6 | 90.4 |
| Sc | 16 | 11 | 14 | 13 | 14 |
| V | 93 | 69 | 87 | 79 | 83 |
| Co | 92 | 93 | 98 | 99 | 99 |
| Ni | 1990 | 1980 | 2110 | 2070 | 2090 |
| Th | 0.01 | 0.004 | 0.01 | 0.09 | 0.05 |
| Nb | 0.17 | 0.15 | 0.21 | 5.8 | 3.0 |
| La | 0.08 | 0.03 | 0.18 | 0.84 | 0.51 |
| Ce | 0.15 | 0.06 | 0.23 | 1.5 | 0.86 |
| Sr | 3.3 | 0.29 | 3.7 | 38 | 21 |
| Nd | 0.13 | 0.06 | 0.19 | 0.71 | 0.45 |
| Zr | 0.73 | 0.27 | 0.96 | 4.7 | 2.8 |
| Hf | 0.03 | 0.02 | 0.03 | 0.10 | 0.06 |
| Sm | 0.08 | 0.06 | 0.09 | 0.20 | 0.14 |
| Eu | 0.04 | 0.02 | 0.04 | 0.08 | 0.06 |
| Ti | 420 | 250 | 430 | 630 | 530 |
| Gd | 0.18 | 0.13 | 0.18 | 0.28 | 0.23 |
| Dy | 0.30 | 0.22 | 0.30 | 0.36 | 0.32 |
| Ho | 0.08 | 0.06 | 0.07 | 0.08 | 0.08 |
| Y | 2.1 | 1.5 | 2.1 | 2.4 | 2.2 |
| Er | 0.25 | 0.18 | 0.22 | 0.25 | 0.24 |
| Yb | 0.26 | 0.19 | 0.24 | 0.26 | 0.25 |
| Lu | 0.04 | 0.03 | 0.04 | 0.04 | 0.04 |

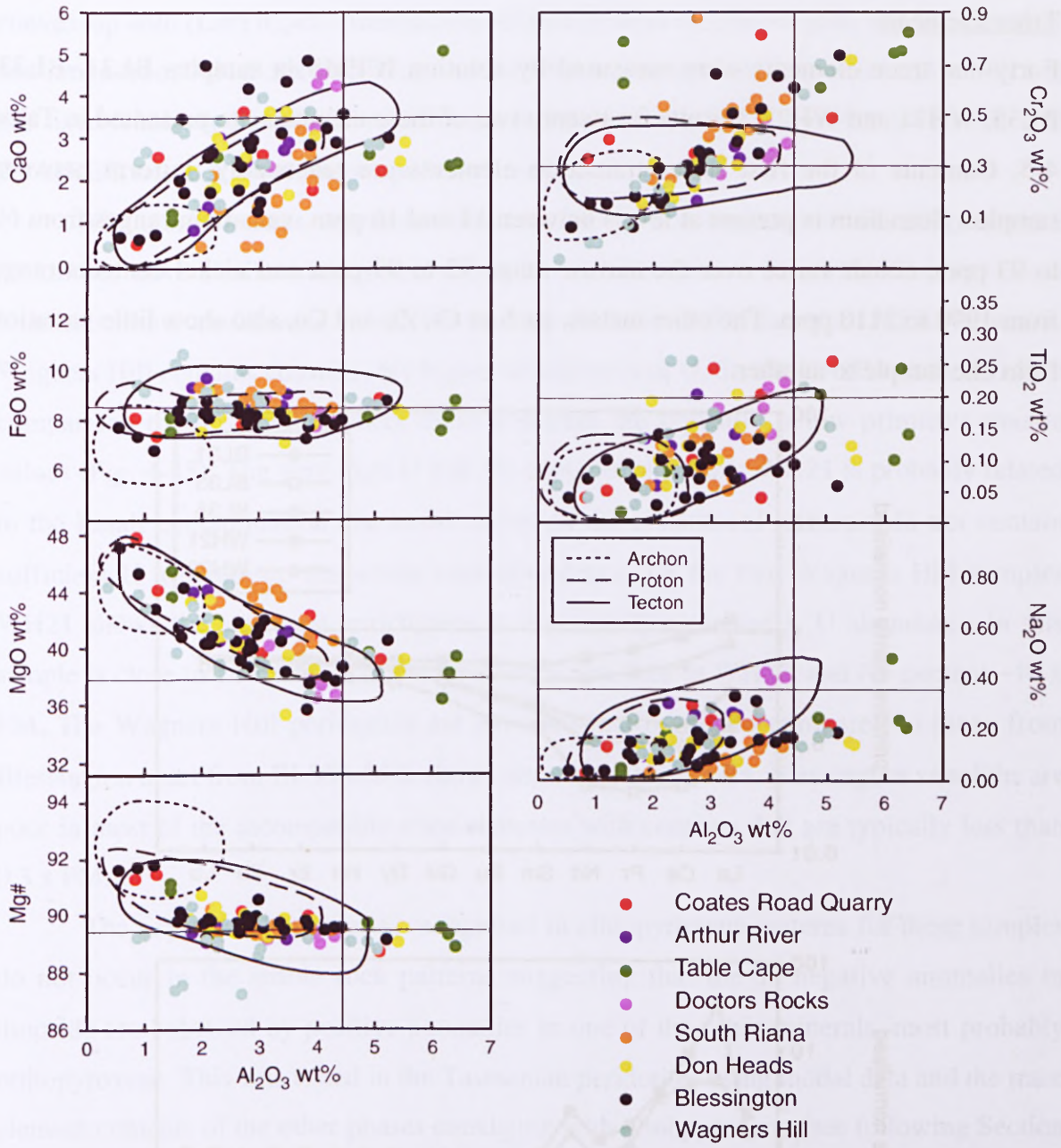


**Figure 4-44.** Concentrations of major elements in Tasmanian mantle xenoliths plotted against $Al_2O_3$ content. Fields are from Griffin *et al.* (1999a). Vertical and horizontal lines mark the primitive mantle values of McDonough and Sun (1995).

Whole-rock $Al_2O_3$ content in peridotites is a convenient measure of depletion in basaltic components (see Section 1.2.3). The Tasmanian xenoliths tend to have high $Al_2O_3$ abundances which suggests that they have undergone only small amounts of melt depletion. The majority of samples fall in the fields for Tecton peridotites for the oxides considered in Fig. 4-44, though there is considerable overlap into the Proton fields. The high-Mg# xenoliths have very low $Al_2O_3$ contents and lie in the Archon fields in Fig. 4-44. The compositional resemblance between the high-Mg# samples and highly-depleted cratonic xenoliths implies that they have experienced a higher degree of partial melting than the more chemically fertile xenoliths.

Trace Elements

Forty-one trace elements were measured by solution ICPMS in samples BL31, BL33, BL35, WH21 and WH22. Results for twenty-two of these elements are presented in Table 4-5. Contents of the first series transition elements are reasonably uniform between samples. Scandium is present at levels between 11 and 16 ppm, vanadium ranges from 69 to 93 ppm, cobalt varies over the narrow range 92 to 99 ppm and nickel contents range from 1990 to 2110 ppm. The other metals, such as Cr, Zn and Cu, also show little variation from one sample to another.

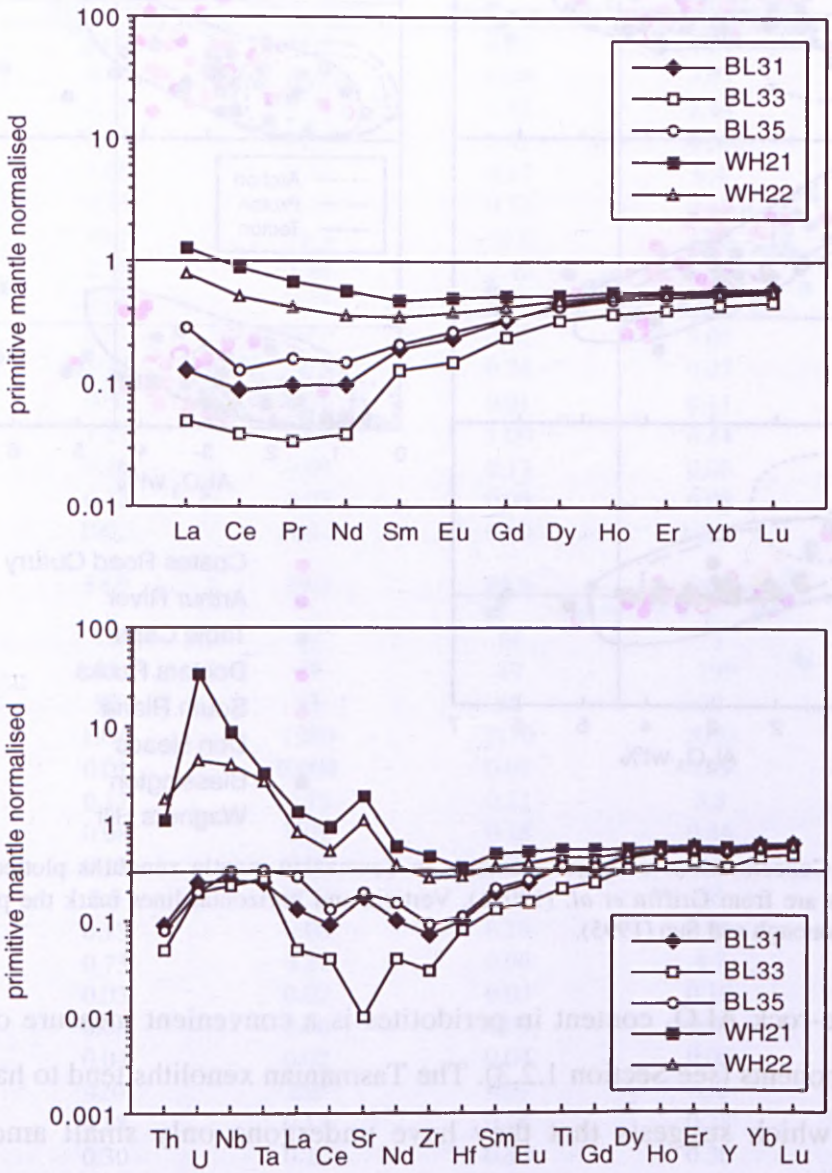


**Figure 4-45.** Primitive mantle normalised REE patterns (top) and trace element abundance patterns (bottom) for Tasmanian spinel peridotites.

The rare-earth element data produce very smooth plots with flat HREE (Fig. 4-45). Both Blessington and Wagners Hill have low HREE contents that are typically ~0.4-0.6 x primitive mantle (PM). LREE patterns in the Blessington samples are spoon-shaped and

convex-up with $(La/Yb)_N<1$. Abundances of the LREE in the Blessington xenoliths are low and range from 0.04-0.3 x PM. Wagners Hill lherzolites are LREE-enriched ($(La/Yb)_N>1$) and have relatively flat MREE ($(Sm/Dy)_N\approx1$). Apart from La (1.5-2 x PM) the LREE, and the MREE, occur at levels below primitive mantle.

The trace element abundance patterns for the Blessington and the Wagners Hill peridotites have similar shapes but very different abundances for some elements. Both localities show enrichment in U, Nb and Ta relative to Th and the LREE, however, Wagners Hill contains considerably higher abundances of U, Sr, the HFSE and the LILE in comparison to Blessington where these elements are typically below primitive mantle values (Fig. 4-45). The very high U and Nb contents of sample WH21 is probably related to the basalt contamination discussed earlier as the constituent minerals do not contain sufficient U to make up the whole rock abundance. Of the two Wagners Hill samples WH21 shows the strongest enrichment in incompatible elements. U abundance in this sample is close to 12 x PM, which is four times that seen in WH22, and Nb content ~10 x PM. The Wagners Hill peridotites are enriched in Rb and Ba compared to those from Blessington apart from BL35 which shows anomalously high Ba. Blessington xenoliths are poor in most of the incompatible trace elements with contents that are typically less than 0.3 x PM.

The negative Ti anomalies recognised in clinopyroxene patterns for these samples do not occur in the whole rock patterns suggesting that the Ti negative anomalies in diopside are balanced by positive anomalies in one of the other minerals, most probably orthopyroxene. This was tested in the Tasmanian peridotites using modal data and the trace element contents of the other phases coexisting with clinopyroxene (see following Section on mass balance). Negative Zr anomalies do occur in the Blessington whole rock patterns, though they are at lower abundances and are not as well-defined as those seen in the clinopyroxenes.

### *4.4.2 Mass balance calculations*

A mass balance calculation has been carried out for those samples for which whole-rock data was available. Firstly, the total trace-element abundances ($\Sigma$ cpx) in clinopyroxene have been calculated by multiplying the cpx modal % (given in Appendix I) by the corresponding trace element concentrations in cpx from Appendix III, and then dividing the result by the whole rock values ($\Sigma$ cpx/rock) to identify the proportion of each trace element concentrated in clinopyroxene (Table 4-7, Fig. 4-46). Patterns for

Blessington and Wagners Hill spinel lherzolites resemble each other and are similar to those calculated for fertile xenoliths from SE China (Xu, 1999). In the Tasmanian samples clinopyroxene accounts for 50 to 80% of the whole rock Y and HREE budget, but less than half of LREE, HFSE, Sr and Ti in the whole-rock resides in clinopyroxene, indicating that the other minerals must account for at least a proportion of these elements.

**Table 4-7.** Results from mass balance calculations.

| Σ Cpx/rock | BL31 | BL33 | BL35 | WH21 | WH22 |
|---|---|---|---|---|---|
| Th | 0.00 | 0.00 | 0.00 | 0.03 | 0.78 |
| Nb | 0.01 | 0.01 | 0.01 | 0.00 | 0.02 |
| La | 0.17 | 0.03 | 0.05 | 0.01 | 0.38 |
| Ce | 0.34 | 0.04 | 0.14 | 0.01 | 0.45 |
| Sr | 0.22 | 0.10 | 0.12 | 0.01 | 0.26 |
| Nd | 0.52 | 0.51 | 0.22 | 0.10 | 0.47 |
| Zr | 0.26 | 0.17 | 0.11 | 0.05 | 0.35 |
| Hf | 0.45 | 0.49 | 0.28 | 0.28 | 0.43 |
| Sm | 0.63 | 0.72 | 0.44 | 0.38 | 0.54 |
| Eu | 0.63 | 0.87 | 0.44 | 0.46 | 0.57 |
| Ti | 0.34 | 0.53 | 0.29 | 0.38 | 0.30 |
| Gd | 0.60 | 0.85 | 0.48 | 0.56 | 0.57 |
| Dy | 0.66 | 0.88 | 0.58 | 0.70 | 0.64 |
| Ho | 0.60 | 0.83 | 0.51 | 0.67 | 0.57 |
| Y | 0.54 | 0.78 | 0.49 | 0.63 | 0.54 |
| Er | 0.57 | 0.78 | 0.57 | 0.69 | 0.59 |
| Yb | 0.56 | 0.73 | 0.54 | 0.71 | 0.56 |
| Lu | 0.51 | 0.65 | 0.42 | 0.64 | 0.49 |

| Σ Minerals/rock | BL31 | BL33 | BL35 | WH21 | WH22 |
|---|---|---|---|---|---|
| Th | 0.00 | 0.00 | 0.98 | 0.05 | 0.94 |
| Nb | 0.09 | 0.07 | 0.06 | 0.01 | 0.03 |
| La | 0.21 | 0.03 | 0.05 | 0.01 | 0.39 |
| Ce | 0.36 | 0.04 | 0.14 | 0.01 | 0.46 |
| Sr | 0.22 | 0.10 | 0.13 | 0.01 | 0.27 |
| Nd | 0.55 | 0.51 | 0.26 | 0.11 | 0.51 |
| Zr | 0.32 | 0.24 | 0.13 | 0.06 | 0.40 |
| Hf | 0.58 | 0.65 | 0.49 | 0.46 | 0.56 |
| Sm | 0.69 | 0.80 | 0.44 | 0.40 | 0.56 |
| Eu | 0.68 | 0.92 | 0.51 | 0.49 | 0.67 |
| Ti | 0.54 | 0.78 | 0.52 | 0.56 | 0.48 |
| Gd | 0.65 | 1.10 | 0.53 | 0.58 | 0.60 |
| Dy | 0.72 | 0.93 | 0.64 | 0.95 | 0.68 |
| Ho | 0.71 | 0.89 | 0.58 | 0.75 | 0.64 |
| Y | 0.60 | 0.87 | 0.57 | 0.69 | 0.60 |
| Er | 0.67 | 0.84 | 0.82 | 0.83 | 0.67 |
| Yb | 0.83 | 1.05 | 0.87 | 0.89 | 0.73 |
| Lu | 1.05 | 0.84 | 1.13 | 0.82 | 0.84 |

Secondly, the proportion of each trace element contained in the major minerals has been calculated by summing the trace-element concentrations in all mineral components (clinopyroxene, orthopyroxene, olivine and spinel) (Σ minerals) and then dividing by the

whole rock values (Σ minerals/rock) (Table 4-6). The results are illustrated in Fig. 4-46. The similarity between patterns for (Σ cpx/rock) and (Σ minerals/rock) indicates that clinopyroxene is the main carrier of trace elements in these peridotites and that the other phases do not significantly contribute to the whole rock trace element budget. The deep Ti anomalies in the Σ cpx/rock pattern are reduced but not eliminated in the Σ minerals/rock pattern suggesting that the other phases contain insufficient Ti to balance the deficit in clinopyroxene.

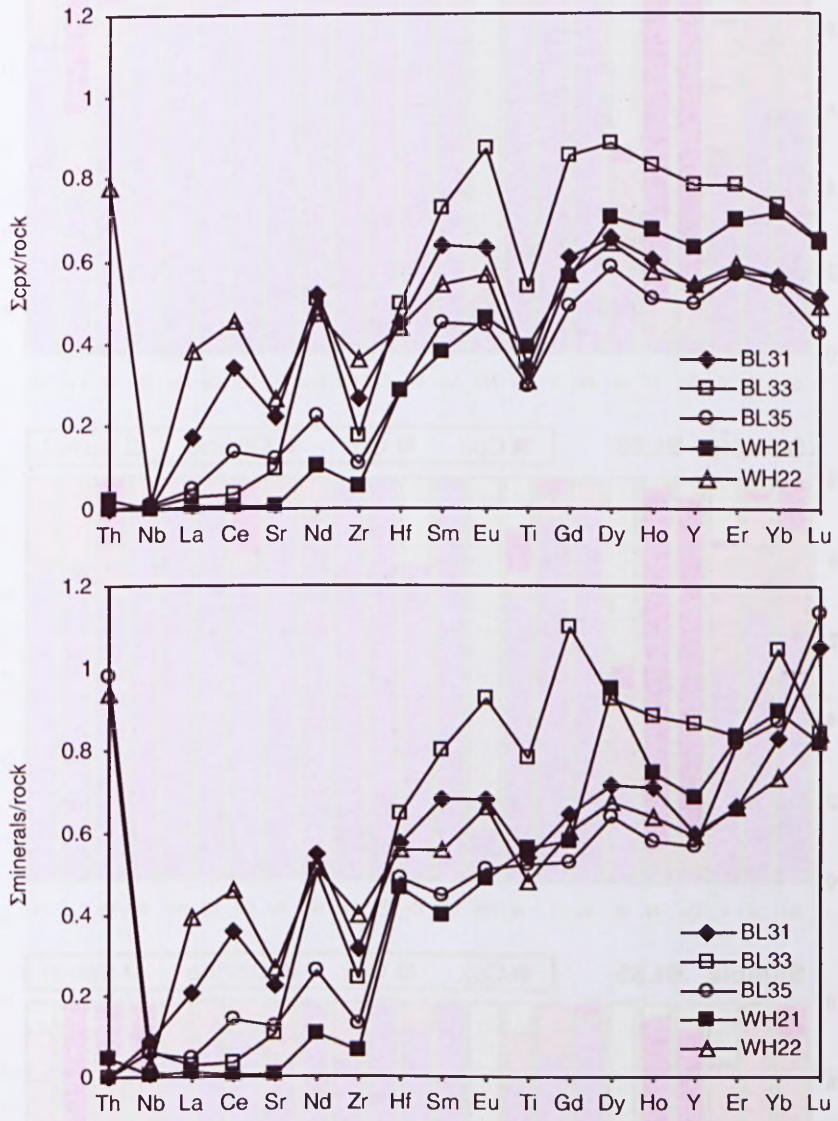


**Figure 4-46.** Mass balance calculation diagrams for Tasmanian spinel lherzolites.

A study of trace-element residence sites in mantle xenoliths from the Kerguelen Islands by Grégoire *et al.* (2000) found that clinopyroxene is the dominant host for REE, Sr, Y, Zr and Th; opx is important for Ti, Zr, HREE, Y, Sc and V; olivine for Ni, Co and Sc; and spinel for V and Ti. Figs. 4-47 and 4-48 show the relative contributions of the individual mineral phases to the trace element budget for Tasmanian spinel lherzolites. The

LREE, Sr, Zr and Y occur almost exclusively in clinopyroxene, confirming the findings of (Grégoire *et al.*, 2000), with minor amounts found in orthopyroxene and, in rare cases, olivine and spinel. Orthopyroxene and olivine are major hosts for the HREE and collectively account for up to 60% of these elements, in particular Yb and Lu.

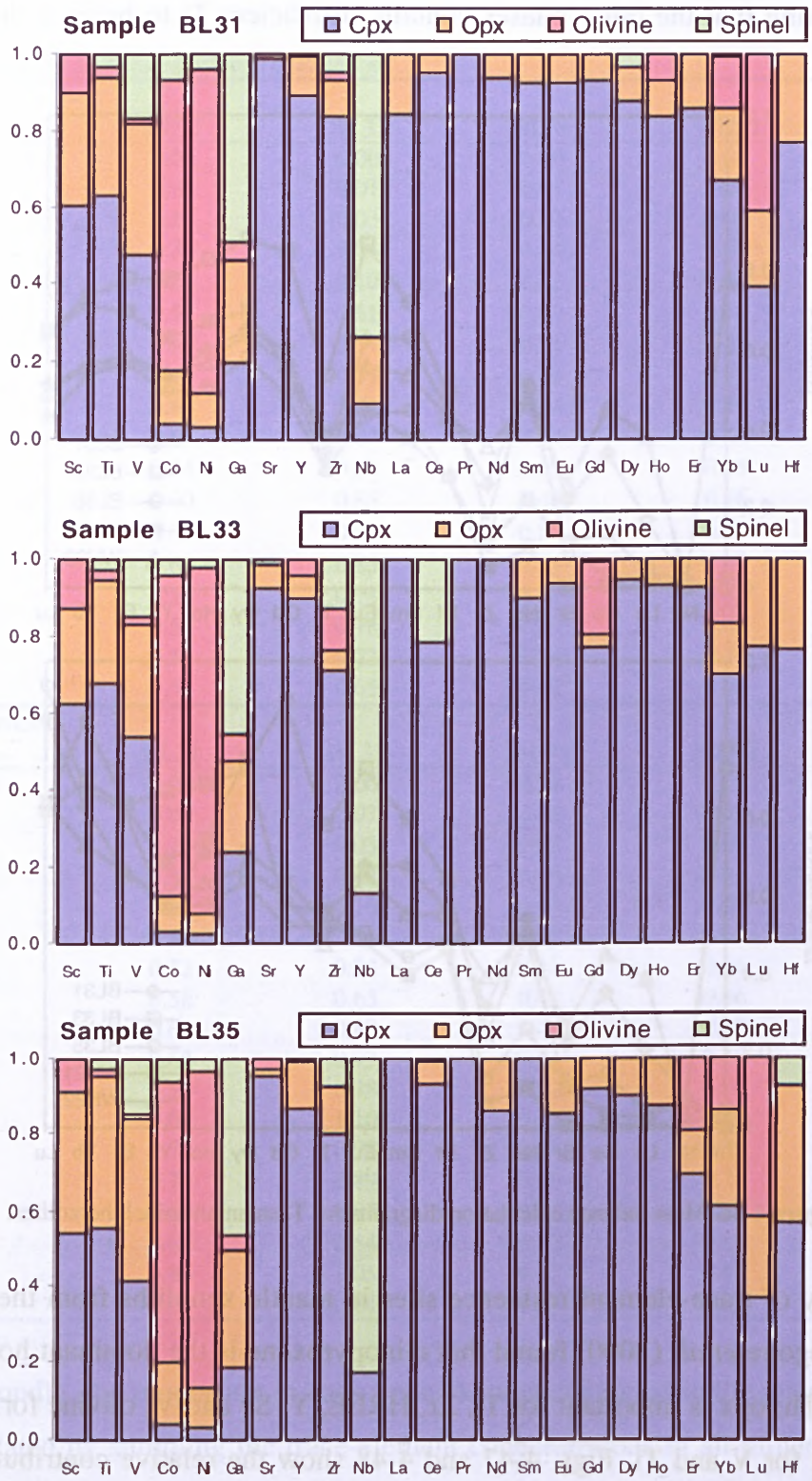


**Figure 4-47.** Relative contributions of the individual mineral phases to the trace element budgets for spinel lherzolites from Blessington.

Clinopyroxene typically contains 50 to 60% of Sc, Ti and V, with orthopyroxene taking up much of the remainder, while olivine is the main repository for Co and Ni. This is similar to the Kerguelen peridotites although olivine in the Tasmanian samples was not found to be a significant site for Sc. Spinel contains very low abundances of most trace elements apart from Ga and Nb, both of which show moderate to strong preference for this phase.

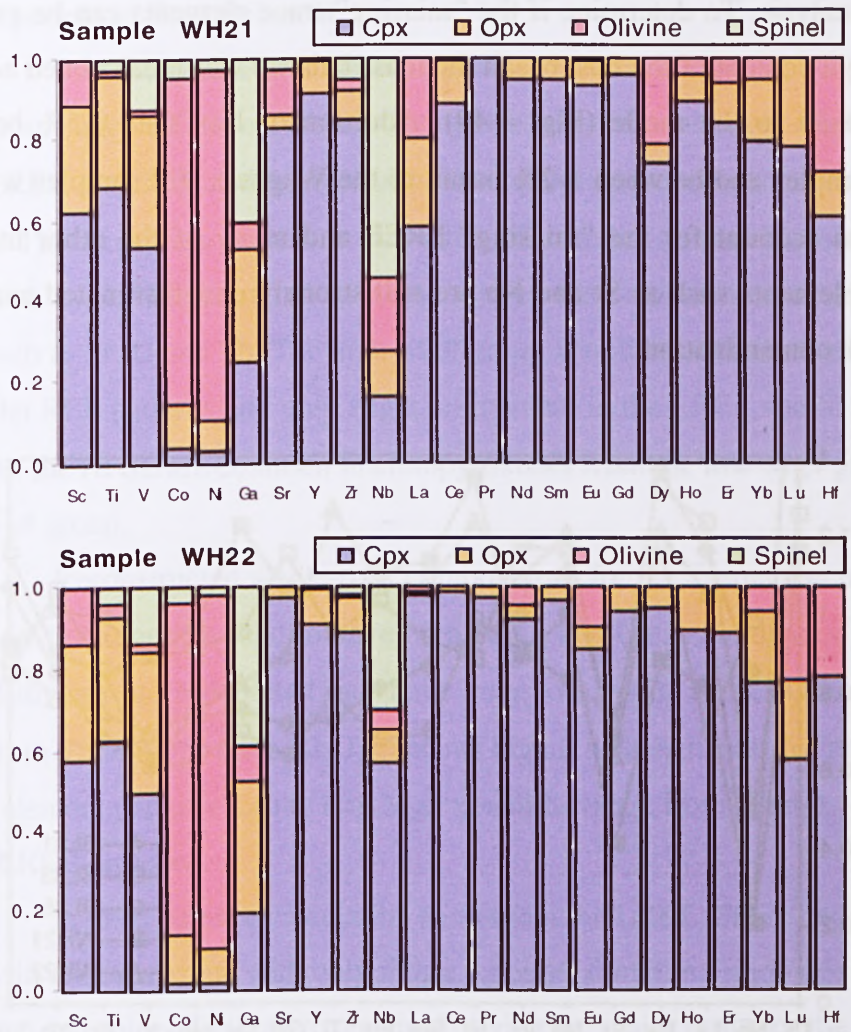


**Figure 4-48.** Relative contributions of the individual mineral phases to the trace element budgets for spinel lherzolites from Wagners Hill.

The ($\Sigma$ minerals/rock) pattern (Fig. 4-46) indicates that a large proportion of the incompatible trace elements do not reside in the major mineral phases, requiring repositories such as grain boundaries, fluid inclusions or exotic accessory minerals. Previous studies (Stosch, 1982; Fraser *et al.*, 1984; Suzuki, 1987; Zindler and Jagoutz, 1988; Ionov *et al.*, 1992) have reported grain boundary enrichment of incompatible elements in some mantle peridotites and (Bodinier *et al.*, 1996) have identified

microphases (titanium oxides and phlogopite) attached to the surfaces of spinels from lherzolites and harzburgites. Fluid inclusions in mantle minerals, in particular olivine and orthopyroxene, have been shown to concentrate LREE as well as K, Rb, Sr and Ba (Stosch, 1982).

Although basalt-hosted mantle xenoliths are erupted very quickly and have little time for modification by their host there is still the possibility of contamination during entrainment. There is also the risk of contamination during sample preparation for geochemical analysis. To determine if the "missing" trace elements can be explained by the trace element content of the host basalt the mass balance was recalculated adding small amounts of basalt to the mode (Fig. 4-49). Addition of less than 0.5% basalt to the Blessington samples and between 1-2% basalt to the Wagners Hill samples was found to be sufficient to account for the "missing" LREE and many of the other incompatible elements, but elements such as Sr and Nb are still strongly underestimated and cannot be related to basalt contamination.

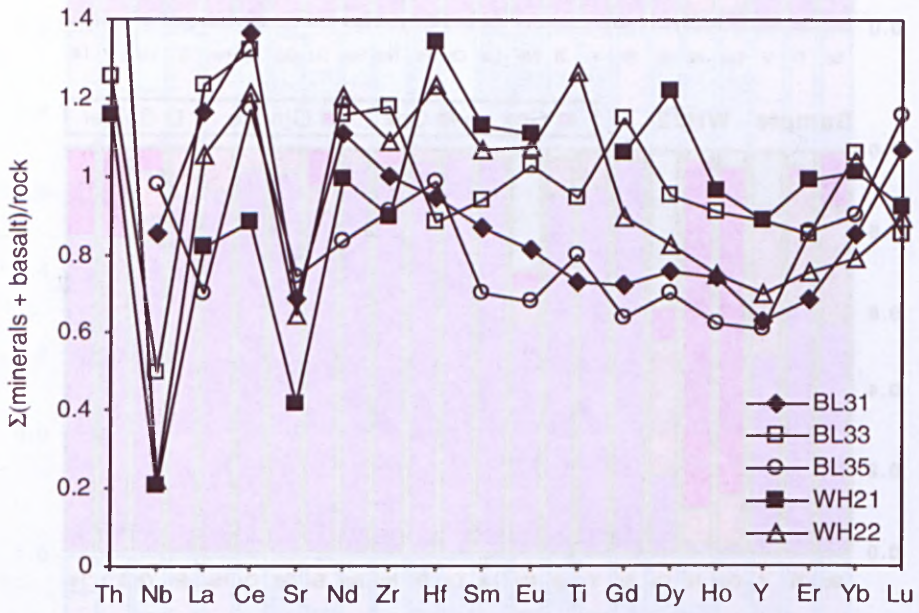


**Figure 4-49.** Mass balance calculation diagram for Tasmanian spinel lherzolites. Small amounts of basalt (0.1-2%) have been included in the calculations to account for some of the "missing" trace elements in the mass balance.

## 4.5 SUMMARY

(1) Tasmanian mantle xenoliths are predominately spinel lherzolites from the Cr-diopside suite with subordinate harzburgites and dunites. All the main microstructural types (coarse, porphyroclastic and granoblastic) defined by Harte (1977) are represented and it is common for xenoliths from a given locality to be dominated by a single

microstructural type.

(2) Samples can be divided into two main groups based on the Mg# of olivine. The majority of the Tasmanian xenoliths belong to the low-Mg# (<91) group. This group typically has high modal clinopyroxene (>25%) and occurs at all localities. The high-Mg# (>91) group is characterised by low modal clinopyroxene (<5%). These samples are less common and have been found at three localities (Coates Road Quarry, Table Cape and Blessington). A third group at Wagners Hill has very low olivine Mg# (<88) and has probably experienced Fe-enrichment.

(3) Trace element abundance patterns for clinopyroxene vary from LREE-depleted to strongly LREE-enriched. Clinopyroxenes from the low-Mg# xenoliths are generally LREE-enriched, and are typically accompanied by concomitant enrichment in Sr, Th and U. The exception to this is the suite of xenoliths from Blessington which is characterised by LREE-depleted clinopyroxenes that are also poor in incompatible elements such as Sr, U and Th. The high-Mg# group xenoliths contain clinopyroxenes with generally flat REE patterns and only slight enrichment in the LREE and Sr. Deep negative anomalies in the HFSE are common in clinopyroxenes from the low-Mg# group but rare in the high-Mg# group.

(4) Reconstructed whole-rock compositions for the Tasmanian peridotites show that the low-Mg# xenoliths tend to have high $Al_2O_3$ and CaO abundances while the high-Mg# xenoliths are more depleted and have very low $Al_2O_3$ and CaO contents. Several xenoliths from Table Cape have $Al_2O_3$ contents higher than estimates for primitive mantle. Rare earth element patterns for the low-Mg# xenoliths range from strongly LREE-depleted to slightly LREE-enriched.

(5) A mass balance calculation shows that the LREE, Sr, Zr and Y occur almost exclusively in clinopyroxene with only minor amounts found in orthopyroxene and, in rare cases, olivine and spinel. Orthopyroxene and olivine are major hosts for the HREE. A large proportion of the incompatible elements apparently reside in intergranular material in the peridotites. Contamination by the host basalt may account for some of these "missing" elements.

# CHAPTER 5
# CHARACTERISATION OF TASMANIAN LITHOSPHERIC MANTLE

## 5.1 INTRODUCTION

In Chapter 4 the major and trace element characteristics of the Tasmanian mantle xenoliths were dealt with quantitatively. This chapter aims to explore the processes causing the geochemical variations identified in these rocks. These processes can then be considered in terms of the lateral and vertical distribution of rock types to build a three-dimensional picture of the northern Tasmanian lithosphere.

Major and trace-element variations seen in minerals from the Tasmanian peridotite xenoliths reflect partial melting and metasomatic processes within the upper mantle. It has been previously noted that, while major element chemistry in many suites of mantle peridotites can be ascribed to partial melting, the incompatible trace-element compositions of the samples require later metasomatic enrichments. Therefore, it is important to distinguish between primary and secondary variations in rock composition. Work on spinel lherzolite xenoliths from Victoria (Frey and Green, 1974) attributed observed differences between major and trace element compositions to mixing of two components. Component A was defined as a depleted harzburgite or lherzolite, residual after partial melting of pyrolite, that controls the major element chemistry. Component B was regarded as a percolating basanitic melt that controls the bulk of incompatible elements. Component B was inferred to be present both in cryptically metasomatised anhydrous rocks (see Section 5.4.1) and in those containing secondary, metasomatically introduced minerals such as amphibole, mica and apatite.

While the conclusions of Frey and Green (1974) have now been modified to some extent (Griffin *et al.*, 1988; O'Reilly and Griffin, 1988) this initial-depletion/subsequent-enrichment pattern has been recognised in both garnet- and spinel-facies peridotites from world-wide localities making it a useful framework for studying Tasmanian xenoliths.

## 5.2 CRUSTAL ELEMENTS AND LITHOSPHERIC COMPOSITION

It has been proposed that the broad correlation recognised between crustal age and SCLM composition is the result of quasi-contemporaneous formation of crustal volumes

and the underlying lithosphere mantle (Griffin *et al.*, 1999a). If this is the case, and given that the relationship has been identified in relatively small terrains (Griffin *et al.*, 1999a), it is possible that each of the crustal Elements of Tasmania (Seymour and Calver, 1995) is coupled to a separate and geochemically distinct mantle section. To identify if mantle heterogeneity in Tasmania is linked to specific crustal terrains the sample localities will be now considered in terms of their relevant crustal Element i.e. Coates Road Quarry, Arthur River, Table Cape and Doctors Rocks belong to the Rocky Cape Element, South Riana and Don Heads are part of the Sheffield Element, and the Sideling, Blessington and Wagners Hill occur in the Northeast Tasmania Element. Wagners Hill xenoliths, however, are considered separately from the other Northeast Tasmania samples to highlight distinct compositional differences within the Element. The localities will also be discussed individually where intra-Element differences are recognised e.g. localised metasomatic events.

### *5.2.1 Variations in mineral major element composition*

The extraction of basaltic melt from a fertile source (rich in oxides such as CaO, $Al_2O_3$ and $TiO_2$) leads to progressively more depleted and Mg-rich compositions in the residue. A plot of modal olivine against olivine Mg# using appropriate data for depleted oceanic peridotites and model fertile, parental upper mantle defines an "oceanic trend" which represents the overall effect of partial melting of dry, fertile peridotite at low pressures (Boyd, 1989). Xenoliths from both oceanic and continental Phanerozoic terrains closely follow the oceanic trend whereas those from older Proterozoic and Archean terrains define fields that lie above the trend (Fig. 5-1).

Most Tasmanian xenoliths are very fertile and lie within, or adjacent to, the Phanerozoic field (Fig. 5-1). The samples that scatter well outside this field, fall either significantly below the oceanic trend or lie at elevated Mg# in, or adjacent to, the Proterozoic field. The samples plotting in the Proterozoic field include the high-Mg# samples already identified at Coates Road, Table Cape and Blessington plus two samples with slightly lower Mg# from Wagners Hill and South Riana. If these xenoliths represent residues of high degrees of partial melting they would be expected to have correspondingly low modal contents of clinopyroxene. This was found to be the case for samples from Blessington and Table Cape but not for those from Coates Road (CQ1), South Riana (SR10) and Wagners Hill (WH22) which contain about 10% diopside. It seems likely that these xenoliths may have been refertilised (i.e. Fe, Ca added) after the partial melting event

which initially depleted them.

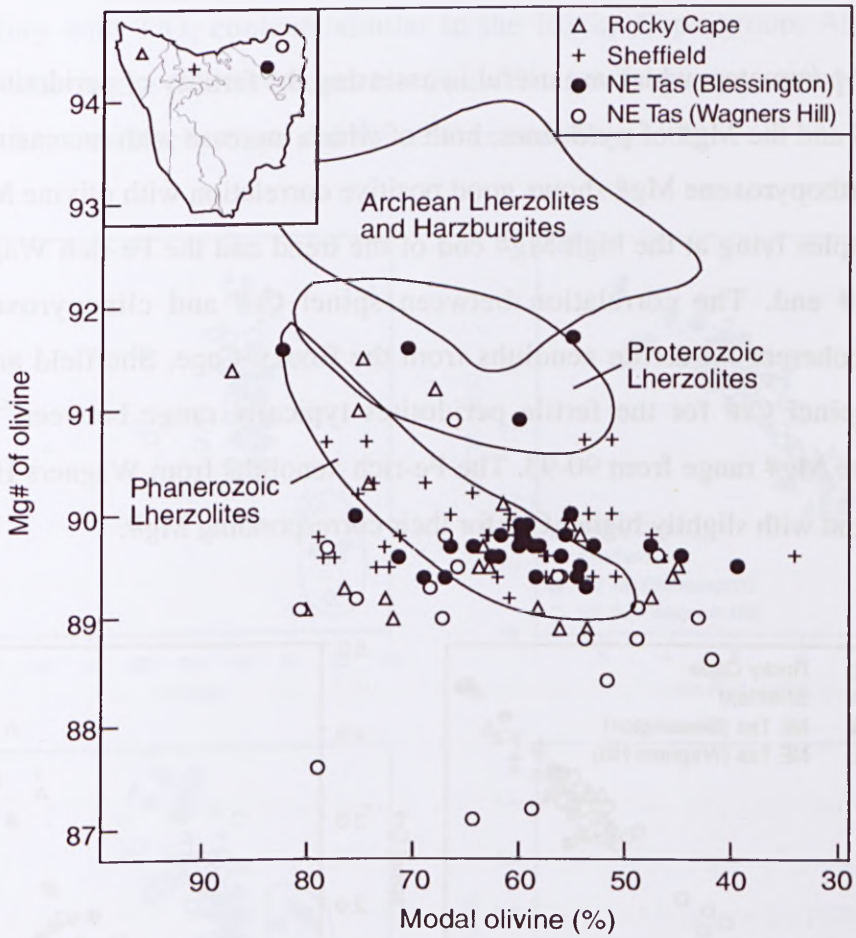


**Figure 5-1.** Modal olivine vs olivine Mg# plot for xenoliths from the different Tasmanian crustal Elements. Phanerozoic and Archean fields from Boyd (1989, 1997). Proterozoic field from Griffin *et al.* (1998b).

There is considerable overlap between the fertile xenoliths from the different crustal Elements (Fig. 5-1). The majority of xenoliths from the Rocky Cape Element scatter at low-Mg# (<89.5) close to or within the Phanerozoic field. Those xenoliths which lie outside the field are from Arthur River (<60% olivine) and Doctors Rocks (>60% olivine). The majority of fertile xenoliths from the Sheffield Element lie in the Phanerozoic field, at Mg# greater than 89.5, and follow the oceanic trend to more depleted compositions; a few samples scatter to higher and lower olivine modes. The Northeast Element xenoliths also plot predominantly in the Phanerozoic field with a narrow range in Mg# from ~89.5-90.

Wagners Hill xenoliths have low olivine Mg# (<90) and typically fall outside the Phanerozoic field at higher or lower modal olivine. Three xenoliths are characterised by very low Mg# (<88) and lie significantly below the field for Phanerozoic lherzolites. Fe-

rich peridotites such as these have been identified at other localities around the world and are considered to be the product of major element metasomatism by a silicate melt (Boyd, 1997).

Other parameters which are useful in assessing the fertility of peridotite include the Cr# of spinel and the Mg# of pyroxenes, both of which increase with increasing depletion. In Fig. 5-2 orthopyroxene Mg# shows good positive correlation with olivine Mg# with the depleted samples lying at the high Mg# end of the trend and the Fe-rich Wagners Hill at the low-Mg# end. The correlation between spinel Cr# and clinopyroxene Mg# is moderately coherent for fertile xenoliths from the Rocky Cape, Sheffield and Northeast Elements. Spinel Cr# for the fertile peridotites typically range between 10-15 while clinopyroxene Mg# range from 90-93. The Fe-rich xenoliths from Wagners Hill lie above the fertile trend with slightly higher Cr# for their corresponding Mg#.

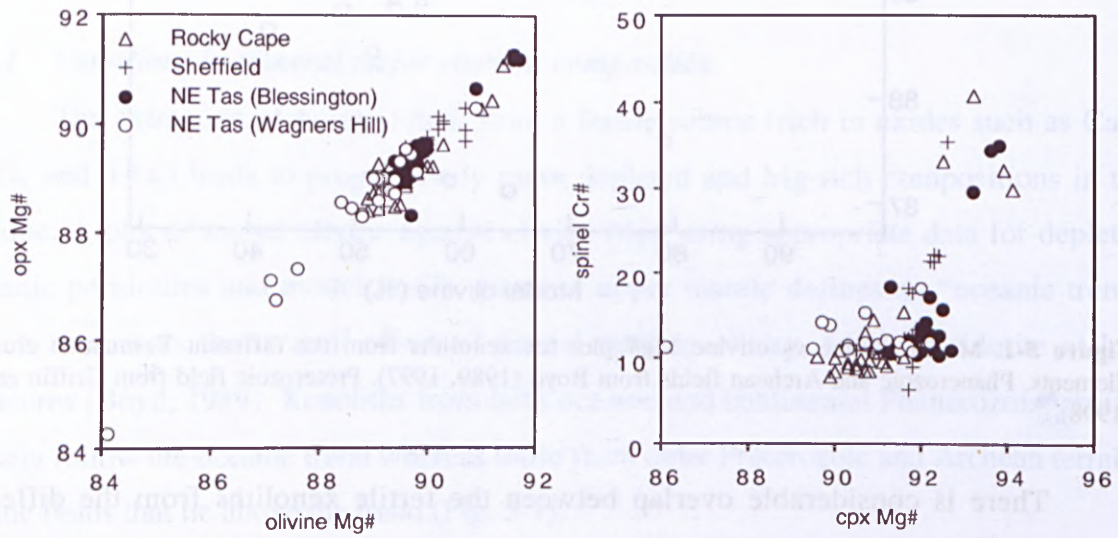


**Figure 5-2.** Compositional comparison between olivine, orthopyroxene, clinopyroxene and spinel.

The depleted peridotites have uniformly high spinel Cr# (>30) and clinopyroxene Mg# (>93) and lie at values that put them above the natural extension of the fertile trend suggesting that they are not genetically related to the fertile xenoliths. The majority of Rocky Cape peridotites cluster at the low-Cr# end of the fertile trend with Cr# typically less than 10. The Rocky Cape peridotites also have the lowest clinopyroxene Mg# of the fertile xenoliths and plot as a distinct group with Mg# below 91.

Clinopyroxene compositions reveal further differences between Rocky Cape mantle peridotites and those from the other crustal Elements. Figure 5-3 shows that Rocky Cape clinopyroxenes have considerably higher contents of $Al_2O_3$, $Na_2O$ and $TiO_2$, and lower

CaO abundances, compared to those from Sheffield and Northeast Tasmania. Clinopyroxenes from Wagners Hill do not fall into either the moderately-fertile or highly-fertile category with $TiO_2$ contents similar to the Rocky Cape group, $Al_2O_3$ and CaO contents similar to the Sheffield and Northeast Tasmania groups, and $Na_2O$ contents intermediate between Rocky Cape and the other crustal Elements.

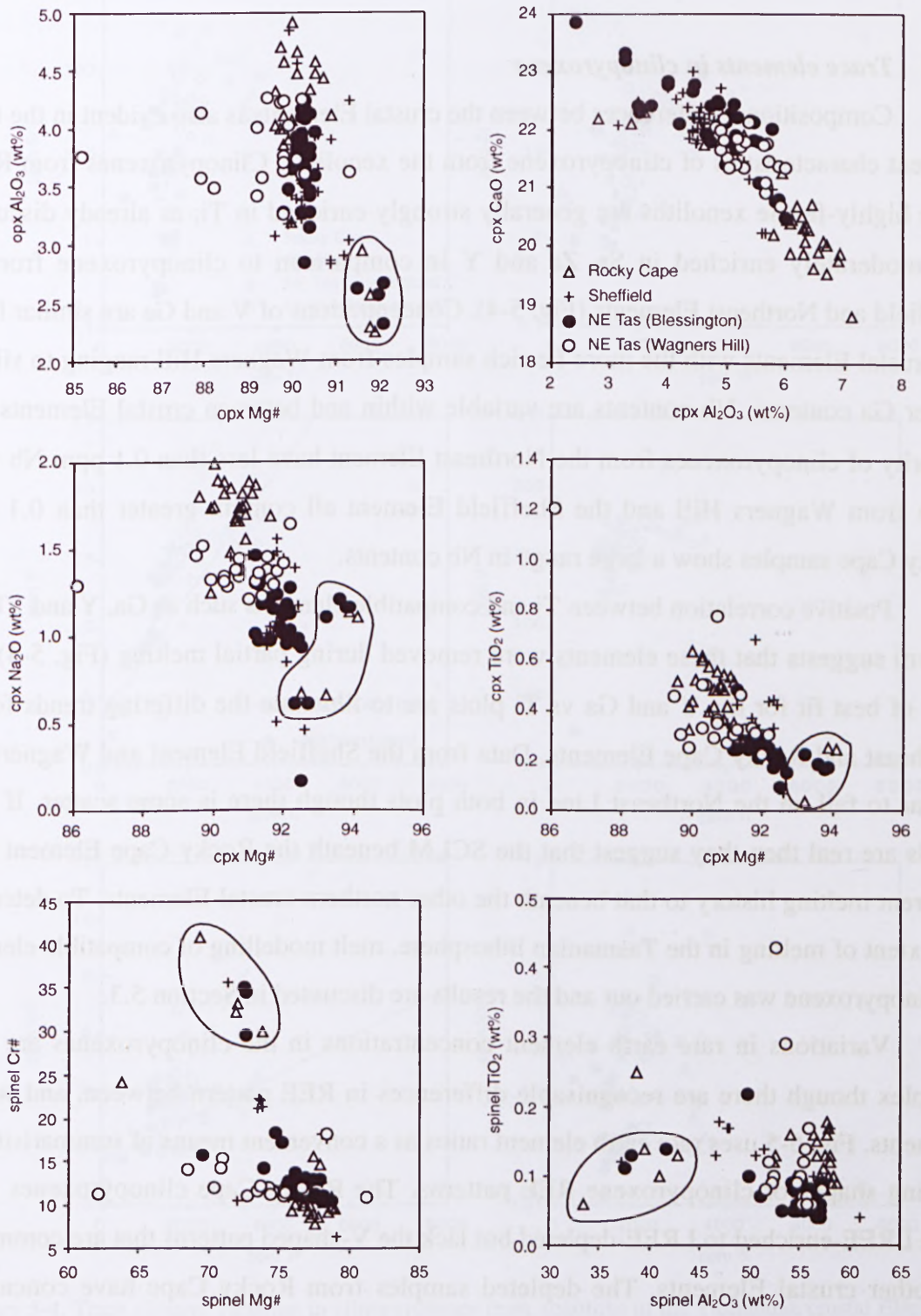


**Figure 5-3.** Major element variation in minerals from xenoliths of the Tasmanian crustal Elements. Depleted samples have been circled.

Orthopyroxene composition is typically more aluminous in the Rocky Cape xenoliths though there is no discernible difference in orthopyroxene Mg# between the different crustal Elements; the Fe-rich Wagners Hill xenoliths have very low orthopyroxene Mg# as expected. Spinel composition displays only minor variation between crustal Elements with Rocky Cape spinels generally having low-Cr#, as already noted, and displaying slight enrichment in $TiO_2$.

### *5.2.2 Trace elements in clinopyroxene*

Compositional differences between the crustal Elements is also evident in the trace-element characteristics of clinopyroxene from the xenoliths. Clinopyroxenes from Rocky Cape highly-fertile xenoliths are generally strongly enriched in Ti, as already discussed, and moderately enriched in Sr, Zr and Y in comparison to clinopyroxene from the Sheffield and Northeast Elements (Fig. 5-4). Concentrations of V and Ga are similar for all the crustal Elements with the more Fe-rich samples from Wagners Hill ranging to slightly higher Ga contents. Nb contents are variable within and between crustal Elements. The majority of clinopyroxenes from the Northeast Element have less than 0.1 ppm Nb while those from Wagners Hill and the Sheffield Element all contain greater than 0.1 ppm. Rocky Cape samples show a large range in Nb contents.

Positive correlation between Ti and compatible elements such as Ga, Y and Yb (not shown) suggests that these elements were removed during partial melting (Fig. 5-4). The lines of best fit for the Y and Ga vs Ti plots are to illustrate the differing trends for the Northeast and Rocky Cape Elements. Data from the Sheffield Element and Wagners Hill appear to fall on the Northeast Line in both plots though there is some scatter. If these trends are real then they suggest that the SCLM beneath the Rocky Cape Element has a different melting history to that beneath the other northern crustal Elements. To determine the extent of melting in the Tasmanian lithosphere, melt modelling of compatible elements in clinopyroxene was carried out and the results are discussed in Section 5.3.

Variations in rare earth element concentrations in the clinopyroxenes are more complex though there are recognisable differences in REE pattern between, and within, Elements. Fig. 5-5 uses rare earth element ratios as a convenient means of summarising the varying shapes of clinopyroxene REE patterns. The Rocky Cape clinopyroxenes range from LREE-enriched to LREE-depleted but lack the V-shaped patterns that are common to the other crustal Elements. The depleted samples from Rocky Cape have concave-up LREE, a feature restricted to this crustal Element, which produce the sinuous patterns

illustrated in the bottom right quadrant in Fig. 5-5B. Clinopyroxenes from the Sheffield Element vary from LREE-depleted to LREE-enriched though enrichment is typically only in La (Fig. 5-5A) and enrichment in the other LREE is apparent in just a couple of samples (top left quadrant in Fig. 5-5B).

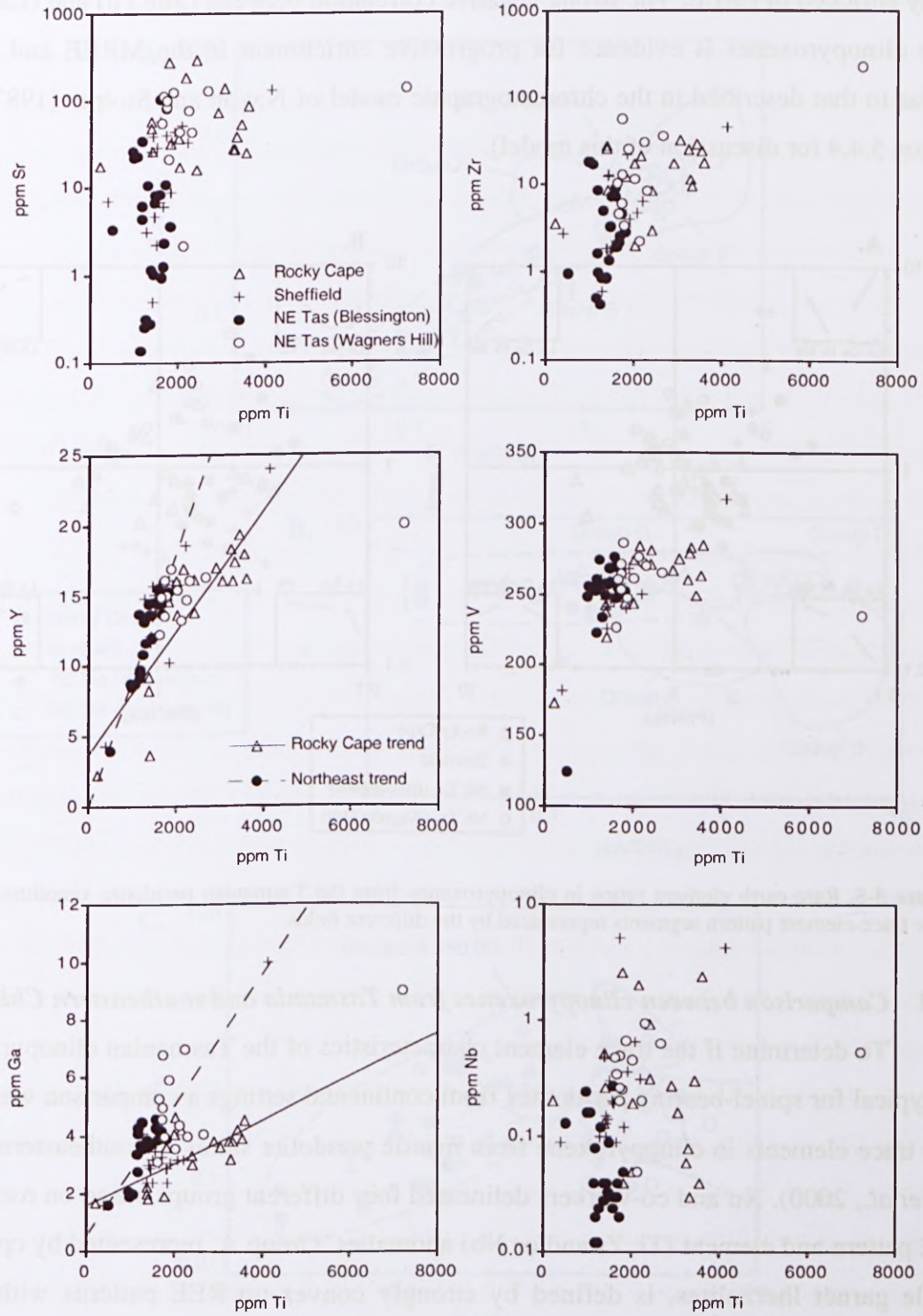


**Figure 5-4.** Trace element variation in clinopyroxenes from xenoliths of the Tasmanian crustal Elements. Also shown are lines of best fit for Rocky Cape (solid line) and Northeast (dashed line) Elements.

REE patterns in clinopyroxenes from the Northeast Element are not easily summarised because its two localities, Blessington and Wagners Hill, have very different patterns. Blessington clinopyroxenes separate into two main groups. The first group (includes the refractory samples) is depleted in the LREE, whereas, the second group is enriched in La relative to the other LREE. In comparison, the Wagners Hill samples are highly enriched in LREE. The strong negative correlation between (Sm/Yb) and (La/Pr) in these clinopyroxenes is evidence for progressive enrichment in the MREE and LREE similar to that described in the chromatographic model of Navon and Stolper (1987) (see Section 5.4.4 for discussion of this model).

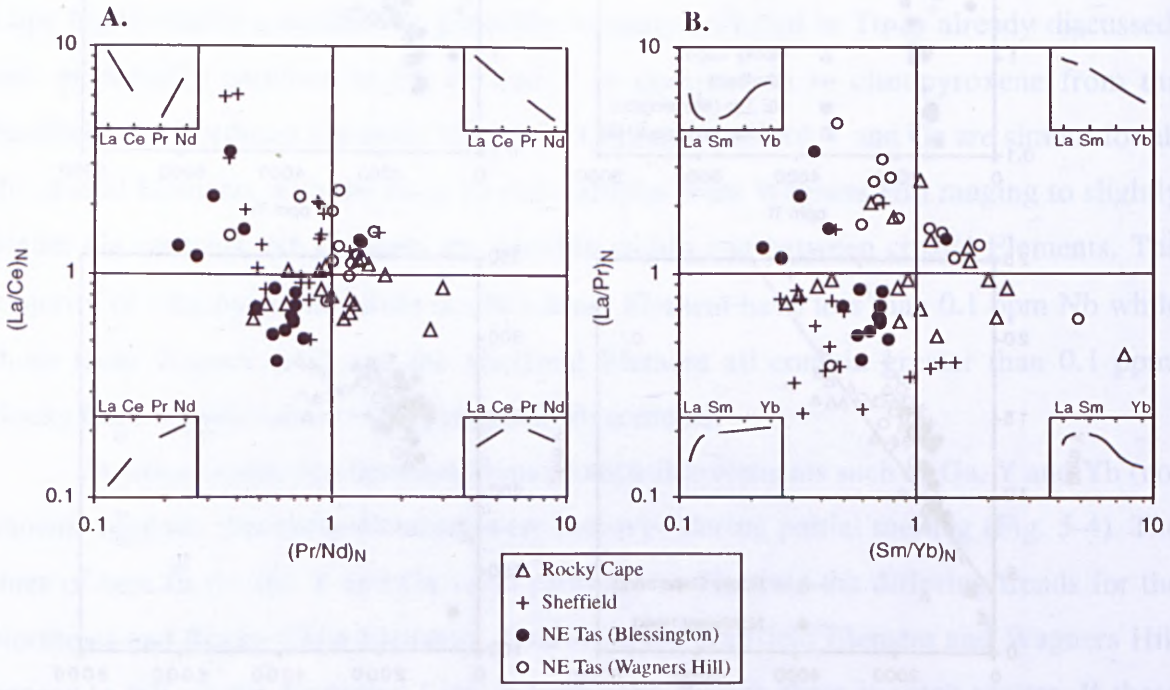


**Figure 5-5.** Rare earth element ratios in clinopyroxenes from the Tasmanian peridotite xenoliths. Insets show trace-element pattern segments represented by the different fields.

### *5.2.3 Comparison between clinopyroxenes from Tasmania and southeastern China*

To determine if the trace element characteristics of the Tasmanian clinopyroxenes are typical for spinel-bearing peridotites from continental settings a comparison was made with trace elements in clinopyroxene from mantle peridotite suites in southeastern China (Xu *et al.*, 2000). Xu and co-workers delineated four different groups based on rock type, REE pattern and element (Ti, Zr and/or Nb) anomalies. Group A, represented by cpx from fertile garnet lherzolites, is defined by strongly convex-up REE patterns with small negative Ti and Zr anomalies. Group B consists of cpx from fertile spinel±garnet lherzolites and is defined by flat HREE, small negative Ti (±Zr) anomalies and depleted

LREE. Group C, represented by amphibole-bearing lherzolites, has high LREE contents and large negative Nb and Ti anomalies. Group D comprises cpx-poor, depleted spinel peridotites and has low HREE contents, high LREE and very low abundances of Zr, Hf and Ti. Fig. 5-6 shows the fields for these four groups on plots of $(La/Sm)_N$ against $(La/Lu)_N$, Y and Zr.

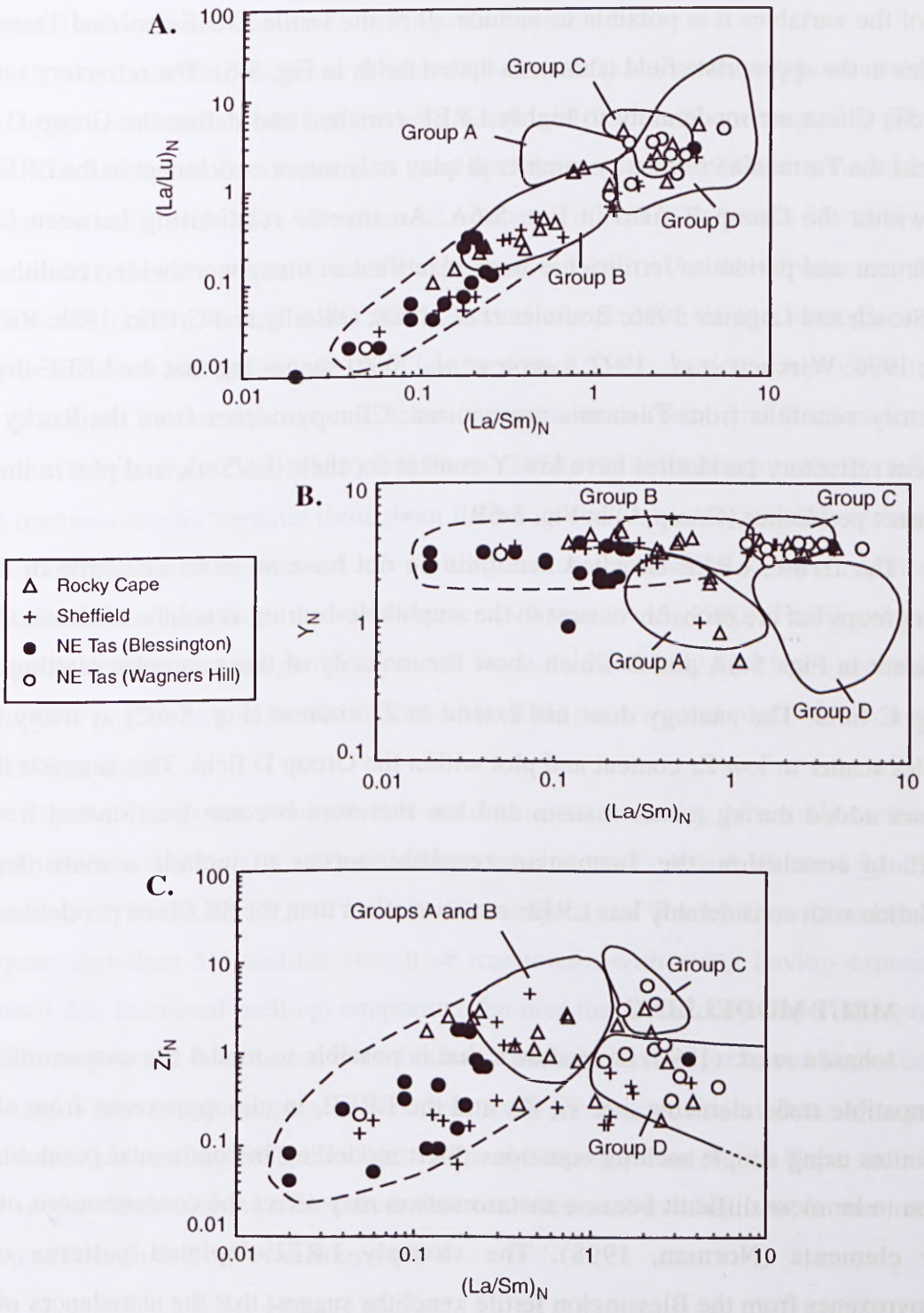


**Figure 5-6.** Plots of La/Sm vs La/Lu, Zr and Y (all normalised to primitive mantle) for clinopyroxene from the Tasmanian peridotite xenoliths. Fields from Xu *et al.* (2000). See text for discussion on Groups A, B, C and D.

The Tasmanian clinopyroxene data do not fit neatly into the fields defined by the SE China data, though the bulk of the Tasmanian samples do plot within Xu's fields. According to Xu's scheme, the fertile, LREE-depleted clinopyroxenes from Tasmania should plot in Group B. This is true for many of the fertile samples from the Rocky Cape and Sheffield Elements but not for those from the Northeast Element which are highly depleted in the LREE. However, by extending the fields for Group B to lower values for each of the variables it is possible to include all of the fertile LREE-depleted Tasmanian samples in the appropriate field (shown as dotted fields in Fig. 5-6). The refractory samples from SE China are moderately to highly LREE-enriched and define the Group D field, whereas the Tasmanian refractory samples display only minor enrichment in the LREE and plot within the Group B field in Fig. 5-6A. An inverse relationship between LREE-enrichment and peridotite fertility has been identified in many worldwide xenolith suites (e.g. Stosch and Lugmair 1986; Bodinier *et al.*, 1988; O'Reilly and Griffin, 1988; Rivalenti *et al.*, 1996; Wiechert *et al.*, 1997; Lenoir *et al.*, 2000) suggesting that the LREE-depleted refractory xenoliths from Tasmania are unusual. Clinopyroxenes from the Rocky Cape Element refractory peridotites have low Y content for their $(La/Sm)_N$ and plot in the field for garnet peridotites (Group A) in Fig. 5-6B.

The fertile, LREE-enriched xenoliths do not have an exact analogue in the SE China groups but are probably closest to the amphibole-bearing xenoliths of Group C. This is evident in Figs 5-6A and B which show the majority of these samples plotting in the Group C field. The analogy does not extend to Zr content (Fig. 5-6C) as many of the samples scatter to low Zr content and plot within the Group D field. This suggests that Zr was not added during metasomatism and has therefore become fractionated from the LREE. In conclusion, the Tasmanian xenoliths appear to include a more depleted population with considerably less LREE-metasomatism than the SE China peridotites.

## 5.3 MELT MODELLING

Johnson *et al.* (1990) have shown that is possible to model the concentrations of incompatible trace elements, i.e. Ti, Zr, and the LREE, in clinopyroxenes from abyssal peridotites using simple melting equations. Melt modelling in continental peridotites has proven to be more difficult because metasomatism may affect the concentrations of these trace elements (Norman, 1998). The strongly LREE-depleted patterns of the clinopyroxenes from the Blessington fertile xenoliths suggest that the abundances of these elements may be controlled by partial melting, but the majority of clinopyroxenes from the

other localities show enrichment in the LREE and MREE and have obviously been metasomatised. These elements, therefore, cannot be used to model partial melting in the Tasmanian peridotites. Instead more compatible elements, such as Y and the HREE have been used (following Norman, 1998), in conjunction with Zr and Ti (following Johnson *et al.*, 1990). The modelling of Johnson *et al.* (1990) has also been used to test the possibility that the Tasmanian xenoliths experienced initial melting in the garnet field before subsequent transport and continued melting in the spinel field.

To constrain the conditions of melt depletion the concentrations of select elements in clinopyroxene were modelled for both batch and fractional melting of a primitive source. The starting bulk composition used by Johnson *et al.* (1990) is a model LREE-depleted lherzolite (1.5-2.5 x CI values of Loubet *et al.*, 1975) whereas Norman (1998) uses a model refractory primitive mantle composition taken as 3 x the CI values of Anders and Grevasse (1989). In this thesis the "pyrolite" composition of McDonough and Sun (1995) is favoured and this set of values has been used as the starting composition in both melting models. The models are calculated from non-modal batch and fractional melting equations derived from Gast (1968) and Shaw (1970, 1979). In batch melting, solid and liquid fractions remain together throughout the entire melting interval, while in fractional melting infinitesimal increments of melting occur, accompanied by instantaneous segregation of the melt from the solid residue (Johnson *et al.*, 1990). Fractional melting depletes the residue in incompatible elements far more effectively than batch melting does and the two processes can be distinguished in REE patterns and plots of incompatible elements in residues.

Fig. 5-7 shows the clinopyroxene modelling results using Norman's method and compatible elements, Y and Yb. The starting compositions for Y and Yb are 4.3 and 0.441 ppm, and $D_Y^{cpx/melt}$ =0.42, $D_{Yb}^{cpx/melt}$ =0.40. The majority of Rocky Cape xenoliths have undergone less than 5% melting (batch or fractional), with many having experienced between 1-3% fractional melting, supporting the idea that the Rocky Cape lithosphere is generally very fertile. In contrast, the refractory xenoliths have experienced higher degrees of melting, ~20% batch melting or ~8% fractional melting at Coates Road Quarry, and ~15% fractional melting at Table Cape. Although the depleted Table Cape samples lie closer to the batch melting curve than that for fractional melting, the former requires unreasonably high degrees of melting (<45%).

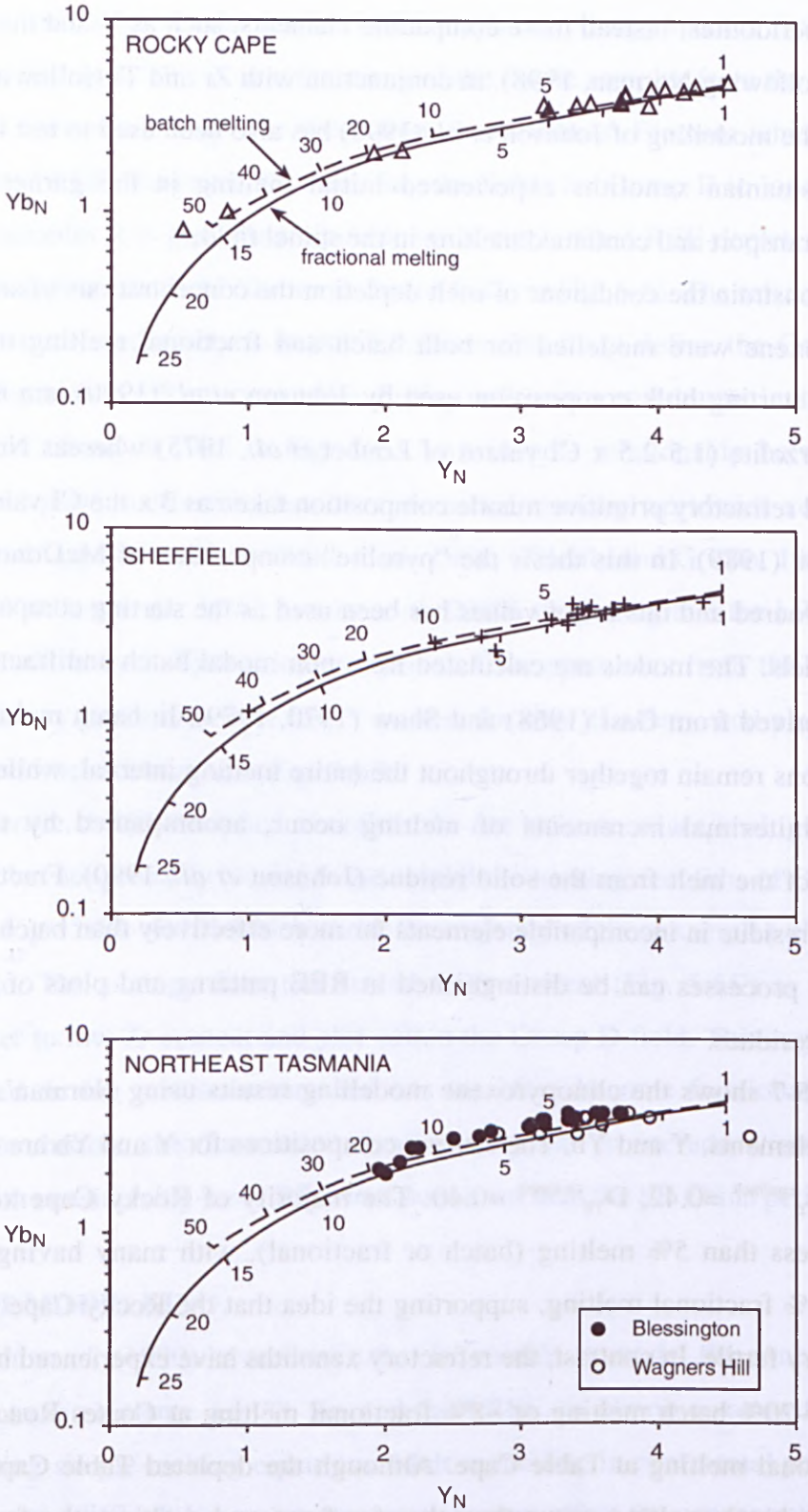


**Figure 5-7.** A comparison of fractional and batch melting models with the Y and Yb contents of clinopyroxene from the Tasmanian mantle peridotites. Method after Norman (1998).

The fertile Sheffield peridotites have moderately high Y and Yb contents, consistent with 3-4% partial melting while the coarse-grained, slightly more refractory, peridotites from South Riana have Y and Yb contents consistent with 5-6% melting. Clinopyroxene from sample SR1b-2 is highly enriched in both Y ($Y_N$=5.58) and Yb ($Yb_N$=6.12) and as a consequence plots above and far to the right of the melting curve implying metasomatic addition of these two trace elements.

In the Northeast Element, the Blessington spinel peridotites plot along the batch melting curve, showing a range in melting from ~3-20%. The more fertile xenoliths typically have undergone less than 5% melting though others have experienced up to 10% melting. The refractory xenoliths fall in between the batch and fractional melting curves, and are residues of either 15-20% batch melting or ~8% fractional melting. The Wagners Hill xenoliths have, in general, experienced less than 5% melting (batch or fractional), the notable exception being sample WH13 which falls to the right of the melting trend suggesting that it has been enriched in Y.

The Ti vs Zr modelling used by Johnson *et al.* (1990) is not appropriate for the majority of Tasmanian peridotites because they fall off the modelling trend on a Ti vs Zr plot (see Fig. 5.8A). This does not apply to the depleted xenoliths from Coates Road Quarry and Blessington which plot close to the Ti-Zr melting curve and can be modelled by ~15% fractional melting which agrees well with the results in Fig. 5-7. Clinopyroxene from the depleted Rocky Cape sample TC7 falls well below the trend due to its anomalously low Ti content (210 ppm).

The crystal/liquid distribution coefficients for Ti and Zr used in (Johnson *et al.*, 1990) are $D_{Ti}^{cpx/melt}$=0.44 and $D_{Zr}^{cpx/melt}$=0.20. Xu (1999) argued that $D_{Ti}^{cpx/melt}$=0.20 and $D_{Zr}^{cpx/melt}$=0.25 are more appropriate values for partial melting in the shallow mantle. Using the revised distribution coefficients of Xu (1999) and the model of Norman (1998) produces a better fit for the Rocky Cape data (Fig. 5-8B) but the majority of datapoints for the other crustal Elements still lie off the melting trend. In Fig. 5-8B the Rocky Cape xenoliths can be modelled by 3-6% fractional melting which is consistent with batch melting results in Fig. 5-7. The poor fit between the Tasmanian data and the Zr-Ti melting trend suggests either that the distribution coefficients are unsuitable for these samples, or that at least one of the two elements has been perturbed, possibly by metasomatism (Fig. 5-8). Johnson *et al.* (1990) found that using garnet in the melting assemblage for the Ti-Zr model did not significantly change the trajectory of the model melting curves.

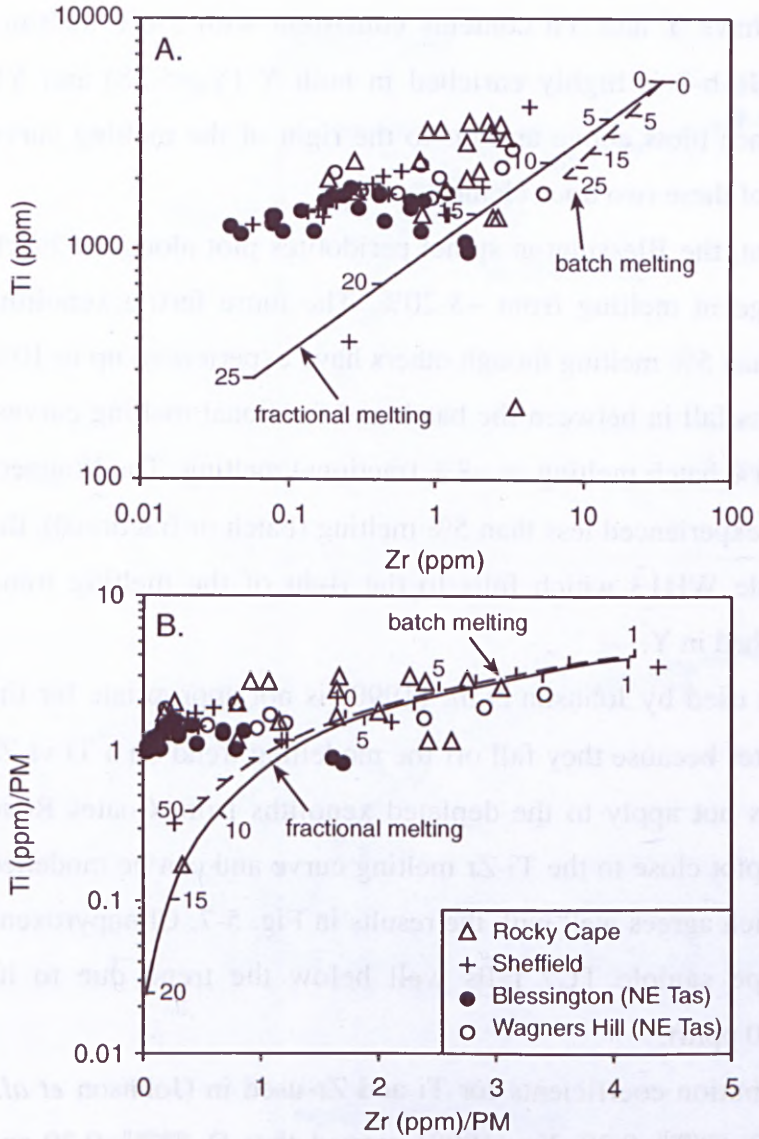


**Figure 5-8.** A comparison of fractional and batch melting models with the Zr and Ti contents of clinopyroxene from the Tasmanian mantle peridotites. (A) Johnson *et al.* (1990) model. (B) Norman (1998) model using $D_{Ti}$=0.20 and $D_{Zr}$=0.25 (after Xu *et al.*,1999).

A potential problem with melt modelling using the method of Norman (1998) is the assumption that melting has only occurred in the spinel stability field when significant intraplate melting may occur in the garnet stability field. There is textural evidence in several of the Tasmanian xenoliths for the prior existence of garnet in the assemblage, including pyroxene-spinel symplectites and pyroxene-spinel clusters, both of which are thought to represent decomposition of garnet at low pressure (Carswell *et al*, 1984; Green and Burnley, 1988). To test this possibility, REE in clinopyroxenes from Blessington xenoliths have been modelled using the method of Johnson *et al.* (1990) and a situation where melting begins in the garnet field but finishes in the spinel field (see Fig. 5-9).

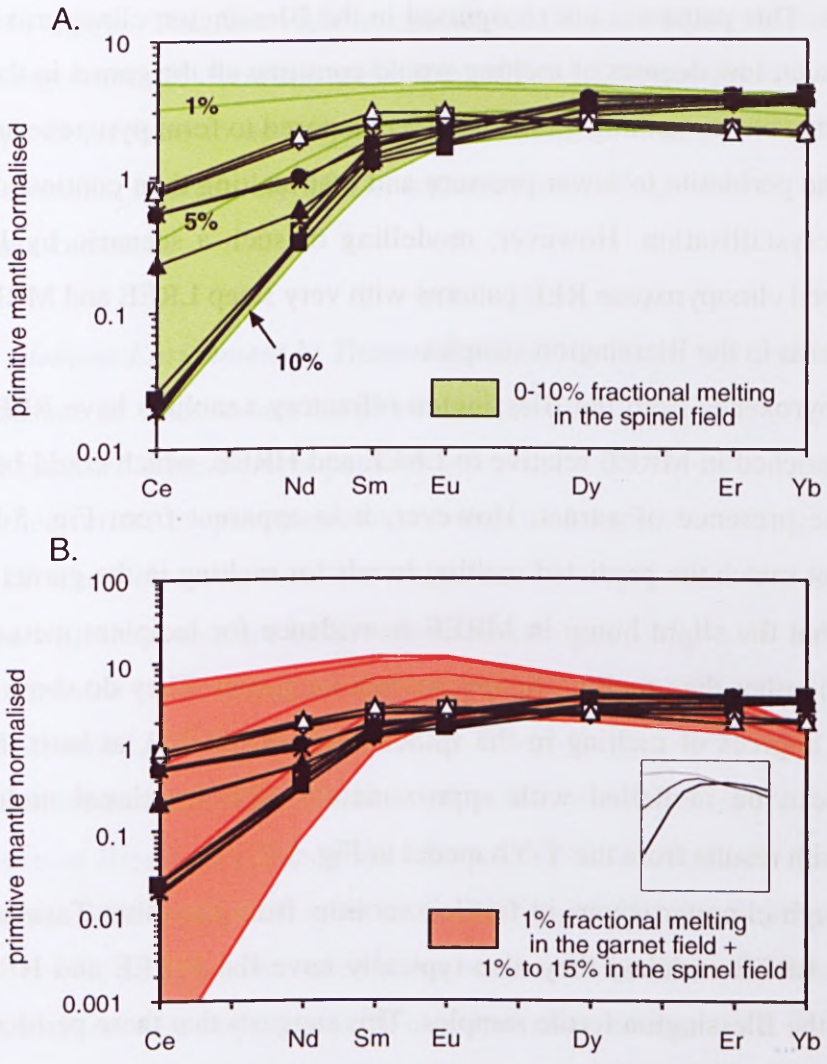


**Figure 5-9.** (A) Melting model for 0-10% fractional melting in the spinel field. Data from Blessington clinopyroxenes (closed symbols – fertile peridotites; open symbols – depleted peridotites) conform to the shape of the model and degree of melting inferred from the Y-Yb model in Fig. 5-7. (B) Melting model in which melting begins in the garnet stability and continues up to an additional 15% in the spinel stability field. The inset is a schematic representation of the evolution of the MREE hump in clinopyroxenes with melting from 1% (upper line) to 10% (bold line) in the presence of garnet.

REE patterns for clinopyroxenes from the Blessington fertile xenoliths are flat in the MREE to HREE with depleted LREE. These patterns are similar to those seen for many of the abyssal peridotites from Johnson *et al.* (1990), which were modelled by varying degrees of batch and fractional melting in the spinel field. Fig. 5-9A illustrates the good match between Blessington clinopyroxene residual compositions and the predicted patterns for melting in the spinel stability field. According to this model the Blessington fertile peridotites have undergone between 1-8% fractional melting which agrees well with the results from the Y-Yb model in Fig. 5-7. Fig. 5-9B shows the predicted REE patterns for clinopyroxene that was melted by 1% in the garnet field but was subsequently melted by up to 15% in the spinel field. Even 1% melting in the garnet field is sufficient to significantly lower the HREE and produce a hump in the MREE in the residual

clinopyroxene. This pattern is not recognised in the Blessington clinopyroxenes, and it is unlikely that such low degrees of melting would consume all the garnet in the assemblage. It is possible that any remaining garnet later decomposed to form pyroxene and spinel after transport of the peridotite to lower pressure and that melting then continued in the spinel field after recrystallisation. However, modelling of such a scenario by Johnson *et al.* (1990) produced clinopyroxene REE patterns with very steep LREE and MREE that do not resemble patterns in the Blessington samples.

Clinopyroxenes from the Blessington refractory xenoliths have REE patterns that are slightly enriched in MREE relative to LREE and HREE, which could be indicative of melting in the presence of garnet. However, it is apparent from Fig. 5-9B that these samples do not match the predicted melting trends for melting in the garnet field and it is more likely that the slight hump in MREE is evidence for incipient metasomatism (see Section 5.4.2) rather than melting in the presence of garnet. They do show a good match for moderate degrees of melting in the spinel field (Fig. 5-9A), at least in terms of the HREE, and can be modelled with approximately 10% fractional melting which is comparable with results from the Y-Yb model in Fig. 5-7.

Although clinopyroxenes in fertile xenoliths from the other Tasmanian localities are generally LREE-enriched they also typically have flat MREE and HREE similar to those seen in the Blessington fertile samples. This suggests that these peridotites were also melted solely in the spinel field.

## 5.4 METASOMATISM

### *5.4.1 Introduction*

Metasomatism is a process whereby the mineralogy and/or chemical composition of a rock is altered by the introduction of chemical components from an external source (Wilshire, 1987). This process can occur either by infiltration (mass movement due to fluid flow) or by diffusion (diffusion of chemical species through stagnant pore fluids) (Dawson, 1980; Wyllie, 1987). The affected region can become either "enriched" or "deficient" in these components relative to the premetasomatic state depending on whether the components were added or removed from the region. The convention, however, is for "mantle metasomatism" to be used only when referring to the enrichment process, whereby the abundances of incompatible trace elements (LREE, LILE, Ti, Nb, Zr, Th and U) are increased relative to the presumed primitive or depleted mantle precursor (Roden and Murthy, 1985). Dawson (1980) recognises two major types of chemical enrichment that are

metasomatic in origin. The first type is termed patent or modal metasomatism and is defined by changes in bulk chemistry associated with modification in modal mineralogy. The other type is referred to as "cryptic metasomatism" and involves enrichment in incompatible elements (particularly LREE) without clear petrographic evidence (modal or textural) of metasomatism.

### *5.4.2 Trace Element Enrichment in Tasmanian Mantle Clinopyroxenes*

The absence of volatile-bearing phases (e.g. amphibole, mica, apatite, carbonate) and the LREE-enriched trace element patterns seen in clinopyroxenes from the Tasmanian fertile peridotites reflect cryptic metasomatic enrichment of the mantle in this region. Comparison of trace element variation diagrams for the LREE-depleted (La-poor) clinopyroxenes with those that are LREE-enriched (La-rich) shows that enrichment in the LREE is accompanied by concomitant enrichment in Sr, Th and U (see Fig. 5-10). The correlation of Sr with La is well-defined for the Rocky Cape Element and Wagners Hill locality in the Northeast Element, but is poorly defined for the Sheffield Element and difficult to assess at Blessington due to the very low concentrations of La at this locality. These relationships with La are also apparent for Th (Fig. 5-10) and U (not shown), and to a lesser degree for Nb and Ta which show some scatter at high contents. As expected there is no correlation between La and compatible elements such as Yb.

Zr, Ti and Hf do not show any obvious correlation with LREE enrichment suggesting that these elements have not been disturbed by metasomatism to any significant extent (Fig. 5-10). Rivalenti *et al.* (1996) have proposed that the apparent immobility of Ti during metasomatism of mantle peridotites may be due to several causes, such as reduced Ti solubility in hydrous fluids, fractionation of Ti-rich phases from percolating silicate melts, or reaction with carbonatite melts formerly equilibrated with amphibole-bearing peridotite. Very little is known about Zr and Hf solubility, but Stosch and Lugmair (1986) suggested, by analogy with Ti, that both of these elements are also insoluble in metasomatic fluids.

Clinopyroxene from the refractory xenoliths does not show the strong LREE-enrichment recognised in the fertile peridotites. The REE patterns for clinopyroxene from the depleted xenoliths are generally quite flat though some show slight enrichment in the MREE relative to the LREE giving them a weak sinuous shape (see Figs. 4-34 and 4-39). Sinuous REE patterns in clinopyroxene and garnet have been recognised in granular garnet peridotites from kimberlites and are interpreted as the onset of metasomatism by a LREE-

enriched melt (Shimizu, 1975). This suggests that the depleted xenoliths from Tasmania could have been affected by the same or a similar melt to that which metasomatised the fertile xenoliths. The similar high abundances of other incompatible elements such as Sr, Nb, U and Th in both xenolith types supports this model (see Fig. 4-32).

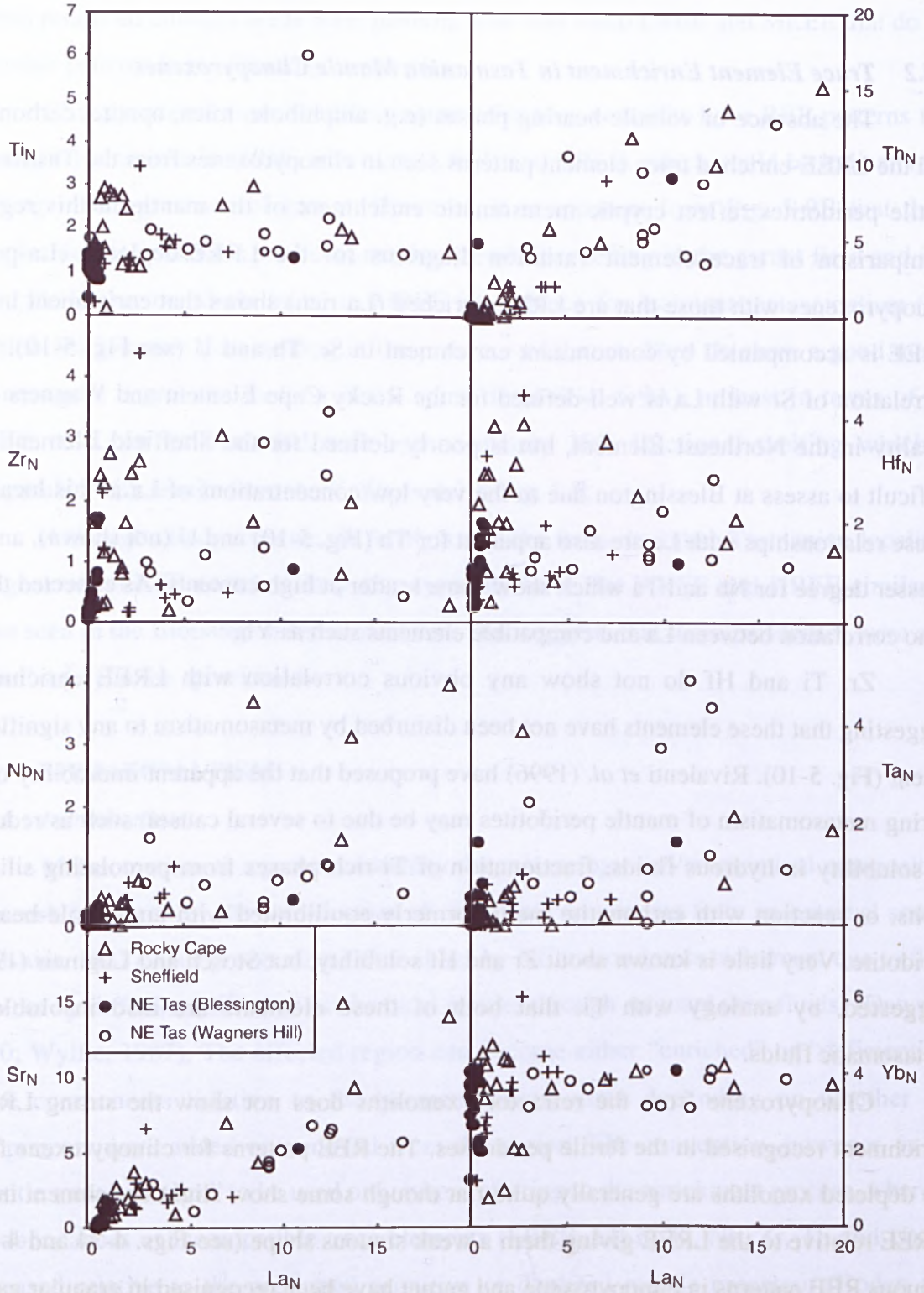


**Figure 5-10.** Plots of primitive mantle normalised trace element compositions of clinopyroxene in Tasmanian peridotites.

Mantle-wall rock closest to the percolating melt will show the strongest evidence for contamination, i.e. Fe-enrichment and high concentrations of incompatible elements, as seen in the Fe-rich fertile xenoliths from Wagners Hill, while volatile-rich fluids, rich in $CO_2$, $H_2O$ and incompatible elements, released from the melt during crystallisation will then migrate into the surrounding rock and produce a progressive decrease in enrichment as the fluid moves further from the source. An alternative model, the chromatographic model of Navon and Stolper (1987), predicts that the most incompatible elements will travel the furthest and therefore the wall-rock closest to the source will be the least enriched (Section 5.4.4).

### *5.4.3 Metasomatic Fluid/Melt*

Metasomatism in mantle xenoliths is the result of interaction between wall-rock peridotite and a fluid, or fluids, which may range from carbonatitic or silicate melts to $CO_2 \pm H_2O$ fluids, and mixtures of the all the possible end-members. Each of these agents has a distinct geochemical signature, which can be seen in both whole-rock and mineral trace element patterns, and enables identification of the metasomatic source (O'Reilly and Griffin, 1996).

The Ti and Zr concentrations of the most strongly LREE-enriched Tasmanian clinopyroxenes are as low as in the unmetasomatised samples (Fig, 5-10), suggesting that the metasomatic agent was poor in high-field strength elements (HFSE). A study of cryptically metasomatised xenoliths from the Atsagin-Dush volcanic centre in SE Mongolia concluded that negative anomalies of Nb, Hf, Zr and Ti, in both whole rock and clinopyroxenes, are an indication of interaction with a carbonate melt (Wiechert *et al.*, 1997). Numerous high-pressure experiments have shown that carbonate melts can exist in equilibrium with peridotite over a range of upper-mantle conditions of pressure, temperature, bulk composition and volatile content (Wallace and Green, 1988; Thibault *et al.*, 1992; Dalton and Wood, 1993; Sweeney, 1994) and, given that carbonate melts are capable of transporting considerable amounts of REE, LILE, U, and Th, they have been identified as a potential contaminant of wall-rock peridotite (Green and Wallace, 1988; Baker and Wyllie, 1992).

A possible way to discriminate between peridotite affected by carbonatite and that affected by silicate melt is illustrated in Figure 5-11. This diagram plots the degree of Ti depletion against the degree of LREE enrichment. Peridotite inferred to have been contaminated by a carbonatitic melt shows greater enrichment in REE and greater relative

depletion in Ti and Zr than those metasomatised by silicate melts (Coltorti *et al.*, 1999). According to Fig. 5-11, the majority of metasomatised Tasmanian xenoliths have been affected by a silicate melt, or fluids associated with a silicate melt. However, it is also apparent that at least a few samples, i.e those with low Ti (<3000ppm) but high La/Yb (>2), may have been modified by a fluid that carries a carbonate component.

To estimate the amount of carbonatite added to LREE-enriched harzburgites from the Olmani cinder cone in Tanzania Rudnick *et al.* (1993) calculated mixing curves between average Ca-carbonatite and both harzburgite and lherzolite(see Fig. 5-12). The authors found that mixing only 0.5% carbonatite into refractory harzburgite can explain the Ti-REE compositions of most spinel peridotite xenoliths from the literature, with only peridotites showing modal carbonatitic metasomatism from SE Australia and Olmani requiring larger amounts of carbonatite (>5% addition). Choosing a peridotite starting composition close to that of primitive mantle (i.e. lherzolite) produces a similar shaped mixing curve but requires greater amounts of carbonatite to shift the trace element ratios to the same extent.

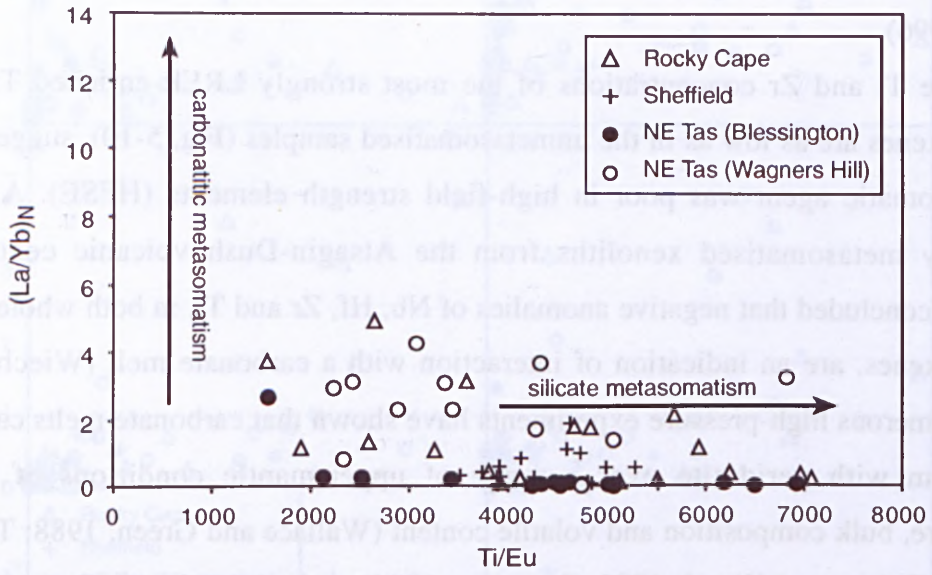


**Figure 5-11.** Ti/Eu vs chondrite-normalised $(La/Yb)_N$ ratios for clinopyroxene from Tasmanian spinel peridotites.

Fig. 5-12 shows that compositions for a subset of the Tasmanian lherzolite xenoliths fall close to the mixing curve for lherzolite and require less than 1% carbonatite addition. According to Rudnick *et al.* (1993), such a small amount of contaminant is more likely to result in cryptic metasomatism of the peridotite rather than the production of new minerals. This is evident in the Tasmanian xenoliths which show enriched clinopyroxene trace element patterns but no evidence for modal metasomatism. Interaction with a

carbonatite melt is apparent in xenoliths from all three Tasmanian crustal Elements. However, the affected Rocky Cape samples exhibit strong Nb-enrichment which is not seen in samples from the other crustal Elements and may indicate later overprinting by a Nb-rich melt.

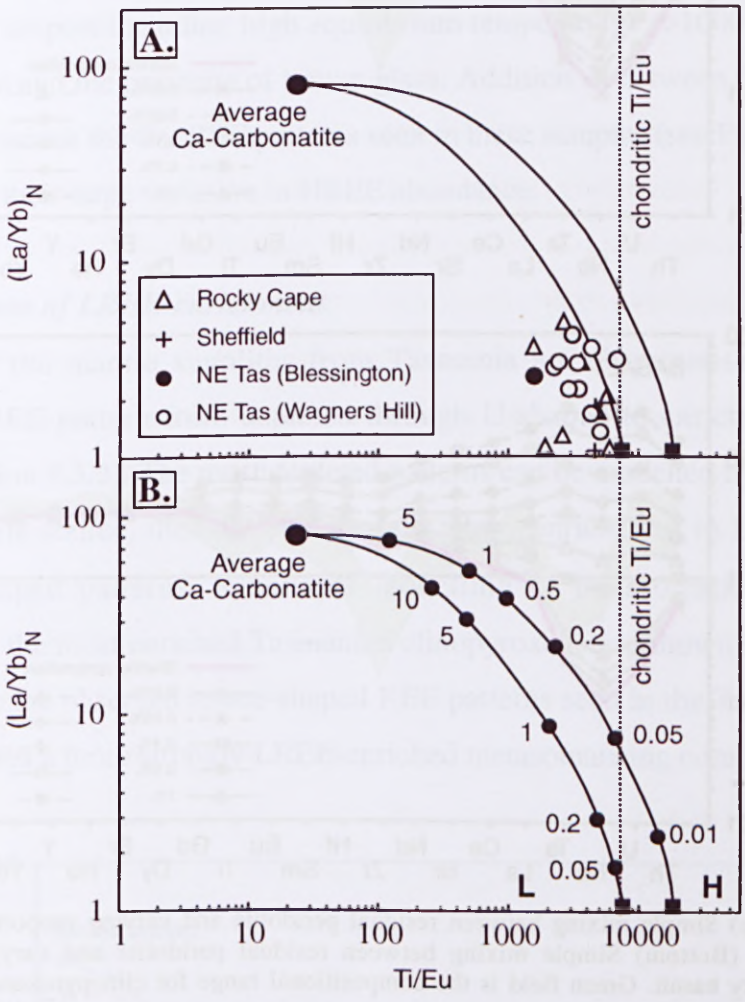


**Figure 5-12.** (A) Ti/Eu versus chondrite-normalised La/Yb ratio for clinopyroxenes from Tasmanian peridotite xenoliths. (B) Same as in (A) but showing mixing curves between lherzolite (*L*) and harzburgite (*H*) and average Ca-carbonatite (after Rudnick *et al.*, 1993). Numbers adjacent to curves represent percentage of average carbonatite added to peridotites.

Possible agents for silicate metasomatism in the Tasmanian xenoliths are the Jurassic dolerites, the Tertiary basalts which host the xenoliths,or fluids from other mantle events. To determine which of these are plausible contaminants, simple mixing calculations between a moderately depleted peridotite and varying proportions of dolerite and basalt were carried out. A residue after 5% partial melting of a primitive mantle source was used as the starting composition as the majority of Tasmanian xenoliths have been shown to be relatively fertile (see Section 5.3). Jurassic dolerite composition is the average cited in Hergt *et al.* (1989) while the basalt composition was provided by M. Zhang.

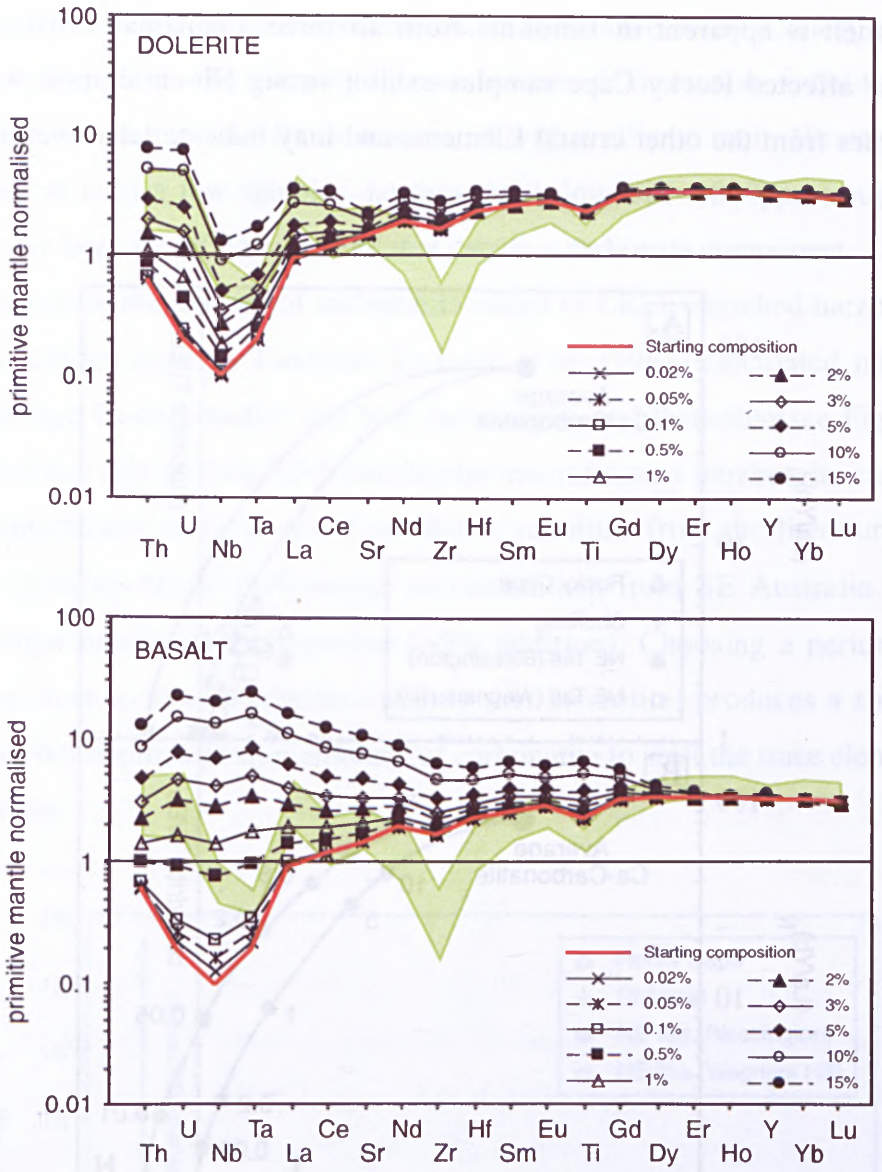


**Figure 5-13.** (Top) Simple mixing between residual peridotite and varying proportions of Tasmanian Jurassic dolerite. (Bottom) Simple mixing between residual peridotite and varying proportions of Tasmanian Tertiary basalt. Green field is the compositional range for clinopyroxenes from Tasmanian peridotite xenoliths.

Fig. 5-13 illustrates the fair match between clinopyroxene composition and contamination of residual peridotite by dolerite: the deep Zr anomaly in cpx cannot be modelled without using an extremely depleted starting composition that is inappropriate for the samples being studied. The trace-element pattern for clinopyroxene can be modelled by addition of 3% dolerite in the least metasomatised samples to 15% dolerite in the most enriched xenoliths. Addition of basalt, however, produces very flat patterns at volumes greater than 0.1% and depleted patterns at volumes less than 0.1%. The lack of correlation between the clinopyroxene pattern and basalt contamination suggests that xenolith residence time in the host basalt was too short to significantly modify mineral composition and that there is no detectable metasomatism by similar basaltic magmas

before entrainment. The Jurassic dolerites, however, may have produced a strong metasomatic imprint in the northern Tasmanian lithosphere implying emplacement and long-term residence at shallow depth.

A group of samples which does appear to have been modified by their host rock are the coarse-grained xenoliths from South Riana. These peridotites show strong evidence for heating during transport including high equilibrium temperatures (>1000°C), spongy rims on clinopyroxene and the presence of brown glass. Addition of between 0.5 and 5% basalt is sufficient to produce the flat REE patterns seen in these samples (see Fig. 4-36) though it does not explain their large variation in HREE abundance.

### *5.4.4 Mechanism of LREE-enrichment*

Many of the mantle xenoliths from Tasmania are characterised by a range in clinopyroxene REE pattern from depleted through U-shaped to enriched in LREE and MREE (see Section 4.3.2). The most depleted patterns can be modelled by <5% melting of a primitive mantle source, though some samples show enrichment in La relative to Ce, producing V-shaped patterns. Results of modelling of metasomatism by a melt in equilibrium with the most enriched Tasmanian clinopyroxene are shown in Fig. 5-14. This does not produce the observed spoon-shaped REE patterns seen in the Tasmanian samples but instead requires a more strongly LREE-enriched metasomatising component.

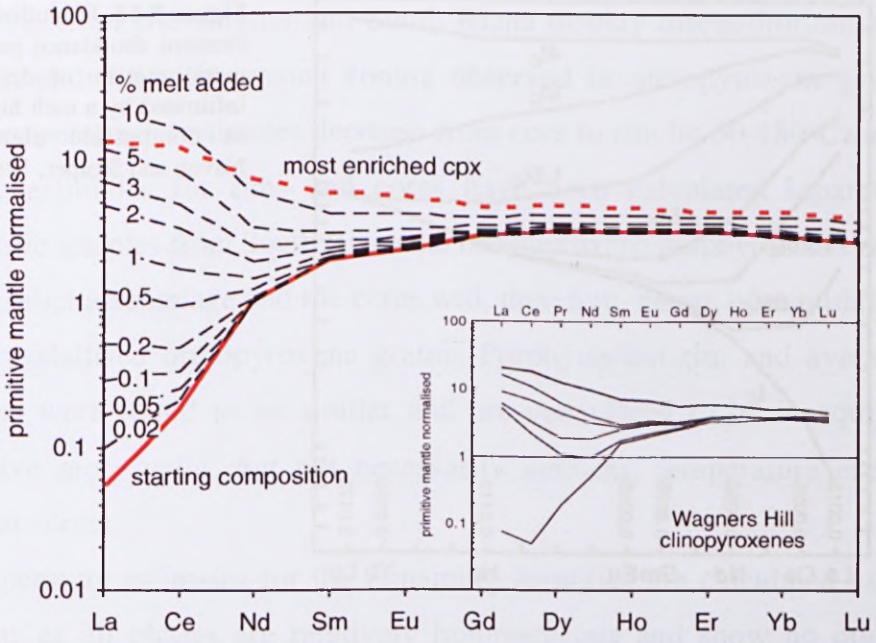


**Figure 5-14.** Modelling of metasomatism of Wagners Hill peridotite by a melt in equilibrium with the most enriched Wagners Hill clinopyroxene. Inset shows the range in REE patterns observed in Wagners Hill clinopyroxenes.

Such an agent may be produced using the chromatographic model of Navon and Stolper (1987). This model was devised as a way of illustrating the evolution of a melt during percolation through rock. As melts and other fluids migrate through the mantle they chemically interact with wall-rock with which they are not initially in equilibrium. This process can be modelled, in a very simplistic way, using the analogy of laboratory column chromatography. Column chromatography is used for the separation of mixtures of chemicals and involves pouring a liquid through a column filled with a porous solid. Components in the liquid are attracted to the surface of the solid to varying degrees, so that weakly attracted components travel more quickly through the column. The various components will, therefore, pass through the column at different rates and become separated as solution flow continues.

In Navon and Stolper's model the "column" is the body of rock through which the liquid percolates (referred to as the matrix), and the solution is a migrating melt or fluid which interacts with the matrix. Enrichment is controlled primarily by differences in fluid/mineral partition co-efficients so that as a fluid passes through the "column" the more incompatible elements will travel faster and therefore equilibrate more slowly than the more compatible elements. This causes a series of broad, overlapping chromatographic fronts to develop in the fluid as it becomes progressively more enriched with time and/or distance.

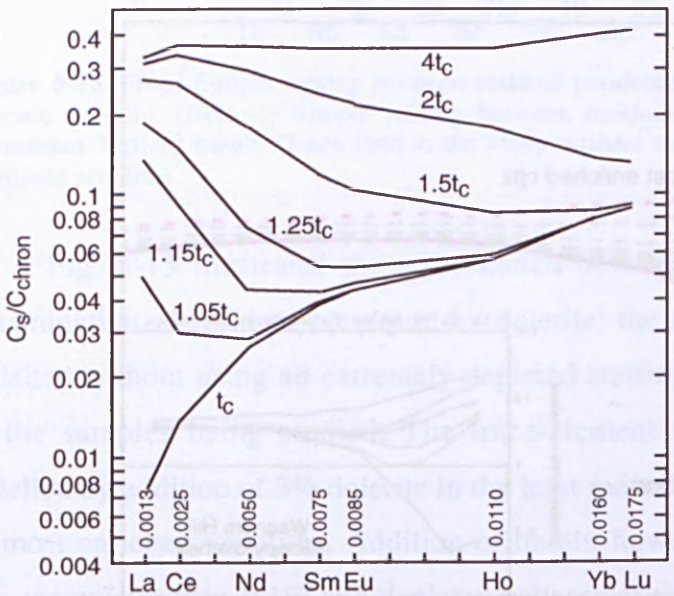


**Figure 5-15.** Evolution of rare earth element abundance patterns during metasomatism of depleted mantle infiltrated by a melt highly enriched in compatible elements (after Navon and Stolper, 1987).

The evolution in REE patterns predicted by the chromatographic model is illustrated in Fig. 5-15. The similarity between the model and the actual patterns observed

in clinopyroxenes from Wagners Hill (see Fig. 5-14) suggests that the chromatographic effect has had a major role in producing the gradual enrichment in incompatible elements seen in samples from this locality. This type of enrichment has also been recognised at other Tasmanian localities such as Arthur River and Doctors Rocks.

## 5.5 GEOTHERMOBAROMETRY

### *5.5.1 Introduction*

Equilibrium temperatures were obtained for all one hundred and thirty xenoliths from Tasmania. The geothermometers used to calculate temperatures for the Tasmanian xenoliths are the orthopyroxene-spinel thermometers of Sachtleben and Seck (1981) and Witt-Eickschen and Seck (1991), the Cr-Al-opx thermometer of Witt-Eickschen and Seck (1991), the Ca-in-orthopyroxene thermometer of Brey and Kohler (1990) and the two-pyroxene thermometer of Wells (1977). As discussed in Section 2.4.1, direct pressure estimates for spinel peridotites are not possible and can only be estimated by extrapolation to the relevant regional geotherm, which in the case of Tasmania is taken as the southeastern Australian geotherm.

When selecting ultramafic xenoliths for temperature calculations it is necessary that mineral assemblages be in equilibrium (i.e. no zoning, coronas). Disequilibrium is apparent in samples from Blessington and South Riana where it is reflected as zoning of $Al_2O_3$ and CaO in orthopyroxene at both localities and zoning of $Al_2O_3$ in clinopyroxene at South Riana. Spinels from Blessington and South Riana display disequilibrium as zoning in $Al_2O_3$, $Cr_2O_3$ and FeO. The strong zoning observed in orthopyroxene greatly affects calculated temperatures (estimates decrease from core to rim by 50-180°C) and therefore temperature estimates for rims and cores have been calculated separately. In the porphyroclastic samples from South Riana the orthopyroxene porphyroclasts represent part of an older, relict assemblage and the cores will, therefore, be out of equilibrium with the smaller, recrystallised orthopyroxene grains. Porphyroclast rim and average neoblast compositions were found to be similar and are considered to be in equilibrium and therefore give more valid, but not necessarily ambient, temperature estimates than porphyroclast cores.

Temperature estimates for the remaining localities are calculated using average compositions as all phases are relatively homogeneous and show no other evidence suggesting disequilibrium.

### 5.5.2 *Comparison of geothermometric methods*

A comparison of geothermometry methods used to obtain temperatures for Tasmanian xenoliths is shown in Figs. 5-16 and 5-17. Agreement between [SS] and [WES-1] estimates is very good although [SS] temperatures are consistently 50°C higher than those calculated using [WES-1]. There is a good correlation between [SS] and [WES-2] with most estimates within ±50°C and the greatest scatter below 850°C and above 950°C. Correlation between the opx-sp and Cr-Al-opx thermometers of Witt-Eickschen and Seck is very good though [WES-2] tends to be slightly elevated (+25-50°C). The generally higher temperatures observed in [WES-2] compared to the opx-sp thermometers of Sachtleben and Seck (1981) and Witt-Eickschen and Seck (1991) may be because the Cr-Al-opx thermometer does not take into account the influence of spinel as the other two methods do. Correlation between the Wells two-pyroxene thermometer and [SS], [WES-1] and [WES-2] is very poor with Wells underestimating by up to 100°C.

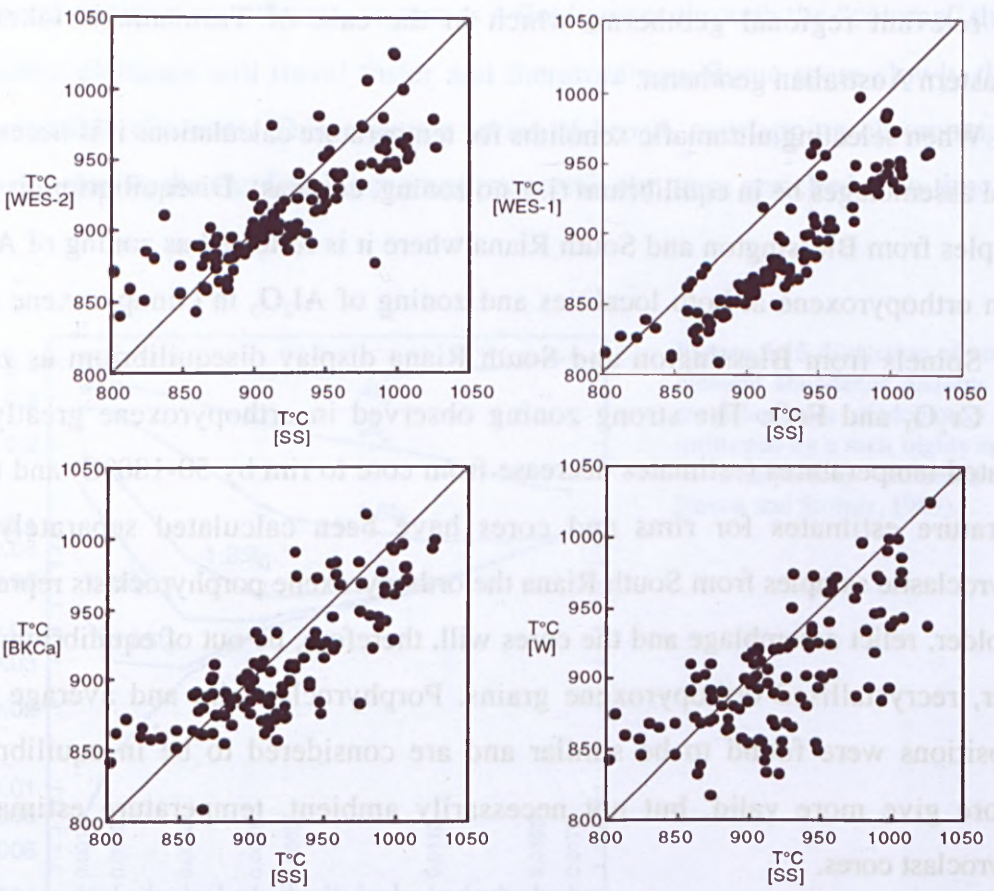


**Figure 5-16.** Comparison of geothermometric methods used for calculating equilibrium temperatures for the Tasmanian peridotite xenoliths.

Brey and Kohler (1990) temperatures have been calculated at pressures of 15 kb as suggested by Sachtleben and Seck (1981). This is an acceptable pressure estimate for

spinel lherzolites and is based on extensive experimental work carried out in the CMS system at this pressure (Lindsley and Dixon, 1976). There is reasonably good agreement between [BKCa] and the other thermometers, though [BKCa] tends to overestimate (up to 100°C) in comparison to [WES-1]. In general, there is very good agreement between [BKCa] and [W]. The Wells (1977) two-pyroxene thermometer shows very poor agreement with the thermometers of Sachtleben and Seck (1981) and Witt-Eickschen and Seck (1991) reflecting the intrinsic differences between the thermometers themselves. That is, the two-pyroxene thermometer of Wells and the Ca-in-opx thermometer of Brey and Kohler are based on exchange reactions whereas the other thermometers are based on the solubility of Al in orthopyroxene. Since Ca diffuses more rapidly than Al, the exchange thermometers respond faster to temperature changes than do the Al-in-opx thermometers.

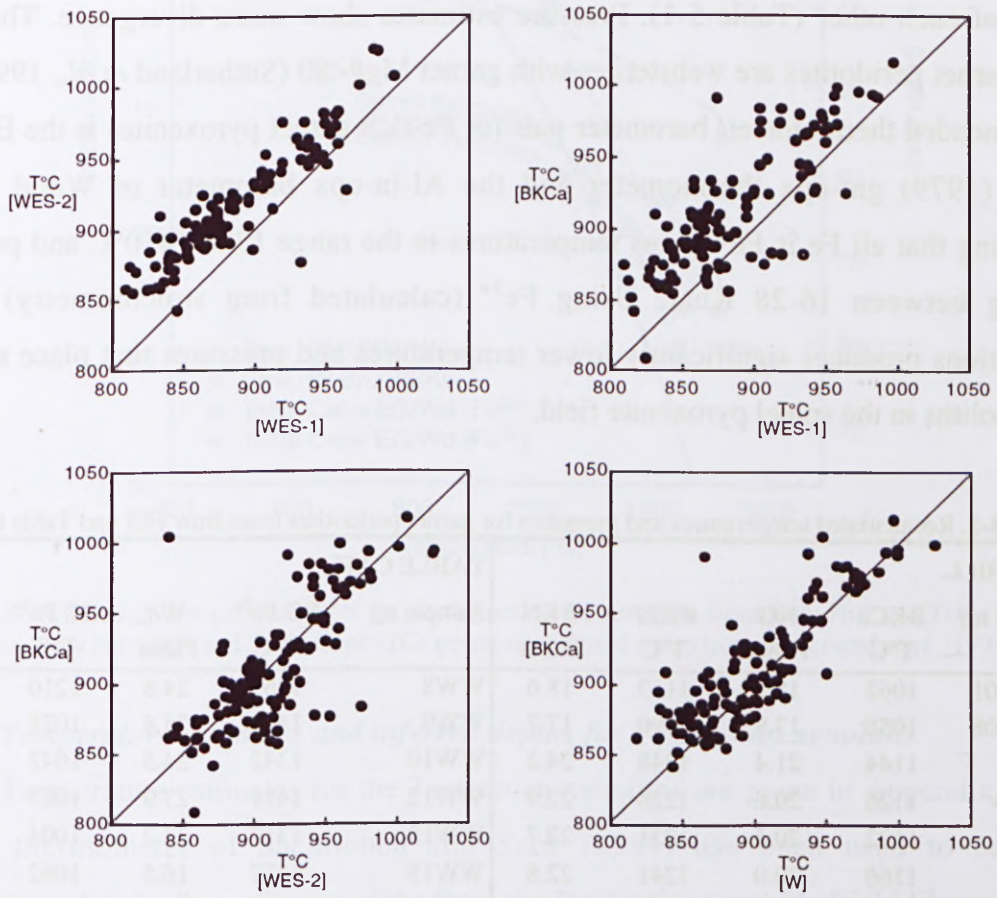


**Figure 5-17.** Comparison of geothermometric methods used for calculating equilibrium temperatures for the Tasmanian peridotite xenoliths.

### *5.5.3 Re-evaluation of the Tasmanian geotherms*

Although the southeastern Australia (SEA) geotherm has been chosen in this study to be the appropriate geotherm for Tasmania, previous workers have constructed specific geotherms for Tasmania based on P-T estimates for garnet peridotites from Table Cape and

Bow Hill (central Tasmania) (Sutherland, 1989; Sutherland *et al.*, 1994). These geotherms are elevated relative to the SEA geotherm. The deviation from the SEA geotherm has been interpreted to reflect higher temperature gradients for Tasmania related to abnormally hot mantle linked with voluminous magmatism during the Cenozoic (Sutherland *et al.*, 1994). Temperature and pressure estimates for the Tasmanian garnet peridotite suites have been recalculated here based on the protocol for basalt-borne xenoliths outlined in Xu *et al.* (1998) to determine if the Tasmanian geotherms can be reproduced using the appropriate geothermometer/ geobarometer pairs.

For the Bow Hill Mg-rich garnet lherzolites (garnet Mg#≥80; Sutherland *et al.*, 1996) the Brey and Kohler (1990) Ca-in-opx thermometer/Nickel and Green (1985) barometer pair, and the Brey and Kohler (1990) two-pyroxene thermometer/ Al-in-opx barometer pair were used. These combinations give temperature estimates within error (± 50°C) of each other (Table 5-1). Pressure estimates show more divergence. The Table Cape garnet peridotites are websterites with garnet Mg#<80 (Sutherland *et al.*, 1996). The recommended thermometer/ barometer pair for Fe-rich garnet pyroxenites is the Ellis and Green (1979) gnt-cpx thermometer and the Al-in-opx barometer of Wood (1974). Assuming that all Fe is $Fe^{2+}$ gives temperatures in the range 1320-1410°C and pressures ranging between 16-28 Kbar. Using $Fe^{3+}$ (calculated from stoichiometry) in the calculations produces significantly lower temperatures and pressures that place many of the xenoliths in the spinel pyroxenite field.

**Table 5-1.** Recalculated temperatures and pressures for garnet peridotites from Bow Hill and Table Cape.

| BOW HILL | | | | | TABLE CAPE | | | | |
|---|---|---|---|---|---|---|---|---|---|
| Sample no | BKCa T°C | NG Pkbar | BK2P T°C | BKN Pkbar | Sample no | EG $Fe^{2+}$ T°C | Wd Pkbar | EG $Fe^{3+}$ T°C | Wd Pkbar |
| DR12501 | 1062 | 18.1 | 1113 | 18.6 | WW8 | 1369 | 24.8 | 1210 | 17.8 |
| DR12508 | 1058 | 17.9 | 1090 | 17.7 | WW9 | 1410 | 25.4 | 1028 | 11.1 |
| BH5 | 1144 | 21.4 | 1248 | 24.2 | WW10 | 1342 | 24.5 | 1042 | 11.4 |
| EBH-D | 1126 | 20.6 | 1226 | 22.9 | WW12 | 1411 | 27.9 | 1063 | 13.5 |
| EBH-E | 1122 | 20.5 | 1221 | 22.7 | WW13 | 1317 | 23.2 | 1004 | 10.1 |
| QQ20 | 1166 | 20.0 | 1241 | 22.8 | WW15 | 1327 | 16.5 | 1082 | 7.2 |
| QQ20a | 1180 | 21.1 | 1222 | 21.9 | | | | | |

Re-calculation of the P-T data using the geothermobarometer pairs suggested by Xu *et al.* (1998) produces temperature and pressure estimates for Bow Hill that lie within error on the SEA geotherm (see Fig. 5-18). However, this is not the case for Table Cape. The few P-T estimates that are available for this locality lie at temperatures above the SEA geotherm (Fig. 5-18). The Table Cape geotherm of Sutherland *et al.* (1994) is based on P-T

estimates calculated using the BK2P/BKN pair of Brey and Kohler (1990). Recalculation of the data using EG79/Wd ($Fe^{2+}$) gives pressures and temperatures that lie well below the Table Cape geotherm. Using EG79/Wd($Fe^{3+}$) produces a better fit to the geotherm but at unreasonably low pressures. Unfortunately there is no detailed petrologic context given for these samples in the literature so there is no mechanism to test equilibrium relationships or unequivocally establish that these xenoliths reflect a higher thermal regime.

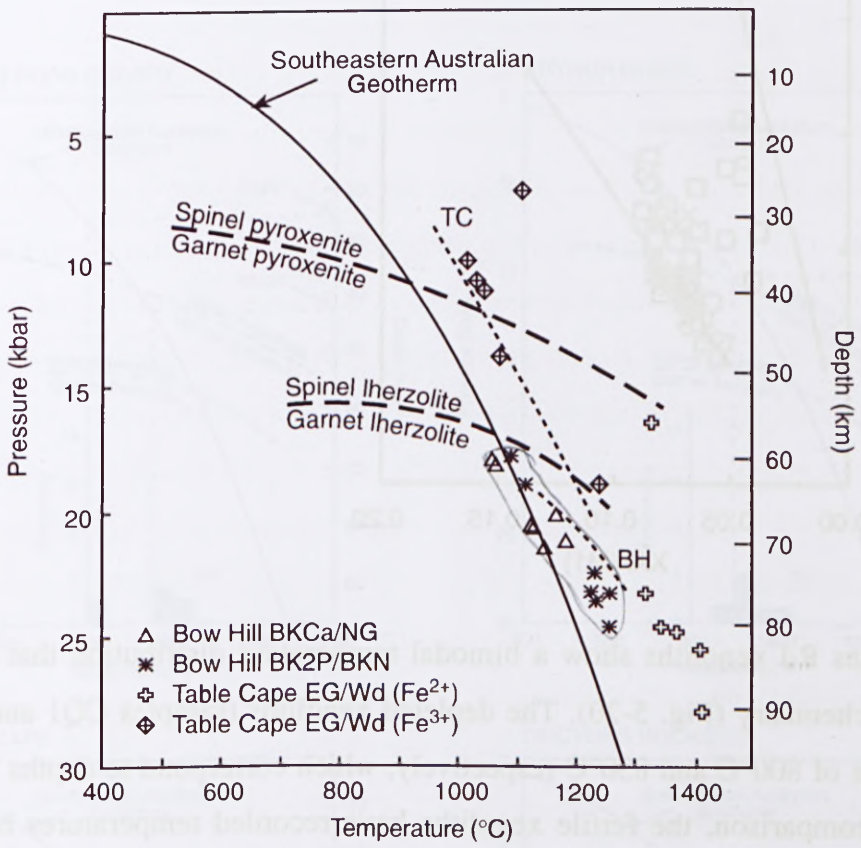


**Figure 5-18.** Pressure-temperature plots for garnet peridotite xenoliths from Bow Hill and Table Cape in Tasmania. Bow Hill (BH) and Table Cape (TC) geotherms (dotted lines) from Sutherland *et al.* (1994).

### *5.5.4 Temperature estimates and inferred depths for Tasmanian xenoliths*

Temperature estimates for the Tasmanian xenoliths are given in Appendix V. The opx-sp thermometer of Sachtleben and Seck (1981) has been used to calculate temperatures for the lherzolite xenoliths from the Rocky Cape and Sheffield Elements. The Cr-Al-opx thermometer (Witt-Eickschen and Seck, 1991) has been used for xenoliths from the Northeast Tasmania Element as many samples from these localities are spinel-free thus precluding the use of the [SS] thermometer. This thermometer has also been used to determine core temperatures for porphyroclasts from the porphyroclastic xenoliths of South Riana. Fig. 5-19 illustrates that temperatures calculated using the Cr-Al-opx

thermometer of Witt-Eickschen and Seck (1991) can be applied to these samples as they lie within the compositional range for which the thermometer was calibrated.

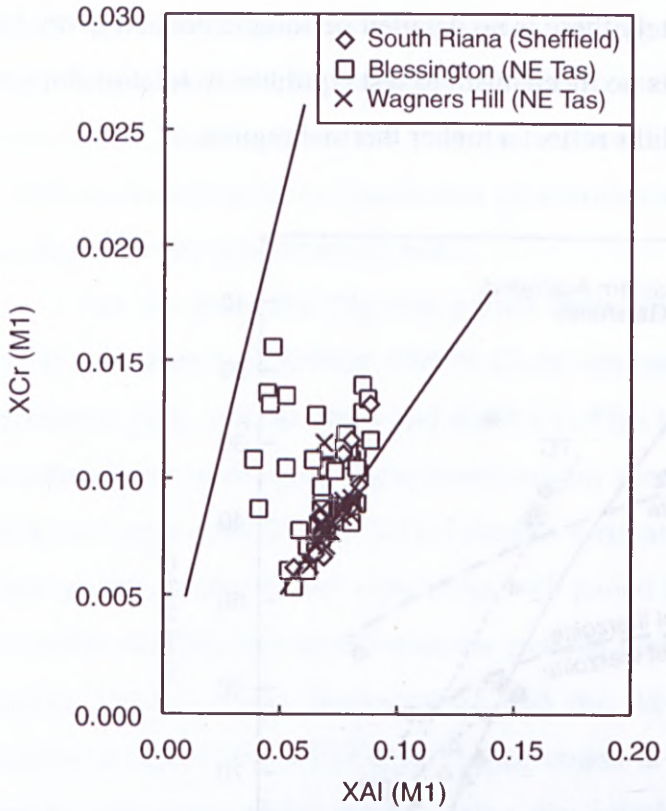


**Figure 5-19.** Plot of XCr on the M1-site of orthopyroxene vs XAl. Solid lines define the compositional range for which the Witt-Eickschen and Seck (1991) Cr-Al-opx thermometer is calibrated.

Coates Rd xenoliths show a bimodal temperature distribution that is related to sample geochemistry (Fig. 5-20). The depleted xenoliths (samples CQ1 and CQ4) have temperatures of 800°C and 830°C respectively, which correspond to depths of 26km and 30km. By comparison, the fertile xenoliths have recorded temperatures between 960-1010°C suggesting derivation from depths of 42-48 km. The temperature difference between the two xenolith types is well outside error (±50°C) and indicates that these two groups have been derived from different levels of the mantle. Most xenoliths from Arthur River give temperatures that range from 910°C to 1030°C, and corresponding depths of 36-52km (Fig. 5-20). Sample AR2 is spinel-free and calculated temperatures for this sample are 845°C [WES-2] and 863°C [BKCa]. These temperatures are equivalent to a depth of about 31-32 km. Table Cape xenoliths have recorded temperatures that range from 930-1010°C which correspond to depths of 40-48 km (Fig. 5-20). There is no apparent difference in temperature between the fertile and depleted xenoliths from this locality. Xenoliths from Doctors Rocks show a temperature range from 910-1010°C with equivalent depths of 36-48 km (Fig. 5-20).

South Riana xenoliths show a bimodal distribution in temperature that is related to petrography. Fine-grained xenoliths lie between 860-910°C at depths of 32-36 km whereas coarse-grained samples lie in the temperature range 980-1025°C (Fig. 5-21). As the latter show evidence for heating (see Section 4.2.2) these estimates are unlikely to represent the ambient temperature of the sample at the time of entrainment and more likely to reflect the conditions during ascent to the surface.

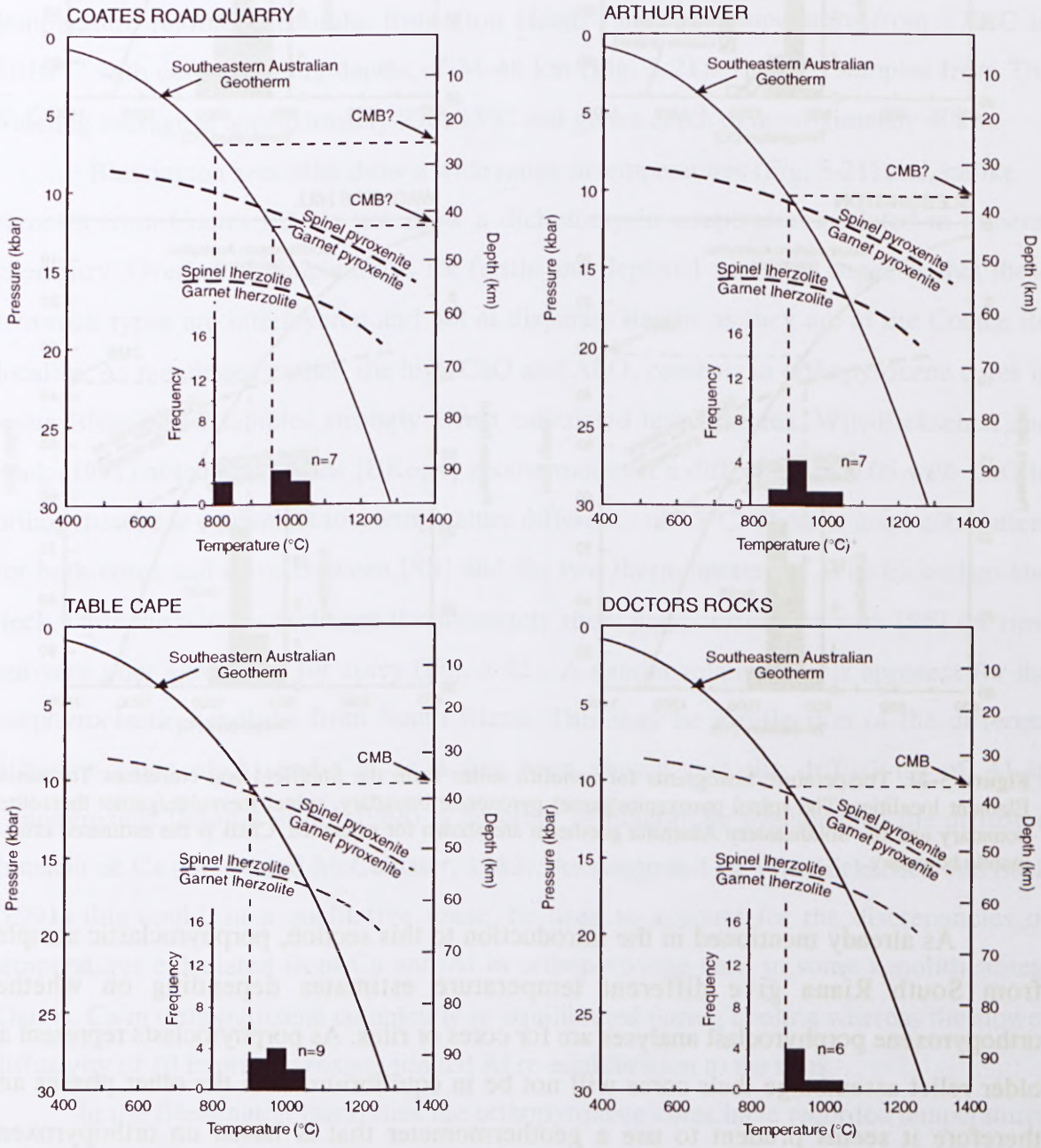


**Figure 5-20.** Temperature histograms for xenolith suites from the Rocky Cape Element localities. The spinel pyroxenite/garnet pyroxenite boundary, spinel lherzolite/garnet lherzolite boundary and the Southeastern Australia geotherm are shown for reference.

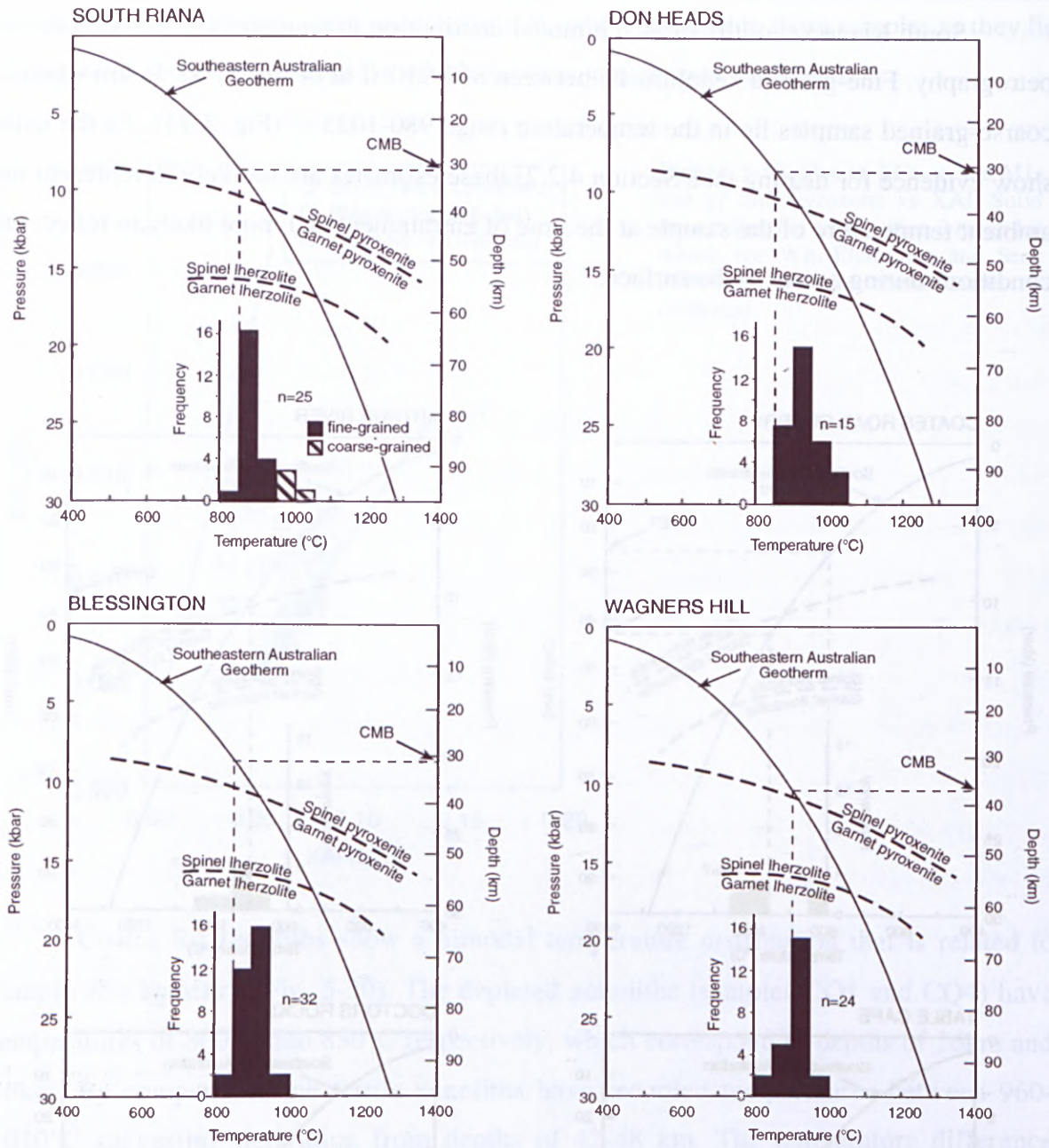


**Figure 5-21.** Temperature histograms for xenolith suites from the Sheffield and Northeast Tasmania Element localities. The spinel pyroxenite/garnet pyroxenite boundary, spinel lherzolite/garnet lherzolite boundary and the Southeastern Australia geotherm are shown for reference. CMB is the estimated crust-mantle boundary.

As already mentioned in the introduction to this section, porphyroclastic samples from South Riana give different temperature estimates depending on whether orthopyroxene porphyroclast analyses are for cores or rims. As porphyroclasts represent an older relict assemblage their cores will not be in equilibrium with the other phases and therefore it seems prudent to use a geothermometer that is based on orthopyroxene composition only i.e. the Cr-Al-opx thermometer of Witt-Eickschen and Seck, (1991) or the Ca-in-opx thermometer of Brey and Kohler (1990). The former has been chosen here because it shows better correlation with [SS] than does [BKCa]. Core temperatures are

invariably higher (+50-140°C) than those for rims and range from 900-1025°C (equivalent to depths of 36-52 km) (Fig. 5-21). Temperature estimates for porphyroclast rims (850-900°C) and temperatures calculated using only neoblast compositions (870-910°C) are very similar and it is reasonable to assume that they are in equilibrium. The temperature range for rims corresponds to depths of 31-36 km. The differences between core and rim data suggests that these xenoliths originally derived from a deep environment, as indicated by core temperatures, and subsequently recrystallised in a shallower environment as indicated by rim and neoblast data. Alternatively, the cores may be relicts from a high-temperature regime. Xenoliths from Don Heads range in temperature from 870°C to 1010°C with corresponding depths of 34-48 km (Fig. 5-21). The two samples from The Sideling average at approximately 930±15°C and give a depth of approximately 40km.

Blessington xenoliths show a wide range in temperatures (Fig. 5-21) and, unlike samples from Coates Rd, do not show a dichotomy in temperatures related to mineral chemistry. Overlap in temperatures for fertile and depleted xenoliths suggests that these two rock types are interlayered and not at disparate depths as they are at the Coates Rd locality. As mentioned earlier, the high CaO and $Al_2O_3$ contents in orthopyroxene cores in some Blessington samples strongly affect calculated temperatures. Witt-Eickschen and Seck (1991) noted that for the [BKopx] geothermometer a difference of 0.05 wt% CaO in orthopyroxene is equivalent to a temperature difference of 15°C. There is good correlation, for both cores and rims, between [SS] and the two thermometers of Witt-Eickschen and Seck while the two Ca exchange thermometers show good correlation with [SS] for rims but very poor agreement for cores (Fig. 5-22). A similar relationship is apparent for the porphyroclastic xenoliths from South Riana. This may be a reflection of the different diffusion rates of Al and Ca, as it has been shown that the diffusivity of Al in clinopyroxene (Sautter *et al.*, 1988) is an order of magnitude smaller than the diffusion constant of Ca (Brady and McCallister, 1983). As suggested by Witt-Eickschen and Seck (1991) this could, in a qualitative sense, be used to account for the discrepancies of temperatures calculated from Ca and Al in orthopyroxene seen in some xenolith suites. That is, Ca in orthopyroxene completely re-equilibrated during cooling whereas the slower diffusivity of Al in orthopyroxene limited Al re-equilibration to the rims.

In the Blessington lherzolites the orthopyroxene cores have recorded temperatures of 1030°C which suggests a high-temperature origin for the earlier assemblage. Later cooling at constant, or decreasing, pressure has seen complete re-equilibration of Ca in orthopyroxene but only partial re-equilibration of Al so that cores still retain evidence of

heating. Rim temperatures vary from 840-920°C and correspond to depths of 31-40 km. This temperature interval is covered by the range in temperatures for the equilibrated samples from Blessington (i.e. those without zoning in any mineral phase) where the majority of temperature estimates lie between 840°C and 940°C (one sample has a T of 975°C) giving depths of 31-42 km.

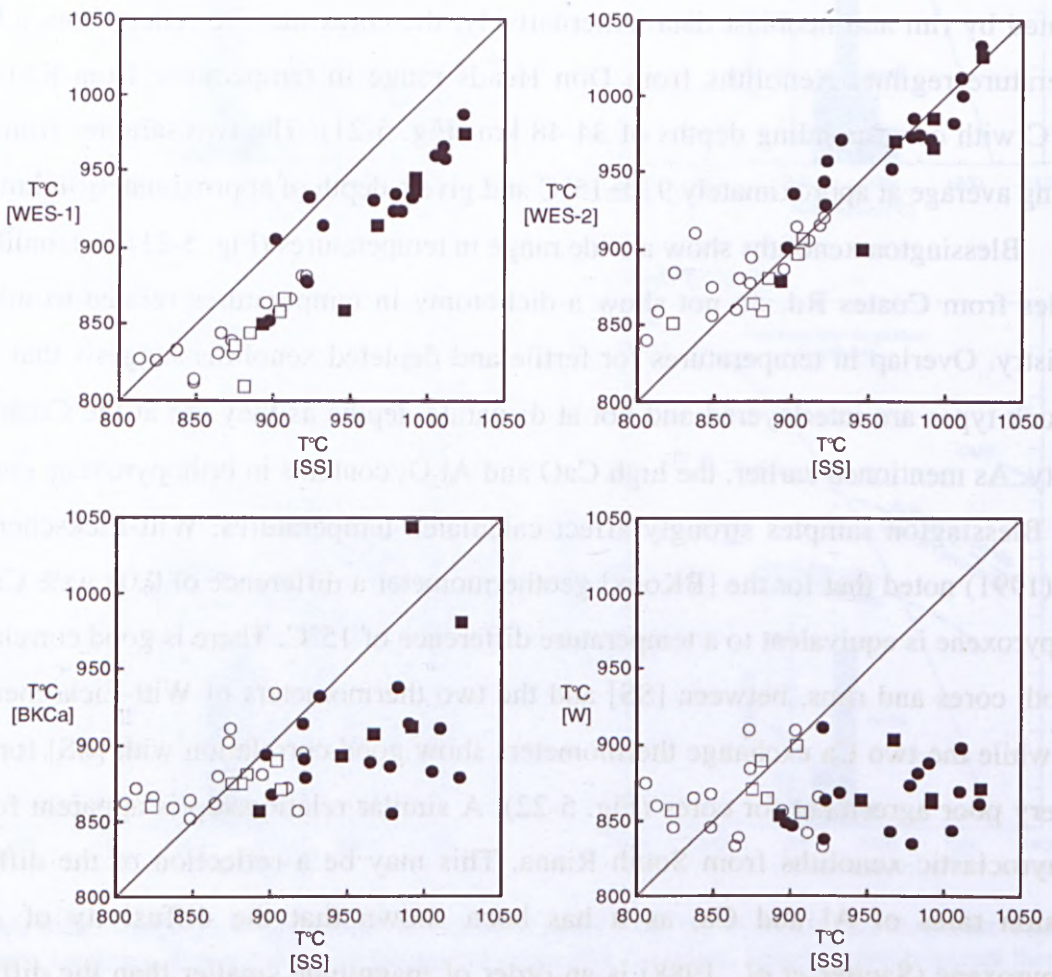


**Figure 5-22.** Comparison of geothermometric results for core and rim analyses for South Riana and Blessington spinel lherzolites. Open circles-Blessington rims. Filled circles-Blessington cores. Open squares-South Riana rims. Filled squares-South Riana cores.

Xenoliths from Wagners Hill show very little variation in temperature estimates with the majority of samples lying between 900-950°C ( a few samples range as low as 800°C). These temperatures place the origin of these xenoliths at depths of approximately 36-42 km (Fig. 5-21). The low-T xenoliths give depths of 32-35 km, putting them in a similar range as two pyroxenites from the same locality and suggesting that these two rock types are interlayered at these depths.

## 5.6 CRUST-MANTLE BOUNDARY

### *5.6.1 Introduction*

A probable deep crust-upper mantle stratigraphy for eastern Australia has been determined using petrologic information including geothermobarometric calculations and recognition of composite xenoliths with lithological contacts. This stratigraphy comprises a lower crust dominated by mafic granulites, then a crust-mantle transition zone (starting at about 25 km) consisting of spinel lherzolite wall-rock intercalated with igneous cumulates, granulites and spinel±garnet pyroxenites (Griffin and O'Reilly, 1987b). These mafic rocks are thought to be frozen basaltic liquids that represent repetitive basaltic underplating and overplating at the crust-mantle boundary by intrusive and tectonic processes (O'Reilly, 1989a). The proportion of spinel lherzolite increases with depth from the crust-mantle boundary until about 55-60 km where garnet peridotite becomes the main rock type (O'Reilly and Griffin, 1991). The crust-mantle boundary (CMB) is therefore defined as the depth at which ultramafic lithologies become dominant and has been found in eastern Australia at depths ranging from 25 to 38 km (Griffin and O'Reilly, 1987a,b; O'Reilly, 1989a).

The seismological definition of the crust-mantle boundary is based on the Mohorovicic Discontinuity or Moho. The Moho represents a seismic discontinuity where compressional wave velocity (Vp) increases from about 6.5-7.0 km/s to about 8.0 km/s and has been inferred to represent a compositional boundary separating the lower crust from the upper mantle (Ringwood, 1975; Griffin and O'Reilly, 1987a; Collins, 1991). The Moho has traditionally been treated as a single sharp discontinuity, however, more detailed study suggests that in some areas the Moho is a transition zone 5-15 km thick (O'Reilly, 1989a). Seismic reflection profiles show that this zone corresponds to a broad band of short discontinuous reflections (Collins, 1991). This transition zone is also apparent in deep crust/upper mantle profiles constructed using xenolith suites as discussed above though there is contention over whether both boundaries occur at the same depth.

Interpretations of xenolith data from eastern Australia imply that the chemically-defined crust-mantle boundary does not always coincide with the Moho as suggested by other workers (Collins, 1991; Finlayson *et al.*, 1993). To demonstrate that the two are not necessarily coincident Griffin and O'Reilly (1987b) distinguish between what they call the "seismic Moho" (the velocity discontinuity) and the CMB or "petrological" Moho (boundary or transition between felsic/mafic crustal rocks and a dominantly ultramafic upper mantle). They have shown that beneath continental rifts and orogenic belts of

Proterozoic or younger age the depth to the seismic Moho will depend on the scale of the transition and on the geothermal gradient, but will probably lie below the petrological Moho (Griffin and O'Reilly, 1987a). This has been demonstrated in stratigraphic profiles constructed from southeastern Australian xenoliths and is related to the lowering of Vp by elevated temperatures so that in areas of high heat flow Vp≥8.0 may not be reached until the spinel lherzolite/garnet lherzolite transition (55-60 km) is crossed even though the crust-mantle boundary is relatively shallow (~25 km) (Griffin and O'Reilly, 1987a).

### *5.6.2 The crust-mantle boundary in Tasmania*

Crustal thickness in Tasmania has been determined using geophysical methods such as seismic refraction and reflection and gravity. Seismic refraction surveys carried out by Richardson (1989b) have indicated that the Tasmanian crust is anomalously thin along the north of the state (23-27 km) and thickens to about 32 km beneath central Tasmania. This has been partly supported by gravity surveys of Tasmania which show crustal thickness varying from 23-24 km along the coasts. However, modelling of gravity data suggests the crust to be only 27 km thick in central Tasmania (Leaman and Richardson, 1989). More recent seismic refraction studies along the western half of the same traverse report crustal thickness as being relatively uniform at 30-32 km supporting seismic reflection data which shows the Moho lying at 30-33 km in northwestern Tasmania (Barton, 1998; Rawlinson *et al.*, 1998).

A complete map of the Tasmanian Moho (Rawlinson *et al.*, 2001) has been constructed from inversion of seismic refraction and wide-angle reflection traveltimes (Fig. 5-23). The Moho is well resolved in northern and western Tasmania but shows poor resolution in the central and northeastern parts of the state due to a lack of sources near central Tasmania and few receivers in NE Tasmania (Rawlinson *et al.*, 2001). The Moho map shows the crust of north-central Tasmania to be considerably thicker (from 32 km at the coast up to 37 km inland) than previous estimates. In contrast, northwestern Tasmania appears to have a thinner crust (~27-30 km) than determined in other studies. A small region on the northeast coast of the Rocky Cape Element is anomalously thin (~25-26 km). Nevertheless there is some indication for a higher geotherm in the Table Cape region. The anomalously shallow mantle (~25 km) apparent on the northeast coast of the Rocky Cape Element (see Tasmanian Moho map in Fig. 5-23) suggests thinned crust and high heat flow which would raise the local geotherm.

In this study the depth to the crust-mantle boundary in Tasmania has been

estimated using geothermometry. The depth to the CMB is poorly constrained for the localities in the Rocky Cape Element due to the small number of samples collected in these places. The crust-mantle boundary at Coates Rd is hard to constrain as there are few samples and they are distributed over depths from 26-48 km (Fig. 5-20). The shallowest depth would place the CMB above the seismic Moho (28-29 km) in this region as established for mantle sections in young extensional areas (Griffin and O'Reilly, 1987a). The depth to the CMB at Arthur River is also difficult to determine but could be similar to that estimated for Coates Rd, despite implications in Fig. 5-20 for a deeper CMB at this locality.

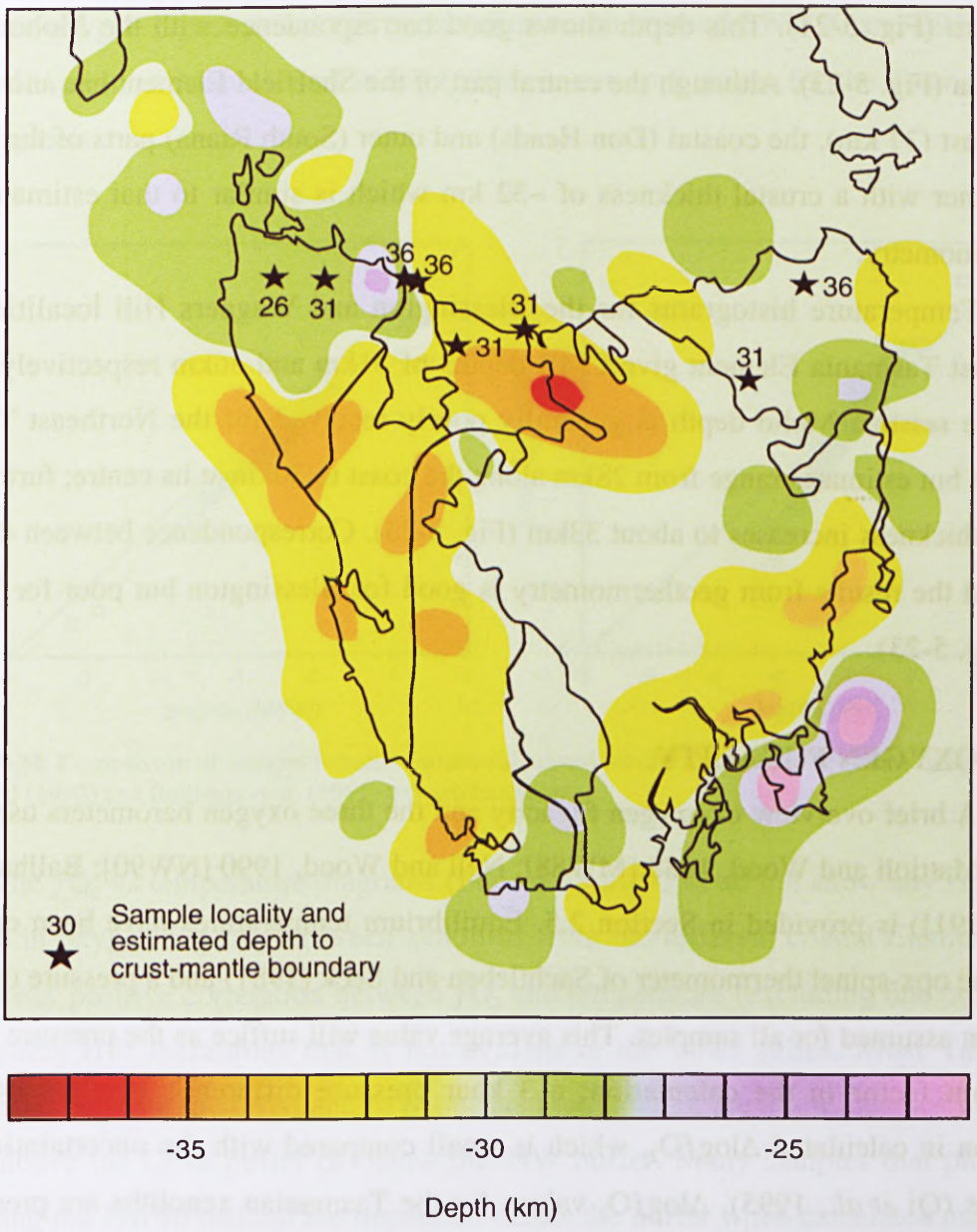


**Figure 5-23.** Comparison between depths to the crust-mantle boundary estimated from mantle xenolith geothermobarometry and Moho depths determined from the TAGSO wide angle seismic survey. Moho map modified after Rawlinson *et al.*, 2001.

Histograms for Table Cape and Doctors Rocks xenoliths, when referred to the southeastern Australian geotherm, place the CMB at depths of approximately 36 km (see Fig. 5-20) which is considerably deeper than defined on the Moho map. As it is generally expected that the seismic Moho will lie below the petrologically defined Moho this might suggest problems in depth estimation for the xenoliths. It has been proposed that the geotherm that exists beneath Tasmania is hotter than that for southeastern Australia (Sutherland *et al*, 1994; see Section 5.5.3) as a result of more recent volcanism. Extrapolating the xenolith temperatures to a higher geotherm would raise the CMB to shallower depths and give better agreement with the seismic Moho.

The crust-mantle boundary at South Riana and Don Heads is well-constrained at 31-32 km (Fig. 5-21). This depth shows good correspondence with the Moho map for Tasmania (Fig. 5-23). Although the central part of the Sheffield Element has anomalously thick crust (37 km), the coastal (Don Heads) and outer (South Riana) parts of the Element are thinner with a crustal thickness of ~32 km which is similar to that estimated using geothermometry.

Temperature histograms for the Blessington and Wagners Hill localities in the Northeast Tasmania Element give CMB depths of 31km and 36km respectively (Fig. 5-21). The seismic Moho depth is generally poorly resolved for the Northeast Tasmania Element but estimates range from 28km along the coast to 30km at its centre; further south crustal thickness increases to about 33km (Fig. 5-23). Correspondence between the Moho map and the results from geothermometry is good for Blessington but poor for Wagners Hill (Fig. 5-23).

## 5.7 OXYGEN FUGACITY

A brief overview of oxygen fugacity and the three oxygen barometers used in this thesis (Mattioli and Wood, 1988 [MW88]; Nell and Wood, 1990 [NW90]; Ballhaus *et al.*, 1991 [B91]) is provided in Section 2.5. Equilibrium temperatures have been calculated using the opx-spinel thermometer of Sachtleben and Seck (1981) and a pressure of 15 kbar has been assumed for all samples. This average value will suffice as the pressure is not an important factor in the calculation; a 3 kbar pressure difference produces <0.1 unit variation in calculated $\Delta \log fO_2$, which is small compared with the uncertainties of the analyses (Qi *et al.*, 1995). $\Delta \log fO_2$ values for the Tasmanian xenoliths are presented in Appendix VI.

The majority of the $fO_2$ values for the Tasmanian spinel peridotites are in the range

QFM to QFM−2, similar to that seen for garnet-free mantle xenolith suites from western Victoria (Chen *et al.*, 1991) and other continental plate settings from around the world (Wood and Virgo, 1989). Oxygen fugacities derived from the NW90 and B91 methods show good agreement (Fig. 5-24) though values calculated from B91 are consistently 0.3-0.4 log units lower than those from the NW90 method. The values given by MW88 show more scatter, particularly at low $fO_2$ (Fig. 5-24), than those calculated by the other two methods, possibly because this calibration was based on experimental data for Cr-free spinels (Wood *et al.*, 1990). As a consequence, this algorithm generates results that are slightly dependent on Cr/(Cr+Al) ratios and can produce spurious correlations of $fO_2$ with spinel Cr content (Wood *et al.*, 1990). For the purposes of this thesis, interpretation of the Tasmanian oxygen fugacity data will be based on results from the NW90 and B91 methods as the calibration of Mattioli and Wood (1988) is not appropriate for the Tasmanian Cr-bearing spinels.

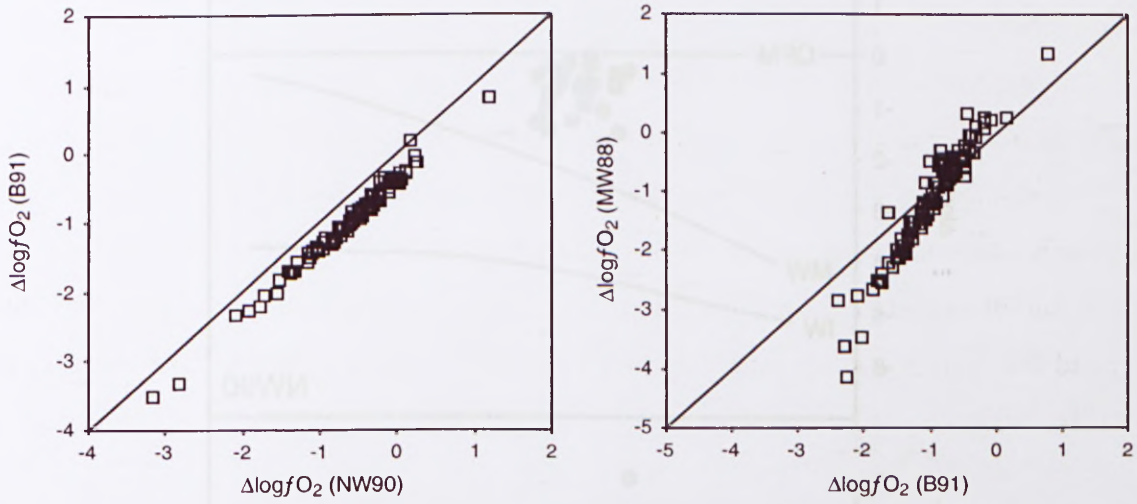


**Figure 5-24.** Comparison of oxygen fugacity values calculated for the Tasmanian xenoliths using the Nell and Wood (1990) and Ballhaus *et al.* (1991) oxygen barometers.

The $fO_2$ vs temperature diagrams (Figs. 5-25 to 5-28) do not show any significant variation in oxygen fugacity between xenoliths from the different crustal Elements apart from a weak positive correlation between $fO_2$ and temperature (excluding one outlier) for the Wagners Hill lherzolites that is not evident in the other suites. Most Tasmanian xenoliths lie between the QFM and MW buffers though there are a few samples which are located above the QFM buffer or below the MW buffer. Many samples that plot above QFM using the NW90 method are depressed below the buffer when calculated using B91. The exceptions to this are two samples from the Northeast Element (BL25a from Blessington and WH13 from Wagners Hill) which appear to he truly oxidized relative to

the other xenoliths. Several samples lie below the MW buffer, for both the NW90 and B91 method, including TC9 and TC10 from the Rocky Cape Element and WH21 from Wagners Hill. In other xenolith suites this has been ascribed to metasomatism by a fluid with lower oxygen fugacity (Chen *et al.*, 1991).

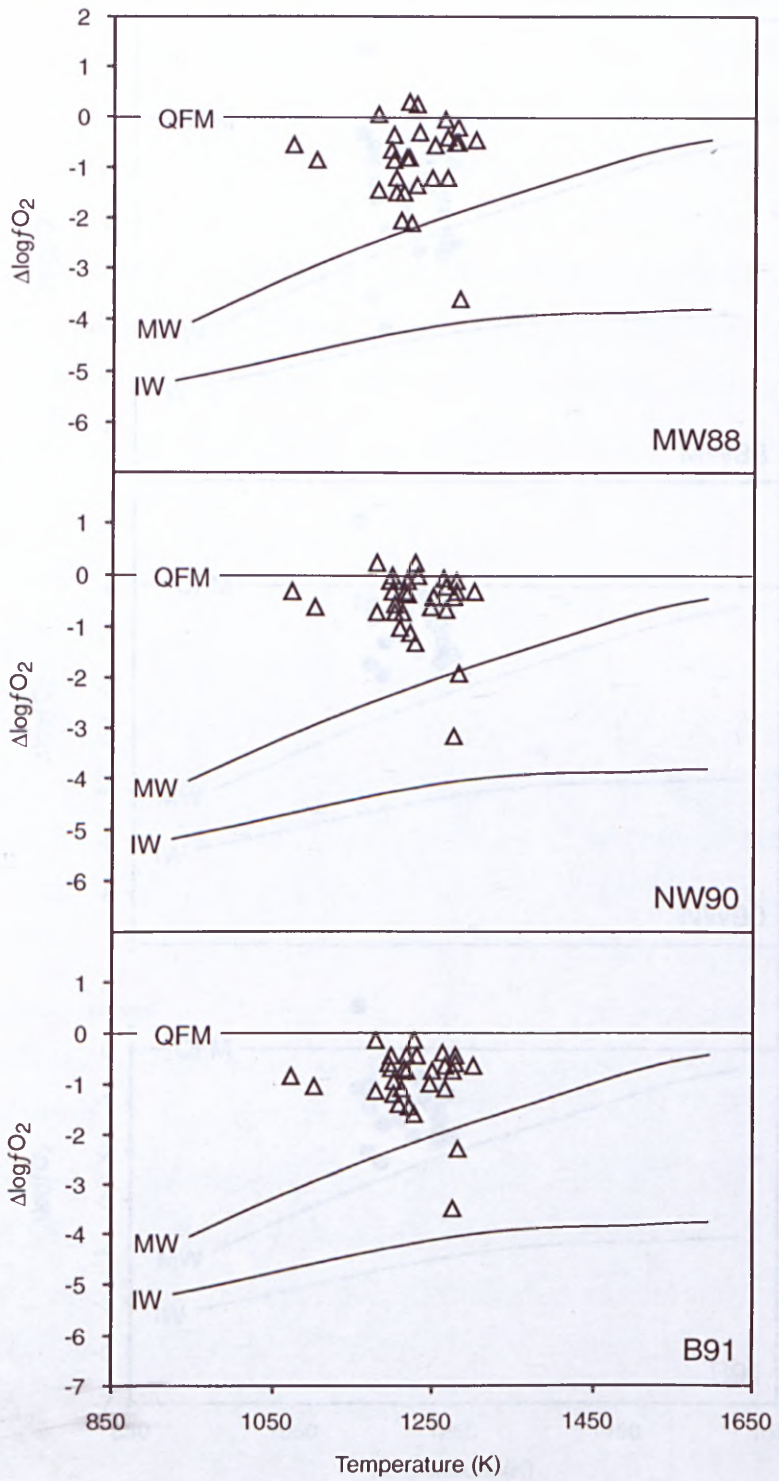


**Figure 5-25.** Comparison of results for the Rocky Cape Element xenolith suite, using three different calibrations of the orthopyroxene-olivine-spinel geobarometer. $\Delta \log fO_2$ is the difference between calculated $\log fO_2$ and the quartz-fayalite-magnetite (QFM) buffer (this applies to all oxygen fugacity diagrams in this thesis). The pressure-corrected (15 kbar) magnetite-wüstite (MW) and iron-wüstite (IW) buffer curves are the same as those used by (O'Neill and Wall, 1987).

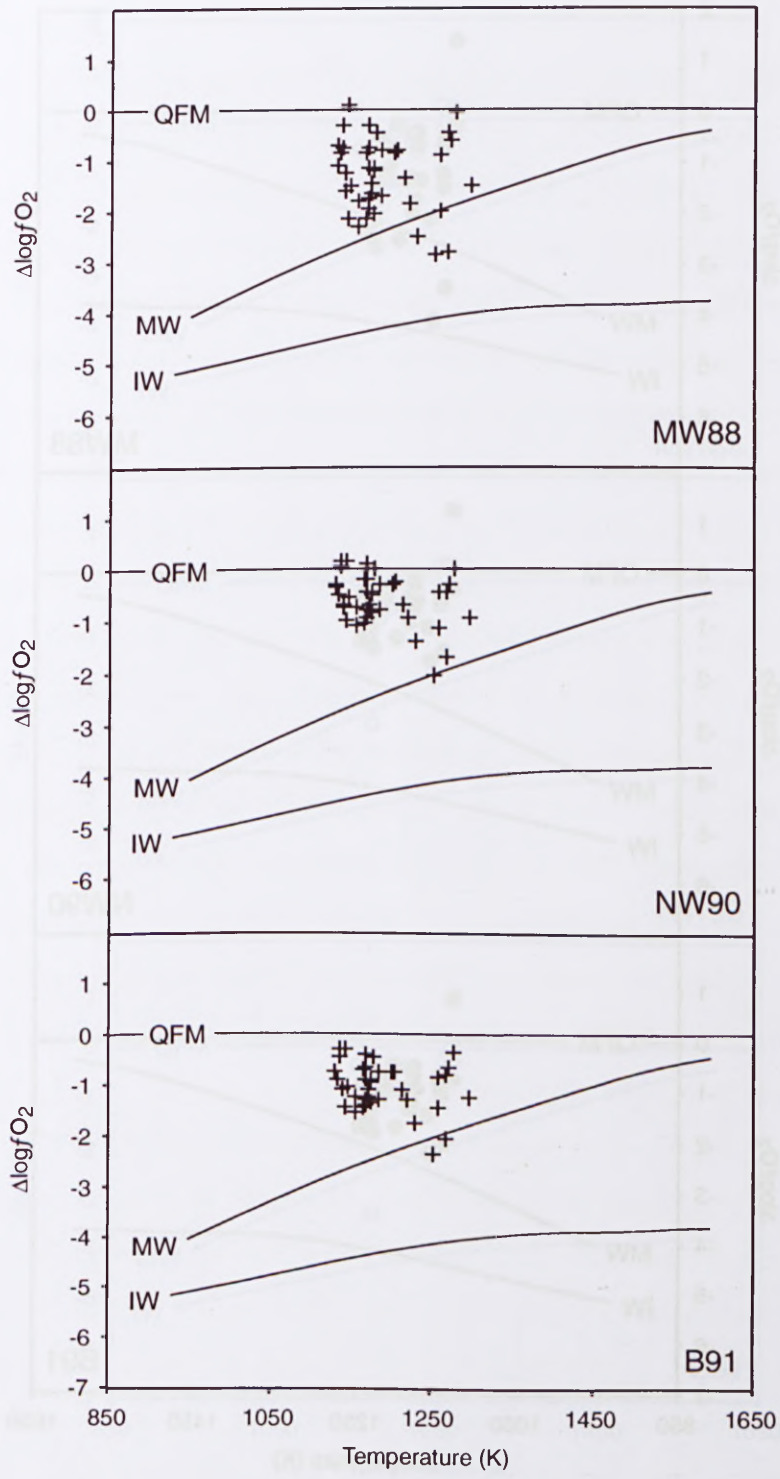


**Figure 5-26** Comparison of results for the Sheffield Element xenolith suite, using three different calibrations of the orthopyroxene-olivine-spinel geobarometer.

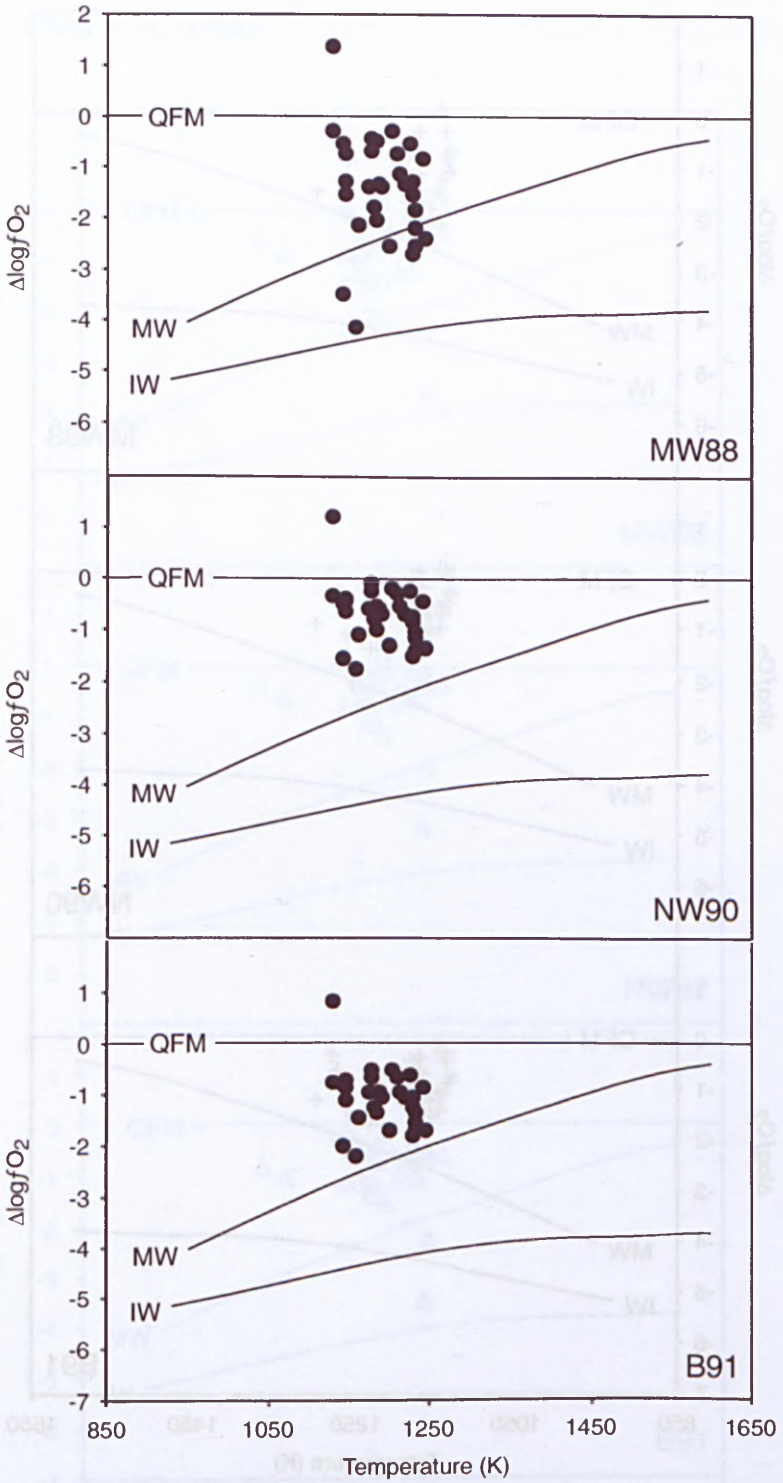


**Figure 5-27.** Comparison of results for the Blessington xenolith suite from the Northeast Tasmanian Element, using three different calibrations of the orthopyroxene-olivine-spinel geobarometer.

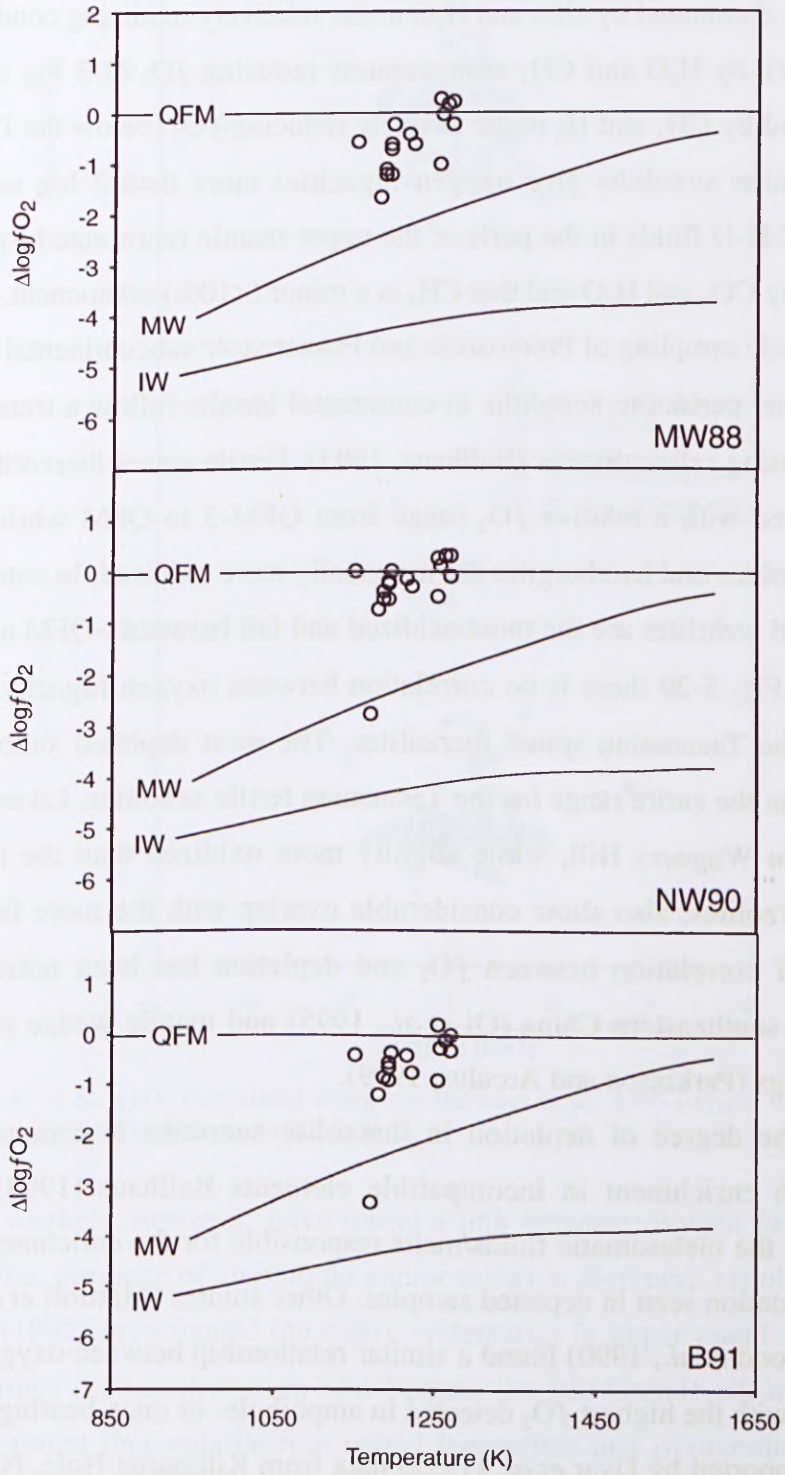


**Figure 5-28.** Comparison of results for the Wagners Hill xenolith suite from the Northeast Tasmanian Element, using three different calibrations of the orthopyroxene-olivine-spinel geobarometer.

It is commonly accepted that mantle fluids commonly lie within the C-H-O-S system (Haggerty and Tompkins, 1983; Taylor and Green, 1988). Given the common occurrence of carbon-bearing material (i.e. carbonates) in mantle lherzolites, the fluid phase should be dominated by $CO_2$ and $H_2O$ under relatively oxidizing conditions (close to the QFM buffer), by $H_2O$ and $CH_4$ at moderately reducing $fO_2$ (2-3 log units below the QFM buffer) and by $CH_4$ and $H_2$ under strongly reducing $fO_2$ (below the IW buffer). The bulk of Tasmanian xenoliths give oxygen fugacities more than 2 log units above IW, implying that C-H-O fluids in the parts of the upper mantle represented by these samples are dominated by $CO_2$ and $H_2O$ and that $CH_4$ is a minor (<10%) component.

Worldwide sampling of Proterozoic and Phanerozoic subcontinental lithosphere has shown that spinel peridotite xenoliths in continental basalts follow a trend of increasing $fO_2$ with increasing refractoriness (Ballhaus, 1993). Fertile spinel lherzolite xenoliths are the most reduced with a relative $fO_2$ range from QFM-3 to QFM while slightly more refractory lherzolites and harzburgites are marginally more oxidized. In contrast, refractory harzburgites and wehrlites are the most oxidized and fall between ~QFM and QFM+1. As can be seen in Fig. 5-29 there is no correlation between oxygen fugacity and indices of depletion for the Tasmanian spinel lherzolites. The most depleted xenoliths have $fO_2$ which fall within the entire range for the Tasmanian fertile xenoliths. Likewise the Fe-rich peridotites from Wagners Hill, while slightly more oxidized than the majority of the Tasmanian lherzolites, also show considerable overlap with the more fertile xenoliths. Similar lack of correlation between $fO_2$ and depletion has been noted in peridotite xenoliths from southeastern China (Qi *et al.*, 1995) and mantle wedge peridotites from island arc settings (Parkinson and Arculus, 1999).

Since the degree of depletion in lherzolite xenoliths is commonly positively correlated with enrichment in incompatible elements Ballhaus (1993) came to the conclusion that the metasomatic fluids/melts responsible for the enrichment are linked to the marked oxidation seen in depleted samples. Other studies (Mattioli *et al.*, 1989; Canil *et al.*, 1990; Wood *et al.*, 1990) found a similar relationship between oxygen fugacity and metasomatism with the highest $fO_2$ detected in amphibole- or mica-bearing xenoliths. This finding was supported by Dyar *et al.* (1992) data from Kilbourne Hole, New Mexico and suggests that metasomatism involving amphibole and mica occurs under conditions of higher $fO_2$ than does metasomatism by anhydrous melts.

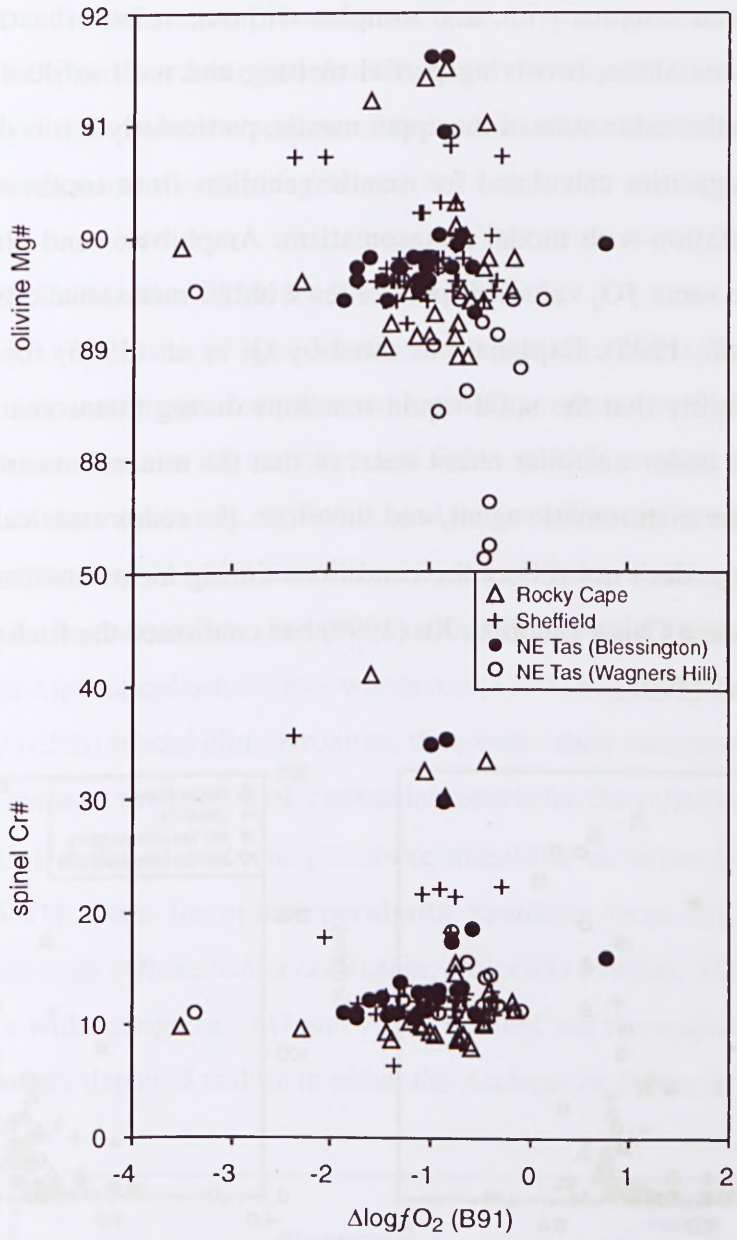


**Figure 5-29.** Plots of $\Delta \log fO_2$ (calculated using the Ballhaus et al, 1990 oxygen barometer) against indices of depletion for the Tasmanian mantle xenoliths.

Not all workers, however, have found a link between oxygen fugacity and high water activity (i.e. presence of amphibole and/or mica) in lherzolite xenoliths. Amundsen and Neumann (1992) investigated the redox systematics in upper mantle xenoliths from continental settings (i.e. northwestern Spitsbergen, the Rio Grande rift and southeastern Australia) and found that volatile-free spinel lherzolites and pyroxenites have similar median $fO_2$ values (QFM-0.5 and QFM-0.7 respectively) as volatile-bearing lherzolites (QFM-0.3) from the same localities. Anhydrous spinel lherzolites and pyroxenite xenoliths from oceanic settings (i.e. the Canary Islands, Hawaii and Tahiti) were found to have consistently high oxygen fugacities with a median value of QFM+1.0. The authors concluded that: (1) The xenolith suites investigated exhibit no systematic difference in

redox state between samples with, and samples without, volatile-bearing minerals. (2) Magmatic processes alone, involving partial melting and melt infiltration, may induce large variations in the redox state of the upper mantle, particularly if it is depleted.

Oxygen fugacities calculated for mantle xenoliths from southeastern China have revealed no correlation with modal metasomatism. Amphibole- and phlogopite-bearing xenoliths give the same $fO_2$ values as peridotites with no metasomatic minerals (Chen *et al.*, 1991; Qi *et al.*, 1995). Explanations cited by Qi *et al.* (1995) for this observation include the possibility that the solid-liquid reactions during metasomatism in the upper mantle took place under a similar redox state, or that the mineral assemblage did not re-equilibrate with the metasomatic agent, and therefore, the redox state calculated from the mineral assemblage does not reflect the conditions during metasomatism. A more recent study of southeastern China xenoliths Xu (1999) has confirmed the findings of Chen *et al.* (1991) and Qi *et al.* (1995).

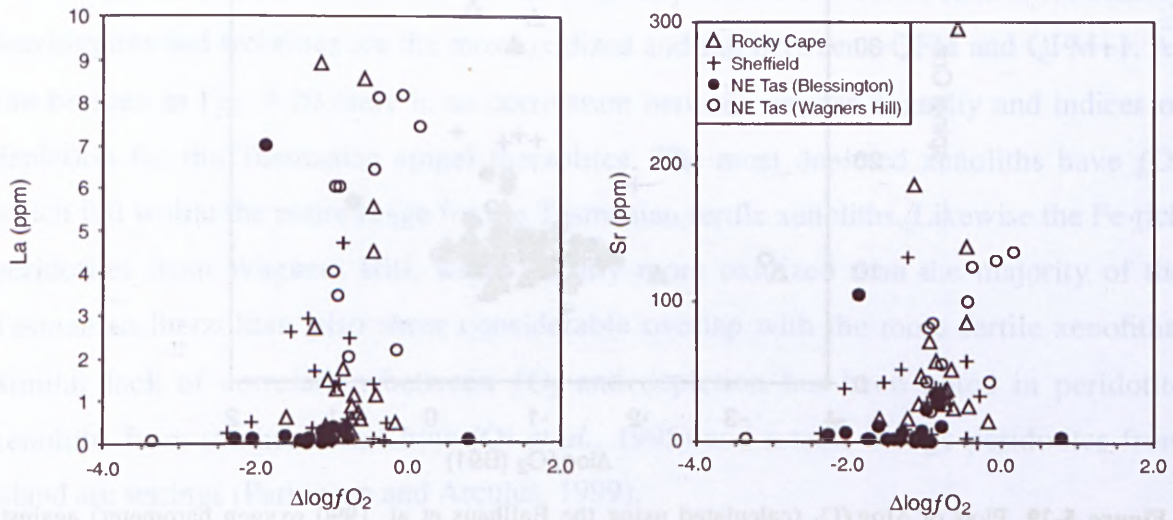


**Figure 5-30.** Plots of La and Sr in clinopyroxene against $\Delta\log fO_2$ for the Tasmanian mantle xenoliths.

The Tasmanian mantle xenoliths do not contain any hydrous minerals but show evidence for widespread cryptic metasomatism. In Fig. 5-30 (above), La and Sr have been plotted against $\Delta\log fO_2$ to determine if there is any correlation between incompatible trace element enrichment and oxygen fugacity in the Tasmanian peridotites. Most of the metasomatised xenoliths have oxygen fugacities ranging from QFM-1.8 to QFM, therefore falling within the whole range for the Tasmanian xenoliths and suggesting that redox state is not related to metasomatism in these rocks. Of the two oxidized samples, one (WH13) is highly enriched in La and Sr whereas the other (BL25a) is extremely depleted in these elements. Xenoliths with oxygen fugacities below QFM-2 have similarly low La and Sr contents as those seen in more oxidized samples. This study confirms that there is no

consistent world-wide relationship between degree of mantle metasomatism and the oxygen fugacity of spinel lherzolite xenoliths in basalts; the direction of change of oxygen fugacity probably depends on the source of the metasomatic fluid and the extent of its equilibration with the mineral assemblage.

## 5.8 PROTEROZOIC MANTLE IN TASMANIA?

The mean composition of subcontinental lithospheric mantle beneath terrains of Archean, Proterozoic and Phanerozoic tectonothermal age shows a secular evolution in all measures of depletion, such as Al, Ca, Mg# and Fe/Al (Griffin *et al.*, 1999a). Unmodified Proterozoic SCLM is moderately depleted, and intermediate in composition between Archean and Phanerozoic SCLM. In Section 5.2.1, it was shown that the depleted xenoliths from Tasmania plot in, or near, the Proterozoic field on a modal olivine vs olivine Mg# diagram. The high-Mg# samples have low whole rock CaO and $Al_2O_3$ contents, a reflection of their very low (<5%) modal clinopyroxene, than commonly accepted primitive mantle compositions. In contrast to the bulk of Tasmanian xenoliths, the refractory samples plot in or near the area of depleted cratonic peridotite xenoliths in terms of their Ca and Al contents (Fig. 5-31). Data for spinel peridotite xenoliths from regions with known Proterozoic crustal ages (Obnezhennaya, Russia; Colorado Plateau, U.S.A; Mt Gambier; Australia) show a wider range in CaO and $Al_2O_3$ content but the majority of samples are moderately to strongly depleted and lie in either the Archean or Proterozoic field.

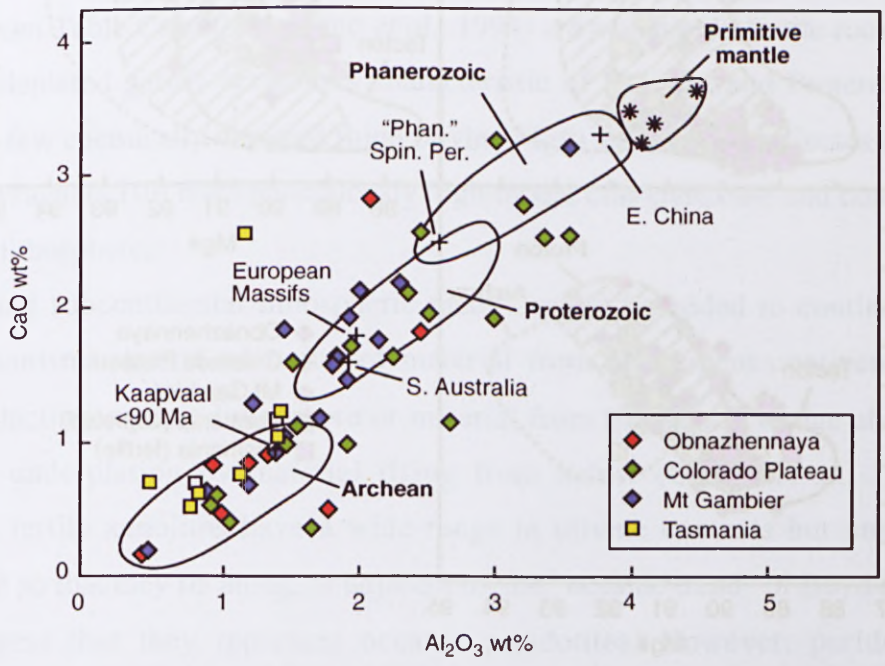


**Figure 5-31.** $Al_2O_3$ vs CaO plot for Tasmanian depleted peridotites. Also shown are data for spinel peridotite xenolith suites from regions of known Proterozoic age. Modified from Griffin *et al*, 1999a.

Other criteria that are used to discriminate between mantle samples of different ages include whole rock compositional parameters such as Mg#, Cr#, Mg/Si and Fe/Al (Fig. 5-32). The fields in Fig. 5-32 are from Griffin *et al.* (1998b) and are based on the tectonothermal age of the crust (i.e. the age of the last major crust-forming event) through which the xenolith was sampled: Archons (>2.5 Ga), Protons (2.5-1 Ga) and Tectons (<1 Ga). While there is considerable overlap between fields for the different age groups, particularly for samples of suspected Proterozoic age, it is apparent that the depleted Tasmanian xenoliths bear a stronger compositional resemblance to the Proton xenoliths than they do to the Tasmanian fertile xenoliths. The data for the depleted peridotites lies at high Mg#, Fe/Al and Mg/Si and plots in the Proton field, with some overlap into the Archon field. By contrast, the fertile xenoliths, while overlapping from the Tecton field into the Proton field, lie well outside the field for Archon samples. The depleted xenoliths have high Cr# that extend from the Proton field to the high values seen in some samples from Obnezhennaya and Mt Gambier.

It may be that the rare depleted xenoliths found at some localities in Tasmania represent relics of the old Proterozoic lithosphere.

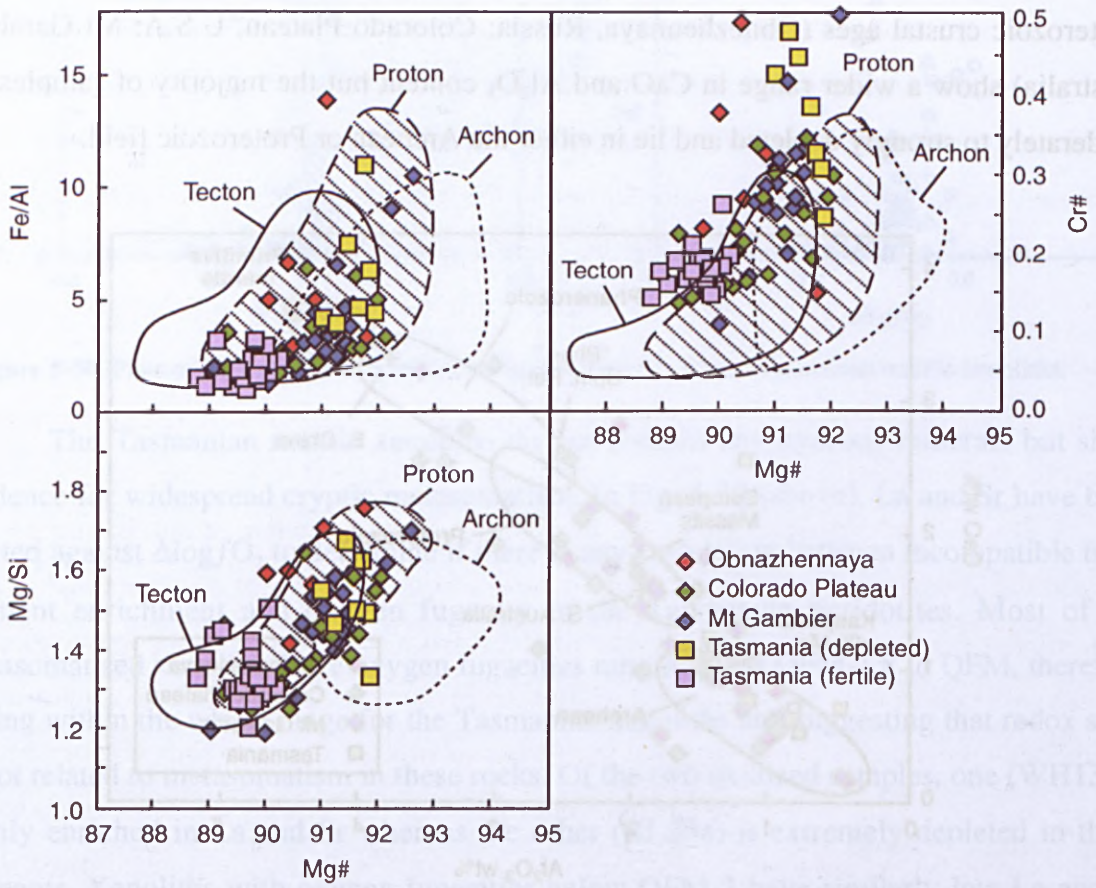


**Figure 5-32.** Whole rock compositional data for spinel peridotites from Tasmania and regions of known Proterozoic crustal age. Fields for Archon, Proton and Tecton xenoliths from Griffin *et al.* (1998b).

## 5.9 DISCUSSION

### *5.9.1 Continental extension and asthenospheric upwelling in northern Tasmania*

One of the principal aims of this study was to determine if a link can be made between mantle geochemistry and crustal terrains of Phanerozoic and Proterozoic age. In Tasmania it was expected that the mantle xenoliths sampled beneath Proterozoic terrains might resemble depleted Proterozoic lithosphere elsewhere, while those associated with Phanerozoic crust might be more fertile and representative of Phanerozoic lithosphere. In fact, the majority of Tasmanian mantle xenoliths are fertile, even in regions where they have been erupted through Proterozoic crust; the xenoliths with the most fertile compositions are found in the Rocky Cape Element, which has yielded some of the oldest crustal ages in Tasmania. This suggests that any depleted Proterozoic lithosphere that was once coupled to Proterozoic crust in Tasmania has been either removed and replaced by younger, chemically fertile lithosphere, or refertilised by the infiltration of asthenospheric melts.

The majority of the Tasmanian mantle xenoliths studied here have whole-rock compositions that are depleted relative to common estimates for primitive mantle (McDonough and Sun, 1995) and, despite evidence for later cryptic metasomatism, they do not appear to have been substantially refertilised. The very low degrees of depletion (<5% partial melting of a primitive source as modelled in Section 5.3) observed in the Tasmanian xenoliths suggest that they represent little-modified asthenospheric mantle, which has been emplaced beneath the continent from below to form new lithosphere. The garnet peridotite xenoliths from Table Cape (Sutherland *et al.*, 1994) are also highly fertile rocks, and quite unlike the depleted garnet peridotites characteristic of Archean and Proterozoic mantle sections. A few chemically depleted (high olivine Mg#) samples from Coates Road, South Riana and Wagners Hill have anomalously high modal clinopyroxene and could represent refertilised lithosphere.

Young subcontinental lithospheric mantle might be added to continents by two basic mechanisms: lateral accretion of material from convergent continental margins (either subducting oceanic lithosphere or material from the mantle wedge above Benioff zones), or underplating by material rising from below (Griffin *et al.*, 1999a). The Tasmanian fertile xenoliths have a wide range in olivine contents but uniformly low olivine Mg# so that they lie along, or adjacent to, the "oceanic trend" of Boyd (1997). This might suggest that they represent oceanic peridotites. However, peridotites from convergent-margin settings are significantly more depleted in terms of Ca and Al than

those from young intraplate settings and typically have lower median Ca/Al and higher Fe/Al than the latter despite their similar Mg# (Griffin *et al.*, 1999a). In addition, most oceanic peridotites have undergone extreme modification of their Ca and Al contents during ocean floor metamorphism so that in detail they do not resemble the fertile peridotites studied here. Therefore, the "oceanic trend" may simply reflect melt extraction at relatively shallow depths; a process that can produce both subcontinental and suboceanic lithosphere (Boyd, 1997).

If the Tasmanian mantle xenoliths represent little-modified asthenospheric mantle accreted beneath the continent then what mechanism effected their emplacement? Generation of Phanerozoic lithospheric mantle is thought to occur either in extensional environments (Jochum *et al.*, 1989) or by accumulation of fossil plume heads in intraplate environments (Stein and Hofmann, 1994). The most recent major extensional event to affect Tasmania was the rifting of Australia from Antarctica during the break-up of Gondwana. This produced the Early Cretaceous failed rift to the north of Tasmania, between Antarctica and mainland Australia (which at that time included Tasmania), the middle Cretaceous to Paleocene rift between Antarctica and Australia along the Tasmanian west coast, and the middle Cretaceous to Paleocene rift between New Zealand and Australia along the Tasmanian east coast. Rifting around Tasmania was accompanied by formation of a number of extensional sedimentary basins, both offshore and onshore, tectonic uplift, crustal magmatism and widespread normal faulting (Seymour and Calver, 1995).

Uplift and magmatism during extension are generally attributed to upwelling of the asthenosphere to shallow depths. Replacement of cold, relatively dense lithosphere by hot, buoyant asthenosphere elevates continental margins as the lithosphere is heated and stretched. Uplift is also thought to be related to underplating by basaltic magmas produced by partial melting of the rising asthenosphere. These magmas are less dense than their parental mantle source and consequently segregate and migrate upwards through the mantle until they reach the density drop at the crust-mantle boundary where they pond and solidify. The extent of uplift in eastern Tasmania is thought to have been on the km-scale, as estimated from denudation rates, following the onset of continental extension in the Tasman Sea at ~96 Ma (O'Sullivan *et al.*, 1998). This uplift has been interpreted as possibly resulting from underplating inward of the rift as postulated for much of the southeastern highlands of Australia.

Asthenosphere upwelling beneath northern Tasmania can be further confirmed by studies of the basalts erupted during Tertiary time. Isotopically, the Tasmanian lavas define the extreme end of the alkaline basaltic field (i.e. they are the most radiogenic in terms of $^{206}Pb/^{204}Pb$), which is interpreted as consistent with an asthenospheric isotopic signature (Ewart, 1989). These rocks also have Nd- and Sr-isotopic compositions that approach those of the present-day depleted mantle, with $\varepsilon_{Nd}$ values in the range +5 to +8 and $^{87}Sr/^{86}Sr$ values commonly <0.7030 (Foden *et al.*, 2002). Some of the alkali basalts from Tasmania are characterised by high-μ (high $^{238}U/^{204}Pb$) type isotopic signatures, which have been interpreted as evidence for interaction between the depleted mantle source and the Balleny plume (Lanyon *et al.*, 1993). This plume is currently situated beneath the Balleny Islands in the Ross Sea region of Antarctica but is believed to have been located just east of Tasmania at ~40-45 Ma (Lanyon *et al.*, 1993).

Other evidence that northern Tasmania is underlain by fertile lithosphere comes from geophysical studies. The seismic velocity of peridotite increases with its degree of depletion. Seismic velocities calculated by Griffin *et al.* (1999a) for typical Tecton, Proton and Archon mantle compositions show that the Vp value calculated for Tecton SCLM at 50 km (i.e. where Tecton mantle will be in the spinel peridotite facies) is 7.86 km/s compared to 8.10 km/s for Proton SCLM and 8.18 km/s for Archon SCLM at the same depth. The relatively low mantle velocities (~7.9 km/s) revealed by recent AGSO seismic surveys of the Tasmanian lithosphere (Rawlinson *et al.*, 1998) are consistent with the Vp estimate for Tecton SCLM and confirm the overall fertile nature of the mantle beneath northern Tasmania.

### *5.9.2 Lithosphere delamination in northern Tasmania*

Both the Rocky Cape and Northeast Tasmania Elements contain a subset of strongly depleted xenoliths that are compositionally similar to spinel peridotites from worldwide Proterozoic terrains (see Section 5.8). Equilibrium temperatures calculated for the depleted peridotites from Coates Road Quarry are low compared to those for fertile samples from the same locality, indicating that the more refractory xenoliths were residing at shallower depth. In the case of Table Cape and Blessington, the depleted xenoliths give similar equilibrium temperatures to the fertile peridotites suggesting that the two mantle types are intercalated at shallow depths. These more depleted peridotites may indicate the presence of remnant Proterozoic SCLM, embedded in the Cenozoic lithosphere, that has persisted to at least the time of xenolith entrainment.

The scarcity of depleted xenoliths suggests that the Proterozoic SCLM in Tasmania has been largely removed and replaced by more fertile material or transformed, but how was this accomplished? Density calculations for SCLM of different ages show that depleted Proterozoic SCLM is quite buoyant relative to "asthenosphere" and is, therefore, difficult to remove by gravitational forces alone (O'Reilly *et al.*, 2001; Poudjom Djomani *et al.*, 2001). While a detailed discussion of possible scenarios for lithosphere replacement is outside the scope of this study, one potential mechanism has been suggested in Yuan (1996) based on geological and geophysical studies of the Sino-Korean craton. Detailed seismic tomography of part of the eastern Sino-Korean craton, an area of very high heat flow, shows a lithospheric mantle made up of vertically and laterally extensive blocks of high-velocity (probably Archean) mantle embedded in a matrix of lower-velocity (presumably Cenozoic) mantle. Yuan (1996) suggests that this heterogeneity reflects the disruption of the Archean lithosphere due to rifting and contemporaneous upwelling of fertile asthenospheric material along breaks in the cratonic root. This has then lead to mechanical dispersal, heating and "dilution" of the ancient SCLM, rather than its simple removal or delamination. Whether this mechanism effected the removal of Proterozoic mantle in Tasmania is difficult to ascertain based on data from scattered localities. More data on the lateral, vertical and temporal variations in the composition of the Tasmanian lithosphere, and integration with regional geophysical data, are required for further discussion of this problem.

Highly fertile SCLM is common beneath Palaeozoic-Mesozoic mobile belts. This is thought to be related to the higher intrinsic density of Phanerozoic mantle sections. These sections are commonly less than 100 km thick and buoyant relative to asthenosphere when the geotherm is sufficiently high, as in many Cenozoic volcanic provinces. However, once they have cooled to typical steady-state conductive geotherms they become denser than the underlying asthenosphere, and therefore gravitationally unstable. As the cooled mantle founders and sinks, upwelling asthenospheric material will fill the resulting "space" and subsequently raise geotherms and possibly cause melting in the crust (Griffin *et al.*, 1998b). As the new lithospheric mantle cools down, it in turn will become unstable and start another cycle of cooling, instability and delamination. This cycle may explain the ubiquitous presence of fertile xenolith suites in basalts erupted through Phanerozoic orogenic belts, where instead it might be expected to find depleted oceanic and arc-related peridotites (Griffin *et al.*, 1999a; Poudjom Djomani *et al.*, 2001).

### *5.9.2 A thermal anomaly in northwestern Tasmania?*

Heat flow studies of Tasmania have shown that it has an unusually high heat flux (>80 $mWm^{-2}$) which may reflect extensive melting in the upper mantle beneath Tasmania (Richardson, 1989a). According to the heat flow maps of Australia produced by Cull (1982) and Cull and Conley (1983) the northwestern part of Tasmania has an anomalous heat flow value of 90 $mWm^{-2}$. This implies a localised thermal perturbation beneath the Rocky Cape Element. Rifting along the western coast of Tasmania between Australia and Antarctica during the Cenozoic resulted in higher heat flow in western Tasmania (O'Sullivan *et al.*, 1998) and could be responsible for the thermal anomaly beneath the Rocky Cape Element.

Mantle xenoliths have revealed that the Rocky Cape Element is underlain by highly fertile material that is not recognised beneath either the Sheffield or Northeast Tasmanian Elements. Crustal thickness at Coates Road Quarry has been estimated at 26 km which suggests thinning of the lithosphere and upwelling of asthenosphere to shallow levels beneath northwestern Tasmania. This could explain the extremely high (>1400°C) equilibrium temperatures calculated for the garnet peridotites from Table Cape (Sutherland *et al.*, 1996). If the geotherm for northwestern Tasmania is raised relative to the southeastern Australia geotherm then this casts some doubt on the usefulness of the temperatures calculated in this study for the spinel-bearing peridotites from the Rocky Cape Element. It is possible, that temperatures extrapolated to the SEA geotherm have been somewhat underestimated and do not represent the true thermal state in the shallow lithosphere beneath northwestern Tasmania.

## 5.10 SUMMARY

(1) The Tasmanian xenoliths can be described in terms of three major compositional groups. The first group is highly fertile and occurs only in the Rocky Cape Element. The second group is moderately fertile and is found in all three Elements. The third group is depleted and is represented in the Rocky Cape and Northeast Tasmania Elements.

(2) Modeling of trace element patterns in clinopyroxenes indicates that the fertile Tasmanian peridotites have experienced less than 5% (batch or fractional) partial melting and the fertile Rocky Cape peridotites have experienced less than 2% melting. The depleted xenoliths from the Rocky Cape Element can be modelled by 8-15% fractional partial melting but require unreasonable degrees of melting (30-50%) if a batch melting

model is used. The refractory peridotites from the Northeast Element can be modelled by ~8% fractional melting or ~20% batch melting. Melt depletion in the Tasmanian xenoliths appears to have occurred in the spinel stability field, based on the good match between clinopyroxene depleted compositions and the predicted patterns for melting in the spinel field.

(3) The majority of Tasmanian xenoliths show evidence for cryptic metasomatism. Clinopyroxene trace element patterns show enrichment in the LREE, Sr, U and Th. These patterns can be modelled by simple mixing between moderately depleted (~5% melting) peridotite and 3-15% dolerite. A few xenoliths are characterised by low Ti/Eu and moderately high La/Yb, and may reflect mixing between fertile peridotite and <1% carbonatite. Many of the samples from Wagners Hill, Arthur River and Doctors Rocks display a range in clinopyroxene REE patterns from depleted through U-shaped to enriched in LREE and MREE that suggests that the chromatographic effect has played a major role in the trace element enrichment of these rocks.

(4) Equilibrium temperatures have been calculated for the Tasmanian mantle xenoliths and comparisons made using the opx-sp thermometer of Sachtleben and Seck (1981) and the Cr-Al-opx thermometer of Witt-Eickschen and Seck (1991). Temperatures have been referred to the southeastern Australian geotherm to estimate pressures and depths. Fertile peridotites from the Rocky Cape Element give temperatures ranging from 900-1030°C which are equivalent to depths of 36-52 km. Depleted peridotites from the Coates Road Quarry locality give low temperatures (800-830°C) suggesting that they were derived from shallow mantle depths (~26 km). Xenoliths from the Sheffield Element show a range in temperature from 850-1030°C. The high temperatures are restricted to a group of coarse-grained peridotites from South Riana which show petrographic evidence for heating by the host basalt during ascent. Temperatures for peridotites from the Northeast Tasmania Element range from ~800-950°C, corresponding to depths of 26-42 km. Compositional zoning in some samples from Blessington gives elevated core temperatures relative to rims suggesting a high-temperature origin for these xenoliths.

(5) The depth to the crust-mantle boundary across northern Tasmania has been determined by extrapolating xenolith temperatures to the southeastern Australian geotherm. The CMB is poorly constrained beneath the Rocky Cape Element but may be as shallow as 26 km. The CMB is well-defined at 31-32 km beneath the Sheffield Element and Blessington in the Northeast Tasmania Element and coincides with Moho depths derived from wide-angle seismic surveys. The depth to the CMB at Wagners Hill is

estimated as 36 km.

(6) Oxygen fugacities calculated for Tasmanian peridotites do not show any obvious correlation with xenolith composition, and also confirm the lack of a consistent world-wide relationship between mantle metasomatism and the oxygen fugacity of spinel peridotites.

(7) The compositional similarity between the depleted xenoliths from Tasmania and spinel peridotites from known Proterozoic terrains suggests that there may be remnants of older lithosphere preserved beneath Tasmania.

(8) The scarcity of such depleted lithosphere remnants, and the extensive occurrence of hot, fertile lithosphere beneath northern Tasmania, are linked to asthenosphere upwelling during rifting between Australia and Antarctica.

(9) The presence of very fertile peridotite beneath the Rocky Cape Element coupled with high heat flow is evidence for upwelling of asthenosphere to shallow levels and thinning of the crust in northwestern Tasmania.

# CHAPTER 6
# MANTLE PERIDOTITES OF THE WESTERN GNEISS REGION, NORWAY

## 6.1 INTRODUCTION

One aim of this thesis is to compare postulated Proterozoic mantle in Tasmania with mantle of established Proterozoic age elsewhere, to evaluate the worldwide similarity in mantle of this age. A direct comparison would, ideally, involve peridotite xenoliths erupted through Proterozoic crust as seen in northern Tasmania. However, there appears to be a worldwide paucity of mantle xenolith suites from areas with Proterozoic crust. An alternative to using mantle xenoliths is to use crustal peridotites from orogenic massifs as they provide an analogous database for the lithospheric mantle and can be used in conjunction with data from basalt-borne and kimberlite-borne xenoliths (Menzies and Dupuy, 1991). In addition, massif peridotites have the advantage of being large enough to establish spatial and temporal relationships among rock types.

Many orogenic massifs have yielded Proterozoic Re-Os depletion ages including the Ronda peridotite in Spain and several Pyreneean and Swiss massifs (Reisberg and Lorand, 1995; Meisel *et al.*, 1996a). Garnet peridotite massifs from the Western Gneiss Region, Norway have yielded Proterozoic Sm-Nd mineral ages (Mearns, 1986; Jamtveit *et al.*, 1991; Brueckner and Medaris, 1998) and may therefore represent relatively unmodified Proterozoic SCLM.

## 6.2 GEOLOGY OF THE WESTERN GNEISS REGION

### *6.2.1 Geological setting*

The Scandinavian Caledonides are a north-south trending, early to middle Palaeozoic mountain belt that evolved during closure of the Iapetus ocean basin and the westward subduction of the Baltic shield beneath Laurentia (Brueckner, 1998). The Caledonides can be divided into five major complexes, the autochthon (and parautochthon), and the lower, middle, upper and uppermost allochthons (Roberts and Gee, 1985; Stephens and Gee, 1985) (Fig. 6-1). The *autochthon* and *parautochthon* consist of Precambrian (Mid-Proterozoic and older) crystalline basement and a sedimentary cover of Upper Proterozoic and/or Lower Paleozoic age. The *lower allochthon* consists of

imbricated thrust slices of Precambrian crystalline rock and Upper Proterozoic and/or Lower Paleozoic sedimentary cover. The *middle allochthon* is made up of sheets of Precambrian crystalline rocks and sandstone-dominated successions of Upper Proterozoic age. The *upper allochthon* comprises high grade metamorphic rocks (Seve Nappes) overlain by several nappes consisting of volcano-sedimentary sequences of ophiolite and island arc affinity. The *uppermost allochthon* (to the north of Fig. 6-1) consists mainly of high-grade metamorphic rocks of continental affinity that are considered to be exotic with respect to Baltoscandia.

The Western Gneiss Region (WGR), or Basal Gneiss Complex, forms an elongate area, 300 km long and 150 km wide, along the western coast of Norway from Bergen in the south to Trondheim in the north (Cuthbert *et al.*, 2000). The WGR is the basement to an assembly of thrust sheets emplaced onto the Baltoscandian continental margin during the final phase of the Caledonian orogeny (Coleman and Wang, 1995). Considered to be autochthonous or parautochthonous crystalline basement of Middle Proterozoic or older age, the WGR contains interfolded nappes that have been divided into two principal lithotectonic units: (1) the HP/UHP (high pressure/ultra-high pressure) metamorphosed Fjordane complex, a mixed assembly of gneiss, supracrustals, anorthosites, augen gneisses and eclogites, exposed to the north and west; (2) the Jøstedal complex, a more monotonous migmatitic orthogneiss unit to the east (Griffin *et al.*, 1985; Ernst *et al.*, 1995).

The gneisses of the Fjordane Complex are associated with rocks that are largely supracrustal in origin and consist of interlayered pelitic and igneous migmatites, marbles, quartzites, and amphibolites. The complex also includes gabbro, anorthosite, eclogite and peridotite which have been interpreted as either tectonic inclusions or intrusives (Ernst *et al.*, 1995). Foliated intermediate to acidic igneous rocks intrude the gneisses; a prominent intrusive type is distinctive "rapakivi granites" or "augen gneisses" (Griffin *et al.*, 1985). These Fjordane Complex units exhibit predominantly amphibolite-facies mineralogy. However, relicts of high-pressure assemblages are locally abundant such as clinopyroxene + garnet + quartz + K-spar + kyanite in the rapakivi granites (Cuthbert *et al.*, 1983; Griffin *et al.*, 1985). Similar granulite-facies assemblages occur in anorthosites and other rock types. These relict granulite-facies assemblages show variable degrees of retrogression to amphibolite-facies assemblages (Griffin *et al.*, 1985). Other high-pressure rocks in the Fjordane Complex are eclogites and garnet-bearing peridotites.

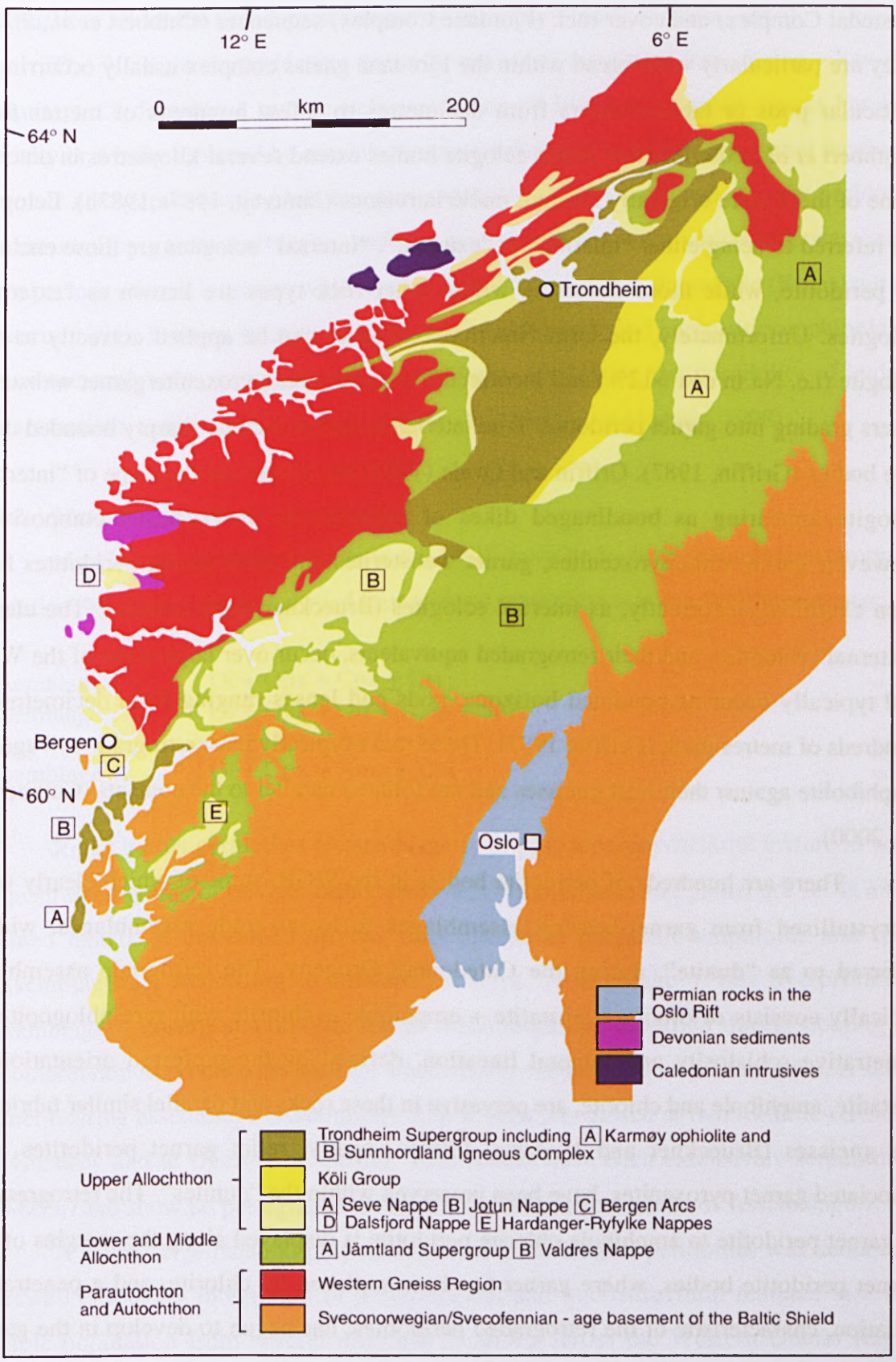


**Figure 6-1.** Map showing the main tectonostratigraphic units of the southern Scandinavian Caledonides After Cuthbert *et al.* (1983).

Eclogites are relatively common throughout the WGR within both basement (Jøstedal Complex) and cover rock (Fjordane Complex) sequences (Cuthbert *et al.*, 2000). They are particularly widespread within the Fjordane gneiss complex usually occurring as lenticular pods or tabular layers from decimetres to a few hundreds of metres thick (Cuthbert *et al.*, 2000). A few larger eclogite bodies extend several kilometres in outcrop; some of these were originally layered, mafic intrusions (Jamtveit, 1987a;1987b). Eclogites are referred to being either "internal" or "external". "Internal" eclogites are those enclosed by peridotite, while those occurring within other rock types are known as "external" eclogites. Unfortunately, the term "internal" eclogites can be applied correctly to true eclogite (i.e. Na in cpx >12%) and incorrectly to garnet clinopyroxenite/garnet websterite layers grading into garnet peridotite. True internal eclogites include sharply bounded dike-like bodies (Griffin, 1987). Griffin and Qvale (1985) recognised another type of "internal" eclogite appearing as boudinaged dikes of superferrian (FeTi) basalt composition. However, garnet clinopyroxenites, garnet websterites and even garnet peridotites have been classified, incorrectly, as internal eclogites (Brueckner, pers. comm.). The classic "external" eclogites, and their retrograded equivalents, occur over large areas of the WGR and typically occur as boudined horizons, pods and lenses ranging from decimetres to hundreds of metres thick (Griffin, 1987). These rocks typically have retrograde selvages of amphibolite against their host gneisses and are foliated parallel to the contacts (Cuthbert *et al.*, 2000).

There are hundreds of peridotite bodies in the WGR, some of which clearly were recrystallised from garnet-bearing assemblages to lower-grade assemblages, widely referred to as "dunite", during the Caledonian Orogeny. The retrograde assemblage typically consists of olivine + enstatite + amphibole + chlorite with rare phlogopite. A penetrative schistosity and mineral lineation, defined by the preferred orientation of enstatite, amphibole and chlorite, are pervasive in these rocks and parallel similar fabrics in the gneisses (Brueckner and Medaris, 1998). Locally, relict garnet peridotites, and associated garnet pyroxenites, have been preserved within the "dunites". The retrogression of garnet peridotite to amphibole-chlorite peridotite is displayed along the margins of the garnet peridotite bodies, where garnet has been replaced by chlorite, and a penetrative foliation, characteristic of the retrograded peridotites, has begun to develop in the garnet peridotite (Medaris, 1984). The peridotites contain several generations of folds that are identical in geometry and orientation to the folds in the surrounding gneisses indicating

that the peridotites and gneisses shared a common ductile structural history during much, and possible all, of the Caledonian Orogeny (Brueckner, 1969; Medaris, 1984).

The WGR garnet peridotites typically consist of the assemblage olivine + low-Al + enstatite + Cr-diopside + pyrope-rich garnet though in some instances garnet has been partially or wholly replaced by amphibole-spinel kelyphite. In addition to garnet lherzolites there are also garnet-bearing harzburgites and dunites. On a local scale, garnet peridotites are intruded by garnet websterite, wehrlite and clinopyroxenite, which indicates one or more periods of melt intrusion while the peridotites were still in the mantle (Brueckner and Medaris, 1998). Primary hydrous phases, such as phlogopite and kaersutitic amphibole, are associated with some garnet-bearing assemblages, suggesting the possibility of hydrous metasomatism, again while still in the mantle (Brueckner and Medaris, 1998).

### *6.2.2 Metamorphism*

Mg-Cr type peridotite bodies in the WGR have had a long, complex metamorphic evolution. Medaris (1984) identified four mineral assemblages in the WGR peridotites.

| | |
|---|---|
| Assemblage 1. | Ol + Opx + Cpx + Grt |
| Assemblage 2. | Ol + Opx + Grt + Amp + Spl |
| Assemblage 3. | Ol + Opx + Amp + Spl |
| Assemblage 4. | Ol + Opx + Amp + Chl |

Relict garnet peridotites (Assemblage 1) display a porphyroclastic texture in which large strained grains of olivine, orthopyroxene, clinopyroxene and garnet are set in a fine-grained matrix of unstrained olivine, orthopyroxene, pargasitic amphibole and spinel (Assemblage 3). According to Medaris' scheme, Assemblage 1 was overprinted by Assemblage 3 during amphibolite facies metamorphism, modified during cooling and decompression to produce assemblage 4 and finally subjected to serpentinisation. A second garnet-bearing assemblage (Assemblage 2) has been recognised at two localities (Rødskar on Gurskøy and at Ugelvik on Otrøy). These rocks have been extensively serpentinised (50-60%) and show no petrographic evidence for the prior existence of Assemblage 1.

A seven-stage metamorphic history for the Norwegian peridotites was deduced by Carswell (1986) by integration of mineralogical and microstructural features in a large sample population from several different localities across the Western Gneiss Region. Most individual Mg-Cr peridotite samples contain disequilibrium mineral assemblages corresponding to at least two, but never all seven, of the metamorphic stages (Jamtveit *et al.*, 1991).

| *Stage* | | *Interpretation* |
|---|---|---|
| I | Ol + Opx + Cpx + Spl + Amp | High-temperature protolith |
| II | Ol + Opx + Cpx + Grt | Coarse-grained eclogite facies |
| III | Ol + Opx + Cpx + Grt + Spl | Fine-grained neoblast eclogite facies |
| IV | Ol + Opx + Cpx + Spl | Kelyphitic granulite facies |
| V | Ol + Opx + Amp + Spl | Coronitic/foliated high amphibolite facies |
| VI | Ol + Opx + Amp + Chl | Foliated low amphibolite facies |
| VII | Serp + Talc + Amp + Chl | Localised greenschist facies |

Stage I was inferred by Carswell and was supposed to be a spinel peridotite (Carswell *et al.*, 1983; Carswell, 1986). This assemblage originally was based on a single sample, the provenance of which is now uncertain (Brueckner, pers. comm.). Stages II (Assemblage 1 of Medaris, 1984) and III (Assemblage 2 of Medaris, 1984) are characterised by garnet-bearing assemblages and while Carswell would now probably consider them to be Stage I and II (Brueckner, pers. comm.) the original classification will be used here to avoid any confusion. Stage II assemblages are four-phase (grt + cpx + opx + ol) garnet peridotite (lherzolite) displaying inequigranular textures with large strained clasts (up to 2 cm across) of orthopyroxene, clinopyroxene, garnet and more rarely olivine in a much finer-grained matrix of essentially strain-free olivine grains. In contrast, the five-phase Stage III assemblage (Stage II phases + spinel) is comprised of smaller (<1 mm) neoblasts adjacent to, and probably formed by strain-induced recrystallisation of, larger Stage II clasts (Jamtveit *et al.*, 1991). The lower Cr content of Stage III garnets (compared to the Stage II garnet), and its co-existence with Cr-rich spinel, is further evidence for the recrystallisation of a high-P Stage II assemblage to a lower pressure Stage III assemblage.

Petrological evidence for an early, high-T pre-stage II assemblage in the WGR peridotites includes reaction coronas of garnet around aluminous spinel (Carswell *et al.*, 1983), orthopyroxene megacrysts with exsolved clinopyroxene and garnet in a garnet pyroxenite from Ulgevik (Carswell, 1973), and clinopyroxene megacrysts with exsolved orthopyroxene and garnet from a garnet clinopyroxenite at Aldalen (Medaris, unpubl.). So far none of these occurrences have provided conclusive proof for a high-T protolith for the Norwegian peridotites. A low-P protolith has been suggested by the presence of chlorite inclusions in stage II garnet from a garnet pyroxenite from Gurskebotn (Jamtveit, 1984). However, stage II garnet in this sample also contains inclusions of pargasitic amphibole, and an alternative interpretation is that garnet host and chlorite and amphibole inclusions represent an early lower temperature, but high pressure, assemblage in pyroxenite (Medaris and Carswell, 1990). The recent discovery of majoritic (high-Si) garnets in garnet

peridotites from Otrøy has been cited as evidence for an early high-P-T stage (6 GPa, 1200°C) (van Roermund and Drury, 1998; van Roermund *et al.*, 2000).

The prevailing pattern of post-garnet peridotite recrystallisation (Stages III to VII) is one of decompression, cooling and the introduction of $H_2O$. The retrograde metamorphic path for these peridotites is characterised by an initial large drop in pressure relative to temperature (Stages III → V) followed by cooling during Stages VI and VII (Carswell, 1986). Stage IV is apparent in most samples and is characterised by development of kelyphites of intergrown pyroxenes + spinel around garnets. These are in turn frequently overgrown by later Stage V (Assemblage 3 of Medaris, 1984) coarse-grained coronas of orthopyroxene + pargasitic amphibole + spinel. Stages VI (Assemblage 4 of Medaris, 1984) and VII reflect the late-stage stability at reduced temperatures of firstly aluminous chlorite and finally serpentine + talc assemblages (Carswell, 1986).

### *6.2.3 Geochronological framework*

The evolution of the WGR is complex and is the result of several orogenic episodes in the period 1700-380 Ma (Kullerud *et al.*, 1986). These episodes can be briefly summarised as follows:

(1) 1700-1600 Ma ⇒ Extensive crustal formation during the Gothian Orogeny as evidenced from Sm-Nd, Rb-Sr whole rock and U-Pb zircon results (Brueckner, 1972; Pidgeon and Råheim, 1972; Brueckner, 1979; Lappin *et al.*, 1979; Mearns, 1984).

(2) 1500-1400 Ma ⇒ a period of relative quiescence with intermittent mafic intrusions and possibly also sporadic granitic magmatism (Gaal and Gorbatschev, 1987).

(3) 1300-900 Ma ⇒ Extensive intrusion, of dolerites and granites, associated with the Sveconorwegian (Grenvillian) Orogeny (Mearns, 1984; Mørk and Mearns, 1986).

(4) ca. 700 Ma ⇒ Rifting to form the Iapetus Ocean, associated intrusion of dolerite dykes, and uplift followed by cooling of lower-crustal rocks (Mearns, 1984).

(5) 500-400 Ma ⇒ Closure of the Iapetus Ocean culminates in the Scandian Orogeny at ca. 410 Ma. Resulting high-P regional metamorphism leads to formation of eclogites and deformation of the Gothian and Sveconorwegian rocks of the WGR (Cuthbert *et al.*, 1983; Mearns, 1986).

(6) 400-380 Ma ⇒ Uplift and cooling of the terrain leads to widespread retrogression of the high-P metamorphic assemblages (Lux, 1985; Jamtveit, 1987a).

The structural and petrological features in the rocks of the present day WGR are largely the result of Caledonian reworking. This reworking appears to have been largely domainal. Where water was introduced or where strain rates were high reworking was extensive and manifested as foliations, and east-plunging mineral lineations and folds, whereas dry areas or zones of low strain preserve "enclaves" of Proterozoic igneous and metamorphic structures and fabrics.

## 6.3 PREVIOUS WORK

Since 1921, when Pentti Eskola published his classic treatise on the eclogites of the Western Gneiss Region, there has been interest in the evolution of these rocks and related rock types. Eskola recognised that the eclogites and associated garnet peridotites must have formed at higher pressures than chemically equivalent basalts and spinel peridotites, and proposed that they represented samples of the upper mantle. O'Hara and Mercy (1963) argued that the Norwegian garnet peridotites and "internal" eclogites are chemically different from similar material found as xenoliths in kimberlite pipes but still came to the conclusion that these rocks were derived from the upper mantle. This interpretation was followed by O'Hara and a series of co-workers (Lappin, 1966; O'Hara, 1967; Carswell, 1968a, 1968b; O'Hara *et al.*, 1971; Lappin, 1974; Lappin and Smith, 1978) and extended to include not only the garnet peridotites but also the "external" eclogites enclosed in the gneisses.

This led to an interesting controversy as another school of thought had suggested that all the external eclogites, and possibly some of the internal ones, found in western Norway may be essentially *in situ* crustal metamorphic rocks (Bryhni, 1966; Bryhni and Green, 1970; Bryhni *et al.*, 1969; Green and Mysen, 1972; Griffin and Råheim, 1973). Carswell (1974) reconsidered the crustal versus mantle origin problem for the garnet lherzolites on the basis of their temperature-pressure estimates and concluded that they equilibrated at depths greater than 70 km along an expected sub-continental geotherm. This result was shown to contrast with previous estimates for the "external" eclogites, and a possible dual paragenesis of the Norwegian garnet-bearing rocks was proposed, with the garnet lherzolites and associated "internal" eclogites being tectonic slices of the upper mantle thrust into the basal crustal rocks during a major orogenic event and the "external" eclogites being deep crustal (i.e. "*in situ*") metamorphic rocks. Further evidence for the crustal origin of the "external" eclogites came from Krogh (1977) who used geothermobarometry and mineral zoning to conclude that the eclogites represent crustal

rocks metamorphosed *in situ* from low-P protoliths during subduction of continental crust to depths of 65-80 km.

A dual origin for Norwegian eclogites and garnet peridotites was also supported by Brueckner's (1977) strontium isotope analyses of clinopyroxene from these rock types. The country-rock eclogites were shown to have high $Sr^{87}/Sr^{86}$ ratios (0.707-0.715) suggesting that they either originated from crustal material or that they originated from mantle material, but were contaminated by crustal fluids before or during eclogite-facies metamorphism (Brueckner, 1977). The latter process requires a rather complex history of intrusion, contamination accompanied by hydration, subsequent dehydration, and finally eclogite-facies metamorphism which seemed rather contrived when compared to the crustal mechanism (Brueckner, 1977). The lower $Sr^{87}/Sr^{86}$ values (0.701-0.703) of cpx from the garnet peridotites indicated that they formed from mantle material and had escaped contamination (Brueckner, 1974; Brueckner, 1977).

The timing of eclogite facies metamorphism in the WGR has also been subject to controversy. Krogh (1977) proposed a Precambrian age for eclogite formation in the WGR based on K-Ar dating of amphiboles (McDougall and Green, 1964). However, U-Pb dating of metamorphic zircons from the eclogites yielded ages of 401±20 Ma (Krogh *et al.*, 1974) and 446 +54/-65 Ma (Gebauer *et al.*, 1985) suggesting that the eclogite facies metamorphism was a Caledonian event. This was substantiated by Sm-Nd cpx-grt dating of external eclogites by Griffin and Brueckner (1980) which gave an average age of 425±20 Ma. Further Sm-Nd dating (Mearns and Lappin, 1982; Griffin and Brueckner, 1985; Mørk and Mearns, 1986) also produced Caledonian ages for the eclogites as has recent U-Pb zircon geochronology which gives ages clustering around 405-410 Ma (Root *et al.*, 2001). These ages were seen to support a crustal origin for the eclogites and it was concluded that the eclogite-forming event in western Norway was the result of high-pressure metamorphism in the subducting Baltic plate during the Caledonian orogeny.

Attempts to date the garnet peridotites using the Sm-Nd isotopic method have given equivocal results. Several Sm-Nd garnet-clinopyroxene-whole rock dates for the garnet peridotites range from 1700-1000 Ma (Jacobsen and Wasserburg, 1980; Mearns, 1986). Mearns (1986) and Jamtveit *et al.* (1991) published a Proterozoic age (1703±29 Ma) for Stage II garnet assemblages but the latter found that two samples with Stage III assemblages gave a younger age (437±58 Ma and 511±18 Ma) that may be related to the Caledonian orogeny. Another interesting outcome from the same study stems from the convergence of whole-rock Nd-isotope evolution curves at 3000-2500 Ma which led the

authors to speculate on a possible Archean age for the peridotite protoliths (Jamtveit *et al.*, 1991). This would imply, they argue, formation of the peridotites long before the crustal rocks of the WGR and suggests that they are genetically unrelated to their host. Consequently the peridotites may reflect a mantle depletion which was not associated with crustal growth in this part of the Baltic Shield.

Recent papers on the WGR have focussed on contrast and comparison with other Eurasian peridotite massifs (Medaris and Carswell, 1990; Ernst *et al.*, 1995; Krogh and Carswell, 1995; Brueckner and Medaris, 1998; Carswell *et al.*, 1999; Medaris, 1999). In the light of geochemical, geothermobarometric and geochronological data it is now widely accepted that the garnet peridotite bodies in the WGR are unique and represent the only current example of ancient subcontinental lithosphere that has been tectonically emplaced into the crust with its upper mantle assemblages intact (Medaris, 1999; Brueckner and Medaris, 2000). In addition, the discoveries of coesite and (micro)diamond in eclogites and gneisses has led several workers (Smith, 1984; Dobrzhinetskaya *et al.*, 1995; Wain, 1997) to redefine the WGR as an ultra-high-pressure metamorphic terrain. This has been supported by the discovery of relict majoritic garnet within garnet peridotites from Otrøy in the northwestern WGR (van Roermund and Drury, 1998; van Roermund *et al.*, 2000; Drury *et al.*, 2001; van Roermund *et al.*, 2001) and has led to the suggestion that the Otrøy peridotites originated in the asthenosphere and were emplaced into the lithosphere by asthenospheric diapirism (van Roermund *et al.*, 2001).

## 6.4 SAMPLES

### *6.4.1 Localities*

The majority of peridotite samples used in this study were collected by S.Y. O'Reilly and W.L. Griffin in 1997; another four samples are from W.L. Griffin's earlier collections. Samples were collected from seven different localities (see Figs 6-2 and 6-3). The southernmost locality is at Levdal in Nordfjord. Another three localities, Raudkleivane, Helgehornsvatn and Ekremseter, are located in the Almklovdalen peridotite mass which is approximately 10 km northeast of Levdal. Two localities, Gurskebotn and Sandvika, are located on the island of Gurskøy about 20 km north of Almklovdalen, while the last locality is at Ugelvik on the island of Otrøy in the northern WGR.

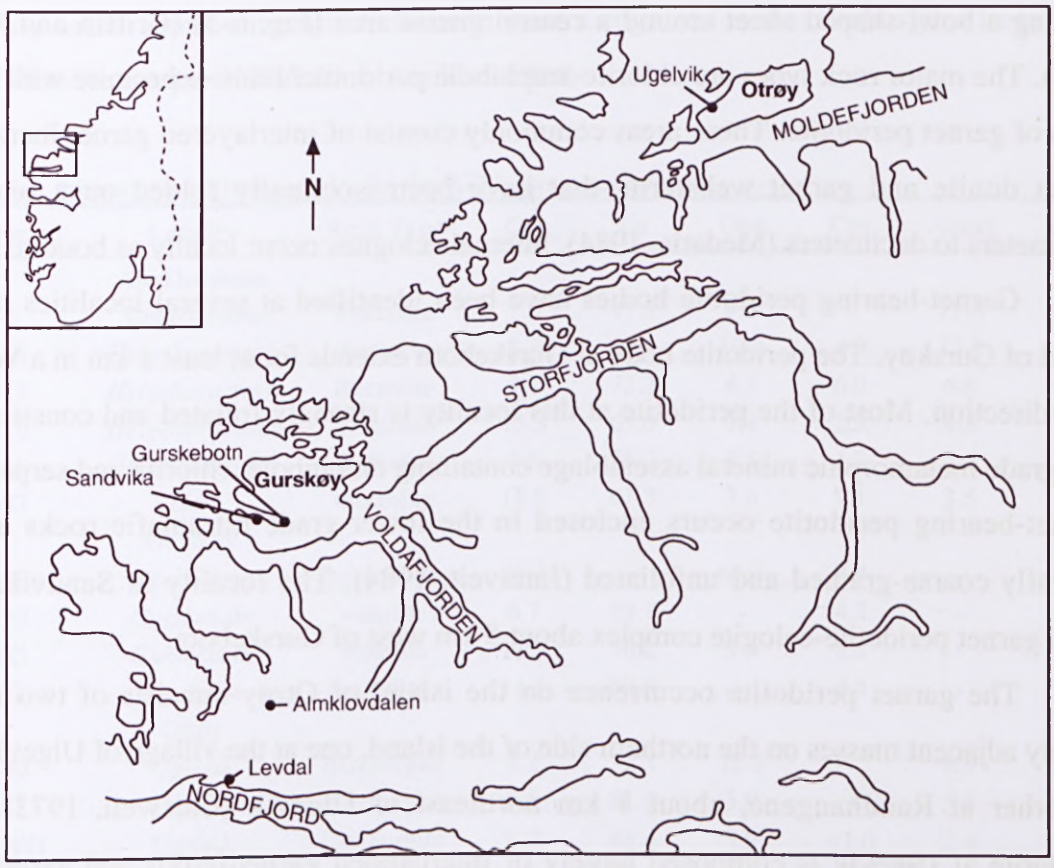


**Figure 6-2.** Map of part of the Western Gneiss Region showing sample localities. Modified after Jamtveit et al. (1991)

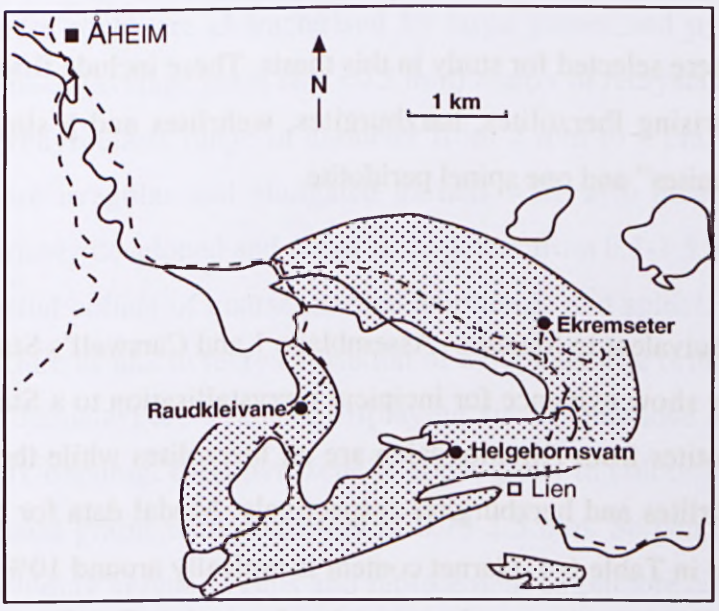


**Figure 6-3.** Map of Almklovdalen peridotite body showing sample localities. Modified after Griffin and Mørk (1981).

The locality at Levdal is a small dunite (chlorite-bearing) body that is being mined underground. Also exposed at this site is a 1 m thick eclogite horizon with large hornblende porphyroblasts (Griffin and Mørk, 1981). The Almklovdalen peridotite consists of several large ultramafic bodies that are thought to be connected in the sub-surface,

forming a bowl-shaped sheet around a central gneiss area (Fig. 6-3) (Griffin and Mørk, 1981). The major rock types are chlorite-amphibole peridotite/dunite±chromite with small areas of garnet peridotite. These areas commonly consist of interlayered garnet lherzolite, garnet dunite and garnet websterite that have been isoclinally folded on a scale of centimeters to decimeters (Medaris, 1984). Internal eclogites occur locally as boudins.

Garnet-bearing peridotite bodies have been identified at several localities on the island of Gurskøy. The peridotite body at Gurskebotn extends for at least 1 km in a WNW-ESE direction. Most of the peridotite at this locality is strongly foliated and consists of a low-grade metamorphic mineral assemblage containing amphibole, chlorite and serpentine. Garnet-bearing peridotite occurs enclosed in the lower-grade ultramafic rocks and is typically coarse-grained and unfoliated (Jamtveit, 1984). The locality at Sandvika is a small garnet peridotite-eclogite complex about 5 km west of Gurskebotn.

The garnet peridotite occurrence on the island of Otrøy consists of two major closely adjacent masses on the northern side of the island, one at the village of Ulgevik and the other at Raudhaugene, about 1 km northeast of Ulgevik (Carswell, 1973). The peridotite at Ulgevik is composed largely of interbanded garnetiferous and garnet-free peridotite, both of which have experienced extensive late stage serpentinisation.

### *6.4.2 Petrography*

Twenty-eight peridotites were selected for study in this thesis. These include fourteen garnet-bearing peridotites, comprising lherzolites, harzburgites, wehrlites and a single pyroxenite, thirteen garnet-free "dunites" and one spinel peridotite.

Garnet peridotite and pyroxenite

The garnet-bearing samples are equivalent to Medaris' Assemblage 1 and Carswell's Stage II assemblage though the majority show evidence for incipient recrystallisation to a Stage III assemblage. The garnet peridotites from Almklovdalen are all lherzolites while those from Gurskøy and Otrøy are wehrlites and harzburgites respectively. Modal data for the garnet-bearing rocks are presented in Table 6-1. Garnet content is typically around 10% or lower, and modes greater than 15% are only seen in a couple of samples. Gurskøy and Otrøy peridotites are generally richer in olivine (72-89%) than the lherzolites from Almklovdalen (61-77%). The pyroxenes make up between 10-20% of the mode for any given sample except for pyroxenite sample N97-29B which contains ~75% pyroxene. Amphibole is common in peridotites from Almklovdalen and Otrøy but absent in the

Gurskøy rocks. Small amounts of chromite were recognised in the harzburgites from Otrøy and lherzolite sample N97-5 from Almklovdalen.

**Table 6-1.** Pointcounted mineral modes for the WGR garnet peridotites.

| Sample no. | Locality | Rock Type | Gnt | Ol | Opx | Cpx | Amph | Chr |
|---|---|---|---|---|---|---|---|---|
| | Almklovdalen | | | | | | | |
| N97-5 | *Raudkleivane* | lherzolite | 1.6 | 77.3 | 9.3 | - | 11.5 | <1.0 |
| N97-14 | *Helgehornsvatn* | lherzolite | 8.2 | 64.1 | 10.4 | 4.3 | 13.0 | - |
| N97-15 | *Helgehornsvatn* | lherzolite | 9.7 | 72.2 | 4.5 | 6.0 | 6.6 | - |
| N97-16 | *Helgehornsvatn* | lherzolite | 15.3 | 65.6 | 7.4 | 2.9 | 8.8 | - |
| N97-18 | *Helgehornsvatn* | lherzolite | 9.5 | 75.3 | 8.5 | 1.2 | 5.5 | - |
| LNWG | *Lien* | lherzolite | 18.5 | 61.3 | 7.6 | 9.1 | 3.5 | - |
| | Gurskøy | | | | | | | |
| N97-29B | *Gurskebotn* | pyroxenite | 25.4 | - | 66.2 | 8.4 | - | - |
| N97-30 | *Gurskebotn* | wehrlite | 6.7 | 89.1 | - | 4.2 | - | - |
| GBWG | *Gurskebotn* | wehrlite | 11.5 | 76.2 | 3.5 | 8.8 | - | - |
| SVWG | *Sandvika* | wehrlite | 11.1 | 80.5 | - | 8.4 | - | - |
| | Otrøy | | | | | | | |
| N97-40 | *Ugelvik* | harzburgite | 5.2 | 72.3 | 15.2 | - | 6.9 | <1.0 |
| N97-41 | *Ugelvik* | harzburgite | 7.5 | 81.4 | 5.9 | - | 5.2 | <1.0 |
| OTRWG | *Ugelvik* | harzburgite | 6.3 | 85.4 | 5.9 | <1.0 | 2.4 | <1.0 |

The garnet lherzolites from Almklovdalen are predominantly porphyroclastic in texture and, with the exception of sample LNWG, moderately serpentinised (see Fig. 6-4). These rocks are characterised by large garnet and pyroxene porphyroclasts in a fine-grained (average grain size <0.5 mm) matrix of recrystallised olivine and pyroxene. Garnet porphyroclasts range in diameter from 2 mm to 1 cm. Grains are often rounded though more irregular and elongated garnets were also noted. Kelyphite rims on garnets are variably developed and range in thickness from 0.1-1.5 mm. Mantling the reaction rims are partial collars of coarse-grained amphibole and spinel. Carswell (1968b) interpreted this texture as due to recrystallisation of kelyphite. The orthopyroxene porphyroclasts (>4 mm in diameter) are strained, displaying strong undulose extinction and, in some instances, kink-banding. Clinopyroxene is apple-green in colour and typically occurs as unstrained, equant grains with diameters of 0.75-2.5 mm. Serpentine veins crosscut porphyroclasts, including kelyphite rims and replacement amphibole collars on garnet. This suggests that serpentinisation postdates formation of the reaction coronas and later recrystallisation as interpreted by Carswell (1968b).

Sample LNWG is very fresh and shows no evidence for serpentinisation. Large garnets (>1 cm in diameter) reside in a fine- to medium-grained matrix of olivine with subordinate pyroxene and amphibole. Kelyphite rims on garnets are absent or poorly

developed (<0.1 mm thick). Patches of coarse-grained amphibole and small garnet neoblasts (~0.2 mm) are observed adjacent to the larger garnet grains. These recrystallised garnets are characteristic of the Stage III assemblage of Carswell (1986). Inclusions in Stage II garnets include clinopyroxene, orthopyroxene and olivine. In addition to the small equant olivines (<1 mm) there are larger tabular olivines (>2 mm in length) which are aligned parallel and define a weak lineation. Pale brown orthopyroxene and apple-green clinopyroxene occur as large (1-3 mm diameter) strained grains that commonly display undulose extinction and fine exsolution lamellae of the complementary pyroxene. Clinopyroxene shows evidence for shear in the form of fine reaction rims of secondary clinopyroxene and/or amphibole that have been drawn out into the foliation plane of the matrix. Small chromite grains occur disseminated along the foliation plane often in association with amphibole stringers.

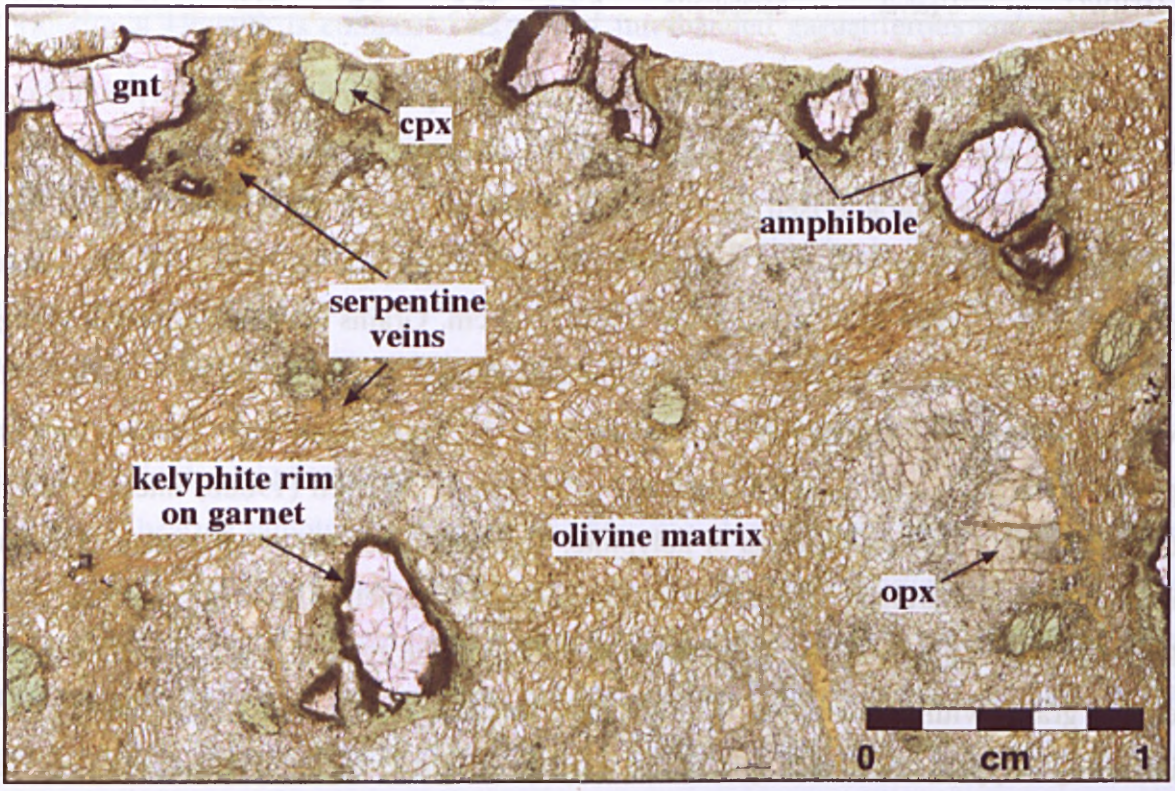


**Figure 6-4.** Porphyroclastic texture in garnet lherzolite N97-14 from Almklovdalen. Kelyphite rims and amphibole mantles are well-developed on garnets. Serpentine veins are abundant and occasionally are observed cross-cutting porphyroclasts (see garnet grain in top lefthand corner).

Sample N97-5 from Almklovdalen has a mosaic-porphyroclastic texture. Garnet and orthopyroxene porphyroclasts (>3 mm) are set in a well-developed, fine- to medium-grained mosaic of olivine (average grain size of 1 mm), pyroxene and amphibole. Garnets have been extensively kelyphitised and collars of amphibole and chromite on the reaction rims are common. Rare garnets have been completely retrograded and appear as amphibole and chromite pseudomorphs. Orthopyroxenes are strained and display undulose extinction. Amphibole occurs in the matrix as fine stringers which show a preferred alignment and define a weak lineation in the rock. Small chromites occur as discrete intergranular grains in the matrix.

The garnet wehrlites from Gurskøy display a coarse texture in which large garnet (2-7 mm) and olivine (2-5 mm) grains are separated by a fine-grained mosaic of olivine and pyroxenes (Fig. 6-5). Garnet grains are rounded and commonly surrounded by well-developed kelyphitic reaction coronas. In several samples garnet has been completely replaced by kelyphite. A rim of very fine-grained amphibole is occasionally observed on the outer edge of the kelyphite. The large olivine grains generally show strong undulose extinction and typically have a heavily fractured and embayed appearance. Recrystallised olivines display an equigranular texture and are strain-free. Pale-green clinopyroxene (0.5-1.0 mm) is commonly found as groups of two or more grains. Exsolution within clinopyroxene, observed in several grains, occurs as long, fine, closely spaced lamellae of chromite. Clinopyroxene was also found in one sample (GBWG) as small (<1 mm) rounded inclusions in garnet. Chromite is present as discrete intergranular grains in the matrix.

Garnet pyroxenite (N97-29B) from Gurskøy consists of large (1-7 mm) orthopyroxene, clinopyroxene and garnet grains separated by a fine-grained mosaic of strain-free clinopyroxene, orthopyroxene and amphibole (Fig. 6-6). Orthopyroxenes commonly are strained and kinked and some show extensive intragrain recrystallisation. Garnets are generally large (2-7 mm in length) and display well-developed kelyphite rims. Inclusions in garnet are common and include small (~ 0.5 mm), rounded clinopyroxenes, randomly oriented flakes of chlorite (< 0.1 mm), and very fine needles of rutile that are often oriented in two approximately perpendicular directions. Clinopyroxene grains are bright apple-green in colour and range from 1-2 mm in diameter. The majority of grains are unstrained though several are kinked and display undulose extinction. Very fine, short exsolution lamellae of orthopyroxene were observed in a few clinopyroxenes.

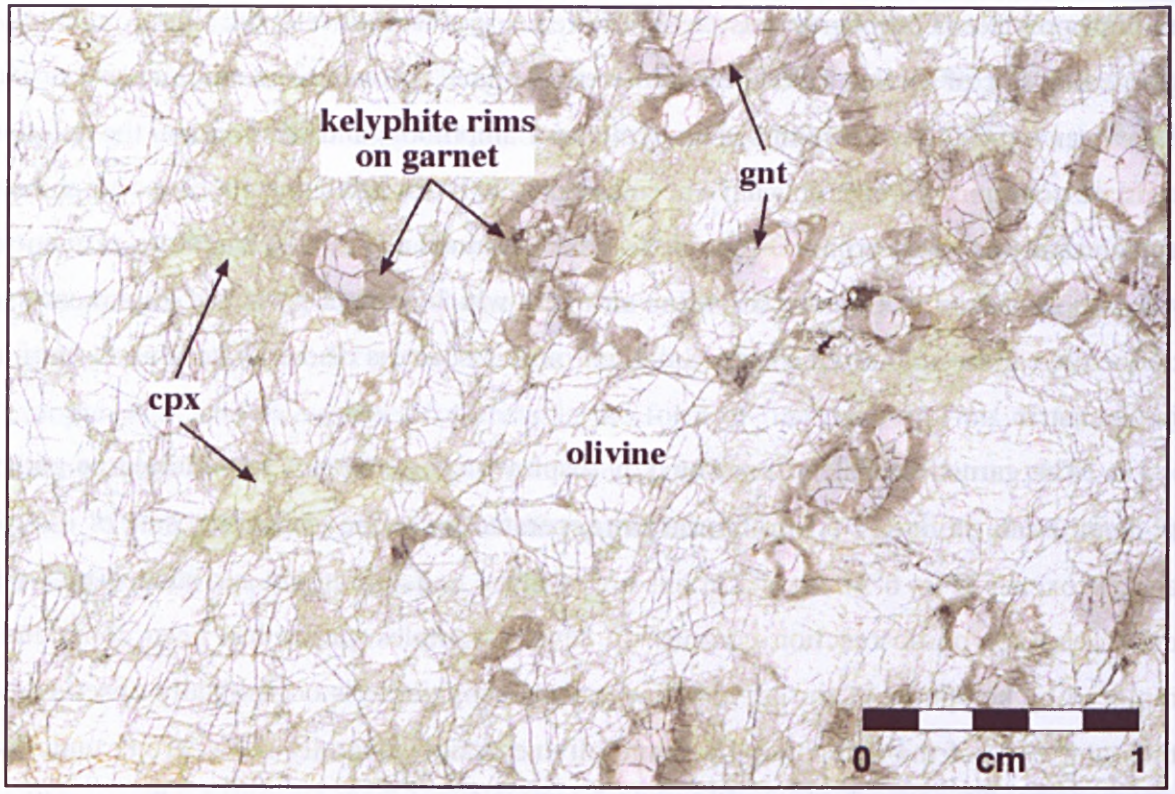


**Figure 6-5.** Coarse texture in garnet wehrlite GBWG from Gurskøy. Kelyphite rims are well-developed on garnet. The garnet grain in the top righthand corner contains a large inclusion of clinopyroxene.

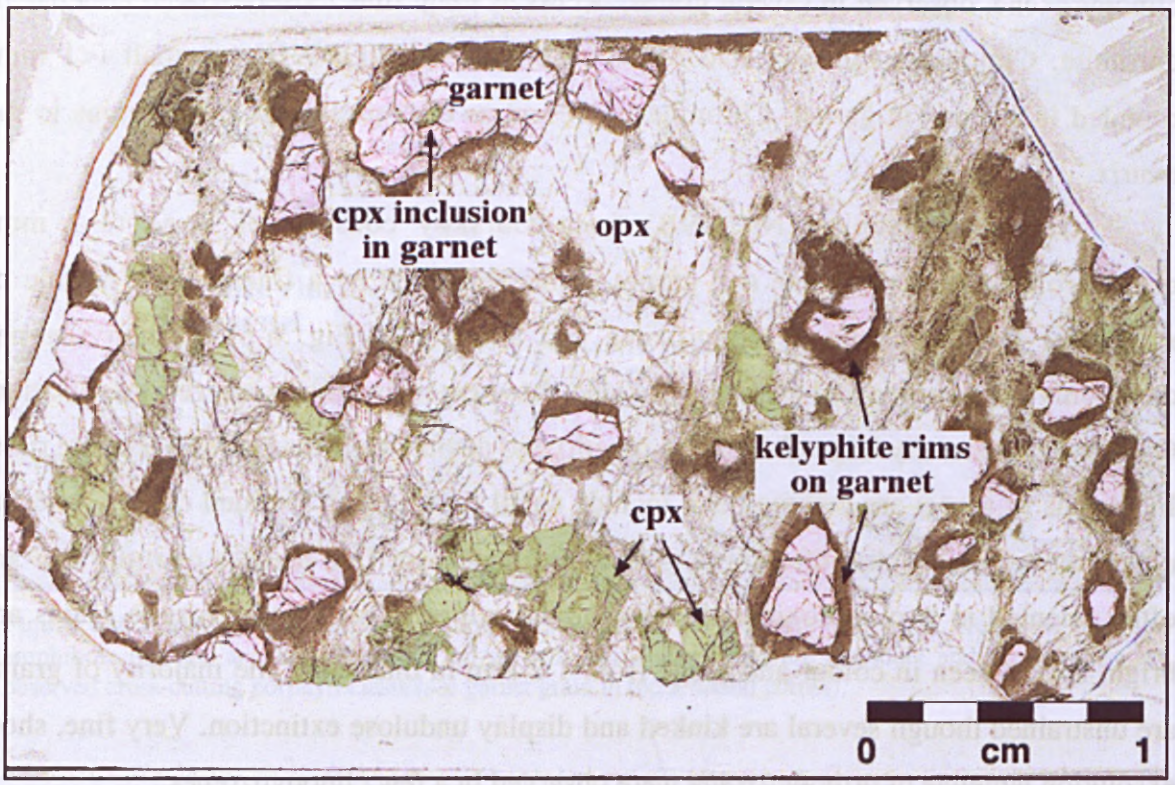


**Figure 6-6.** Porphyroclastic texture in garnet pyroxenite N97-29B from Gurskøy. Kelyphite rims are well-developed on garnet. Large inclusions of clinopyroxene were noted in some garnet grains.

The garnet harzburgites from Otrøy have the assemblage garnet-olivine-orthopyroxene-pargasitic amphibole-spinel (Table 6-1). The rocks are porphyroclastic, with garnet up to 7 mm in diameter residing in a fine-to medium-grained (<1 mm) matrix of olivine, orthopyroxene and amphibole. Extensive serpentinisation, 50% or more, obscures most grain contacts (see Fig. 6-7), but sufficient texture is preserved to reveal that garnet grains interlock on a coarse scale with the other silicates, presumably representing an equilibrium assemblage. The majority of garnets are small (~2 mm) and rounded, though rare grains are larger (>7 mm) and more elongate in shape. Kelyphitic reaction rims on garnet are common but are generally poorly-developed. Small (<1 mm) clear grains of unstrained orthopyroxene and amphibole, with tiny chromite inclusions, are occasionally observed around the external margins of the reaction rims.

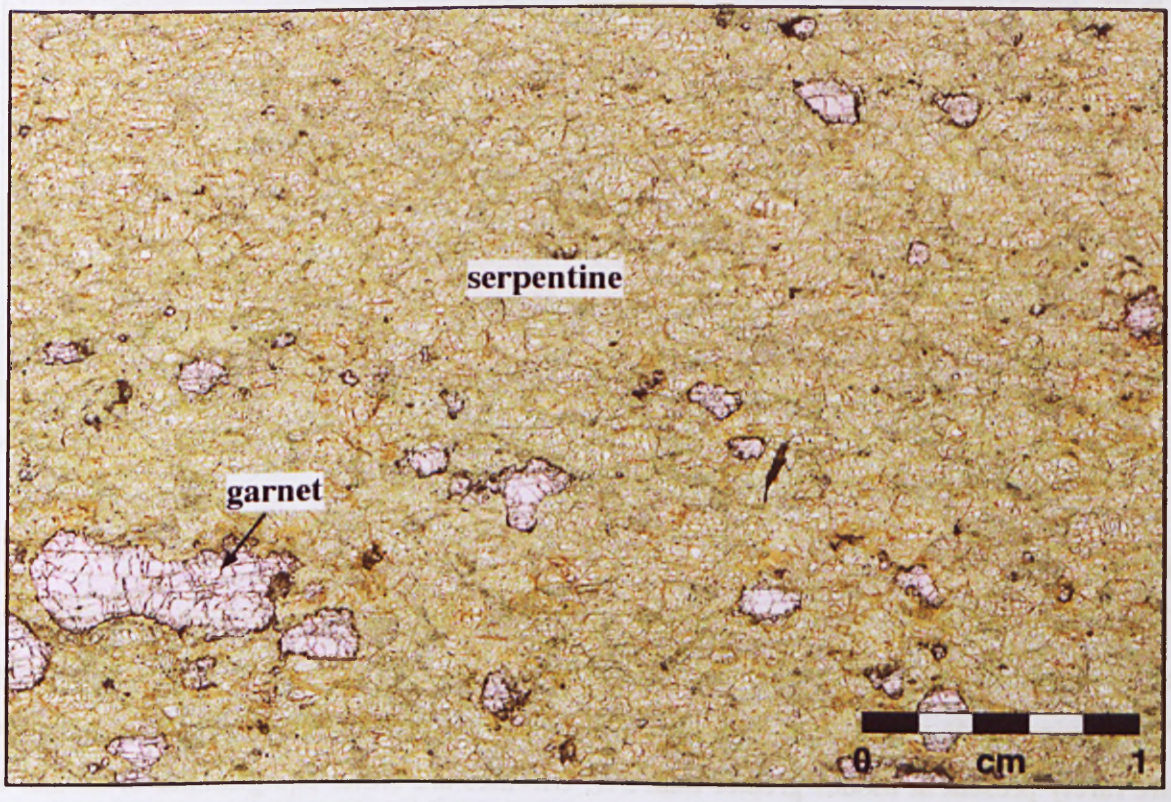


**Figure 6-7.** Porphyroclastic texture in garnet harzburgite OTRWG from Otrøy. Serpentinisation is extensive and obscures most grain contacts. Kelyphite rims on garnet are poorly developed or absent.

Spinel peridotite

Spinel peridotite sample N97-25 from Almklovdalen contains the assemblage olivine-orthopyroxene-chromite-amphibole (see Table 6-2) and corresponds to Carswell's Stage V assemblage. Large amphibole porphyroclasts (>7 mm in length) and smaller orthopyroxenes (av. 2 mm) are set in a fine-grained mosaic of equant olivine grains (Fig. 6-8). The amphibole porphyroclasts are brown and fibrous in appearance and mantled by

laths of clear, pale-green amphibole that are observed to flow around the larger grains. Orthopyroxene grains are pale brown in colour and dusty looking. Chromite is found disseminated in the matrix as large (>1.5 mm) discrete grains or as fine trains associated with amphibole.

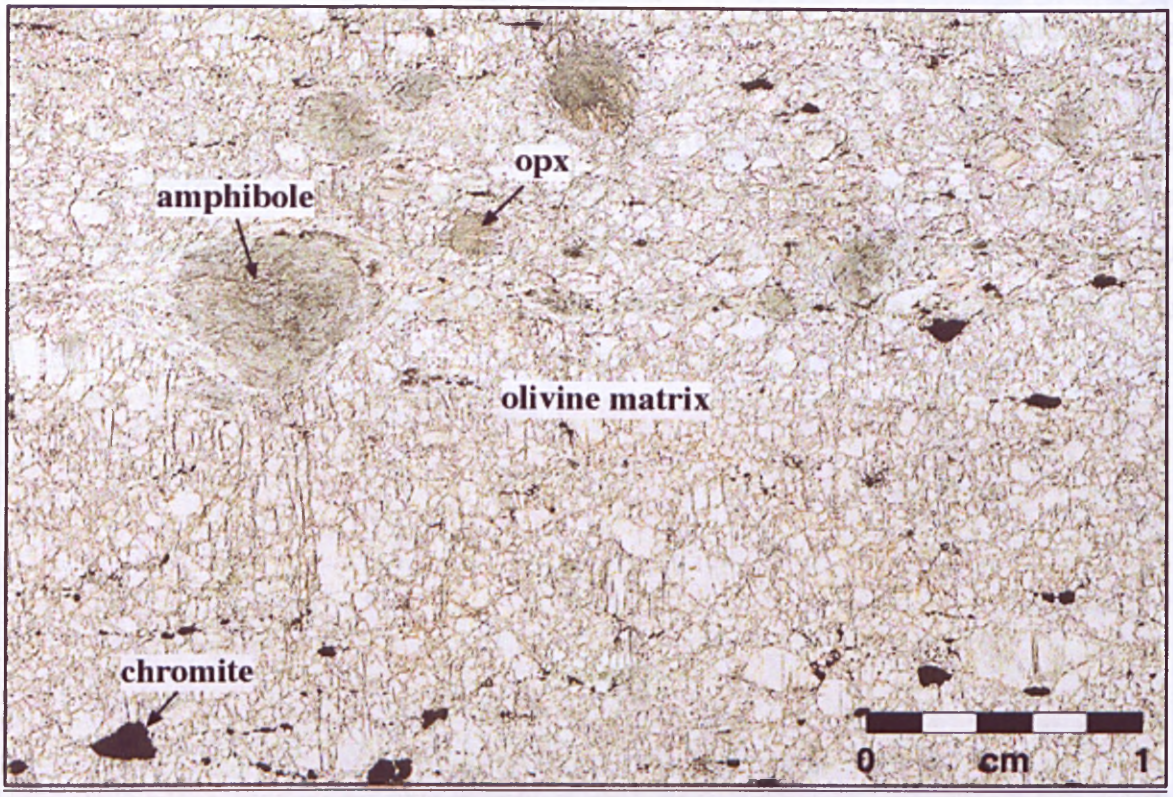


**Figure 6-8.** Porphyroclastic texture in spinel peridotite N97-25 from Almklovdalen. Large fibrous amphibole porphyroclasts are set in a fine-grained olivine matrix.

Dunite

The WGR dunites have the assemblage olivine±orthopyroxene±chromite±amphibole± chlorite±phlogopite (Table 6-2). This assemblage is equivalent to Carswell's (1986) Stage VI. Olivine mode varies from ~88-98% while the other phases, apart from orthopyroxene, are rarely present at modes greater than 5%. Olivines are either equigranular or tabular in shape with the latter showing a parallel alignment and defining a pronounced lineation. Grain size varies from 0.1 mm to 1.0 cm though large grains are rare and average grain size is only ~0.4 mm. Large relict olivine grains (>2.0 mm) are rare and typically strongly embayed. Orthopyroxene is present in several samples as large (>2.0 mm) strained porphyroclasts which make up <10% of the mode. These porphyroclasts are often brown and fibrous in appearance and are commonly attenuated in the direction of the foliation.

**Table 6-2.** Pointcounted mineral modes for the WGR dunites and harzburgite.

| Sample no. | Locality | Rock Type | Ol | Opx | Chr | Chl | Amph | Phlog |
|---|---|---|---|---|---|---|---|---|
| N97-1 | *Levdal* Almklovdalen | dunite | 91.6 | 6.3 | <1.0 | 1.5 | - | - |
| N97-6 | *Raudkleivane* | dunite | 93.4 | 4.3 | <1.0 | 1.0 | - | <1.0 |
| N97-7 | *Raudkleivane* | dunite | 94.6 | - | <1.0 | 3.2 | 1.5 | <1.0 |
| N97-8 | *Raudkleivane* | dunite | 92.0 | 6.1 | <1.0 | 1.6 | <1.0 | <1.0 |
| N97-9 | *Raudkleivane* | dunite | 94.7 | - | <1.0 | 1.6 | 3.5 | - |
| N97-11 | *Raudkleivane* | dunite | 98.3 | - | <1.0 | 1.2 | - | <1.0 |
| N97-13 | *Raudkleivane* | dunite | 91.3 | 6.8 | <1.0 | 1.6 | <1.0 | - |
| N97-17 | *Helgehornsvatn* | dunite | 94.5 | - | <1.0 | 1.2 | 3.9 | - |
| N97-22 | *Ekremseter* | dunite | 87.8 | 7.5 | 1.1 | <1.0 | 3.6 | - |
| N97-23 | *Ekremseter* | dunite | 93.4 | 5.8 | <1.0 | - | <1.0 | <1.0 |
| N97-24 | *Ekremseter* | dunite | 97.0 | - | - | 3.0 | - | - |
| N97-25 | *Ekremseter* | harzburgite | 85.6 | 5.1 | 2.7 | - | 6.6 | - |

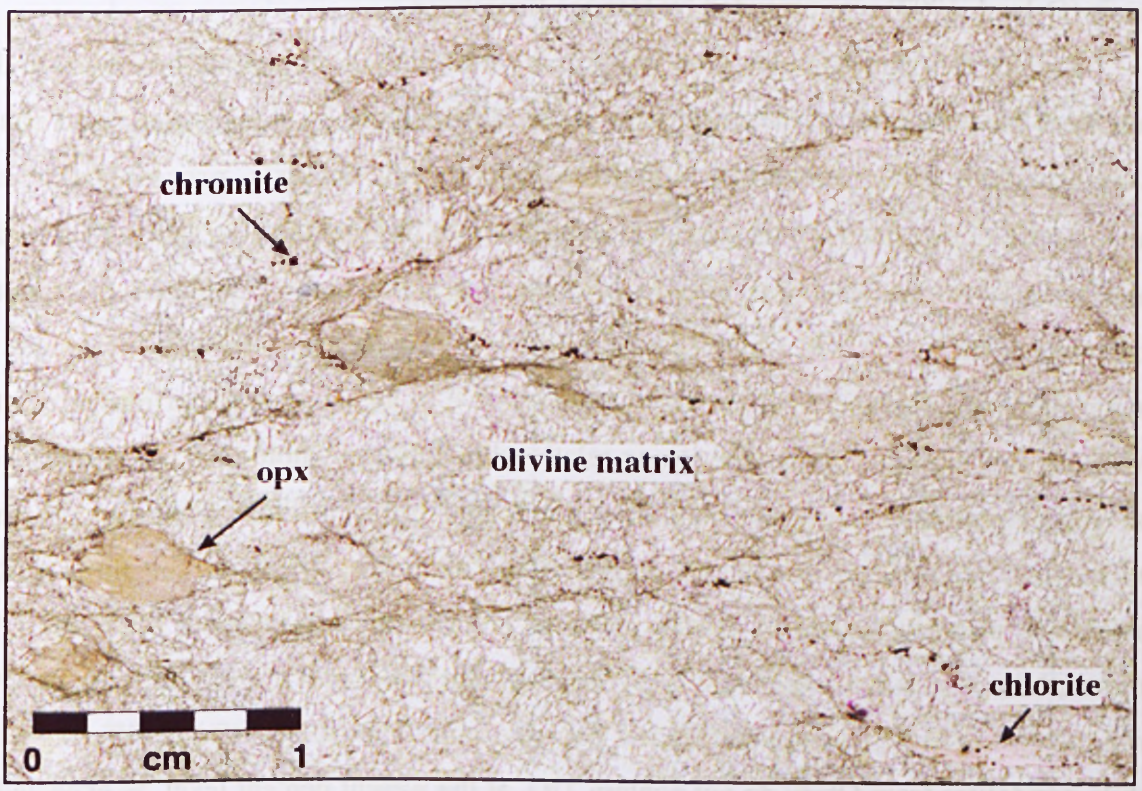


**Figure 6-9.** Porphyroclastic texture in dunite N97-8 from Almklovdalen. Large orthopyroxene porphyroclasts are set in a fine-grained olivine matrix.

Pale purple chlorite occurs as small discrete flakes (0.4-0.5 mm) or as ribbons of larger interlocking grains (0.5-1.0 mm in length) that are associated with trains of fine-grained (<0.5 mm) disseminated chromite. Large (~1 mm) chromites were identified in the matrix in some samples. Amphibole and phlogopite typically occur as single pale green flakes (lengths of <0.6 mm and <0.2 mm respectively) in close association with chlorite. Sample N97-17 is unusual in that it is coarse-grained (olivine grain size ranges from 0.5-4.0 mm with an average of ~2.0 mm) and contains pale green chlorite and variegated

(bright green/pale green) amphibole. Recrystallisation of olivine is minimal and there is no obvious lineation of accessory minerals. Associated with the amphibole is a fine-grained (<0.5 mm) red-brown chromite.

## 6.5 WHOLE ROCK GEOCHEMISTRY

### *6.5.1 Major elements*

Twenty Eight samples from the WGR were analysed by XRF for whole rock major element abundances at Macquarie University using glass fusion discs (see Section 2.2.1). Two of these samples are average "mine run" dunites, provided by A/S Olivin, from two quarries in Almklovdalen. Analytical results are presented in Appendix VII. An additional major-element dataset for nine dunites from Almklovdalen from an unpublished PhD thesis (Osland, 1997) was provided by Hannes Brueckner.

Major element data may preserve primary information on melting processes in the mantle as the behaviour of these elements is governed largely by stoichiometry and phase equilibria both under subsolidus conditions and during anatexis, processes that are intrinsically constrained by the physical conditions in the mantle. Extraction of a mafic melt from a primitive source should produce a residue that is depleted in basaltic components such as $Al_2O_3$, CaO, $TiO_2$ and $Na_2O$. Fig. 6-10 illustrates the differences in major element abundances for the peridotites relative to an estimate for primitive mantle (McDonough and Sun, 1995). The strong relationship between whole rock Mg# and Cr# in the garnet peridotites suggests that they are linked by a common depletion process. Decreasing $Al_2O_3$, CaO and $Na_2O$ content with increasing Mg# for the three suites indicates a primary control by partial melting. The relationship between Mg# and $TiO_2$ content, however, is not so clear. While Almklovdalen peridotites show a decrease in $TiO_2$ with increasing Mg#, Gurskøy peridotites have the same $TiO_2$ (0.07 wt%) at differing Mg# while peridotites from Otrøy do not contain $TiO_2$ at the weight percent level, as expected if these samples are the most depleted. The different trends of Mg# vs Al, Ca, and Na in the Gurskøy data may imply that these peridotites experienced different melting (or different metasomatic enrichment) processes from the Almklovdalen and Otrøy samples.

The dunites from Almklovdalen are strongly depleted with Mg# in the range 92-93.6. These rocks are extremely poor in Al and other magmaphile elements, as expected from their high modal olivine content and lack of Ca-Al phases such as garnet and clinopyroxene (see Figs. 6-10 and 6-11). High Mg# coupled with strong depletion in $Al_2O_3$, CaO and $TiO_2$ is indicative of high degrees of partial melting. Similar levels of

depletion have been noted in dunite xenoliths from Russia (Boyd and Finnerty, 1980), Tanzania (Rudnick *et al.*, 1993) and Greenland (Scott Smith, 1987; Bernstein *et al.*, 1998). Data for the "mine run" dunites show that the bulk of the Almklovdalen body is very depleted. This suggests that the olivine-rich rocks from the WGR, particularly those that are extremely poor in Al, are not simply retrograded garnet peridotites, as suggested by Medaris (1984), but in fact primary dunites and harzburgites.

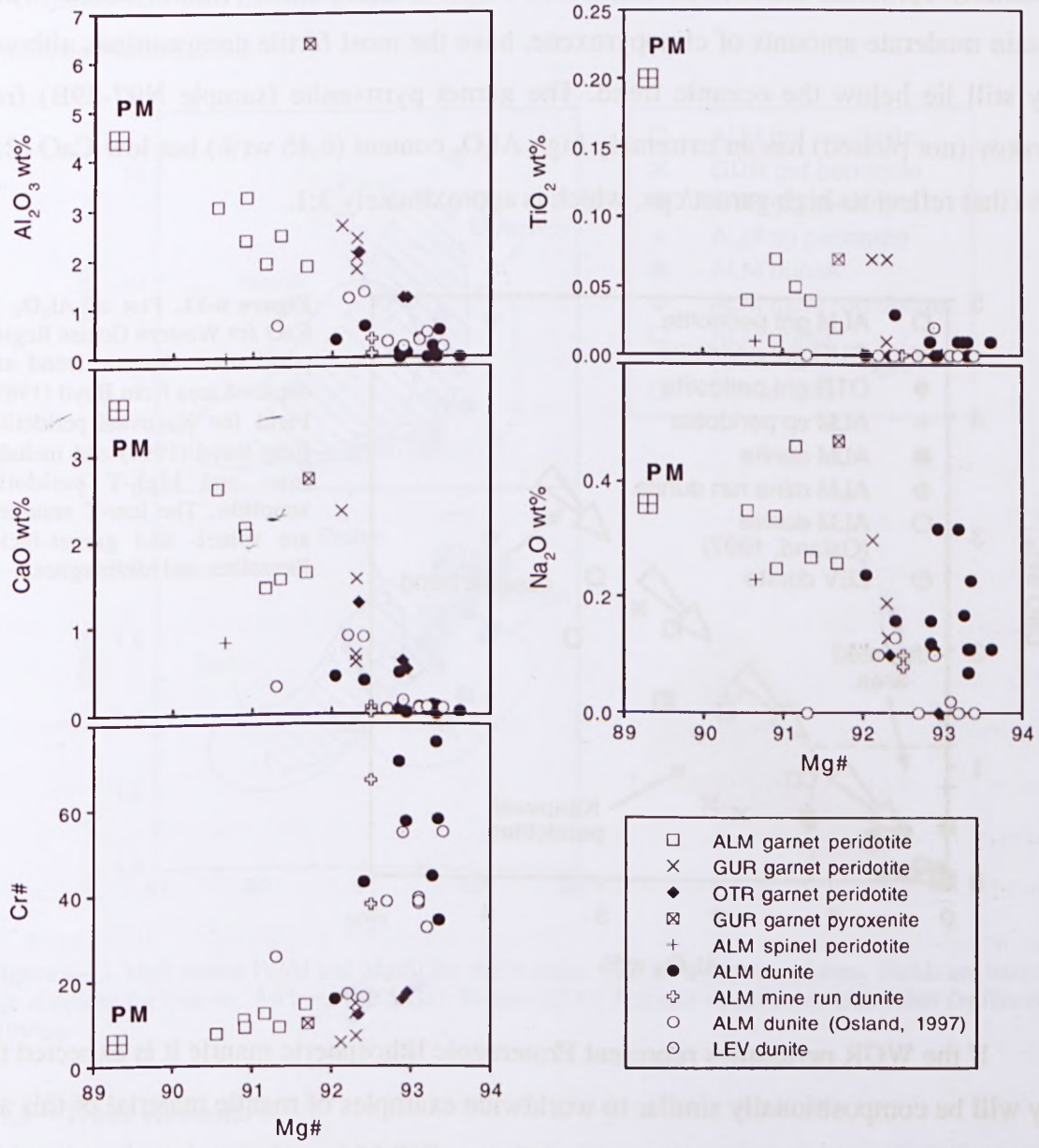


**Figure 6-10.** Whole rock major element oxides plotted against whole rock Mg# for peridotites from the Western Gneiss Region, Norway. Primitive mantle (PM) composition from McDonough and Sun (1995).

On a plot of $Al_2O_3$ vs CaO the garnet peridotites from the WGR define a strong trend of decreasing $Al_2O_3$ content with decreasing CaO content (Fig. 6-11). This relationship, first recognised in world-wide oceanic peridotite data, represents the

compositional progression from fertile to depleted peridotite (Boyd, 1989). The WGR garnet peridotites are depleted relative to primitive mantle and show a small but significant enrichment in $Al_2O_3$, relative to a given CaO, to the trend for oceanic peridotites. Low Ca/Al values are characteristic of garnet peridotite xenoliths from the Kaapvaal Craton and correlated with a lesser proportion of diopside in cratonic peridotites (Boyd, 1989). This is also the case for the Norwegian peridotites where samples from Otrøy, which are essentially cpx-free, are the most depleted whereas those from Almklovdalen, which contain moderate amounts of clinopyroxene, have the most fertile compositions although they still lie below the oceanic trend. The garnet pyroxenite (sample N97-29B) from Gurskøy (not plotted) has an extremely high $Al_2O_3$ content (6.46 wt%) but low CaO (2.76 wt%) that reflect its high garnet/cpx, which is approximately 3:1.

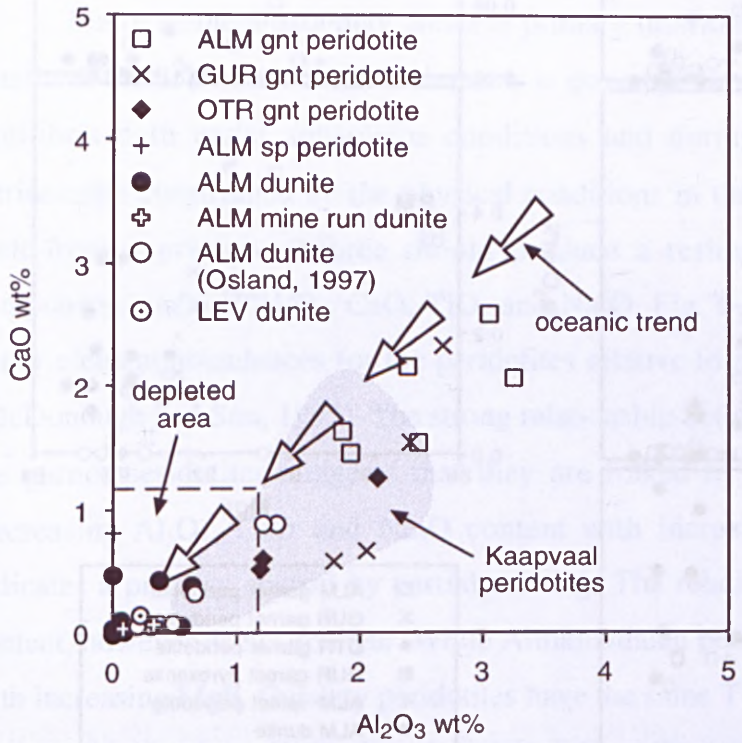


**Figure 6-11.** Plot of $Al_2O_3$ vs CaO for Western Gneiss Region peridotites. Oceanic trend and depleted area from Boyd (1989). Field for Kaapvaal peridotites from Boyd (1997) and includes low- and high-T peridotite xenoliths. The low-T xenoliths are spinel- and garnet-facies lherzolites and harzburgites.

If the WGR peridotites represent Proterozoic lithospheric mantle it is expected that they will be compositionally similar to worldwide examples of mantle material of this age. Key element ratios for Archon, Proton and Tecton SCLM have been plotted against Mg# in Fig. 6-12. In the Tecton suites, Mg/Si (atomic ratio) increases with degree of depletion as measured by Mg#, corresponding to the "oceanic trend" of Boyd (1989). A similar trend is shown by the Proton data but it is displaced to higher Mg# while Archon lithospheric mantle is displaced to still higher Mg#, without a corresponding increase in Mg/Si. Fe/Al (atomic ratio) increases with increasing Mg# for the Tecton and Proton datasets but the

Archon samples have anomalously low Fe/Al given their high Mg#. The garnet peridotites from Almklovdalen lie in the Proton field on both plots and thus have compositions that resemble Proterozoic SCLM. The garnet-bearing samples from Gurskøy and Otrøy are more depleted and plot in, or near, the Archon field in both diagrams. The dunites have high Mg# that put them above the extension of the Proton field on a Mg/Si vs Mg# plot, though a few have typical Archon compositions. Many of the dunites have extremely low Al contents and plot off the graph to high Fe/Al ratios or, in some cases, are Al-free and cannot be plotted at all.

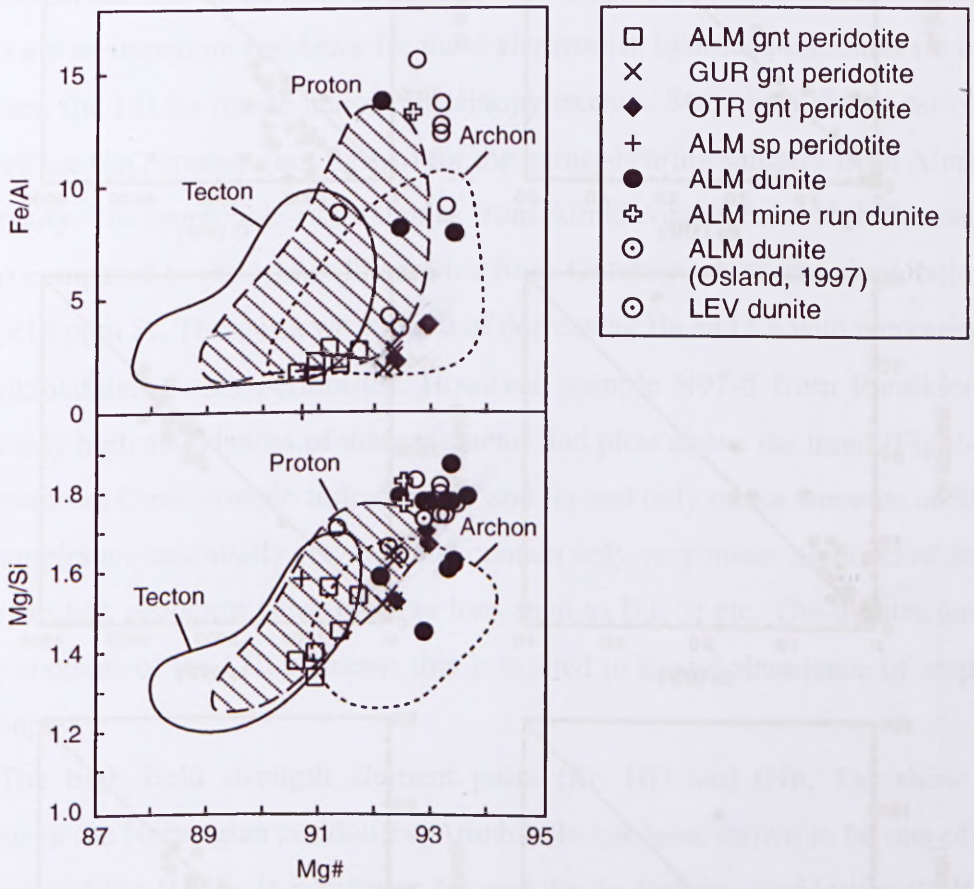


**Figure 6-12.** Mg# versus Fe/Al and Mg/Si for the Western Gneiss Region peridotites. Fields are based on age divisions for cratons: Archons (>2.5 Ga), Protons (2.5-1 Ga) and Tectons (<1 Ga). After Griffin *et al.* (1999a).

### *6.5.2 Trace elements*

Trace element data, obtained by both the XRF and solution ICPMS methods, have been collected for the twenty-eight peridotites already analysed for major elements and are tabled in Appendices VIIA (ICPMS) and VIIB (XRF). Only a limited number of elements was analysed by XRF, i.e. Ba, Cr, Cu, Ni, V and Zn, while these plus numerous other trace elements, including U, Th and REE, were analysed by solution ICPMS. Agreement between the available XRF data and ICPMS data is reasonably good for Ba, Cu, Ni and V

but poor for Cr and Zn (Fig. 6-13). This is ascribed to the incomplete dissolution of chromite during the ICPMS analysis. For the purposes of this thesis the ICPMS data are used because they provide a more complete trace element dataset for the Western Gneiss Region peridotites than the XRF data which are limited and do not include key elements such as Zr, Y and Sr.

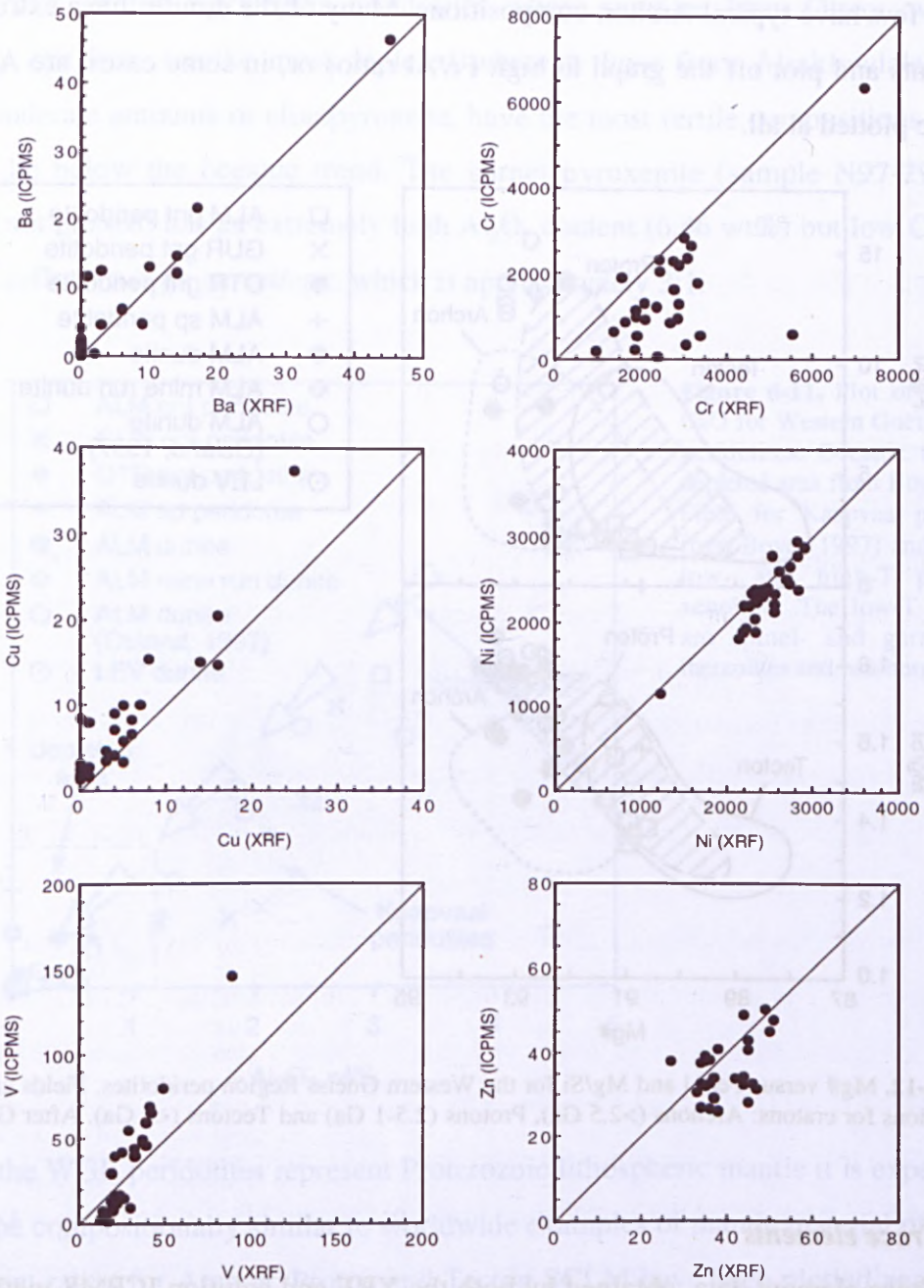


**Figure 6-13.** Comparison of trace element data determined by XRF and solution ICPMS methods.

Trace element analyses of whole rocks show that Ni is positively correlated with Mg# in the garnet peridotites and the dunites (Fig. 6-14) as expected if these rocks are residues after partial melting. Ni content in the garnet peridotites is relatively similar between localities (1800-2500 ppm) though sample N97-29B from Gurskøy has

anomalously low Ni (1150 ppm) that is related to its very low modal olivine. The dunites have Ni contents that overlap those for the garnet peridotites but the majority of samples contain between 2400-3000 ppm Ni, which is a reflection of their high olivine content. The spinel peridotite (N97-25) from Almklovdalen has a similar Ni content to the garnet peridotites from this locality.

Correlation between the large ion lithophile elements (LILEs i.e. Rb, Cs, Sr, Ba) and Mg# is generally poor for the WGR peridotites (data for Sr and Ba shown in Fig. 6-14) implying that most of these elements were introduced after melt extraction. The presence of these elements can be directly correlated with amphibole and/or mica content as these minerals are an important residence for these elements in hydrous peridotites (in anhydrous peridotites, the LILEs reside mainly in clinopyroxene). Strontium shows no correlation with Mg# nor CaO content (not shown) for the garnet-bearing samples from Almklovdalen and Gurskøy. The amphibole-rich samples from Almklovdalen have high Sr contents (17-36 ppm) compared to the garnet lherzolites from Gurskøy which are amphibole-free and contain <15 ppm Sr. There is a weak trend of decreasing Ba and Cs with increasing Mg# in the Almklovdalen garnet peridotites. However, sample N97-5 from Raudkleivane has anomalously high abundances of these elements and plots above the trend (Fig. 6-14). The peridotites from Otrøy contain little or no Sr and Ba and only minor amounts of Rb and Cs. These samples are essentially cpx-free and contain only very minor amounts of amphibole, so there are few residence sites for large ions such as Ba, Sr etc. The dunites have highly variable contents of the LIL elements that is related to modal abundance of amphibole in these samples.

The high field strength element pairs (Zr, Hf) and (Nb, Ta) show variable behaviour in the Norwegian peridotites. Amphibole has been shown to be one of the main repositories of the HFSE, in particular Nb and Ta, in hydrous peridotites (O'Reilly and Griffin, 1988). Zr shows a weak negative correlation with Mg# in the Almklovdalen garnet peridotites implying that Zr abundance in the whole rock may be related to degree of partial melting. The garnet peridotite samples from Gurskøy fall into a high-Zr group (>2.5 ppm) and a low-Zr group (<0.5 ppm). The samples with high Zr contents define a positive trend that lies above that for the Almklovdalen peridotites. The high-Zr rocks are considerably fresher than the two low-Zr samples (which display extensive kelyphitisation of garnet) and it possible that Zr has been lost from the latter during alteration. As the Gurskøy peridotites do not contain amphibole Zr has instead been partitioned into clinopyroxene and, to a lesser extent, garnet (see Tables 6-5 and 6-7). Hf shows similar

behaviour to Zr. The garnet peridotites from Otrøy and the dunites have very low abundances of Zr and Hf. The other HFSE (Nb, Ta) do not show any correlation with Mg# for any of the peridotite groups. The highest concentrations of Nb (and Ta) occur in the amphibole-rich garnet peridotites from Almklovdalen while the lowest abundances of these elements are found in the garnet peridotites from Otrøy.

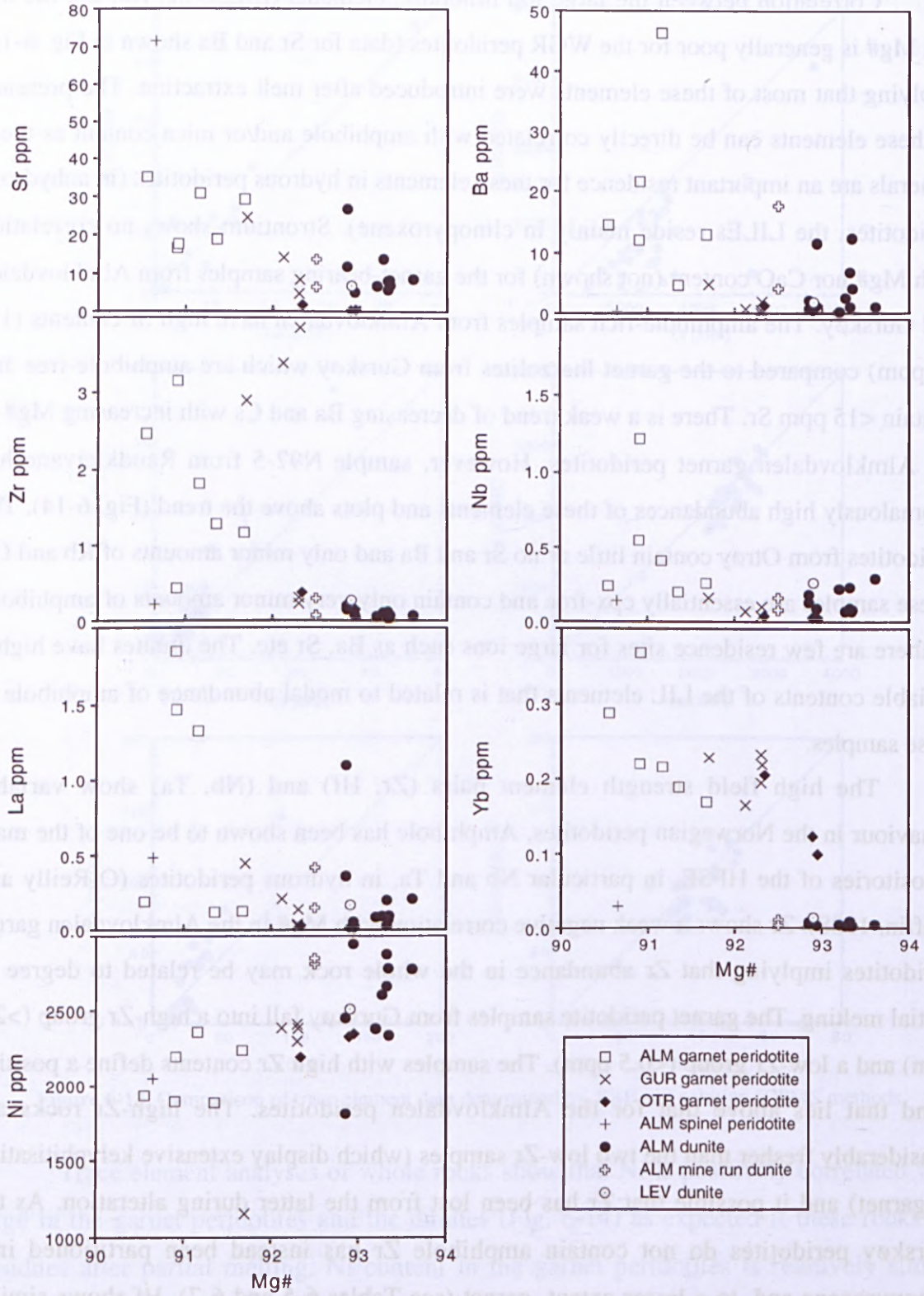


**Figure 6-14.** Whole rock trace element abundances vs Mg# for Western Gneiss Region peridotites.

There is no correlation between light rare earth element abundance, as represented by La, and Mg# in the WGR peridotites. The Almklovdalen garnet peridotites divide into two very distinct groups based on La content (Fig. 6-14). One group exhibits strong La-enrichment while the second is depleted in La. As amphibole modes are similar for both groups it appears that the first group has been enriched in La possibly as a result of interaction with, and metasomatism by, a LREE-enriched fluid/melt. The garnet peridotites from the other localities and the dunites have La contents (<0.5 ppm) comparable to the La-poor group from Almklovdalen. Dunite sample N97-17 has an anomalously high La content of 1.1 ppm.

The heavy rare earth elements will preferentially partition into garnet and it is expected that garnet-rich samples will be enriched in these elements. This is evident for the WGR peridotites in the Yb vs Mg# plot in Fig. 6-14 which shows that the garnet peridotites have uniformly high Yb contents whereas the dunite and spinel peridotite (N97-25) contain negligible ytterbium. There is a very strong negative correlation between Yb and Mg# in the Almklovdalen and Otrøy garnet peridotites which reflects the highly compatible nature of the HREE during partial melting.

Rare earth element patterns for the garnet peridotites from Almklovdalen can be divided into two basic shapes: convex-upwards and convex-downwards. The convex-upwards patterns are defined by high MREE abundances [$(La/Nd)_N<1$] relative to HREE and LREE while the convex-downwards patterns are LREE-enriched [$(La/Nd)_N>1$] relative to MREE, with LREE abundances varying from 0.02 x PM (primitive mantle) to 3 x PM in the most enriched samples. Convex-downwards (U-shaped) patterns in residual peridotites have been interpreted as reflecting either (i) mixing of LREE-enriched melts with depleted residues (Song and Frey, 1989), or (ii) differential ascent rates of REE as ascending melts interact with peridotite wall-rock (Navon and Stolper, 1987). The latter is known as the chromatographic model and this has been discussed in some detail in Section 5.4.4. The sinuous shape of the convex-upwards patterns have previously been attributed to a three-step process; (i) partial melting, (ii) metasomatism by a melt/fluid enriched in incompatible elements, and (iii) a second partial melting event (Nixon, 1987). However, these patterns are more likely simply a result of mineral control on REE abundances in the whole-rock. LREE are depleted relative to MREE in clinopyroxene and amphibole and this is reflected in the whole-rock patterns. Depletion in the HREE seen in cpx and amphibole is balanced, in the whole-rock, by garnet. The difference in LREE-enrichment between the peridotites with U-shaped and sinuous patterns is probably related to the extent of metasomatism.

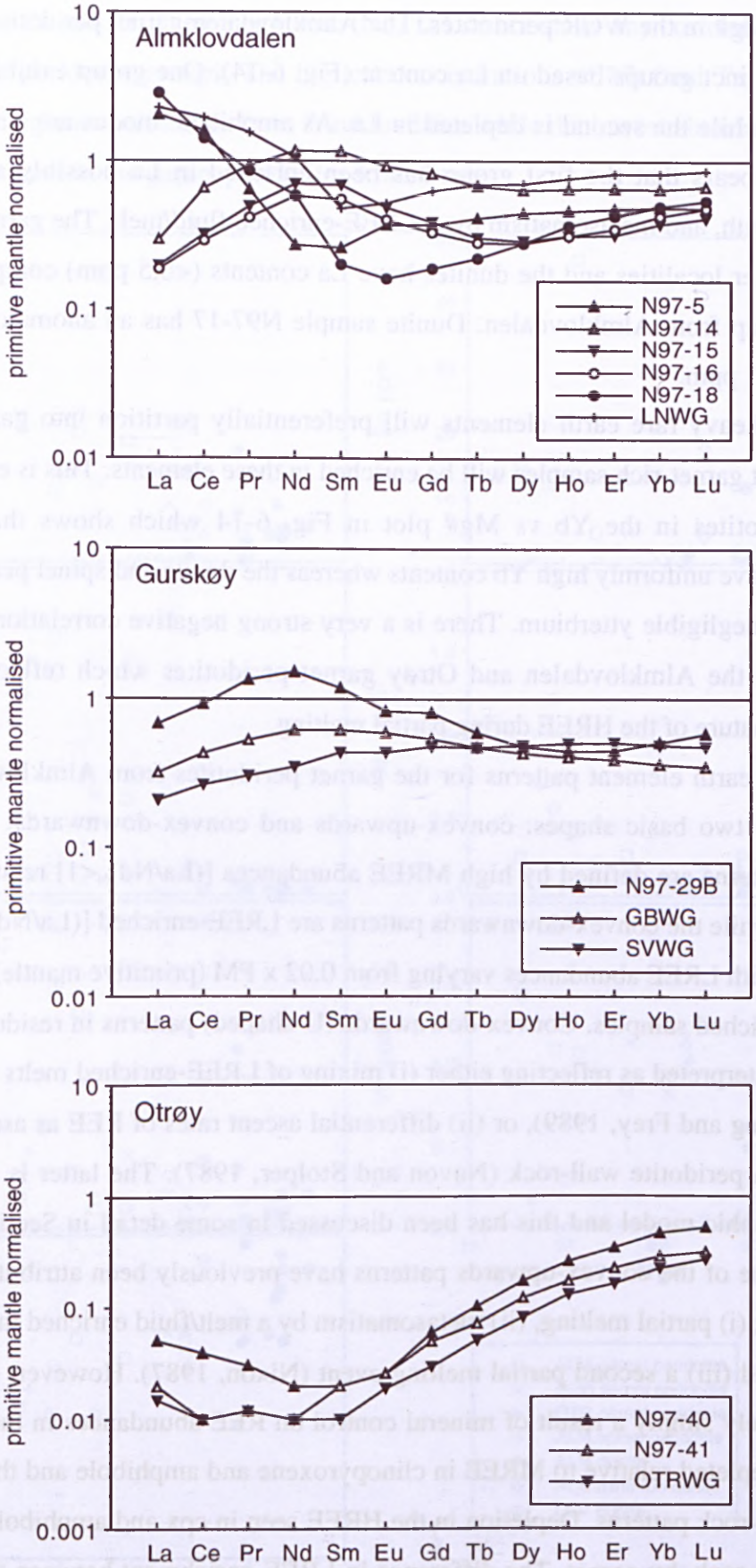


**Figure 6-15.** Whole rock primitive mantle normalised REE patterns for Western Gneiss Region garnet peridotites.

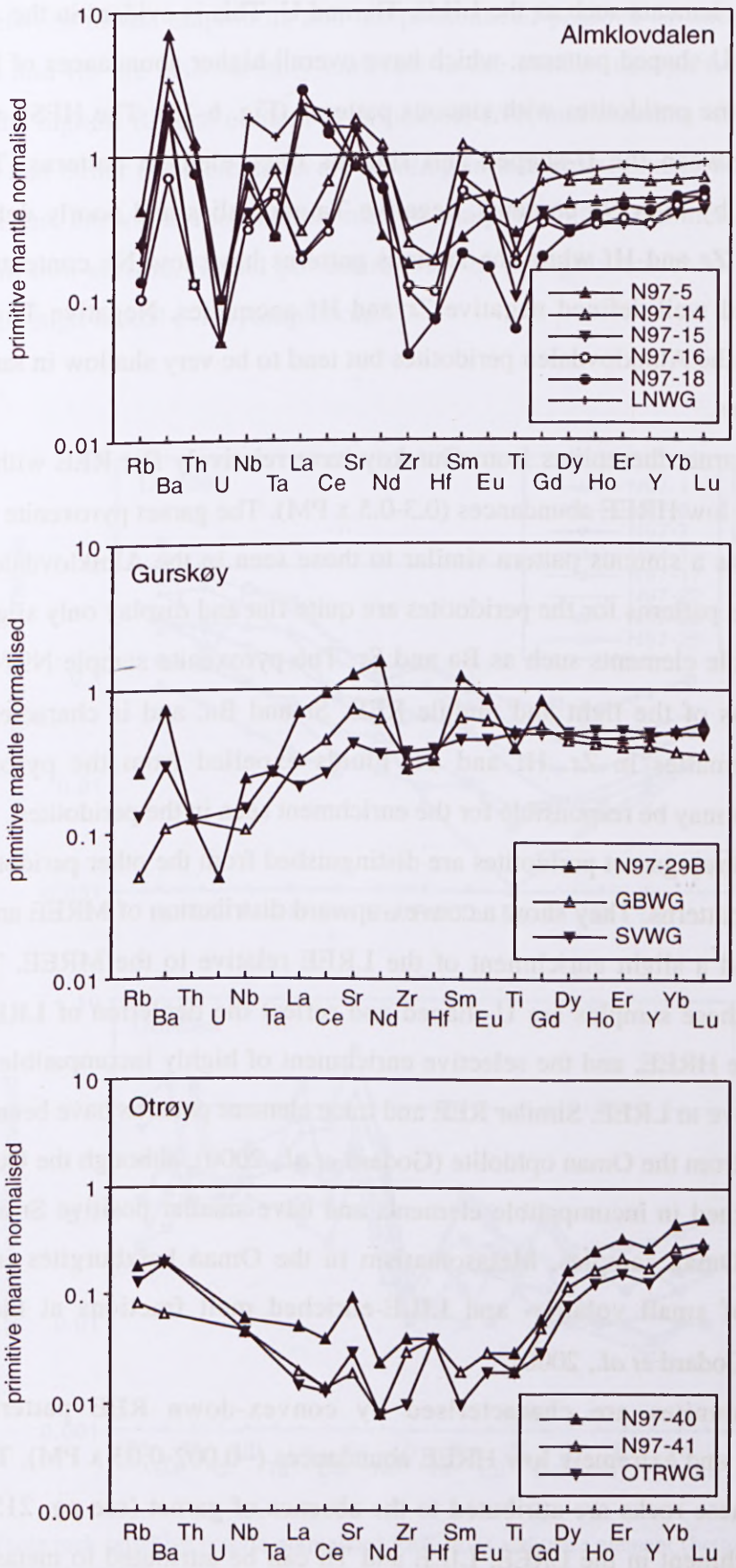


**Figure 6-16.** Whole rock primitive mantle normalised trace element patterns for Western Gneiss Region garnet peridotites.

LREE-enrichment in peridotite is commonly accompanied by enrichment in other incompatible elements such as the LILE, Th, and U. This is evident in the Almklovdalen samples with U-shaped patterns, which have overall higher abundances of Ba, Sr and Th compared to the peridotites with sinuous patterns (Fig. 6-16). The HFSE show variable behaviour between the U-shaped and sinuous trace element patterns. The first are characterised by high Nb contents, negative Ta anomalies and poorly defined negative anomalies in Zr and Hf while the sinuous patterns have low Nb contents, positive Ta anomalies and well-defined negative Zr and Hf anomalies. Negative Ti anomalies are ubiquitous in the Almklovdalen peridotites but tend to be very shallow in samples with U-shaped patterns.

The garnet lherzolites from Gurskøy have relatively flat REE with slight LREE depletion and low HREE abundances (0.3-0.5 x PM). The garnet pyroxenite from Gurskøy (N97-29B) has a sinuous pattern similar to those seen in the Almklovdalen peridotites. Trace element patterns for the peridotites are quite flat and display only slight enrichment in incompatible elements such as Ba and Sr. The pyroxenite sample N97-29B has high concentrations of the light and middle REE, Sr and Ba, and is characterised by deep negative anomalies in Zr, Hf and Ti. Fluids expelled from the pyroxenite during crystallisation may be responsible for the enrichment seen in the peridotites.

The Otrøy garnet peridotites are distinguished from the other peridotites by spoon-shaped REE patterns. They show a convex-upward distribution of MREE and HREE from Eu to Lu, and a slight enrichment of the LREE relative to the MREE. Trace element patterns for these samples are U-shaped and reflect the depletion of LREE, Zr and Hf relative to the HREE, and the selective enrichment of highly incompatible elements (i.e. Rb, Ba) relative to LREE. Similar REE and trace element patterns have been recognised in harzburgites from the Oman ophiolite (Godard *et al.*, 2000), although the Otrøy peridotites are less enriched in incompatible elements and have smaller positive Sr anomalies than seen in the Oman samples. Metasomatism in the Oman harzburgites is attributed to infiltration of small volatile- and LILE-enriched melt fractions at the base of the lithosphere (Godard *et al.*, 2000).

The dunites are characterised by convex-down REE patterns that have [$(La/Yb)_N$>1] and extremely low HREE abundances (~0.002-0.03 x PM). The low HREE contents is these rocks are attributed to the absence of garnet (see pg. 215) whereas the relative enrichment in the LREE, LILE and Th can be attributed to metasomatism by a volatile-rich fluid. These elements are probably residing in amphibole or phlogopite as

chlorite is not a significant carrier of LIL elements. This is supported by the positive correlation between modal amphibole and the pronounced positive Sr anomalies seen in Fig. 6-17. Ba and Rb are also variably enriched in the dunites though interestingly the sample with the highest Rb and content is amphibole-free, and contains <1% phlogopite. This suggests that either these elements are residing in interstitial phases not identified in thin-section or that the whole-rock sample used in analysis contained a metasomatic phase not sampled in thin-section. Spinel peridotite N97-25 is highly enriched in Sr and has correspondingly high modal (~7%) amphibole.

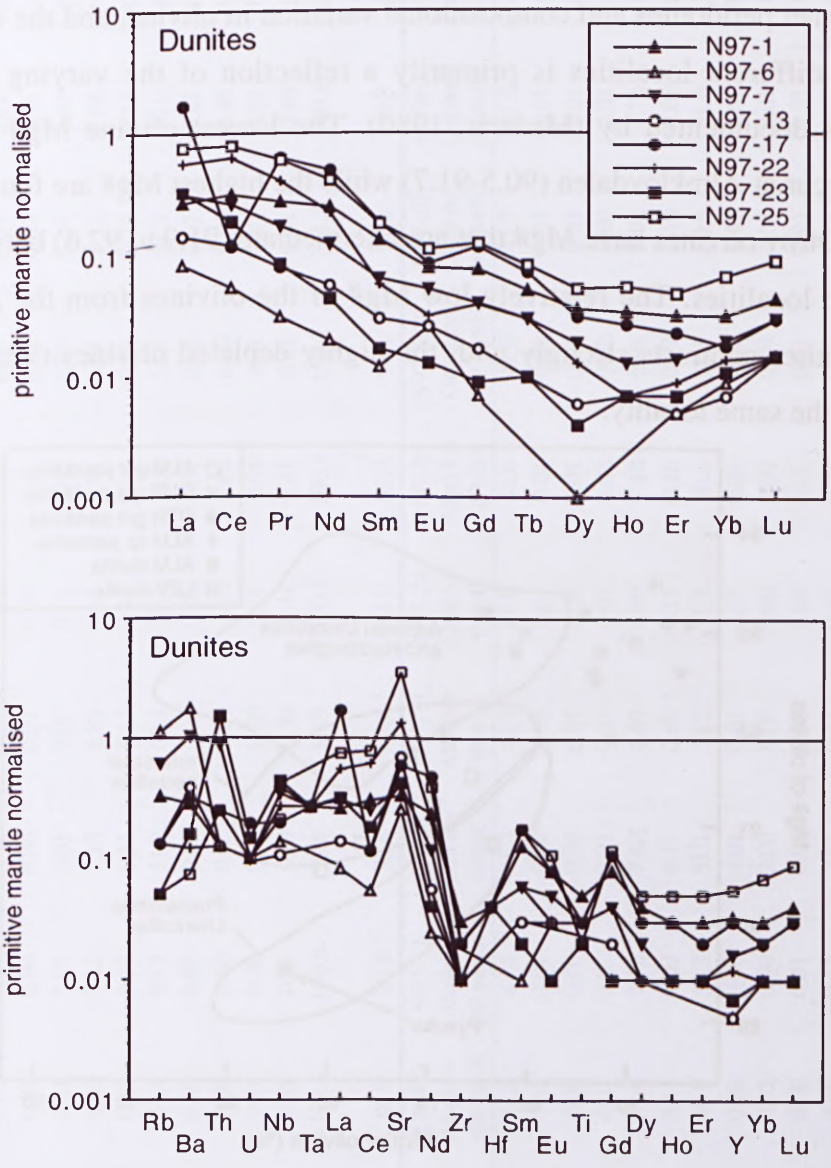


**Figure 6-17.** Whole rock primitive mantle normalised REE (top) and trace element (bottom) patterns for Western Gneiss Region dunites.

## 6.6 MINERAL GEOCHEMISTRY

Major element data for all mineral phases of the Western Gneiss Region peridotites are given in the relevant mineral section. Garnet, clinopyroxene, amphibole and orthopyroxene from the garnet peridotites were analysed for 30 trace elements and results are tabulated in the relevant mineral section. Mineral trace elements were not analysed in the dunites.

### *6.6.1 Olivine*

Olivine grains in the WGR peridotites are unzoned and variation in Fo within an individual sample is less than ±0.2. Olivine Mg# is typically high (>90.5) in the WGR (see Fig. 6-18) garnet peridotites and compositional variation in olivine, and the other silicates, between the different localities is primarily a reflection of the varying Mg# in bulk chemistry, as documented by (Medaris, 1980). The lowest olivine Mg# in the garnet peridotites occur at Almklovdalen (90.5-91.7) while the highest Mg# are found at Gurskøy (92.9-93.2). Otrøy olivines have Mg# that are intermediate (91.9 to 92.6) between those for the other two localities. The relatively low Mg# of the olivines from the Almklovdalen garnet peridotites contrasts strongly with the highly depleted olivines (92.5-93.5) in the dunites from the same locality.

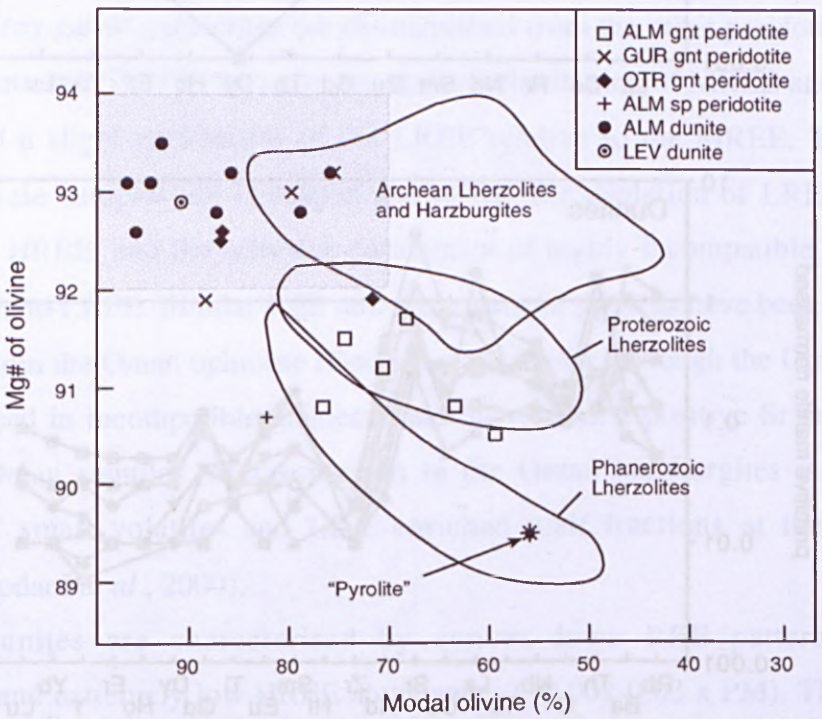


**Figure 6-18.** Modal olivine vs olivine Mg# plot for the WGR peridotites. Phanerozoic and Archean fields from (Boyd, 1989; Boyd, 1997). Proterozoic field from (Griffin *et al.*, 1998b). Grey field encloses data for olivine-rich peridotite xenoliths from Wiedemann Fjord (Greenland; Bernstein *et al.*, 1998), the Slave craton (Boyd and Canil, 1997), the Tanzanian craton (Lee and Rudnick, 1999) and Ubekendt Ejland (Greenland; Bernstein and Brooks, 1999).

**Table 6-3.** Major element abundances (wt%) of olivine from Western Gneiss Region peridotites.

| Sample no. | N97-1 | N97-5 | N97-6 | N97-7 | N97-8 | N97-9 | N97-11 | N97-13 | N97-14 | N97-15 | N97-16 | N97-17 | N97-18 |
|---|---|---|---|---|---|---|---|---|---|---|---|---|---|
| Locality | Levdal | Almklov | Almklov | Almklov | Almklov | Almklov | Almklov | Almklov | Almklov | Almklov | Almklov | Almklov | Almklov |
| Rock type | dunite | gnt lherz | dunite | dunite | dunite | dunite | dunite | dunite | gnt lherz | gnt lherz | gnt lherz | dunite | gnt lherz |
| $SiO_2$ | 41.9 | 40.6 | 40.2 | 40.3 | 40.7 | 41.1 | 41.1 | 41.9 | 41.0 | 40.9 | 41.53 | 41.0 | 41.5 |
| $TiO_2$ | 0.01 | 0.01 | 0.01 | 0.01 | 0.01 | 0.00 | 0.00 | 0.00 | 0.02 | 0.02 | 0.01 | 0.01 | 0.01 |
| $Al_2O_3$ | 0.01 | 0.00 | 0.00 | 0.01 | 0.00 | 0.01 | 0.01 | 0.00 | 0.01 | 0.00 | 0.00 | 0.00 | 0.00 |
| $Cr_2O_3$ | 0.01 | 0.01 | 0.01 | 0.02 | 0.01 | 0.02 | 0.02 | 0.03 | 0.02 | 0.01 | 0.01 | 0.01 | 0.01 |
| FeO | 6.96 | 9.12 | 7.19 | 6.89 | 6.95 | 6.74 | 6.74 | 7.12 | 9.08 | 8.33 | 8.25 | 7.31 | 8.25 |
| MnO | 0.10 | 0.12 | 0.11 | 0.11 | 0.11 | 0.09 | 0.09 | 0.10 | 0.12 | 0.13 | 0.09 | 0.11 | 0.09 |
| MgO | 51.4 | 50.3 | 51.8 | 52.1 | 51.9 | 51.8 | 51.8 | 51.7 | 50.0 | 50.6 | 50.9 | 51.3 | 50.9 |
| CaO | 0.00 | 0.00 | 0.01 | 0.01 | 0.00 | 0.01 | 0.01 | 0.01 | 0.01 | 0.01 | 0.01 | 0.01 | 0.01 |
| $Na_2O$ | 0.00 | 0.00 | 0.00 | 0.00 | 0.00 | 0.00 | 0.00 | 0.00 | 0.00 | 0.00 | 0.00 | 0.01 | 0.00 |
| $K_2O$ | 0.01 | 0.00 | 0.00 | 0.00 | 0.01 | 0.01 | 0.01 | 0.01 | 0.01 | 0.00 | 0.01 | 0.00 | 0.01 |
| NiO | 0.38 | 0.43 | 0.39 | 0.39 | 0.44 | 0.41 | 0.41 | 0.01 | 0.40 | 0.39 | 0.41 | 0.41 | 0.41 |
| Total | 100.8 | 100.6 | 99.8 | 99.9 | 100.1 | 100.3 | 100.2 | 101.3 | 100.8 | 100.4 | 101.2 | 100.2 | 101.5 |
| Mg# | 92.9 | 90.8 | 92.8 | 93.1 | 93.0 | 93.2 | 93.1 | 92.8 | 90.8 | 91.5 | 91.7 | 92.6 | 90.5 |

| Sample no. | LNWG | N97-21 | N97-22 | N97-23 | N97-24 | N97-25 | N97-29B | N97-30 | GBWG | SVWG | N97-40 | N97-41 | OTRWG |
|---|---|---|---|---|---|---|---|---|---|---|---|---|---|
| Locality | Almklov | Almklov | Almklov | Almklov | Almklov | Almklov | Gurskøy | Gurskøy | Gurskøy | Gurskøy | Otrøy | Otrøy | Otrøy |
| Rock type | gnt perid | ol augen | dunite | dunite | dunite | sp harz | gnt pyro | gnt wehr | gnt wehr | gnt wehr | gnt harz | gnt harz | gnt harz |
| $SiO_2$ | 41.2 | 41.4 | 41.3 | 41.9 | 41.9 | 41.6 | 41.9 | 41.7 | 41.5 | 41.7 | 40.8 | 41.3 | 41.5 |
| $TiO_2$ | 0.01 | 0.01 | 0.00 | 0.01 | 0.01 | 0.01 | 0.02 | 0.01 | 0.01 | 0.01 | 0.02 | 0.01 | 0.01 |
| $Al_2O_3$ | 0.00 | 0.00 | 0.00 | 0.01 | 0.00 | 0.01 | 0.01 | 0.01 | 0.01 | 0.00 | 0.01 | 0.01 | 0.01 |
| $Cr_2O_3$ | 0.01 | 0.01 | 0.01 | 0.01 | 0.01 | 0.02 | 0.02 | 0.00 | 0.01 | 0.01 | 0.01 | 0.01 | 0.01 |
| FeO | 8.56 | 7.10 | 7.40 | 6.67 | 6.89 | 9.10 | 6.98 | 8.02 | 6.75 | 6.91 | 8.01 | 7.63 | 7.21 |
| MnO | 0.11 | 0.09 | 0.12 | 0.09 | 0.11 | 0.16 | 0.07 | 0.10 | 0.05 | 0.06 | 0.12 | 0.10 | 0.09 |
| MgO | 49.5 | 51.7 | 51.1 | 52.2 | 51.8 | 50.1 | 51.5 | 50.9 | 51.6 | 51.5 | 51.2 | 51.4 | 50.6 |
| CaO | 0.00 | 0.00 | 0.01 | 0.01 | 0.01 | 0.01 | 0.00 | 0.01 | 0.01 | 0.01 | 0.02 | 0.01 | 0.01 |
| $Na_2O$ | 0.01 | 0.00 | 0.00 | 0.00 | 0.00 | 0.00 | 0.00 | 0.01 | 0.01 | 0.01 | 0.00 | 0.00 | 0.00 |
| $K_2O$ | 0.00 | 0.01 | 0.01 | 0.00 | 0.00 | 0.01 | 0.01 | 0.01 | 0.01 | 0.00 | 0.01 | 0.01 | 0.00 |
| NiO | 0.40 | 0.43 | 0.42 | 0.41 | 0.40 | 0.32 | 0.49 | 0.44 | 0.32 | 0.34 | 0.41 | 0.40 | 0.41 |
| Total | 99.8 | 100.8 | 100.4 | 101.3 | 101.1 | 101.4 | 101.0 | 101.2 | 100.2 | 100.6 | 100.6 | 100.9 | 99.8 |
| Mg# | 91.2 | 92.8 | 92.5 | 93.3 | 93.1 | 90.7 | 92.9 | 91.9 | 93.2 | 93.0 | 91.9 | 92.3 | 92.6 |

Olivine compositions and modes from the Almklovdalen garnet peridotites fall in or near the Proterozoic field in Fig. 6-18 and show an overall increase in olivine Mg# with increasing olivine content. The same is true for the Otrøy peridotites though they extend to higher Mg# and modal olivine and plot outside the Proterozoic field. The garnet peridotites from Gurskøy have uniformly high Mg# and variable modal olivine. Two of these samples plot in the Archean field and appear to be quite different from the other garnet peridotites. The dunites have very high modal olivine and fall in the compositional field defined by the Wiedemann Fjord (east Greenland) peridotites (Bernstein *et al.*, 1998) and other similar olivine-rich mantle xenoliths (see Fig. 6-18). The Wiedemann Fjord spinel dunites are extremely depleted and have been modelled as residues after ~40% melting of a primitive mantle source. The depleted compositions of the dunites are similarly consistent with high degrees of partial melting.

### *6.6.2 Orthopyroxene*

The orthopyroxenes in the WGR garnet-bearing peridotites are enstatites with compositions that range from $En_{90.9}$ to $En_{93.4}$. A significant feature of the orthopyroxene is the consistently low content of $Al_2O_3$, which ranges from 0.59% to 1.71%, though the majority of grains contain less than 1.0% (Fig. 6-19). $Cr_2O_3$ contents are low and vary from 0.08-0.23 while Cr# is typically between 12 and 15; an exception is orthopyroxene from sample GBWG from Gurskøy which has an anomalously low Cr# of 3 (Fig. 6-19). There is no significant difference in chemistry between orthopyroxene in garnet-bearing lherzolite and pyroxenite from Gurskøy (Fig. 6-19). Orthopyroxene in garnet kelyphite rims is Al-rich with $Al_2O_3$ contents of up to 6 wt%.

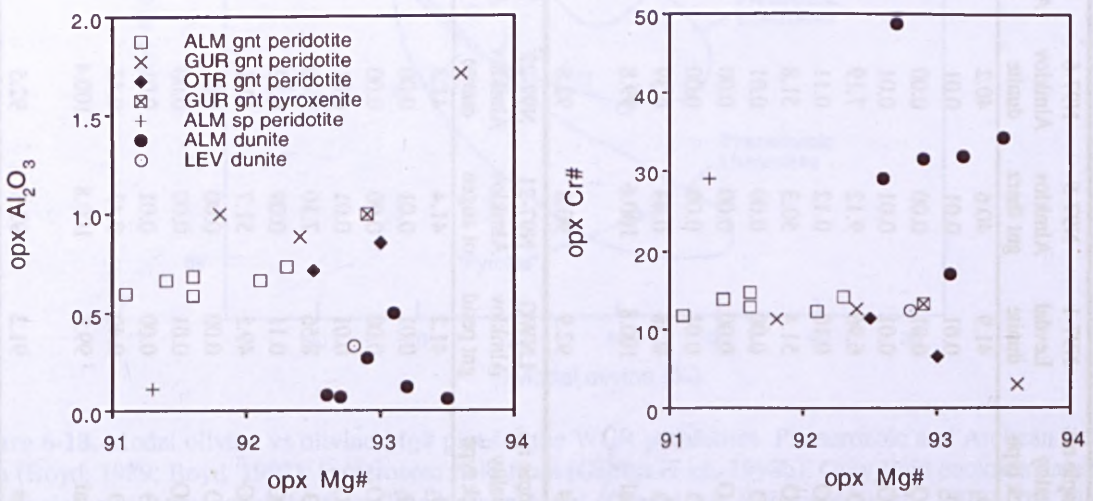


**Figure 6-19.** Compositional variation diagrams for orthopyroxene in peridotites from the Western Gneiss Region, Norway.

**Table 6-4.** Major element oxide abundances (wt%) of orthopyroxene from Western Gneiss Region peridotites.

| Sample no. | N97-5 | N97-14 | N97-15 | N97-16 | N97-18 | LNWG | N97-29A |
|---|---|---|---|---|---|---|---|
| Locality | Almklov | Almklov | Almklov | Almklov | Almklov | Almklov | Gurskøy |
| Rock type | gnt perid | gnt perid | gnt perid | gnt perid | gnt perid | gnt perid | gnt perid |
| $SiO_2$ | 57.5 | 58.3 | 57.7 | 58.9 | 58.5 | 58.3 | 58.3 |
| $TiO_2$ | 0.03 | 0.01 | 0.02 | 0.03 | 0.03 | 0.03 | 0.04 |
| $Al_2O_3$ | 0.67 | 0.60 | 0.73 | 0.67 | 0.69 | 0.59 | 0.89 |
| $Cr_2O_3$ | 0.17 | 0.12 | 0.18 | 0.14 | 0.19 | 0.13 | 0.18 |
| FeO | 6.00 | 6.15 | 5.34 | 5.47 | 5.83 | 5.72 | 5.19 |
| MnO | 0.13 | 0.12 | 0.11 | 0.10 | 0.10 | 0.12 | 0.14 |
| MgO | 35.7 | 35.5 | 35.8 | 35.9 | 35.6 | 34.8 | 36.0 |
| CaO | 0.12 | 0.11 | 0.11 | 0.11 | 0.12 | 0.10 | 0.15 |
| $Na_2O$ | 0.00 | 0.00 | 0.00 | 0.00 | 0.00 | 0.01 | 0.02 |
| $K_2O$ | 0.00 | 0.01 | 0.00 | 0.01 | 0.01 | 0.00 | 0.01 |
| NiO | 0.07 | 0.07 | 0.07 | 0.05 | 0.06 | 0.09 | 0.08 |
| Total | 100.4 | 101.0 | 100.1 | 101.3 | 101.1 | 99.9 | 101.0 |
| Mg# | 91.4 | 91.1 | 92.3 | 92.1 | 91.6 | 91.6 | 92.4 |

| Sample no. | N97-29B | N97-31 | GBWG | GBWG | N97-41 | OTRWG | N97-1 |
|---|---|---|---|---|---|---|---|
| Locality | Gurskøy | Gurskøy | Gurskøy | Gurskøy | Otrøy | Otrøy | Levdal |
| Rock type | gnt pyrox | gnt perid | gnt perid | kelyphite | gnt perid | gnt perid | dunite |
| $SiO_2$ | 58.7 | 58.7 | 58.2 | 54.8 | 58.0 | 58.4 | 59.0 |
| $TiO_2$ | 0.03 | 0.03 | 0.04 | 0.01 | 0.01 | 0.00 | 0.02 |
| $Al_2O_3$ | 1.00 | 1.00 | 1.71 | 6.01 | 0.72 | 0.86 | 0.33 |
| $Cr_2O_3$ | 0.23 | 0.23 | 0.08 | 0.38 | 0.14 | 0.09 | 0.09 |
| FeO | 4.87 | 4.87 | 4.39 | 3.84 | 5.20 | 4.75 | 4.96 |
| MnO | 0.07 | 0.07 | 0.08 | 0.08 | 0.10 | 0.09 | 0.16 |
| MgO | 36.0 | 36.0 | 36.0 | 33.6 | 36.2 | 35.5 | 36.3 |
| CaO | 0.13 | 0.13 | 0.14 | 0.69 | 0.16 | 0.16 | 0.07 |
| $Na_2O$ | 0.01 | 0.01 | 0.00 | 0.00 | 0.01 | 0.02 | 0.00 |
| $K_2O$ | 0.01 | 0.01 | 0.00 | 0.01 | 0.01 | 0.01 | 0.01 |
| NiO | 0.07 | 0.07 | 0.00 | 0.01 | 0.08 | 0.13 | 0.07 |
| Total | 101.2 | 101.2 | 100.6 | 99.4 | 100.8 | 100.0 | 101.0 |
| Mg# | 92.9 | 92.9 | 93.6 | 94.0 | 92.5 | 93.0 | 92.8 |

| Sample no. | N97-6 | N97-8 | N97-13 | N97-21 | N97-22 | N97-23 | N97-25 |
|---|---|---|---|---|---|---|---|
| Locality | Almklov | Almklov | Almklov | Almklov | Almklov | Almklov | Almklov |
| Rock type | dunite | dunite | dunite | dunite | dunite | dunite | sp perid |
| $SiO_2$ | 57.6 | 58.0 | 59.13 | 58.7 | 58.6 | 59.1 | 59.3 |
| $TiO_2$ | 0.00 | 0.01 | 0.00 | 0.01 | 0.02 | 0.01 | 0.02 |
| $Al_2O_3$ | 0.07 | 0.12 | 0.27 | 0.50 | 0.08 | 0.06 | 0.11 |
| $Cr_2O_3$ | 0.10 | 0.09 | 0.18 | 0.14 | 0.05 | 0.04 | 0.07 |
| FeO | 5.15 | 4.75 | 4.97 | 4.84 | 5.16 | 4.59 | 6.08 |
| MnO | 0.18 | 0.13 | 0.12 | 0.14 | 0.14 | 0.12 | 0.18 |
| MgO | 36.5 | 36.8 | 36.4 | 36.7 | 36.2 | 36.9 | 35.7 |
| CaO | 0.08 | 0.09 | 0.11 | 0.14 | 0.09 | 0.08 | 0.12 |
| $Na_2O$ | 0.00 | 0.01 | 0.00 | 0.02 | 0.00 | 0.00 | 0.01 |
| $K_2O$ | 0.00 | 0.00 | 0.01 | 0.01 | 0.00 | 0.00 | 0.01 |
| NiO | 0.04 | 0.09 | 0.01 | 0.07 | 0.07 | 0.06 | 0.05 |
| Total | 99.8 | 100.1 | 101.3 | 101.2 | 100.4 | 100.9 | 101.6 |
| Mg# | 92.7 | 93.2 | 92.9 | 93.1 | 92.6 | 93.5 | 91.3 |

Orthopyroxenes from the dunites have homogeneous compositions with high Mg# (92.5-93.5), but very low $Al_2O_3$ contents (0.06-0.5 wt%), and fall below the trend defined by the garnet peridotites (see Fig. 6-19). These orthopyroxenes have high $Cr_2O_3$ relative to $Al_2O_3$, compared to the garnet peridotites, and consequently have higher Cr#. In terms of $Al_2O_3$ content and Cr# the orthopyroxene from the spinel peridotite (N97-25) is similar to that seen in the dunites though it has a Mg# closer to the Almklovdalen garnet peridotites.

Compositional zoning was noted in orthopyroxenes from garnet peridotite from all three main localities. At Almklovdalen the cores of the orthopyroxene grains are moderately enriched in $Al_2O_3$ and $Cr_2O_3$ relative to the rims, a trend previously reported by Medaris (1980), though the latter work detected a increase in $Al_2O_3$ content in the outermost parts of the rim. Mg# shows a small decrease from core to rim that is the result of minor Fe-enrichment in rims compared to cores. In contrast to Almklovdalen, orthopyroxenes from Gurskøy and Otrøy show a pattern of increasing $Al_2O_3$ from 0.4-0.9 wt% in cores to 0.7-1.7% at rims, the highest value occurring in a rim in contact with garnet. The Otrøy grains also display a slight decrease in Mg# from core to rim. It has been suggested by Medaris (1984) that the increase in Al content in orthopyroxene rims (in equilibrium with garnet) is a response to a decrease in pressure and temperature. Orthopyroxenes from the dunites are generally homogeneous except for those from sample N97-1 from Levdal which display strong Al-enrichment in cores (1.27 wt%) relative to rims (0.33 wt%).

### *6.6.3 Clinopyroxene*

Clinopyroxenes from the WGR garnet peridotites and pyroxenites are exclusively diopsides ($En_{47-50}Fs_{1.8-3.4}Wo_{48-51}$). Major and trace element abundances for the Norwegian clinopyroxenes are given in Table 6-5. Two types of clinopyroxene have been recognised at Almklovdalen. The first type is relatively fresh in appearance and is characterised by high $Al_2O_3$, $Na_2O$ and $Cr_2O_3$, and low MgO and CaO (see Table 6-5 and Fig. 6-20). Mg# for the type 1 cpx ranges from 93.4-94.6 while Cr# varies from 24.9-31.2. The second type is grainy in appearance due to the presence of numerous, densely-packed dark inclusions, and is distinguished by low $Al_2O_3$, $Na_2O$, and $Cr_2O_3$, and high MgO and CaO. Both Mg# and Cr# are higher in type 2 compared to type 1 and have average values of 95.6 and 32.3 respectively. Type 2 clinopyroxene was identified in samples N87-18 and LNWG and occurs either as discrete grains in the matrix or as rims on type 1 clinopyroxene which suggests that it may be a breakdown product of type 1.

Clinopyroxene from the Gurskøy peridotites is closer in composition to type 1 from Almklovdalen than to type 2 though there are some significant differences. Gurskøy clinopyroxenes have higher Mg# (~95-96) and higher abundances of Al, Ti and Na compared to type 1 diopside (Fig. 6-20). The harzburgites from Otrøy are by definition cpx-free, however, a single small grain of diopside was found in sample OTRWG. The Otrøy clinopyroxene is similar in composition to type 1 from Almklovdalen but has a higher Cr content.

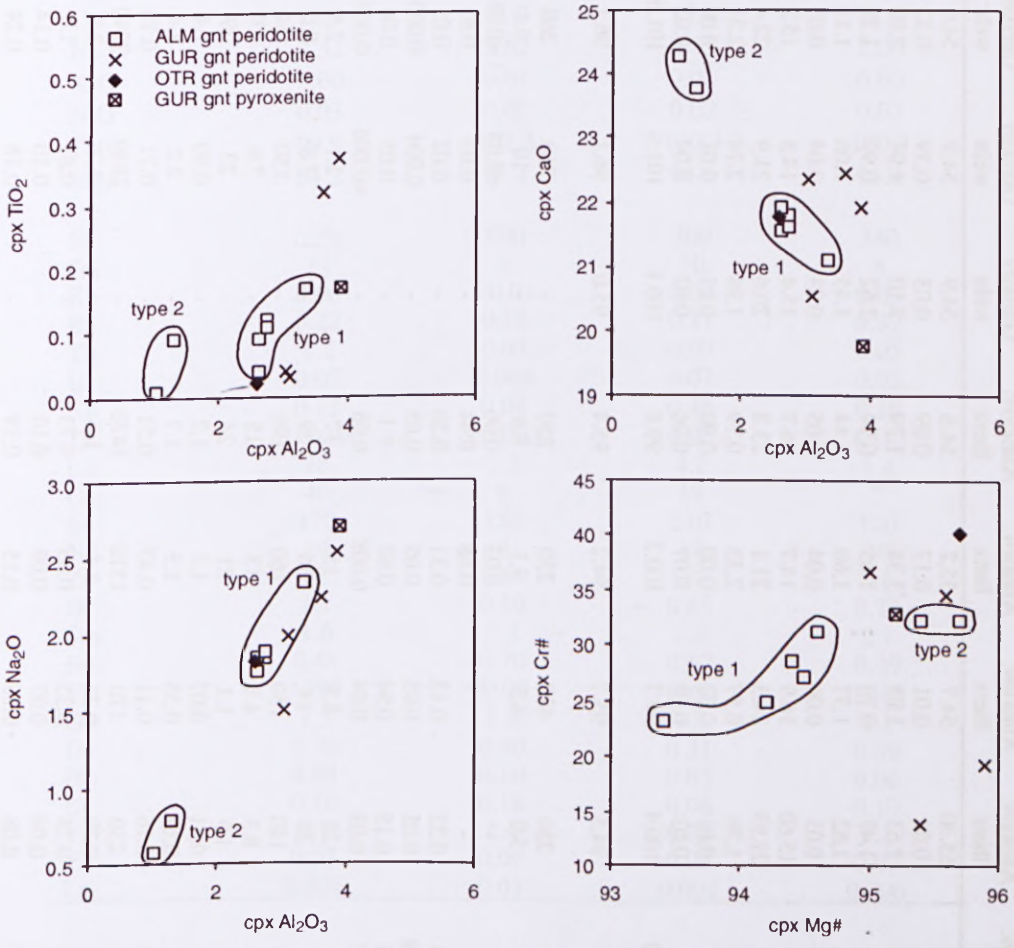


**Figure 6-20.** Compositional variation diagrams for clinopyroxene in peridotites from the Western Gneiss Region, Norway. Type 1 and 2 clinopyroxenes from Almklovdalen are circled.

Zoning in clinopyroxene is most apparent in terms of Al and Na content and shows a similar pattern to zoning recognised in orthopyroxene. At Almklovdalen, $Al_2O_3$ and $Na_2O$ decrease from core to rim which, according to Medaris (1984), reflects the extraction of jadeite component from clinopyroxene during the formation of amphibole. In contrast, clinopyroxenes from Gurskøy display an increase of $Al_2O_3$ and $Na_2O$ from core to rim, that Medaris (1984) suggested may signify the return of jadeite component to clinopyroxene during the regeneration of garnet, though there is no evidence for post-kelyphite, regenerated garnet in these samples.

**Table 6-5.** Major (wt%) and trace element (ppm) abundances of clinopyroxene from Western Gneiss Region garnet peridotites.

| Sample no. | N97-14 | N97-15 | N97-16 | N97-18(1) | N97-18(2) | LNWG(1) | LNWG(2) | N97-30 | GBWG | SVWG | N97-29B | OTRWG |
|---|---|---|---|---|---|---|---|---|---|---|---|---|
| Locality | Almklov. | Almklov. | Almklov. | Almklov. | Almklov. | Almklov. | Almklov. | Gurskøy | Gurskøy | Gurskøy | Gurskøy | Otrøy |
| Rock type | lherz | lherz | lherz | lherz | lherz | lherz | lherz | wehr | wehr | wehr | pxenite | harz |
| $SiO_2$ | 54.6 | 54.5 | 54.9 | 55.30 | 54.7 | 55.2 | 54.6 | 54.9 | 54.9 | 54.9 | 55.3 | 54.5 |
| $TiO_2$ | 0.09 | 0.09 | 0.10 | 0.04 | 0.01 | 0.17 | 0.09 | 0.03 | 0.39 | 0.32 | 0.16 | 0.02 |
| $Al_2O_3$ | 2.52 | 2.62 | 2.40 | 2.63 | 1.04 | 3.34 | 1.29 | 3.10 | 4.94 | 3.92 | 3.29 | 2.60 |
| $Cr_2O_3$ | 1.26 | 1.77 | 1.59 | 1.47 | 0.76 | 1.65 | 0.94 | 2.62 | 0.99 | 1.28 | 2.37 | 2.60 |
| FeO | 1.96 | 1.56 | 1.66 | 1.62 | 1.37 | 1.60 | 1.44 | 1.45 | 1.06 | 1.11 | 1.33 | 1.23 |
| MnO | 0.03 | 0.02 | 0.03 | 0.03 | 0.06 | 0.04 | 0.05 | 0.03 | 0.04 | 0.03 | 0.01 | 0.02 |
| MgO | 15.5 | 15.4 | 15.8 | 15.60 | 16.9 | 14.7 | 16.7 | 15.4 | 14.5 | 15.2 | 14.8 | 15.2 |
| CaO | 22.0 | 21.6 | 21.9 | 21.93 | 24.3 | 21.1 | 23.8 | 20.6 | 21.9 | 22.4 | 20.7 | 21.8 |
| $Na_2O$ | 1.69 | 1.85 | 1.60 | 1.76 | 0.57 | 2.33 | 0.79 | 1.98 | 2.74 | 2.21 | 2.41 | 1.82 |
| $K_2O$ | 0.00 | 0.01 | 0.01 | 0.01 | 0.01 | 0.00 | 0.00 | 0.01 | 0.01 | 0.00 | 0.00 | 0.00 |
| NiO | 0.02 | 0.05 | 0.02 | 0.03 | 0.08 | 0.07 | 0.06 | 0.02 | 0.04 | 0.03 | 0.04 | 0.07 |
| Total | 99.7 | 99.5 | 100.0 | 100.4 | 99.7 | 100.2 | 99.8 | 100.1 | 101.5 | 101.5 | 100.4 | 99.9 |
| Mg# | 93.4 | 94.6 | 94.4 | 94.5 | 95.7 | 94.2 | 95.4 | 95.0 | 96.1 | 96.1 | 95.2 | 95.7 |
| Ni | 300 | 270 | 280 | 280 | 420 | 230 | 250 | - | 260 | 260 | 280 | 450 |
| Ga | 7.8 | 4.9 | 6.4 | 5.0 | 4.5 | 9.1 | 9.6 | - | 10 | 9.1 | 12 | 2.2 |
| Rb | - | - | - | - | - | 0.03 | 0.06 | - | <0.05 | <0.05 | <0.05 | 0.10 |
| Ba | - | - | - | - | - | 0.68 | 0.44 | - | 0.03 | 0.65 | 0.03 | 0.15 |
| Th | 0.07 | 0.05 | 0.03 | 0.22 | 0.12 | 0.31 | 0.20 | - | 0.02 | 0.05 | 0.04 | 0.01 |
| U | 0.03 | 0.01 | 0.009 | 0.05 | 0.05 | 0.05 | 0.05 | - | 0.004 | 0.003 | 0.02 | 0.004 |
| Nb | 0.15 | 0.34 | 0.26 | 0.15 | 0.94 | 0.61 | 1.1 | - | 0.05 | 0.06 | 0.16 | 0.11 |
| Ta | 0.06 | 0.07 | 0.02 | 0.03 | 0.04 | 0.008 | 0.08 | - | <0.006 | 0.008 | 0.02 | <0.002 |
| La | 2.2 | 2.1 | 2.4 | 20 | 8.8 | 15 | 17 | - | 2.1 | 2.5 | 4 | 0.35 |
| Ce | 11 | 9.2 | 8.7 | 26 | 14 | 36 | 39 | - | 7.8 | 8.0 | 19 | 0.92 |
| Sr | 320 | 310 | 310 | 140 | 150 | 160 | 190 | - | 150 | 150 | 210 | 27 |
| Nd | 17 | 16 | 16 | 8.3 | 4.8 | 13 | 15 | - | 7.9 | 7.9 | 20 | 0.43 |
| Zr | 16 | 9 | 10 | 1.9 | 1.1 | 21 | 24 | - | 23 | 29 | 10 | 1.5 |
| Hf | 0.52 | 0.30 | 0.41 | 0.11 | 0.07 | 1.1 | 1.2 | - | 0.90 | 1.4 | 0.72 | 0.11 |
| Sm | 4.9 | 3.4 | 3.4 | 0.69 | 0.35 | 1.5 | 1.7 | - | 2.2 | 2.4 | 3.2 | 0.08 |
| Eu | 0.98 | 0.70 | 0.70 | 0.16 | 0.11 | 0.47 | 0.51 | - | 0.71 | 0.78 | 0.63 | 0.03 |
| Ti | 820 | 500 | 890 | 230 | 170 | 1510 | 1470 | - | 2830 | 2240 | 1190 | 120 |
| Gd | 1.8 | 1.2 | 1.2 | 0.38 | 0.21 | 1.4 | 1.6 | - | 1.7 | 2.1 | 1.3 | 0.13 |
| Dy | 0.57 | 0.31 | 0.33 | 0.28 | 0.35 | 0.65 | 0.73 | - | 0.81 | 1.0 | 0.31 | 0.18 |
| Ho | 0.07 | 0.04 | 0.04 | 0.04 | 0.07 | 0.09 | 0.10 | - | 0.10 | 0.14 | 0.04 | 0.04 |
| Er | 0.12 | 0.08 | 0.09 | 0.08 | 0.18 | 0.15 | 0.19 | - | 0.18 | 0.24 | 0.07 | 0.08 |
| Y | 1.6 | 0.98 | 1.1 | 0.95 | 1.5 | 1.9 | 2.2 | - | 2.4 | 3.2 | 0.87 | 0.87 |
| Yb | 0.06 | 0.06 | 0.05 | 0.06 | 0.12 | 0.06 | 0.11 | - | 0.09 | 0.13 | 0.05 | 0.05 |
| Lu | <0.014 | 0.01 | <0.015 | 0.02 | 0.03 | 0.007 | 0.01 | - | 0.01 | 0.01 | 0.006 | 0.005 |

**Table 6-6.** Major (wt%) and trace element (ppm) abundances of clinopyroxene inclusions from Western Gneiss Region garnet peridotites.

| Sample no. | LNWG | GBWG | N97-29B | N97-29B |
|---|---|---|---|---|
| Locality | Almklovdalen | Gurskøy | Gurskøy | Gurskøy |
| Rock type | lherzolite | wehrlite | pyroxenite | pyroxenite |
| Host mineral | garnet | garnet | garnet | opx |
| $SiO_2$ | 55.0 | 55.4 | 55.8 | 54.8 |
| $TiO_2$ | 0.22 | 0.41 | 0.18 | 0.17 |
| $Al_2O_3$ | 3.21 | 3.81 | 3.79 | 3.82 |
| $Cr_2O_3$ | 1.72 | 0.93 | 2.24 | 2.49 |
| FeO | 1.65 | 1.33 | 1.47 | 0.97 |
| MnO | 0.03 | 0.06 | 0.01 | 0.00 |
| MgO | 14.9 | 15.5 | 14.6 | 14.6 |
| CaO | 20.9 | 21.3 | 19.4 | 21.4 |
| $Na_2O$ | 2.32 | 2.62 | 2.85 | 2.00 |
| $K_2O$ | 0.00 | 0.01 | 0.01 | 0.00 |
| NiO | 0.03 | 0.02 | 0.02 | 0.03 |
| Total | 99.9 | 101.4 | 100.3 | 100.3 |
| Mg# | 94.2 | 95.4 | 94.6 | 96.4 |
| | | | | |
| Ni | 220 | 300 | 300 | 340 |
| Ga | 11 | 9 | 10 | 8 |
| Rb | 0.05 | <0.04 | 0.04 | 0.05 |
| Ba | 0.22 | 0.18 | 0.21 | 0.37 |
| Th | 1.2 | 0.03 | 0.09 | 0.05 |
| U | 0.05 | 0.004 | 0.02 | 0.02 |
| Nb | 0.12 | 0.04 | 0.46 | 0.16 |
| Ta | 0.008 | <0.005 | 0.05 | 0.01 |
| La | 18 | 2.2 | 4.2 | 1.4 |
| Ce | 40 | 8 | 19 | 7 |
| Sr | 170 | 150 | 210 | 120 |
| Nd | 14 | 8 | 19 | 10 |
| Zr | 22 | 20 | 8 | 11 |
| Hf | 1.1 | 0.89 | 0.65 | 0.74 |
| Sm | 1.6 | 2.2 | 2.9 | 2.1 |
| Eu | 0.48 | 0.70 | 0.57 | 0.49 |
| Ti | 1890 | 3100 | 1160 | 1240 |
| Gd | 1.5 | 1.8 | 1.2 | 1.1 |
| Dy | 0.70 | 0.80 | 0.31 | 0.39 |
| Ho | 0.09 | 0.10 | 0.03 | 0.06 |
| Er | 0.16 | 0.18 | 0.06 | 0.10 |
| Y | 2.1 | 2.4 | 0.78 | 1.2 |
| Yb | 0.07 | 0.09 | 0.03 | 0.07 |
| Lu | 0.006 | 0.01 | 0.004 | 0.006 |

Type 1 clinopyroxenes from the Almklovdalen garnet peridotites display variable trace element behaviour. Rare earth element patterns show a range in shape from concave-up LREE and MREE, and low HREE abundances, to steep patterns with a negative slope that show a progression from LREE-enrichment to depleted HREE (Fig. 6-21). Trace element patterns typically show strong negative anomalies in U, Zr, Hf and Ti, and enrichment in the LREE, Th, Sr and Y (Fig. 6-22). The exception to this is clinopyroxene from sample LNWG which does not have a Hf anomaly and has only shallow negative anomalies for Zr and Ti. The type 2 clinopyroxenes from have very similar patterns to type 1 though at slightly lower abundances. The HREE in type 2 from sample LNWG are moderately enriched compared to type 1 from the same rock.

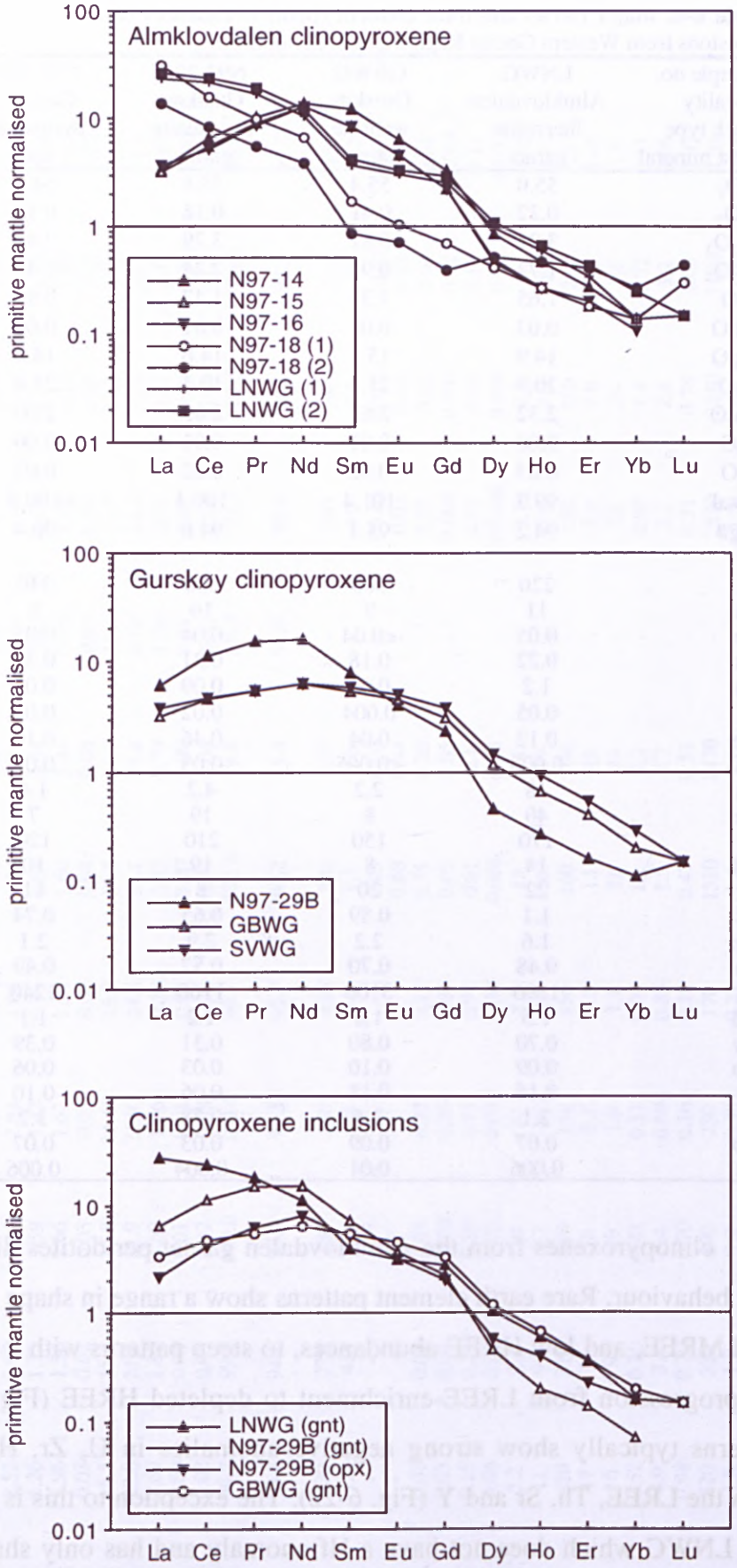


**Figure 6-21.** Primitive mantle normalised REE patterns of clinopyroxene in garnet peridotites from the Western Gneiss Region, Norway. Host mineral for clinopyroxene inclusions in shown in brackets.

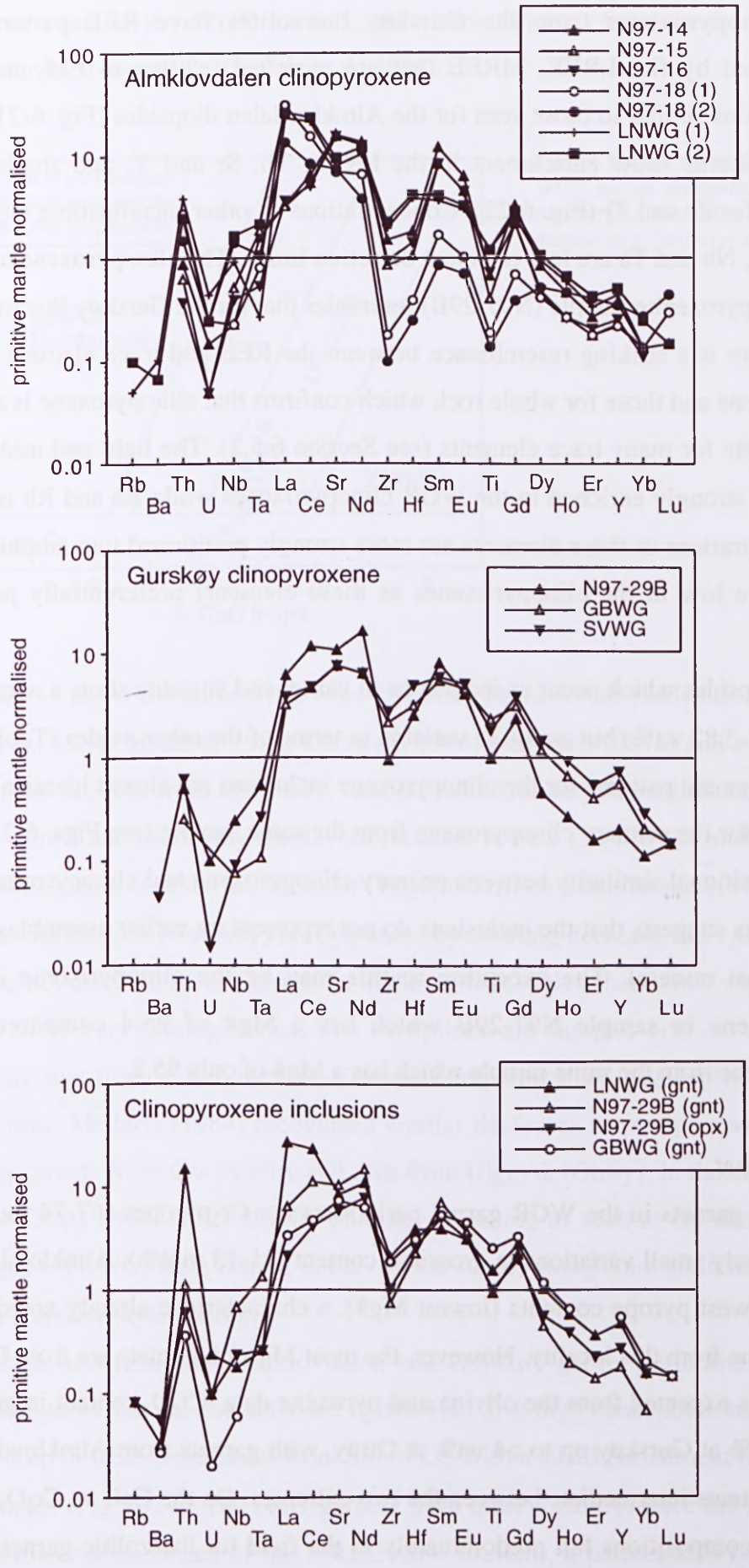


**Figure 6-22.** Primitive mantle normalised trace element patterns of clinopyroxene in garnet peridotites from the Western Gneiss Region, Norway.

Clinopyroxenes from the Gurskøy lherzolites have REE patterns that are characterised by flat LREE, MREE that are enriched relative to PM, and HREE at concentrations similar to those seen for the Almklovdalen diopsides (Fig. 6-21). The trace element patterns show enrichment in the LREE, Th, Sr and Y, and shallow negative anomalies for Zr and Ti (Fig. 6-22). Concentrations of other incompatible elements, such as U, LILE, Nb and Ta are low or below detection limits. The clinopyroxene trace element pattern for pyroxenite sample (N97-29B) resembles that for the Gurskøy lherzolites.

There is a striking resemblance between the REE and trace element patterns for clinopyroxene and those for whole rock which confirms that clinopyroxene is an important residence site for many trace elements (see Section 6.5.2). The light and middle REE, Sr and Th are strongly enriched in the WGR clinopyroxenes while Ba and Rb occur at very low concentrations as these elements are more strongly partitioned into amphibole. HREE contents are low in the clinopyroxenes as these elements preferentially partition into garnet.

Diopsides which occur as inclusions in garnet and enstatite show a narrow range in $Al_2O_3$ (3.21-3.82 wt%) but are quite variable in terms of the other oxides (Table 6-6). REE and trace element patterns for the clinopyroxene inclusions are almost identical in shape to the pattern for the primary clinopyroxene from the same sample (see Figs. 6-21 and 6-22). The compositional similarity between primary clinopyroxene and clinopyroxene occurring as inclusions suggests that the inclusions do not represent an earlier assemblage preserved in their host mineral. The exception to this may be the clinopyroxene inclusion in orthopyroxene in sample N97-29B which has a Mg# of 96.4 compared to matrix clinopyroxene from the same sample which has a Mg# of only 95.2.

### *6.6.4 Garnet*

The garnets in the WGR garnet peridotites are Cr-pyropes (67-74 mol% pyrope) that show only small variations in grossular content (11-13 mol%). Almklovdalen garnets have the lowest pyrope contents (lowest Mg#), a characteristic already noted for olivine and pyroxene from this locality. However, the most Mg-rich garnets are from Gurskøy and not Otrøy as expected from the olivine and pyroxene data. $Cr_2O_3$ content in garnet ranges from <2 wt% at Gurskøy up to >4 wt% at Otrøy, with garnets from Almklovdalen having chrome contents intermediate between the two extremes. On the CaO vs $Cr_2O_3$ plot in Fig. 6-23 these compositions fall predominantly in the field for lherzolitic garnets except for two samples from Gurskøy which lie in the field for low-Cr garnets. Ca-rich compositions,

such as those seen in the WGR garnets, are characteristic of garnet from fertile to moderately depleted lherzolite (Griffin *et al.*, 1998b).

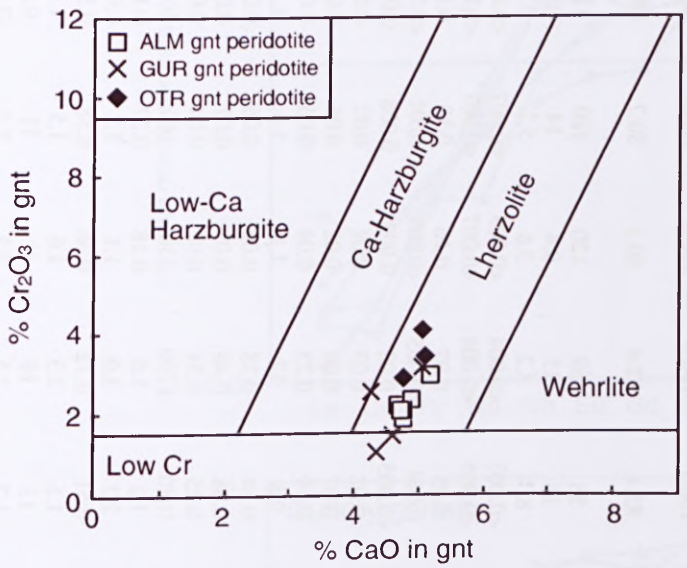


**Figure 6-23.** CaO vs $Cr_2O_3$ plot for WGR garnet peridotites. Fields for harzburgite, lherzolite and wehrlite garnets after Griffin *et al.* (1999d).

Zoning in the WGR garnets has been discussed in numerous publications (Medaris, 1980; Jamtveit, 1984; Medaris, 1984; Carswell, 1986; Jamtveit, 1987a) and is recognised in several of the samples from this study. Garnets from Gurskøy lherzolite and pyroxenite are strongly zoned and uniformly display an increase in FeO (>1.5 wt%) and decrease in MgO (>1.0 wt%) from core to rim. Jamtveit (1984) described a similar pattern of zoning in garnets from Gurskebotn (Gurskøy) accompanied by a strong decrease in $Cr_2O_3$ content at rims that was not detected here. Garnets from the Almklovdalen lherzolites were found, in most cases, to be very homogeneous. The exceptions are samples N97-16 and N97-18 which display marginal enrichment of Fe, and complementary Mg-depletion, in rims relative to cores. Medaris (1984) recognised similar decreases in pyrope and increase in almandine in garnets from this locality and also from Ulgevik (Otrøy). In the current study, garnets from Otrøy show either similar patterns of zoning as seen at Gurskøy or, in the case of sample OTRWG, have zoning in the reverse sense, though one grain in this sample does exhibit Gurskøy-style zoning.

Most garnets from the Almklovdalen and Gurskøy garnet peridotites have very similar REE patterns that are characterised by flat HREE at high concentrations (5-7 x PM) and a sharp drop in REE abundances from Sm to Ce, with a small enrichment in La present in a few samples (Fig. 6-24). The other garnets from these localities have the same HREE patterns but lower abundances of the MREE (Sm, Eu, Gd), a pattern also typical of the Otrøy garnets.

**Table 6-7.** Major (wt%) and trace element (ppm) abundances of garnet from Western Gneiss Region garnet peridotites.

| Sample no. | N97-5 | N97-14 | N97-15 | N97-16 | N97-18 | LNWG | N97-29B | N97-30 | GBWG | SVWG | N97-40 | N97-41 | OTRWG |
|---|---|---|---|---|---|---|---|---|---|---|---|---|---|
| Locality | Almklov. | Almklov. | Almklov. | Almklov. | Almklov. | Almklov. | Gurskøy | Gurskøy. | Gurskøy | Gurskøy | Otrøy | Otrøy | Otrøy |
| Rock type | lherz | lherz | lherz | lherz | lherz | lherz | pxenite | wehr | wehr | wehr | harz | harz | harz |
| $SiO_2$ | 41.4 | 41.6 | 41.3 | 41.9 | 42.0 | 41.9 | 42.6 | 42.1 | 42.5 | 42.4 | 41.6 | 41.8 | 42.1 |
| $TiO_2$ | 0.06 | 0.04 | 0.05 | 0.06 | 0.02 | 0.06 | 0.08 | 0.03 | 0.17 | 0.19 | 0.02 | 0.02 | 0.02 |
| $Al_2O_3$ | 21.9 | 21.8 | 21.1 | 21.5 | 21.8 | 22.1 | 21.7 | 20.9 | 23.2 | 22.7 | 21.2 | 20.7 | 21.6 |
| $Cr_2O_3$ | 2.30 | 1.92 | 3.02 | 2.42 | 2.14 | 2.12 | 2.59 | 3.20 | 1.15 | 1.57 | 3.48 | 4.18 | 2.96 |
| FeO | 9.69 | 9.68 | 8.91 | 9.71 | 10.3 | 9.65 | 8.58 | 8.58 | 7.72 | 7.96 | 8.80 | 8.57 | 8.32 |
| MnO | 0.43 | 0.45 | 0.44 | 0.46 | 0.47 | 0.45 | 0.34 | 0.39 | 0.31 | 0.34 | 0.41 | 0.45 | 0.39 |
| MgO | 19.9 | 19.4 | 19.6 | 19.3 | 19.1 | 18.8 | 20.8 | 19.7 | 21.3 | 21.0 | 19.9 | 20.1 | 19.6 |
| CaO | 4.70 | 4.81 | 5.21 | 4.93 | 4.80 | 4.73 | 4.31 | 5.07 | 4.38 | 4.61 | 5.14 | 5.07 | 4.81 |
| $Na_2O$ | 0.02 | 0.02 | 0.01 | 0.02 | 0.01 | 0.02 | 0.02 | 0.01 | 0.04 | 0.04 | 0.01 | 0.01 | 0.01 |
| $K_2O$ | 0.00 | 0.00 | 0.01 | 0.00 | 0.00 | 0.01 | 0.01 | 0.01 | 0.00 | 0.01 | 0.00 | 0.01 | 0.00 |
| NiO | 0.02 | 0.01 | 0.01 | 0.02 | 0.03 | 0.01 | 0.01 | 0.01 | 0.00 | 0.01 | 0.01 | 0.03 | 0.01 |
| Total | 100.4 | 99.8 | 99.5 | 100.3 | 100.7 | 99.8 | 100.9 | 100.0 | 100.7 | 100.9 | 100.6 | 100.9 | 99.8 |
| Mg# | 78.5 | 78.1 | 79.6 | 78.0 | 76.8 | 77.6 | 81.2 | 80.4 | 83.1 | 82.4 | 80.1 | 80.7 | 80.8 |
| Sc | 83 | 77 | 110 | 94 | 94 | 94 | 110 | - | 58 | 69 | 120 | 120 | 110 |
| Ni | 11 | 8.8 | 13 | 13 | 10 | 10 | 21 | - | 16 | 15 | 9.4 | 14 | 13 |
| Ga | 7.7 | 6.6 | 4.6 | 5.4 | 4.6 | 7.1 | 8.2 | - | 8.3 | 8.2 | 3.6 | 5.2 | 3.6 |
| Th | 0.02 | <0.02 | 0.01 | <0.02 | 0.02 | <0.005 | <0.004 | - | <0.007 | <0.004 | <0.003 | <0.007 | <0.008 |
| U | 0.02 | 0.01 | 0.002 | 0.01 | 0.03 | 0.007 | 0.009 | | <0.005 | <0.004 | <0.007 | <0.007 | <0.002 |
| Nb | 0.03 | 0.03 | 0.04 | 0.03 | 0.05 | 0.09 | 0.16 | - | 0.05 | 0.07 | 0.16 | 0.19 | 0.13 |
| Ta | <0.02 | <0.02 | 0.01 | <0.02 | 0.01 | <0.005 | 0.005 | | 0.004 | <0.005 | <0.009 | <0.01 | <0.004 |
| La | 0.03 | 0.02 | <0.02 | 0.02 | 0.07 | 0.02 | 0.04 | - | <0.005 | 0.02 | 0.003 | 0.008 | 0.006 |
| Ce | 0.13 | 0.05 | 0.04 | 0.03 | 0.12 | 0.13 | 0.26 | - | 0.02 | 0.03 | 0.02 | 0.02 | 0.02 |
| Sr | 0.04 | 0.16 | 0.13 | 0.11 | 0.07 | 0.21 | 1.5 | - | 0.07 | 0.08 | 0.02 | 0.05 | 0.05 |
| Nd | 0.18 | 0.67 | 0.86 | 0.61 | 0.47 | 0.43 | 0.86 | - | 0.19 | 0.25 | 0.04 | 0.06 | 0.02 |
| Zr | 11 | 10 | 6.1 | 6.0 | 1.5 | 9.2 | 5.9 | - | 9.8 | 17 | 1.1 | 1.4 | 1.1 |
| Hf | 0.17 | 0.11 | 0.08 | 0.09 | 0.06 | 0.13 | 0.15 | - | 0.14 | 0.38 | 0.05 | 0.06 | 0.04 |
| Sm | 0.33 | 0.98 | 1.2 | 0.92 | 0.22 | 0.35 | 0.75 | - | 0.38 | 0.48 | 0.03 | 0.07 | 0.03 |
| Eu | 0.25 | 0.51 | 0.49 | 0.39 | 0.12 | 0.22 | 0.32 | - | 0.25 | 0.31 | 0.02 | 0.04 | 0.02 |
| Ti | 470 | 290 | 200 | 350 | 120 | 480 | 750 | - | 1680 | 1790 | 130 | 160 | 160 |
| Gd | 1.3 | 1.9 | 1.4 | 1.1 | 0.47 | 1.3 | 1.2 | - | 1.2 | 1.6 | 0.18 | 0.27 | 0.17 |
| Dy | 2.9 | 2.7 | 1.8 | 1.7 | 1.7 | 2.9 | 1.1 | - | 2.2 | 3.0 | 1.1 | 1.2 | 0.98 |
| Ho | 0.74 | 0.63 | 0.49 | 0.40 | 0.50 | 0.74 | 0.25 | - | 0.51 | 0.72 | 0.36 | 0.38 | 0.35 |
| Er | 2.1 | 1.8 | 1.4 | 1.3 | 1.8 | 2.4 | 0.79 | - | 1.6 | 2.3 | 1.6 | 1.5 | 1.4 |
| Y | 18 | 17 | 12 | 10 | 13 | 19 | 6.5 | - | 13 | 19 | 11 | 11 | 9.6 |
| Yb | 2.6 | 2.1 | 1.9 | 1.8 | 2.4 | 2.8 | 0.99 | - | 1.7 | 2.5 | 2.3 | 2.2 | 2.2 |
| Lu | 0.40 | 0.32 | 0.32 | 0.31 | 0.38 | 0.43 | 0.17 | - | 0.25 | 0.37 | 0.40 | 0.38 | 0.36 |

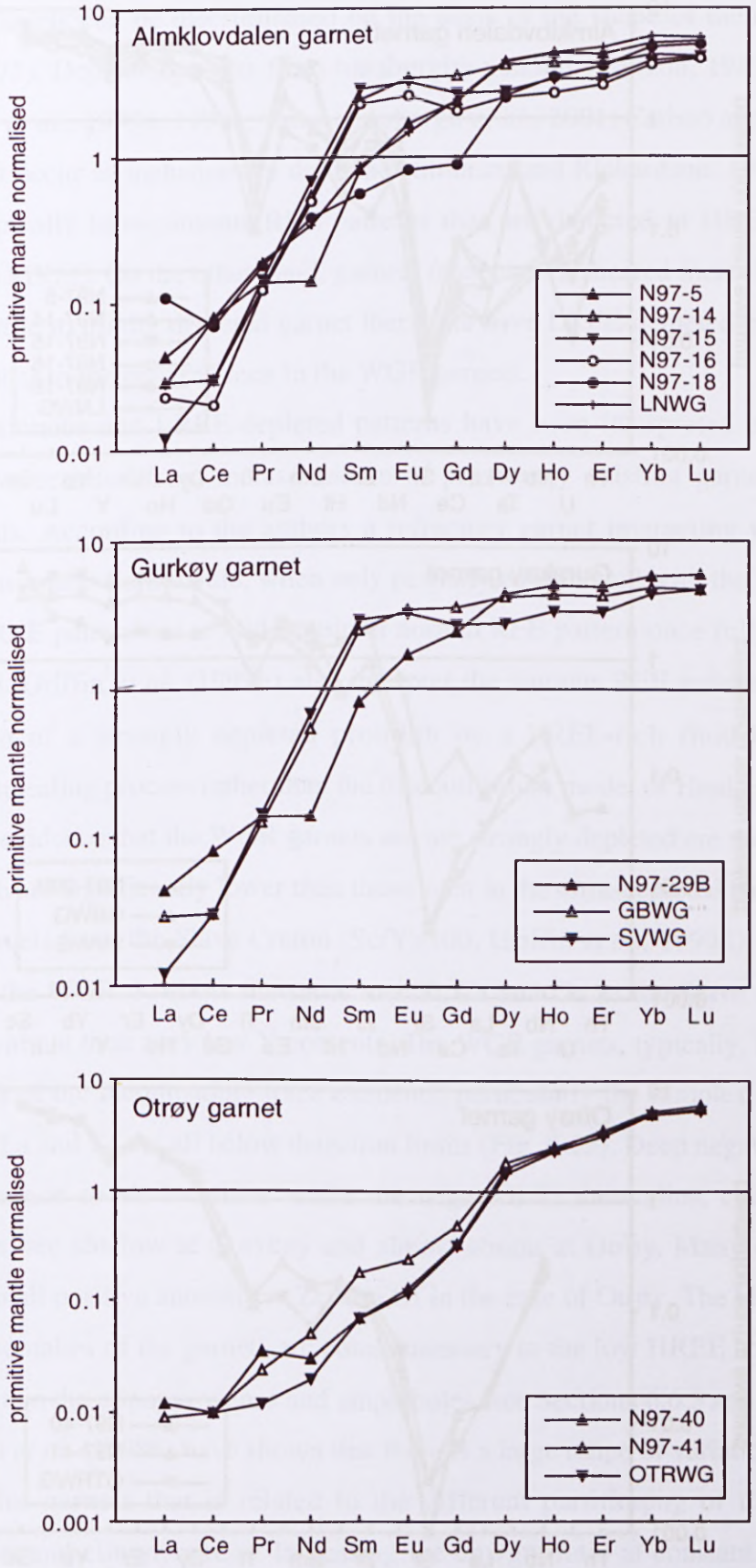


**Figure 6-24.** Primitive mantle normalised REE patterns of garnet in garnet peridotites from the Western Gneiss Region, Norway.

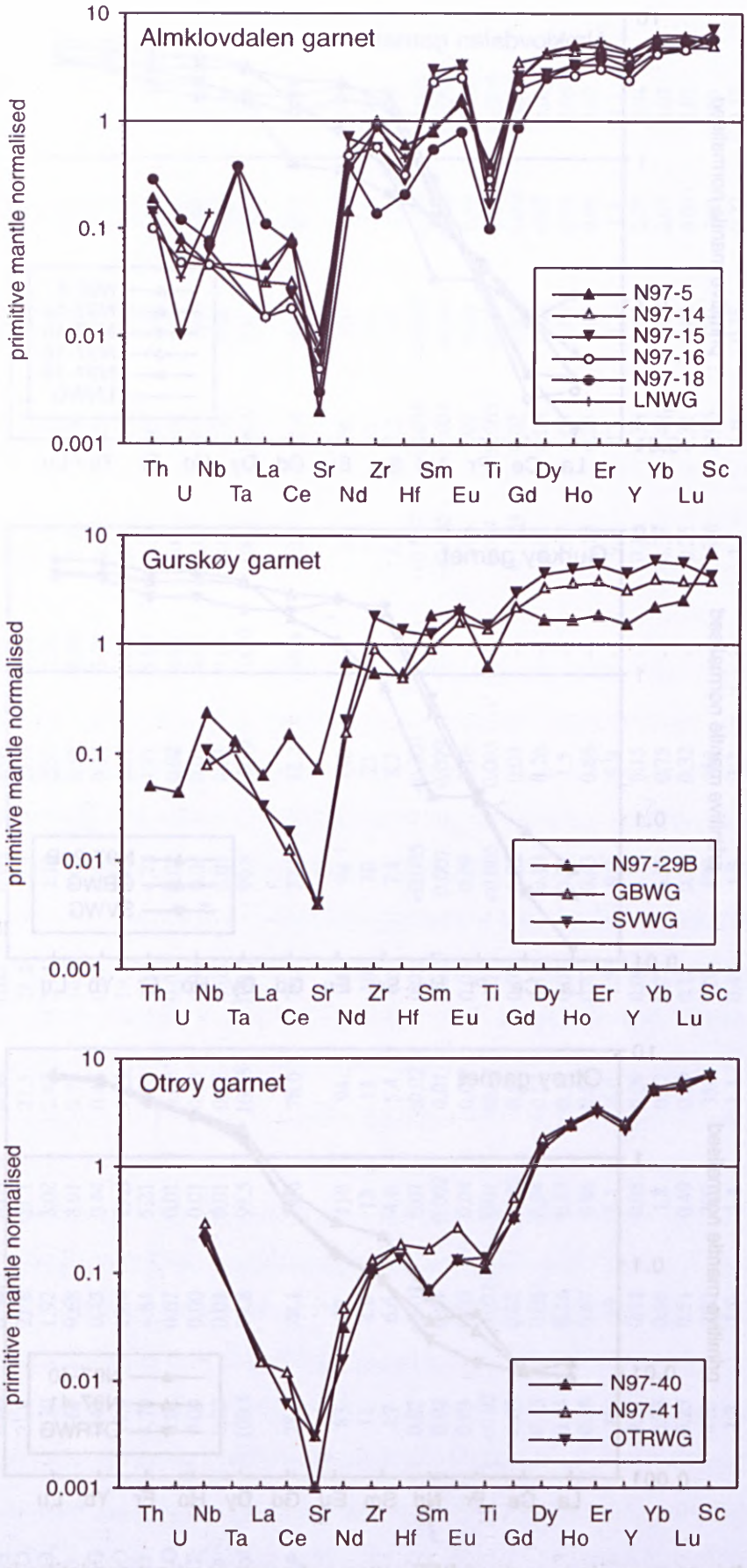


**Figure 6-25.** Primitive mantle normalised trace element patterns of garnet in garnet peridotites from the Western Gneiss Region, Norway.

Rare earth element studies of garnets from kimberlite-borne garnet lherzolite have shown that garnets can be discriminated on the basis of the shape of their REE pattern (Shimizu, 1975). Depleted garnets from harzburgite xenoliths (Nixon, 1987; Hoal *et al.*, 1994; Griffin *et al.*, 1999a, 1999c; van Achterbergh *et al.*, 2001; Carbno and Canil, 2002) and those that occur as inclusions in diamond (Shimizu and Richardson, 1987; Stachel *et al.*, 1998) typically have sinuous REE patterns that are depleted in HREE and LREE relative to the MREE. On the other hand, garnets from high-T sheared lherzolites and those from most fertile to mildly depleted garnet lherzolite have LREE-depleted patterns (Xu *et al.*, 2000) similar to the patterns seen in the WGR garnets.

Both sinuous and LREE-depleted patterns have been interpreted by Hoal *et al.* (1994) to have resulted from metasomatism of previously existing garnets by LREE-enriched fluids. According to the authors a refractory garnet interacting with a LREE-enriched metasomatic fluid would, when only partially equilibrated with the fluid, produce a sinusoidal REE pattern but would acquire a normal REE pattern once fully-equilibrated with the fluid. Griffin *et al.* (1999b) also interpret the sinuous REE pattern as reflecting metasomatism of a strongly depleted protolith by a LREE-rich fluid but prefer an overgrowth-annealing process rather than the disequilibrium model of Hoal *et al.* (1994).

Other evidence that the WGR garnets are not strongly depleted are their Sc/Y ratios (4 to16) which are significantly lower than those seen in the ultra-depleted harzburgitic and lherzolitic garnets from the Slave Craton (Sc/Y>100; Griffin *et al.*, 1999d). However, the garnets from the WGR do show the same low Ti, Zr and Ga as the Slave ultra-depleted garnets, but without their very low Y contents. The WGR garnets, typically, have very low concentrations of the incompatible trace elements, particularly the samples from Otrøy in which U, Th, La and Ta are all below detection limits (Fig. 6-25). Deep negative anomalies in Sr are common to all localities while the negative Ti anomalies, characteristic of Almklovdalen, are shallow at Gurskøy and almost absent at Otrøy. Many of the garnets also show a small positive anomaly in Zr, and Hf in the case of Otrøy. The high HREE and positive Zr anomalies of the garnets are complementary to the low HREE and negative Zr anomalies seen in the clinopyroxenes and amphiboles (see Sections 6.6.3 and 6.6.5).

Griffin *et al.* (1998b) have shown that there is a large range of variation in Zr/Y and Y/Ga ratios for garnets that is related to the different partitioning of these elements between garnet and clinopyroxene. Increasing the cpx/gnt ratio at constant T (by raising modal cpx content at constant garnet content) decreases Zr/Y in the garnet and increases Y/Ga, while a decrease in cpx/gnt has the opposite effect (Griffin *et al.*, 1998b). Fig. 6-26

is a plot of Zr/Y vs Y/Ga for garnets from the WGR peridotites. Compositions for the Almklovdalen and Gurskøy garnets plot close to the field for worldwide Proton garnet suites whereas those from Otrøy, while having similar Y/Ga ratios to the other two WGR localities, have extremely low Zr/Y ratios and lie well away from the Proton field. The low Zr/Y in the WGR garnets suggests that either the WGR garnet peridotites have higher cpx/gnt than most cratonic lherzolites or, alternatively, that the peridotites were equilibrated at lower T than most garnet lherzolite xenoliths.

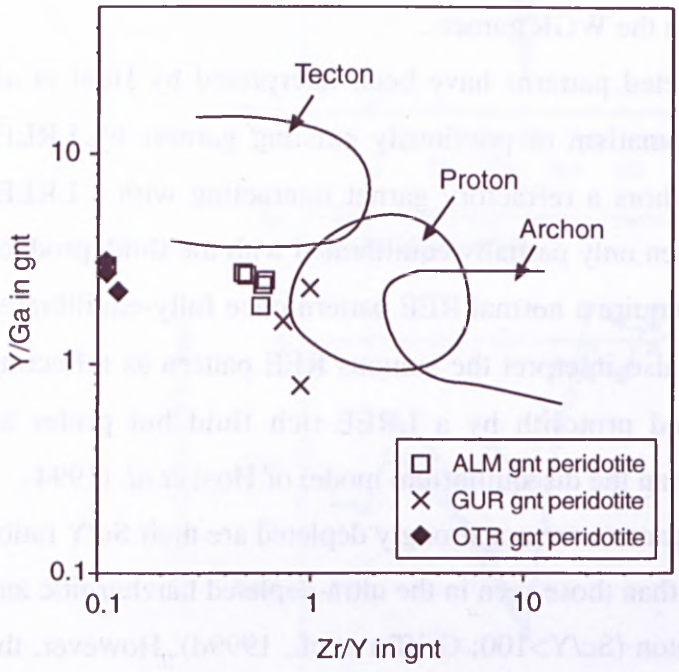


**Figure 6-26.** Zr/Y vs Y/Ga ratios in garnet from WGR garnet peridotites. Fields for lherzolitic garnets from (Griffin *et al.*, 1998b).

### *6.6.5 Chromite*

The chromites from the WGR peridotites show a wide variation in composition from the extreme Cr-rich examples in the dunites to the Cr-poor chromites in garnet peridotite from Gurskøy (Table 6-8; Fig. 6-27). Chromites from the Almklovdalen dunites and spinel peridotite sample N97-25 cluster at low Mg# (22-35) and high-Cr# (89-94). These high Cr# are related to the very low (2-3wt%) $Al_2O_3$ contents of chromite in the dunites. The Levdal dunite contains chromite that is Al-rich (12.9wt%) but with similar Mg# to the Almklovdalen chromites. Chromites in the garnet peridotites from Almklovdalen and Otrøy have Mg# in the range 36-57 and Cr# of 57-67. This is in strong contrast to spinel from the Gurskøy garnet peridotite, sample SVWG, which has very high-$Al_2O_3$ and very low-$Cr_2O_3$ giving a low Cr# (7.9) that is matched by a Mg# of 82.5.

**Table 6-8.** Major element oxide abundances (wt%) of chromite from Western Gneiss Region peridotites.

| Sample no. | N97-5 | N97-15 | N97-16 | SVWG | N97-41 | OTRWG | N97-25 | N97-1 | N97-6 | N97-7 |
|---|---|---|---|---|---|---|---|---|---|---|
| Locality | Almklov | Almklov | Almklov | Gurskøy | Otrøy | Otrøy | Almklov. | Levdal | Almklov. | Almklov. |
| Rock type | gnt perid | gnt perid | gnt perid | gnt perid | gnt perid | gnt perid | sp perid | dunite | dunite | dunite |
| $SiO_2$ | 0.01 | 0.04 | 0.05 | 0.03 | 0.05 | 0.04 | 0.02 | 0.05 | 0.01 | 0.27 |
| $TiO_2$ | 0.16 | 0.12 | 0.10 | 0.02 | 0.02 | 0.02 | 0.15 | 0.19 | 0.01 | 0.22 |
| $Al_2O_3$ | 16.4 | 16.0 | 22.0 | 60.6 | 20.9 | 19.3 | 3.44 | 12.9 | 2.61 | 3.04 |
| $Cr_2O_3$ | 49.2 | 47.2 | 43.4 | 7.71 | 47.2 | 49.5 | 53.8 | 49.0 | 58.4 | 56.9 |
| FeO | 24.0 | 25.4 | 21.3 | 7.85 | 18.3 | 16.2 | 34.1 | 27.1 | 31.1 | 29.7 |
| MnO | 0.00 | 0.00 | 0.00 | 0.00 | 0.00 | 0.00 | 0.00 | 0.00 | 0.00 | 0.00 |
| MgO | 8.28 | 8.17 | 10.4 | 20.8 | 11.3 | 12.15 | 5.24 | 7.31 | 5.06 | 6.00 |
| CaO | 0.00 | 0.02 | 0.00 | 0.02 | 0.03 | 0.04 | 0.01 | 0.00 | 0.00 | 0.01 |
| $Na_2O$ | 0.01 | 0.00 | 0.03 | 0.02 | 0.01 | 0.02 | 0.01 | 0.02 | 0.04 | 0.03 |
| $K_2O$ | 0.01 | 0.01 | 0.00 | 0.00 | 0.00 | 0.00 | 0.01 | 0.01 | 0.01 | 0.05 |
| NiO | 0.04 | 0.04 | 0.11 | 0.23 | 0.04 | 0.06 | 0.09 | 0.06 | 0.03 | 0.05 |
| Total | 98.0 | 97.0 | 97.3 | 97.2 | 97.9 | 97.3 | 96.9 | 96.6 | 97.3 | 96.2 |
| Mg# | 38.1 | 36.4 | 46.4 | 82.5 | 52.1 | 57.2 | 21.6 | 32.5 | 22.5 | 26.4 |
| Cr# | 66.9 | 66.4 | 57.0 | 7.9 | 60.5 | 63.3 | 91.6 | 71.7 | 93.8 | 92.6 |

| Sample no. | N97-8 | N97-9 | N97-11 | N97-13 | N97-17 | N97-21 | N-97-22 | N97-23 | N97-24 |
|---|---|---|---|---|---|---|---|---|---|
| Locality | Almklov. | Almklov | Almklov | Almklov | Almklov. | Almklov | Almklov | Almklov | Almklov |
| Rock type | dunite | dunite | dunite | dunite | dunite | dunite | dunite | dunite | dunite |
| SiO2 | 0.01 | 0.02 | 0.01 | 0.01 | 0.00 | 0.02 | 0.02 | 0.01 | 0.04 |
| $TiO_2$ | 0.01 | 0.02 | 0.04 | 0.00 | 0.14 | 0.08 | 0.16 | 0.09 | 0.14 |
| $Al_2O_3$ | 2.70 | 3.25 | 3.01 | 2.75 | 3.18 | 3.17 | 3.39 | 5.00 | 4.33 |
| $Cr_2O_3$ | 59.9 | 59.5 | 57.9 | 62.1 | 57.7 | 59.4 | 58.2 | 59.4 | 56.8 |
| FeO | 28.5 | 26.8 | 29.2 | 27.9 | 30.1 | 29.2 | 29.3 | 25.5 | 30.1 |
| MnO | 0.00 | 0.00 | 0.41 | 0.00 | 0.00 | 0.00 | 0.00 | 0.00 | 0.00 |
| MgO | 5.22 | 6.32 | 6.21 | 5.04 | 6.00 | 5.39 | 6.27 | 7.65 | 6.11 |
| CaO | 0.00 | 0.01 | 0.01 | 0.01 | 0.01 | 0.02 | 0.01 | 0.00 | 0.01 |
| $Na_2O$ | 0.02 | 0.01 | 0.00 | 0.02 | 0.02 | 0.01 | 0.00 | 0.01 | 0.02 |
| $K_2O$ | 0.01 | 0.00 | 0.00 | 0.01 | 0.01 | 0.00 | 0.00 | 0.01 | 0.01 |
| NiO | 0.06 | 0.05 | 0.03 | 0.00 | 0.06 | 0.03 | 0.06 | 0.04 | 0.07 |
| Total | 96.4 | 96.1 | 97.2 | 97.9 | 97.2 | 97.4 | 97.5 | 97.7 | 97.5 |
| Mg# | 24.6 | 29.6 | 27.5 | 24.4 | 26.3 | 24.7 | 27.6 | 35.0 | 26.6 |
| Cr# | 93.7 | 92.5 | 92.8 | 93.8 | 92.4 | 92.6 | 92.0 | 89.1 | 89.8 |

Fig. 6-27A shows fields for chromites from a variety of ultramafic rock types. The majority of the WGR chromites fall outside the field for chromite from peridotite xenoliths apart from those from Otrøy which lie at the depleted end (i.e. high Cr#) of the xenolith trend. As the chromite in the WGR rocks is not primary but a breakdown product of garnet it was not expected that the WGR compositions would lie along the partial melting trend for mantle peridotites. Likewise the WGR chromites do not plot within the field for Archon and Proton compositions as anticipated but appear to lie at a high Cr# extension of the Tecton field.

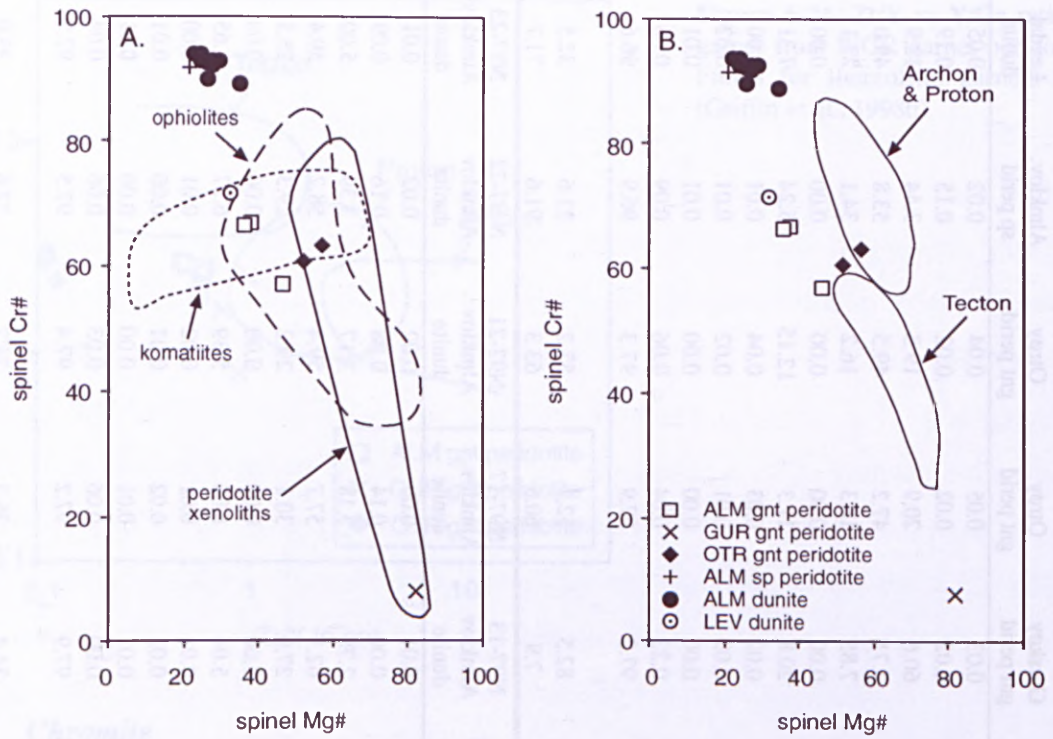


**Figure 6-27.** Compositional variation diagrams for chromites from the WGR peridotites. Fields are from Yao (1999).

### *6.6.6 Amphibole*

Amphibole is widespread in both the garnet-bearing peridotites and dunites from the Western Gneiss Region. In the garnet peridotites it occurs predominantly as partial rims around garnet whereas in the dunites it appears in association with chlorite. The amphiboles found in the WGR peridotites are exclusively calcic amphiboles (range in CaO content is 11.2-13.0 wt%) though there is significant variation in composition between the different rock types (Table 6-9). Amphibole in the garnet peridotites is pargasite though compositions tend towards magnesio-hornblende, particularly in amphiboles from Almklovdalen (Fig. 6-28). The dunite from Levdal (N97-1) also contains pargasite. In the dunites and spinel peridotite from Almklovdalen, amphibole is high in Si but very poor in alkalis and, therefore, can be classified as tremolite (Fig. 6-28).

**Table 6-9.** Major element oxide abundances (wt%) of amphibole from Western Gneiss Region peridotites.

| Sample no. | N97-5 | N97-14 | N97-15 | N97-16 | N97-18 | LNWG | SVWG | N97-40 | N97-41 | OTRWG |
|---|---|---|---|---|---|---|---|---|---|---|
| Locality | Almklov. | Almklov. | Almklov. | Almklov. | Almklov. | Almklov. | Gurskøy | Otrøy | Otrøy | Otrøy |
| Rock type | gnt lherz | gnt lherz | gnt lherz | gnt lherz | gnt lherz | gnt lherz | gnt lherz | gnt harz | gnt harz | gnt harz |
| $SiO_2$ | 46.6 | 45.7 | 45.4 | 46.6 | 44.9 | 45.6 | 44.6 | 45.6 | 45.0 | 45.2 |
| $TiO_2$ | 0.31 | 0.28 | 0.18 | 0.27 | 0.09 | 0.28 | 1.05 | 0.06 | 0.11 | 0.11 |
| $Al_2O_3$ | 11.5 | 12.2 | 12.7 | 11.8 | 13.9 | 12.8 | 13.9 | 12.8 | 13.1 | 13.4 |
| $Cr_2O_3$ | 1.54 | 1.18 | 1.30 | 1.60 | 1.67 | 1.52 | 0.87 | 2.03 | 1.99 | 1.82 |
| FeO | 2.81 | 3.67 | 3.44 | 3.00 | 3.13 | 3.07 | 2.16 | 2.66 | 2.47 | 2.15 |
| MnO | 0.03 | 0.03 | 0.06 | 0.03 | 0.03 | 0.07 | 0.06 | 0.05 | 0.02 | 0.03 |
| MgO | 19.0 | 18.4 | 18.3 | 18.8 | 18.0 | 18.8 | 18.7 | 18.7 | 18.8 | 18.7 |
| CaO | 12.6 | 12.7 | 12.3 | 12.5 | 12.5 | 11.9 | 13.0 | 12.5 | 12.2 | 12.1 |
| $Na_2O$ | 2.07 | 2.10 | 1.92 | 2.19 | 2.67 | 2.86 | 3.05 | 2.50 | 2.97 | 3.18 |
| $K_2O$ | 0.10 | 0.12 | 0.41 | 0.20 | 0.03 | 0.04 | 0.14 | 0.09 | 0.01 | 0.03 |
| NiO | 0.09 | 0.12 | 0.08 | 0.13 | 0.08 | 0.09 | 0.15 | 0.10 | 0.09 | 0.11 |
| F | 0.18 | 0.02 | 0.01 | - | - | - | - | - | - | - |
| Cl | 0.02 | 0.17 | 0.14 | - | - | - | - | - | - | - |
| Total | 96.6 | 96.6 | 96.0 | 97.1 | 97.1 | 97.0 | 97.7 | 96.9 | 96.8 | 96.9 |
| Mg# | 92.0 | 89.9 | 90.4 | 91.8 | 91.1 | 91.6 | 93.9 | 92.6 | 93.2 | 94.0 |

| Sample no. | N97-25 | N97-1 | N97-7 | N97-8 | N97-9 | N97-13 | N97-17 | N97-22(1) | N-97-22(2) | N97-23 |
|---|---|---|---|---|---|---|---|---|---|---|
| Locality | Almklov. | Levdal | Almklov. | Almklov. | Almklov. | Almklov. | Almklov. | Almklov. | Almklov. | Almklov. |
| Rock type | spinel harz. | dunite | dunite | dunite | dunite | dunite | dunite | dunite | dunite | dunite |
| SiO2 | 58.6 | 46.0 | 53.7 | 52.9 | 53.3 | 53.5 | 52.7 | 58.2 | 54.8 | 55.7 |
| $TiO_2$ | 0.03 | 0.30 | 0.14 | 0.01 | 0.01 | 0.00 | 0.07 | 0.03 | 0.08 | 0.07 |
| $Al_2O_3$ | 0.56 | 11.1 | 3.35 | 3.93 | 4.07 | 4.40 | 4.58 | 0.65 | 3.71 | 2.99 |
| $Cr_2O_3$ | 0.27 | 1.54 | 0.79 | 1.00 | 0.86 | 1.24 | 1.04 | 0.21 | 0.54 | 0.58 |
| FeO | 1.87 | 2.99 | 2.21 | 2.51 | 2.48 | 2.48 | 2.44 | 1.59 | 2.23 | 2.03 |
| MnO | 0.05 | 0.02 | 0.06 | 0.05 | 0.05 | 0.04 | 0.04 | 0.04 | 0.04 | 0.06 |
| MgO | 23.7 | 19.2 | 23.0 | 22.8 | 22.7 | 22.2 | 22.4 | 23.7 | 22.7 | 23.2 |
| CaO | 12.4 | 12.1 | 11.8 | 11.2 | 11.7 | 11.9 | 11.5 | 12.6 | 12.1 | 11.8 |
| $Na_2O$ | 0.51 | 2.24 | 1.02 | 1.05 | 1.03 | 1.27 | 1.25 | 0.36 | 1.22 | 1.17 |
| $K_2O$ | 0.07 | 1.02 | 0.46 | 0.59 | 0.50 | 0.42 | 0.71 | 0.05 | 0.35 | 0.35 |
| NiO | 0.06 | 0.09 | 0.06 | 0.06 | 0.11 | 0.01 | 0.12 | 0.09 | 0.13 | 0.13 |
| F | - | - | 0.05 | 0.04 | 0.02 | 0.03 | 0.04 | - | - | - |
| Cl | - | - | 0.01 | 0.00 | 0.03 | 0.01 | 0.00 | - | - | - |
| Total | 98.1 | 96.7 | 96.6 | 96.2 | 96.9 | 97.5 | 96.9 | 97.5 | 98.0 | 98.1 |
| Mg# | 95.8 | 92.0 | 94.9 | 94.2 | 94.2 | 94.1 | 94.2 | 96.4 | 94.8 | 95.3 |

**Table 6-10.** Trace element abundances (ppm) of amphibole from Western Gneiss Region peridotites.

| Sample no. | N97-5 | N97-14 | N97-15 | N97-16 | N97-18 | LNWG | N97-40 | N97-41 | OTRWG |
|---|---|---|---|---|---|---|---|---|---|
| Locality | Almklov. | Almklov. | Almklov. | Almklov. | Almklov. | Almklov. | Otrøy | Otrøy | Otrøy |
| Rock type | lherz | lherz | lherz | lherz | lherz | lherz | harz | harz | harz |
| Sc | 56 | 44 | 58 | 43 | 41 | 47 | 33 | 36 | 26 |
| Ni | 770 | 820 | 680 | 790 | 840 | 730 | 470 | 500 | 710 |
| Ga | 14 | 14 | 7.5 | 13 | 12 | 35 | 6.6 | 6.1 | 14 |
| Rb | - | - | - | - | - | 1.43 | 1.4 | 0.54 | 2.1 |
| Ba | - | - | - | - | - | 170 | 48 | 28 | 80 |
| Th | 0.18 | 0.03 | 0.02 | 0.02 | 0.06 | 0.10 | 0.02 | 0.02 | 0.005 |
| U | 0.04 | 0.02 | 0.01 | 0.01 | 0.07 | 0.04 | 0.06 | 0.01 | 0.007 |
| Nb | 2.4 | 2.7 | 4.7 | 2.1 | 9.1 | 2.4 | 0.14 | 0.20 | 0.20 |
| Ta | 0.06 | 0.23 | 0.37 | 0.18 | 0.17 | 0.08 | 0.004 | 0.01 | 0.007 |
| La | 13 | 2.2 | 1.5 | 2.1 | 19 | 9.5 | 0.69 | 0.59 | 0.46 |
| Ce | 30 | 12 | 7.6 | 9.6 | 30 | 30 | 1.5 | 1.2 | 1.1 |
| Sr | 200 | 310 | 310 | 270 | 160 | 150 | 38 | 12 | 29 |
| Nd | 5.2 | 19 | 16 | 20 | 11 | 13 | 0.61 | 0.73 | 0.65 |
| Zr | 14 | 12 | 13 | 13 | 3.3 | 17 | 1.9 | 3.7 | 3.1 |
| Hf | 0.68 | 0.47 | 0.38 | 0.54 | 0.13 | 0.77 | 0.09 | 0.18 | 0.18 |
| Sm | 1.5 | 5.1 | 4.4 | 5.0 | 1.0 | 1.7 | 0.12 | 0.28 | 0.16 |
| Eu | 0.59 | 1.5 | 1.1 | 1.1 | 0.27 | 0.56 | 0.05 | 0.10 | 0.06 |
| Ti | 1680 | 1440 | 1170 | 1550 | 600 | 1990 | 310 | 480 | 710 |
| Gd | 2.0 | 3.1 | 2.2 | 2.0 | 0.73 | 1.77 | 0.23 | 0.44 | 0.28 |
| Dy | 2.0 | 1.9 | 1.2 | 0.87 | 0.89 | 1.4 | 0.59 | 0.64 | 0.43 |
| Ho | 0.40 | 0.36 | 0.23 | 0.15 | 0.19 | 0.24 | 0.15 | 0.11 | 0.09 |
| Er | 1.1 | 0.91 | 0.56 | 0.34 | 0.49 | 0.60 | 0.49 | 0.30 | 0.25 |
| Y | 10 | 9.2 | 5.5 | 3.7 | 4.8 | 6.0 | 4.0 | 2.9 | 2.3 |
| Yb | 0.96 | 0.81 | 0.53 | 0.32 | 0.40 | 0.40 | 0.54 | 0.21 | 0.21 |
| Lu | 0.13 | 0.11 | 0.07 | 0.05 | 0.06 | 0.05 | 0.09 | 0.03 | 0.03 |

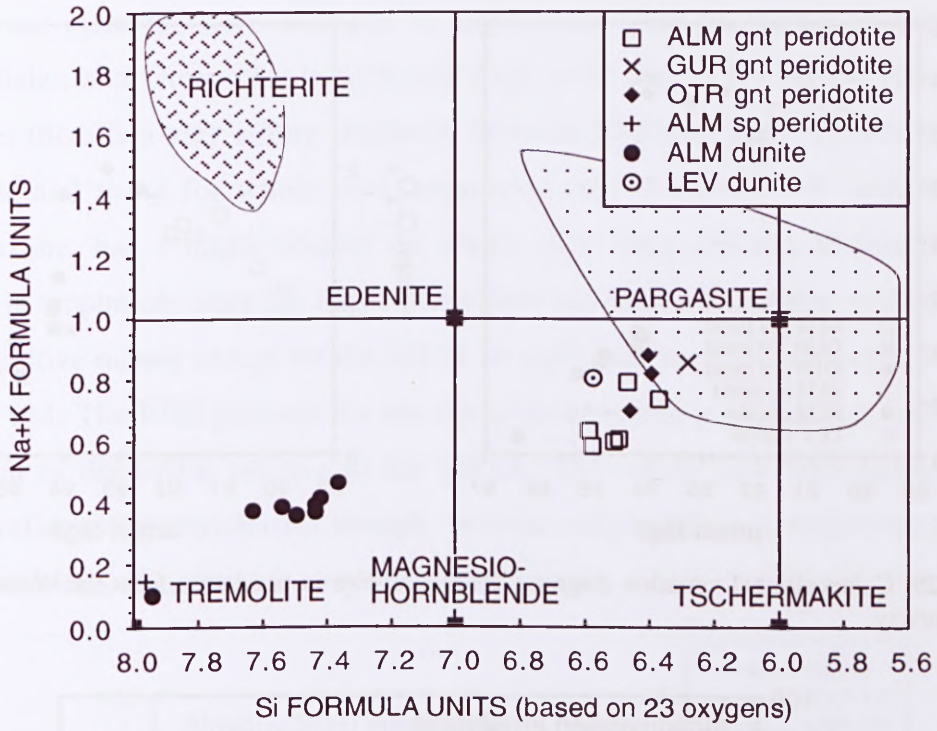


**Figure 6-28.** Variation in Na+K versus Si for amphiboles from the WGR peridotites. Fields are for amphiboles in garnet peridotites from kimberlites (hatches) and spinel peridotites from alkali basalts (dots). After Menzies *et al.* (1987).

$Al_2O_3$ content in amphiboles from the garnet peridotites is high and ranges from 11.5-13.9 wt% compared to 0.65-4.58 wt% in amphibole from the Almklovdalen dunites. Abundances of $Cr_2O_3$ and $TiO_2$ are similar for both rock types though values are overall slightly lower in the dunitic rocks. Amphibole Mg# varies with locality in the garnet peridotites as already seen with the other silicates. The dunites from Almklovdalen contain amphibole with uniformly high Mg# (94.1-96.4) compared to the Levdal dunite which has a low Mg# of 92.0. The positive correlation between $Al_2O_3$ and $Cr_2O_3$, and Mg# for the garnet peridotites (Fig. 6-29) can be related to the breakdown of garnet and clinopyroxene during retrograde metamorphism which will produce progressively more Al- and Cr-rich amphibole.

Volatile elements in amphibole, such as F and Cl, were analysed in about half the samples (Table 6-9). Amphibole from the Almklovdalen garnet peridotites contains very low concentrations of fluorine but up to 0.18 wt% chlorine. High abundances of Cl (0.19-0.45 wt%) in amphiboles from Gurskøy garnet peridotites were reported by Jamtveit (1984). Fluorine and chlorine contents are very low (<0.05 wt%) in amphiboles from the dunites.

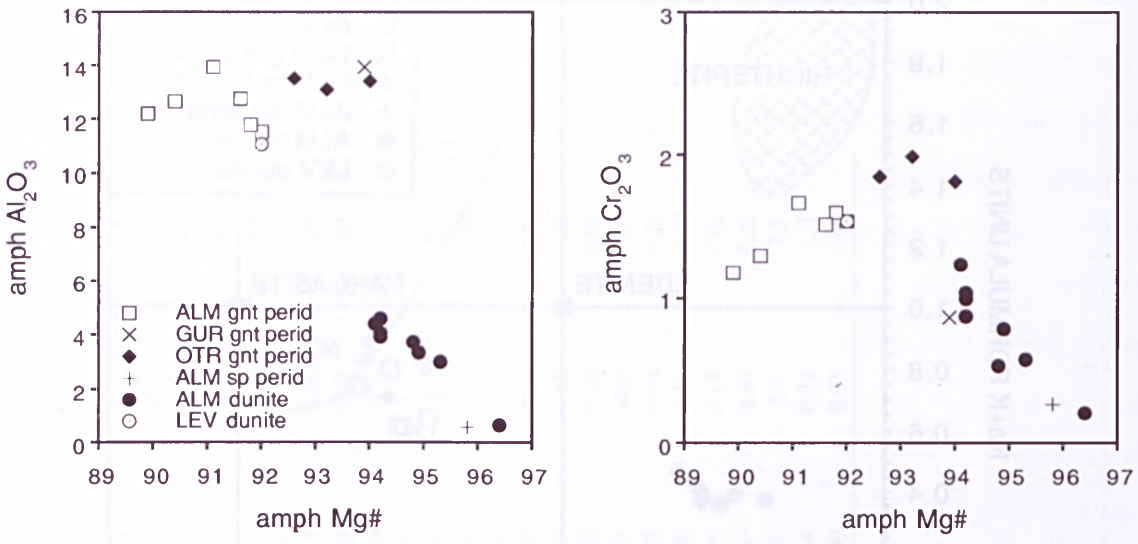


**Figure 6-29.** Compositional variation diagrams for amphiboles in peridotites from the Western Gneiss Region, Norway.

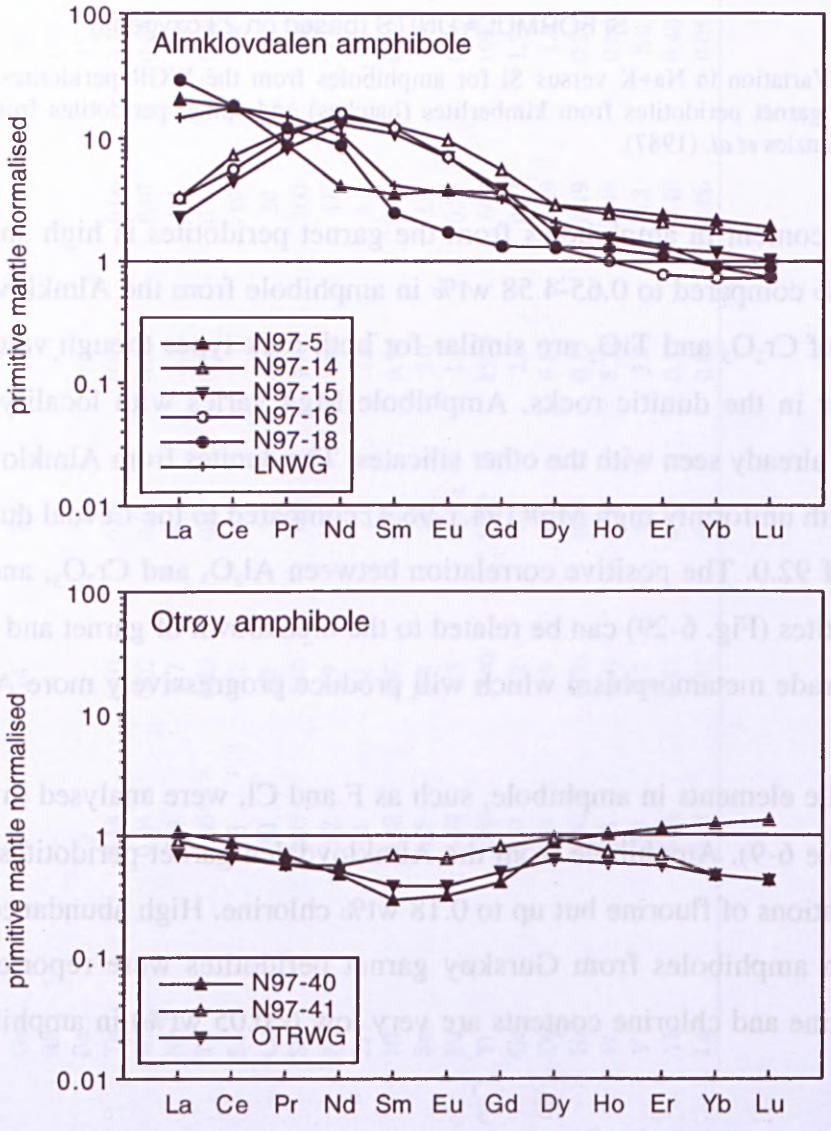


**Figure 6-30.** Primitive mantle normalised REE patterns of amphibole in garnet peridotites from the Western Gneiss Region, Norway.

Trace elements were analysed in amphiboles from the garnet peridotites from Almklovdalen and Otrøy (Table 6-10 and Figs. 6-30 and 6-31). In the Almklovdalen peridotites there is a very strong similarity between REE and trace element patterns for amphibole and those for whole rock suggesting that this phase, in conjunction with clinopyroxene, has a major control on whole rock trace element abundances. Trace elements in amphibole from the Otrøy peridotites are nearly all present at concentrations below primitive mantle except for the LILEs, in particular Ba which occurs at abundances of ~10 x PM. The REE patterns for the Otrøy amphiboles are quite flat with marginal enrichment in the LREE relative to the MREE. The whole rock REE patterns for the samples reflects this enrichment though, because amphibole is a volumetrically minor phase, total LREE abundance is very low in these rocks.

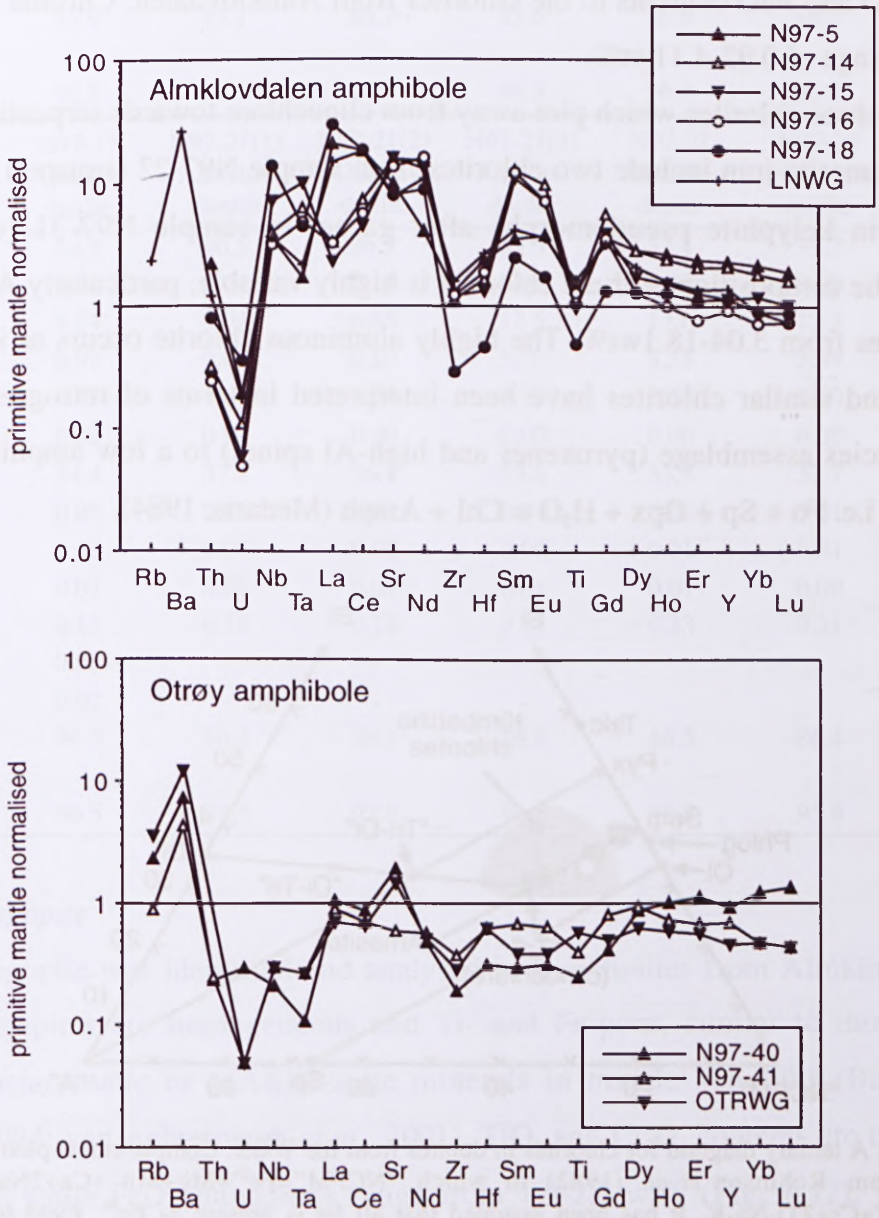


**Figure 6-31.** Primitive mantle normalised trace element patterns of amphibole in garnet peridotites from the Western Gneiss Region, Norway.

### *6.6.7 Chlorite*

Chlorite was analysed in thirteen dunites from the WGR; one from Levdal and twelve from Almklovdalen (see Table 6-11). In order to consider all elements on a single two-dimensional plot, the ternary diagram of Robinson *et al.* (1982) has been adopted (Fig. 6-32). The majority of chlorites from Almklovdalen and Levdal (crosses in Fig. 6-32) plot near the point for ideal tri-octahedral ("Tri") clinochlore (Mg-rich chlorite) and coincidentally lie within the field for kimberlitic chlorites. Clinochlores from Almklovdalen display a very narrow range in composition with MgO contents varying from 33.4-33.9wt% and $Al_2O_3$ contents ranging from 13.1-13.7wt%; sample N97-17 is an exception with slightly higher MgO (34.4wt%) and significantly lower $Al_2O_3$ (9.34wt%). The clinochlore from the Levdal peridotite sample has very high $Al_2O_3$ (17.4wt%) but similar MgO and FeO contents to the chlorites from Almklovdalen. Chrome values show an overall range of 0.92-4.11wt%.

The three chlorites which plot away from clinochlore towards serpentine along the serpentine-amesite join include two chlorites from sample N97-22 (squares) and chlorite inclusions in kelyphite pseudomorphs after garnet in sample N97-31 (circle) from Gurskøy. The composition of these chlorites is highly variable, particularly $Al_2O_3$ content which ranges from 3.04-18.1wt%. The highly aluminous chlorite occurs as inclusions in kelyphite and similar chlorites have been interpreted in terms of retrogression of the granulite facies assemblage (pyroxenes and high-Al spinel) to a low amphibolite facies assemblage i.e. Fo + Sp + Opx + $H_2O$ = Chl + Amph (Medaris, 1984).

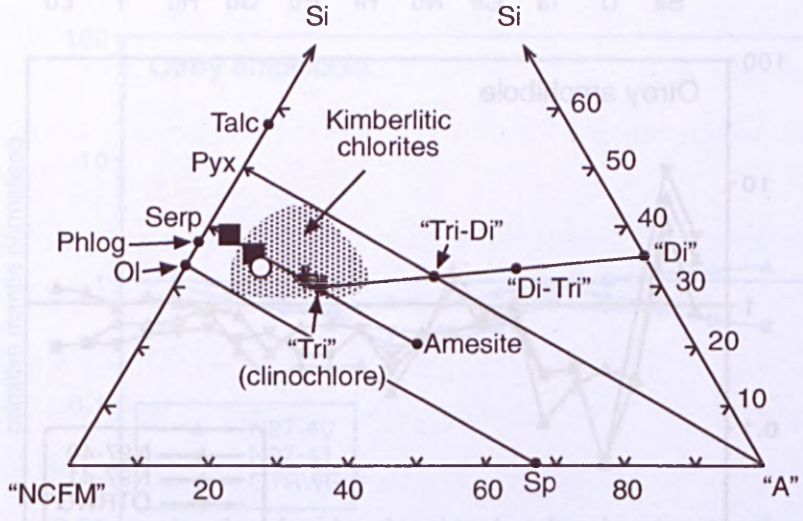


**Figure 6-32.** A ternary diagram for chlorites in dunites from the WGR. Compositional plotting scheme is adopted from Robinson *et al.* (1982) in which "NCFM"=$Fe^{2+}$+Mg+Mn +Ca+2Na+2K-Ti, and "A"=Al+$Fe^{3+}$+Cr+2Ti-Na-K. It has been assumed that all Fe is present as $Fe^{2+}$. Field for kimberlitic chlorites from Tompkins *et al.* (1984).

**Table 6-11.** Major element oxide abundances (wt%) of chlorite in dunites from Levdal and Almklovdalen.

| Sample no. | N97-1 | N97-6 | N97-7 | N97-8 | N97-9 | N97-11 | N97-13 |
|---|---|---|---|---|---|---|---|
| Locality | Levdal | Almklov | Almklov | Almklov | Almklov | Almklov | Almklov |
| Rock type | dunite | dunite | dunite | dunite | dunite | dunite | dunite |
| $SiO_2$ | 31.5 | 31.9 | 32.4 | 32.4 | 32.9 | 33.1 | 33.3 |
| $TiO_2$ | 0.06 | 0.01 | 0.02 | 0.01 | 0.01 | 0.00 | 0.00 |
| $Al_2O_3$ | 17.4 | 13.7 | 13.1 | 13.7 | 13.3 | 13.5 | 13.6 |
| $Cr_2O_3$ | 2.04 | 3.17 | 3.55 | 3.09 | 4.11 | 3.39 | 3.97 |
| FeO | 2.07 | 2.46 | 2.34 | 2.28 | 2.27 | 2.41 | 2.26 |
| MnO | 0.00 | 0.00 | 0.00 | 0.00 | 0.00 | 0.00 | 0.00 |
| MgO | 32.5 | 33.6 | 33.9 | 33.9 | 33.9 | 33.9 | 33.7 |
| CaO | 0.01 | 0.02 | 0.01 | 0.02 | 0.01 | 0.00 | 0.00 |
| $Na_2O$ | 0.01 | 0.01 | 0.02 | 0.01 | 0.00 | 0.01 | 0.01 |
| $K_2O$ | 0.18 | 0.02 | 0.03 | 0.00 | 0.01 | 0.00 | 0.01 |
| NiO | 0.17 | 0.22 | 0.28 | 0.21 | 0.28 | 0.21 | 0.00 |
| F | - | 0.00 | 0.03 | 0.01 | 0.01 | 0.02 | 0.02 |
| Cl | - | 0.02 | 0.01 | 0.01 | 0.02 | 0.00 | 0.00 |
| Total | 85.9 | 85.1 | 85.7 | 85.6 | 86.9 | 86.4 | 87.1 |
| Mg# | 96.5 | 96.1 | 96.3 | 96.3 | 96.4 | 96.2 | 96.4 |

| Sample no. | N97-17 | N97-21(1) | N97-21(2) | N97-21(3) | N97-22 | N97-24 | N97-31 |
|---|---|---|---|---|---|---|---|
| Locality | Almklov | Almklov | Almklov | Almklov | Almklov | Almklov | Gurskøy |
| Rock type | dunite | dunite | dunite | dunite | dunite | dunite | gnt lherz |
| $SiO_2$ | 34.5 | 40.5 | 36.9 | 33.3 | 33.1 | 33.2 | 30.6 |
| $TiO_2$ | 0.09 | 0.04 | 0.11 | 0.01 | 0.01 | 0.00 | 0.01 |
| $Al_2O_3$ | 9.34 | 3.04 | 6.86 | 13.5 | 13.6 | 13.3 | 18.1 |
| $Cr_2O_3$ | 0.92 | 0.06 | 0.80 | 3.70 | 3.58 | 3.39 | 0.68 |
| FeO | 6.43 | 4.64 | 5.04 | 2.32 | 2.54 | 2.60 | 2.61 |
| MnO | 0.02 | 0.01 | 0.00 | 0.00 | 0.00 | 0.00 | 0.02 |
| MgO | 34.4 | 37.7 | 36.4 | 33.8 | 33.4 | 33.7 | 31.1 |
| CaO | 0.06 | 0.06 | 0.01 | 0.01 | 0.00 | 0.01 | 0.02 |
| $Na_2O$ | 0.42 | 0.07 | 0.02 | 0.00 | 0.01 | 0.01 | 0.00 |
| $K_2O$ | 0.01 | 0.02 | 0.01 | 0.01 | 0.01 | 0.00 | 0.00 |
| NiO | 0.15 | 0.14 | 0.12 | 0.22 | 0.23 | 0.21 | 0.19 |
| F | 0.03 | - | - | - | - | - | 0.03 |
| Cl | 0.02 | - | - | - | - | - | 0.01 |
| Total | 86.3 | 86.2 | 86.3 | 86.8 | 86.5 | 86.4 | 83.4 |
| Mg# | 90.5 | 93.5 | 92.8 | 96.3 | 95.9 | 95.8 | 95.5 |

### *6.6.8 Phlogopite*

Phlogopite was identified and analysed in five dunites from Almklovdalen. The WGR phlogopites are homogeneous and Ti- and Fe-poor, similar to those found as primary, metasomatic or MARID-suite minerals in mantle xenoliths (Bachinski and Simpson, 1984; van Achterbergh *et al.*, 2001). $TiO_2$ and $Cr_2O_3$ contents are typically less than 1 wt% while FeO abundances range from 1.9-2.2 wt% (Fig. 7-12). The greatest variation in composition between samples is in the alkalis with $Na_2O$ content ranging from

0.78-7.41wt% and $K_2O$ content varying from 4.46-7.43wt%. Abundances of Cl and F are low and similar to those seen in the amphiboles from Almklovdalen. Mg# range from 95.5-96.2 which places them at the high end of the compositional range for micas in garnet peridotite xenoliths in kimberlites (Carswell, 1975; Bachinski and Simpson, 1984). The origin of the phlogopite in the WGR peridotites is uncertain. However, the presence of phases such as phlogopite in garnet peridotites is thought to be evidence for hydrous metasomatism.

**Table 6-12.** Major element oxide abundances (wt%) of phlogopite in dunites from Almklovdalen.

| Sample no. | N97-6 | N97-7 | N97-8 | N97-11 | N97-23 |
|---|---|---|---|---|---|
| Rock type | dunite | dunite | dunite | dunite | dunite |
| $SiO_2$ | 42.5 | 42.2 | 42.5 | 41.1 | 42.7 |
| $TiO_2$ | 0.01 | 0.30 | 0.02 | 0.04 | 0.23 |
| $Al_2O_3$ | 12.3 | 12.4 | 12.7 | 11.4 | 11.6 |
| $Cr_2O_3$ | 0.43 | 0.61 | 0.66 | 0.61 | 1.05 |
| FeO | 2.24 | 1.99 | 2.09 | 1.90 | 1.89 |
| MnO | 0.01 | 0.00 | 0.02 | 0.00 | 0.02 |
| MgO | 26.7 | 26.3 | 26.3 | 26.7 | 27.1 |
| CaO | 0.01 | 0.01 | 0.01 | 0.16 | 0.15 |
| $Na_2O$ | 1.60 | 1.55 | 1.80 | 7.41 | 0.78 |
| $K_2O$ | 7.37 | 7.43 | 6.71 | 4.46 | 5.84 |
| NiO | 0.22 | 0.21 | 0.22 | 0.16 | 0.21 |
| F | 0.01 | 0.06 | 0.01 | 0.03 | n/a |
| Cl | 0.04 | 0.02 | 0.05 | 0.01 | n/a |
| Total | 93.5 | 92.9 | 93.1 | 93.9 | 91.6 |
| Mg# | 95.5 | 95.9 | 95.7 | 96.2 | 96.2 |

## 6.7 GEOTHERMOBAROMETRY

### *6.7.1 Introduction*

Reliable estimates of equilibrium temperatures and pressures should ideally enable determination of the conditions and depths of formation of garnet peridotite assemblages. The main problem in estimating the temperatures and pressures of a mineral assemblage is to know which phases formed in equilibrium with one another. It is reasonable to assume that minerals in contact with each other without visible reaction are at equilibrium, but the phases in the Norwegian garnet peridotites are seldom in direct contact, except in the case of inclusions in garnet, and many of the garnets and pyroxenes are compositionally zoned. For these reasons, P-T estimates were determined separately for cores and rims. There is no consensus in the literature as to whether the cores or the rims will provide the most reliable temperatures and pressures. Several workers (Evans and Trommsdorff, 1978;

Carswell and Gibb, 1980; Medaris, 1980) have used mineral cores to calculate equilibration conditions for various European garnet peridotites. However, Carswell *et al.* (1985) has pointed out that there is no assurance that the cores of isolated grains have ever been in equilibrium with each other and that the margins of grains in direct contact may represent the only equilibrium compositions recorded in these rocks. These authors have suggested that the low-$Al_2O_3$ cores of orthopyroxene may never have been in equilibrium with garnet and that pressures calculated from such compositions may be anomalously high. Despite these reservations, other studies (Medaris, 1984; Medaris and Carswell, 1990; Krogh and Carswell, 1995) have continued to use core compositions because of the relative uniformity of core compositions of minerals from the Norwegian garnet peridotites and the restriction of zoning to grain margins. Ideally, grains to be used in the calculations should be in direct contact or separated by a thin zone of kelyphite or recrystallised matrix. Medaris (1984) recommends not to use samples where garnet rims have been extensively kelyphitised.

The P-T conditions of formation for the WGR garnet peridotites have been investigated by numerous workers (Carswell, 1973; Carswell, 1974; Carswell and Gibb, 1980; Medaris, 1980; Jamtveit, 1984; Medaris, 1984; Carswell, 1986; Jamtveit *et al.*, 1991; Krogh and Carswell, 1995; Brueckner and Medaris, 1998) using a variety of geothermometer-geobarometer pairs. Table 6-13 is a compilation of published P-T estimates for garnet peridotites from Almklovdalen, Gurskøy and Otrøy. There is a strong trend of decreasing temperature and pressure from core to rim for the Almklovdalen and Gurskøy garnet peridotites for a variety of geothermometer/geobarometer pairs. Core temperatures show a range of 750-800°C while rim temperatures are closer to 700°C at Almklovdalen and as low as 610°C at Gurskøy. Core pressures for the Almklovdalen peridotites are ~24 kb whereas pressures calculated for rims are ~21 kb. Differences between core and rim pressures are more profound for the Gurskøy peridotites where rims have recorded pressures up to 13 kb lower than those for cores. Variations in pressure estimates for the Otrøy peridotites show either the same or opposite sense to the other localities. At Ugelvik pressures are typically higher in rims by ~5-10 kb compared to cores and temperatures slightly lower in cores compared to rims. Raudhaugene cores are up to 10 kb (depending on geobarometer) higher than rims while temperatures are generally uniform between cores and rims.

Fig. 6-33 is a synoptic P-T-t path for the metamorphic evolutionary Stages II ± VII in the Mg-Cr type peridotite bodies (Krogh and Carswell, 1995). It is thought unlikely that

these rocks followed a direct P-T path between Stages IIa and III on Fig. 6-33, in view of the long time interval between these assemblages. It seems more reasonable, as argued by (Jamtveit *et al.*, 1991), that prior to the Caledonian orogeny, these peridotites were held at appreciably lower P-T conditions in the subcontinental mantle with their Stage IIa mid-Proterozoic assemblage metastably preserved. The pressure increase from Stage IIb to III would, therefore, relate to the tectonic emplacement of the peridotite into the crust during subduction during the Caledonian plate collision and subsequent crustal thickening (Jamtveit *et al.*, 1991; Krogh and Carswell, 1995). It is envisaged that the P-T-t paths for the mantle-derived Mg-Cr type peridotites converged, at the P-T conditions of their Stage III mineral assemblages, with the clockwise prograde paths for the development of the Caledonian high-pressure assemblages in the country-rock eclogites (Medaris, 1980; Krogh and Carswell, 1995) and in the Fe-Ti type garnet peridotites. The increase in P-T estimates from core to rim for the Otrøy peridotites is difficult to reconcile with the P-T paths illustrated in Fig. 6-33.

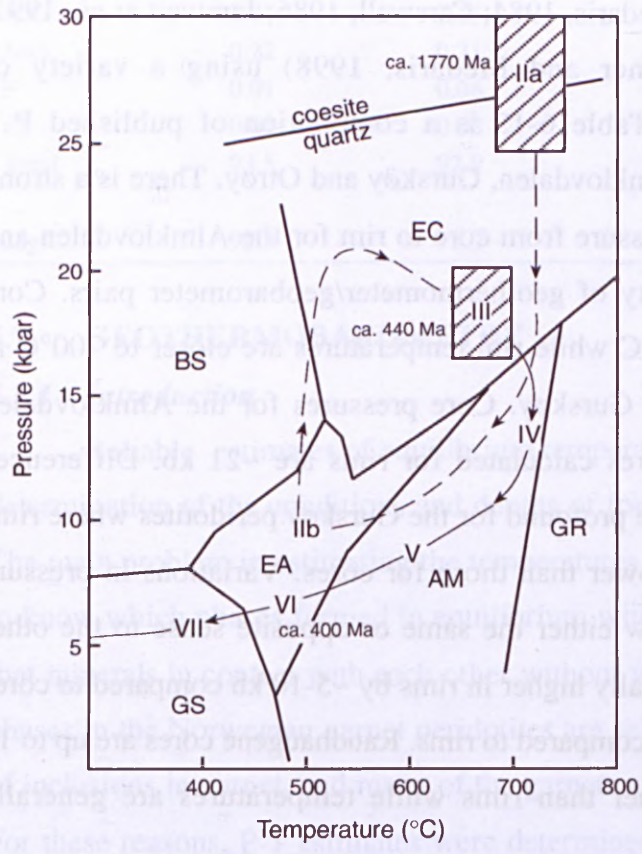


**Figure 6-33.** P-T-t path for metamorphic evolution of Mg-Cr type peridotites from the Western Gneiss Region. P-T estimates for Stage II and III assemblages are based on data from the localities on Otrøy. Diagram taken from (Krogh and Carswell, 1995).

**Table 6-13.** Compilation of published temperature and pressure estimates for garnet peridotites from the Western Gneiss Region. Thermometers: ONW79 (O'Neill and Wood, 1979); H84 (Harley, 1984); P85 (Powell, 1985); EG79 (Ellis and Green, 1979); MG78 (Mori and Green, 1978). Barometers: W74 (Wood, 1974).

| Locality | Mineral | T°C Ol/Gnt ONW79 | T°C Opx/Gnt H84 | T°C Cpx/Gnt P85 | T°C Cpx/Gnt EG79 | P kb Opx-Gnt W74 | T°C Cpx/Gnt MG78 | P kb Opx/Gnt W74 |
|---|---|---|---|---|---|---|---|---|
| Almklovdalen[b] | cores | 804 ± 55 (30kb) | | | 805 ± 24 | 24.3 ± 3.1 | 772 ± 31 (30kb) | |
| | rims | 714 ± 30 (30kb) | | | 734 ± 32 | 20.7 ± 2.5 | 701 ± 42 (30kb) | |
| Lien[a] (Almklovdalen) | average | 808 ± 52 (30kb) | 847 ± 21 (30kb) | 794 ± 27 (30kb) | | | | |
| Gurskebøtn[c] (Gurskøy) | cores | | | | 750-810 | 28-32 | 750-790 | 28-31 |
| | rims | | | | 630-660 | 16-18 | 610-640 | 15-17 |
| Sandvika[b] (Gurskøy) | cores | 849 ± 58 (30kb) | | | 855 ± 37 | 32.4 ± 2.8 | 821 ± 48 (30kb) | |
| | rims | 719 ± 57 (30kb) | | | 704 ± 24 | 19.5 ± 3.3 | 706 ± 32 (30kb) | |
| Ugelvik[b] (Otrøy) | cores | 711 ± 33 (30kb) | | | | 31.8 ± 5.1 | | |
| | rims | 776 ± 35 (30kb) | | | | 24.5 ± 2.4 | | |
| Raudhaugene[d] (Otrøy) | cores | 715 (18.4kb[#]) | 847 (29.3kb[*]) | | 805 | 23.5 | 779 | 22.0 |
| | rims | | 853 (35.5kb[*]) | | 831 | 30.4 | 772 | 26.7 |
| Raudhaugene[e] (Otrøy) | cores | 795 (36kb[‡]) | 870 (40kb[‡]) | 701 (31kb[‡]) | | | | |
| | rims | 791 (28kb[‡]) | 847 (30kb[‡]) | 704 (23kb[‡]) | | | | |

REFERENCES
a Medaris (1980)
b Medaris (1984)
c Jamtveit (1984)
d Carswell (1986)
e Jamtveit et al. (1991)

# Wood (1974)
* Harley and Green (1982)
‡ Nickel and Green (1985)

### *6.7.2 Results*

Temperatures and pressures have been calculated for cores and rims for eleven of the fifteen garnet peridotites from the Western Gneiss Region; three samples contain heavily kelyphitised garnets making them unsuitable for geothermobarometric calculations. Mineral phases in sample N97-5 were shown to be compositionally homogeneous and, in this case, average compositions were used. The calculated univariant curves for a number of different exchange reaction equilibria have been plotted in P-T space (see Appendix VIII) in order to identify samples in which there is reasonable overall equilibrium between the selected mineral pairs. The calculated reaction equilibria that show close correspondence (solid lines) have been judged to yield the most reliable results for the individual samples. These results indicate that the "best" agreement is between the ON79, K88 and BKCa thermometers and the NG85 and BKN barometers. The two barometers give results typically within 2-3 kb of each other though in some samples the difference can be up to 5 kb.

The two-pyroxene thermometer of Brey and Kohler (1990) produces significantly lower temperatures than the other methods whereas the Fe-Mg exchange thermometers of Ellis and Green (1979) and Harley (1984) have a tendency to give higher temperatures. The problems with the Fe-Mg thermometers may relate to unidentified variations in $Fe^{3+}/Fe^{2+}$ ratios between the paired minerals. In addition, Carswell and Gibb (1987) judged EG79 to be the most accurate calibration of the Fe-Mg thermometer only at T >1200°C which puts it well outside the temperature range for the WGR peridotites. Problems with the H84 thermometer include its limited precision at low temperatures due to analytical uncertainties (serious doubts were expressed in Carswell and Gibb (1987) over whether satisfactory Fe-Mg equilibration between the mineral phases was achieved during the experiments), and its failure to take into account important minor constituents such as Mn, $Cr^{3+}$ and $Fe^{3+}$.

Table 6-14 lists the P-T results for the WGR garnet peridotites derived from the univariant curves in Appendix VIII. Indicated mean P-T estimates for Gurskøy cores are 770±30°C and 32±5 kb, and for Otrøy cores 745±40°C and 34±4 kb, which puts them well above the quartz-coesite stability boundary. This criterion, according to Krogh and Carswell (1995), qualifies Stage II Mg-Cr garnetiferous assemblages as UHP (ultra-high pressure) assemblages. This is supported by a recent evaluation of P-T conditions for coesite stability (Hemingway *et al.*, 1998) which indicates that the minimum pressure required for UHP metamorphism is ~2.63 GPa at 600°C and 2.73 GPa at 700°C. By

contrast, the rim compositions, representing recrystallised Stage III assemblages, appear to have equilibrated at much lower pressures within the quartz stability field i.e. pressure estimates for Gurskøy and Otrøy rims are 19±3 kb and 23±5 kb respectively. Indicated rim temperatures for Gurskøy are 645±40°C and for Otrøy, 710±50°C. There is close concordance between the P-T estimates calculated for the Gurskøy and Otrøy peridotites here and those published in the literature.

**Table 6-14.** Indicated temperatures and pressures for WGR garnet peridotites derived from calculated univariant curves for a number of different exchange reaction equilibria (see text for details). Ni-in-garnet temperatures calculated using the thermometer of Ryan *et al.* (1996).

| Locality | Sample no. | T°C | | P kbar | | T°C Ni-in-gnt |
|---|---|---|---|---|---|---|
| Almklovdalen | N97-5 | 730±20 | | 28±2 | | 677 |
| | | Core | | Rim | | |
| | | T°C | P kbar | T°C | P kbar | |
| | N97-14 | 730±20 | 27±3 | 730±30 | 30±4 | 640 |
| | N97-15 | 685±50 | 21±5 | 715±40 | 24±4 | 706 |
| | N97-16 | 700±30 | 26±1 | 650±40 | 23±3 | 706 |
| | N97-18 | 715±40 | 28±4 | 680±30 | 25±3 | 661 |
| | LNWG | 685±10 | 25±2 | 685±20 | 27±3 | 661 |
| Gurskøy | N97-29B | 790±15 | 37±2 | 640±70 | 19±5 | 802 |
| | GBWG | 745±20 | 27±1 | 650±30 | 14±2 | 745 |
| | SVWG | 770±70 | 32±4 | 645±40 | 25±2 | 733 |
| Otrøy | N97-40 | 775±35 | 37±4 | 735±45 | 23±5 | 651 |
| | N97-41 | 770±60 | 37±5 | 710±50 | 25±6 | 720 |
| | OTRWG | 690±30 | 28±2 | 690±50 | 22±4 | 706 |

Mean P-T estimates for the Almklovdalen garnet peridotites are similar for cores and rims. Core temperatures are 710±30°C for cores and slightly lower at 690±30°C for rims while core and rim pressures are both 26±3 kb. These estimates lie below the quartz-coesite reaction curve indicating recrystallisation to dominantly lower pressure assemblages, though individual samples may have core and/or rim P-T values that lie in the coesite stability field. The overall lower P-T conditions revealed for the Almklovdalen peridotites are consistent with the apparent southeastward decrease in metamorphic temperatures and pressure defined by regional geotherms for country rock eclogites and granulites (Griffin *et al.*, 1985). However, given the errors on the Almklovdalen temperatures and the small distance between Almklovdalen and Gurskøy it is unlikely that this variation is related to metamorphic gradient. Medaris (1984) has argued that the regional metamorphic gradient recorded by granulites and eclogites is not reflected by the garnet-bearing assemblages in the WGR, based on the similarity of P-T estimates for localities across the region. It is more probable that the Almklovdalen peridotites were

sampled at higher levels in the upper mantle, and therefore lower temperatures and pressures, than the peridotites preserved at Otrøy and Gurskøy.

Temperature estimates for the garnet peridotites calculated using the exchange thermometers and the two-pyroxene thermometers have been independently tested using the Ni-in-garnet thermometer (Griffin *et al.*, 1989; Ryan *et al.*, 1996. Also see Section 2.4.3). Results are listed in Table 6-14. This thermometer is based on the temperature dependence of Ni in Cr-pyrope garnet in equilibrium with olivine. Consequently this thermometer may only have a limited application to the WGR peridotites as it cannot be assumed that these phases are in equilibrium in these rocks. However, disequilibrium is less of a problem with this thermometer as Ni content can be used to estimate the T of a pyrope grain without knowledge of the exact composition of the coexisting olivine. This is because it has been shown that the range of Ni content in olivine is small compared to the observed range in garnet over the temperature range 640-1400°C (Ryan *et al.*, 1996).

There is considerable heterogeneity in Ni contents in the WGR garnets, not only within individual grains but also between grains in the same sample. As only a single core and rim analysis was taken for each garnet in this study it was impossible to recognise any zoning in the grains though a study of trace element zoning in garnets from the WGR peridotites has shown evidence for zoning in elements such as Ti, V and Cr (Brueckner *et al.*, 1996). The Ni content for cores has been used were possible though most $T_{Ni}$ calculations were carried out using grain averages as intra- and inter-grain variation in Ni content for a given sample was found to be too complex. Despite this problem 75% of the $T_{Ni}$ temperatures are within error of temperature estimates for cores derived using univariant curves though for other samples $T_{Ni}$ is up to 100°C lower. Griffin *et al.* (1996) have argued that Ni is the most rapidly diffusing trace element in garnet and is therefore expected to give lower temperatures. To use the Ni-in-garnet thermometer more effectively for the WGR peridotites, a more detailed investigation of Ni distribution in garnet is required.

The P-T estimates for the WGR garnet peridotites are plotted in Figure 6-34, in which are included for reference, the stability fields for diamond and graphite, coesite and quartz, garnet and spinel peridotite, and two steady-state conductive geotherms, one for 200km thick lithosphere and another for 100 km thick lithosphere, assuming a 35 km thick crust and taking the lithosphere-asthenosphere boundary to be at 1350°C (Brueckner and Medaris, 1998). The garnet peridotites show a tight distribution along a single "cold" geotherm that closely matches the conductive geotherm for 200 km thick lithosphere and

lies below the graphite-diamond stability curve. By comparison, the field for WGR garnet peridotites taken from Medaris and Carswell (1990), and shown in Fig. 6-34, is above the 200 km conductive geotherm and lies predominantly in the stability field for diamond.

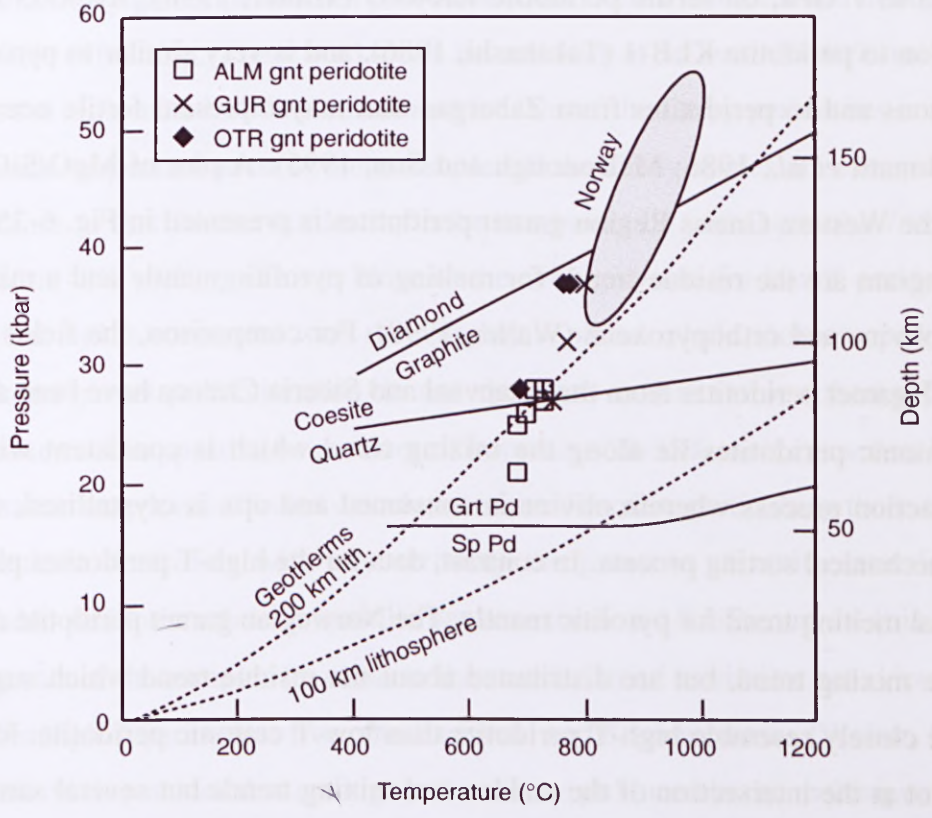


**Figure 6-34.** P-T conditions for garnet peridotites from the WGR. Grey field taken from Medaris and Carswell (1990). Steady-state conductive geotherms for 100- and 200-km thick lithosphere (Brueckner and Medaris, 1998) are shown for reference.

The pressure and temperature estimates from Medaris and Carswell (1990) were calculated using averaged results of three Fe-Mg exchange thermometers (O'Neill and Wood, 1979; Harley, 1984; Powell, 1985) with the orthopyroxene Al barometer of Nickel and Green (1985). The resulting P-T estimates show a range from about 800°C, 30 kb to almost 1000°C, 55 kb. The authors expressed some concern regarding the use of Fe-Mg thermometers in conjunction with Nickel and Green's barometer, and the difference in the P-T range calculated here and that of Medaris and Carswell (1990) is most likely due to inappropriate choice of geothermometers and/or geobarometers. In particular, the garnet-opx thermometer of Harley (1984) has been shown to overestimate temperature (as discussed on p. 250 of this Section) and will therefore lead to artificially high pressures.

## 6.8 MODELLING OF DEPLETION PROCESSES

The extraction of mafic and ultramafic melts from fertile peridotite leaves behind a depleted residue, the composition of which is determined by the initial peridotite

composition and the melt composition at the conditions of segregation. To estimate the extent of melting in the WGR peridotites their major element and modal compositions have been compared to residue trends derived from melting experiments, over a pressure range of 3 to 7 GPa, on fertile peridotite KR4003 (Walter, 1998). KR4003 is close in composition to peridotite KLB-1 (Takahashi, 1986), and is very similar to pyrolite model compositions and to peridotites from Zabargad that may represent fertile oceanic upper mantle (Bonatti *et al.*, 1986; McDonough and Sun, 1995). A plot of $MgO/SiO_2$ vs $SiO_2$ showing the Western Gneiss Region garnet peridotites is presented in Fig. 6-35. Included in this diagram are the residue trends for melting of pyrolitic mantle and a mixing trend between olivine and orthopyroxene (Walter, 1998). For comparison, the fields for low-T and high-T garnet peridotites from the Kaapvaal and Siberia Cratons have been added. The low-T cratonic peridotites lie along the mixing trend which is consistent with a melt-mantle reaction process wherein olivine is consumed and opx is crystallised, or it could imply a mechanical sorting process. In contrast, data for the high-T peridotites plot close to the residual melting trend for pyrolitic mantle. The Norwegian garnet peridotite data do not follow the mixing trend, but are distributed about the residue trend which suggests that they more closely resemble high-T peridotite than low-T cratonic peridotite. Most of the dunites plot at the intersection of the residue and mixing trends but several samples lie at higher $SiO_2$ contents along the mixing trend within the field for low-T peridotites.

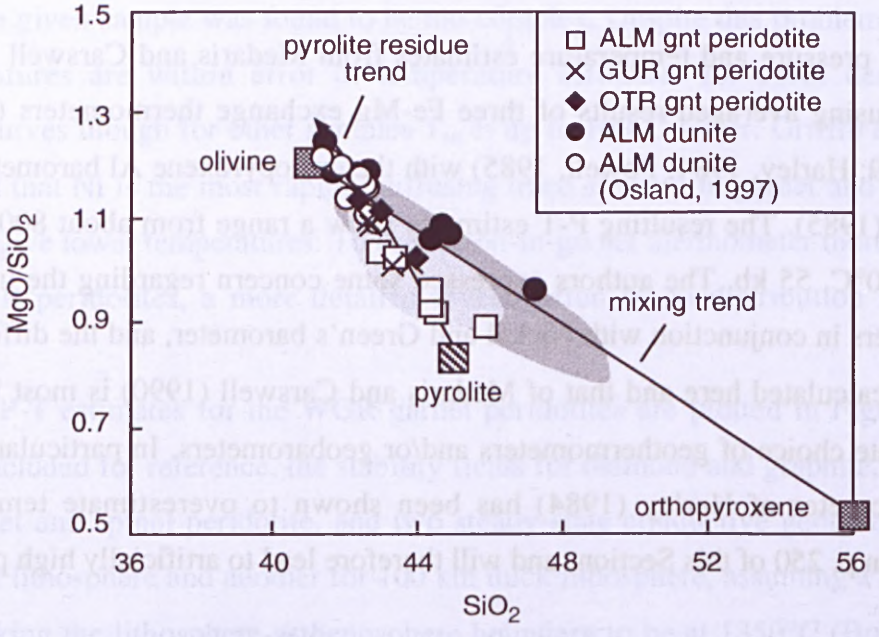


**Figure 6-35.** $Mg/SiO_2$ vs $SiO_2$ (wt%) showing peridotites from the Western Gneiss Region relative to the residue trend for pyrolite (KR4003), and to a mixing trend between olivine and opx (Walter, 1998). Dark grey area is the field for low-temperature garnet peridotites from the Kaapvaal and Siberia Cratons. Pale grey area is field for high-temperature garnet peridotites from the Kaapvaal and Siberia Cratons.

A plot of whole rock Mg# vs modal olivine showing WGR peridotites relative to pyrolite residue trends for melting from 2 to 7 GPa (Walter, 1998) is shown in Fig. 6-36A. There is a large spread in the data though some broad inferences can be made. The Gurskøy and Otrøy garnet peridotites plot close to the 5 GPa residue trend indicating high-pressure melt extraction. These rocks can be residues of at least 20-40% melting. It is likely that the high modal olivine calculated for two of the Otrøy peridotites is an artefact of the extreme serpentinisation of these samples. If the Otrøy modes are extrapolated back to values close to that for the third sample the datapoints lie just above the 7 GPa residue trend at about 40% melting. This is close to the average value for low-T peridotites from the Kaapvaal and is consistent with their highly depleted whole rock compositions. The Almklovdalen garnet peridotite data do not show any consistent or coherent behaviour. Overall, these rocks appear to be residues of between ~18-35% melt extraction but, again, serpentinisation may have affected calculated mineral modes, particularly those for olivine. It is difficult to determine with any certainty the pressure of melt extraction for the Almklovdalen peridotites though most lie between the 5 and 7 GPa curves. It is also worth noting that two of the samples lie close to the oceanic trend as similar behaviour has been observed for high-T peridotites from the Kaapvaal and Siberia cratons (Walter, 1998). The dunites have olivine modes that are higher than those produced in the melting experiments, though if the 3 and 5 GPa residue trends are extrapolated to higher modal olivine then the dunites lie somewhere in between these two melting contours. Although Fig. 6-36A implies that these rocks require unreasonably high degrees of melting (~60%?) it is conceivable that at least some of the dunites represent residues after mid- to high-pressure melting of a fertile source, comparable to that modelled for low-T cratonic peridotite.

The Almklovdalen garnet peridotites show a strong correlation between opx content and rock Mg# that lies just below the oceanic trend (grey field in Fig. 6-36B) which is consistent with melt extraction at low pressures (<2 GPa). The data for the Gurskøy and Otrøy garnet peridotites are not well-constrained. Only one sample (GBWG) from Gurskøy contains a measurable amount of orthopyroxene. This sample lies at the low opx extension of the 2 GPa residue trend which is at variance with the results seen in Fig. 6-36A. Despite probable inaccuracies in calculated mineral modes for the Otrøy peridotites the indication in Fig. 6-36B is that these rocks could be residues of high degrees of melting (~40%) at high pressures. This may also be true for some of the dunites from Almklovdalen as suggested by Fig. 6-34A. Other dunites from this locality are opx-free and thus more ambiguous.

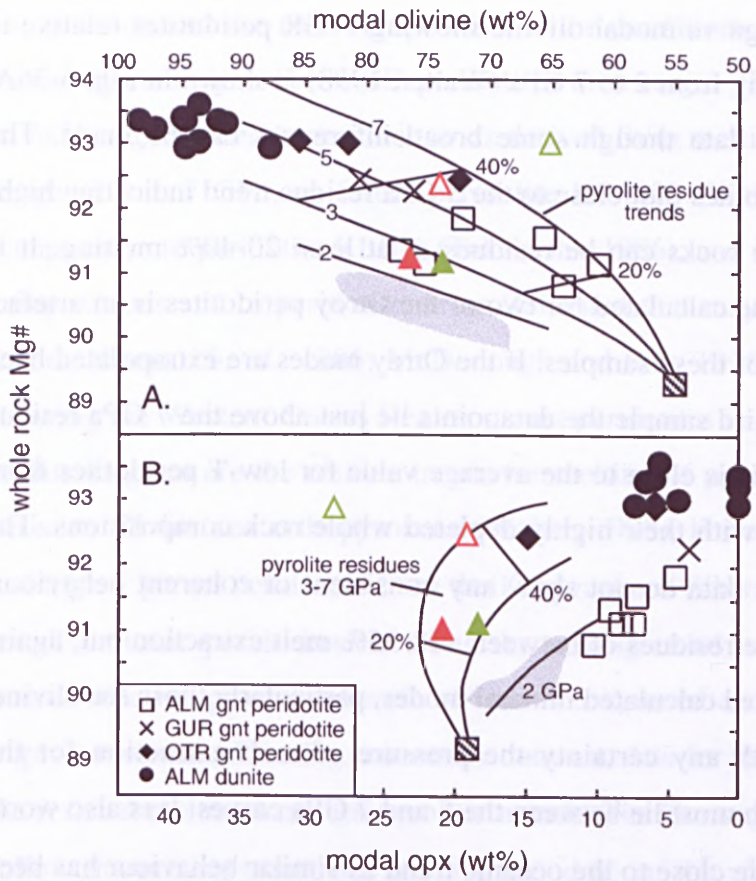


**Figure 6-36.** Whole rock Mg# vs modal olivine (A) and modal opx (B) showing residue trends for melting of pyrolitic mantle (3-7 GPa, KR4003, (Walter, 1998); 2GPa, KLB-1, (Hirose and Kushiro, 1993)). Residue contours are labeled according to pressure (GPa) and percent melting. After (Walter, 1998). Red triangles represent average low-T (open) and high-T (closed) peridotites from Kaapvaal. Green triangles represent average low-T (open) and high-T (closed) peridotites from Siberia. Grey field is for oceanic peridotites.

## 6.9 DISCUSSION

### *6.9.1 A possible origin for the WGR garnet peridotites*

Garnet peridotites in the Western Gneiss Region occur as discrete bodies within larger masses of "dunite". Previous work on the WGR peridotites has had a tendency to treat the garnet peridotites as the main rock type but this is misleading and disregards the most volumetrically significant part of the peridotite bodies. The dunites have long been interpreted as retrograded garnet peridotite based on the close spatial relationship between the two rock types and evidence for retrogression of garnet to chlorite along the margins of the garnet peridotite bodies. However, this study has shown that the bulk of the dunites, at least at the Almklovdalen locality, are highly refractory and do not in fact represent retrograded garnet peridotite. This poses the problem of how to reconcile the presence of small volumes of relatively fertile material within large bodies of extremely depleted material. The discrepancy in the pressure estimates for the garnet peridotites ( 2 GPa) and dunites (5-7 GPa) at Almklovdalen, as revealed by melt modelling in Fig. 6-34B, suggests that the relationship between the rock types is not related to a simple melt-depletion process. A possible solution to the problem may lie in the fertile nature of the

Almklovdalen garnet peridotites and their resemblance to high-T sheared peridotite xenoliths found in kimberlites.

The WGR garnet peridotites have previously been interpreted by Brueckner and Medaris (1998) as representing cold, melt-depleted, buoyant lithospheric mantle based on their apparent similarity to low-T coarse garnet peridotite xenoliths found in kimberlites (Carswell, 1968). However, this study has found evidence from whole-rock and mineral compositions which suggests that the WGR garnet peridotites may be more closely related to high-T sheared peridotite xenoliths than low-T coarse peridotites. High-T sheared peridotite xenoliths typically have less depleted major element compositions than the more common low-T peridotites. They are enriched in Fe relative to low-T peridotites, with Mg# that are usually below 92 (Boyd, 1997), and have previously been regarded as samples of asthenospheric material that have underplated cratons or young subducted oceanic lithosphere accreted on the bottom of cratonic keels (Boyd and Mertzman, 1987; Kesson and Ringwood 1989). High-T sheared garnet peridotite xenoliths are now thought to represent old lithospheric keel that has been strongly metasomatised by the recent infiltration of asthenosphere-related melts. This conclusion was initially based on zoning in garnet from sheared peridotites (Smith and Boyd, 1987; Smith, 1988; Griffin *et al.*, 1989; Smith and Boyd, 1992), which was argued as evidence for melt infiltration, and was later supported by Archean Re-Os depletion ages that revealed that these rocks are in fact fragments of ancient cratonic lithosphere that have been refertilised (Walker *et al.*, 1989; Pearson *et al.*, 1995b).

Refertilisation of a depleted protolith by silicate melts will introduce elements such as Ti, Fe, Ca, Al, Na, and P. Evidence for this re-enrichment has been recognised in suites of sheared garnet peridotite xenoliths from many localities worldwide. Compositional zoning patterns in garnet have been particularly revealing. A study of garnets from sheared garnet peridotites from the Thumb diatreme on the Colorado Plateau found core-to-rim depletions in MgO to be accompanied by enrichment in Fe, Ti and Na (Smith and Ehrenberg,1984; Smith, 1988). Core-to-rim enrichments in FeO, $TiO_2$, $Na_2O$ and $P_2O_5$ have also been documented for garnets from Lesotho (southern Africa) sheared lherzolites (Smith and Boyd, 1987; Smith,1988). Other studies of garnet zoning (Griffin *et al.*, 1989; 1996) have shown that Fe and Ti enrichment in garnet rims is often accompanied by enhanced Zr, Y and Ga contents and, according to Kesson and Ringwood (1989), it is expected that HREE would have been introduced in parallel with Y.

Zoning data on garnet in peridotite xenoliths restrict some metasomatic processes to geologically short time-spans (10-$10^4$ years) prior to the eruption of the host magmas, and suggest that the metasomatism is genetically linked to the magmatic events or their immediate precursors (Griffin *et al.*, 1996). Changes in composition from core to rim for garnets from the Western Gneiss Region peridotites has been widely documented (Carswell *et al.*, 1983; Jamtveit, 1984; Medaris, 1984; Carswell, 1986; Jamtveit, 1987a; Brueckner *et al.*, 1996) and has been interpreted as a response to cooling and decompression of the peridotites (Medaris, 1984). This is the probably the more viable explanation as zoning in garnets from massif peridotites is unlikely to be related to mantle metasomatism as garnets have been shown to homogenise in less than 1 Ma at mantle temperatures (Griffin *et al.*, 1999b).

### *6.9.2 Classification of WGR garnets using the CARP scheme*

The WGR garnets have been classified according to the CARP (Cluster Analysis by Regressive Partitioning) scheme of Griffin *et al.* (2001b). CARP is a statistical approach that has been used to define compositional populations within a large database of Cr-pyrope garnets from the subcontinental lithospheric mantle. The rules defining the populations (classes) are expressed in simple compositional variables (major oxides, Zn, Ga, Sr, Y and Zr) and are therefore applicable to new samples and other databases (Griffin *et al.*, 2001b). The classes are divided into four groups: (1) depleted harzburgites and lherzolites, little metasomatism; (2) depleted, metasomatised (± phlogopite) peridotites; (3) fertile to moderately depleted (metasomatised) lherzolites; and (4) melt-related metasomatised lherzolites.

The Norwegian garnets fall into CARP classes L9, L10A and L10B and, therefore, belong to Group 3 (Griffin *et al.*, 2001b). Class L9 represents low-Cr garnets from very fertile lherzolites (low-Fo olivine) which may have been subjected to Fe-metasomatism. L9 garnets are characterised by high HREE and low LREE, consistent with relatively low degrees of depletion. Class L10A represents garnets from a range of fertile to moderately depleted lherzolites, many of which show evidence for phlogopite-related, or in some cases Ca/Al, metasomatism. These rocks contain abundant cpx and garnet, but have highly magnesian olivine (mean=$Fo_{92}$). The REE patterns of L10A garnets are similar to those of L9 garnets. Class L10B represents low-Cr garnets from fertile lherzolites with Fo-poor olivine (mean=$Fo_{90}$). It is likely that many of the L10B rocks, especially those from

Tectons, never experienced much melt depletion. L10B garnets have trace element patterns similar to the L9 and L10A garnets.

The garnets from Almklovdalen fall into Classes L9 and L10A (Table 6-15). These peridotites are relatively fertile, as evidenced by their low-Mg# olivine (90.5-91.7), and contain Cr-poor, LREE-depleted garnets as expected in these classes. The lack of K-enrichment in the L10A peridotites suggests that these rocks have not been affected by phlogopite-related metasomatism but their high Ca and Al abundances (see Fig. 6-11) may indicate Ca-Al metasomatism. Class L10A garnets are also found in the more depleted peridotites from Otrøy. The Otrøy rocks have more magnesian olivine ($Fo_{91.9-92.6}$) than the samples from Almklovdalen, but again have the low-Cr, LREE-depleted garnets typical of Class L10A. The garnets from Gurskøy fall into Class L10B. However, the Gurskøy peridotites are strongly depleted with high-Mg# olivine ($Fo_{93}$) and do not resemble the fertile lherzolites typical of this class. Despite this discrepancy, the Gurskøy garnets are poor in Cr and LREE-depleted and therefore similar to Class 10B garnets.

**Table 6-15.** CARP classification for garnets from the WGR garnet peridotites.

| Sample no. | Locality | Garnet Type* | CARP Class | Rock Type | Texture** | Olivine Mg# |
|---|---|---|---|---|---|---|
| N97-5 | Almklovdalen | lherz | L10A | lherzolite | D | 90.8 |
| N97-14 | Almklovdalen | lherz | L10A | lherzolite | D | 90.8 |
| N97-15 | Almklovdalen | lherz | L10A | lherzolite | D | 91.5 |
| N97-16 | Almklovdalen | lherz | L10A | lherzolite | D | 91.7 |
| N97-18 | Almklovdalen | lherz | L9 | lherzolite | D | 90.5 |
| LNWG | Almklovdalen | lherz | L9 | lherzolite | D | 91.2 |
| GBWG | Gurskøy | low-Cr | L10B | wehrlite | C | 93.2 |
| SVWG | Gurskøy | low-Cr | L10B | wehrlite | C | 93.0 |
| N97-40 | Otrøy | lherz | L10A | harzburgite | D | 91.9 |
| N97-41 | Otrøy | lherz | L10A | harzburgite | D | 92.3 |
| OTRWG | Otrøy | lherz | L10A | harzburgite | D | 92.6 |

* based on garnet Ca-Cr classification scheme in Fig. 6-23
** C = coarse granular; D = deformed (sheared)

Class L9 and L10A garnets are abundant in the shallow layers of both Archon and Proton mantle sections and are interpreted as refertilisation of depleted harzburgites and lherzolites to depleted/metasomatised lherzolites (Griffin *et al.*, 2001b). Further metasomatism is thought to produce fertile lherzolites, represented by the Class L10B garnets, which show no evidence of previous depletion. Mantle sections for Proterozoic terrains (i.e. Botswana, Yangtze and Birekte) considered in Griffin *et al.* (2001b) all show a concentration of depleted/ metasomatised garnets and some depleted ones towards the base of the sections; these grade upward into dominantly fertile lherzolite and downward into lherzolites affected by melt-related metasomatism. The dominance of metasomatised

garnets in Proterozoic mantle sections has led Griffin *et al.* (2001b) to conclude that at least some Proterozoic lithosphere may represent strongly reworked Archean lithospheric mantle. If this is the case for the garnet peridotite bodies from the WGR then it might be expected that Archean isotopic signatures may be preserved in the reworked peridotite. This possibility is explored in Chapter 7 using the Re-Os isotopic system.

### *6.9.3 A depleted precursor for the WGR garnet peridotites*

The discussion in Sections 6.9.1 and 6.9.2 suggests that the WGR garnet peridotites represent refertilisation of a depleted precursor and raises the question of the nature of the original depleted protolith. The obvious choice is the dunite which encloses the garnet-bearing peridotites. The close structural relationship between the garnet peridotites and their enclosing dunites presents the possibility that the garnet peridotites could represent zones of melt percolation and refertilisation of the dunites. Refertilisation of dunite has been noted in a suite of xenoliths from the Kimberley-Bultfontein kimberlite pipes (Boyd *et al.*, 1993). In that study it was found that olivine in coarse dunites was overall more forsteritic than olivine porphyroclasts in sheared dunites i.e. $Fo_{89-94}$ compared to $Fo_{85-93}$. In the porphyroclastic samples, olivine neoblasts were observed to be enriched in Ti, Fe, Cr, Al, Ca and Na relative to the more forsteritic porphyroclasts, while orthopyroxene porphyroclasts ($En_{93}$) have rims of $En_{89}$ that are comparatively enriched in Ti, Fe, Cr, Al and Na. The South African sheared dunites were found to contain ilmenite, a common accessory phase in some suites of sheared peridotite xenoliths. In this study, ilmenite was recognised in one garnet peridotite from Gurskøy.

Garnet peridotites in the WGR are locally intruded by garnet-bearing websterites, wehrlites and clinopyroxenites. At Almklovdalen, the close spatial relationship between the garnet peridotite and associated rock types and the similarity in their whole-rock trace element patterns have been cited as good evidence for at least one episode of melt intrusion while the peridotites were still in the mantle (Brueckner and Medaris, 1998). Whether or not this intrusion event was the one that refertilised the dunites is difficult to ascertain. Preliminary Sm-Nd mineral dating from Almklovdalen suggests that intrusion of the pyroxenites occurred at ~1.82 Ga (Brueckner and Medaris, 1998). This implies that the peridotites were already stabilised by the Early Proterozoic; this is verified by the 1.76 Ga Sm-Nd mineral age established for an Almklovdalen garnet peridotite (Mearns, 1986), and rules out refertilisation by subduction-related melts during the Caledonian.

The exact nature of the refertilising agent is difficult to constrain but evidence from whole-rock compositions for the garnet peridotites suggests that the melt was rich in Fe, Ca, Al and Na but not Ti. The low Ti contents in the peridotites are supported by correspondingly low Ti in the pyroxenites. Na contents are particularly high in the peridotites and in some cases are higher than the estimates for primitive mantle, which suggests that the melt was alkali-rich. This is supported by the high $Na_2O$ content in the pyroxenite from Gurskøy. The melt is also likely to have been rich in incompatible trace elements such as the LREE, LILE (except Rb) and Th as whole-rock compositions for the peridotites are variably enriched in these elements.

## 6.10 SUMMARY

(1) Peridotites were collected from three main localities in the Western Gneiss Region. Rock types include garnet-bearing lherzolite, harzburgite and wehrlite, chlorite-amphibole "dunite", and spinel-bearing harzburgite. Textures are predominantly porphyroclastic though coarse microstructures are also recognised.

(2) The WGR peridotites have whole-rock compositions that are depleted relative to estimates for primitive mantle. The Almklovdalen garnet peridotites have the least depleted bulk compositions. They have the lowest whole-rock Mg# and Mg/Si of the three localities and range to higher whole-rock Ca and Al contents than the samples from Gurskøy and Otrøy. Dunites from Almklovdalen have extremely depleted compositions and appear to be residues after high degrees of partial melting.

(3) Whole-rock REE patterns for the garnet peridotites at Almklovdalen can be divided into two types; convex-upwards (sinuous) and convex downwards (U-shaped). The convex-upwards patterns are defined by high MREE abundances relative to HREE and LREE while the convex-downwards patterns are LREE-enriched relative to MREE. These patterns reflect REE patterns for the constituent minerals. The garnet lherzolites from Gurskøy have relatively flat REE with slight LREE depletion and low HREE abundances. The Otrøy garnet peridotites have spoon-shaped REE patterns that are defined by a convex-upward distribution of MREE and HREE from Eu to Lu, and slight enrichment of the LREE relative to the MREE. The dunites are characterised by convex-down REE patterns that have extremely low HREE abundances that are attributed to the absence of garnet.

(4) The presence of amphibole in garnet peridotites from Almklovdalen and Otrøy is evidence for modal metasomatism by a volatile-rich fluid/melt. Garnet and

clinopyroxene are variably enriched in incompatible trace elements and indicate that the metasomatising agent was rich in LREE, LILE (except Rb) and Th. The Gurskøy garnet peridotites are amphibole-free but show evidence for cryptic metasomatism in garnet and clinopyroxene. The dunites are relatively enriched in whole-rock LREE, LILE (including Rb) and Th. These elements are probably residing in amphibole or phlogopite as chlorite is not a significant carrier of LIL elements.

(5) The garnets in the WGR peridotites are Cr-pyropes and resemble garnets from fertile to moderately depleted lherzolite from worldwide localities. Rare earth patterns for the WGR garnets have high HREE and depleted LREE similar to garnets from high-T sheared peridotite xenoliths in kimberlites. The WGR garnets have very low Zr/Y indicating low-T equilibration.

(6) Calculated univariant curves for a number of different exchange reaction equilibria were plotted in P-T space for mineral cores and rims for each garnet peridotite. Core P-T estimates for the Gurskøy and Otrøy peridotites are typically higher than for rims and indicate that core assemblages equilibrated above the quartz-coesite stability curve and qualify as ultrahigh-pressure (UHP) assemblages. By comparison, rim P-T estimates for these rocks lie below the quartz-coesite stability boundary and indicate re-equilibration at lower pressures and temperatures. Both core and rim P-T estimates for the Almklovdalen peridotites lie below the quartz-coesite stability boundary. This suggests that either these peridotites do not have a high-P origin or that they were recrystallised at low-P. $T_{Ni}$ temperatures for the WGR peridotites are within error of temperature estimates for cores derived using univariant curves.

(7) Garnet peridotites from Gurskøy and Otrøy can be modelled as residues after 20-40% melt extraction at pressures between 5 and 7 GPa. The dunites can also be modelled as residues after high-P melting but require higher degrees (60%?) of melt extraction. Melt modelling for the Almklovdalen garnet peridotites is more complicated but overall the Almklovdalen rocks appear to be residues after ~20-35% partial melting at low pressure (2 GPa). The discrepancy in the pressure estimates for the garnet peridotites and dunites at Almklovdalen suggests that these rock types are not related by a simple melt-depletion process.

(8) The resemblance between the WGR garnet peridotites and high-T sheared peridotite xenoliths in kimberlites suggests that the WGR rocks represent refertilisation of a depleted precursor as modelled for high-T cratonic peridotites. The close structural relationship between the fertile garnet peridotites and the highly depleted dunites at

Almklovdalen presents the possibility that the garnet peridotite bodies represent zones of refertilised dunite.

(9) The exact nature of the refertilising agent is difficult to constrain but evidence from whole-rock compositions for the Almklovdalen garnet peridotites suggests that the melt was rich in Fe, Ca, Al and Na but not Ti. This is supported by pyroxenite compositions.

# CHAPTER 7
# MANTLE SULFIDES AND RE-OS DATING

## 7.1 INTRODUCTION

Sulfide phases are common in mantle rocks but typically only occur at modal abundances less than 0.1%. Sulfides are thought to be a key site for siderophile elements in the mantle (Alard *et al.*, 2000 and references therein) and are therefore crucial for further understanding of the Re-Os isotopic system in mantle rocks. The Re-Os system is a powerful tool that has become applicable to a variety of geochemical problems, particularly in the study of the upper mantle materials. The development of new instruments, such as the multi-collector LAM-ICPMS (see Section 2.2.2), allows *in situ* isotope analysis of sulfide minerals which has the advantage of removing much of the ambiguity inherent in whole rock studies due to the usual presence of at least two generations of sulfide within a given sample (Alard *et al.*, 2000). It also allows for a relatively rapid acquisition of data compared to conventional methods.

Two main types of sulfides have been recognised in mantle materials based on relationships between sulfide phases and silicate matrix. The first type is "enclosed" sulfide which typically occurs as inclusions within the major phases. The second type is "interstitial" which refers to sulfides situated between grains of the dominant phases. In selecting sulfides for analysis in this study both sulfide types were considered. Sulfides trapped within mineral phases are thought to be primary in origin and may therefore yield information about the melting history of the rock, while interstitial sulfides are not shielded from interaction with infiltrating fluids, and are therefore more susceptible to modification.

The petrographic study of polished thin sections and electron microprobe analysis (point analyses and chemical mapping) have been used to investigate the mineralogy, abundance and distribution of the base metals in mantle sulfides.

## 7.2 MANTLE SULFIDES

Sulfide minerals in peridotites are thought to originate from immiscible sulfide melts trapped in mantle residues during partial melting events (Frick, 1973; Dromgoole and Pasteris, 1987; Szabó and Bodnar, 1995). The "immiscible sulfide melt" hypothesis was based partly on the subspherical shape of sulfide aggregates which is generally

considered to indicate that a sulfide droplet remained liquid as the host solidified, following segregation of the sulfide liquid from the parental silicate melt and subsequent inclusion within either silicate minerals or in the matrix (Guo *et al.*, 1999). A study of sulfide assemblages in a suite of xenoliths from Kilbourne Hole (Dromgoole and Pasteris, 1987) concluded that no contamination mechanism can explain the occurrence and chemistry of the sulfides and that their most likely origin is partial retention of an immiscible sulfide liquid during mantle melting. Szabó and Bodnar (1995) reached a similar conclusion regarding sulfide minerals in unmetasomatised peridotite xenoliths from eastern Europe.

In the Cu-Fe-Ni-S system, the monosulfide phase FeS crystallises on the Fe-S tie-line at 1192°C. Upon cooling, Ni and Cu increase in the FeS phase to form the monosulfide solid solution (MSS) $(Fe,Ni)_{1-x}S$. Melting of MSS between 900-1100°C is incongruent, leaving MSS as the residual solid phase and producing a Ni-and Cu-rich sulfide liquid. Fe-Ni-Cu-S-O sulfide is molten at temperatures below the anhydrous peridotite solidus which implies that in active geodynamic settings, where advective geotherms predominate, sulfide melt could become mobilised before any partial melting of peridotite (e.g. Lorand *et al.*, 1993). Experimental work has shown that, at oxygen fugacities typical of the lithospheric mantle, small amounts of sulfide melt will form an interconnected network in olivine-rich rocks enabling the melt to migrate in the mantle via porous flow (Gaetani and Grove, 1999; Rose and Brenan, 2001). Sulfide melt also has low viscosity compared to silicate melt. These characteristics, as well as their affinity for volatile-rich melts, means that base metal sulfides are likely to be mobile in the mantle and could be introduced during metasomatism.

A relationship between sulfide enrichment and metasomatism by volatile-rich small-volume melts has been demonstrated in several studies. Fine-grained aggregates of late reactional phases (i.e. Cr-rich cpx + alkali feldspar + olivine + chromite) have been found in association with sulfide and glass in xenoliths from In Teria, Algeria (Kogarko *et al.*, 1995). Amundsen *et al.* (1987) and Ionov *et al.* (1993) described metasomatic pockets in carbonate-bearing lherzolite from Spitsbergen where sulfide occurs with the assemblage carbonate + glass + cpx2 + ol2. Kogarko *et al.* (1995) found similar reaction pockets in harzburgite xenoliths from the Canary Islands, where they identified Mg-carbonate + glass + altered sulfide ± ol2 ± cpx2 ± Cr-rich spinel.

## 7.3 SULFIDES IN TASMANIAN MANTLE XENOLITHS

### *7.3.1 Sulfide petrography and occurrence*

Detailed petrographic data and major element compositions were determined for sulfides in four xenolith suites; Coates Rd Quarry and Table Cape from the Rocky Cape Element, and Blessington and Wagners Hill from the Northeast Element. The majority of the fertile mantle xenoliths contain small amounts of sulfide, either as interstitial grains in the matrix or as inclusions in silicate minerals, while the depleted xenoliths, particularly those from the Rocky Cape Element, are essentially sulfide-free. The majority of Tasmanian sulfides occur as polymineralic aggregates and monomineralic grains are rare. Sulfide modes were determined using the image analysis program RockMAS (**Rock** **M**odal-**A**nalysis-**S**oftware). RockMAS allows calculation of the modal abundances of mineral phases in petrographic thin sections using element distribution maps obtained by EMP (Figs. 7-1 and 7-2). This technique determines modes faster and more accurately than the traditional point-counting method; the relative error calculated from counting statistics is less than 0.5% for a 256x256 image. Modes determined with this method should, however, be used with caution as sectioning of the sulfide is random and certain phases may be under- or over-estimated.

Eight phases have been identified in the Tasmanian sulfides: common phases are pentlandite (pn), chalcopyrite (cp), pyrrhotite (po), Ni-poor monosulfide solid solution (mss) and a low-T Ni-Fe-sulfide that appears transitional between pn and mss (pn-mss trans); less common ones include an intermediate solid solution (iss), cubanite (cb), and bornite (bo). Pentlandite occurs in 80% of the sulfides analysed, followed by chalcopyrite (and other Cu-rich phases) (67%), pyrrhotite (42%), pn-mss trans (38%) and mss (17%). Modal proportions of phases in individual sulfide grains from the Tasmanian peridotite xenoliths are summarised in Table 7-1.

The most abundant sulfide type in Tasmanian mantle xenoliths is interstitial sulfide. The interstitial sulfides are present either as small irregular blebs and stringers along grain contacts, or as subhedral grains at the 120°C triple junctions between major phases. Grain size is variable with most sulfides ranging from 10-100 μm in diameter and rarer grains up to 450 μm across. These grains most commonly consist of pn and po aggregates with blocky rims of cp. Cu-rich phases also occur as fine veins or minute exsolved rods and blebs throughout pn. The transitional pn-mss occurs as blebs in pn, often at the centre of the grain, while Ni-poor mss is found either as discrete grains with fine rims of cp or as blebs in po. Alteration is generally low (<10% iron hydroxide) except in sulfides from

Coates Road Quarry which are often highly altered (>40% iron hydroxide).

**Table 7-1.** Modal proportions of phases in individual sulfide grains from Tasmanian peridotite xenoliths. Interstitial sulfides denoted by "i" and enclosed sulfides by "e".

| Sample no. | Sulfide type | Host mineral | Pn | Po | Cp* | Ni-poor Mss | Pn-Mss Trans |
|---|---|---|---|---|---|---|---|
| CQ3(1) | i | | 50.0 | - | 50.0 | - | - |
| CQ3(2) | i | | 60.7 | - | 39.3 | - | - |
| CQ7 | i | | 87.0 | - | 13.0 | - | - |
| TC1(1) | i | | 75.7 | - | 24.3 | - | - |
| TC1(2) | i | | 28.0 | 72.0 | - | - | - |
| TC1(3) | i | | 76.4 | 16.3 | 7.3 | - | - |
| TC1(4) | i | | - | 48.5 | - | 51.5 | - |
| TC6 | e | cpx | 29.0 | - | 19.0 | 51.0 | - |
| TC10(1) | i | | 45.5 | - | - | 54.5 | - |
| TC10(2) | i | | 30.0 | 51.0 | 19.0 | - | - |
| BL1 | i | | 90.6 | - | 9.4 | - | - |
| BL8 | e | olivine | 77.4 | - | 22.6 | - | - |
| BL10 | e | olivine | 82.0 | - | 18.0 | - | - |
| BL12 | e | opx | 24.5 | - | 11.6 | 63.9 | - |
| BL13(2) | i | | 38.7 | - | 30.6 | 30.7 | 30.7 |
| BL13(3) | i | | 51.1 | 43.9 | 5.0 | - | - |
| BL14 (1) | e | olivine | 37.9 | 62.1 | - | - | - |
| BL14(2) | e | cpx | 60.7 | 32.9 | 6.4 | - | - |
| BL16(1) | i | | - | 78.9 | 14.4 | 7.7 | - |
| BL16(2) | i | | - | 4.0 | - | 96.0 | - |
| BL17(2) | e | olivine | - | - | - | 100 | - |
| BL17(3) | e | cpx | 56.8 | - | - | - | 43.2 |
| BL17(4) | e | olivine | - | 65.1 | 10.3 | 24.6 | - |
| BL21 | e | cpx | 30.1 | - | 13.1 | 56.8 | - |
| BL27 | i | | 84.0 | - | 16.0 | - | - |
| WH2B | e | cpx | 14.7 | - | 1.4 | - | 83.9 |
| WH6 | e | cpx | 14.6 | - | - | - | 85.4 |
| WH20 | e | cpx | 23.4 | - | - | - | 76.6 |

*this includes chalcopyrite and other Cu-rich phases (i.e. cubanite, bornite, iss etc).

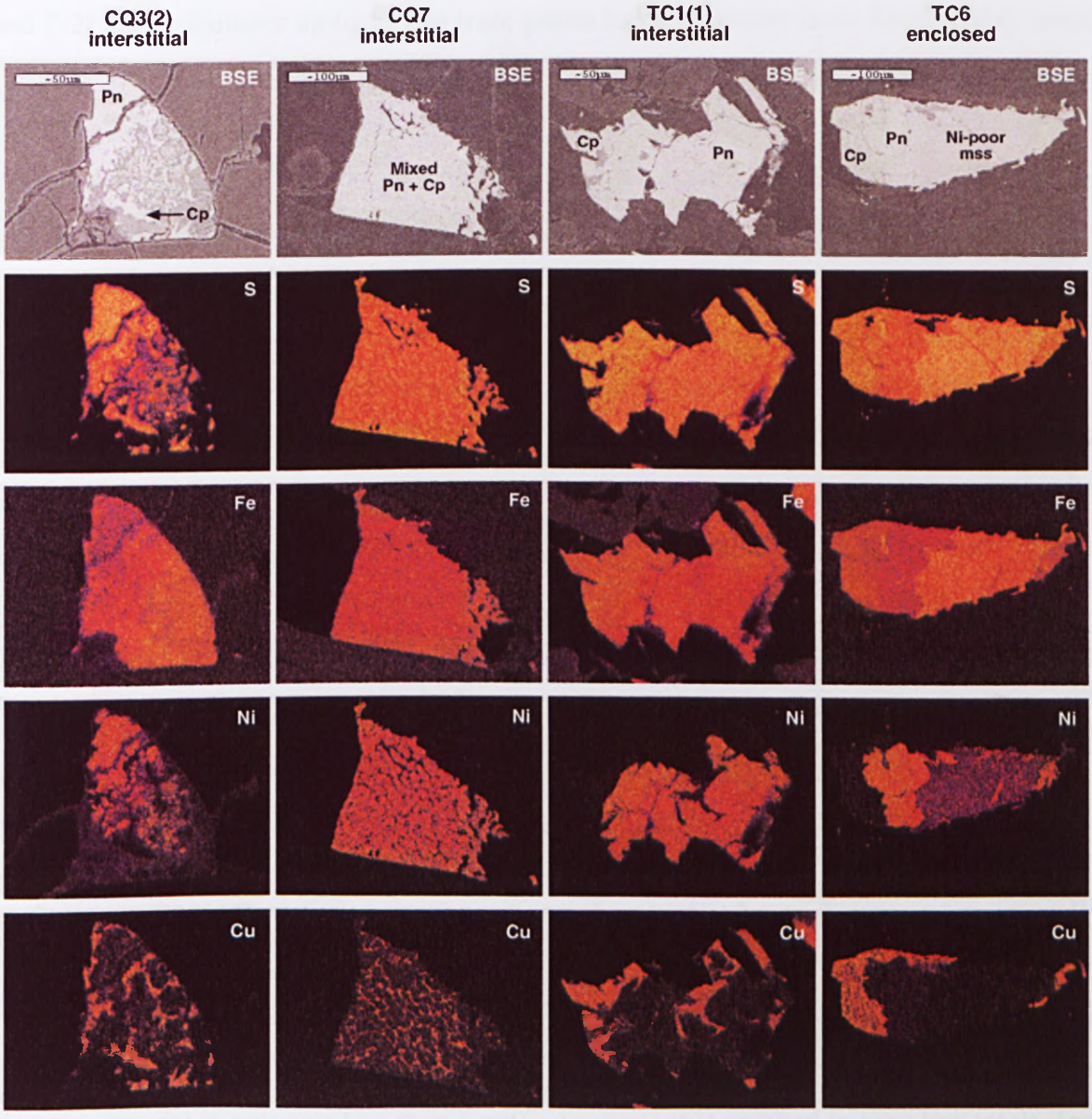


**Figure 7-1.** Chemical maps of sulfide grains in Coates Road Quarry and Table Cape spinel peridotite xenoliths. Maps were made using a LINK energy dispersive X-ray detector coupled to the electron microprobe at GEMOC (Macquarie University). Colour scale indicates the relative abundance of a given element. Intensity depends on the abundance of the element and also on the analysis time and the energy of the X-ray selected. False colours were produced using the SXM-NIH64 freeware package (http://www.nih.com). BSE: Back-Scattered Electron image.

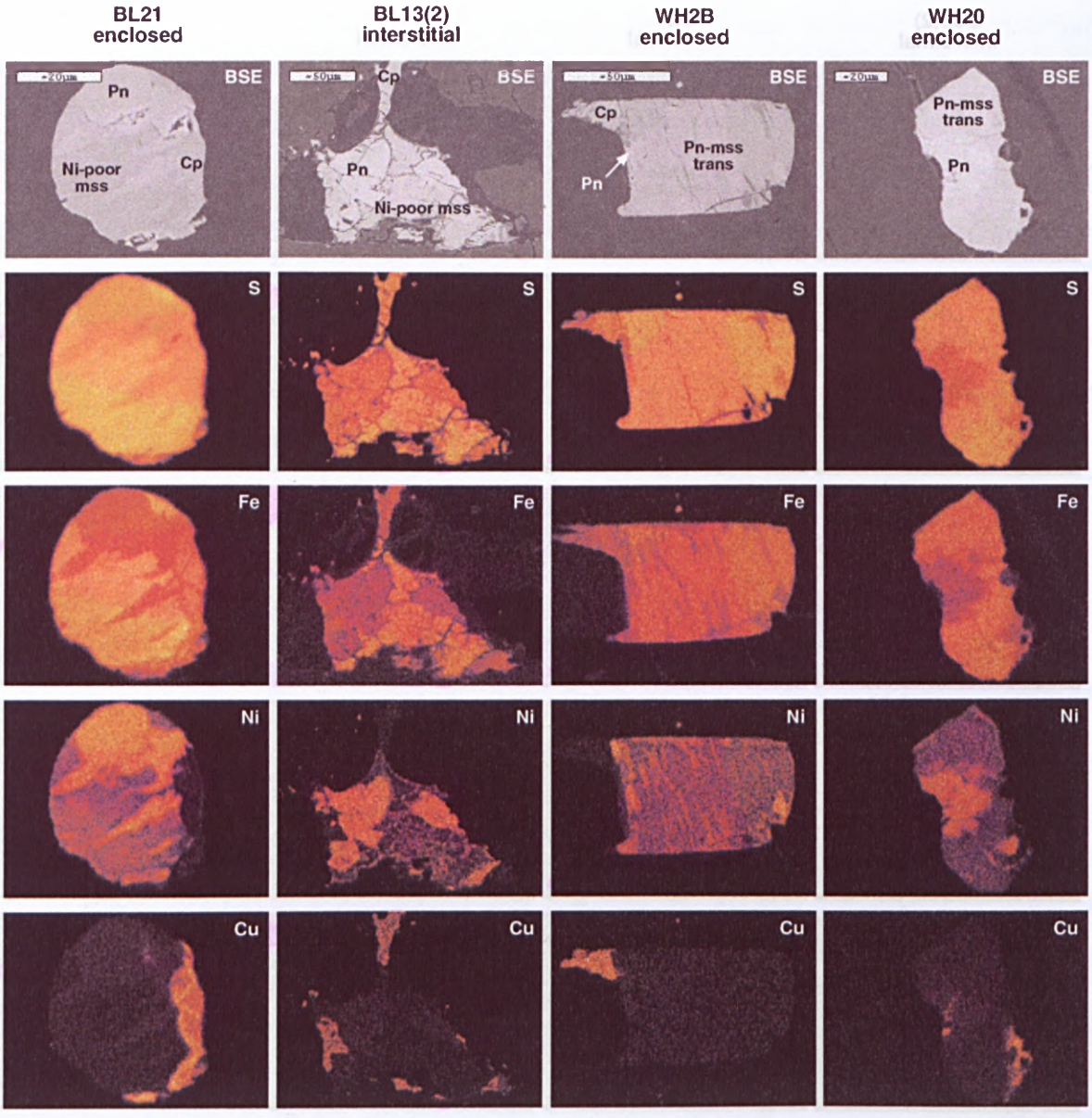


**Figure 7-2.** Chemical maps of sulfide grains in Blessington and Wagners Hill spinel peridotite xenoliths. Maps were made using a LINK energy dispersive X-ray detector coupled to the electron microprobe at GEMOC (Macquarie University). Colour scale indicates the relative abundance of a given element. Intensity depends on the abundance of the element and also on the analysis time and the energy of the X-ray selected. False colours were produced using the SXM-NIH64 freeware package (http://www.nih.com). BSE: Back-Scattered Electron image.

The second major type of sulfide in Tasmanian peridotites is sulfide enclosed in primary silicates but not spinel. Enclosed sulfides occur in all silicate phases but most commonly in clinopyroxene. They typically have round or oval cross-sections (Figs. 7-1 and 7-2) and a diameter up to 50 µm (rare grains have diameters from 50-150 µm). Small sulfide droplets are sometimes associated with large sulfide inclusions, in fracture planes radiating outwards from the large sulfide grain. According to Andersen *et al.* (1987), these trails are the result of expansion of the sulfide grain during melting which forces the sulfide melt out into the cracks. Frick (1973) and Guo *et al.* (1999) interpreted the trails as sulfide droplets trapped along silicate sub-boundaries that are controlled by the cleavage or slip planes of the silicate phases. The original fracture may be completely annealed so that the sulfide droplets have become discrete inclusions on a small scale. Most of the enclosed sulfides consist of >50% mss and/or transitional pn-mss interfingered with pn or po. Rims of fine or blocky cp are common on these grains and in rare cases cp is found as tiny blebs and veinlets in the pn. Aggregates of pn and po without mss, similar to those seen as interstitial sulfides, are uncommon. Bornite is present in an isolated occurrence with iss.

Obviously metasomatic sulfides such as those that occur in reaction patches with carbonates were not recognised in the Tasmanian xenoliths.

### *7.3.2 Chemical composition of sulfide phases*

The compositional data for the sulfide phases given in Appendix IX are single spot analyses or averages of 2-4 spot analyses for each phase. Phases are generally homogenous. Standard deviations for the averaged compositions of the individual phases are within 2.7 wt% for elements present in excess of 10 wt%, 1.2 wt% for elements present in the range of 5-10 wt%, 0.8 wt% for elements in the range of 1-5 wt%, and 0.25 wt% for elements present in amounts less than 1 wt%. Analyses that resulted in very low totals (less than 95%) were not included in the averaged values.

Pentlandite

Pentlandite is the most common phase in the Tasmanian sulfides (Fig. 7-3). Nickel contents in pentlandite range from 29-37wt%. Ni/(Ni+Fe) ratios vary from 0.45-0.57 which overlaps the range for the Qilin sulfides (Guo *et al.*, 1999) but is generally more Ni-poor. Most Cu contents are <0.7 wt% with one analysis of 1.2 wt%. Co contents are low and show a range of 0.3-0.8 wt%. Metal/sulfur (Me/S) ratios vary over a very narrow range (1.10-1.11) in the interstitial pentlandites while the enclosed pentlandites have Me/S ratios

that lie mainly between 1.05-1.10 with one sample displaying a metal deficit (Me/S=0.94). This low Me/S ratio, coupled with a low Ni content, reflects a mixture of pn + mss as noted by Guo *et al.* (1999). Oxygen is ubiquitous in pentlandite with contents varying from 0.28-1.08 wt%.

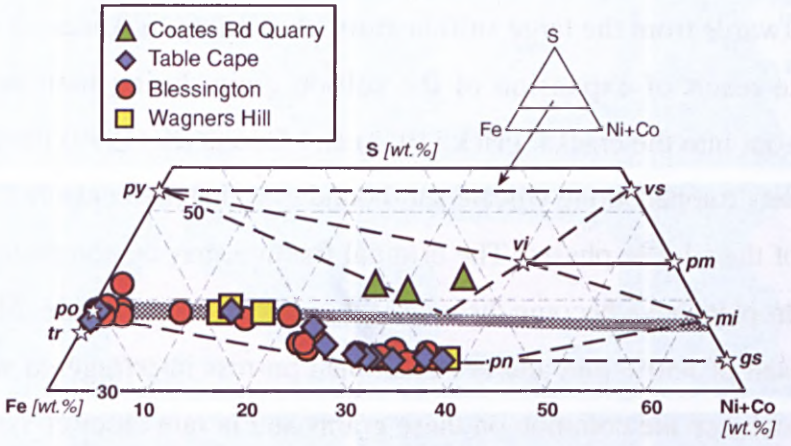


**Figure 7-3.** Sulfide phase composition in Tasmanian spinel peridotite xenoliths. Phase diagram at 300°C taken from Craig (1973). Stars represent the stoichiometric compositions for the minerals **tr**: troilite (FeS), **po**: pyrrhotite ($Fe_7S_8$-FeS), **py**: pyrite ($FeS_2$), **pn**: pentlandite ($(Fe,Ni)_9S_8$), **gs**: godlevskite ($Ni_7S_6$), **mi**: millerite (NiS), **pm**: polydymite ($Ni_3S_4$), **vi**: violarite ($Ni,FeS_4$), **vs**: vaesite ($NiS_2$).

Pyrrhotite

Pyrrhotite is a common phase in the interstitial sulfides and less common in the enclosed sulfides. Pyrrhotite was not identified in the Wagners Hill sulfides (Fig. 7-3). Here the name pyrrhotite is applied to mss containing less than 5 wt% Ni. This is regarded as the maximum nickel solubility in the pyrrhotite structure (Cabri, 1973). Pyrrhotite composition was found to be similar for both interstitial and enclosed sulfides. Ni contents range from 0.36-3.08 wt% while Cu and Co contents are 0.02-2.79 wt% and <0.1 wt% respectively. The higher Cu values may be due to Cu-rich micro-inclusions in the pyrrhotite. Metal/sulfur ratios are low with an overall range of 0.89-0.91, similar to the range (0.88-0.92) for pyrrhotite from Kilbourne Hole xenoliths (Dromgoole and Pasteris, 1987).

Monosulfide solid solution

At mantle temperatures the only possible solid phase in the Cu-Fe-Ni-S system is the monosulfide solid solution (MSS) $(Fe,Ni)_{1-x}S$ which is stable to at least 400°C. Between 400 and 300°C the continuity of the MSS phase field breaks down and further cooling to below 300°C causes the MSS field to withdraw away from the Ni-S join and separate into Ni-poor (mss1) and Ni-rich (mss2) monosulfide solid solutions and pentlandite; the solvus between mss1 and mss2 centres around 33-35 wt% Fe (Craig, 1973; Misra, 1973).

The low-T mss identified in the Tasmanian xenoliths corresponds to experimental mss1 of Craig (1973) and Misra (1973), and closely resembles the mss1 phase described in lherzolite xenoliths from southeast China (Guo *et al.*, 1999). The metal/sulfur ratios of the Tasmanian mss range from 0.87-0.92, corresponding to a metal deficit of approximately 0.1 in the monosulfide structure, making it "pyrrhotite-like". Cu and Co contents are low and have respective ranges of 0.00-0.07 wt% and 0.16-0.27 wt%.

There also exists another low-T Ni-Fe-sulfide phase in the Tasmanian xenoliths which lies above the pn-po tie-line, and midway between pn and mss1 compositions (pn-mss trans), on a Fe-Ni-S phase diagram at 300°C (Fig. 7-3.).

Chalcopyrite

Chalcopyrite is the most common Cu-rich sulfide in the Tasmanian xenolith suite (see Fig. 7-4). Analysis of chalcopyrite indicates that it is nearly stoichiometric (Cu/Fe ratios range from 0.95-1.04), with generally less than 0.4 at% Ni, although two samples contain >1.2 at%. These compositions are similar to those for chalcopyrite from the Qilin xenolith suite (Guo *et al.*, 1999). Oxygen contents show a wide range from 0.27-7.93 wt%. There is no difference in composition in chalcopyrite between interstitial and enclosed sulfides.

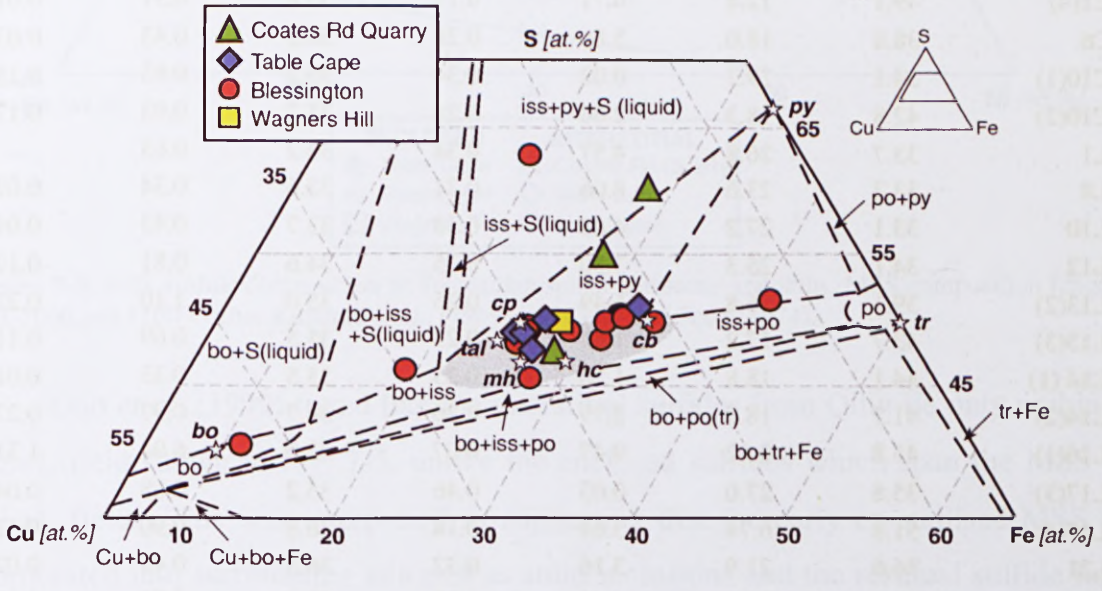


**Figure 7-4.** Sulfide phase composition in Tasmanian spinel peridotite xenoliths. Phase relations in the central portion of the Cu-Fe-S system at 600°C from Cabri (1973). Grey area is the field for intermediate solid solution (iss). Stars represent the stoichiometric compositions for the minerals **cp**: chalcopyrite ($CuFeS_2$), **py**: pyrite ($FeS_2$), **cb**: cubanite ($Fe_2CuS_3$), **tal**: talnakhite ($Cu_9Fe_8S_{16}$), **mh**: mooihoekite ($Cu_9Fe_9S_{16}$), **hc**: haycockite ($Cu_4Fe_5S_8$), **bo**: bornite ($Cu_5FeS_4$), **tr**: troilite (FeS).

Minor phases

Both the interstitial and enclosed sulfides contain Cu-rich phases other than chalcopyrite. These phases include cubanite, bornite and a variety of intermediate solid solutions (see Fig. 7-4). Cubanite was identified in several samples occurring as aggregates with pn±pn-mss trans. Bornite was found in one sulfide grain in sample BL17 from Blessington.

### *7.3.3 Sulfide bulk compositions*

At mantle temperatures MSS is the only possible solid phase in the Cu-Fe-Ni-S system. Pentlandite is a major constituent of the Tasmanian sulfide grains. As pentlandite is stable in the Fe-S-Ni system only at temperatures below 610°C, the polyphase assemblages are not of primary origin. Sulfide phase geochemistry and modes were used to reconstruct the original high-temperature bulk sulfide compositions (Table 7-2).

**Table 7-2.** Reconstructed bulk sulfide compositions. Values given in wt%.

| Sample no. | Fe | Ni | Cu | Co | S | O | Si |
|---|---|---|---|---|---|---|---|
| CQ3(1) | 26.8 | 17.7 | 12.1 | 0.91 | 34.7 | 6.32 | 0.96 |
| CQ3(2) | 23.7 | 19.8 | 15.8 | 0.24 | 37.2 | 2.18 | 0.43 |
| CQ7 | 28.2 | 22.7 | 3.67 | 0.51 | 38.1 | 5.05 | 1.01 |
| TC1(1) | 32.2 | 24.3 | 8.83 | 0.25 | 33.6 | 0.38 | 0.02 |
| TC1(2) | 52.6 | 8.73 | 0.18 | 0.22 | 36.9 | 0.34 | 0.01 |
| TC1(3) | 38.9 | 22.5 | 2.86 | 0.30 | 34.3 | 0.39 | 0.02 |
| TC1(4) | 49.1 | 12.8 | 0.71 | 0.17 | 35.8 | 0.51 | 0.01 |
| TC6 | 38.8 | 18.0 | 5.86 | 0.28 | 36.5 | 0.43 | 0.03 |
| TC10(1) | 34.1 | 29.2 | 0.02 | 0.34 | 35.2 | 0.83 | 0.15 |
| TC10(2) | 42.8 | 18.3 | 2.66 | 0.28 | 35.2 | 0.93 | 0.17 |
| BL1 | 33.7 | 26.8 | 4.57 | 0.34 | 33.2 | 0.65 | - |
| BL8 | 33.3 | 23.6 | 8.06 | 0.31 | 33.6 | 0.34 | 0.02 |
| BL10 | 33.1 | 27.2 | 4.82 | 0.33 | 33.7 | 0.43 | 0.04 |
| BL12 | 34.1 | 25.3 | 3.50 | 0.35 | 34.6 | 0.81 | 0.19 |
| BL13(2) | 39.1 | 16.8 | 6.49 | 0.25 | 35.0 | 1.10 | 0.22 |
| BL13(3) | 43.7 | 17.2 | 1.65 | 0.23 | 35.5 | 0.69 | 0.11 |
| BL14 (1) | 44.1 | 18.8 | 1.20 | 0.25 | 35.5 | 0.33 | 0.01 |
| BL14(2) | 41.2 | 18.7 | 2.79 | 0.36 | 34.7 | 0.97 | 0.27 |
| BL16(1) | 45.8 | 2.52 | 9.47 | 0.07 | 33.9 | 6.04 | 1.31 |
| BL17(3) | 35.8 | 27.0 | 0.03 | 0.46 | 35.2 | 0.68 | 0.04 |
| BL17(4) | 51.8 | 6.74 | 3.64 | 0.14 | 36.8 | 0.90 | 0.12 |
| BL21 | 36.6 | 21.9 | 3.16 | 0.32 | 36.5 | 0.48 | 0.02 |
| BL27 | 32.2 | 28.6 | 4.44 | 0.35 | 33.6 | 0.76 | 0.10 |
| WH6 | 44.5 | 14.5 | 0.52 | 0.44 | 38.5 | 1.01 | 0.15 |
| WH20 | 41.9 | 18.2 | 0.09 | 0.26 | 38.1 | 0.74 | 0.13 |

The reconstructed bulk sulfides are all Fe-rich monosulfide solid solution (MSS) (see Fig. 7-5). The abbreviation MSS describes inferred primary mantle monosulfide solid

solutions equivalent to the experimentally derived high-T MSS of Kullerud *et al.* (1969). Tasmanian MSS has Fe contents that vary from 23.7 to 53.6 wt% with an average of 38.3 wt%. This range is similar to those found in other studies of sulfides in spinel peridotites (Dromgoole and Pasteris, 1987; Szabó and Bodnar, 1995; Guo *et al.*, 1999). Most Ni contents lie in the range 12 to 30 wt% which is a reflection of high modal pentlandite and/or mss in the sulfides. In contrast, those sulfides with low Ni contents (2-9 wt%) have assemblages that are dominated by pyrrhotite. The majority of sulfides contain between 0.1 to 6.5 wt% Cu with the more Cu-rich sulfides containing up to 16 wt% Cu. This range in values reflects the highly variable abundance of chalcopyrite and other Cu-rich minerals in the assemblage. Co contents are typically very low (<0.5 wt%) as is O content (<1.0 wt%). The three sulfides from the Coates Road Quarry (CQ) locality have unusually high O contents (2.2-6.3 wt%).

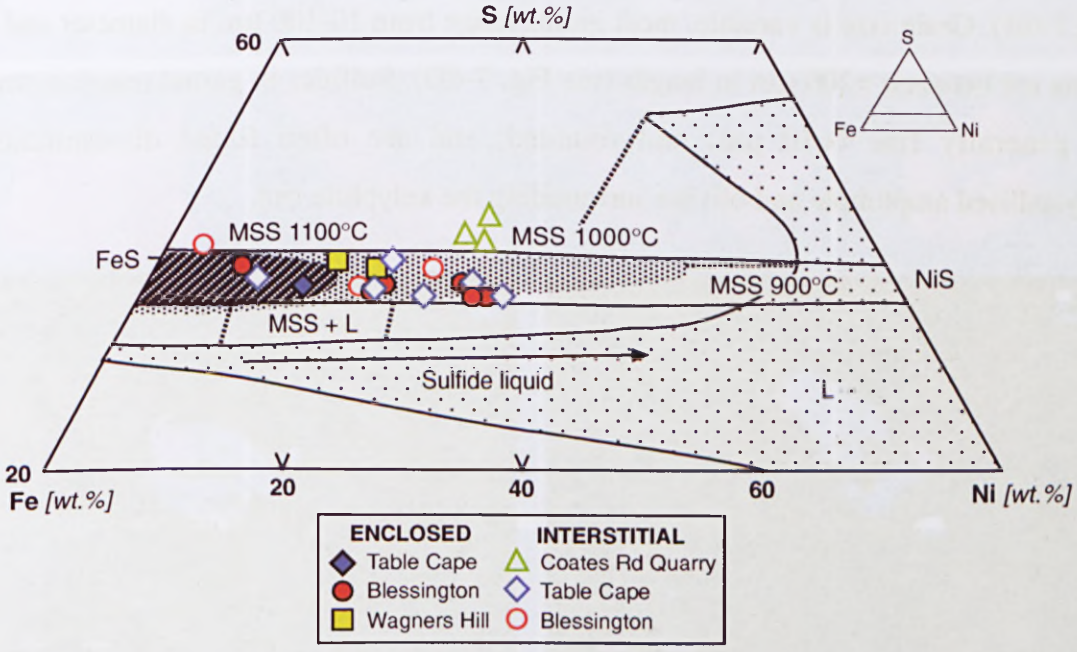


**Figure 7-5.** Bulk sulfide composition in Tasmanian spinel peridotite xenoliths. MSS composition range at 900, 1000 and 1100°C after Kullerud *et al.*, (1969) and Craig and Scott (1974).

Guo *et al.* (1999) found that the interstitial sulfides from Qilin lie only within the MSS+L field shown in Fig. 7-5, unlike the enclosed sulfides which span the MSS and MSS+L fields. This was interpreted as suggesting that the early crystallised MSS was incorporated into surrounding silicates as solid inclusions and the residual sulfide liquid was trapped between the larger silicate mineral grains. The bulk compositions for both the interstitial and enclosed sulfides from Tasmania fall predominantly in the MSS fields at 1000°C and 1100°C. As the calculated temperatures for the xenoliths are less than 1100°C this suggests that the sulfides in the Tasmanian xenoliths were solid at the time of xenolith

entrainment. The interstitial sulfides may have been residual sulfide liquid at higher temperatures but have since been recrystallised at lower T.

## 7.4 SULFIDES IN WESTERN GNEISS REGION GARNET PERIDOTITES

### *7.4.1 Sulfide petrography and occurrence*

Sulfides are abundant in many of the Western Gneiss Region garnet peridotites, excluding those from Otrøy, and occur either interstitially or, less commonly, as inclusions in silicate minerals. The sulfides are generally fresh though several of the larger grains show a moderate degree (<20%) of alteration to Fe-hydroxide. Interstitial sulfides display a wide variety of shapes ranging from irregular blebs through to angular subhedral forms and more rounded grains (Figs. 7-6 and 7-7). Sulfides are typically found in serpentinite veins between and cross-cutting silicate minerals (Fig. 7-6C) and also in kelyphite rims on garnet (Fig.7-6B). Grain size is variable, most grains range from 10-100 μm in diameter and rarer grains are between >200 μm in length (see Fig. 7-6D). Sulfides in garnet reaction coronas are generally fine (<10 μm) and rounded, and are often found disseminated in recrystallised amphibole and olivine surrounding the kelyphite rim.

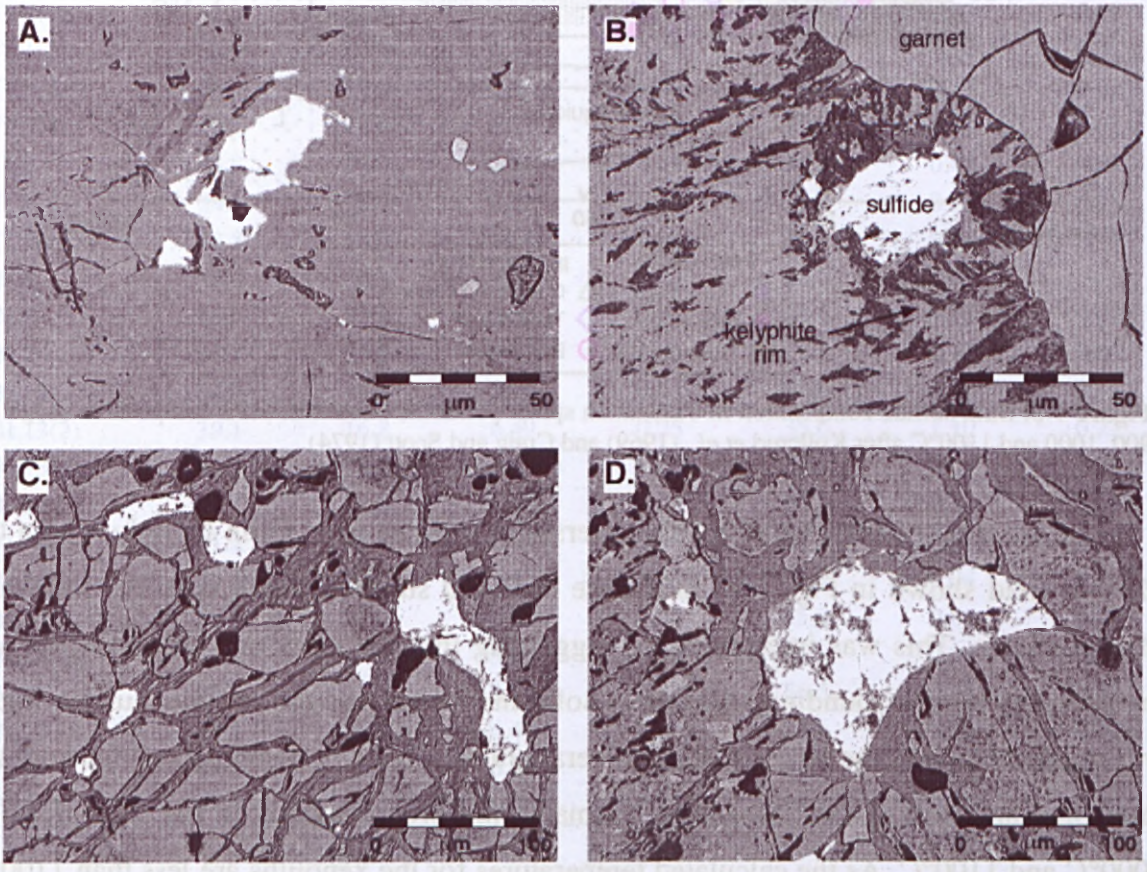


**Figure 7-6.** Sulfide in Western Gneiss Region garnet peridotites. Black and white photomicrographs taken in reflected light. (A) enclosed sulfide in olivine. (B) sulfide in kelyphite rim on garnet. (C) and (D) interstitial sulfides.

Enclosed sulfides occur predominantly in olivine (Fig. 7-6A) though rare grains were found in garnet and orthopyroxene. Grains are typically small (<50 μm) and rounded and often appear as fine inclusion trails and patches in the host mineral. Other sulfides are larger (>100 μm) and more angular or irregular in shape (Fig. 7-7). These grains are generally found in partially annealed fractures and cracks in the host mineral and probably do not represent primary sulfide trapped during partial melting.

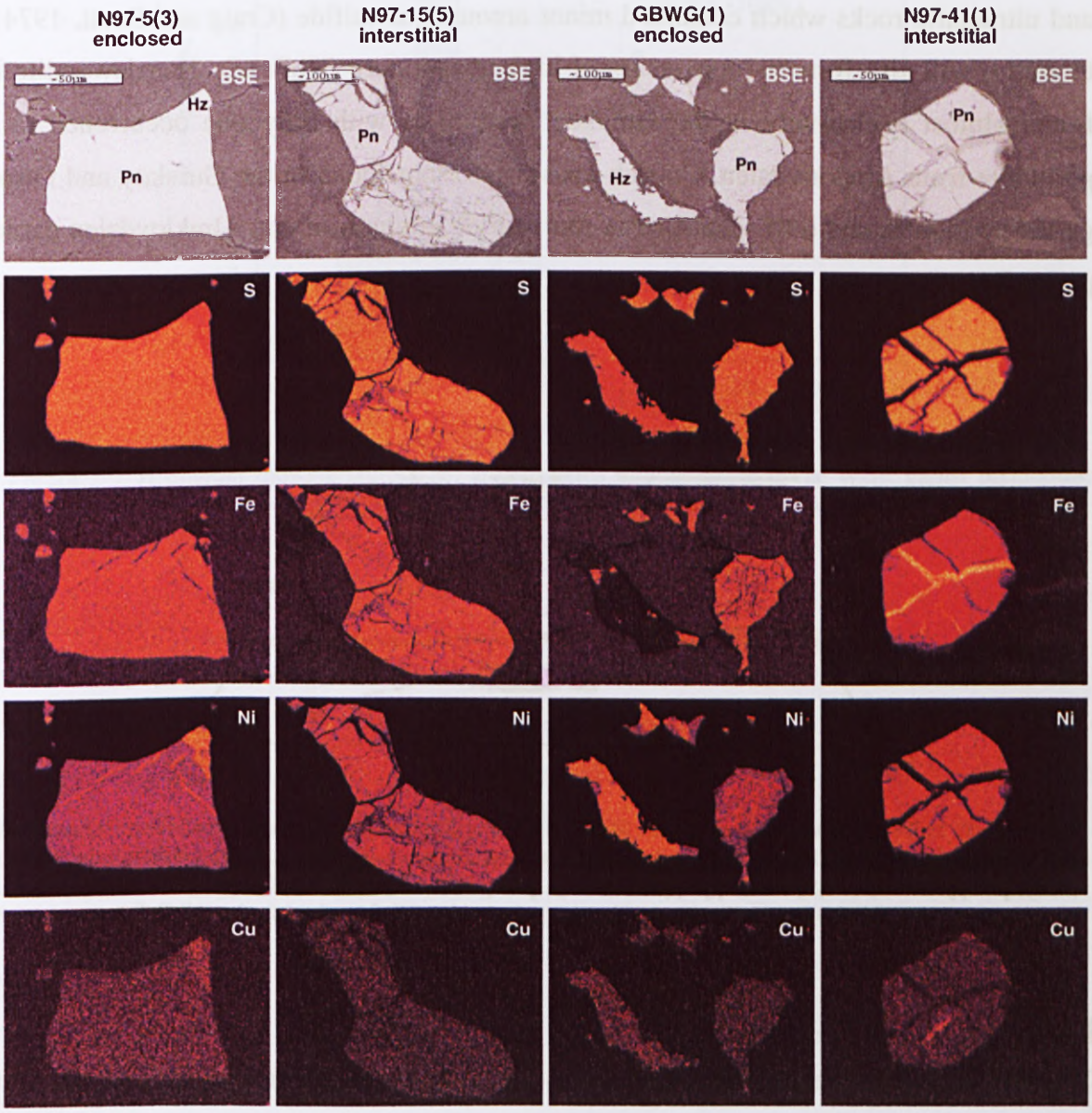


**Figure 7-7.** Chemical maps of sulfide in Western Gneiss Region garnet peridotites. Maps were made using a LINK energy dispersive X-ray detector coupled to the electron microprobe at GEMOC (Macquarie University). Colour scale indicates the relative abundance of a given element. Intensity depends on the abundance of the element and also on the analysis time and the energy of the X-ray selected. False colours were produced using the SXM-NIH64 freeware package (http://www.nih.com). BSE: Back-Scattered Electron image.

### *7.4.2 Chemical composition of sulfide minerals*

Sulfides in the WGR garnet peridotites are dominated by pentlandite (pn) and heazlewoodite (hz) and are nearly devoid of Cu-bearing and pure Fe-S phases (Appendix X; Figs. 7-7 and 7-8). The majority of the Norwegian sulfides are monomineralic pentlandites. Heazlewoodite occurs as discrete monomineralic grains or as alteration of pentlandite, appearing as partial blocky rims or a jagged "network" radiating out from the centre of the pentlandite grain. Heazlewoodite is only stable at temperatures below 556°C and is usually a product of pentlandite reduction resulting from serpentinisation of mafic and ultramafic rocks which contained minor amounts of sulfide (Craig and Scott, 1974), though it will also form by conversion of high-temperature $(Ni,Fe)_3S_2$. Heazlewoodite is found almost exclusively in the Gurskøy peridotites with only one occurrence in a peridotite from Almklovdalen. Cu-rich phases were not found in the Gurskøy and Otrøy garnet peridotites and only identified in four sulfide grains from the Almklovdalen garnet peridotites.

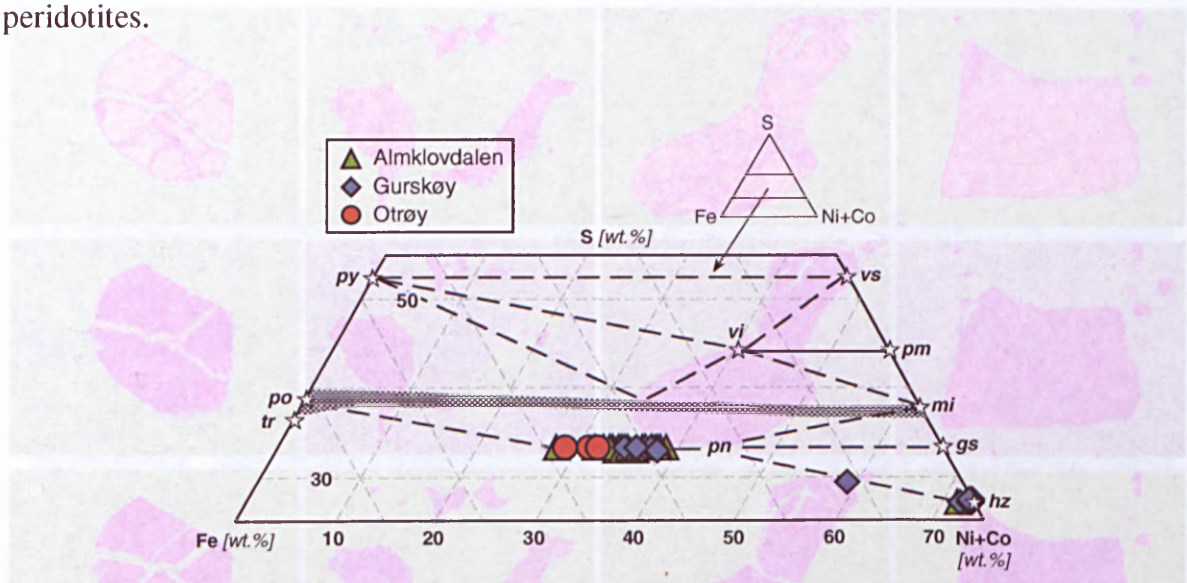


**Figure 7-8.** Sulfide phase composition in Western Gneiss Region garnet peridotites. Phase diagram at 300°C taken from Craig (1973). Stars represent the stoichiometric compositions for the minerals **tr**: troilite (FeS), **po**: pyrrhotite ($Fe_7S_8$-FeS), **py**: pyrite ($FeS_2$), **pn**: pentlandite ($(Fe,Ni)_9S_8$), **gs**: godlevskite ($Ni_7S_6$), **hz**: heazlewoodite ($Ni_3S_2$), **mi**: millerite (NiS), **pm**: polydymite ($Ni_3S_4$), **vi**: violarite ($Ni,FeS_4$), **vs**: vaesite ($NiS_2$).

Pentlandite

There is no difference in pentlandite composition between the interstitial and enclosed sulfides. Nickel content shows a very large variation from 28-38 wt% though most grains contain between 33 and 36 wt% Ni. Ni/(Ni+Fe) ratios vary from 0.42-0.56 which overlaps the range reported for the Qilin xenoliths (Guo *et al.*, 1999) (Fig. 7-10) but tend towards more Ni-poor compositions. Cu contents range from zero to 0.69 wt% though most samples contain less than 0.1 wt%. Co contents are also low with most grains containing

between 0.4 and 1.2 wt%; this is within the range for pentlandite that occurs in xenoliths (Guo *et al.*, 1999) and massif peridotites (Garuti *et al.*, 1984), and as inclusions in diamond (Deines and Harris, 1995). Oxygen abundance is generally less than 0.5 wt% though a few samples are slightly more oxygen-rich (~1 wt%).

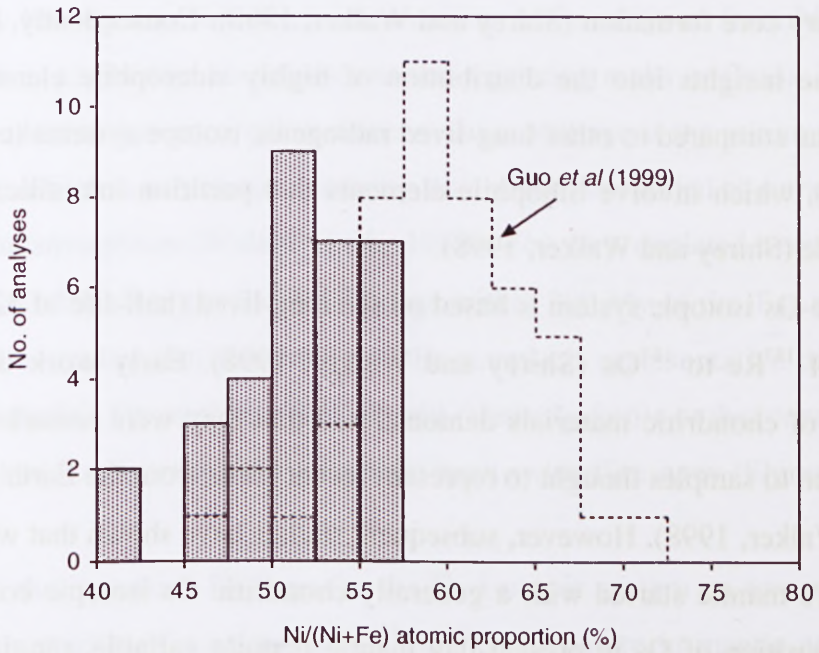


**Figure 7-9.** Histogram showing Ni/(Ni+Fe) atomic ratios of pentlandite in the WGR garnet peridotites. The dotted line represents pentlandite data from the peridotites of Qilin in southeast China (Guo *et al.*, 1999).

Heazlewoodite

Heazlewoodite composition shows little variation from grain to grain. Nickel content ranges from 70.4-72.7 wt% while sulfur content varies from 25.8-26.6 wt%. Fe, Cu and Co are generally only present at abundances less than 1 wt% apart from the heazlewoodite from Almklovdalen which contains ~2 wt% Fe. O content is low and typically less than 0.5 wt%.

Minor phases

The Cu-rich sulfides include chalcopyrite, chalcocite and a phase rich in oxygen (11-32at%) which is probably an alteration product (copper hydroxide) of a Cu-rich sulfide. A Ni-rich sulfide from Gurskøy has a composition that is intermediate between pentlandite and heazelwoodite and falls on the tie-line between the two end-members (see Fig. 7-9).

## 7.5 THE RE-OS ISOTOPIC SYSTEM

### *7.5.1 Introduction*

The elements Re and Os are termed "highly siderophile" meaning that they strongly prefer metal (or sulfide) phases over silicate minerals. The bulk of these elements were likely stripped from the silicate portions of the Earth, Mars and other differentiated bodies during planetary core formation (Shirey and Walker, 1998). Consequently, Re and Os can provide unique insights into the distribution of highly siderophile elements (HSE) in mantle domains compared to other long-lived radiogenic isotope systems (e.g. Rb-Sr, Sm-Nd, U-Th-Pb), which involve lithophile elements that partition into silicate rather than metal or sulfide (Shirey and Walker, 1998).

The Re-Os isotopic system is based on the long-lived (half-life of 42 billion years) β-transition of $^{187}Re$ to $^{187}Os$ (Shirey and Walker, 1998). Early work on Os isotopic compositions of chondritic materials demonstrated that they were remarkably similar in $^{187}Os/^{188}Os$ ratio to samples thought to represent recent melts from the Earth's upper mantle (Shirey and Walker, 1998). However, subsequent studies have shown that while it is likely that the Earth's mantle started with a generally chondritic Os isotopic composition, the isotopic composition of Os in present-day mantle is quite variable, ranging from $^{187}Os$-depleted in ancient subcontinental lithospheric mantle to enriched in some plume-related rocks (Shirey and Walker, 1998). This heterogeneity in Os isotopic compositions is because Os, unlike the elements comprising other commonly applied radiometric systems, is compatible in the mantle during melting (Pearson *et al.*, 1995a). Conversely, Re is mildly incompatible and partitions into the melt during melt extraction, so melt depletion reduces the Re/Os of mantle residues. As a result, mantle melting produces marked fractionations of Re from Os that rapidly evolve into distinct time-integrated isotopic signatures for both melts and reservoirs (Pearson, 1999).

The Re-Os system has distinct advantages in geochemical and geochronological studies of mantle materials compared with other radiogenic isotopic systems. Firstly, the high relative abundances of Os (0.8-9 ppb) in continental peridotite xenoliths, as compared with host magmas such as alkali basalts and kimberlites, make the Os abundance and Os isotopic composition of xenoliths difficult to change by infiltration of the host or post-crystallisation metasomatic fluids/melts (Shirey and Walker, 1998). This is illustrated by Pearson (1999) who showed that a mass fraction of the host kimberlite in excess of 10% is required to obscure direct isotopic evidence of an Archean origin for an entrained peridotite xenolith. Re-Os data should, therefore, provide a clearer view of the timing and

nature of melt extraction from the continental lithosphere and its relation to continent formation and stabilisation (Walker *et al.*, 1989).

Secondly, minimum ages of separation of peridotites from the convecting mantle can still be obtained, even if parent-daughter ratios have been disturbed. A complicating factor in determining Re-Os model ages for mantle melting is that mantle rocks, because of their relatively low Re concentration, are sensitive to Re addition from high-Re content materials, such as kimberlite, recycled crust and migrating melts or fluids. In cases where secondary Re addition has occurred, a more useful model age is the minimum time of Re-depletion ($T_{RD}$) which is calculated assuming that all Re was added at some point such as eruption, or metamorphism (Walker *et al.*, 1989). For very depleted xenoliths, this is a good assumption that often produces a $T_{RD}$ age within 200 My of the $T_{MA}$ age (the model age calculated assuming that the Re/Os of the sample is representative of its long-term history in the mantle). For xenoliths that are still relatively fertile or that contain introduced Re, the $T_{RD}$ model ages represent minimum melt-extraction ages (Shirey and Walker, 1998).

One of the important findings for the Os isotopic system on terrestrial rocks has been the demonstration of a unique low $^{187}Os/^{188}Os$ signature in mantle peridotite suites from beneath continents (Shirey and Walker, 1998). Some portions of ancient subcontinental lithospheric mantle are severely depleted in Re and have correspondingly subchondritic $^{187}Os/^{188}Os$, indicating long-term isolation from the convecting mantle. Elevated initial Os isotopic compositions have, to date, only been detected in deep-seated ultramafic magmas younger than the Early Proterozoic (Shirey and Walker, 1998). Speculative mechanisms to explain the post-Archean appearance of deep mantle sources with enriched Os signatures include recycling of Archean crust in subduction zones and plumes originating from the lower mantle (Shirey and Walker, 1998). Subduction of oceanic crust and transport of osmium into the mantle wedge in chlorine-rich, slab-derived fluids has been suggested as a possible explanation for the radiogenic Os-isotope ratios found in mantle xenoliths from the Cascade arc in the United States (Brandon et al., 1996).

### *7.5.2 Terminology*

<u>$\gamma$Os</u>

The parameter $\gamma$Os was formulated by Walker et al. (1989) to describe the isotopic composition of Os relative to a reference mantle value (the convention is to use chondrite) at a specific time, and is defined by the relationship:

$$\gamma Os = \left[ \frac{\left[ \frac{^{187}Os}{^{188}Os} \right]_{sample}}{\left[ \frac{^{187}Os}{^{188}Os} \right]_{chond}} - 1 \right] \times 100$$

Samples with positive γOs are described as enriched or radiogenic and imply long-term $^{187}Os$ in-growth in a high $^{187}Re/^{188}Os$ environment. Samples with negative γOs are referred to as depleted or unradiogenic and reflect retarded $^{187}Os$ in-growth relative to chondrite, implying a Re-depleted environment.

$T_{MA}$ (mantle extraction model age)

Calculation of a $T_{MA}$ age for a sample is carried out using the equation:

$$T_{MA} = \frac{1}{\lambda} \ln \left[ \frac{\left[ \frac{^{187}Os}{^{188}Os} \right]_{chond} - \left[ \frac{^{187}Os}{^{188}Os} \right]_{sample}}{\left[ \frac{^{187}Re}{^{188}Os} \right]_{chond} - \left[ \frac{^{187}Re}{^{188}Os} \right]_{sample}} + 1 \right]$$

Where $\lambda = ^{187}Re$ decay constant (1.64 x 10-11yr$^{-1}$, (Lindner *et al.*, 1989)), $^{187}Os/^{188}Os$ and $^{187}Re/^{188}Os$ ratios of the asthenospheric mantle are 0.1271 and 0.40076 respectively, corresponding to the mean of carbonaceous chondrites (values from Walker and Morgan (1989)), and $^{187}Os/^{188}Os$ and $^{187}Re/^{188}Os$ are measured in the sample.

$T_{RD}$ (rhenium depletion model age)

Calculation of a $T_{RD}$ age for a sample is carried out using the equation:

$$T_{RD} = \frac{1}{\lambda} \ln \left[ \frac{\left[ \frac{^{187}Os}{^{188}Os} \right]_{chond} - \left[ \frac{^{187}Os}{^{188}Os} \right]_{sample(t)}}{\left[ \frac{^{187}Re}{^{188}Os} \right]_{chond}} + 1 \right]$$

Re-depletion ages are usually determined via a two-step process whereby the $^{187}Os/^{188}Os$ of the sample is first back-calculated to the time t when Re is thought to have been added, and then this value is used to calculate the $T_{RD}$ age by projection to the CHUR evolution curve. The initial Re/Os of the sample is assumed to be zero, the other values are the same as for $T_{MA}$. Corrected initial $^{187}Os/^{188}Os$ will be lower than the measured $^{187}Os/^{188}Os$ ratio, increasing the resulting $T_{RD}$ age.

## 7.6 RE-OS RESULTS

### *7.6.1 Tasmania*

Whole-rock Re-Os isotopic data were collected for five spinel lherzolite samples from Tasmania; three from Blessington and two from Wagners Hill. Re-Os data were also obtained for thirteen large sulfide grains from six spinel peridotites; collectively from Blessington, Wagners Hill and South Riana. Both enclosed and interstitial sulfides were analysed. Total Os and Pt concentrations were estimated by comparing the signal intensity on the sample to that obtained on the PGE-A standard. The accuracy of these data is limited by variations in ablation conditions, the lack of an internal standard, the small compositional heterogeneity of the isotopic standard, and the probability that maximum signals are not achieved during short runs on some small grains (Griffin *et al.*, 2001a). The analysed sulfides are small (<50μm) with mainly low Os concentrations (<10 ppm; Table 7-3) so the internal precision for $^{187}Os/^{188}Os$ is likely to be poor (1-2% 2SE) (Griffin *et al.*, 2001a). Pt concentrations in the analysed sulfides are very low and range from 0.03 to 8.8 ppm.

Comparison of whole-rock and sulfide data

Re and Os data for the Tasmanian peridotites are reported in Table 7-3. Os contents in the xenoliths are generally higher (3.91-5.25 ppb) than the estimated primitive mantle value (~3.4 ppb: McDonough and Sun, 1995) apart from sample BL35 which contains only 3.1 ppb Os. Re contents vary from 0.06-0.23 ppb. The highest value is close to that estimated for the primitive mantle (0.3 ppb: McDonough and Sun, 1995) while the lower values are consistent with Re-removal during partial melting. $^{187}Re/^{188}Os$ ratios range from 0.0544 to 0.2830 while $^{187}Os/^{188}Os$ varies from 0.1251 to 0.1490.

A comparison of whole-rock Os isotopic composition with indices of depletion (i.e. whole-rock Mg# and $Al_2O_3$) is illustrated in Fig. 7-10. The Tasmanian Os data show a positive correlation with whole-rock Mg# which is contrary to the expected trend and suggests that the Re-Os system has been disturbed since the time of partial melting. The high $^{187}Os/^{188}Os$ ratios for the most refractory xenoliths require either addition of radiogenic Os or ancient Re-addition which has allowed long-term in-growth of $^{187}Os$. However, given that the xenoliths have been shown to be representative of young, fertile lithosphere (see Chapter 5) the latter interpretation seems unlikely. $Al_2O_3$ content shows little variation between samples and is not correlated with $^{187}Os/^{188}Os$.

**Table 7-3.** Whole-rock and sulfide Re-Os isotopic data and model ages for Tasmanian spinel peridotites.

| Whole rock sample no. | Re (ppb) | Os (ppb) | $^{187}Re/^{188}Os$ | ±2SE | $^{187}Os/^{188}Os$ | ±2SE | γOs | $T_{RD}$ (Ga) | $T_{MA}$** (Ga) |
|---|---|---|---|---|---|---|---|---|---|
| BL31 | 0.241 | 4.77 | 0.2454 | 0.0228 | 0.14899 | 0.00062 | 17.3 | f | f |
| BL33 | 0.228 | 4.36 | 0.2529 | 0.0259 | 0.12507 | 0.00062 | -1.5 | 0.30±0.09 | 0.82±0.29 |
| BL35 | 0.169 | 3.09 | 0.2830 | 0.183 | 0.12957 | 0.00048 | 2.0 | f | f |
| WH21 | 0.090 | 3.91 | 0.1123 | 0.0199 | 0.14152 | 0.00043 | 11.4 | f | f |
| WH22 | 0.058 | 5.25 | 0.0544 | 0.0122 | 0.14418 | 0.00033 | 13.5 | f | f |

| Sulfide no. | Sulfide type | $^{187}Re/^{188}Os$ | ±2SE | $^{187}Os/^{188}Os$ | ±2SE | Os (ppm) | Pt (ppm) | γOs | $T_{RD}$* (Ga) | $T_{MA}$** (Ga) |
|---|---|---|---|---|---|---|---|---|---|---|
| BL8 | enclosed | 0.2026 | 0.0028 | 0.1240 | 0.0014 | 16 | 0.03 | -2.4 | 0.48±0.21 | 0.93±0.21 |
| BL10 | enclosed | 0.4932 | 0.0090 | 0.1096 | 0.0118 | - | - | -13.7 | 2.62±1.73 | 2.57±1.73 |
| BL13/1 | interstitial | 0.9405 | 0.0116 | 0.1441 | 0.0086 | 1.9 | 1.1 | 13.5 | f | 1.86±0.47 |
| BL13/2 | interstitial | 0.4631 | 0.0154 | 0.1333 | 0.0046 | 9.0 | 8.8 | 4.9 | f | e |
| BL13/3 | interstitial | 0.2643 | 0.0056 | 0.1281 | 0.0022 | 22 | 4.3 | 0.9 | f | f |
| BL13/4 | interstitial | 0.4051 | 0.0380 | 0.1366 | 0.0102 | 2.2 | 0.17 | 7.6 | f | e |
| BL16/1 | interstitial | 0.4075 | 0.0900 | 0.1347 | 0.0076 | 2.1 | 7.2 | 6.1 | f | e |
| BL16/2 | interstitial | 0.3260 | 0.0058 | 0.1288 | 0.0022 | 10 | 0.8 | 1.4 | f | f |
| SR8a/1 | interstitial | 0.0901 | 0.0120 | 0.1524 | 0.0048 | 7.1 | 0.39 | 20.0 | f | f |
| SR8a/3 | interstitial | 0.5199 | 0.0620 | 0.2115 | 0.0240 | 1.2 | 0.12 | 66.6 | f | e |
| SR8a/4 | interstitial | 0.6044 | 0.1100 | 0.2082 | 0.0200 | 3.6 | 0.21 | 63.9 | f | e |
| WH2b/1 | enclosed | 0.3091 | 0.0112 | 0.1350 | 0.0034 | 5.0 | 1.3 | 6.3 | f | f |
| WH2b/2 | enclosed | 0.9334 | 0.0720 | 0.1395 | 0.0110 | 3.3 | 2.4 | 9.8 | f | 1.38±0.62 |

* calculated at 40 Ma

** propagated 2SE analytical uncertainties on $^{187}Re/^{188}Os$ and $^{187}Os/^{188}Os$

'f' indicates future model age

'e' indicates model age older than the Earth

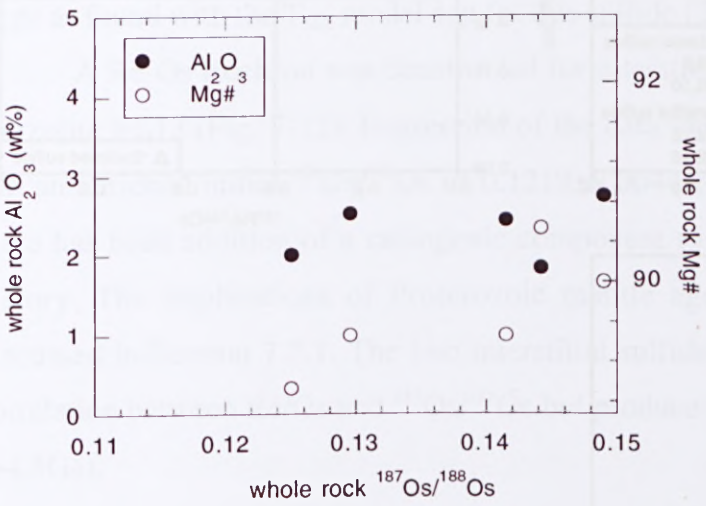


**Figure 7-10.** Whole-rock $^{187}Os/^{188}Os$ against whole-rock $Al_2O_3$ and Mg# for Tasmanian spinel peridotites.

Plots of $^{187}Re/^{188}Os$ vs $^{187}Os/^{188}Os$ for enclosed and interstitial sulfide from three localities are shown in Fig. 7-11. Two enclosed and six interstitial sulfides were analysed from Blessington xenoliths. The two enclosed sulfides (BL8 and BL10) have unradiogenic $^{187}Os/^{188}Os$ ratios, consistent with their residence in a reservoir with low Re/Os i.e. the lithospheric mantle. The high Re/Os ratio for sulfide BL10 suggests that there has been Re-addition, though this is probably recent, perhaps during xenolith entrainment, as there appears to have been little time for significant in-growth of radiogenic Os. The four interstitial sulfides from sample BL13 have $^{187}Os/^{188}Os$ ratios that range from 0.1281 to 0.1441 and Re/Os between 0.2643 and 0.9405. Re/Os is positively correlated with $^{187}Os/^{188}Os$ and it could be argued that these sulfides define an age. This is discussed below.

The interstitial sulfides from BL16 have high Re/Os ratios which suggest that they have experienced Re–addition (Fig. 7-11). As the host xenolith is fertile and most likely only Phanerozoic in age, the radiogenic Os isotopic compositions for the sulfides suggest that there has been $^{187}Os$-addition as well as there has not been sufficient time for substantial in-growth of $^{187}Os$. Addition of both Re and Os can account for the isotopic ratios measured in the enclosed sulfides from Wagners Hill and the interstitial sulfides from South Riana as well, as they all have high Re/Os ratios coupled with radiogenic Os, particularly the interstitial sulfides from sample SR8a which have $^{187}Os/^{188}Os$ ratios up to 0.21.

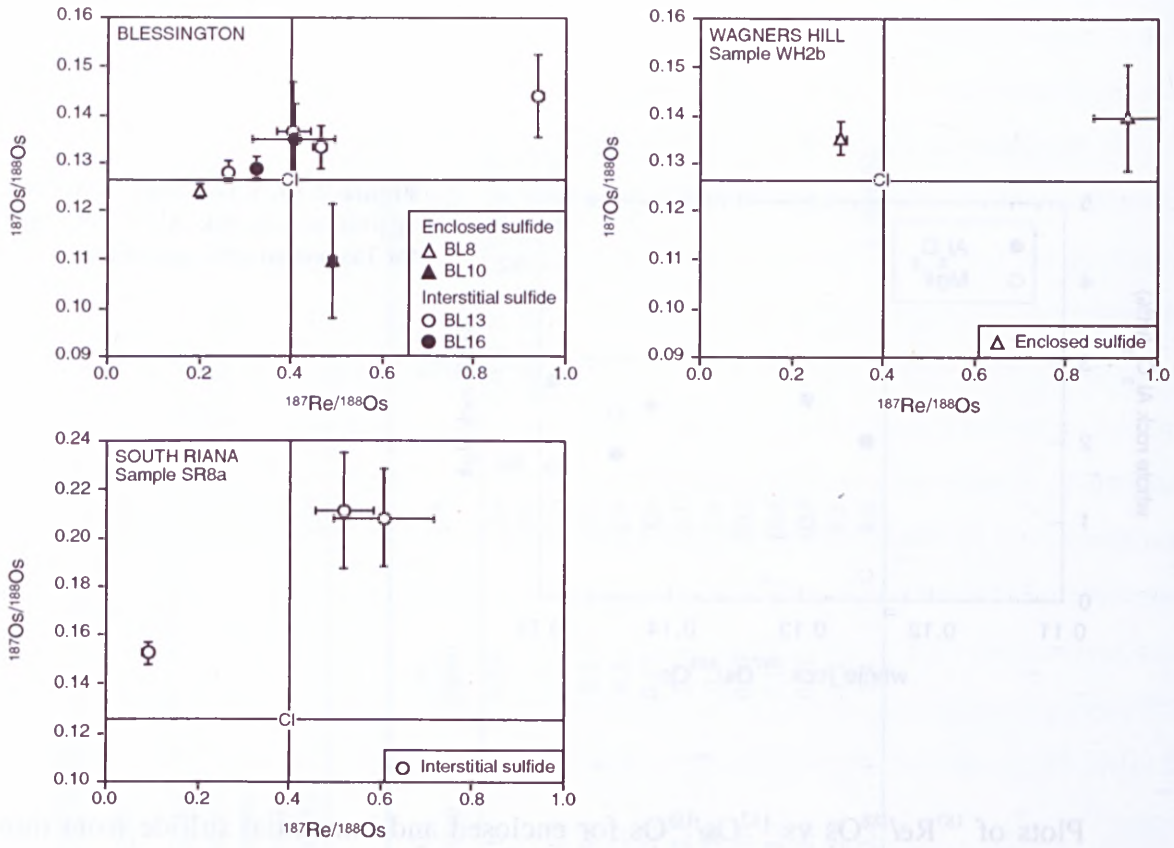


**Figure 7-11.** $^{187}Re/^{188}Os$ vs $^{187}Os/^{188}Os$ plot for whole rock and sulfides from Tasmanian spinel lherzolites. Analytical uncertainties are shown by the error bars. CI values are from Shirey and Walker (1997).

## Model ages and isochrons

Three sulfides from Blessington and one from Wagners give geologically reasonable $T_{MA}$ model ages ranging from 0.93 to 2.57 Ga (Table 7-3). These ages are surprising as both localities are in the Northeast Tasmania Element which has no crustal ages older than the Early Ordovician (Seymour and Calver, 1995). Even taking into account the uncertainty on the youngest age, its model age is 300 Ma older than the oldest crustal age in northeastern Tasmania. However, given the very high $^{187}Re/^{188}Os$ ratios and poor internal precision on $^{187}Os/^{188}Os$ (>11%; 2SE) for these sulfides these model ages should be treated with caution. However, it is worth noting that the oldest $T_{MA}$ age was obtained from a sulfide grain in depleted peridotite BL10.

$^{187}Re/^{188}Os$ ratios in the Tasmanian sulfides are generally very high suggesting Re-addition. Re-addition in basalt-borne xenoliths is usually considered to occur at the time of entrainment in the host rock. Tertiary volcanism in northeastern Tasmania ranges in age from ~16.0 to 58 Ma and an age of 40 Ma has been chosen here. Corrections using such a young age have very little effect on initial $^{187}Os/^{188}Os$ ratios and only increase the $T_{RD}$ age by 20 Ma. Os isotopic compositions for the majority of the Tasmanian sulfides are superchondritic, giving future $T_{RD}$ ages. The exception is sulfide BL8 which gives a $T_{RD}$

age of 0.48±0.21 Ga. This age is within error of the whole-rock $T_{RD}$ age (0.30±0.09 Ga) for sample BL33 and may reflect a real event in the mantle beneath northeastern Tasmania during the Palaeozoic. A sulfide $T_{RD}$ age was also obtained for BL10 but the error is very large as found with the $T_{MA}$ model age for this sulfide (Table 7-3).

A Re-Os isochron was constructed for interstitial sulfides from Blessington spinel lherzolite BL13 (Fig. 7-12). Regression of the data yields a Model 3 age of 1.45±0.70Ga and an enriched initial $^{187}Os/^{188}Os$ of 0.1219±0.0044 ($\gamma Os_{initial}$ = +4.0). This suggests that there has been addition of a radiogenic component to the sulfides at some stage in their history. The implications of Proterozoic mantle ages for northeastern Tasmania are discussed in Section 7.7.1. The two interstitial sulfides from BL16 also show a positive correlation between Re/Os and $^{187}Os/^{188}Os$ but produce an isochron with an unrealistic age (>4.5Ga).

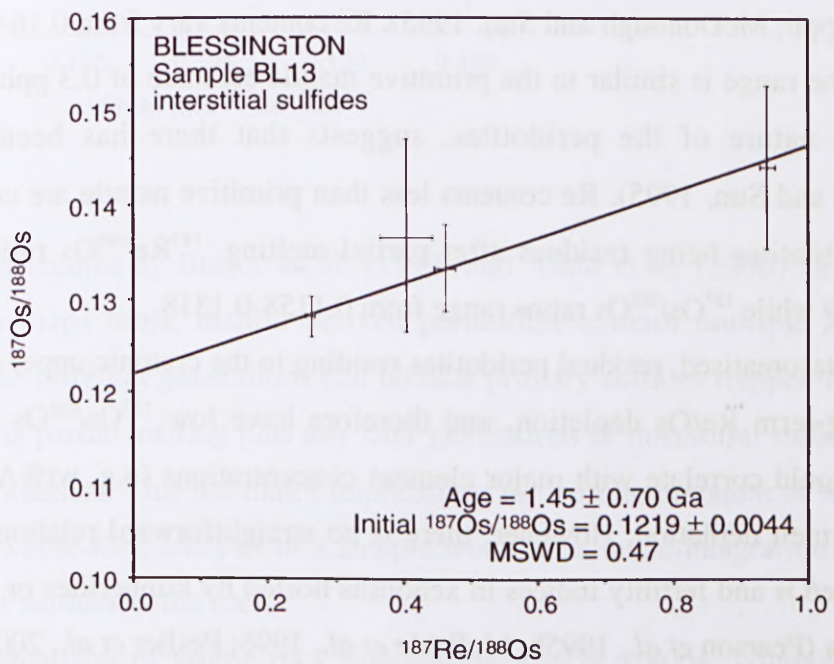


**Figure 7-12.** Re-Os isochron diagram for spinel lherzolite sample BL13 from Blessington. MSWD (Mean Square of Weighted Deviates) is a measure of the ratio of the observed scatter of points (from the best fit line) to the expected scatter (from the assigned errors and error correlations).

### *7.6.2 Western Gneiss Region*

Whole-rock Re-Os isotopic data were collected for three garnet peridotite samples from Almklovdalen. *In-situ* Re-Os data were also collected for sulfides in seven garnet peridotites; four from Almklovdalen (samples N97-5, N97-14, N97-15 and LNWG) and three from Gurskøy (samples GBWG, SVWG and pyroxenite N97-29B). The garnet peridotites from Otrøy were found to be extremely poor in sulfide and have been excluded

from this study. Both enclosed and interstitial sulfides were analysed to determine if there is any recognisable difference in isotopic ratios between the two sulfide types. All enclosed sulfides were hosted by olivine. Estimated abundances of Os and Pt have been extracted from the multi-collector LA-ICPMS data (see Section 7.6.1 and Table 7-4). Os contents in the enclosed sulfides range from 3 to 87 ppm and Pt abundances vary from <1 to 65 ppm. The interstitial sulfides typically have high Os contents (>300 ppm) though a few grains range down to <1 ppm Os. Such high Os contents are unusual in interstitial sulfides and more typical of enclosed sulfides (Griffin *et al.*, 2001a). Pt contents are low in the interstitial sulfides, ranging from 0.17-16 ppm.

Comparison of whole-rock and sulfide data

Whole-rock Re and Os data for the Almklovdalen peridotites are reported in Table 7-4. Os contents range from 4.3-4.5 ppb which is slightly higher than the estimate for primitive mantle (~3.4 ppb; McDonough and Sun, 1995). Re contents vary from 0.16-0.31 ppb. The high end of the range is similar to the primitive mantle estimate of 0.3 ppb which, given the depleted nature of the peridotites, suggests that there has been Re-addition (McDonough and Sun, 1995). Re contents less than primitive mantle are consistent with the other peridotites being residues after partial melting. $^{187}Re/^{188}Os$ ratios vary from 0.1872-0.3489 while $^{187}Os/^{188}Os$ ratios range from 0.1158-0.1318.

Unmetasomatised, residual peridotites residing in the cratonic upper mantle should preserve long-term Re/Os depletion, and therefore have low $^{187}Os/^{188}Os$. Furthermore, $^{187}Os/^{188}Os$ should correlate with major element concentrations (e.g. wt%$Al_2O_3$) that are indicative of melt depletion. However, there is no straightforward relationship between $^{187}Os/^{188}Os$, Re/Os and fertility indices in xenoliths hosted by kimberlites or alkali basalts. Many workers (Pearson *et al.*, 1995b; McBride *et al.*, 1996; Peslier *et al.*, 2000; Hanghøj *et al.*, 2001) have found little or no correlation, while a review of osmium isotopic compositions of mantle xenoliths by Meisel *et al.* (2001) reports a positive trend between $Al_2O_3$ and $^{187}Os/^{188}Os$ for a range of xenolith suites. In contrast to the data for xenoliths, peridotites from orogenic massifs generally show a good correlation between Os isotopic compositions and indices of melt extraction (Reisberg *et al.*, 1991; Reisberg and Lorand, 1995).

As only three samples from the WGR were analysed for whole rock Re-Os isotopes any apparent trends, or lack thereof, in the data should be treated with caution (see Fig. 7-13). Despite the limitations of the data it is evident that the most depleted sample (N97-15)

has the most radiogenic Os composition whereas the more fertile peridotites have less radiogenic $^{187}Os/^{188}Os$ ratios. This is contrary to the trend expected for residues of partial melting and suggests that there has been some disturbance of the Re-Os systematics since the time of melt extraction.

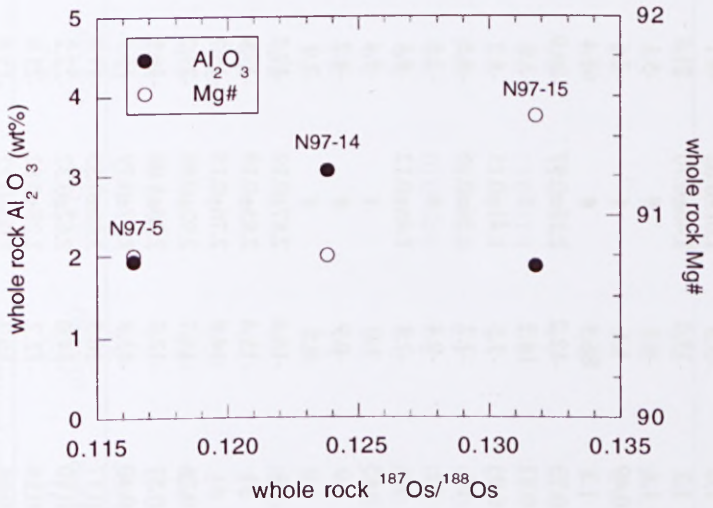


**Figure 7-13.** Whole rock $^{187}Os/^{188}Os$ against whole $Al_2O_3$ and Mg# for WGR garnet peridotites.

Recent studies by Burton et al. (1999) and Alard et al. (2000) have shown that many, and perhaps most, mantle derived peridotites contain multiple generations of sulfides. These different generations can include primary sulfides trapped in crystallising silicates during partial melting plus any later generations of interstitial sulfides introduced during metasomatism. This has major implications for the interpretation of whole-rock Re-Os data as a whole-rock analysis of a sample would thus be an integration of the various generations of sulfides in the rock.

A comparison of whole rock and sulfide Re-Os isotopic compositions for the Western Gneiss Region garnet peridotites is shown in Fig. 7-14. Enclosed sulfides from Almklovdalen have $^{187}Re/^{188}Os$ ratios ranging from 0.0527-1.3173 and $^{187}Os/^{188}Os$ varying from 0.1067-0.2458 (see Table 7-3). Interstitial sulfides from Almklovdalen show a similar range in $^{187}Re/^{188}Os$ (0.0344-1.0401) to the enclosed sulfides but exhibit a smaller variation in $^{187}Os/^{188}Os$ values (0.1113-0.1597). Sulfides analysed in the peridotites from Gurskøy are interstitial and typically characterised by high $^{187}Re/^{188}Os$ (0.3894-0.4963) though one grain had a very low ratio of 0.0445. $^{187}Os/^{188}Os$ ratios are superchondritic and vary from 0.1306-0.1423. Whole-rock data for each sample show an intermediate Re/Os and Os isotopic composition, plotting in the middle of the sulfide array.

**Table 7-4.** Whole-rock and sulfide Re-Os isotopic data and model ages for Western Gneiss Region garnet peridotites.

| Whole rock sample no. | Re (ppb) | Os (ppb) | $^{187}Re/^{188}Os$ | ±2SE | $^{187}Os/^{188}Os$ | ±2SE | γOs (0.4 Ga) | $T_{RD}$ (0.4 Ga) | γOs (1.6 Ga) | $T_{RD}$ (1.6 Ga) | $T_{MA}$* (Ga) |
|---|---|---|---|---|---|---|---|---|---|---|---|
| N97-5 | 0.209 | 4.51 | 0.2278 | 0.0096 | 0.11581 | 0.00041 | -9.8 | 1.84±0.02 | -14.1 | 2.62±0.02 | 3.80±0.25 |
| N97-14 | 0.163 | 4.33 | 0.1872 | 0.0110 | 0.12380 | 0.00031 | -3.6 | 0.68±0.05 | -6.6 | 1.24±0.05 | 0.92±0.10 |
| N97-15 | 0.305 | 4.28 | 0.3489 | 0.0166 | 0.13177 | 0.00021 | 1.8 | f | -3.7 | 0.71±0.03 | f |

| Sulfide no. | Sulfide type | $^{187}Re/^{188}Os$ | ±2SE | $^{187}Os/^{188}Os$ | ±2SE | Os (ppm) | Pt (ppm) | γOs (0.4 Ga) | $T_{RD}$ (0.4 Ga) | γOs (1.6 Ga) | $T_{RD}$ (1.6 Ga) | $T_{MA}$* (Ga) |
|---|---|---|---|---|---|---|---|---|---|---|---|---|
| N97-5/1a | interstitial | 0.1959 | 0.0096 | 0.1115 | 0.0020 | 197 | 2.5 | -13.3 | 2.48±0.29 | -16.4 | 3.05±0.29 | 4.41±0.60 |
| N97-5/1b | interstitial | 0.2132 | 0.0096 | 0.1113 | 0.0018 | 299 | 4.2 | -13.6 | 2.53±0.26 | -17.0 | 3.15±0.26 | e |
| N97-5/1c | interstitial | 0.2369 | 0.0184 | 0.1219 | 0.0042 | 77 | 1.0 | -5.3 | 1.01±0.62 | -9.1 | 1.71±0.06 | # |
| N97-5/2 | interstitial | 0.5396 | 0.0170 | 0.1139 | 0.0048 | 89 | 1.2 | -13.2 | 2.46±0.70 | -21.8 | 4.02±0.70 | f |
| N97-5/3a | interstitial | 0.3128 | 0.0440 | 0.1291 | 0.0034 | 91 | 1.1 | -0.1 | # | -5.1 | # | f |
| N97-5/3b | interstitial | 0.2300 | 0.0260 | 0.1300 | 0.0016 | 82 | 0.49 | 1.1 | f | -2.6 | 0.49±0.24 | f |
| N97-14/2 | enclosed | 1.3173 | 0.0800 | 0.2458 | 0.0130 | 4.6 | 1.3 | 86.5 | # | 65.4 | # | e |
| N97-14/3a | enclosed | 1.1082 | 0.0840 | 0.1190 | 0.0066 | 4.7 | 0.73 | -12.2 | 2.27±0.97 | -29.9 | e | f |
| N97-15/1b | enclosed | 0.6472 | 0.0260 | 0.1495 | 0.0019 | 11 | 0.82 | 14.2 | f | 3.8 | f | e |
| N97-15/2a | enclosed | 0.0741 | 0.0068 | 0.1181 | 0.0010 | 20 | 0.93 | -7.5 | 1.41±0.15 | -8.7 | 1.63±0.15 | 1.63±0.09 |
| N97-15/2b | enclosed | 0.0781 | 0.0038 | 0.1184 | 0.0011 | 20 | 65 | -7.2 | 1.36±0.16 | -8.5 | 1.59±0.16 | 1.59±0.10 |
| N97-15/2c | enclosed | 0.1146 | 0.0082 | 0.1273 | 0.0032 | 21 | 62 | -0.4 | # | -2.3 | # | f |
| N97-15/2d | enclosed | 0.0671 | 0.0086 | 0.1177 | 0.0008 | 13 | 3.9 | -7.8 | 1.46±0.12 | -8.8 | 1.66±0.12 | 1.67±0.07 |
| N97-15/4a | interstitial | 0.4019 | 0.0220 | 0.1310 | 0.0011 | 17 | 0.65 | 1.0 | f | -5.4 | 1.03±0.16 | e |
| N97-15/4b | interstitial | 0.4511 | 0.0096 | 0.1289 | 0.0008 | 27 | 1.0 | -0.9 | # | -8.2 | 1.53±0.12 | e |
| N97-15/5 | interstitial | 0.4032 | 0.0300 | 0.1406 | 0.0013 | 11 | 1.0 | 8.5 | f | 2.0 | f | e |
| N97-15/6a | enclosed | 0.1258 | 0.0062 | 0.1083 | 0.0013 | 87 | 28 | -15.4 | 2.87±0.19 | -17.5 | 3.23±0.19 | 3.97±0.29 |
| N97-15/6b | enclosed | 0.1606 | 0.0200 | 0.1087 | 0.0013 | 63 | 31 | -15.4 | 2.85±0.19 | -17.9 | 3.32±0.19 | 4.44±0.49 |
| N97-15/7a | enclosed | 0.0527 | 0.0180 | 0.1086 | 0.0010 | 85 | 41 | -14.8 | 2.76±0.15 | -15.7 | 2.91±0.15 | 3.11±0.12 |
| N97-15/7b | enclosed | 0.3420 | 0.0181 | 0.1094 | 0.0034 | 3.1 | 0.26 | -15.7 | 2.92±0.50 | -21.2 | 3.90±0.49 | e |
| N97-15/7c | enclosed | 0.2966 | 0.0106 | 0.1137 | 0.0072 | 3.0 | 0.57 | -12.2 | 2.26±1.06 | -16.9 | 3.13±1.05 | e |
| N97-15/7d | enclosed | 0.1492 | 0.0360 | 0.1105 | 0.0054 | 7.0 | 0.40 | -13.8 | 2.57±0.79 | -16.2 | 3.01±0.79 | 3.83±0.68 |
| N97-15/7e | enclosed | 0.0844 | 0.0196 | 0.1067 | 0.0036 | 10 | 0.17 | -16.5 | 3.06±0.53 | -17.8 | 3.30±0.53 | 3.74±0.35 |
| N97-15/8a | enclosed | 0.5096 | 0.0152 | 0.1127 | 0.0022 | 3.9 | 0.10 | -14.0 | 2.62±0.32 | -22.2 | 4.08±0.32 | f |
| N97-15/8b | enclosed | 0.6023 | 0.0540 | 0.1156 | 0.0056 | 3.5 | 0.19 | -12.2 | 2.28±0.82 | -21.8 | 4.02±0.81 | f |
| N97-15/9a | enclosed | 0.3177 | 0.0118 | 0.1156 | 0.0015 | 4.6 | 0.05 | -10.7 | 2.00±0.22 | -15.8 | 2.93±0.22 | e |

**Table 7-4.** Whole-rock and sulfide Re-Os isotopic data and model ages for Western Gneiss Region garnet peridotites.

| Sulfide no. | Sulfide type | $^{187}Re/^{188}Os$ | ±2SE | $^{187}Os/^{188}Os$ | ±2SE | Os (ppm) | Pt (ppm) | γOs (0.4 Ga) | $T_{RD}$ (0.4 Ga) | γOs (1.6 Ga) | $T_{RD}$ (1.6 Ga) | $T_{MA}$* (Ga) |
|---|---|---|---|---|---|---|---|---|---|---|---|---|
| N97-15/9b | enclosed | 0.3317 | 0.0070 | 0.1168 | 0.0018 | 7.3 | 0.002 | -9.8 | 1.84±0.27 | -15.1 | 2.81±0.26 | e |
| N97-15/9c | enclosed | 0.3013 | 0.0088 | 0.1172 | 0.0030 | 3.8 | 0.03 | -9.4 | 1.76±0.44 | -14.2 | 2.65±0.44 | e |
| N97-15/10a | interstitial | 0.0344 | 0.0014 | 0.1334 | 0.0026 | 16 | 3.6 | 4.8 | f | 4.2 | f | f |
| N97-15/10b | interstitial | 1.0401 | 0.0980 | 0.1597 | 0.0048 | 1.8 | 6.7 | 20.1 | f | 3.5 | f | 2.98±0.32 |
| N97-15/10c | interstitial | 0.2883 | 0.0013 | 0.1324 | 0.0058 | 1.4 | 4.2 | 2.6 | f | -2.0 | # | f |
| N97-15/11a | interstitial | 0.3697 | 0.0400 | 0.1378 | 0.0064 | 2.0 | 0.38 | 6.5 | f | 0.5 | f | f |
| N97-15/11b | interstitial | 0.0628 | 0.0086 | 0.1262 | 0.0054 | 2.0 | 4.9 | -1.1 | # | -2.1 | # | # |
| N97-29B | interstitial | 0.3503 | 0.0540 | 0.1338 | 0.0050 | 3.4 | 16 | 3.4 | f | -2.2 | # | f |
| GBWG/1 | interstitial | 0.4226 | 0.0240 | 0.1410 | 0.0080 | 0.8 | 0.45 | 8.7 | f | 2.0 | f | e |
| GBWG/2 | interstitial | 0.4963 | 0.0280 | 0.1423 | 0.0058 | 2.1 | 0.29 | 9.3 | f | 1.4 | f | e |
| LNWG/1a | interstitial | 0.1336 | 0.0015 | 0.1182 | 0.0006 | 8.2 | 0.33 | -7.7 | 1.45±0.10 | -9.9 | 1.85±0.09 | 1.97±0.07 |
| LNWG/1c | interstitial | 0.3702 | 0.0480 | 0.1236 | 0.0014 | 13 | 0.25 | -4.7 | 0.89±0.20 | -10.6 | 1.99±0.20 | e |
| LNWG/1d | interstitial | 0.8315 | 0.0104 | 0.1370 | 0.0038 | 8.6 | 0.33 | 3.4 | f | -9.9 | 1.85±0.56 | 1.36±0.26 |
| LNWG/1e | interstitial | 0.1781 | 0.0174 | 0.1204 | 0.0008 | 6.0 | 0.17 | -6.2 | 1.17±0.12 | -9.0 | 1.69±0.12 | 1.77±0.13 |
| LNWG/1f | interstitial | 0.1483 | 0.0024 | 0.1196 | 0.0007 | 6.6 | 0.20 | -6.7 | 1.26±0.11 | -9.0 | 1.70±0.11 | 1.75±0.09 |
| LNWG/2 | interstitial | 0.2748 | 0.0013 | 0.1289 | 0.0015 | 14 | 1.4 | 0.0 | # | -4.4 | 0.83±0.23 | f |
| SVWG/1 | interstitial | 0.3894 | 0.0044 | 0.1340 | 0.0009 | 14 | 3.3 | 3.4 | f | -2.8 | 0.54±0.13 | f |
| SVWG/2 | interstitial | 0.3744 | 0.0140 | 0.1396 | 0.0032 | 3.6 | 0.58 | 7.9 | f | 1.9 | f | f |
| SVWG/4b | interstitial | 0.0445 | 0.0110 | 0.1306 | 0.0010 | 2.5 | 16 | 2.5 | f | 1.8 | f | f |

* propagated 2SE analytical uncertainties on $^{187}Re/^{188}Os$ and $^{187}Os/^{188}Os$

'f' indicates future model age

'e' indicates model age older than the Earth

'#' indicates model age that is less than its calculated error

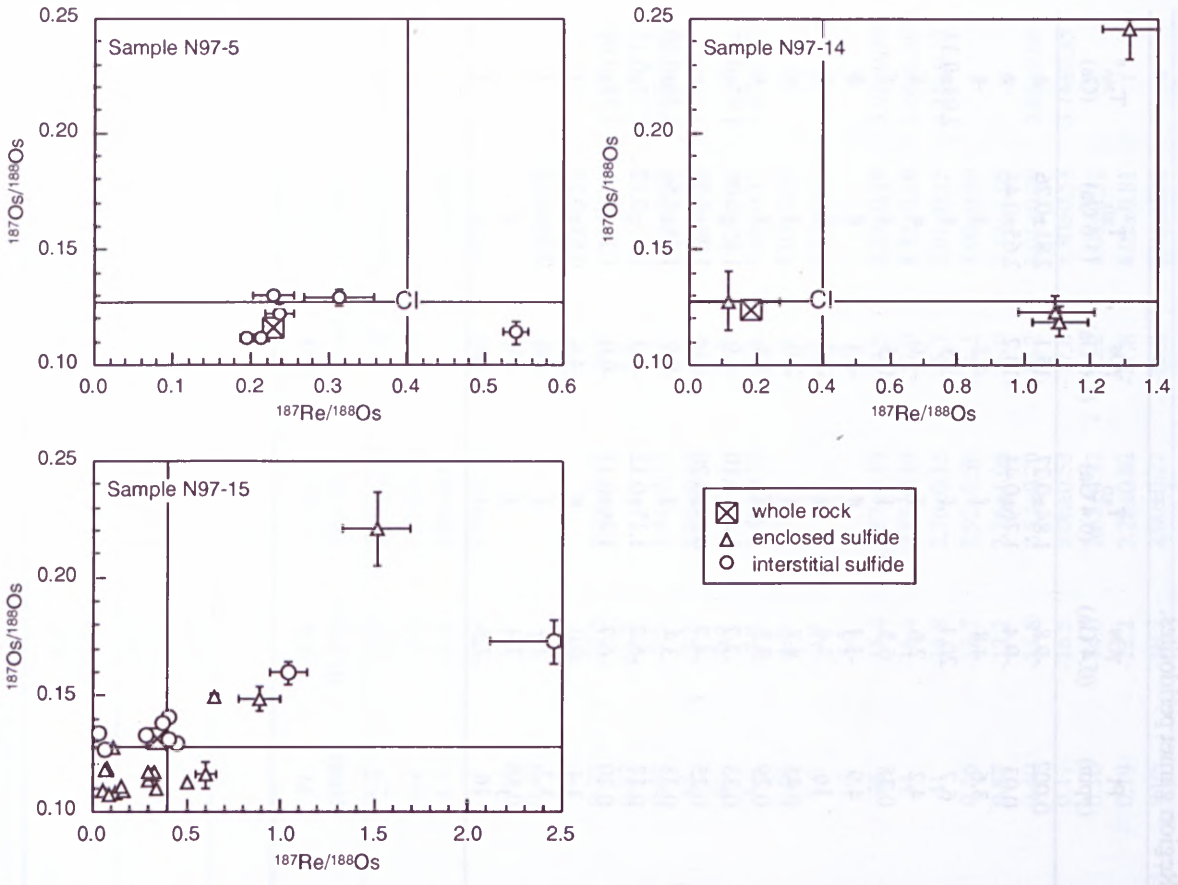


**Figure 7-14.** $^{187}Re/^{188}Os$ against $^{187}Os/^{188}Os$ for whole rock and sulfide from three Almklovdalen garnet peridotites. Analytical uncertainties are shown by the error bars. CI values are from Shirey and Walker (1998).

## Model ages

Calculation of Re-Os model ages for mantle peridotites is complicated by the possibility that measured Re concentrations in the samples may include a component derived from fluid or melt infiltration either from the host rock or earlier metasomatism. Walker *et al.* (1989) addressed this potential problem by making the limiting assumption that all Re was removed during a melting event and that the present-day Re content was added from an exotic source. In xenoliths, the time of Re-addition is generally taken as the time of eruption; for massif peridotites, the timing is less straightforward, and must be based on assumptions about the age of major magmatic or tectonic events that affected the peridotites. In the case of the Western Gneiss Region there are two main events which may have affected the peridotites. The first is the Gothian orogeny between 1.6-1.7 Ga which saw widespread magmatic activity and crustal generation in Norway. The second is the Caledonian subduction event at about 0.4 Ga, which marks the likely time for emplacement of the peridotites into the crust.

Fig. 7-15 illustrates the effect of back-calculating initial $^{187}Os/^{188}Os$ ratios to 0.4 Ga and 1.6 Ga (data from Table 7-4) for twenty-three sulfides from Almklovdalen. Calculation of initial $^{187}Os/^{188}Os$ at 0.4 Ga shifts ratios to slightly less radiogenic compositions and reduces the number of peaks in the measured values. While many of the corrected values are still superchondritic and give future ages there are three well-defined peaks with subchondritic ratios that can be matched with maximums in the corresponding $T_{RD}$ plot in Fig. 7-15B. The broad peak in the $^{187}Os/^{188}Os$ data at approximately 0.11 in Fig. 7-15A produces the peak at ~2.5-2.8 Ga in Fig. 7-15B. Likewise the sharp peak at about 0.118 in the Os plot defines a corresponding sharp peak in the age data at ~1.4 Ga. The difference between the corrected and uncorrected $T_{RD}$ model ages is about 0.1-0.2 Ga. This is sufficient to confirm an Archean age for many of the enclosed sulfides while maintaining a strong Proterozoic signature in the interstitial sulfides.

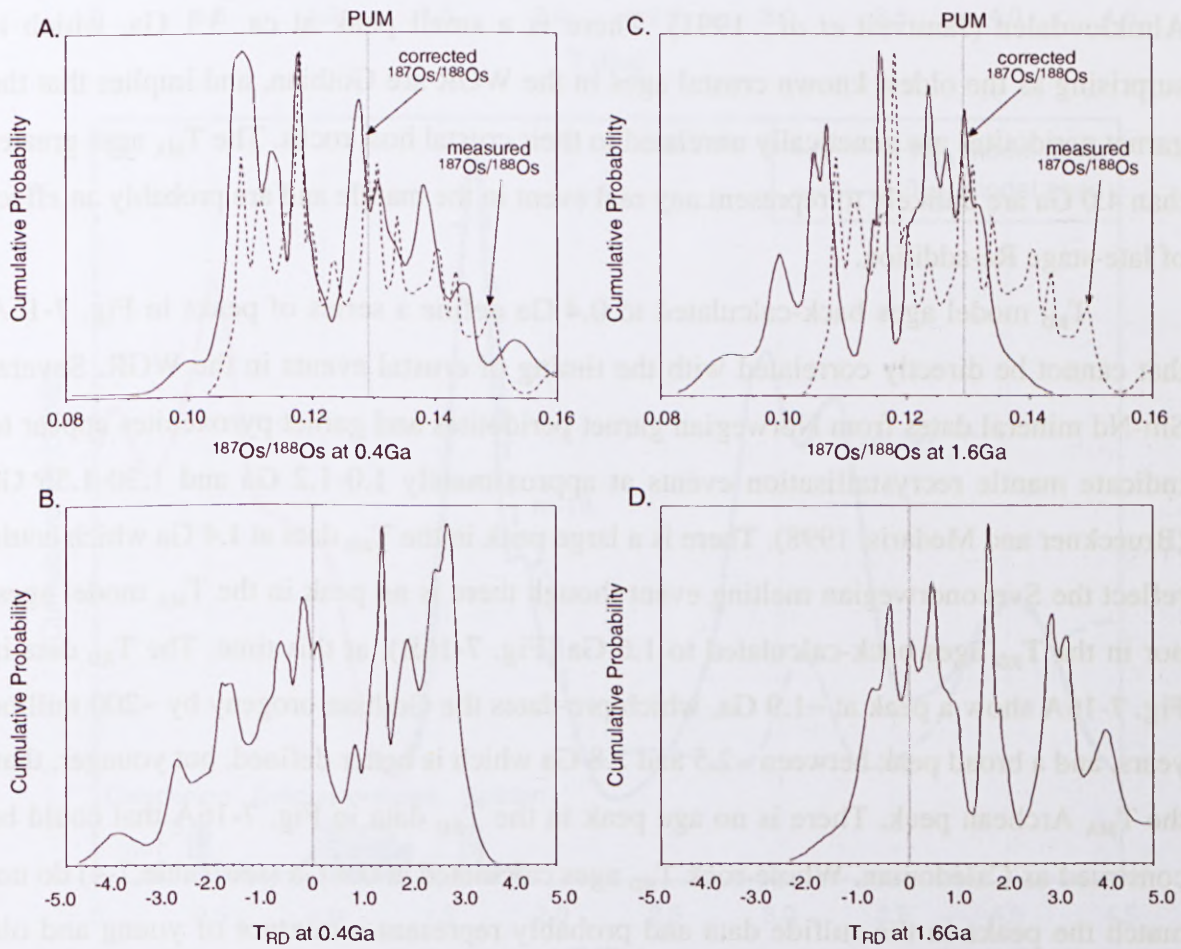


**Figure 7-15.** Cumulative probability diagrams for initial $^{187}Os/^{188}Os$ and $T_{RD}$ calculated at 0.4 Ga and 1.6 Ga. PUM line is the value for primitive upper mantle ($^{187}Os/^{188}Os$ =0.1290±0.0009) after Meisel *et al.*, 1996b.

The shift to older ages is even more apparent if measured $^{187}Os/^{188}Os$ ratios are back-calculated to 1.6 Ga. The majority of Os compositions are now subchondritic with very few values falling to the right of the PUM line (Fig. 7-15C). $T_{RD}$ model ages calculated using the corrected Os data are shown in Fig.7-15D. There is a large spread in ages from 1.0 Ga to the present day with a small peak at ~0.5 Ga. Ages greater than 1.5 Ga are clearly resolved into distinct Proterozoic and Archean peaks with little overlap. The Proterozoic peak has a maximum at ~1.65 Ga while the broad Archean peak ranges from 2.9-3.2 Ga.

Fig. 7-16 is a cumulative probability plot comparing $T_{MA}$ and $T_{RD}$ model ages for the Almklovdalen sulfides. The model age data define a series of peaks, some of which can be matched to major crustal events in Norway. There are three main peaks in the $T_{MA}$ data (Fig. 7-16A). The most prominent peak is at approximately 1.65 Ga which falls within the age range for the Gothian orogeny (1.60-1.75 Ga) and is close to the calculated Sm-Nd mineral age of 1703±29 Ma for garnet peridotites from the Raudkleivane locality in Almklovdalen (Jamtveit *et al.*, 1991). There is a small peak at ca. 3.1 Ga, which is surprising as the oldest known crustal ages in the WGR are Gothian, and implies that the garnet peridotites are genetically unrelated to their crustal host rocks. The $T_{MA}$ ages greater than 4.0 Ga are unlikely to represent any real event in the mantle and are probably an effect of late-stage Re-addition.

$T_{RD}$ model ages back-calculated to 0.4 Ga define a series of peaks in Fig. 7-16A that cannot be directly correlated with the timing of crustal events in the WGR. Several Sm-Nd mineral dates from Norwegian garnet peridotites and garnet pyroxenites appear to indicate mantle recrystallisation events at approximately 1.0-1.2 Ga and 1.30-1.55 Ga (Brueckner and Medaris, 1998). There is a large peak in the $T_{RD}$ data at 1.4 Ga which could reflect the Sveconorwegian melting event though there is no peak in the $T_{MA}$ model ages, nor in the $T_{RD}$ ages back-calculated to 1.6 Ga (Fig. 7-16B), at this time. The $T_{RD}$ data in Fig. 7-16A show a peak at ~1.9 Ga, which pre-dates the Gothian orogeny by ~200 million years, and a broad peak between ~2.5 and 2.8 Ga which is better defined, but younger, than the $T_{MA}$ Archean peak. There is no age peak in the $T_{RD}$ data in Fig. 7-16A that could be construed as Caledonian. Whole-rock $T_{RD}$ ages calculated at 0.4 Ga (see Table 7-4) do not match the peaks in the sulfide data and probably represent a mixture of young and old sulfide ages.

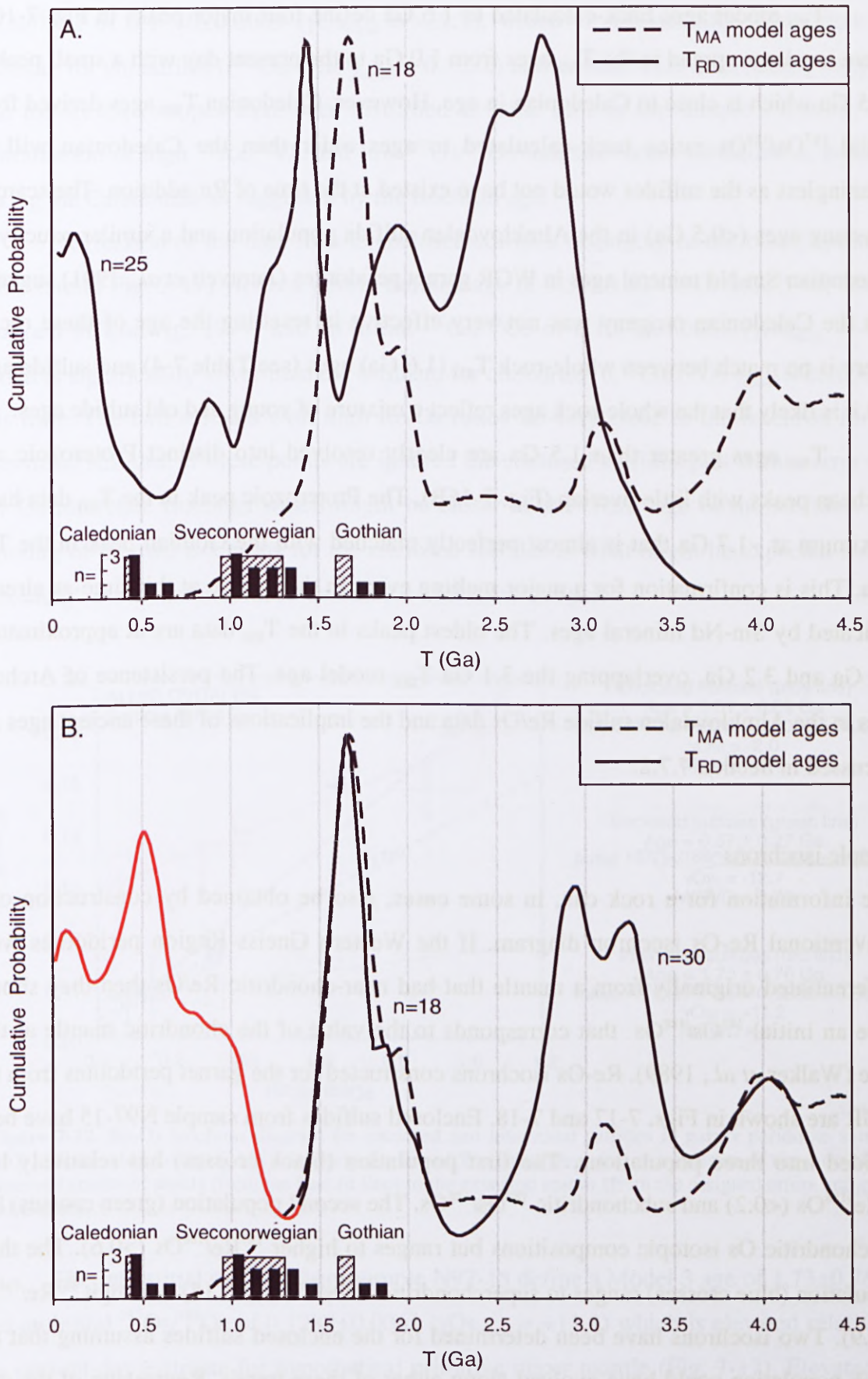


**Figure 7-16.** Cumulative probability plot of $T_{MA}$ and $T_{RD}$ model ages for sulfides from Almklovdalen garnet peridotites. (A) $T_{RD}$ calculated at 0.4 Ga and (B) $T_{RD}$ calculated as 1.6 Ga. The red line indicates meaningless $T_{RD}$ ages. Striped boxes show age ranges for major crustal orogenies in Norway. Black boxes are Sm-Nd mineral ages for WGR garnet pyroxenites and peridotites (Brueckner and Medaris, 1998).

$T_{RD}$ model ages back-calculated to 1.6 Ga define four major peaks in Fig. 7-16B. There is a large spread in the $T_{RD}$ ages from 1.0 Ga to the present day with a small peak at ~0.5 Ga which is close to Caledonian in age. However, Caledonian $T_{RD}$ ages derived from initial $^{187}Os/^{188}Os$ ratios back-calculated to ages older than the Caledonian will be meaningless as the sulfides would not have existed at the time of Re-addition. The scarcity of young ages (<0.5 Ga) in the Almklovdalen sulfide population and a similar paucity of Caledonian Sm-Nd mineral ages in WGR garnet peridotites (Jamtveit *et al.*, 1991) suggests that the Caledonian orogeny was not very effective in resetting the age of these rocks. There is no match between whole-rock $T_{RD}$ (1.6 Ga) ages (see Table 7-4) and sulfide ages and it is likely that the whole-rock ages reflect a mixture of young and old sulfide ages.

$T_{RD}$ ages greater than 1.5 Ga are clearly resolved into distinct Proterozoic and Archean peaks with little overlap (Fig. 7-16B). The Proterozoic peak in the $T_{RD}$ data has a maximum at ~1.7 Ga that is almost perfectly matched with the Gothian peak in the $T_{MA}$ data. This is confirmation for a major melting event in the mantle at this time as already indicated by Sm-Nd mineral ages. The oldest peaks in the $T_{RD}$ data are at approximately 2.9 Ga and 3.2 Ga, overlapping the 3.1 Ga $T_{MA}$ model age. The persistence of Archean ages in the Almklovdalen sulfide Re/Os data and the implications of these ancient ages are discussed in Section 7.7.2.

Sample isochrons

Age information for a rock can, in some cases, also be obtained by construction of a conventional Re-Os isochron diagram. If the Western Gneiss Region peridotites were differentiated originally from a mantle that had near-chondritic Re/Os then they should have an initial $^{187}Os/^{188}Os$ that corresponds to the value of the chondritic mantle at that time (Walker *et al.*, 1989). Re-Os isochrons constructed for the garnet peridotites from the WGR are shown in Figs. 7-17 and 7-18. Enclosed sulfides from sample N97-15 have been divided into three populations. The first population (black crosses) has relatively low $^{187}Re/^{188}Os$ (<0.2) and subchondritic $^{187}Os/^{188}Os$. The second population (green crosses) has subchondritic Os isotopic compositions but ranges to higher $^{187}Re/^{188}Os$ (>0.6). The third population (blue crosses) ranges to superchondritic $^{187}Os/^{188}Os$ (>0.15) and high $^{187}Re/^{188}Os$ (>0.9). Two isochrons have been determined for the enclosed sulfides assuming that the black population could have evolved along either of these trends. Regression of the data for the enclosed sulfides belonging to the green population (green line in Fig. 7-17) yields an age of 0.57±0.27 Ga (Model 3 fit; Isoplot program of Ludwig, 1999) and an initial

$^{187}Os/^{188}Os$ of 0.1076±0.0009 ($\gamma Os_{initial}$ = -12.7), which is substantially lower than the estimate for chondrites (($^{187}Os/^{188}Os$ )$_{chond}$ = 0.1232) at this time. This discrepancy suggests that the Re-Os isotopes have been disturbed at some time in the sample's history. The combination of high $^{187}Re/^{188}Os$ and low $^{187}Os/^{188}Os$ indicate recent Re-addition, possibly during the Caledonian as suggested by the isochron age.

Regression of the data for the enclosed sulfides belonging to the blue population (blue line in Fig. 7-17) yields a poorly defined age of 3.51±0.89 Ga (Model 3 fit; Isoplot program of Ludwig, 1999) and an initial $^{187}Os/^{188}Os$ of 0.1008±0.0057 ($\gamma Os_{initial}$ = -2.0) which is significantly lower than the estimate for chondrites (($^{187}Os/^{188}Os$ )$_{chond}$ = 0.1030) at this time. The two sulfides with high Re/Os ratios lie very close to the isochron for the interstitial sulfides. If these points are ignored the enclosed sulfides plot within error of a 2.4 Ga reference isochron which might be closer to the "real" age of the sulfides. The crossing of the two isochrons for the enclosed sulfides is what might be expected from a "resetting" event that mobilised Os and Re within the sample.

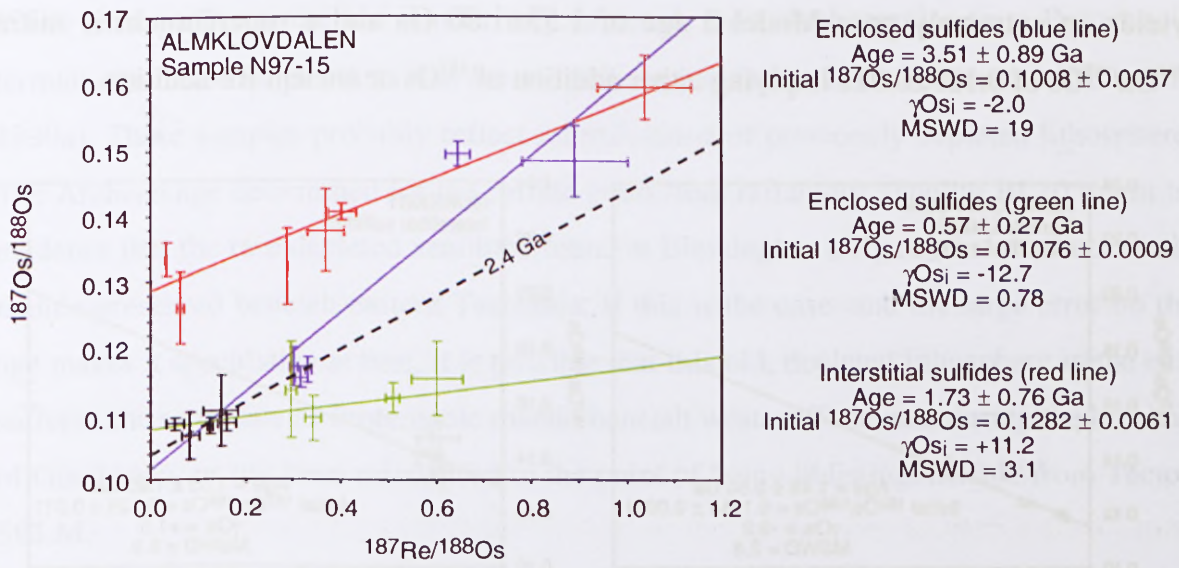


**Figure 7-17.** Re-Os isochron diagram for enclosed and interstitial sulfides in garnet peridotite sample N97-15 from Almklovdalen. MSWD (Mean Square of Weighted Deviates) is a measure of the ratio of the observed scatter of points (from the best fit line) to the expected scatter (from the assigned errors and error correlations).

The interstitial sulfides from sample N97-15 define a Model 3 age of 1.73±0.76 Ga and an initial $^{187}Os/^{188}Os$ of 0.1282±0.0061 ($\gamma Os_{initial}$ = +11.2) which is elevated relative to the present-day estimate for hypothetical primitive upper mantle (Fig. 7-17). Elevated Os isotopic compositions have been attributed to either addition of radiogenic $^{187}Os$ or ancient Re-addition followed by in-growth of $^{187}Os$ (McBride *et al.*, 1996). The first case requires an agent that has evolved in a reservoir with high Re/Os to allow for substantial in-growth

of radiogenic Os while the second case is dependent on a source with high Re concentrations and high Re/Os ratios relative to the mantle. The obvious disturbance in the Re/Os ratios of the Almklovdalen interstitial sulfides means that an isochron age calculated using these data may not reflect any real event in the mantle. However, it is worth noting that the interstitial sulfide age falls within error of the Sm-Nd mineral isochron age (1703±26Ma) determined for Almklovdalen garnet peridotite (Mearns, 1986).

Regression of the data from interstitial sulfides in another Almklovdalen peridotite (sample LNWG) yields a Model 3 age of 1.48±0.50 Ga and an initial $^{187}Os/^{188}Os$ of 0.1154±0.0021 ($\gamma Os_{initial}$ = -1.37) (Fig. 7-18). The fit of the data to the isochron is quite good (MSWD=2.8) and the initial Os composition is close to the chondritic value at that time ($(^{187}Os/^{188}Os)_{chond}$=0.1169 at 1.49 Ga). This suggests that the isochron may represent isotopic evolution of a Proterozoic chondritic mantle reservoir undisturbed by post-formation Re-addition. The interstitial sulfide isochron for Gurskøy sulfides was constructed using data from three different peridotite samples from two localities; samples GBWG and N97-29B from Gurskebotn, and SVWG from Sandvika. Regression of the data yields an extremely poor Model 3 age of 1.53±1.80 Ga and a superchondritic initial $^{187}Os/^{188}Os$ of 0.129±0.011 implying either addition of $^{187}Os$ or ancient Re-addition.

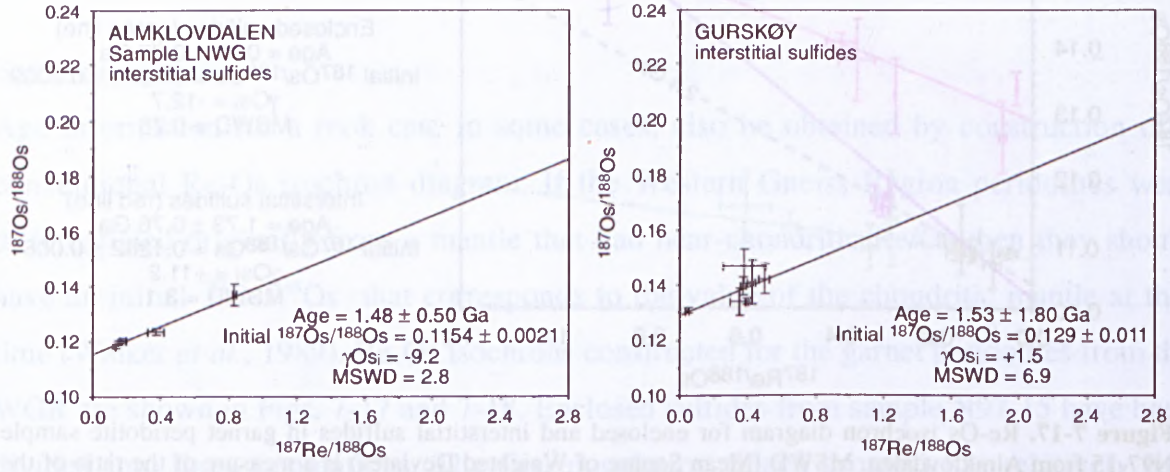


**Figure 7-18.** Re-Os isochron diagram for interstitial sulfides in garnet peridotites from the Western Gneiss Region. MSWD (Mean Square of Weighted Deviates) is a measure of the ratio of the observed scatter of points (from the best fit line) to the expected scatter (from the assigned errors and error correlations).

## 7.7 DISCUSSION

### *7.7.1 Tasmania*

The presence of depleted mantle peridotites in Tertiary basalts in northeastern Tasmania suggests that there might once have been old, melt-depleted lithosphere beneath the Northeast Tasmania Element. Despite the lack of known Precambrian crustal ages in

eastern Tasmania, there is some evidence for Proterozoic material in the lower levels of the crust, from granite protolith ages. S-type granites in northeastern Tasmania have been shown to have high initial $^{86}Sr/^{86}Sr$ ratios (>0.7119) which indicate a continental crust protolith with a high Rb/Sr ratio (Cocker, 1982). Protolith ages for the source rock of the granites, estimated from the intersection of the projected Sr-evolution curves of the upper mantle and the source rock with a known or assumed Rb/Sr ratio, range between 800-1700 Ma (Cocker, 1982). I-type granites have yielded slightly younger protolith ages of 1250-1400 Ma. These ages for the granite source rocks indicate a Proterozoic age for rocks of the lower crust in eastern Tasmania.

Proterozoic crustal ages in eastern Tasmania raise the possibility that the Northeast Tasmania Element was at one time underlain by Proterozoic mantle. If this is the case, then it is possible that the Re-Os isochron age determined for Blessington reflects a real mantle event beneath eastern Tasmania during the Proterozoic. This is complicated by the overall fertility of the northern Tasmanian lithosphere (see Chapter 5) and suggests that there might have been extensive refertilisation of old mantle in the northeast. While average Proton SCLM is relatively depleted, individual samples from Proterozoic terrains can have compositions that are as fertile as peridotites from Tectons (Griffin *et al.*, 1999a). These samples probably reflect refertilisation of previously depleted lithosphere. The Archean age determined for the sulfide grain from refractory xenolith BL10 might be evidence that the rare depleted xenoliths found at Blessington truly represent relicts of old mantle preserved beneath eastern Tasmania. If this is the case, and the large error on the age makes it speculative at best, it is possible that this old, depleted lithosphere in the east suffered the same fate as Proterozoic mantle beneath western Tasmania during the breakup of Gondwana, or has been refertilised to the point of being indistinguishable from Tecton SCLM.

### *7.7.2 Western Gneiss Region*

The implications of Archean ages in the WGR garnet peridotites are twofold. Firstly, the dichotomy in calculated ages between enclosed and interstitial sulfides implies that enclosed sulfides have been shielded by their silicate host and are able to preserve the signature of an ancient melting event despite late stage modification by more recent melting and multiple metamorphic episodes. This is supported by a study of Re-Os isotopes for silicates and sulfides in a spinel lherzolite xenolith from Kilbourne Hole, New Mexico. Burton *et al.* (1999) found that Os isotope compositions for silicates and

interstitial sulfides were indistinguishable, suggesting that these phases were in equilibrium at the time of xenolith eruption. However, enclosed sulfides in silicate minerals were observed to have retained significantly less radiogenic Os isotope compositions, suggesting that they had been protected from reaction or diffusion by their silicate hosts. It was concluded that sulfide inclusions trapped in silicates may be unable to equilibrate either with other minerals or with intergranular melt, and in principle may preserve significantly older Re-Os age information than coexisting phases. Similar findings have been published by Burton *et al.* (2000) for silicates and sulfides from Tanzanian xenoliths. The old ages for the WGR enclosed sulfides therefore imply that the sulfides were trapped in their host minerals during an early, probably Archean, melting event and were protected from subsequent melting events and metamorphism.

This suggests that the most "realistic" Os melt depletion age will be found in sulfides from olivine as it is a mineral that is rarely involved in metasomatic reaction except in cases where large volume of melt is involved. However, recent work on sulfides enclosed in olivines from Siberian mantle peridotites has suggested that sulfide liquids could penetrate olivine crystals along cracks, and that both melts and crystallising sulfide could be trapped by necking-down processes like those that produce fluid inclusions in crustal rocks (Griffin *et al.*, 2001a). This may explain the young ages found in some enclosed sulfides. The interstitial sulfides most likely represent sulfide trapped in the silicate matrix during metasomatism and recrystallisation triggered by the Gothian orogeny. Evidence for metasomatism at this time comes from initial Sm-Nd ratios for garnet lherzolite from Almklovdalen (Mearns, 1986). Mantle metasomatism at ca. 1700 Ma has been invoked by Mearns (1986) to explain the change in Sm-Nd ratios in the garnet peridotite from >CHUR before 1700 Ma to <CHUR at the present day. He postulates that some process, possibly metasomatism, at ca. 1700 Ma led to a shift from LREE-depleted to LREE-enriched compositions in the mantle, implying that the peridotites represent metasomatised mantle material which had a long history prior to 1700 Ma.

The second, and most important, implication of the Archean ages is that the WGR garnet peridotites experienced an Archean partial melting event. Previously, Proterozoic ages for the garnet-bearing peridotites and the basement crustal rocks of the WGR led to the suggestion that the mantle and crust in the southern Caledonides of Norway, as well as other terrains adjacent at the time, were coupled throughout much of the Proterozoic (Brueckner and Medaris, 1998). However, an Archean (2.5-3.0 Ga) whole-rock Sm-Nd

errorchron (Jamtveit *et al.*, 1991) and the Archean Re-Os sulfide ages found in this study provide evidence for a much older melting event in the mantle beneath the Baltic Shield.

This suggests that the peridotites reflect a mantle depletion that was not associated with crustal growth in this part of the Baltic Shield or, alternatively, the Archean crust corresponding to this mantle depletion event may have been reworked in Proterozoic time, to the point of being unrecognisable. To date, there is very little evidence for Archean crust in the WGR, although according to early interpretations, the rocks in the WGR were "believed to have been mainly formed by high-grade metamorphism, migmatization, and granitization of pre-existing rocks (Archean, Eo-Cambrian, Cambro-Silurian)" (Bryhni and Grimstad, 1970). Bryhni and Grimstad (1970) also state that "it could not be doubted that Precambrian (Archean) rocks formed part of the Gneiss region". The Archean Sm-Nd errorchron determined for WGR garnet peridotites by Jamtveit *et al.* (1991) may suggest reworking of Archean crust during the Proterozoic, assuming the crust and mantle have been coupled since Archean time. On the other hand, perhaps crust formed during the Archean only exists at structural levels below those exposed in the Caledonides.

Despite the lack of crustal evidence for an Archean event it appears that mantle material that underwent depletion in Archean time has survived in relatively shallow parts of the lithospheric mantle. Its survival through a major episode of crustal generation in Proterozoic time is almost certainly linked to the buoyancy of these highly depleted peridotites, relative to the underlying asthenosphere (Griffin et al., 1999a).

The preservation of Archean ages in the WGR garnet peridotites is further evidence that at least some mantle material that has, in the past, been identified as Proterozoic SCLM, using radiogenic systems that partition into silicate phases rather than sulfide, may in fact be refertilised Archean lithospheric mantle. CARP analysis (see Section 6.9.1) of other Proterozoic mantle sections has revealed a higher abundance of depleted/ metasomatised garnets near their base, grading upward into more fertile lherzolites. A similar pattern in garnet distribution for SCLM sampled by young kimberlites (<100 Ma) in the Kaapvaal Craton is thought to reflect the metasomatism of depleted harzburgites and lherzolites, as sampled by older kimberlites (>100 Ma), to produce depleted/metasomatised lherzolites (Griffin *et al.*, 2001b). It has been suggested that the Proterozoic sections represent a continuation of the same sorts of metasomatic processes, in which case at least part of the observed secular evolution trend, from Archean to Proterozoic, probably reflects modification of pre-existing SCLM (Griffin *et al.*, 2001b). Given that Archean SCLM is virtually indestructible due to its refractory and buoyant nature (Poudjom Djomani *et al.*,

2000; O'Reilly *et al.*, 2001) it is perhaps not surprising that it can persist beneath Proterozoic orogenic belts.

## 7.8 SUMMARY

(1) Base metal sulfides are common in Tasmanian peridotite xenoliths. The sulfides occur predominantly as small (<50 μm) polymineralic aggregates either enclosed in silicate phases or as interstitial grains in the silicate matrix. Common sulfide phases include pentlandite, pyrrhotite, chalcopyrite and low-T monosulfide solid solutions.

(2) Reconstructed bulk sulfides are all Fe-rich high-T monosulfide solid solution. These compositions lie in the MSS fields at 1000°C and 1100°C suggesting that the sulfides were solid at the ambient temperatures of the xenoliths.

(3) Base metal sulfides are abundant in many of the garnet peridotites from the Western Gneiss Region, and occur either interstitially or, less commonly, as mineral inclusions in silicate minerals. Sulfides in the WGR peridotites are dominated by pentlandite and heazelwoodite and are nearly devoid of Cu-bearing and pure Fe-S phases.

(4) Tasmanian sulfides generally have radiogenic Os isotopic compositions and high Re/Os ratios. This is ascribed to Os- and Re-addition as there has been little time for significant in-growth of $^{187}Os$.

(5) A Re-Os isochron constructed for sulfides in a xenolith from the Northeast Tasmania Element yields an age of 1.45±0.7 Ga. This suggests that northeastern Tasmania might be underlain in part by refertilised Proterozoic lithospheric mantle.

(6) Sulfides from the Western Gneiss Region show a wide range in Re-Os isotopic compositions. Enclosed sulfides tend to have unradiogenic $^{187}Os/^{188}Os$ implying long-term isolation from the convecting mantle. $^{187}Re/^{188}Os$ is generally high (>0.1) implying late Re-addition. Interstitial sulfides typically have high $^{187}Os/^{188}Os$ and $^{187}Re/^{188}Os$. The radiogenic Os compositions imply either addition of radiogenic $^{187}Os$ or ancient Re-addition followed by in-growth of $^{187}Os$.

(7) Isochrons constructed for enclosed sulfides from one sample show that there has been resetting of the Re-Os system, possibly during the Caledonian. Interstitial sulfides from the same sample give a Proterozoic age that might reflect remobilisation of sulfide during the Gothian crustal event.

(8) $T_{RD}$ model ages (back-calculated to 1.6 Ga) for Almklovdalen sulfides define a series of peaks on a cumulative probability diagram, some of which can be matched with known crustal events. The peak at ~1.7 Ga corresponds with the timing of

the Gothian crustal orogeny while the peaks in the Archean do not correspond with any known crustal event in the WGR. The Archean ages suggest that the peridotites experienced an Archean partial melting event.

(9) The preservation of Archean ages in the WGR garnet peridotites supports compositional evidence that some Proterozoic mantle sections represent strongly modified Archean lithospheric mantle.

# CONCLUSIONS

(1) Mantle-derived xenoliths entrained in Tertiary alkali basalts erupted through Proterozoic and Phanerozoic crust in northern Tasmania are predominately Cr-diopside spinel lherzolites with subordinate harzburgites and dunites. Most of the lherzolites are fertile in terms of whole-rock $Al_2O_3$ and CaO contents and Mg# and lie in, or adjacent, to the "oceanic peridotite trend" in the olivine Mg# vs modal olivine diagram. The harzburgites have depleted compositions more typical of refractory cratonic peridotites and plot in the Proterozoic field on a olivine Mg# vs modal olivine diagram.

(2) The Tasmanian xenoliths can be divided into three major compositional groups based on sample fertility. The first group is highly fertile (olivine Mg#<89.5) and occurs only in the Rocky Cape Element. The second group is moderately fertile (olivine Mg# between 89.5-90.5) and is found in all three Elements. The third group is depleted (olivine Mg#>91.5) and is represented in the Rocky Cape and Northeast Tasmania Elements. Rare xenoliths from Wagners Hill (Northeast Tasmania Element) have very low olivine Mg# (<88) that is considered to be the result of metasomatism by an Fe-rich melt.

(3) Trace element patterns of clinopyroxenes in the Tasmanian peridotites reflect interplay between different degrees of partial melting, and subsequent enrichment by metasomatism. Modelling of compatible trace element abundances in clinopyroxene indicates that the fertile Tasmanian peridotites have experienced less than 5% (batch or fractional) partial melting in the spinel stability field and some Rocky Cape peridotites have experienced less than 2% melting. The depleted xenoliths require higher degrees of partial melting (8-15% fractional melting) in the spinel field. Most Tasmanian xenoliths show evidence for cryptic metasomatism. Clinopyroxene trace element patterns show enrichment in the LREE, Sr, U and Th which can be modelled by simple mixing between moderately depleted (~5% melting) peridotite and 3-15% dolerite. A few xenoliths have compositions that might reflect mixing between fertile peridotite and <1% carbonatite.

(4) The depth to the crust-mantle boundary across northern Tasmania has been determined by extrapolating xenolith temperatures to the southeastern Australian (SEA) geotherm. The CMB is well-defined at 31-32 km beneath the Sheffield and Northeast Tasmania Elements and coincides with Moho depths derived from wide-angle seismic surveys. The CMB is poorly constrained beneath the Rocky Cape Element but may be as shallow as 26 km. Estimates of crustal thickness in northwestern Tasmania are complicated

by high heat flow in this region which would raise the local geotherm and thus raise the estimated depth to the crust-mantle boundary.

(5) A Re-Os isochron age of 1.45±0.7 Ga for sulfides from a fertile xenolith from Blessington suggests that northeastern Tasmania might be underlain in part by refertilised Proterozoic lithospheric mantle. An ancient origin for the depleted xenoliths is supported by an Archean Re-Os sulfide age for a xenolith from northeastern Tasmania.

(6) Rare depleted xenoliths found at some localities in Tasmania may represent relics of old Proterozoic lithosphere preserved in the shallow lithosphere. The scarcity of these xenoliths, and the extensive occurrence of hot, fertile lithosphere beneath northern Tasmania suggests that there has been large-scale removal or refertilisation of the original depleted lithosphere. This is attributed to asthenosphere upwelling and lithosphere thinning during rifting between Australia and Antarctica.

(7) Peridotites from the Western Gneiss Region include garnet-bearing lherzolite, harzburgite and wehrlite, chlorite-amphibole "dunite", and spinel-bearing harzburgite. The WGR peridotites have whole-rock compositions that are depleted relative to estimates for primitive mantle. The Almklovdalen garnet peridotites have the least depleted bulk compositions. They have the lowest whole-rock Mg# and Mg/Si of the three localities and range to higher whole-rock Ca and Al contents than the samples from Gurskøy and Otrøy. Dunites from Almklovdalen have extremely depleted compositions and appear to be residues after high degrees of partial melting.

(8) The garnets in the WGR peridotites are Cr-pyropes and resemble garnets from fertile to moderately depleted lherzolite from worldwide localities. Rare earth patterns for the WGR garnets have high HREE and depleted LREE similar to garnets from high-T sheared peridotite xenoliths in kimberlites.

(9) Garnet peridotites from Gurskøy and Otrøy can be modelled as residues after 20-40% melt extraction at pressures between 5 and 7 GPa. The dunites can also be modelled as residues after high-P melting but require higher degrees (60%?) of melt extraction. Melt modelling for the Almklovdalen garnet peridotites is more complicated but overall the Almklovdalen rocks can be modelled as residues after ~20-35% partial melting at low pressure (2 GPa). The discrepancy in the pressure estimates for the garnet peridotites and dunites at Almklovdalen suggests that these rock types are not related by a simple melt-depletion process.

(10) The resemblance between the WGR garnet peridotites and high-T sheared peridotite xenoliths in kimberlites suggests that the WGR rocks represent refertilisation of

a depleted precursor as modelled for high-T cratonic peridotite. The close structural relationship between the fertile garnet peridotites and the highly depleted dunites at Almklovdalen presents the possibility that the garnet peridotite bodies represent zones of refertilised dunite. Evidence from whole-rock compositions for the Almklovdalen garnet peridotites suggests that the refertilising agent was rich in Fe, Ca, Al and Na but not Ti.

(11) Re-Os $T_{RD}$ model ages for Almklovdalen sulfides define a series of peaks on a cumulative probability diagram, some of which can be matched with known crustal events. However, peaks in the Archean do not correspond with any known event in the WGR crust and suggest that the peridotites experienced an Archean partial melting event. The preservation of Archean ages in the WGR garnet peridotites supports compositional evidence that some Proterozoic mantle sections elsewhere represent strongly modified Archean lithospheric mantle.

(12) In conclusion, this study has shown that crustal age is not a definitive indicator of the composition and age of the underlying mantle. Processes such as lithosphere removal and modification can spatially or temporally decouple crust and mantle so that what is seen at the surface does not necessarily reflect what lies beneath. Methodologies which integrate geochemical, thermal and chronological information such as 4-D Lithosphere Mapping are therefore essential when studying the evolution of the lithospheric mantle.

# REFERENCES


Alard, O., Griffin, W.L., Lorand, J.P., Jackson, S.E. and O'Reilly, S.Y., 2000. Non-chondritic distribution of the highly siderophile elements in mantle sulfides. Nature, 407: 891-894.

Amundsen, H.E.F. and Neumann, E.-R., 1992. Redox control during mantle/melt interaction. Geochimica et Cosmochimica Acta, 56: 2405-2416.

Amundsen, H.E.F., Griffin, W.L. and O'Reilly, S.Y., 1987. The lower crust and upper mantle beneath northwestern Spitsbergen: evidence from xenoliths and geophysics. Tectonophysics, 139: 169-185.

Anders, E. and Grevasse, N., 1989. Abundances of the elements: meteoritic and solar. Geochimica et Cosmochimica Acta, 53: 197-214.

Andersen, T., Griffin, W.L. and O'Reilly, S.Y., 1987. Primary sulphide melt inclusions in mantle-derived megacrysts and pyroxenites. Lithos, 20: 279-294.

Anderson, D.L., 1995. Lithosphere, asthenosphere, and perisphere. Reviews of Geophysics, 33: 125-149.

Antonini, P., Piccirillo, E.M., Petrini, R., Civetta, L., D'Antonio, M. and Orsi, G., 1999. Enriched mantle–Dupal signature in the genesis of the Jurassic Ferrar tholeiites from Prince Albert Mountains (Victoria Land, Antarctica). Contributions to Mineralogy and Petrology, 136: 1-19.

Arculus, R.J. and Delano, J.W., 1981. Intrinsic oxygen fugacity measurements: techniques and results for spinels from upper mantle peridotite and megacryst assemblages. Geochimica et Cosmochimica Acta, 45: 899-913.

Bachinski, S.W. and Simpson, E.L., 1984. Ti-phlogopites of the Shaw's Cove minette: a comparison with micas of other lamprophyres, potassic rocks, kimberlites, and mantle xenoliths. American Mineralogist, 69: 41-56.

Baker, M.B. and Wyllie, P.J., 1992. High-pressure apatite solubility in carbonate-rich liquids: implications for mantle metasomatism. Geochimica et Cosmochimica Acta, 56: 3409-3422.

Ballhaus, C., 1993. Redox states of lithospheric and asthenospheric upper mantle. Contributions to Mineralogy and Petrology, 114: 331-348.

Ballhaus, C., Berry, R.F. and Green, D.H., 1991. High pressure experimental calibration of the olivine-orthopyroxene-spinel oxygen geobarometer: implications for the oxidation state of the upper mantle. Contributions to Mineralogy and Petrology, 107: 27-40.

Barrell, J., 1914. The strength of the Earth's crust. Geology, 22: 28-48.

Barton, T.J., 1998. A geophysical transect across northern Tasmania. 14th Australian Geological Convention Abstracts (Townsville), 49: 24.

Belshaw, N.S., Freedman, P.A., O'Nions, R.K., Frank, M. and Guo, Y., 1998. A new variable dispersion double-focussing plasma mass spectrometer with performance illustrated for Pb isotopes. Int. J. Mass. Spec. Ion. Proc., 181: 51-58.

Bernstein, S. and Brooks, C.K., 1999. Mantle xenoliths from tertiary lavas and dykes at Ubekendt Ejland, West Greenland. Geological Survey of Greenland Bulletin, 180: 152-154.

Bernstein, S., Keleman, P.B. and Brooks, C.K., 1998. Depleted spinel harzburgite xenoliths in Tertiary dykes from East Greenland; restites from high degree melting. Earth and Planetary Science Letters, 154: 221-235.

Berry, R.F., 1994. Tectonics of western Tasmania: Late Precambrian-Devonian. In: David R. Cooke and Paul A. Kitto (Editors), Contentious issues in Tasmanian geology. Geological Society of Australia Abstracts, 39: pp. 6-8.

Berry, R.F., Elliott, C.G. and Grey, D.R., 1990. Structure and tectonics of western and northern Tasmania. 10th Australian Geological Convention (Hobart), Excursion Guide E3, 53 pp.

Black, L.P., Seymour, D.B., Corbett, K.D., Cox, S.E., Streit, J.E., Bottrill, R.S., Calver, C.R., Everard, J.L., Green, G.R., McClenaghan, M.P., Pemberton, J., Taheri, J. and Turner, N.J., 1997. Dating Tasmania's oldest events. Australian Geological Survey Organisation, Record 1997/15: 57 pp.

Bodinier, J.-L., Dupuy, C. and Dostal, J., 1988. Geochemistry and petrogenesis of Eastern Pyrenean peridotites. Geochimica and Cosmochimica Acta, 52: 2893-2907.

Bodinier, J.-L., Merlet, C., Bedini, R.M., Simien, F., Remaidi, M. and Garrido, C.J., 1996. Distribution of niobium, tantalum, and other highly incompatible trace elements in the lithospheric mantle: the spinel paradox. Geochimica et Cosmochimica Acta, 60(3): 545-550.

Bonatti, E., Ottonello, G. and Hamlyn, P.R., 1986. Peridotites from the island of Zabargad (St John), Red Sea: petrology and geochemistry. Journal of Geophysical Research, 91: 599-631.

Boyd, F.R., 1989. Compositional distinction between oceanic and cratonic lithosphere. Earth and Planetary Science Letters, 96: 15-26.

Boyd, F.R., 1997. Origins of peridotite xenoliths: major element considerations. In: G. Ranalli, F.R. Luchi, C.A. Ricci and T. Tromunsdorff (Editors), High pressure and high temperature research on lithosphere and mantle materials. University of Siena, pp. 89-106.

Boyd, F.R. and Canil, D., 1997. Peridotite xenoliths from the Slave Craton, Northwest Territories (abstract), Seventh Annual Goldschmidt Conference, Houston, pp. 34-35.

Boyd, F.R. and Finnerty, A.A., 1980. Conditions of origin of natural diamonds of peridotite affinity. Journal of Geophysical Research, 85(B12): 6911-6918.

Boyd, F.R. and Mertzman, S.A., 1987. Composition and structure of the Kaapvaal lithosphere, southern Africa. In: B.O. Mysen (Editor), Magmatic Processes: Physicochemical Principles. The Geochemical Society, pp. 13-24.

Boyd, F.R., Jones, R.A. and Nixon, P.H., 1983. Mantle metasomatism: the Kimberley dunites. Carnegie Institute Washington Yearbook, 82: 330-337.

Boyd, F.R., Pokhilenko, N.P., Pearson, D.G., Mertzman, S.A., Sobolev, N.V. and Finger, L.W., 1997. Composition of the Siberian cratonic mantle: evidence from Udachnaya peridotite xenoliths. Contributions to Mineralogy and Petrology, 128: 228-246.

Brady, J.B. and McCallister, R.H., 1983. Diffusion data for clinopyroxenes from homogenisation and self-diffusion experiments. American Mineralogist, 68: 95-105.

Brandon, A.D., Creaser, R.A., Shirey, S.B. and Carlson, R.W., 1996. Osmium recycling in subduction zones. Science, 272: 861-864.

Brauns, C.M., Hergt, J.M., Woodhead, J.D. and Maas, R., 2000. Os isotopes and the origin of the Tasmanian dolerites. Journal of Petrology, 41(7): 905-918.

Brewer, T.S., Hergt, J.M., Hawkesworth, C.J., Rex, D. and Storey, B.C., 1992. Coats Land dolerites and the generation of Antarctic continental flood basalts. In: B.C. Storey, T. Alabaster and R.J. Pankhurst (Editors), Magmatism and the causes of continental break-up. Geological Society Special Publication, pp. 185-208.

Brey, G. and Green, D.H., 1975. The role of $CO_2$ in the genesis of olivine melilitite. Contributions to Mineralogy and Petrology, 49: 93-103.

Brey, G.P. and Kohler, T., 1990. Geothermobarometry in four-phase lherzolites II. New thermobarometers and practical assessment of existing thermobarometers. Journal of Petrology, 31(6): 1353-1378.

Brey, G.P., Kohler, T. and Nickel, K.G., 1990. Geothermobarometry in four-phase lherzolites I. Experimental results from 10 to 60 kb. Journal of Petrology, 31(6): 1313-1352.

Brown, A.V., 1989. Radiometric age dating. In: A.V. Brown (Editor), Geological atlas 1:50 000 Series Sheet 21 (7916S) Smithton. Explanatory Report Geological Survey of Tasmania, pp. 84.

Brown, A.V. and McClenaghan, M.P., 1982. Tertiary basaltic rocks. In: M.P. McClenaghan, N.J. Turner, P.W. Baillie, A.V. Brown, P.R. Williams and W.R. Moore (Editors), Geology of the Ringarooma-Boobyalla area. Geological Survey of Tasmania Survey, pp. 92-114.

Brueckner, H.K., 1969. Timing of ultramafic intrusions in the core zone of the Caledonides of southern Norway. American Journal of Science, 267: 195-212.

Brueckner, H.K., 1972. Interpretation of Rb-Sr ages from the Precambrian rocks of southern Norway. American Journal of Science, 272: 334-358.

Brueckner, H.K., 1974. "Mantle" Rb/Sr and $^{87}Sr/^{86}Sr$ ratios for clinopyroxenes from Norwegian garnet peridotites and pyroxenites. Earth and Planetary Science Letters, 24: 26-32.

Brueckner, H.K., 1977. A crustal origin for eclogites and a mantle origin for garnet peridotites: strontium isotopic evidence from clinopyroxenes. Contributions to Mineralogy and Petrology, 60: 1-15.

Brueckner, H.K., 1979. Precambrian ages from Geiranger-Tafjord-Grotli area of the Basal Gneiss Region, west Norway. Norsk Geologisk Tidsskrift, 59: 141-153.

Brueckner, H.K., 1998. Sinking intrusion model for the emplacement of garnet-bearing peridotites into continental collision orogens. Geology, 26(7): 631-634.

Brueckner, H.K. and Medaris, L.G., 1998. A tale of two orogens: the contrasting T-P-t history and geochemical evolution of mantle in high- and ultrahigh-pressure metamorphic terranes of the Norwegian Caledonides and the Czech Variscides. Schweiz. Mineral. Petrogr. Mitt., 78: 293-307.

Brueckner, H.K. and Medaris, L.G., 2000. A general model for the intrusion and evolution of "mantle" garnet peridotites in high-pressure and ultra-high-pressure metamorphic terranes. Journal of Metamorphic Geology, 18: 123-133.

Brueckner, H.K., Blusztajn, J. and Bakun-Czubarow, N., 1996. Trace element and Sm-Nd "age" zoning in garnets from peridotites of the Caledonian and Variscan Mountains and tectonic implications. Journal of Metamorphic Petrology, 14: 61-73.

Bryhni, I., 1966. Reconnaissance studies of gneisses, ultrabasites, eclogites and anorthosites in Outer Nordfjord, western Norway. Norges Geologiske Undersökelse, 241: 1-68.

Bryhni, I. and Green, D.H., 1970. On the occurrence of eclogites in western Norway. Contributions to Mineralogy and Petrology, 26: 12-19.

Bryhni, I. and Grimstad, E., 1970. Supracrustal and infracrustal rocks in the Gneiss Region of the Caledonides west of Breimsvatn. Norges Geologiske Undersökelse, 266: 105-140.

Bryhni, I., Bollingberg, H.J. and Graff, P.R., 1969. Eclogites in quartzo-felspathic gneisses of Nordfjord, west Norway. Norsk Geologisk Tidsskrift, 49: 193-225.

Burns, K.L., 1964. One mile geological map series-Devonport. Explanatory Report Department of Mines Tasmania: 122-123.

Burton, K.W., Schiano, P., Birck, J.L. and Allegre, C.J., 1999. Osmium isotope disequilibrium between mantle minerals in a spinel-lherzolite. Earth and Planetary Science Letters, 172: 311-322.

Burton, K.W., Schiano, P., Birck, J.L., Allegre, C.J., Rehkämper, M., Halliday, A.N. and Dawson, J.B., 2000. The distribution and behaviour of rhenium and osmium amongst mantle minerals and the age of the lithospheric mantle beneath Tanzania. Earth and Planetary Science Letters, 183: 93-106.

Cabri, L.J., 1973. New data on phase relations in the Cu-Fe-S system. Economic Geology, 68: 443-454.

Canil, D., Virgo, D. and Scarfe, C.M., 1990. Oxidation state of mantle xenoliths from British Columbia, Canada. Contributions to Mineralogy and Petrology, 104: 453-462.

Canil, D., O'Neill, H.S.C., Pearson, D.G., Rudnick, R.L., McDonough, W.F. and Carswell, D.A., 1994. Ferric iron in peridotites and mantle oxidation states. Earth and Planetary Science Letters, 123: 205-220.

Carbno, G.B. and Canil, D., 2002. Mantle structure beneath the SW Slave Craton, Canada: constraints from garnet geochemistry in the Drybones Bay Kimberlite. Journal of Petrology, 43(1): 129-142.

Carroll Webb, S.A. and Wood, B.J., 1986. Spinel-pyroxene-garnet relationships and their dependence on Cr/Al ratio. Contributions to Mineralogy and Petrology, 92: 471-480.

Carswell, D.A., 1968a. Picritic magma-residual dunite relationships in garnet peridotite at Kalskaret near Tafjord, south Norway. Contributions to Mineralogy and Petrology, 19: 97-124.

Carswell, D.A., 1968b. Possible primary upper mantle peridotite in Norwegian basal gneiss. Lithos, 1: 322-355.

Carswell, D.A., 1973. Garnet pyroxenite lens within Ugelvik layered garnet peridotite. Earth and Planetary Science Letters, 20: 347-352.

Carswell, D.A., 1974. Comparative equilibration temperatures and pressures of garnet lherzolites in Norwegian gneisses and in kimberlite. Lithos, 7: 113-121.

Carswell, D.A., 1975. Primary and secondary phlogopites and clinopyroxenes in garnet lherzolite xenoliths. Physics and Chemistry of the Earth, 9: 417-429.

Carswell, D.A., 1986. The metamorphic evolution of Mg-Cr type Norwegian garnet peridotites. Lithos, 19: 279-297.

Carswell, D.A. and Gibb, F.G.F., 1980. The equilibrium conditions and petrogenesis of European crustal garnet lherzolites. Lithos, 13: 19-29.

Carswell, D.A. and Gibb, F.G.F., 1987. Evaluation of mineral thermometers and barometers applicable to garnet lherzolite assemblages. Contributions to Mineralogy and Petrology, 95: 499-511.

Carswell, D.A., Cuthbert, S.J. and Krogh Ravna, E.J., 1999. Ultrahigh-pressure metamorphism in the Western Gneiss Region of the Norwegian Caledonides. International Geology Review, 41: 955-966.

Carswell, D.A., Griffin, W.L. and Kresten, P., 1984. Peridotite nodules from the Ngopetsoeu and Lipelaneng kimberlites, Lesotho: a crustal or mantle origin. Third International Kimberlite Conference, Clermont-Ferrand, 2, pp. 229-247.

Carswell, D.A., Harvey, M.A. and Al-Samman, A.H., 1983. The petrogenesis of contrasting Fe-Ti and Mg-Cr garnet peridotite types in the high grade gneiss complex of western Norway. Bulletin de Minèralogie, 106: 727-750.

Carswell, D.A., Krogh, E.J. and Griffin, W.L., 1985. Norwegian orthopyroxene eclogites: calculated equilibration conditions and petrogenetic implications. In: D.G. Gee and B.A. Sturt (Editors), The Caledonide Orogen - Scandinavia and Related Areas. John Wiley and Sons Ltd, London, pp. 823-841.

Chen, Y.D., Pearson, N.J., O'Reilly, S.Y. and Griffin, W.L., 1991. Applications of olivine-orthopyroxene-spinel oxygen geobarometers to the redox state of the upper mantle. Journal of Petrology, Special Lherzolite Issue: 291-306.

Cocker, J.D., 1982. Rb-Sr geochronology and Sr isotopic composition of Devonian granitoids, eastern Tasmania. Journal Geological Society of Australia, 29: 139-157.

Cohen, A.S., 1996. Separation of osmium from geological materials by solvent extraction for analysis by thermal ionisation mass spectrometry. Anal. Chim. Acta, 332: 269-275.

Coleman, R.G. and Wang, X., 1995. Overveiw of the geology and tectonics of UHPM. In: R.G. Coleman and X. Wang (Editors), Ultrahigh pressure metamorphism. Cambridge University Press, Cambridge, pp. 1-33.

Colhoun, E.A., 1989. Quaternary. In: C.F. Burrett and E.L. Martin (Editors), Geology and mineral resources of Tasmania. Special Publication Geological Society of Australia, pp. 410-418.

Collins, C.D.N., 1991. The nature of the crust-mantle boundary under Australia from seismic evidence. In: B.J. Drummond (Editor), The Australian lithosphere. Special Publication Geological Society of Australia, pp. 67-80.

Coltorti, M., Bonadiman, C., Hinton, R.W., Siena, F. and Upton, B.G.J., 1999. Carbonatite metasomatism of the oceanic upper mantle: evidence from clinopyroxenes and glasses in ultramafic xenoliths of Grande Comore, Indian Ocean. Journal of Petrology, 40(1): 133-165.

Corbett, K., 1994. Stratigraphic mapping, Tyennan connections, Cambrian orogenies, the Arthur Lineament, and the tectonic context of the Mount Read Volcanics. A fresh look at Western Tasmania. Contentious issues in Tasmanian geology. Geological Society of Australia Abstracts, 39: 35-37.

Cox, S.F., 1989. Cape Wickham. In: C.F. Burrett and E.L. Martin (Editors), Geology and Mineral Resources of Tasmania: A Bicentennial Volume. Special Publication Geological Society of Australia, pp. 26-27.

Craig, J.R., 1973. Pyrite-pentlandite assemblages and other low temperature relations in the Fe-Ni-S system. American Journal of Science, 273A, 496-510.

Craig, J.R. and Scott, S.D., 1974. Sulfide phase equilibria. In: P.H. Ribbe (Editor), Sulfide mineralogy. Mineralogical Society Of America Short Course Notes, 1, pp. CS-1–CS-110.

Cull, J.P., 1982. An appraisal of Australian heat-flow data. BMR Journal of Australian Geology and Geophysics, 7: 11-21.

Cull, J.P. and Conley, D., 1983. Geothermal gradients and heat flow in Australia sedimentary basins. BMR Journal of Australian Geology and Geophysics, 8: 329-337.

Cuthbert, S.J., Harvey, M.A. and Carswell, D.A., 1983. A tectonic model for the metamorphic evolution of the Basal Gneiss Complex, Western South Norway. Journal of Metamorphic Geology, 1: 63-90.

Cuthbert, S.J., Carswell, D.A., Krogh-Ravna, E.J. and Wain, A., 2000. Eclogites and eclogites in the Western Gneiss Region, Norwegian Caledonides. Lithos, 52: 165-195.

Dalton, J.A. and Wood, B.J., 1993. The compositions of primary carbonate melts and their evolution through wallrock interaction in the mantle. Earth and Planetary Science Letters, 119: 511-525.

Danckwerth, P.A. and Newton, R.C., 1978. Experimental determination of spinel peridotite to garnet peridotite reaction in the system $MgO$-$Al_2O_3$-$SiO_2$ in the range 900-1100°C and $Al_2O_3$ isopleths of enstatite in the spinel field. Contributions to Mineralogy and Petrology, 66: 189-201.

Dawson, J.B., 1980. Kimberlites and their xenoliths. Springer-Verlag, Berlin, 252 pp.

Dawson, J.B., 1984. Contrasting types of upper-mantle metasomatism? In: J.Kornprobst (Editor), Kimberlites II: the mantle and crust-mantle relationships. Elsevier Science Publishers, Amsterdam, pp. 289-294.

Debayle, E. and Kennett, B.L.N., 2000. The Australian continental upper mantle: structure and deformation inferred from surface waves. Journal of Geophysical Research, 105(B11): 25423-25450.

Deines, P. and Harris, J.W., 1995. Sulfide inclusion chemistry and carbon isotopes of African diamonds. Geochimica et Cosmochimica Acta, 59(15): 3173-3188.

Dobrzhinetskaya, L.F., Eide, E.A., Larsen, R.B., Sturt, B.A., Tronnes, R.G., Taylor, W.R. and Posukhova, T.V., 1995. Microdiamonds in high-grade metamorphic rocks from the Western Gneiss Region, Norway. Geology, 23: 597-600.

Dromgoole, E.L. and Pasteris, J.D., 1987. Interpretation of the sulfide assemblages in a suite of xenoliths from Kilbourne Hole and Porillo Maar, New Mexico. In: E. Morros and J.D. Pasteris (Editors), Mantle metasomatism and alkaline magmatism. Geological Society of America, pp. 25-46.

Drummond, B.J., Barton, T.J., Korsch, R.J., Rawlinson, N., Yeates, A.N., Collins, C.D.N. and Brown, A.V., 2000. Evidence for crustal extension and inversion in eastern Tasmania, during the Neoproterozoic and Early Palaeozoic. Tectonophysics, 329: 1-21.

Drury, M.R., van Roermund, H.L.M., Carswell, D.A., de Smet, J.H., van den Berg, A.P. and Vlaar, N.J., 2001. Emplacement of deep upper-mantle rocks into cratonic lithosphere by convection and diapiric upwelling. Journal of Petrology, 42(1): 131-140.

Duncan, R.A., Hooper, P.R., Rehacek, J., Marsh, J.S. and Duncan, A.R., 1997. The timing and duration of the Karoo igneous event, southern Gondwana. Journal of Geophysical Research, 102: 18127-18138.

Dyar, M.D., McGuire, A.V. and Harrell, M.D., 1992. Crystal chemistry of iron in two styles of metasomatism in the upper mantle. Geochimica et Cosmochimica Acta, 56: 2579-2586.

Dyar, M.D., McGuire, A.V. and Ziegler, R.D., 1989. Redox equilibria and crystal chemistry of coexisting minerals from spinel lherzolite mantle xenoliths. American Mineralogist, 74: 969-980.

Eggler, D.H., Meen, J.K., Welt, F., Dudas, F.O., Furlong, K.P., McCallum, M.E. and Carlson, R.W., 1988. Tectonomagmatism of the Wyoming Province. Colorado School of Mines Quarterly, 83: 25-40.

Ellis, D.J. and Green, D.H., 1979. An experimental study of the effect of Ca upon garnet-clinopyroxene Fe-Mg exchange equilibria. Contributions to Mineralogy and Petrology, 71: 13-22.

Encarnacion, J., Fleming, T.H., Elliot, D.H. and Eales, H.V., 1996. Synchronous emplacement of Ferrar and Karoo dolerites and the early break-up of Gondwana. Geology, 24: 535-538.

Ernst, W.G., Liou, J.G. and Coleman, R.G., 1995. Comparative petrotectonic study of five Eurasian ultrahigh-pressure metamorphic complexes. International Geology Review, 37: 191-211.

Eskola, P., 1921. On the eclogites of Norway. Skrift. Videnskaps-selsk. Christiana Mat.-Naturv, K1 18, 1-118.

Evans, B.W. and Trommsdorff, V., 1978. Petrogenesis of garnet lherzolite, Cima di Gagnone, Lepontine Alps. Earth and Planetary Science Letters, 40: 333-348.

Ewart, A., 1989. Fractionation, assimilation and source melting: a petrogenetic overview. In: R.W. Johnson (Editor), Intraplate volcanism in eastern Australia and New Zealand. Cambridge University Press, Cambridge, pp. 249-253.

Faure, G., Pace, K.K. and Elliot, D.H., 1982. Systematic variations of $^{87}Sr/^{86}Sr$ ratios and major element concentrations in the Kirkpatrick Basalt of Mount Falla, Queen

Alexandra range, Transantarctic Mountains. In: C. Craddock (Editor), Antarctic Geoscience. University of Wisconsin Press, Madison, pp. 715-723.

Finlayson, D.M., Owen, A., Johnstone, D. and Wake-Dyster, K.D., 1993. Moho and petrologic crust-mantle boundary coincide under southeastern Australia. Geology, 21: 707-710.

Fleming, T.H., Foland, K.A. and Elliot, D.H., 1995. Isotopic and chemical constraints on the crustal evolution and source signature of Ferrar magmas, north Victoria Land, Antarctica. Contributions to Mineralogy and Petrology, 121: 217-236.

Foden, J., Song, S.H., Turner, S., Elburg, M., Smith, P.B., Van der Steldt, B. and Van Penglis, D., 2002. Geochemical evolution of lithospheric mantle beneath S.E. South Australia. Chemical Geology, 182: 663-695.

Fraser, D.G., Watt, F., Grime, G.W. and Takacs, J., 1984. Direct determination of strontium enrichment on grain boundaries in a garnet lherzolite xenolith by proton microprobe analysis. Nature, 312: 352-354.

Frey, F.A. and Green, D.H., 1974. The mineralogy, geochemistry and origin of lherzolite inclusions in Victorian basanites. Geochimica et Cosmochimica Acta, 39: 1023-1059.

Frey, F.A. and Prinz, M., 1978. Ultramafic inclusions from San Carlos, Arizona: petrologic and geochemical data bearing of their petrogenesis. Earth and Planetary Science Letters, 38: 129-176.

Frick, C., 1973. The sulphides in griquaite and garnet-peridotite xenoliths in kimberlite. Contributions to Mineralogy and Petrology, 39: 1-16.

Fujii, T., 1976. Solubility of $Al_2O_3$ in enstatite coexisting with forsterite and spinel. Carnegie Institute Washington Yearbook, 75: 566-571.

Gaal, G. and Gorbatschev, R., 1987. An outline of the Precambrian evolution of the Baltic Shield. Precambrian Research, 35: 15-52.

Gaetani, G.A. and Grove, T.L., 1999. Wetting of mantle olivine by sulfide melt: implications for Re/Os ratios in mantle peridotite and late-stage core formation. Earth and Planetary Science Letters, 169: 147-163.

Garuti, G., Gorgoni, C. and Sighinolfi, G.P., 1984. Sulfide mineralogy and chalcophile and siderophile element abundances in the Ivrea-Verbano mantle peridotites (Western Italian Alps). Earth and Planetary Science Letters, 70: 69-87.

Gasparik, T. and Newton, R.C., 1984. The reversed alumina contents of orthopyroxene in equilibrium with spinel and forsterite in the system $MgO$-$Al_2O_3$-$SiO_2$. Contributions to Mineralogy and Petrology, 85: 186-196.

Gast, P.W., 1968. Trace element fractionation and the origin of tholeiitic and alkaline magma types. Geochimica et Cosmochimica Acta, 32: 1057-1086.

Gebauer, D., Lappin, M.A., Grünenfelder, M. and Wyttenbach, A., 1985. The age and origin of some Norwegian eclogites. A U-Pb zircon and REE study. Chemical Geology, 52: 227-247.

Godard, M., Jousselin, D. and Bodinier, J.-L., 2000. Relationships between geochemistry and structure beneath a palaeo-spreading centre: a study of the mantle section in the Oman ophiolite. Earth and Planetary Science Letters, 180: 133-148.

Green, D.H. and Wallace, M.E., 1988. Mantle metasomatism by ephemeral carbonatite melts. Nature, 336: 459-462.

Green, H.W. and Burnley, P.C., 1988. Pyroxene-spinel symplectites: origin by decomposition of garnet confirmed. EOS, 69(44): 1514.

Green, D.H. and Mysen, B.O., 1972. Genetic relationship between eclogite and hornblende + plagioclase pegmatite in western Norway. Lithos, 5: 147-161.

Grégoire, M., Moine, B.N., O'Reilly, S.Y., Cottin, J.Y. and Giret, A., 2000. Trace element residence and partitioning in mantle xenoliths metasomatised by highly alkaline, silicate- and carbonate-rich melts (Kerguelen Islands, Indian Ocean). Journal of Petrology, 41(4): 477-509.

Griffin, W.L., 1987. 'On the eclogites of Norway' - 65 years later. Mineralogical Magazine, 51(361): 333-343.

Griffin, W.L. and Brueckner, H.K., 1980. Caledonian Sm-Nd ages and a crustal origin for Norwegian eclogites. Nature, 285: 319-321.

Griffin, W.L. and Brueckner, H.K., 1985. REE, Rb-Sr and Sm-Nd studies of Norwegian eclogites. Chemical Geology, 52: 249-271.

Griffin, W.L. and Mørk, M.B.E., 1981. Eclogites and basal gneisses in western Norway., Uppsala Caledonide Symposium. Mineralogisk-Geologisk Museum, Excursion Guide B1, 88 pp.

Griffin, W.L. and O'Reilly, S.Y., 1987a. The composition of the lower crust and the nature of the continental Moho-xenolith evidence. In: P.H. Nixon (Editor), Mantle Xenoliths. John Wiley and Sons Ltd, New York, pp. 413-430.

Griffin, W.L. and O'Reilly, S.Y., 1987b. Is the continental Moho the crust-mantle boundary? Geology, 15: 241-244.

Griffin, W.L. and Qvale, H., 1985. Superferrian eclogites and the crustal origin of garnet peridotites, Almklovdalen, Norway. In: D.G. Gee and B.A. Sturt (Editors), The Caledonide Orogen - Scandinavia and Related Areas. John Wiley and Sons Ltd, London, pp. 803-812.

Griffin, W.L. and Råheim, A. 1973. Convergent metamorphism of eclogites and dolerites, Kristiansund area, Norway. Lithos, 6: 21-40.

Griffin, W.L., O'Reilly, S.Y. and Ryan, C.G., 1999a. The composition and origin of subcontinental lithospheric mantle. In: Y. Fei, C.M. Bertka and B.O. Mysen (Editors), Mantle petrology: field observations and high pressure experimentation: a tribute to Francis F. (Joe) Boyd. The Geochemical Society, pp. 13-45.

Griffin, W.L., O'Reilly, S.Y. and Stabel, A., 1988. Mantle metasomatism beneath western Victoria, Australia II: Isotopic geochemistry of Cr-diopside lherzolites and Al-augite pyroxenites. Geochimica et Cosmochimica Acta, 52: 449-459.

Griffin, W.L., Sutherland, F.L. and Hollis, J.D., 1987. Geothermal profile and crust-mantle transition beneath east-central Queensland: volcanology, xenolith petrology and seismic data. Journal of Volcanology and Geothermal Research, 31: 177-203.

Griffin, W.L., Wass, S.Y. and Hollis, J.D., 1984. Ultramafic xenoliths from Bullenmerri and Gnotuk Maars, Victoria, Australia: Petrology of a subcontinental crust-mantle transition. Journal of Petrology, 25(1): 53-87.

Griffin, W.L., Andi, Z., O'Reilly, S.Y. and Ryan, C.G., 1998a. Phanerozoic evolution of the lithosphere beneath the Sino-Korean craton. In: M.F.J. Flower, S.L. Chung, C.H. Lo and Y.Y. Lee (Editors), Mantle dynamics and plate interactions in east Asia. Geodynamics Series 27. American Geophysical Union, Washington, D.C., pp. 107-126.

Griffin, W.L., Spetsius, Z., Pearson, N.J. and O'Reilly, S.Y., 2001a. In-situ Re-Os analysis of sulfide inclusions in kimberlitic olivine: new constraints on depletion events in the Siberian lithospheric mantle. Geochemistry Geophysics Geosystems (subm.).

Griffin, W.L., Austrheim, H., Brastad, K., Bryhni, I., Krill, A.G., Krogh, H.K., Mørk, M.B.E., Qvale, H. and Tørudbakken, B., 1985. High-pressure metamorphism in the Scandinavian Caledonides. In: D.G. Gee and B.A. Sturt (Editors), The Caledonide Orogen - Scandinavia and Related Areas. John Wiley and Sons Ltd, London, pp. 783-801.

Griffin, W.L., Cousens, D.R., Ryan, C.G., Sie, S.H. and Suter, G.F., 1989. Ni in chrome pyrope garnets: a new geothermometer. Contributions to Mineralogy and Petrology, 103: 199-202.

Griffin, W.L., O'Reilly, S.Y., Ryan, C.G., Gaul, O. and Ionov, D.A., 1998b. Secular variation in the composition of subcontinental lithospheric mantle: geophysical and geodynamic implications. In: J. Braun, J.C. Dooley, B.R. Goleby, R.D.van der Hilst and C.T. Klootwijk (Editors), Structure and evolution of the Australian continent. American Geophysical Union, Washington D.C., pp. 1-26.

Griffin, W.L., Fisher, N.I., Friedman, J.H., O'Reilly, S.Y. and Ryan, C.G., 2001b. Cr-pyrope garnets in the lithospheric mantle. II. Compositional populations and their distribution in time and space. Geochemistry Geophysics Geosystems (submitted).

Griffin, W.L., Shee, S.R., Ryan, C.G., Win, T.T. and Wyatt, B.A., 1999b. Harzburgite to lherzolite and back again: metasomatic processes in ultramafic xenoliths from the Wesselton kimberlite, Kimberley, South Africa. Contributions to Mineralogy and Petrology, 134: 232-250.

Griffin, W.L., Smith, D., Ryan, C.G., O'Reilly, S.Y. and Win, T.T., 1996. Trace-element zoning in mantle minerals: metasomatism and thermal events in the upper mantle. The Canadian Mineralogist, 34: 1179-1193.

Griffin, W.L., Pearson, N.J., Belousova, E., Jackson, S.E., van Achterbergh, E., O'Reilly, S.Y. and Shee, S.R., 2000. The Hf isotope composition of cratonic mantle: LAM-MC-ICP-MS analysis of zircon megacrysts in kimberlites. Geochimica et Cosmochimica Acta, 64(1): 133-147.

Griffin, W.L., O'Reilly, S.Y., Abe, N., Aulbach, S., Davies, R.M., Pearson, N.J., Doyle, B.J. and Kivi, K., 2002. The origin and evolution of Archean lithospheric mantle. Precambrian Research (subm.).

Griffin, W.L., Ryan, C.G., Kaminsky, F.V., O'Reilly, S.Y., Natapov, L.M., Win, T.T., Kinny, P.D. and Ilupin, I.P., 1999c. The Siberian lithosphere traverse: mantle terranes and the assembly of the Siberian Craton. Tectonophysics, 310: 1-35.

Griffin, W.L., Doyle, B.J., Ryan, C.G. Pearson, N.J., O'Reilly, S.Y., Davies, R., Kivi, K., van Achterbergh, E. and Natapov, L.M., 1999d. Layered mantle lithosphere in the Lac de Gras area, Slave Craton: composition, structure and origin. Journal of Petrology, 40(5), 705-727.

Guo, J., Griffin, W.L. and O'Reilly, S.Y., 1999. Geochemistry and origin of sulphide minerals in mantle xenoliths: Qilin, Southeastern China. Journal of Petrology, 40(7): 1125-1149.

Haggerty, S.E. and Tompkins, L.A., 1983. Redox state of Earth's upper mantle from kimberlitic ilmenites. Nature, 303: 295-300.

Hanghøj, K., Keleman, P., Bernstein, S., Blusztajn, J. and Frei, R., 2001. Osmium isotopes in the Wiedemann Fjord mantle xenoliths: a unique record of cratonic mantle formation by melt depletion in the Archaean. Geochemistry Geophysics Geosystems, 2.

Harley, S.L., 1984. An experimental study of the partitioning of Fe and Mg between garnet and orthopyroxene. Contributions to Mineralogy and Petrology, 86: 359-373.

Harley, S.L. and Green, D.H., 1982. Garnet-orthopyroxene barometry for granulites and peridotites. Nature, 300: 697-701.

Hart, S.R. and Zindler, G.A., 1986. In search of a bulk-Earth composition. Chemical Geology, 57: 247-267.

Harte, B., 1977. Rock nomenclature with particular relation to deformation and recrystallisation textures in olivine-bearing xenoliths. Journal of Geology, 85: 279-288.

Harte, B., 1987. Metasomatic events recorded in mantle xenoliths: an overview. In: P.H. Nixon (Editor), Mantle xenoliths. John Wiley and Sons, New York, pp. 625-640.

Hemingway, B.S., Bohlen, S.R., Hankins, W.B., Westren, E.J. and Kuskov, O.L., 1998. Heat capacity and thermodynamic properties for coesite and jadeite, reexamination of the quartz-coesite equilibrium boundary. American Mineralogist, 83: 419-433.

Hergt, J.M., Peate, D.W. and Hawkesworth, C.J., 1991. The petrogenesis of Mesozoic Gondwana low-Ti flood basalts. Earth and Planetary Science Letters, 105: 134-148.

Hergt, J.M., Chappell, B.W., McCulloch, M.T., McDougall, I. and Chivas, A.R., 1989. Geochemical and isotopic constraints on the origin of the Jurassic dolerites of Tasmania. Journal of Petrology, 30(4): 841-883.

Hirose, K. and Kushiro, I., 1993. Partial melting of dry peridotites at high pressures: determination of compositions of melts segregated from peridotite using aggregates of diamond. Earth and Planetary Science Letters, 114: 477-489.

Hoal, B.G., Hoal, K.E.O., Boyd, F.R. and Pearson, D.G., 1995. Age constraints on crustal and mantle lithosphere beneath the Gibeon kimberlite field, Namibia. South African Journal of Geology, 98(2): 112-118.

Hoal, K.E.O., Hoal, B.G., Erlank, A.J. and Shimizu, N., 1994. Metasomatism of the mantle lithosphere recorded by rare earth elements in garnets. Earth and Planetary Science Letters, 126: 303-313.

Hofmann, A.W., 1997. Mantle geochemistry: the message from oceanic volcanism. Nature, 385: 219-229.

Ionov, D.A., Kramm, U. and Stosch, H.-G., 1992. Evolution of the upper mantle beneath the southern Baikal rift zone: an Sr-Nd isotope study of xenoliths from the Bartoy volcanoes. Contributions to Mineralogy and Petrology, 111: 235-247.

Ionov, D.A., Dupuy, C., O'Reilly, S.Y., Kopylova, M.G. and Genshaft, Y.S., 1993. Carbonated peridotite xenoliths from Spitsbergen: implications for trace element

signature of mantle carbonate metasomatism. Earth and Planetary Science Letters, 119: 283-297.

Jacobsen, S.B. and Wasserburg, G.J., 1980. Nd and Sr isotopes of the Norwegian garnet peridotites and eclogites. EOS, 61(17): 389.

Jagoutz, E., Palme, H., Baddenhausen, H., Blum, K., Cendales, M., Dreibus, G., Spettel, B., Lorenz, V. and Wänke, H., 1979. The abundances of major, minor and trace elements in the earth's mantle as derived from primitive ultramafic nodules. Proceedings of the Tenth Lunar Planetary Science Conference, pp. 2031-2050.

Jamtveit, B., 1984. High-P metamorphism and deformation of the Gurskebotn garnet peridotite, Sunnmøre, western Norway. Norsk Geologisk Tidsskrift, 64: 97-110.

Jamtveit, B., 1987a. Metamorphic evolution of the Eiksunddal eclogite complex, western Norway, and some tectonic implications. Contributions to Mineralogy and Petrology, 95: 82-99.

Jamtveit, B., 1987b. Magmatic and metamorphic controls on chemical variations within the Eiksunddal eclogite complex, Sunnmøre, western Norway. Lithos, 20: 369-389.

Jamtveit, B., Carswell, D.A. and Mearns, E.W., 1991. Chronology of the high-pressure metamorphism of Norwegian garnet peridotites/pyroxenites. Journal of Metamorphic Geology, 9: 125-139.

Janse, A.J.A., 1994. Is Clifford's Rule still valid? Affirmative examples from around the world. In: H.O.A. Meyer and O. Leonardos (Editors), Diamonds: characterisation, genesis and exploration. Dept. Nacional da Prod. Mineral., Brazilia, pp. 215-235.

Jochum, K.P., McDonough, W.F., Palme, H. and Spettel, B., 1989. Compositional constraints on the continental lithospheric mantle from trace elements in spinel peridotite xenoliths. Nature, 350: 548-550.

Johnson, K.T., Dick, H.J.B. and Shimizu, N., 1990. Melting in the oceanic upper mantle: an ion microprobe study of diopsides in abyssal peridotites. Journal of Geophysical Research, 95(B3): 2661-2678.

Jordan, T.H., 1979. Mineralogies, densities and seismic velocities of garnet lherzolites and their geophysical implications. In: F.R. Boyd and H.O.A. Meyer (Editors), The Mantle Sample: Inclusions in Kimberlites and Other Volcanics, Proceedings of the Second International Kimberlite Conference. American Geophysical Union, Washington D.C., pp. 1-14.

Kelley, S.P. and Wartho, J.-A., 2000. Rapid kimberlite ascent and the significance of Ar-Ar ages in xenolith phlogopites. Science, 289: 609-611.

Kesson, S.E. and Ringwood, A.E., 1989. Slab-mantle interactions I. Sheared and refertilised garnet peridotites - samples of Wadati-Benioff zones? Chemical Geology, 78: 83-96.

Kogarko, L.N., Henderson, C.M.B. and Pacheno, H., 1995. Primary Ca-rich carbonatite magma and carbonate-silicate-sulfide liquid immiscibility in the upper mantle. Contributions to Mineralogy and Petrology, 121: 267-274.

Kohler, T.P. and Brey, G.P., 1990. Calcium exchange between olivine and clinopyroxene calibrated as a geothermobarometer for natural peridotites from 2 to 60 kb with applications. Geochimica et Cosmochimica Acta, 54: 2375-2388.

Kretz, R., 1982. Transfer and exchange equilibria in a portion of the pyroxene quadrilateral as deduced from natural and experimental data. Geochimica et Cosmochimica Acta, 46: 411-421.

Krogh, E.J., 1977. Evidence of Precambrian continent-continent collision in Western Norway. Nature, 267: 17-19.

Krogh, E.J., 1988. The garnet-clinopyroxene Fe-Mg geothermometer - a reinterpretation of existing experimental data. Contributions to Mineralogy and Petrology, 99: 44-48.

Krogh, E.J. and Carswell, D.A., 1995. HP and UHP eclogites and garnet peridotites in the Scandinavian Caledonides. In: R.G. Coleman and X. Wang (Editors), Ultrahigh Pressure Metamorphism. Cambridge University Press, Cambridge, pp. 244-299.

Krogh, E.J., Mysen, B.O. and Davis, G.L., 1974. A Palaeozoic age for the primary minerals of a Norwegian eclogite. Carnegie Institution Washington Yearbook, 73: 575-576.

Kullerud, L., Törudbakken, B. and Ilebekk, S., 1986. A compilation of radiometric age determinations from the Western Gneiss Region, South Norway. Norges Geologiske Undersøkelse, 406: 17-42.

Kullerud, G., Yund, R.A. and Moh, G.H., 1969. Phase relations in the Cu-Fe-S, Cu-Ni-S, and Fe-Ni-S systems. Economic Geology, 4: 323-343.

Kushiro, I., Yoder Jr, H.S. and Mysen, B.O., 1976. Viscosities of basalt and andesite melts at high pressures. Journal of Geophysical Research, 81(35): 6351-6356.

Lambert, D.D., Foster, J.G., Frick, L.R., Li, C. and Naldrett, A.J., 1999. Re-Os isotopic systematics of the Voisey's Bay Ni-Cu-Co magmatic arc system, Labrador, Canada. Lithos, 47: 69-88.

Lanyon, R., Varne, R. and Crawford, A.J., 1993. Tasmanian Tertiary basalts, the Balleny plume, and opening of the Tasman Sea (southwest Pacific Ocean). Geology, 21: 555-558.

Lappin, M.A., 1966. The field relationships of basic and ultrabasic masses in the basal gneiss complex of Stadlandet and Almklovdalen, Nordfjord, southwestern Norway. Norsk Geologisk Tidsskrift, 46(4): 439-496.

Lappin, M.A., 1974. Eclogites from the Sunndal-Grubse ultramafic mass, Almklovdalen, Norway and the T-P history of the Almklovdalen masses. Journal of Petrology, 15(3): 567-601.

Lappin, M.A. and Smith, D.C., 1978. Mantle-equilibrated orthopyroxene eclogite pods from the basal gneisses in the Selje district, western Norway. Journal of Petrology, 19: 530-584.

Lappin, M.A., Pidgeon, R.T. and van Breeman, O., 1979. Geochronology of basal gneisses and mangerite syenites of Stadtlandet, west Norway. Norsk Geologisk Tidsskrift, 59: 161-181.

Leaman, D.E., 1992. Finding Cambrian keys: an essay in controversy, prospectivity and tectonic implications. Geological Survey of Tasmania Bulletin, 70: 58-69.

Leaman, D.E., 1994a. Geological note. The Tamar Fracture System in Tasmania: does it exist? Australian Journal of Earth Sciences, 41: 73-74.

Leaman, D.E., 1994b. Tectonic history of Tasmania from the Proterozoic to the Devonian-discussion session. In: David R. Cooke and Paul A. Kitto (Editors), Contentious issues in Tasmanian geology. Geological Society of Australia Abstracts, 39: 9-12.

Leaman, D.E. and Richardson, R.G., 1989. Production of a residual gravity field map for Tasmania and some implications. Exploration Geophysics, 20: 181-184.

Lee, C.-T. and Rudnick, R., 1999. Compositionally stratified cratonic lithosphere: petrology and geochemistry of peridotite xenoliths from the Labait volcano, Tanzania. In: J.J. Gurney, J.L. Gurney, M.D. Pascoe and S.H. Richardson (Editors), Proceedings of Seventh International Kimberlite Conference, Capetown, pp. 503-521.

Lenoir, X., Garrido, C.J., Bodinier, J.-L. and Dautria, J.-M., 2000. Contrasting lithospheric mantle domains beneath the Massif Central (France) revealed by geochemistry of peridotite xenoliths. Earth and Planetary Science Letters, 181: 359-375.

Lindner, M., Leich, D.A., Russ, G.P., Bazan, J.M. and Borg, R.G., 1989. Direct determination of the half-life of $^{187}$Re. Geochimica et Cosmochimica Acta, 53: 1597-1606.

Lindsley, D.H. and Dixon, S.A., 1976. Diopside-enstatite equilibria at 850 to 1400°C, 5 to 35 kb. American Journal of Science, 276: 1285-1301.

Longerich, H.P., Jackson, S.E. and Günther, D., 1996. Laser ablation inductively coupled plasma mass spectrometric transient signal data acquisition and analyte concentration calculation. Journal of Analytical Atomic Spectroscopy, 11: 899-904.

Lorand, J.P., Keays, R.R. and Bodinier, J.-L., 1993. Copper and noble metal enrichments across the lithosphere-asthenosphere boundary of mantle daipirs: evidence from the Lanzo lherzolite massif. Journal of Petrology, 34(6): 1111-1140.

Loubet, M., Shimizu, N. and Allègre, C.J., 1975. Rare earth elements in alpine peridotites. Contributions to Mineralogy and Petrology, 53: 1-12.

Ludwig, K.R., 1999. Isoplot/Ex version 2.00; a geochronological toolkit for Microsoft Excel. Berkeley Geochronological Center Special Publication, 1a: 46 pp.

Lux, D.R., 1985. K/Ar ages from the Basal Gneiss Region, Stadlandet area, western Norway. Norsk Geologisk Tidsskrift, 65: 277-286.

Maaløe, S. and Aoki, K., 1977. The major element composition of the upper mantle estimated from the composition of lherzolites. Contributions to Mineralogy and Petrology, 63: 161-173.

Mattioli, G.S. and Wood, B.J., 1988. Magnetite activities across the $MgAl_2O_4$-$Fe_2O_4$ spinel join, with application to thermobarometric estimates of upper mantle oxygen fugacity. Contributions to Mineralogy and Petrology, 98: 148-162.

Mattioli, G.S., Baker, M.B., Rutter, M.J. and Stolper, E.M., 1989. Upper mantle oxygen fugacity and its relationship to metasomatism. Journal of Geology, 97: 521-536.

McBride, J.S., Lambert, D.D., Greig, A. and Nicholls, I.A., 1996. Multistage evolution of Australian subcontinental mantle: Re-Os isotopic constraints from Victorian mantle xenoliths. Geology, 24(7): 631-634.

McDonough, W.F. and Sun, S.-s., 1995. The composition of the Earth. Chemical Geology, 120: 223-253.

McDougall, I. and Green, D.H., 1964. Excess radiogenic argon in pyroxenes and isotopic ages on minerals from Norwegian eclogites. Norsk Geologisk Tidsskrift, 44: 183-196.

McKay, D.B. and Mitchell, R.H., 1988. Abundance and distribution of gallium in some spinel and garnet lherzolites. Geochimica et Cosmochimica Acta, 52: 2867-2870.

McKenzie, D. and Bickle, M.J., 1988. The volume and composition of melt generated by extension of the lithosphere. Journal of Petrology, 29(3): 625-679.

Mearns, E.W., 1984. Isotopic studies of crustal evolution in western Norway. Unpubl. PhD thesis, University of Aberdeen.

Mearns, E.W., 1986. Sm-Nd ages for Norwegian garnet peridotite. Lithos, 19: 269-278.

Mearns, E.W. and Lappin, M.A., 1982. A Sm-Nd isotopic study of "internal" and "external" eclogites, garnet lherzolite and grey gneiss from Almklovdalen, western Norway. Terra Cognita, 2: 324.

Medaris, L.G., 1980. Convergent metamorphism of eclogite and garnet-bearing ultramafic rocks at Lien, West Norway. Nature, 283: 470-472.

Medaris, L.G., 1984. A geothermobarometric investigation of garnet peridotites in the Western Gneiss Region of Norway. Contributions to Mineralogy and Petrology, 87: 72-86.

Medaris, L.G., 1999. Garnet peridotites in Eurasian high-pressure and ultrahigh-pressure terranes: a diversity of origins and thermal histories. International Geology Review, 41: 799-815.

Medaris, L.G. and Carswell, D.A., 1990. The petrogenesis of Mg-Cr garnet peridotites in European metamorphic belts. In: D.A. Carswell (Editor), Eclogite Facies Rocks. Chapman and Hall, New York,, pp. 260-290.

Meisel, T., Biino, G.G. and Nagler, T.F., 1996a. Re-Os, Sm-Nd, and rare earth element evidence for Proterozoic oceanic and possible subcontinental lithosphere in tectonised ultramafic lenses from the Swiss Alps. Geochimica et Cosmochimica Acta, 60(14): 2583-2593.

Meisel, T., Walker, R.J. and Morgan, J.W., 1996b. The osmium isotopic composition of the Earth's primitive upper mantle. Nature, 383: 517-520.

Meisel, T., Walker, R.J., Irving, A.J. and Lorand, J.-P., 2001. Osmium isotopic compositions of mantle xenoliths: a global perspective. Geochimica et Cosmochimica Acta, 65(8): 1311-1323.

Menzies, M.A., 1976. Rare earth geochemistry of fused ophiolitic and alpine lherzolites-I. Othris, Lanzo and Troodos. Geochimica et Cosmochimica Acta, 40: 645-656.

Menzies, M.A., 1990a. Petrology and geochemistry of the continental mantle. In: M.A. Menzies (Editor), Continental mantle. Clarendon Press, Oxford, pp. 31-54.

Menzies, M.A., 1990b. Archaean, Proterozoic and Phanerozoic lithospheres. In: M.A. Menzies (Editor), Continental mantle. Clarendon Press, Oxford, pp. 67-86.

Menzies, M.A. and Dupuy, C., 1991. Orogenic massifs: protolith, process and provenance. Journal of Petrology, Special Lherzolites Issue: 1-16.

Menzies, M.A., Rogers, N.W., Tindle, A. and Hawkesworth, C.J., 1987. Metasomatic enrichment processes in lithospheric peridotites, an effect of asthenosphere-

lithosphere interaction. In: M.A. Menzies and C.J. Hawkesworth (Editors), Mantle metasomatism. Academic Press Inc., London, pp. 313-361.

Milligan, P.K. and Tarlowski, C., 1999. Magnetic anomaly map of Australia (third edition), scale 1:5 000 000. Australian Geological Survey Organisation, Canberra.

Misra, K.C. and Fleet, M.E., 1973. The chemical compositions of synthetic and natural pentlandite assemblages. Economic Geology, 68, 518-539.

Molzahn, M., Reisberg, L. and Wörner, G., 1996. Os, Sr, Nd, Pb, O isotope and trace element data from the Ferrar flood basalts, Antarctica: evidence for an enriched subcontinental lithospheric source. Earth and Planetary Science Letters, 144: 529-546.

Moore, A.C. and Qvale, H., 1977. Three varieties of alpine-type ultramafic rocks in the Norwegian Caledonides and Basal Gneiss Complex. Lithos, 10: 149-161.

Mori, T and Green, D.H., 1978. Laboratory duplication of phase equilibria observed in natural garnet lherzolites. Journal of Geology, 86: 83-97.

Mørk, M.B.E. and Mearns, E.W., 1986. Sm-Nd isotopic systematics of a gabbro-eclogite transition. Lithos, 19: 255-267.

Murray, C.G., Scheibner, E. and Walker, R.J., 1989. Regional geological interpretation of a digital coloured residual Bouguer gravity image of eastern Australia with a wavelength cut-off of 250 km. Australian Journal of Earth Sciences, 36: 423-449.

Navon, O. and Stolper, E., 1987. Geochemical consequences of melt percolation: the upper mantle as a chromatographic column. Journal of Geology, 95(3): 285-307.

Nickel, K.G. and Green, D.H., 1985. Empirical geothermobarometry for garnet peridotites and implications for the nature of the lithosphere, kimberlites and diamonds. Earth and Planetary Science Letters, 73: 158-170.

Nicolas, A., Bouchez, J.L., Boudier, F. and Mercier, J.-C., 1971. Textures, structures and fabrics due to solid state flow in some European lherzolites. Tectonophysics, 12: 55-86.

Niu, Y., 1997. Mantle melting and melt extraction processes beneath ocean ridges: evidence from abyssal peridotites. Journal of Petrology, 38: 1047-1074.

Nixon, P.H., 1987. Kimberlitic xenoliths and their cratonic setting. In: P.H. Nixon (Editor), Mantle xenoliths. John Wiley and Sons Ltd, New York, pp. 215-239.

Norman, M.D., 1998. Melting and metasomatism in the continental lithosphere: laser ablation ICPMS analysis of minerals in spinel lherzolites from eastern Australia. Contributions to Mineralogy and Petrology, 130: 240-255.

Norman, M.D., Pearson, N.J., Sharma, A. and Griffin, W.L., 1996. Quantitative analysis of trace elements in geological materials by laser ablation ICPMS: Instrumental operating conditions and calibration values of NIST glasses. Geostandards Newsletter, 20(2): 247-261.

Norrish, K. and Chappell, B., 1977. X-ray fluorescence spectrometry. In: J. Zussman (Editor), Physical methods in determinative mineralogy. Academy Press, London, pp. 201-272.

Norrish, K. and Hutton, J.T., 1969. An accurate x-ray spectrographic method for the analysis of a wide range of geological samples. Geochimica et Cosmochimica Acta, 33: 431-453.

O'Hara, M.J., 1967. Mineral facies in ultrabasic rocks., Ultramafic and related rocks. John Wiley and Sons Ltd, New York, pp. 7-18.

O'Hara, M.J. and Mercy, E.L.P., 1963. Petrology and petrogenesis of some garnetiferous peridotites. Royal Society of Edinburgh Transactions, 65: 251-314.

O'Hara, M.J., Richardson, S.W. and Wilson, G., 1971. Garnet peridotite stability and occurrence in crust and mantle. Contributions to Mineralogy and Petrology, 32: 48-68.

O'Neill, H.S.C., 1980. Corrections. Contributions to Mineralogy and Petrology, 72: 337.

O'Neill, H.S.C., 1981. The transition between spinel lherzolite and garnet lherzolite, and its use as a geobarometer. Contributions to Mineralogy and Petrology, 77: 185-194.

O'Neill, H.S.C. and Wall, V.J., 1987. The olivine-orthopyroxene-spinel oxygen geobarometer, the nickel precipitation curve, and the oxygen fugacity of the Earth's upper mantle. Journal of Petrology, 28(6): 1169-1191.

O'Neill, H.S.C. and Wood, B.J., 1979. An experimental study of Fe-Mg partitioning between garnet and olivine and its calibration as a geothermometer. Contributions to Mineralogy and Petrology, 70: 59-70.

O'Reilly, S.Y., 1989a. Nature of the east Australian lithosphere. In: R.W. Johnson (Editor), Intraplate volcanism in eastern Australia and New Zealand. Cambridge University Press, Cambridge, pp. 290-297.

O'Reilly, S.Y., 1989b. Xenolith types, distribution and transport. In: R.W. Johnson (Editor), Intraplate volcanism in eastern Australia and New Zealand. Cambridge University Press, Cambridge, pp. 249-253.

O'Reilly, S.Y. and Griffin, W.L., 1985. A xenolith-derived geotherm for southeastern Australia and its geophysical implications. Tectonophysics, 111: 41-63.

O'Reilly, S.Y. and Griffin, W.L., 1987. Eastern Australia - 4000 kilometers of mantle samples. In: P.H. Nixon (Editor), Mantle xenoliths. John Wiley and Sons Ltd, New York, pp. 267-280.

O'Reilly, S.Y. and Griffin, W.L., 1988. Mantle metasomatism beneath western Victoria, Australia: I. Metasomatic processes in Cr-diopside lherzolites. Geochimica et Cosmochimica Acta, 52: 433-447.

O'Reilly, S.Y. and Griffin, W.L., 1991. Petrologic constraints on geophysical modelling, southeastern Australia. In: B.J. Drummond (Editor), The Australian lithosphere. Special Publication Geological Society of Australia, pp. 157-162.

O'Reilly, S.Y. and Griffin, W.L., 1996. 4-D lithosphere mapping: methodology and examples. Tectonophysics, 262: 3-18.

O'Reilly, S.Y., Griffin, W.L. and Pearson, N.J., 1989a. Xenoliths of crustal origin. In: R.W. Johnson (Editor), Intraplate volcanism in eastern Australia and New Zealand. Cambridge University Press, Cambridge, pp. 275-288.

O'Reilly, S.Y., Griffin, W.L. and Poudjom-Djomani, Y.H., 1999. Are lithospheres forever? Seventh International Kimberlite Conference, Cape Town, pp. 646-648.

O'Reilly, S.Y., Jackson, I. and Bezant, C., 1990. Seismic and thermal parameters of upper mantle rocks from eastern Australia: implications for seismic modelling. Tectonophysics, 185: 67-82.

O'Reilly, S.Y., Nicholls, I.A. and Griffin, W.L., 1989b. Xenoliths and megacrysts of mantle origin. In: R.W. Johnson (Editor), Intraplate volcanism in eastern Australia and New Zealand. Cambridge University Press, Cambridge, pp. 254-274.

O'Reilly, S.Y., Chen, D., Griffin, W.L. and Ryan, C.G., 1997. Minor elements in olivine from spinel lherzolite: implications for thermobarometry. Mineralogical Magazine, pp. 257-269.

O'Reilly, S.Y., Griffin, W.L., Poudjom Djomani, Y.H. and Morgan, P., 2001. Are lithospheres forever? Tracking changes in subcontinental lithospheric mantle through time. GSA Today, 11(4): 4-10.

Osland, R. (1997). Modelling of variations in Norwegian olivine deposits, causes of variation and estimation of key quality factors. Norwegian University of Science and Technology (Doktor Ingeniør), 189 pp.

O'Sullivan, A.J., 1994. Apatite fission track thermochronology of northeastern Tasmania and the southern Bass Basin. In: David R. Cooke and Paul A. Kitto (Editors), Contentious issues in Tasmanian geology. Geological Society of Australia Abstracts , 39: 129.

O'Sullivan, P.B., Kohn, B.P. and O'Sullivan, A.J., 1998. Cretaceous and Tertiary thermotectonic evolution of Tasmania. Australian Geological Survey Organisation, Record 1998/2: 144-146.

Parkinson, I.J. and Arculus, R.J., 1999. The redox state of subduction zones: insights from arc-peridotites. Chemical Geology, 160: 409-423.

Pearson, D.G., 1999. The age of continental roots. Lithos, 48: 171-194.

Pearson, D.G. and Woodland, S.J., 2000. Solvent extraction/anion exchange separation and determination of PGEs (Os, Ir, Pt, Pd, Ru) and Re/Os isotopes in geological samples by isotope dilution ICP-MS. Chemical Geology, 165: 87-107.

Pearson, D.G., Carlson, R.W., Shirey, S.B., Boyd, F.R. and Nixon, P.H., 1995a. Stabilisation of Archaean lithospheric mantle: a Re-Os isotope study of peridotite xenoliths from the Kaapvaal craton. Earth and Planetary Science Letters, 134: 341-357.

Pearson, D.G., Boyd, F.R., Hoal, K.E.O., Hoal, B.G., Nixon, P.H. and Rogers, N.W., 1994. A Re-Os isotopic and petrological study of Namibian peridotites: contrasting petrogenesis and composition of on- and off-craton lithospheric mantle. Mineralogical Magazine, 58A: 703-704.

Pearson, D.G., Shirey, S.B., Carlson, R.W., Boyd, F.R., Pokhilenko, N.P. and Shimizu, N., 1995b. Re-Os, Sm-Nd, and Rb-Sr isotope evidence for thick Archaean lithospheric mantle beneath the Siberian craton modified by multistage metasomatism. Geochimica et Cosmochimica Acta, 59(5): 959-977.

Pearson, N.J., Alard, O., Griffin, W.L., Jackson, S.E. and O'Reilly, S.Y., 2002. In situ measurement of Re-Os isotopes in mantle sulfides by laser ablation multicollector-inductively coupled plasma mass spectrometry: analytical methods and preliminary results. Geochimica et Cosmochimica Acta, 66(6): 1037-1050.

Peslier, A.H., Reisberg, L., Ludden, J. and Francis, D., 2000. Re-Os constraints on harzburgite and lherzolite formation in the lithospheric mantle: a study of Northern Canadian Cordillera xenoliths. Geochimica et Cosmochimica Acta, 64(17): 3061-3071.

Pidgeon, R.T. and Raheim, A., 1972. Geochronological investigation of the gneiss and minor intrusive rocks from Kristiansund, west Norway. Norsk Geologisk Tidsskrift, 52: 241-256.

Plumb, K.A., 1979. The tectonic evolution of Australia. Earth Science Review, 14: 205-249.

Pollack, H.N. and Chapman, D.S., 1977. On the regional variation of heat flow, geotherms and lithospheric thickness. Tectonophysics, 38: 279-296.

Pouchou, J.L. and Pichoir, F., 1984. A new model for quantitative X-ray microanalysis. Part 1: application to the analysis of homogeneous samples. Recherche Aerospatiale, 5: 13-38.

Poudjom Djomani, Y.H., O'Reilly, S.Y., Griffin, W.L. and Morgan, P., 2001. The density structure of subcontinental lithosphere through time. Earth and Planetary Science Letters, 184: 605-621.

Powell, R., 1985. Regression diagnostics and robust regression in geothermometer/ geobarometer calibration: the garnet-clinopyroxene geothermometer revisited. Journal of Metamorphic Geology, 3: 231-243.

Qi, Q., Taylor, L.A. and Zhou, X., 1995. Petrology and geochemistry of mantle peridotite xenoliths from SE China. Journal of Petrology, 36(1): 55-79.

Råheim, A. and Compston, W., 1977. Correlation between metamorphic events and Rb-Sr ages in metasediments and eclogites from western Tasmania. Lithos, 10: 271-289.

Rampone, E., Bottazzi, P. and Ottolini, L., 1991. Complementary Ti and Zr anomalies in orthopyroxene and clinopyroxene from mantle peridotites. Nature, 354: 518-520.

Rawlinson, N., Houseman, G.A., Collins, C.D.N. and Drummond, B.J., 2001. New evidence of Tasmania's tectonic history from a novel seismic experiment. Geophysical Research Letters, 28(17): 3337-3340.

Rawlinson, N., Semenova, T.O., Collins, C.D.N. and Houseman, G.A., 1998. Crustal structure beneath the north and east coasts of Tasmania from seismic refraction data. 14th Australian Geological Convention Abstracts (Townsville), 49, 372.

Reisberg, L. and Lorand, J.P., 1995. Longevity of subcontinental mantle lithosphere from osmium isotope systematics in orogenic peridotite massifs. Nature, 376: 159-162.

Reisberg, L., Allègre, C.J. and Luck, J.-M., 1991. The Re-Os systematics of the Ronda ultramafic complex of southern Spain. Earth and Planetary Science Letters, 105: 196-213.

Richardson, R.G., 1989a. Geophysics - summary. In: C.F. Burrett and E.L. Martin (Editors), Geology and mineral resources of Tasmania. Special Publication Geological Society Of Australia, pp. 450-451.

Richardson, R.G., 1989b. Geophysics - crustal structure. In: C.F. Burrett and E.L. Martin (Editors), Geology and mineral resources of Tasmania. Special Publication Geological Society Of Australia, pp. 465-466.

Ringwood, A.E., 1962. A model for the upper mantle. Journal of Geophysical Research, 67: 857-867.

Ringwood, A.E., 1966. The chemical composition and origin of the Earth. In: P.M. Hurley (Editor), Advances in Earth Sciences. MIT Press, Cambridge, pp. 287-356.

Ringwood, A.E., 1975. Composition and petrology of the Earth's mantle. McGraw Hill, New York, 618 pp.

Rivalenti, G., Vannucci, R., Rampone, E., Mazzucchelli, M., Piccardo, G.B., Piccarillo, E.M., Bottazzi, P. and Ottolini, L., 1996. Peridotite clinopyroxene chemistry reflects mantle processes rather than continental versus oceanic settings. Earth and Planetary Science Letters, 139: 423-437.

Roberts, D. and Gee, D.G., 1985. An introduction to the structure of the Scandinavian Caledonides., The Caledonide Orogen-Scandinavia and Related Areas. John Wiley and Sons, Chichester, pp. 55-68.

Robinson, P., Spear, F.S., Schumacher, J.C., Laird, J., Klein, C., Evans, B.W. and Doolan, B.L., 1982. Phase relations of metamorphic amphiboles: natural occurrence and theory. In: D.R. Veblen and P.H. Ribbe (Editors), Amphiboles: Petrology and experimental phase relations. Reviews in Mineralogy, Mineralogical Society of America, Washington D.C., pp. 1-228.

Roden, M.F. and Murthy, V.R., 1985. Mantle metasomatism. Annual Review of Earth and Planetary Science, 13: 269-296.

Root, D.B., Mattinson, J.M., Hacker, B.R. and Wooden, J.L., 2001. U-Pb geochronology of an ultrahigh-pressure eclogite from the Western Gneiss Region, Norway. EOS, 82(47): 1035.

Rose, L.A. and Brenan, J.M., 2001. Wetting properties of Fe-Ni-Co-Cu-O-S melts against olivine: implications for sulfide melt mobility. Economic Geology, 96: 145-157.

Rudnick, R.L., McDonough, W.F. and Chappell, B.W., 1993. Carbonatite metasomatism in the northern Tanzanian mantle: petrographic and geochemical characteristics. Earth and Planetary Science Letters, 114: 463-475.

Ryan, C.G., Griffin, W.L. and Pearson, N.J., 1996. Garnet geotherms: pressure-temperature data from Cr-pyrope garnet xenocrysts in volcanic rocks. Journal of Geophysical Research, 101(B3): 5611-5625.

Sachtleben, T. and Seck, H.A., 1981. Chemical control of Al-solubility in orthopyroxene and its implications on pyroxene geothermometry. Contributions to Mineralogy and Petrology, 78: 157-165.

Sautter, V., Jaoul, O. and Abel, F., 1988. Aluminium diffusion in diopside using the $^{27}Al$ (p, $\gamma$) $^{28}Si$ nuclear reaction: preliminary results. Earth and Planetary Science Letters, 89: 109-114.

Scheibner, E. and Veevers, J.J., 2000. Tasman fold belt system. In: J.J. Veevers (Editor), Billion year earth history of Australia and neighbours in Gondwanaland. GEMOC Press, Sydney, pp. 154-233.

Schmidt, P.W. and McDougall, I., 1977. Palaeomagnetic and potassium-argon studies of the Tasmanian dolerites. Geological Society of Australia Journal, 24: 321-328.

Scott Smith, B.H., 1987. Greenland. In: P.H. Nixon (Editor), Mantle xenoliths. John Wiley and Sons, New York, pp. 23-32.

Seymour, D.B. and Calver, C.R., 1995. Explanatory notes for the Time-Space diagram and stratotectonic elements map of Tasmania. Australian Geological Survey Organisation, Record 1995/01: 62 pp.

Seymour, D.B. and Calver, C.R., 1998. Proterozoic rock sequences of western Tasmania. 14th Australian Geological Convention (Townsville), 49, 399.

Shaw, D.M., 1970. Trace element fractionation during anatexis. Geochimica et Cosmochimica Acta, 34: 237-243.

Shaw, D.M., 1979. Trace element melting models. Physical Chemistry of the Earth, 11: 577-586.

Shaw, R.D., Wellman, P., Gunn, P., Whitaker, A.J., Tarlowski, C. and Morse, M., 1996a. Users guide to the Australian Crustal Elements map. Australian Geological Survey Organisation, Record 1996/30.

Shaw, R.D., Wellman, P., Gunn, P., Whitaker, A.J., Tarlowski, C. and Morse, M., 1996b. Australian crustal elements (1:5 000 000 scale map), based on the distribution of geophysical domains. Australian Geological Survey Organisation.

Shimizu, N., 1975. Rare earth elements in garnets and clinopyroxenes from garnet lherzolite nodules in kimberlites. Earth and Planetary Science Letters, 25: 26-32.

Shimizu, N. and Richardson, S.H., 1987. Trace element abundance patterns of garnet inclusions in peridotite-suite diamonds. Geochimica et Cosmochimica Acta, 51: 755-758.

Shirey, S.B. and Walker, R.J., 1995. Carius tube digestion for low-blank rhenium-osmium analysis. Analytical Chemistry, 67: 2136-2141.

Shirey, S.B. and Walker, R.J., 1998. The Re-Os isotope system in cosmochemistry and high-temperature geochemistry. Annual Reviews of Earth and Planetary Science, 26: 423-500.

Smith, D.C., 1984. Coesite in clinopyroxene in the Caledonides and its implications for geodynamics. Nature, 310: 641-644.

Smith, D., 1988. Implications of zoned garnets for the evolution of sheared lherzolites: examples from northern Lesotho and the Colorado Plateau. Journal of Geophysical Research, 93(B5): 4895-4905.

Smith, D., 1999. Temperatures and pressures of mineral equilibrium in peridotite xenoliths: review, discussion, and implications. In: Y. Fei, C.M. Bertka and B.O. Mysen (Editors), Mantle petrology: field observations and high-pressure experimentation. The Geochemical Society, Houston, pp. 171-188.

Smith, D. and Boyd, F.R., 1987. Compositional heterogeneities in a high-temperature lherzolite nodule and implications for mantle processes. In: P.H. Nixon (Editor), Mantle xenoliths. John Wiley and Sons, New York, pp. 625-640.

Smith, D. and Boyd, F.R., 1992. Compositional zonation in garnets in peridotite xenoliths. Contributions to Mineralogy and Petrology, 112: 134-147.

Smith, D. and Ehrenberg, S.N., 1984. Zoned minerals in garnet peridotite nodules from the Colorado Plateau: implications for mantle metasomatism and kinetics. Contributions to Mineralogy and Petrology, 86: 274-285.

Song, Y. and Frey, F.A., 1989. Geochemistry of peridotite xenoliths in basalt from Hannuoba, Eastern China: implications for subcontinental mantle heterogeneity. Geochimica et Cosmochimica Acta, 53: 97-113.

Spetsius, Z.V., 1995. Occurrence of diamond in the mantle: a case study from the Siberian Platform. Journal of Geochemical Exploration, 53: 25-40.

Stachel, T., Viljoen, K.S., Brey, G. and Harris, J.W., 1998. Metasomatic processes in lherzolitic and harzburgitic domains of diamondiferous lithospheric mantle: REE in

garnets from xenoliths and inclusions in diamonds. Earth and Planetary Science Letters, 159: 1-12.

Stein, M. and Hofmann, A.W., 1994. Mantle plumes and episodic crustal growth. Nature, 372: 63-68.

Stephens, M.B. and Gee, D.G., 1985. A tectonic model for the evolution of the eugeoclinal terranes in the central Scandinavian Caledonides., The Caledonide Orogen-Scandinavia and Related Areas. John Wiley and Sons, Chichester, pp. 953-978.

Stosch, H.-G., 1982. Rare earth element partitioning between minerals from anhydrous spinel peridotite xenoliths. Geochimica et Cosmochimica Acta, 46: 793-811.

Stosch, H.-G. and Lugmair, G.W., 1986. Trace element and Sr and Nd isotope geochemistry of peridotite xenoliths from the Eifel (West Germany) and their bearing on the evolution of the subcontinental lithosphere. Earth and Planetary Science Letters, 80: 281-298.

Streckeisen, A., 1976. To each plutonic rock its proper name. Earth-Science Reviews, 12: 1-33.

Sun, S.-s., 1982. Chemical composition and origin of the Earth's primitive mantle. Geochimica et Cosmochimica Acta, 46: 179-192.

Sutherland, F.L., 1969a. The mineralogy, petrochemistry and magmatic history of the Tamar lavas, northern Tasmania. Papers and Proceedings of the Royal Society of Tasmania, 103: 17-33.

Sutherland, F.L., 1969b. A review of the Tasmanian Cainozoic volcanic province. Special Publication Geological Society of Australia, 2: 133-144.

Sutherland, F.L., 1971. The geology and petrology of the Tertiary volcanic rocks of the Tamar Trough, northern Tasmania. Records of the Queen Victoria Museum, 36.

Sutherland, F.L., 1973. Igneous rocks, Central Plateau., The Lake Country of Tasmania. Royal Society of Tasmania, Hobart, pp. 43-54.

Sutherland, F.L., 1974. High-pressure inclusions in tholeiitic basalts and the range of lherzolite-bearing magmas in the Tasmanian Volcanic Province. Earth and Planetary Science Letters, 24: 317-324.

Sutherland, F.L., 1976. Cainozoic volcanic rocks. In: D.E. Leaman (Editor), Geological atlas 1:50 000 Series Sheet 82 (8312S) Hobart. Explanatory Report Geological Survey of Tasmania.

Sutherland, F.L., 1980. Aquagene volcanism in the Tasmanian Tertiary, in relation to coastal seas and river systems. Papers and Proceedings of the Royal Society of Tasmania, 114: 177-199.

Sutherland, F.L., 1984. Cainozoic basalts. In: S.M. Forsyth (Editor), Geological atlas 1:50 000 Series Sheet 68 (8313S) Oatlands. Explanatory Report Geological Survey of Tasmania, pp. 102-120.

Sutherland, F.L., 1989a. Tertiary volcanism. In: C.F. Burrett and E.L. Martin (Editors), Geology and Mineral Resources of Tasmania: A Bicentennial Volume. Special Publication Geological Society of Australia, pp. 383-386.

Sutherland, F.L., 1989b. Tasmania and Bass Strait. In: R.W. Johnson (Editor), Intraplate volcanism in eastern Australia and New Zealand. Cambridge University Press, pp. 143-149.

Sutherland, F.L., 1989c. Cainozoic volcanic rocks. In: S.M. Forsyth (Editor), Geological atlas 1:50 000 Series Sheet 61 (83123N) Interlaken. Explanatory Report Geological Survey of Tasmania, pp. 48-51.

Sutherland, F.L. and Hale, G.E.A., 1970. Cainozoic volcanism in and around Great Lake, central Tasmania. Papers and Proceedings of the Royal Society of Tasmania, 104: 17-32.

Sutherland, F.L. and Hollis, J.D., 1982. Mantle-lower crust petrology from inclusions in basaltic rocks in eastern Australia - an outline. Journal of Volcanology and Geothermal Research, 14: 1-29.

Sutherland, F.L. and Wellman, P., 1986. Potassium-Argon ages of Tertiary volcanic rocks, Tasmania. Papers and Proceedings of the Royal Society of Tasmania, 120: 77-86.

Sutherland, F.L., Hollis, J.D. and Barron, L.M., 1984. Garnet lherzolite and other inclusions from a basalt flow, Bow Hill, Tasmania. In: J. Kornprobst (Editor), Kimberlites II: The mantle and crust-mantle relationships. Elsevier Science Publishers, Amsterdam, pp. 145-160.

Sutherland, F.L., Raynor, L.R. and Pogson, R.E., 1994. Spinel to garnet lherzolite transition in relation to high temperature palaeogeotherms, eastern Australia. Australian Journal of Earth Sciences, 41: 205-220.

Sutherland, F.L., Ewart, A., Raynor, L.R., Hollis, J.D. and McDonough, W.D., 1989. Tertiary basaltic magmas and the Tasmanian lithosphere. In: C.F. Burrett and E.L. Martin (Editors), Geology and Mineral Resources of Tasmania. Special Publication Geological Society of Australia, pp. 386-398.

Sutherland, F.L., Hendry, D.F., Barron, B.J., Matthews, W.L. and Hollis, J.D., 1996. An unusual Tasmanian Tertiary basalt sequence, near Boat Harbour, northwest Tasmania. Records of the Australian Museum, 48(2): 131-161.

Suzuki, K., 1987. Grain-boundary enrichment of incompatible elements in some mantle peridotites. Chemical Geology, 63: 319-334.

Sweeney, R.J., 1994. Carbonatite melt compositions in the Earth's mantle. Earth and Planetary Science Letters, 128: 259-270.

Szabó, C.S. and Bodnar, R.J., 1995. Chemistry and origin of mantle sulfides in spinel peridotite xenoliths from alkaline basaltic lavas, Nógrád-Gömör Volcanic Field, northern Hungary and southern Slovakia. Geochimica et Cosmochimica Acta, 59(19): 3917-3927.

Takahashi, E., 1986. Melting of a dry peridotite KLB-1 up to 14 GPa: implications on the origin of peridotitic upper mantle. Journal of Geophysical Research, 91: 9367-9382.

Taylor, W.R. and Green, D.H., 1988. Measurement of reduced peridotite-C-O-H solidus and implications for redox melting of the mantle. Nature, 332: 349-352.

Thibault, Y., Edgar, A.D. and Lloyd, F.E., 1992. Experimental investigation of melts from a carbonated phlogopite lherzolite: implications for metasomatism in the continental lithospheric mantle. American Mineralogist, 77: 784-794.

Tompkins, L.A., Bailey, S.W. and Haggerty, S.E., 1984. Kimberlitic chlorites from Sierra Leone, West Africa: unusual chemistries and structural polytypes. American Mineralogist, 69: 237-249.

Turner, N.J., 1989. Precambrian. In: C.F. Burrett and E.L. Martin (Editors), Geology and mineral resources of Tasmania. Special Publication Geological Society of Australia, pp. 5-46.

Turner, N.J., Black, L.P. and Kamperman, M., 1994. Pre-Middle Cambrian stratigraphy, orogenesis and geochronology in western Tasmania. In: David R. Cooke and Paul A. Kitto (Editors), Contentious issues in Tasmanian geology. Geological Society of Australia Abstracts, 39: pp. 51-56.

Turner, N.J., Black, L.P. and Kamperman, M., 1998. Dating of Neoproterozoic and Cambrian orogenies in Tasmania. Australian Journal of Earth Sciences, 45: 789-806.

Turner, N.J., Bottrill, R.S., Crawford, A.J. and Villa, I., 1992. Geology and prospectivity of the Arthur Mobile Belt. Bulletin Geological Survey of Tasmania, 70: 227-233.

van Achterbergh, E., Griffin, W.L. and Stiefenhofer, J., 2001. Metasomatism in mantle xenoliths from the Letlhakane kimberlites: estimation of element fluxes. Contributions to Mineralogy and Petrology, 141: 397-414.

van Achterbergh, E., Ryan, C.G. and Griffin, W.L., 1999. GLITTER: online interactive data reduction for the laser ablation inductively coupled plasma mass spectrometry microprobe. Ninth Annual Goldschmidt Conference, Cambridge, pp: 305.

van Roermund, H.L.M. and Drury, M.R., 1998. Ultrahigh pressure (P>6 GPa) garnet peridotites in Western Norway: exhumation of mantle rocks from >185 km. Terra Nova, 10: 295-301.

van Roermund, H.L.M., Drury, M.R., Barnhoorn, A. and de Ronde, A.A., 2000. Super-silicic garnet microstructures from an orogenic garnet peridotite, evidence for an ultra-deep (>6 GPa) origin). Journal of Metamorphic Geology, 18: 135-147.

van Roermund, H.L.M., Drury, M.R., Barnhoorn, A. and de Ronde, A.A., 2001. Relict majoritic garnet microstructures from ultra-deep orogenic peridotites in western Norway. Journal of Petrology, 42(1): 117-130.

Varne, R., 1977. On the origin of spinel lherzolite inclusions in basaltic rocks from Tasmania and elsewhere. Journal of Petrology, 18(1): 1-23.

Veevers, J.J., 2000a. Appendix 1: Tasmanian terranes. In: J.J. Veevers (Editor), Billion year earth history of Australia and neighbours in Gondwanaland. GEMOC Press, Sydney, pp. 349-352.

Veevers, J.J., 2000b. Permian-Triassic basins and foldbelts on Panthalassian margin. In: J.J. Veevers (Editor), Billion year earth history of Australia and neighbours in Gondwanaland. GEMOC Press, Sydney, pp.235-252.

Veevers, J.J. and Ettreim, S.L., 1988. Reconstruction of Antarctica and Australia at breakup (95±5 Ma) and before rifting (160 Ma). Australian Journal of Earth Sciences, 35: 355-362.

Wain, A., 1997. New evidence for coesite in eclogite and gneisses: defining an ultrahigh-pressure province in the Western Gneiss Region of Norway. Geology, 25(10): 927-930.

Walker, R.J. and Morgan, J.W., 1989. Re-Os isotope systematics of carbonaceous chondrites. Science, 243: 519-522.

Walker, R.J., Carlson, R.W., Shirey, S.B. and Boyd, F.R., 1989. Os, Sr, Nd, and Pb isotope systematics of southern African peridotite xenoliths: implications for the chemical

evolution of subcontinental mantle. Geochimica et Cosmochimica Acta, 53: 1583-1595.

Wallace, M. and Green, D.H., 1988. An experimental determination of primary carbonatite composition. Nature, 335: 343-345.

Walter, M.J., 1998. Melting of garnet peridotite and the origin of komatiite and depleted lithosphere. Journal of Petrology, 39(1): 29-60.

Wass, S.Y. and Irving, A.J., 1976. XENMEG: a catalogue of occurrences of xenoliths and megacrysts in basic volcanic rocks of eastern Australia., The Australian Museum, Sydney.

Wellman, P., 1995. Tasman orogenic system; a model for the subdivision and growth history based on gravity and magnetic anomalies. Economic Geology, 90: 1430-1442.

Wellman, P. and McDougall, I., 1974. Cainozoic igneous activity in eastern Australia. Tectonophysics, 23: 49-65.

Wells, P.R.A., 1977. Pyroxene thermometry in simple and complex systems. Contributions to Mineralogy and Petrology, 62: 129-139.

Wiechert, U., Ionov, D.A. and Wedepohl, K.H., 1997. Spinel peridotite xenoliths from the Atsagin-Dush volcano, Dariganga lava plateau, Mongolia: a record of partial melting and cryptic metasomatism in the upper mantle. Contributions to Mineralogy and Petrology, 126: 345-364.

Williams, E., 1978. Tasman fold belt system in Tasmania. Tectonophysics, 48: 159-205.

Williams, E., 1989. Summary and synthesis. In: C.F. Burrett and E.L. Martin (Editors), Geology and mineral resources of Tasmania. Special Publication Geological Society of Australia, pp. 468-499.

Wilshire, H.G., 1987. A model of mantle metasomatism. Geological Society of America Special Paper, 215: 47-60.

Wilshire, H.G. and Shervais, J.W., 1975. Al-augite and Cr-diopside ultramafic xenoliths in basaltic rocks from western United States. Physical Chemistry of the Earth, 9: 257-271.

Witt-Eickschen, G. and Seck, H.A., 1991. Solubility of Ca and Al in orthopyroxene from spinel peridotite: an improved version of an empirical geothermometer. Contributions to Mineralogy and Petrology, 106: 431-439.

Wood, B.J., 1974. The solubility of alumina in orthopyroxene coexisting with garnet. Contributions to Mineralogy and Petrology, 46: 1-15.

Wood, B.J. and Banno, S., 1973. Garnet-orthopyroxene and orthopyroxene-clinopyroxene relationships in simple and complex systems. Contributions to Mineralogy and Petrology, 42: 109-124.

Wood, B.J. and Virgo, D., 1989. Upper mantle oxidation state: ferric iron contents of lherzolite spinels by $^{57}Fe$ Mossbauer spectroscopy and resultant oxygen fugacities. Geochimica et Cosmochimica Acta, 53: 1277-1291.

Wood, B.J., Bryndzia, L.T. and Johnson, K.E., 1990. Mantle oxidation state and its relationship to tectonic environment and fluid speciation. Science, 248: 337-345.

Wyllie, P.J., 1987. Metasomatism and fluid generation in mantle xenoliths. In: P.H. Nixon (Editor), Mantle xenoliths. John Wiley and Sons, New York, pp. 609-621.

Xu, X., 1999. The nature and evolution of the lithospheric mantle, SE China. PhD Thesis, Macquarie University, Sydney, 237 pp.

Xu, X., O'Reilly, S.Y., Griffin, W.L. and Zhou, X., 2000. Genesis of young lithospheric mantle in southeastern China: a LAM-ICPMS trace element study. Journal of Petrology, 40: 111-148.

Xu, X., O'Reilly, S.Y., Griffin, W.L., Zhou, X. and Huang, X., 1998. The nature of the Cenozoic lithosphere at Nushan, Eastern China. In: M.F.J. Flower, S.L. Chung, C.H. Lo and Y.Y. Lee (Editors), Mantle dynamics and plate interactions in East Asia. Geodynamics Series 27. American Geophysical Union, Washington, D.C.

Yao, S., 1999. Chemical composition of chromites from ultramafic rocks: application to mineral exploration and petrogenesis. PhD Thesis, Macquarie University, Sydney, 191 pp.

Yuan, X., 1996. Velocity structure of the Qinling lithosphere and mushroom cloud model. Science in China, Series D, 39: 235-244.

Zhang, M., Stephenson, P.J., O'Reilly, S.Y., McCulloch, M.T. and Norman, M., 2001. Petrogenesis and geodynamic implications of late Cenozoic basalts in North Queensland, Australia: trace element and Sr-Nd-Pb isotope evidence. Journal of Petrology, 42: 685-719.

Zheng, J.P., O'Reilly, S.Y., Griffin, W.L., Lu, F.X. and Zhang, M., 1998. Nature and evolution of Cenozoic lithospheric mantle beneath Shandong Peninsula, Sino-Korean Craton. International Geology Review, 40: 471-499.

Zheng, J.P., O'Reilly, S.Y., Griffin, W.L., Fu, F.X., Zhang, M. and Pearson, N.J., 2000. Relict refractory mantle beneath the Eastern North China Block: significance for lithosphere evolution. Lithos, 57: 43-66.

Zindler, A. and Jagoutz, E., 1988. Mantle cryptology. Geochimica et Cosmochimica Acta, 52: 319-333.

# APPENDIX I

## List of Tasmanian peridotite xenoliths

| Locality | Sample no. | Rock Type | Texture | Ol | Opx | Cpx | Sp |
|---|---|---|---|---|---|---|---|
| Coates Rd Quarry | CQ1 | sp lherzolite | granoblastic | 74.8 | 12.9 | 11.0 | 1.3 |
| | CQ2 | sp lherzolite | granoblastic | 74.2 | 7.2 | 13.3 | 5.3 |
| | CQ3 | sp lherzolite | granoblastic | 61.4 | 20.1 | 17.1 | 1.4 |
| | CQ4 | sp lherzolite | coarse | 87.2 | 9.5 | 2.0 | 1.3 |
| | CQ5 | sp lherzolite | mosaic porphyroclastic | 56.0 | 28.9 | 9.9 | 5.2 |
| | CQ6 | sp lherzolite | granoblastic | 54.1 | 32.5 | 11.8 | 1.6 |
| | CQ7 | sp lherzolite | granoblastic | 59.2 | 29.9 | 7.6 | 3.3 |
| Arthur River | AR1 | sp lherzolite | granoblastic | 80.1 | 11.3 | 6.4 | 2.2 |
| | AR2 | sp dunite | coarse | 97.2 | - | - | 2.8 |
| | AR3 | lherzolite | granoblastic | | | | |
| | AR4 | sp lherzolite | granoblastic | 76.4 | 18.6 | 3.5 | 1.5 |
| | AR5 | sp lherzolite | granoblastic | 62.7 | 24.3 | 11.7 | 1.3 |
| | AR6 | sp lherzolite | granoblastic | | | | |
| | AR7 | sp lherzolite | granoblastic | 63.3 | 21.2 | 12.5 | 3.0 |
| | AR8 | sp lherzolite | granoblastic | 72.5 | 10.3 | 13.4 | 3.8 |
| | AR9 | sp lherzolite | granoblastic | 63.7 | 21.4 | 13.9 | 1.0 |
| Table Cape | TC1 | sp lherzolite | coarse | 71.8 | 15.0 | 11.6 | 1.6 |
| | TC2 | sp lherzolite | granoblastic | | | | |
| | TC3 | sp lherzolite | granoblastic | 75.2 | 19.0 | 3.8 | 2.0 |
| | TC4 | sp lherzolite | granoblastic | 46.5 | 36.3 | 10.3 | 6.9 |
| | TC5 | sp lherzolite | granoblastic | 55.2 | 27.0 | 13.0 | 4.8 |
| | TC6 | sp lherzolite | granoblastic | 56.6 | 24.5 | 10.8 | 8.1 |
| | TC7 | sp lherzolite | granoblastic | 67.9 | 25.5 | 4.5 | 2.1 |
| | TC9 | sp lherzolite | granoblastic | | | | |
| | TC10 | sp lherzolite | granoblastic | 55.1 | 13.5 | 24.7 | 6.7 |
| Doctors Rocks | DR1 | sp lherzolite | granoblastic | 44.8 | 37.8 | 14.0 | 3.4 |
| | DR2 | sp harzburgite | granoblastic | | | | |
| | DR3 | sp lherzolite | granoblastic | 58.1 | 29.2 | 10.4 | 2.3 |
| | DR4 | sp lherzolite | granoblastic | 53.4 | 22.2 | 21.2 | 3.2 |
| | DR5 | sp lherzolite | granoblastic | 45.3 | 32.2 | 20.6 | 1.9 |
| | DR6 | sp lherzolite | granoblastic | 47.3 | 29.6 | 19.9 | 3.2 |
| South Riana | SR1 | sp lherzolite | granoblastic | 78.5 | 10.3 | 6.4 | 4.8 |
| | SR1a | sp lherzolite | granoblastic | 73.7 | 20.5 | 1.4 | 4.4 |
| | SR1b | sp lherzolite | granoblastic | 72.6 | 19.7 | 3.0 | 4.7 |
| | SR1b-2 | sp lherzolite | granoblastic | 60.8 | 28.3 | 10.7 | 0.2 |
| | SR2 | sp lherzolite | granoblastic | 74.4 | 22.0 | 2.9 | 0.7 |
| | SR2a | sp lherzolite | granoblastic | 78.9 | 17.0 | 1.8 | 2.3 |
| | SR2b | sp lherzolite | granoblastic | 62.8 | 26.6 | 5.9 | 4.7 |
| | SR3 | sp lherzolite | granoblastic | 66.4 | 24.7 | 5.5 | 3.4 |
| | SR3a | sp lherzolite | granoblastic | 57.3 | 29.7 | 8.0 | 5.0 |
| | SR3b | sp lherzolite | granoblastic | 57.5 | 29.9 | 8.4 | 4.2 |
| | SR4 | sp lherzolite | granoblastic | 77.4 | 14.3 | 4.1 | 4.2 |
| | SR5 | sp lherzolite | granoblastic | 71.3 | 21.2 | 4.1 | 3.4 |
| | SR6 | sp lherzolite | granoblastic | 78.2 | 1.6 | 19.9 | 0.3 |
| | SR7 | sp lherzolite | granoblastic | 72.2 | 19.7 | 5.7 | 2.4 |
| | SR8 | sp lherzolite | porphyroclastic | | | | |
| | SR8a | sp lherzolite | granoblastic | | | | |
| | SR9 | sp lherzolite | granoblastic | 61.9 | 33.9 | 1.1 | 3.1 |
| | SR10 | sp lherzolite | granoblastic | 53.7 | 26.9 | 18.4 | 1.0 |
| | SR11 | sp lherzolite | granoblastic | 63.0 | 20.9 | 11.3 | 4.8 |